

Green Energy and Technology



Katsumi Kaneko

Francisco Rodríguez-Reinoso *Editors*

# Nanoporous Materials for Gas Storage



Springer

# **Green Energy and Technology**

More information about this series at <http://www.springer.com/series/8059>

Katsumi Kaneko • Francisco Rodríguez-Reinoso  
Editors

# Nanoporous Materials for Gas Storage

 Springer

*Editors*

Katsumi Kaneko  
Research Initiative for Supra-Materials  
Shinshu University  
Nagano, Japan

Francisco Rodríguez-Reinoso  
Laboratorio de Materiales Avanzados  
Departamento de Química  
Inorgánica-Instituto  
Universitario de Materiales  
Universidad de Alicante  
Alicante, Spain

ISSN 1865-3529

Green Energy and Technology

ISBN 978-981-13-3503-7

<https://doi.org/10.1007/978-981-13-3504-4>

ISSN 1865-3537 (electronic)

ISBN 978-981-13-3504-4 (eBook)

Library of Congress Control Number: 2019933412

© Springer Nature Singapore Pte Ltd. 2019

This work is subject to copyright. All rights are reserved by the Publisher, whether the whole or part of the material is concerned, specifically the rights of translation, reprinting, reuse of illustrations, recitation, broadcasting, reproduction on microfilms or in any other physical way, and transmission or information storage and retrieval, electronic adaptation, computer software, or by similar or dissimilar methodology now known or hereafter developed.

The use of general descriptive names, registered names, trademarks, service marks, etc. in this publication does not imply, even in the absence of a specific statement, that such names are exempt from the relevant protective laws and regulations and therefore free for general use.

The publisher, the authors, and the editors are safe to assume that the advice and information in this book are believed to be true and accurate at the date of publication. Neither the publisher nor the authors or the editors give a warranty, express or implied, with respect to the material contained herein or for any errors or omissions that may have been made. The publisher remains neutral with regard to jurisdictional claims in published maps and institutional affiliations.

This Springer imprint is published by the registered company Springer Nature Singapore Pte Ltd.

The registered company address is: 152 Beach Road, #21-01/04 Gateway East, Singapore 189721, Singapore

# Preface

Depletion of global oil reserves and increasing concerns over climate change mainly due to the growing CO<sub>2</sub> levels in the atmosphere are promoting the need to find new, abundant, and cleaner sources of alternative energy while also reducing the amount of industrial CO<sub>2</sub> being produced nowadays. Although there is a noticeable increase in the use of non-emitting non-fossil energy technologies such as renewable energies, the International Energy Agency (IEA) predicts the world's energy consumption to increase by over 40% in the period to 2040, when the use of fossil fuels will mean more than 75% of the world energy. On the other hand, the alarming information provided by the US National Oceanic and Atmospheric Administration in 2017 about the CO<sub>2</sub> level reaching 410 ppm, this meaning an increase in global surface temperature, is adding extra pressure to the urgent need for developing efficient CO<sub>2</sub> capture and storage technologies. The solutions to these two important problems for the wellness of human being are just excellent examples of what scientists and engineers can do to help the human being to reach a better and safer way of living. This book is an attempt to show the actual state of the art in finding alternative energy sources to gasoline and diesel and, at the same time, decreasing the grave problem of global climate change. Development of nanoporous materials and appropriate adsorption processes to store large amounts of gases such as hydrogen and methane (natural gas) or carbon dioxide produced in the actual emitting fossil energy technologies are the main topics of this book. The storage of these gases is also indispensable to promote renewable energy technologies. The conversion of renewable energies into those clean energy gases is demanded in addition to the technologies of batteries and supercapacitors for the stationary supplying. Even storage of CO<sub>2</sub> is the key technology for utilization of CO<sub>2</sub>.

The material concerning the storage of supercritical gases on nanoporous materials is organized into 14 chapters written by internationally recognized experts in their field. Chapter 1 is a short introduction to the state of the art and objectives of the book, with a description of the need for gas storage as a solution to both the depletion of fossil fuels and the climate change produced by the large amount of CO<sub>2</sub> being produced in the actual energy consumption trend. Chapter 2 is

devoted to the fundamentals on adsorption of supercritical gases. Understanding the difference between vapor and supercritical gas is indispensable to develop better nanoporous materials for gas storage. We need to transform a supercritical gas into the vapor (quasi-vaporization) with the nanoporous materials to increase the storage capacity; some examples are shown. As the adsorption amount of supercritical gas on nanoporous materials up to 101 kPa is quite small, high-pressure gas adsorption is necessary for sufficient storage capacity. The analysis of vapor adsorption cannot be applied to high-pressure gas adsorption. Chapter 3 provides how to understand high-pressure gas adsorption, and Chap. 4 helps to define the useful quantities for gas storage. The following three chapters are devoted to the three types of nanoporous materials more frequently used in the storage of supercritical gases: nanoporous carbons (Chap. 5), metal organic frameworks (MOFs) (Chap. 6), and zeolites and related materials (Chap. 7). Authors do a thorough job in introducing these nanomaterials, thus facilitating the understanding by the reader of the main characteristics able to explain the high capacity to adsorb/store supercritical gases such as methane, hydrogen, and carbon dioxide.

Chapters 8, 9, 10, 11, 12, and 13 cover the storage of the three main supercritical gases from the point of view of both looking for cleaner sources of energy and helping to decrease the growing problem of climate change (methane, hydrogen, and carbon dioxide) on the three types of nanoporous materials. Since hydrogen storage on zeolites and related materials has not provided up to now very positive practical results, there is not a specific chapter for this adsorbent-gas interaction, but Chap. 7 also includes some of the more characteristic data already published. Then, Chap. 8 describes the state of the art of the storage of methane (as the main constituent of natural gas) on nanoporous carbons, mainly obtained by chemical activation of natural by-product precursors or petroleum residues, with very high surface area and volume of micro- and narrow mesopores. These materials offer the advantage of additional good mechanical properties allowing for the conformation into monoliths and appropriate packing density. Chapter 9 does the same but for MOFs, the new attractive nanoporous materials with extremely high surface area and porosity. Great expectations exist around these materials of high potential for gas storage, provided the actual efforts in increasing both their mechanical and thermal stabilities and the frequently found poor packing density after conformation are successful. The storage of hydrogen is covered in Chap. 10, with a very good summary of the best results described to present on the storage of this important gas over several nanoporous materials.

The three following chapters are devoted to the adsorption/capture of carbon dioxide on nanoporous carbons (Chap. 11), MOFs (Chap. 12), and zeolites (Chap. 13). Although the most widely used approach for the capture of CO<sub>2</sub> is absorption using amine solutions, this technology exhibits many drawbacks, and this has prompted a fast development of promising more reliable adsorption processes (PSA, TSA, and VSA), based on the three typical adsorbents described in this book.

Chapter 14 is devoted to a promising storage technology based on natural structures embracing gas molecules, i.e., the storage of gases in the form of clathrates. Under specific pressure and temperature conditions, pre-humidified nanoporous solids can entrap gas molecules in ice-based cages with an improved storage capacity, in volumetric basis, compared to the dry material.

It should be noted that this is a multiauthored book, and this could mean some differences in style for the different chapters, but we have tried to minimize the overlaps and repetitions as much as possible. In this respect, we would like to thank the authors for their efforts to adapt to the instructions from the publishers and to introduce the modifications requested by the editors along the time needed to prepare the chapters. In this sense, the assistance from Heather Feng and Haiqin Dong from Springer Nature along the preparation of the book is gratefully acknowledged. We hope that this effort has ended into a book that can be useful for scientists and engineers in the promotion of a better sustainable human society.

Alicante, Spain  
Nagano, Japan

Francisco Rodríguez-Reinoso  
Katsumi Kaneko

# Contents

<b>1</b>	<b>Introduction</b> .....	1
	Francisco Rodríguez-Reinoso and Katsumi Kaneko	
<b>2</b>	<b>Fundamental Aspects of Supercritical Gas Adsorption</b> .....	13
	Fernando Vallejos-Burgos, Tomonori Ohba, and Katsumi Kaneko	
<b>3</b>	<b>Fundamental Science of Gas Storage</b> .....	41
	Tomonori Ohba, Fernando Vallejos-Burgos, and Katsumi Kaneko	
<b>4</b>	<b>Physical Chemistry and Engineering for Adsorptive Gas Storage in Nanoporous Solids</b> .....	65
	Orhan Talu	
<b>5</b>	<b>Nanoporous Carbons with Tuned Porosity</b> .....	91
	Conchi O. Ania and Encarnacion Raymundo-Piñero	
<b>6</b>	<b>Metal-Organic Frameworks</b> .....	137
	V. Bon, I. Senkowska, and S. Kaskel	
<b>7</b>	<b>Zeolites and Other Adsorbents</b> .....	173
	Eduardo Pérez-Botella, Miguel Palomino, Susana Valencia, and Fernando Rey	
<b>8</b>	<b>Methane Storage on Nanoporous Carbons</b> .....	209
	Francisco Rodríguez-Reinoso and Joaquín Silvestre-Albero	
<b>9</b>	<b>Methane Storage on Metal-Organic Frameworks</b> .....	227
	Anne Dailly and Matthew Beckner	
<b>10</b>	<b>Storage of Hydrogen on Nanoporous Adsorbents</b> .....	255
	Philip L. Llewellyn	
<b>11</b>	<b>CO<sub>2</sub> Storage on Nanoporous Carbons</b> .....	287
	Marta Sevilla, Guillermo A. Ferrero, and Antonio B. Fuertes	

<b>12</b>	<b>CO<sub>2</sub> Storage on Metal-Organic Frameworks</b> .....	331
	Yunsheng Ma, Hideki Tanaka, and Ryotaro Matsuda	
<b>13</b>	<b>CO<sub>2</sub> Storage on Zeolites and Other Adsorbents</b> .....	359
	Maria João Regufe, Ana Mafalda Ribeiro, Alexandre F. P. Ferreira, and Alírio Rodrigues	
<b>14</b>	<b>Clathrate-Mediated Gas Storage in Nanoporous Materials</b> .....	383
	J. Silvestre-Albero	

# Chapter 1

## Introduction



**Francisco Rodríguez-Reinoso and Katsumi Kaneko**

### 1.1 Introduction

The depletion of the global oil reserves and the problem of possible climate changes due to increasing levels of carbon dioxide in the atmosphere have led to an increasing search for both new alternative clean energy sources and, simultaneously, for finding a good way to safely remove the large amount of CO<sub>2</sub> being produced with the actual energy systems. In the particular case of transportation, the main energy-consuming sector in developed countries, it accounted in the European Union (UE) in the early 2000s for over 30% of energy use and almost 70% of the oil-derived fuels demand, these figures being thought to continue increasing in the next few years [1]. A relatively recent report (2011), also from the UE, indicated that the CO<sub>2</sub> emissions from transportation represented 42% of the total emissions from consumers, emissions from cars meaning over half of the total emissions from the transportation sector [2]. The International Energy Agency has reported that the average CO<sub>2</sub> concentration has been recorded to be in 2016 above 400 ppm and that it is growing at a rate of more than 2 ppm per year, with the subsequently expected global climate change [3]. This is shown in Fig. 1.1 [4, 5], where the sharp increase in CO<sub>2</sub> concentration in air since 1960 is clearly noted.

It is easy to understand that finding an appropriate alternative source of energy to conventional fossil fuels such as gasoline and diesel would clearly reduce the oil dependence and environmental pressures from CO<sub>2</sub> and other emissions. Fig. 1.2

---

F. Rodríguez-Reinoso (✉)

Laboratorio de Materiales Avanzados, Departamento de Química Inorgánica-Instituto Universitario de Materiales, Universidad de Alicante, Alicante, Spain  
e-mail: [reinoso@ua.es](mailto:reinoso@ua.es)

K. Kaneko

Research Initiative for Supra-Materials, Shinshu University, Nagano, Japan  
e-mail: [kkaneko@shinshu-u.ac.jp](mailto:kkaneko@shinshu-u.ac.jp)

© Springer Nature Singapore Pte Ltd. 2019

K. Kaneko, F. Rodríguez-Reinoso (eds.), *Nanoporous Materials for Gas Storage*, Green Energy and Technology, [https://doi.org/10.1007/978-981-13-3504-4\\_1](https://doi.org/10.1007/978-981-13-3504-4_1)

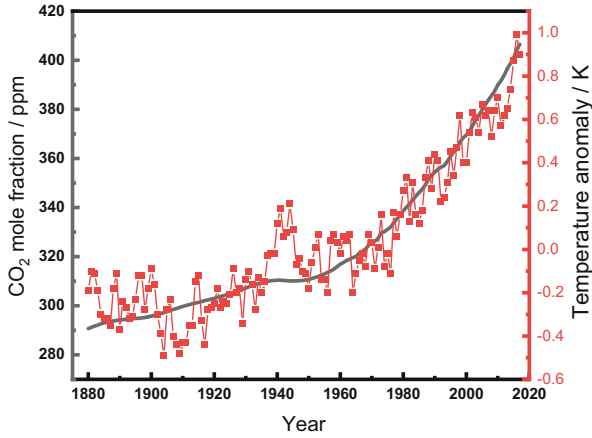


Fig. 1.1 Annual CO<sub>2</sub> concentration and global mean temperature change since 1880

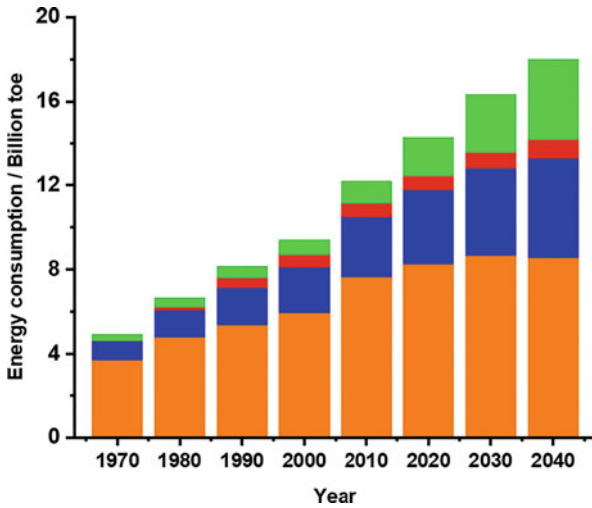


Fig. 1.2 Primary energy consumption and its forecast. Orange, coal and oil; blue, natural gas; red, nuclear energy; green, renewable energy. The toe means tonne of oil equivalent consumption

shows the consumption of different energy sources over the last years and a forecast for the consumption expected up to 2040 [6]. Although there has been in the recent past an increasing contribution from non-fossil energy sources (nuclear, hydro, solar wind, etc.), the contribution of fossil fuels is gradually increasing, and, consequently, there is the need for a real alternative to fossil fuels; in addition, it is also urgent to find the way to capture and store the so large amounts of CO<sub>2</sub> being produced by the combustion of fossil fuels. The chapters of this book intend to present the state of the art in the development of experimental systems devoted

to use alternative fuels (mainly methane and hydrogen), able to produce a cleaner combustion and, meanwhile, to develop materials able to capture the  $\text{CO}_2$  produced in the traditional combustion processes.

## 1.2 The Need for the Storage of Hydrogen, Methane, and Carbon Dioxide

It should be clear that the ideal fuel for production of energy would be hydrogen, since its combustion produces a large amount of energy and, at the same time, the reaction product is water, a clean residue. Hydrogen can be stored physically as either a gas or a liquid. Storage of hydrogen as a gas typically requires high-pressure tanks (350–700 bar tank pressure). On the other hand, storage of hydrogen as a liquid requires cryogenic temperatures, because the boiling point of hydrogen at one atmosphere pressure is 20.3 K. Theoretically, hydrogen can also be stored near ambient temperature on nanoporous solids (by adsorption) or within solids (by absorption), although the amount of gas stored is far from the desired target.

Hydrogen has the highest energy per unit mass of any fuel, but its very low density at ambient temperature results in a very low energy per unit volume. On a mass basis, hydrogen has nearly three times the energy content of gasoline, 120 MJ/kg for hydrogen versus 44 MJ/kg for gasoline. However, the situation is very different on a volume basis; liquid hydrogen has a density of 8 MJ/L, whereas gasoline has a density of 32 MJ/L, as shown in Fig. 1.3, when comparing energy densities of fuels based on lower heating values [7]. Presently available storage

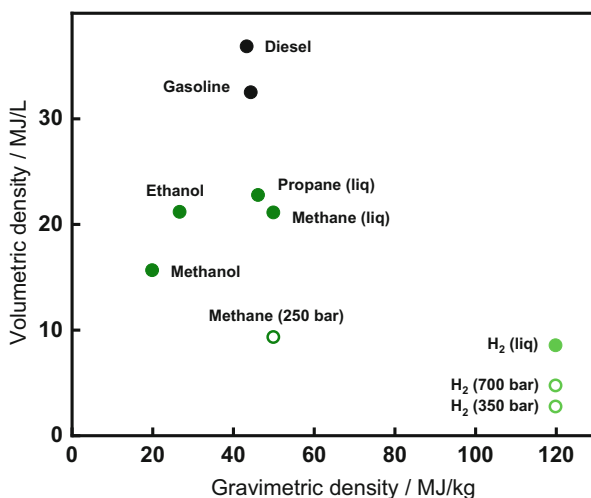


**Fig. 1.3** Comparison of gravimetric and volumetric energy density for different fuels. Solid and open symbols denote liquid and gas, respectively

options typically require large-volume systems that store hydrogen in gaseous form. This is not a great problem for large stationary applications, where the compressed gas tanks may be voluminous. However, in the case of fuel cell-powered vehicles, they will require enough hydrogen to provide a driving range of more than 500 km, with the ability to quickly and easily refuel the vehicle; something similar applies to other portable applications. Thus, onboard hydrogen storage capacities of 5–13 kg hydrogen will be required to meet the driving range for the full range of light-duty vehicles. The goal would be then to provide adequate hydrogen storage to meet the US Department of Energy (DOE) hydrogen storage targets [7] for onboard light-duty vehicles, [material handling equipment](#), and [portable power](#) applications: (1) 0.045 kg H<sub>2</sub>/kg system and (2) 0.030 kg H<sub>2</sub>/L system.

The simplest and easiest approach for actual hydrogen storage would be to use advanced pressure vessels made of fiber-reinforced composites that are capable of reaching 70 MPa pressure, but the long-term solution passes through the materials-based hydrogen storage technologies, including [adsorbents](#), [chemical hydrogen storage materials](#), and [metal hydrides](#), with properties allowing potential to reach the DOE hydrogen storage targets. Although a lot of research has been devoted worldwide in the last years to develop adsorbent nanomaterials for the storage of hydrogen, the results were not very satisfactory from the point of view of reaching the DOE target, as shown later in this book.

The alternative case of methane, as the main constituent of natural gas, is very attractive because it emits the least amount of CO<sub>2</sub> in the combustion of all hydrocarbons. In fact, the production and consumption of natural gas have been increasing almost linearly with time, as shown in Fig. 1.4 [8]. Although natural gas has been mainly used for power generation, it is a very promising fuel for the transportation energy demand in a more environmentally friendly way. Natural gas

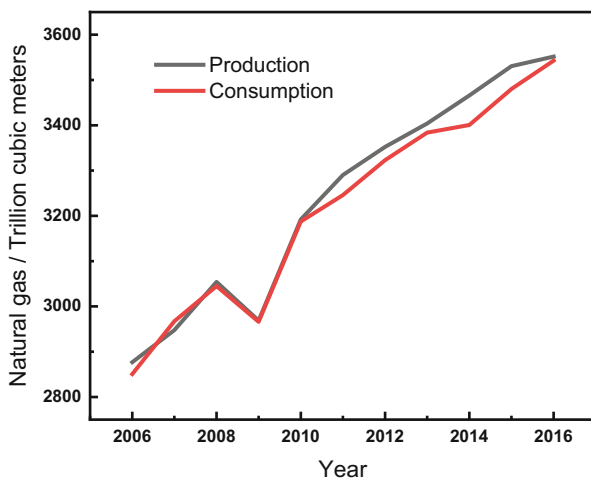


**Fig. 1.4** Production and consumption of natural gas over the last year

(methane) storage is interesting because the gas exhibits several advantages over conventional fuels, such as cleaner burning properties and availability (there is a huge amount of methane in the natural gas hydrates distributed in the oceans and also in the permafrost). From the environmental point of view, a vehicle running on methane would produce 70% less CO, 87% less non-methane organic gas, 87% less nitrogen oxide, and 20% less CO<sub>2</sub> than a vehicle running on gasoline [9]. The main drawback for the use of natural gas vehicles is the low energy density of the fuel (Fig. 1.1), which demands a refinement of existing technologies or finding a new technology or suitable system for storing an acceptable volume of natural gas to provide a reasonable driving distance.

Combustion of 1 L of natural gas at standard temperature and pressure (STP) will yield 0.033 MJ, whereas combustion of 1 L of gasoline will yield 34.2 MJ. Since, in addition, the space available for onboard storage is limited, the driving range of a natural gas vehicle would be very small when compared to a vehicle running with gasoline. This means that to make the use of natural gas attractive in transportation, a larger amount of energy must be stored in an acceptable volume at a reasonable pressure. There are many countries in which natural gas is already being used in vehicles as compressed natural gas (CNG) at 20–25 MPa, this requiring the use of very heavy thick cylindrical or spherical stainless steel tanks. The energy density of CNG at 25 MPa is 9.2 MJ/L as compared with 34.2 MJ/L for gasoline. This limits the driving range of the car to no more than 300 km.

An alternative to compressed natural gas is to use stored liquefied natural gas (LNG) cooled to down below the boiling temperature, 111.7 K. The energy density of LNG (22.2 MJ/L) is more than double that of CNG at 25 MPa, but just around 65% of that of gasoline. The main problem lies in the need of using large, heavy, and highly insulated tanks to keep the fuel cold. For this reason, LNG is only used in heavy-duty vehicles where the gas is burned in daily runs, but not in passenger cars in which the gas deposit may last several days.

Storing methane at relatively low pressures and room temperature by adsorption could be the solution to the problems described above for CNG and LNG, and, for this reason, adsorbed natural gas (ANG) has been considered a promising approach for vehicle transportation. Similarly, it could be used perhaps even in long-distance transportation of very large amounts of natural gas through the seas. The research in this area has been very extensive in the last few years, in an attempt to reach the same energy density of CNG at 25 MPa but at a much lower pressure and room temperature. The accepted target for the adsorption capacity needed for a reasonable driving range in automotive applications was provided by the US Department of Energy (DOE), which set a target in 1995 of 150 V/V at 3.5 MPa and 298 K, which was increased in 2000 to 180 V/V [10, 11]. It should be understood that these figures represent the amount of natural gas delivered (neither adsorbed nor stored) per unit volume of container. The pressure of 3.5 MPa was chosen because it does not require heavy thick wall cylindrical or spherical tanks or multistage compressors for charging the gas; the gas container can then be conformed to the space and shape available in the vehicle.

It is perhaps the occasion to note that the large majority of articles published in the literature of gas storage provide the data corresponding to the uptake of gas adsorbed as excess Gibbs adsorption, the quantity measured in standard volumetric or gravimetric adsorption equipment. However, once the excess adsorption isotherm has been determined, the uptake can be corrected by using both the sample packing and helium densities to obtain the storage capacity [12]. Of course, this value will be larger than the actual gas delivered as a function of the lowest pressure used along desorption, the delivery being the value implied in the DOE target.

Even although the literature shows that reaching the target of 180 V/V was almost impossible (taking into account that the values published correspond to excess adsorption), more recently the DOE has initiated a new methane storage program with the aim to reach the target of 0.5 g CH<sub>4</sub>/g sorbent for gravimetric capacity and/or 263 cm<sup>3</sup>/cm<sup>3</sup> for volumetric capacity, much higher than the previous 180 V/V [13].

Storage of hydrogen and methane is important for the promotion of renewable energy technologies in order to establish a stable supply system, although the batteries and supercapacitors can directly store electricity. This is because the electrical productivity from renewable energy sources is unstable and dependent on the region even under the support by the well-established smart grid system. The stationary electricity supply needs the highly reliable supplementary energy of clean energy substances such as hydrogen or methane. For example, the excessive electricity produced from renewable energy sources can be transformed into hydrogen, which will be used for power generation for stable electricity supply. Hydrogen has several advantages as an ideal energy carrier [14].

The efficient on-site power generation becomes possible with the development of fuel cell technology [15–17]. The fuel cell can convert hydrogen or methane gas directly into electricity at high efficiency through the catalytic oxidation at low temperature, being a promising power source. Automakers have supported ongoing efforts for pushing fuel cell electric vehicles and other applications. The fuel cell energy can play as an important supplement for conventional power sources in the near future. One of the most important issues on the fuel cell energy is the efficient and safe storage of hydrogen or methane, which can become possible by the use of appropriate nanoporous materials. This has prompted a very large amount of research programs to include porous carbons and, especially, very large surface area metal-organic frameworks (MOFs), and the state of the art of the research for the types of materials is described in later chapters.

In addition to these two cases of gas storage related to energy production and considering that for a few years the use of fossil fuels will be remaining as the basic source of energy in industrialized countries (it is estimated to be a minimum of 80% of the total energy supply), the reduction of the amount of emissions in the ambient air is a must. This means that the reduction of the amount of CO<sub>2</sub> by using cleaner and more efficient capture and storage systems must be implemented as soon as possible. In this case of CO<sub>2</sub>, the term storage is usually applied in a different sense to the previous two gases, hydrogen and methane, because the first step is the capture of the CO<sub>2</sub> produced in combustion processes and this would

be followed by the storage of the gas captured. Although the main technological process used for the capture of CO<sub>2</sub> is absorption by amine solutions, this has many practical application problems, and, consequently, the main alternative under research is the use of nanoporous materials for separation and adsorption processes such as PSA (pressure swing adsorption), VSA (vacuum swing adsorption), or TSA (temperature swing adsorption). Just to advance that the two apparently more competitive materials for the capture of CO<sub>2</sub> seem to be carbon and MOFs, the possibilities for both materials being discussed in detail later in this book.

### 1.3 Nanoporous Materials

As shown above, the main gases of interest in this book for storage are methane, hydrogen, and carbon dioxide, and the important aspect of the storage is to know the amount of gas that can be stored inside the deposit where the adsorbent is located. From the logical point of view, the volumetric capacity is the value of interest since the deposit must occupy the minimum volume for the maximum storage of gas. This means that it is important to define the amount of gas that can be stored not from the value that it is obtained from a classical experimental adsorption isotherm (Gibbs excess adsorption, the value provided in most published articles), but the storage capacity, this including the whole volume of gas contained inside the gas tank filled with the adsorbent. Furthermore, the application value of interest is the delivery capacity per unit volume of the tank, not the storage capacity. The deliverable capacity is defined as the difference between the amount of gas at the storage pressure and the amount remaining after the desorption step, which changes from 0.1 to 0.5 MPa as a function of the gas and the final application.

Nanoporous materials are the most promising to provide the target storage of the concerned gases. The molecular size of hydrogen, methane, and CO<sub>2</sub> is less than 1 nm, and the above requirements can be satisfied by physical adsorption. Therefore, the porous materials having the pore size of which is comparable to the target molecular size are the most promising. The detailed explanation is given in Chaps. 2 and 3. Just to recall that the IUPAC has recommended [18] the terminology of porosity as follows:

1. Pores with widths exceeding 50 nm are called macropores.
2. Pores of widths between 2 and 50 nm are called mesopores.
3. Pores with widths not exceeding 2 nm are called micropores.

The term nanopore embraces the above three categories of pores but with an upper limit of about 100 nm. On the other hand, micropores are often divided into narrow micropores (also called ultramicropores) of approximated width <0.7 nm and wide micropores (also called supermicropores, with width >0.7 nm).

Of course, narrow micropores (ultramicropores) have the strongest interaction potential for hydrogen, methane, and CO<sub>2</sub>, and they are the most important in the storage of these gases. However, the rapid diffusion is perturbed in the ultramic-

pores, depending on the temperature. Supermicropores and/or narrow mesopores can often accelerate the adsorption rate in ultramicropores, and they become critical in storing gas at higher pressures. Some porous materials have hierarchical pore structure, and, consequently, we frequently use the wider term of nanopores in this book.

## 1.4 Requested Properties for Nanoporous Adsorbents

Under the above conditions, the properties sought for a nanoporous adsorbent to be used for gas storage could be summarized as follows:

1. *High adsorption capacity and adequate pore structure.* Since the adsorption potential for the molecules of interest ( $\text{CH}_4$ ,  $\text{H}_2$ ,  $\text{CO}_2$ ) is a function of the pore structure and it is maximum in small pores – micropores (up to 2 nm) – the adsorbent should be predominantly microporous, with a pore dimension able to enhance the adsorption of molecules within the pore. Of course, the adsorption potential will be higher in a micropore able to adsorb only one molecule, but the adsorption capacity will be then limited in these narrow micropores. In addition, the strong adsorption potential in very narrow micropores will reduce the amount of gas delivered because part of it will be retained inside the pores, thus reducing the delivery capacity. Furthermore, since the storage is at a given pressure for each gas, this pressure will condition the pore size distribution more appropriate for each gas and pressure. Thus, the presence of wider micropores and even narrow mesopores is a need to reach high values of storage capacity at medium pressures (for instance, 3.5 MPa for methane). Furthermore, the shape of the narrow pores is also very important to reach high storage values. Thus, it is widely recognized that the packing density of spherical molecules in slit-shaped micropores is rather higher than in cylindrical micropores, and, consequently, the former porosity would be preferred for gas storage of most supercritical gases.
2. *High kinetics of adsorption/desorption.* In a practical application of gas storage, the rate at which the adsorbent is filled with gas and later emptied is the additional condition for the adsorbent. Since the main adsorption of the gas inside the adsorbent takes place in small pores, this means that the adsorption kinetics will be conditioned by the access of the gas to the interior of the adsorbent particle. This means that the microporosity must be either directly accessible from the exterior of the particle or that an adequate proportion of larger pores/spaces are provided to facilitate the access of the gas to the micropores. If the adsorbent is a powder or shaped in fibres the access of the gas to the micropores is easier but the problem is the large volume that corresponds to the interparticle space, where adsorption does not take place (see below). If the adsorbent is in the form of monolith having only micropores, the access of the gas to the interior is more difficult, and the kinetics of adsorption and desorption are slower if no larger pores or cracks are not available. Hence the monolith adsorbent of hierarchical pore structure consisting of ultramicropores and mesopores is the most promising.

3. *Reversibility of storage.* Since in most cases the storage of the supercritical gases is intended for applications in which the storage and delivery work continuously, it is clear that an additional condition for the adsorbent is reversibility. This means that once the application conditions are defined, the storage capacity and delivery must keep as constant as possible through use. It must be clear that in the first delivery of stored gas, some of the gas adsorbed in very narrow micropores will remain adsorbed, but the problem should not be present thereafter. Of course, a possible additional problem in the practical application may be the composition of the gas stored. For instance, in the case of natural gas, methane is the main but not the unique component, and the presence of species that can be adsorbed more strongly than methane may be a problem for the reversibility of the system.
4. *Packing density.* Since the value of interest in gas storage is the volumetric capacity, a very high adsorption capacity coupled with a high packing/bulk density will be required for the adsorbent, thus maximizing the amount of gas adsorbed in the minimum volume of adsorbent. As mentioned above, this is very important for practical applications such as onboard vehicle transportation since the gas tank should be as small as possible for a competitive reasonable mileage. If the adsorbent is granular, the interparticle space will be large, and consequently, the amount adsorbed and packed within the porosity will be relatively low since the density of the gas outside the porosity will be that of the gas at the given temperature, much lower than the gas adsorbed in micropores. From the logical point of view, a monolith of adsorbent will exhibit higher bulk density than the granular form of the same adsorbent and, consequently, the volumetric storage capacity will be higher for the former. However, care must be taken in preparing the monolith of adsorbent because the practical application is based in adsorption and desorption processes, both accompanied by thermal effects. Since adsorption is an exothermic process, heat will be evolved along the process, thus enhancing the temperature of the adsorption bed and reducing the adsorption capacity (see Chapter 3, section 3.4). The opposite effect corresponds to desorption, decreasing the delivery of gas. Since the volume occupied by the adsorbent must be as near as possible to the volume of the tank (with the limitations indicated above), the adsorbent must be conformable without losing its adsorption capacity, and this means that the mechanical properties must be as large as possible and requiring as little as possible of the appropriate binder (the ideal would be to find a binderless adsorbent).
5. *Mechanical and chemical stability.* The above adsorptive properties for gas storage are clearly a function of the stability of the adsorbent. Since the adsorbent will work under cycling conditions it is important that all properties keep constant along the use. If the application is mobile, as it is the case for onboard fueling, the mechanical stability is critical because it must withstand the continuous movement of the tank and avoid the subsequent possible erosion. Most usual adsorbents (nanoporous carbons, zeolites, etc.) exhibit chemical stability under the usual working conditions used in gas storage, but it is not so clear in the case of metal-organic frameworks (MOFs), a more recent addition to adsorbents of interest for gas storage.

6. *Inertness*. Since gas storage works at relatively high pressure, the chemical inertness of the adsorbent is important. Again, one should not expect problem for some typical adsorbent used in gas storage such as activated carbons and zeolites, but it is not so clear in the case of MOFs, where the presence of metal centers and organic linkers could make them somewhat reactive to the gas to store under pressure.
7. *Thermal conductivity*. Because physical adsorption taking place in gas storage is exothermic, the rate of adsorption produces a rise in the temperature of the adsorbent bed that will influence the rate of adsorption and the storage capacity. Of course, this problem will increase if the filling rate of the tank is increased. Because the desorption occurring when discharging the stored gas is endothermic, the temperature of the bed decreases by a significant amount, thus decreasing the discharging rate and the amount desorbed. Of course, both problems could be practically solved by decreasing the temperature of the bed along adsorption or heating it along desorption, but this is not so easy in the case of on-board application for transportation. Research is now carried out to increase the heat transfer properties of the bed in addition to the use of the above external heating/cooling accessories. Thus, zeolites are thermal insulators, and even carbons are not sufficiently conductive, and, consequently, the research is trying to increase the thermal conductivity to help to dissipate the heat evolved/supplied during the adsorption/desorption process. Little work has been carried out up to now for MOFs and similar adsorbents, but given their potential in this field, some progress is expected in the near future.

In the above, crucial requirements for nanoporous adsorbents are described. The requirements must be fulfilled for the establishment of the adsorption-aided gas storage technology. However, there are several scientific issues on storage of supercritical gases in nanopores like unveiling phase diagram of supercritical gas adsorbed in nanopores and obtaining molecular-level structural information on molecular assemblies of the concerned gas in nanopores. The intermolecular distribution of molecules as a function of the temperature, pore width (gas-solid interaction), and time are needed for the determination of the in-pore phase diagram and molecular simulation can show the plausible in-pore phase diagram, although the theoretical approach is not easy. For example, molecular simulation-aided synchrotron X-ray scattering [19] enables the determination of the in-pore intermolecular structure, being helpful to obtain the in-pore phase diagram. If the critical point of gas adsorbed in nanopores can be increased, it is easier to increase the storage amount of the concerned gas. The determination of the thickness of adsorbed layer or adsorbed volume of supercritical gas is another essential issue in the storage of supercritical gas. The indirect determination method of the adsorbed layer thickness (or volume) using the high-pressure adsorption isotherm is described in Chap. 3. However, we need new challenges for direct determination of the adsorbed layer thickness using ellipsometry [20] or near-field nano-/atom optics [21], because the thickness of adsorbed layer of supercritical gas can determine accurately the absolute adsorption amount. The collaboration between engineering and science on gas storage is intensively necessary.

From the above point of view, the fundamentals and actual potential of gas storage and representative nanoporous materials and some of the main problems found in the practical application are described in this book. For this reason, the book was planned to describe the main aspects of supercritical gases, the analysis of the fundamentals of adsorptive gas storage, and physical chemistry aspects of high pressure gas adsorption in the first three Chaps. (2, 3, and 4) in an attempt to cover all sides of this important subject. Chapters 5, 6, and 7 are devoted to describing the main characteristics (structure, texture, and physicochemical properties) of the adsorbents more frequently used in gas storage: nanoporous carbons (mainly activated carbon), MOFs, and zeolites or related inorganic materials. The storage of methane/natural gas will be discussed in two chapters, one devoted to nanoporous carbons (Chap. 8) and the other to MOFs (Chap. 9). Given the much lower amount of publications devoted to storage of methane on zeolites, this aspect was directly covered in Chap. 7, when the structure and properties of zeolites were described in detail. On the other hand, given that the large effort devoted to the storage of hydrogen has not been as successful as originally expected, only one chapter (Chap. 10) will be included in which the best results obtained using the different porous materials will be described. The adsorption/capture of CO<sub>2</sub> is covered in Chaps. 11, 12, and 13, one for each one of the three main adsorbents described above. Finally, Chap. 14 is devoted to an emerging area of increasing interest, the gas hydrates, and the description of the latest experimental results published on the use of confinement effect on nanospaces to grow these hydrates (mainly methane and CO<sub>2</sub> hydrates) under milder conditions and faster kinetics than nature.

**Acknowledgments** Dr. S. Wang (Shinshu University) helped to make figures.

## References

1. Kavalov B (2004) Techno-economic analysis of natural gas application as an energy source for road transport in the EU; European Commission. [https://www.researchgate.net/publication/265217576\\_Technoeconomicanalysisofnaturalgasapplicationasanenergysourceforroad\\_transportintheEU](https://www.researchgate.net/publication/265217576_Technoeconomicanalysisofnaturalgasapplicationasanenergysourceforroad_transportintheEU). Accessed Mar 2018
2. Vasanth KK, Preuss K, Titirici MM, Rodríguez-Reinoso F (2017) Nanoporous materials for the onboard storage of natural gas. *Chem Rev* 117:1796–1825
3. CO<sub>2</sub> emissions overview. International Energy Agency 2017. <https://www.iea.org/publications/freepublications/publication/CO2EmissionsFromFuelCombustion2017Overview.pdf>. Accessed Mar 2018
4. See <https://www.CO2.earth/>. Accessed Mar 2018
5. See <https://data.giss.nasa.gov/>. Accessed Mar 2018
6. See BP energy outlook, 2018 edition, P14
7. Fuel Cell Technologies Office of the US DOE (Hydrogen storage) 2017. See <https://www.energy.gov/eere/fuelcells/hydrogen-storage>. Accessed Mar 2018
8. See <https://www.bp.com/>. Accessed Mar 2018
9. How you can benefit from CNG conversion. CNG United, San Clemente, CA. <http://www.cngunited.com/support/howyoucanbenefitfromcngconversion>. Accessed Mar 2018
10. Wegrzyn J, Gurevich M (1996) Adsorbent storage of natural gas. *Appl Energy* 55:71–83

11. Burchell T, Rogers M (2000), Low pressure storage of natural gas for vehicular applications SAE Technical Paper 2000-01-2205, SAE International, Warrendale PA
12. Casco ME, Martínez-Escandell M, Gadea-Ramos E, Kaneko K, Silvestre-Albero J, Rodríguez-Reinoso F (2015) High-pressure methane storage in porous materials: are carbon materials in the pole position? *Chem Mater* 27:959–964
13. See US' DOE MOVE Program at <https://arpa-e-foa.energy.gov/>. Accessed March 2018
14. Veziroglu TN, Barbir F (1992) Hydrogen: the wonder fuel. *Int J Hydrog Energy* 17:391–404
15. Murray EP, Tsai T, Barnett SA (1999) A direct-methane fuel cell with a ceria-based anode. *Nature* 400:649–651
16. Steele BC, Heinzel A (2001) Materials for fuel-cell technologies. *Nature* 414:345–352
17. Debe MK (2012) Electrocatalyst approaches and challenges for automotive fuel cells. *Nature* 486:43–51
18. Thommes M, Kaneko K, Neimark AV, Olivier JP, Rodríguez-Reinoso F, Rouquerol J, Sing KSW (2015) Physisorption of gases, with special reference to the evaluation of surface area and pore size distribution. *Pure Appl Chem* 87:1051–1069
19. Futamura R, Iiyama T, Takasaki Y, Gogotsi Y, Biggs MJ, Salanne M, Ségolini J, Simon P, Kaneko K (2017) Partial breaking of the Coulombic ordering of ionic liquids confined in carbon nanopores. *Nat Mater* 16:1163–1273
20. Bourgeois A, Turcant Y, Walsh C, Defranoux C (2009) Ellipsometry porosimetry (EP): thin film porosimetry by coupling an adsorption setting with an optical measurement, highlights on diffusion results. *Appl Surf Sci* 256:S26–S29
21. Ohtsu M (ed) (1998) *Near-field Nano/atom optics and technology*. Springer, Tokyo

# Chapter 2

## Fundamental Aspects of Supercritical Gas Adsorption



Fernando Vallejos-Burgos, Tomonori Ohba, and Katsumi Kaneko

### 2.1 Equation of State for Gases

Most gases near room temperature and atmospheric pressure can be described by the so-called perfect gas or ideal gas equation of state (Eq. 2.1).

$$PV_m = RT, \quad (2.1)$$

Here,  $V_m$ ,  $P$ , and  $T$  are volume occupied by one mole of gas, pressure, and the temperature of the gas, respectively;  $R$  is the gas constant. Equation 2.1 gives a relation between variables of a gaseous substance. The perfect gas equation of states is valid when the intermolecular interactions are negligibly small compared to the thermal energy. The perfect gas equation of states cannot describe real gases, because in the real gas molecules interact each other. Johannes van der Waals succeeded in modifying the perfect gas equation of states in 1873 [1], leading to his famous van der Waals equation expressed as (Eq. 2.2):

$$\left(P + \frac{a_V}{V_m^2}\right)(V_m - b_V) = RT \quad (2.2)$$

Here,  $a_V$  and  $b_V$  are constants inherent to each gas. The correction term ( $a_V$ ) in the pressure is related to the internal pressure coming from the intermolecular attractive interaction (van der Waals interaction), and the repulsion interaction is

---

F. Vallejos-Burgos · K. Kaneko (✉)  
Research Initiative for Supra-Materials, Shinshu University, Nagano, Japan  
e-mail: [fvb@vallejos.cl](mailto:fvb@vallejos.cl); [kkaneko@shinshu-u.ac.jp](mailto:kkaneko@shinshu-u.ac.jp)

T. Ohba  
Graduate School of Science, Chiba University, Inage, Chiba, Japan  
e-mail: [ohba@chiba-u.jp](mailto:ohba@chiba-u.jp)

included in the volume ( $b_V$ ) through the excluded volume by the hard-sphere molecules. The van der Waals interaction is the dispersion interaction which will be introduced in Chap. 3. The van der Waals equation simplifies to the perfect gas equation in the limit of high temperature and large molar volume. However, an inflection point appears in the  $PV$  relation by lowering the temperature, which is called the critical temperature  $T_c$ . The volume and pressure associated to the inflection point are the critical volume  $V_c$  and critical pressure  $P_c$ , respectively. Those critical parameters arise from the van der Waals equation by the conditions of the inflection point (Eq. 2.3):

$$\left(\frac{\partial P}{\partial V_m}\right)_T = 0, \left(\frac{\partial^2 P}{\partial V_m^2}\right)_T = 0 \quad (2.3)$$

as  $T_c = \frac{8a_V}{27b_V R}$ ,  $V_c = 3b_V$ , and  $P_c = \frac{a_V}{27b_V^2}$ . These relations describe considerably well the experimentally determined critical parameters of real gases. For example, the experimentally determined  $T_c$  values for  $\text{CH}_4$  and  $\text{H}_2$  are 191 and 33 K, respectively, being quite close to the values ( $\text{CH}_4$ , 190 K, and  $\text{H}_2$ , 34 K) derived from the above relation by use of the van der Waals parameters [2]:  $a_V(\text{CH}_4) = 2.28 \times 10^{-1} \cdot \text{m}^6 \cdot \text{Pa} \cdot \text{mol}^{-2}$  and  $b_V(\text{CH}_4) = 4.28 \times 10^{-5} \text{m}^3 \cdot \text{mol}^{-1}$  and  $a_V(\text{H}_2) = 0.25 \times 10^{-1} \text{m}^6 \cdot \text{Pa} \cdot \text{mol}^{-2}$  and  $b_V(\text{H}_2) = 2.66 \times 10^{-5} \cdot \text{m}^3 \cdot \text{mol}^{-1}$ . The van der Waals equation can describe the liquid-vapor coexistence below  $T_c$  in the pressure-volume isotherm [3]. Figure 2.1 shows the van der Waals isotherms of  $\text{CH}_4$  at 160, 170, 180, 190, and 200 K.

The P-V isotherm at 190 K ( $T_c$ ) has an inflection point. The P-V isotherms below  $T_c$  have an S-shaped curve with a maximum and a minimum. The horizontal line AB at 160 K being drawn to obtain the equal areas of C and D represents the gas-liquid coexistent region with properties A and B. The coexistent region becomes narrower by increasing temperature and disappears at  $T_c$ . When temperature becomes much higher than  $T_c$ , the isotherm obeys the perfect gas law. Thus, the van der Waals

**Fig. 2.1** van der Waals isotherms of  $\text{CH}_4$  near critical temperature. Shaded region represents vapor-liquid equilibrium. The green curve is the isotherm plotted at the critical temperature  $T_c$

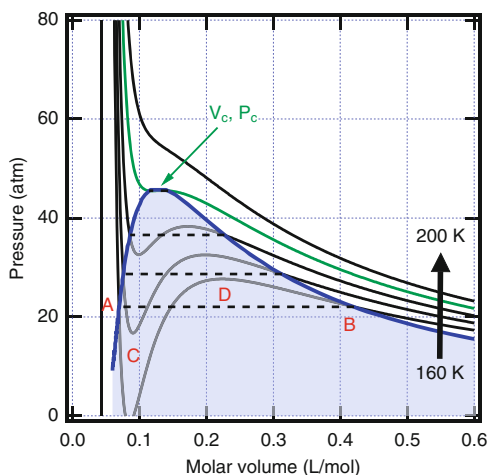


**Fig. 2.2**

Pressure-temperature projection of the phase diagram. Supercritical gas is gas above  $T_c$ , including supercritical fluid.  $T_{\text{triple}}$  and  $P_{\text{triple}}$  denote the temperature and pressure at the triple point, respectively

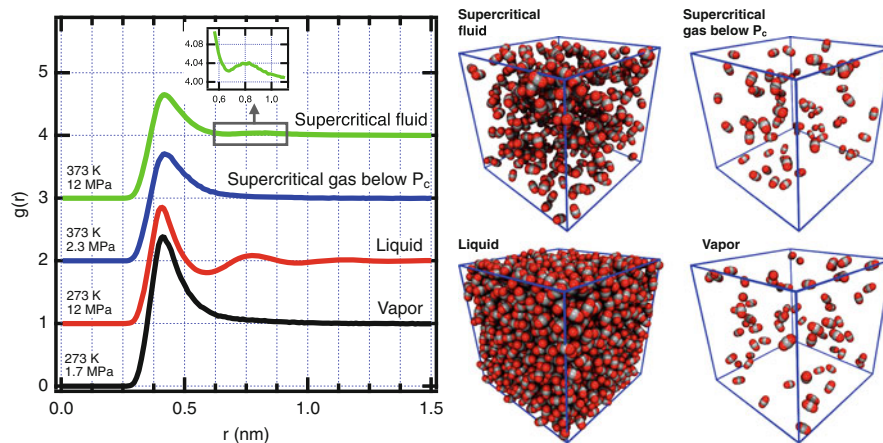
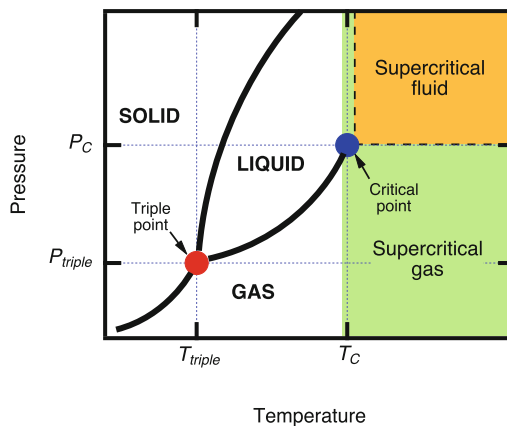


**Fig. 2.3** Radial distribution functions and snapshots obtained from computer simulation for  $\text{CO}_2$  in different phases: supercritical fluid, supercritical gas, liquid, and vapor. TraPPE model [4] is assumed for  $\text{CO}_2$

equation shows the presence of critical points and provides a brief sketch of the liquid-vapor transition.

Here we need to introduce the terminology of supercritical gas. The supercritical fluid is defined as the phase above  $T_c$  and  $P_c$  in Fig. 2.2. However, here we define the supercritical gas as the supercritical fluid plus the gas above  $T_c$  and below  $P_c$  (i.e., all the zone above  $T_c$ ). This is because we cannot liquefy the supercritical gas by compression and the saturated vapor pressure cannot be defined. Accordingly it is difficult to form the high-density state of supercritical gas even using the nanoporous solids; this is the reason why storing supercritical hydrogen and methane using nanoporous materials is not easy. Figure 2.3 shows snapshots obtained from molecular simulation. Of course, supercritical fluid can be regarded as a mixture of gas and liquid; the supercritical gas has the characteristic of the supercritical fluid

**Table 2.1** Virial coefficient  $B$  of representative gases in  $\text{cm}^3/\text{mol}$  [5]

T (K)	H <sub>2</sub>	N <sub>2</sub>	O <sub>2</sub>	CH <sub>4</sub>	CO <sub>2</sub>
15	-239.3				
50	-32.7				
75	-13.2	-276.8	-328.5		
115	1.2	-123.3	-150.4	-305.1	
220	12.1	-26.8	-40.1	-86.14	-247.9
273.15	14.0	-10.4	-22.1	-53.4	-150.9
298	13.8	-5.0	-16.2	-42.9	-123.5
400	15.6	8.9	-0.49	-15.5	-59.9
500	16.2	16.4	8.3	-1.0	-30.3
600		21.1		8.1	-12.9
700		24.2		14.2	-1.5

with less density. The radial distribution function  $g(r)$  of the supercritical fluid has a broad second peak around  $r = 0.7$  nm. The radial distribution function of liquid has a clear second peak indicating, together with the sharp first peak, the slight ordering in addition to the nearest neighbor coordination. Thus, the supercritical gas below  $P_c$  has a short range order different from the supercritical fluid.

Gas storage must form the high density of the target gas. As the van der Waals equation cannot describe the many-body interaction which is not negligible for the high-density gas, we need an effective equation of state which describes the highly pressurized gas. The virial equation is fit for such purpose. The compression factor  $Z$  is defined as  $PV_m/RT$  and is given by the virial expression (Eqs. 2.4 and 2.5). When  $Z = 1$ , the gas is an ideal gas. Here,  $B'(T)$ ,  $C'(T)$ ,  $D'(T)$ , etc. are the second, third, fourth, etc. virial coefficients (Table 2.1).

$$Z = PV_m/RT = 1 + B'(T) + C'(T)P^2 + D'(T)P^3 + \dots \quad (2.4)$$

An equivalent expression as a function of molar volume  $V_m$  is

$$Z = 1 + B(T)/V_m + C(T)/V_m^2 + D(T)/V_m^3 + \dots \quad (2.5)$$

where the virial coefficients are related by

$$B = B'RT, \quad C = (B'^2 + C')(RT)^2, \quad D = (B'^3 + 3B'C' + D')(RT)^3 \quad (2.6)$$

The intermolecular interactions are significant at high-pressure conditions; attractive interactions between molecules decrease the pressure, while repulsive interaction increases it. Then, pressure is not a good measure of the escaping tendency for a high-pressure gas. A better concept is fugacity ( $f$ ); it is defined by Eq. 2.7. When the gas pressure is low, the ideal gas equation is obtained.

$$\left( \frac{\partial \ln f}{\partial P} \right)_T = \frac{V_m}{RT} \quad (2.7)$$

**Table 2.2** Fugacity coefficients of H<sub>2</sub>, N<sub>2</sub>, O<sub>2</sub>, CH<sub>4</sub>, and CO<sub>2</sub> at different pressures and temperatures calculated [6] with the Peng-Robinson [7] equation of state

T (K)	P (MPa)	H <sub>2</sub>	N <sub>2</sub>	O <sub>2</sub>	CH <sub>4</sub>	CO <sub>2</sub>
150	0.01	1.000	0.9993	0.9992	0.9985	0.9965
	0.1	0.9997	0.9932	0.9919	0.9847	0.9648
	1	0.9974	0.9333	0.9200	0.8497	0.0067
	10	0.9983	0.5160	0.3448	0.1174	0.0008
298	0.01	1.000	1.000	0.9999	0.9998	0.9995
	0.1	1.000	0.9996	0.9991	0.9978	0.9945
	1	1.003	0.9957	0.9909	0.9782	0.9460
	10	1.033	0.9727	0.9238	0.8190	0.4678
500	0.01	1.000	1.000	1.000	1.000	0.9999
	0.1	1.000	1.000	1.000	0.9998	0.9992
	1	1.003	1.003	1.001	0.9982	0.9919
	10	1.028	1.033	1.011	0.9887	0.9290

The fugacity  $f$  is usually expressed by the fugacity coefficient  $\lambda$  (as in  $f = \lambda P$ ) which is determined experimentally or calculated from equations of state (see Table 2.2). The fugacity must be used for showing the correct adsorption isotherm of supercritical gas, because the pressure compressing the target gas is not the real pressure which varies depending on the intermolecular interactions. In particular, usage of pressures above 10 MPa should be done with caution according to Table 2.2. However, the term “pressure” can be conveniently used for applications in loading the gas on porous materials.

## 2.2 Intermolecular Interactions Between Molecules in Gas Phase

We must distinguish the intermolecular and intramolecular interactions at first. The latter is so-called chemical bonding which combines atoms through electron exchange interaction over a molecule. If two atoms [a] and [b] interact between each other at the mutual distance  $R'$ , the total wave function  $\Psi_{ab}$  of atoms [a] and [b] is given by Eq. 2.8:

$$\Psi_{ab} = \frac{1}{\sqrt{2}} \{ \psi_a(1)\psi_b(2) + \psi_a(2)\psi_b(1) \} \quad (2.8)$$

Here, (1) and (2) indicate three-dimensional coordinates  $(x_1, y_1, z_1)$  and  $(x_2, y_2, z_2)$  of electrons [1] and [2].  $\psi_x(n)$  is the wave function of atom [x] with an electron [n] and  $x = a$  or  $b$  and  $n = 1$  or  $2$ . When  $R'$  is smaller than the contact distance between the atoms, two electrons exchange their position from atom [a] to atom

**Table 2.3** Characteristic properties and Lennard-Jones parameters of selected gases

Molecule	Interaction	$T_b$ (K)	$T_c$ (K)	$P_c$ (MPa)	$\sigma$ (nm)	$\epsilon/k_B$ (K)
H <sub>2</sub>	Quadrupole	20.3	33.0	1.29	0.292	38.0
O <sub>2</sub>	Quadrupole, Paramagnetism	90.2	154.6	5.04	0.338	126.3
N <sub>2</sub>	Quadrupole	77.3	126.2	3.39	0.363	104.2
NO	Dipole, Paramagnetism	121.4	180	6.48	0.347	119
CO <sub>2</sub>	Quadrupole	194.7	304.2	7.48	0.376	245.3
CH <sub>4</sub>	Octupole	111.6	190.5	4.60	0.372	161.3

[b] or vice versa. The exchange of electrons lowers the total energy of atoms [a] and [b], resulting in a chemical bonding energy of an order of  $(2-10) \times 10^2$  kJ/mol. The thermal energy  $RT$  at 300 K is 2.5 kJ/mol, and then the chemical bonding is quite stable at room temperature. This explains why important atmospheric gases such as N<sub>2</sub>, O<sub>2</sub>, H<sub>2</sub>, CH<sub>4</sub>, and CO<sub>2</sub> are quite stable at ambient temperature. These gaseous molecules have different electronic structures, giving inherent macroscopic and physical properties as summarized in Table 2.3.

Electrons in polyatomic molecules are not uniformly distributed. The molecule then exhibits a polar nature (see Fig. 2.4), with the concept of multipole moment being used for description of their electrostatic interactions. A heteronuclear diatomic molecule has a dipole due to the electronegativity difference between its atoms. Even a homonuclear diatomic molecule such as H<sub>2</sub> and O<sub>2</sub> exhibits a polar nature, because electrons are attracted by the nuclei, resulting in a quadrupole. A CH<sub>4</sub> molecule of  $T_d$  symmetry has an octupole. Multipole moments interact with each other and with the local electrostatic field of solid surfaces; the lower-order multipole moment results in stronger interactions than higher-order multipoles. The interaction energy of an octupole is then negligibly small compared with the dispersion interaction described later. However, the quadrupole moment-associated interaction is often meaningful at low temperature: N<sub>2</sub> and O<sub>2</sub> are stabilized by 3 and 2 kJ/mol, respectively, due to the quadrupole moment and the local electrostatic field arising from a subnanoscale structure [8]. A representative electrostatic interaction is the intermolecular interaction between water molecules, which is so-called hydrogen bonding. In water, its energy is three times larger than the dispersion interaction [9]. This is exceptional, because the contributions from the electrostatic interaction even for HCl and NH<sub>3</sub> are 11% and 48% of their dispersion interaction, respectively. Water molecules thus tend to form a hydrogen-bonded network structure. A hydrogen-bonded cage can accept various neutral molecules such as H<sub>2</sub> and CH<sub>4</sub> to form hydrated compounds [10].

The electrostatic interaction described above is an important intermolecular interaction. Except for water, the predominant attractive intermolecular interaction is dispersion. We will describe the dispersion interaction in terms of quantum

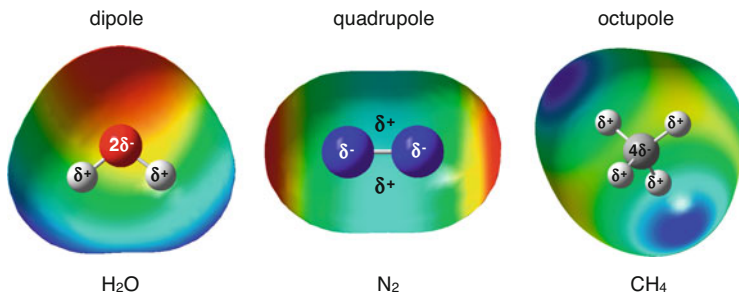


Fig. 2.4 Schematic representation of electric multipoles for important molecules

mechanics. Using Eq. 2.8 for the situation of  $R'$  greater than the [a]-[b] bond distance no electron exchange occur. When electrons [1] and [2] interact with each other by approaching the opposite atom, the perturbation term  $\hat{H}'$  becomes important:

$$\hat{H}' \approx \frac{e^2}{R'^3} (x_1 x_2 + y_1 y_2 - 2z_1 z_2) \quad (2.9)$$

The primary perturbation energy becomes zero, and the secondary perturbation is suggestive. When the wave functions of two atoms without electron exchange are given by  $\psi_a(1)$  and  $\psi_b(2)$ , the total wave function  $\psi_{ab}$  of the system may be written as

$$\psi_{ab} = \psi_a(1)\psi_b(2) \quad (2.10)$$

This theory can also be applied to two molecules instead of two atoms and thereby Eqs. 2.9 and 2.10 can be applied to two molecular systems in order to evaluate their intermolecular dispersion interaction, as given below. The second-order perturbation energy  $E''_0$  is

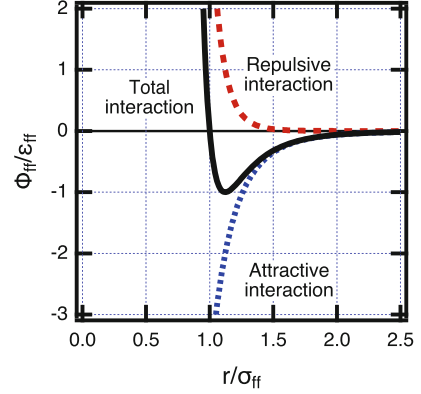
$$E''_0 = -(\text{coefficient}) \frac{e^4}{r_0^6} \bar{r}_1^2 \bar{r}_2^2 \quad (2.11)$$

Here

$$\bar{r}_1^2 = \int \Psi_a^*(1) r_1^2 \Psi_a(1) d\tau_1 \quad (2.12)$$

$$\bar{r}_2^2 = \int \Psi_b^*(2) r_2^2 \Psi_b(2) d\tau_2 \quad (2.13)$$

**Fig. 2.5** Potential energy contributions to the LJ potential in reduced units



$R'$  was replaced by  $r$  in order to give a general meaning in the following discussion. In  $\mu_i^2 = e^2 \bar{r}_i^2$ ,  $\mu_i$  is the mean value of a dipole moment when the electron is continuously moving in a neutral molecule. Then, the dispersion interaction  $U_{disp}$  is described by Eq. 2.14:

$$\Phi_{disp} = -\frac{(\text{coefficient})\bar{\mu}_1^2\bar{\mu}_2^2}{r^6} = -\frac{C_6}{r^6} \quad (2.14)$$

where  $C_6$  is the lumped constant. The dispersion interaction is inversely proportional to the 6th power of the intermolecular distance. Since  $\mu_i$  arises from an instantaneous deviation of an electron, larger molecules have stronger dispersion interactions.

In addition to the dispersion interaction, we must take into account the repulsion force, as discussed previously regarding the van der Waals equation. This force occurs due to the repulsive overlap between negatively charged electron clouds of two molecules. The repulsive interaction is approximated by a constant divided by  $r^{12}$  in the popular Lennard-Jones (LJ) pair potential  $\Phi_{ff}$ , as described in Eq. 2.15.

$$\Phi_{ff}(r) = 4\epsilon_{ff} \left[ \left( \frac{\sigma_{ff}}{r} \right)^{12} - \left( \frac{\sigma_{ff}}{r} \right)^6 \right] \quad (2.15)$$

Here,  $ff$  indicates interaction between fluid molecules.  $\sigma_{ff}$  is the size parameter at  $\Phi_{ff} = 0$ , and  $\epsilon_{ff}$  is the potential energy depth (see Fig. 2.5). The units of  $\epsilon_{ff}$  are conventionally expressed by the absolute temperature times  $k_B$  (the Boltzmann constant). The  $\sigma_{ff}$  and  $\epsilon_{ff}$  (LJ parameters) are determined experimentally [11], and those for molecules relevant to this topic are shown in Table 2.3.

The LJ pair potential also describes well the intermolecular interaction potential  $\Phi_{fj}(r)$  between different molecules  $f$  and  $j$  which are separated by  $r$ .

$$\Phi_{fj}(r) = 4\epsilon_{fj} \left[ \left( \frac{\sigma_{fj}}{r} \right)^{12} - \left( \frac{\sigma_{fj}}{r} \right)^6 \right] \quad (2.16)$$

Here,  $\sigma_{fj}$  and  $\epsilon_{fj}$  are the crossed-interaction parameters having the physical meaning corresponding to Eq. 2.15.  $\sigma_{fj}$  and  $\epsilon_{fj}$  are usually approximated by Lorentz-Berthelot rules (Eq. 2.17).

$$\epsilon_{fj} = \sqrt{\epsilon_{ff}\epsilon_{jj}} \quad , \quad \sigma_{fj} = (\sigma_{ff} + \sigma_{jj})/2 \quad (2.17)$$

Equation 2.16 can also be applied to the fluid-solid interaction. In this case, the LJ parameters of the component atoms in the solid are used for evaluation of  $\sigma_{fj}$  and  $\epsilon_{fj}$ , as will be described in Chap. 3.

We cannot directly discuss the interaction difference between supercritical gas and vapor using the intermolecular potential. However, we have qualitative estimations from the magnitude of  $\epsilon_{ff}$ . For a supercritical gas at ambient temperature,  $\epsilon_{ff}/k_B$  is less than 300 K: 37 K for H<sub>2</sub>, 48 K for N<sub>2</sub>, 150–203 K for CO<sub>2</sub>, and 140–156 K for CH<sub>4</sub>. On the other hand, the values of  $\epsilon_{ff}/k_B$  for vapor molecules such as ethanol and dimethyl ether are 415 and 412 K, respectively. We must then enhance the intermolecular interaction to increase the stored amount of a supercritical gas in the pores of a solid, because larger  $\epsilon_{ff}$  gives the molecule-solid interaction as shown by the Lorentz-Berthelot rule.

As a word of caution, even though the LJ parameters are obtained from experimental studies on bulk fluids, the dispersion interaction strongly depends on the dielectric properties of the surroundings [12]. Then, the routine application of LJ potential to understand the interfacial behavior of gases should be done carefully.

### 2.3 Four Types of Molecule-Solid Interaction for Gas Storage

To achieve efficient gas storage, we must form a highly concentrated molecular assembly of target gas on nanoporous materials. Fundamental understanding of the gas-solid interaction is then necessary for gas storage studies. Although the detailed description on gas-solid interaction based on physical adsorption is given in Sect. 2.4, we will now explain four types of molecule-solid interaction.

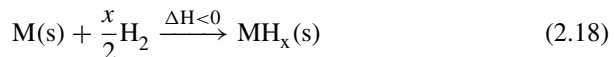
There are four types of gas-solid interactions: physical adsorption, chemisorption, absorption, and occlusion. Here “physical adsorption” is often expressed by simply “adsorption.” These four concepts are not clearly understood. Brunauer [13] described in his book “The molecules that disappear from the gas phase either enter the inside of the solid, or remain on the outside, attached to its surface. The former phenomenon is called absorption, the latter adsorption. Often the two occur simultaneously; the total uptake of the gas is then designated by the term *sorption*.” Although this definition is quite phenomenological, this definition on *adsorption*, *absorption*, and *sorption* is still valid. The book by Rouquerol, Rouquerol, and Sing [14] adopts a similar description, although *adsorption* is now defined as “enrichment of one or more of the components in the region between two bulk phases.” Thus, the definition on *adsorption*, *absorption*, and

*sorption* is too phenomenological and unclear. Hattori et al. [15] clarified the concepts physical adsorption, chemisorption, absorption, and occlusion considering the structural change of molecules and/or solids according to their interaction. *Physical adsorption* induces no structural change neither in the molecule nor the solid. As in *physical adsorption*, the main attractive interaction is dispersion interaction; it does not modify the chemical bonds. On the other hand, *chemisorption* changes the structure of chemisorbed molecules on the solid surface; it does not change the bulk solid structure in general but only varies it slightly at the chemisorption site. For example, when  $\text{SO}_2$  is chemisorbed on  $\alpha$ - $\text{FeOOH}$ ,  $\text{SO}_2$  is transformed into  $\text{SO}_4^{2-}$  by depriving the surface of oxygens;  $\text{SO}_2$  chemically bonds with surface oxygens, creating oxygenated defects in the solid surface [16].

In the case of *absorption*, the major attractive interaction between the molecule and the solid is also dispersion interaction. Absorption of molecules modifies the solid structure without any molecular structural change. A typical example of absorption is the swelling of graphene oxide upon exposure to water vapor, by increasing its d-spacing 23% [17].

Absorption occurs when the sum of the intermolecular energy and molecule-solid interaction energy is larger than the lattice energy of the solid. Gate adsorption in the Cu-based MOF is also a good example of absorption; the Cu-based MOF repeatedly expands the lattice along c-axis by 28% in order to absorb  $\text{CO}_2$  [18, 19]. Although the gate adsorption has been widely used already, the real adsorption mechanism must be ascribed to absorption.

Pd is a representative hydrogen storage metal. Pd solid forms Pd hydride by accepting the hydrogen atoms split from an  $\text{H}_2$  molecule according to the exothermic reaction (Eq. 2.18):



This is a typical example of occlusion. The occlusion of  $\text{H}_2$  by a metal is exothermic, releasing heat  $\Delta H$ . The equilibrium of  $\text{H}_2$  at ambient temperature often occurs at modest hydrogen pressures ( $<0.1 - 1$  MPa), resulting in  $-\Delta H$  of 20–43 kJ/mol [20].

Storage of gases by physical adsorption and absorption has the advantage of high storage/release rate with less energy, but we need to find optimum adsorbents having enough adsorption capacity for a target gas at ambient temperature. Searching and designing promising nanoporous materials are still challenging, inducing plenty of active studies, as will be shown in later chapters. As chemisorption needs active local sites for fixation of the target gas molecules and its rate is much slower compared to physical adsorption, gas storage with chemisorption is in general not promising. Occlusion has been challenged for hydrogen storage. The storage of hydrogen by hydrogen-adsorbing alloys has still various issues for application. The explicit classification of these four concepts associated with the essential properties

of gas molecules and nanoporous materials helps to design better nanomaterials for target gas storage. The fundamental routes for controlling physical adsorption of supercritical gases will be given in the following sections.

## 2.4 Origin of Physical Adsorption

Although four types of molecule-solid interaction are described in Sect. 2.3, the dispersion interaction of a molecule with a solid surface, being the key interaction in physical adsorption, will be addressed here in more detail. Here we use graphite as a model solid, because of its simple periodic structure and reliable analysis.

To calculate the interaction between a molecule  $f$  and a solid slab, we have to sum all the interaction potentials between the molecule  $f$  and all the atoms  $j$  in the solid slab (see Fig. 2.6a):

$$\phi = \int \int \int 4\epsilon_{fj} \left[ \left( \frac{\sigma_{fj}}{r} \right)^{12} - \left( \frac{\sigma_{fj}}{r} \right)^6 \right] dx dy dz \quad (2.19)$$

In order to avoid a heavy calculation that takes into account all atoms in the solid slab, a structureless solid-surface model neglecting the slab structure is often used (see Fig. 2.6b). The interaction potential function is obtained in terms of the vertical distance,  $z$ , between a molecule and solid surface of semi-infinite thickness.

$$\phi(z) = \int_{x=0}^{\infty} 2n\pi x dx \times 4\epsilon_{fj} \left[ \left( \frac{\sigma_{fj}}{r} \right)^{12} - \left( \frac{\sigma_{fj}}{r} \right)^6 \right] \quad (2.20)$$

Here  $n$  is the number density of atoms in the solid. The integration of Eq. 2.20 using  $r^2 = x^2 + z^2$  leads to Eq. 2.21.

$$\phi(z) = 4n\pi\epsilon_{fj}\sigma_{fj}^2 \left[ \frac{1}{5} \left( \frac{\sigma_{fj}}{z} \right)^{10} - \frac{1}{2} \left( \frac{\sigma_{fj}}{z} \right)^4 \right] \quad (2.21)$$

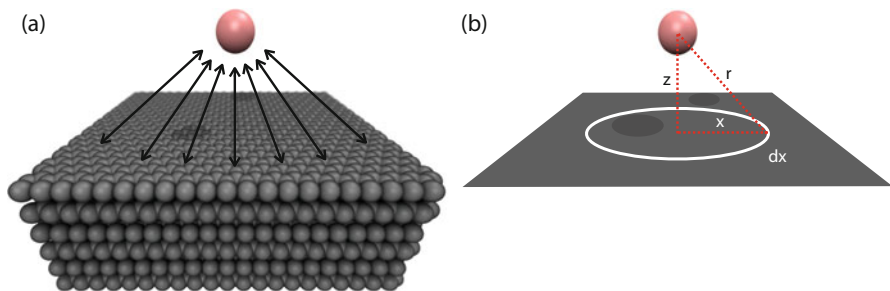


**Fig. 2.6** (a) Pairwise interaction of a molecule with solid-surface atoms and (b) model for an analytical integration of interaction between a molecule and structureless solid surface

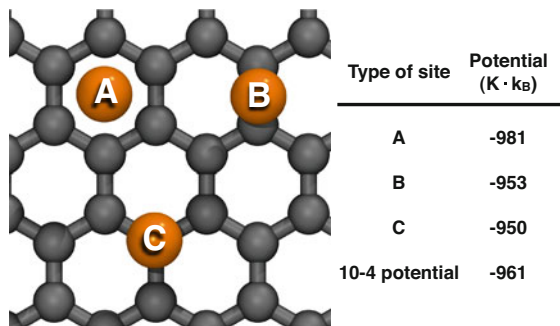
This formula is known as 10 – 4 potential; the potential energy minimum and the equilibrium distance from surface are  $\frac{6}{5}\pi n\epsilon_{fj}\sigma_{fj}^2$  and  $\sigma_{fj}$ , respectively. The presence of the deep interaction potential minimum is the origin of physical adsorption. The distance  $\sigma_{fj}$  at the 10 – 4 potential minimum is shorter than the distance in LJ ( $f, j$ ) pair potential,  $1.122\sigma_{fj}$ , which comes from the summation of attractive pair potentials between a molecule and solid atoms. Steele took into account the stacking structure in a graphite slab with an interlayer distance of  $\Delta$ , providing the so-called 10 – 4 – 3 potential, as given by Eq. 2.22 [21].

$$\phi(z) = 4n\pi\rho_s\epsilon_{fj}\sigma_{fj}^3 \left[ \frac{1}{5} \left( \frac{\sigma_{fj}}{z} \right)^{10} - \frac{1}{2} \left( \frac{\sigma_{fj}}{z} \right)^4 - \frac{\sigma_{fj}^4}{6\Delta(z + 0.61\Delta)^3} \right] \quad (2.22)$$

where  $\rho_s$  is the number density of the solid. The 10 – 4 – 3 potential has been widely used for molecular simulation of gas adsorption on carbon materials. Even though it neglects the surface structure, it gives good agreement with experimental results. The basal plane of graphite is uniform and flat, and then the surface can be well approximated by the structureless model, agreeing well with the small changes in energy for  $N_2$ -graphite system where gas is adsorbed in different positions of the surface of the graphite crystal. The sites (A), (B), and (C) of graphene shown in Fig. 2.7 have different interaction energies to each other; the positions (A) and (C) give  $-981 \text{ K} \cdot k_b$  and  $-950 \text{ K} \cdot k_b$ , respectively. Those values are close to  $-960 \text{ K} \cdot k_b$  from the 10 – 4 potential, and the difference (maximum  $21 \text{ K} \cdot k_b$ ) is unimportant in supercritical gas adsorption at ambient temperature.

The dependences of the stacking structure on the interaction potential and the corresponding adsorption isotherms are shown in Fig. 2.8a [22]. Here the potential parameters used are as follows:  $\sigma(N_2) = 0.3632 \text{ nm}$ ,  $\sigma(C) = 0.34 \text{ nm}$ ,  $\epsilon(N_2) = 104.2 \text{ K}$ ,  $\epsilon(C) = 28.0 \text{ K}$ ,  $\rho_C = 114.0 \text{ nm}^{-3}$ , and  $\Delta = 0.335 \text{ nm}$ . The potential well depths in  $k_B$  units of  $N_2$  adsorbed on the graphene are  $-961 \text{ K}$  for single-layer graphene,  $-1071 \text{ K}$  for two-layer graphene,  $-1094 \text{ K}$  for three-layer graphene, and  $-1104 \text{ K}$  for graphite. The difference of the interaction potential minimum of graphenes having different layer number is less than  $100 \text{ K}$ . A thinner solid surface is more preferable for fixation of molecules at ambient temperature, because single

**Fig. 2.7** The site dependence of interaction potential energy of an  $N_2$  molecule with graphene. (a) at the center of carbon hexagon, (b) on the intermediate on C-C bond, (c) on the C atom. Here, the ideal graphene plane is depicted by the ball-and-stick model



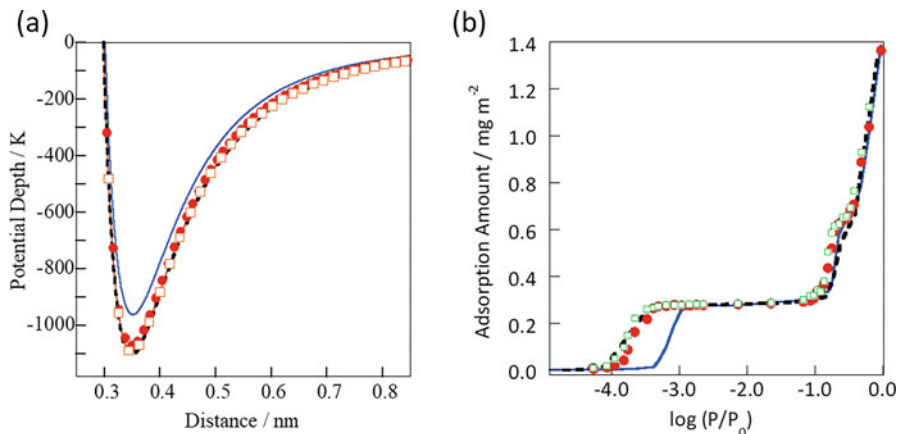


**Fig. 2.8** Interaction potential profiles of  $N_2$  on graphite and graphene of 1–3 layers (a) and  $N_2$  adsorption isotherms at 77 K (b). Solid curves, one-layer graphene; circle symbols, two-layer graphene; square symbols, three-layer graphene; and dashed curves, graphite

wall material has roughly twice the specific surface area of double-wall materials, even though the interaction potential is slightly weaker. Figure 2.8b shows their  $N_2$  adsorption isotherms at 77 K. Here adsorption amount is defined by adsorbed molecules per surface area. The initial uptake relative pressures of the monolayer adsorption are  $10^{-3}$  for one-layer graphene and  $10^{-4}$  for the others; the difference in the uptake relative pressures for more than two layers is only slight. The relative pressure of the second step due to bilayer adsorption is around  $10^{-1}$  for two- and three-layer graphenes and graphite, whereas that of single-layer graphene is larger than others. The relative pressures of bilayer adsorption are less sensitive to the number of graphene layers. As the initial uptake relative pressure measures the strength of physical adsorption, the bilayer graphene-like structure, for example, is a promising candidate structure for gas storage, because it guarantees a strong interaction and large surface area.

Here, we will show the interaction potential of a molecule with slit-shaped graphitic walls of semi-infinite thickness. The inter-wall distance is expressed by the physical width,  $H$ . As the molecule interacts with both graphite walls which are distant from  $z$  and  $H - z$ , respectively, the total interaction potential  $\Phi(z)$  is given by the sum of the interaction potential functions with both graphitic walls (see Eq. 2.23).

$$\Phi(z) = \phi(z) + \phi(H - z) \quad (2.23)$$

As many porous carbons consist of finite graphitic units composed of two to four layers [23], the 10 – 4 – 3 potential is often used for evaluation of  $\Phi(z)$  as a function of the pore width  $w$  experimentally determined. The relationship between the physical pore width  $H$  and  $w$  is given by Eq. 2.24 [24].

$$w = H - (2 \times 0.8506\sigma_{sf} - \sigma_{ff}) \quad (2.24)$$

**Fig. 2.9** Interaction potential profiles of  $N_2$  in a graphitic slit pore of different  $w$  values. The abscissa is the distance of an  $N_2$  molecule from the geometric center of the pore toward the walls

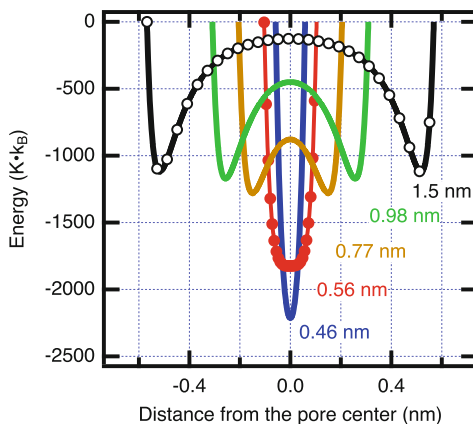


**Fig. 2.10** Dependence of interaction potential depth for  $N_2$  in pores of different shape as a function of the pore width. Porous systems are activated carbon ( $\Delta$ ), SWCNT ( $\square$ ), or fullerene ( $\circ$ )

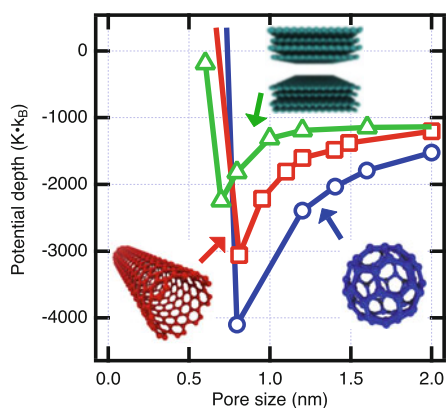


Figure 2.9 shows interaction potential profiles between a graphitic slit-shaped pore and a  $N_2$  molecule. The potential minima in  $k_B$  for  $w = 0.46, 0.56, 0.77, 0.98,$  and  $1.5$  nm were  $-2215, -1825, -1282, -1173,$  and  $-1121$  K, respectively. The potential minimum of the  $1.5$  nm pore is close to that of graphite surface, while the  $0.46$  and  $0.56$  nm pores have very deep interaction potential. The deep interaction potential minimum of micropores leads to a predominant physical adsorption of vapors. Micropores are then excellent candidates even for supercritical gas storage, although we need to apply high pressure on the supercritical gas to increase its adsorbed amount. This interaction potential minimum provides an essential information on designing better storage materials for a target gas.

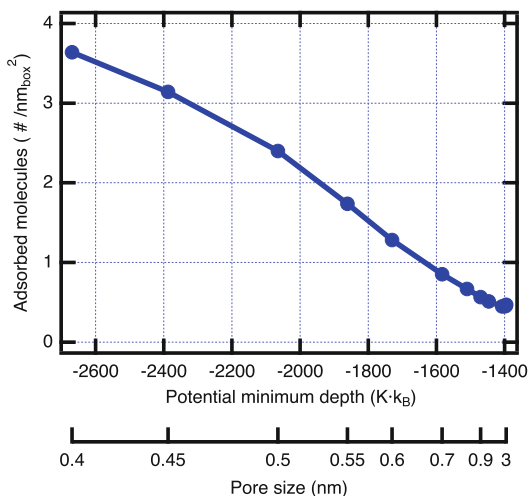
The interaction potential depth is also strongly dependent on the pore geometry. Molecules inside graphitic tubes and cage spaces interact more effectively with these carbon walls than inside the slit-shaped pore, giving a deeper potential interaction well. Ohba et al. (unpublished) evaluated the interaction potential dependence of  $N_2$  confined in the graphitic slit-shaped pore and internal space of SWCNT and fullerene of different pore width (see Fig. 2.10). The pore width of fullerene is defined as the effective diameter of the internal space.

The interaction potential remarkably depends on the pore geometry. Fullerenes with an internal cage space give the deepest interaction potential of the three pore geometries, while the stronger repulsion from the fullerene wall shifts the equilibrium position to a larger value. The strong confinement of molecules within a pore framework structure can induce predominant adsorption from a lower pressure.

The physical adsorption of supercritical methane stems from the deep interaction potential minimum. The interaction potential minimum drops rapidly with the increase of the pore width. Promising porous carbons for supercritical methane storage should be ultramicroporous carbons with a pore width less than about twice of the molecular size. Figure 2.11 shows GCMC simulation results for the relationship between the pore width and adsorption amount of methane at 303 K and 100 kPa. Clearly, the theoretically predicted adsorption amount intensively depends on the pore size. In case of nanoporous carbons, their small micropores can adsorb plenty of supercritical methane; the corresponding vol. % at 3.5 MPa at 303 K is 190 v(STP)/v under the ideal assumption of the complete packing of ACFs [25].

The above discussion can also be applicable to adsorption of other supercritical gases. In general, micropores are promising due to their deep interaction potential minimum. The optimum pore size depends on the molecular size of the target gas. Small mesopores are important for adsorption of larger molecules at a relatively lower temperature, because they guarantee better intrapore diffusion. We discuss these nanoporous materials in this book. The following sections introduce basic science for understanding and designing better nanoporous materials for gas storage as examples of nanoporous carbons.

**Fig. 2.11** Change of adsorption amount of methane with interaction potential minimum and pore width in a slit-shaped graphitic pore at 303 K and 100 kPa



## 2.5 Quasi-Vaporization of Supercritical Gas for Gas Storage

Molecules in the supercritical state do not interact strongly compared with the thermal energy at ambient temperature, as mentioned above. To achieve better gas storage with nanoporous materials, we have to enhance the intermolecular interaction or stability of the target molecules in the surroundings. Vapor can be easily and abundantly adsorbed on nanoporous materials, and thereby we need to convert supercritical gas to the pseudo-vapor, as described later. The pseudo-vaporization is possible by enhancement of intermolecular interactions. Another approach is to introduce an enhanced pressure near the surface. Since gas storage increases by raising the gas pressure, the higher pressure shift of the effective pressure near the surface can increase the adsorption amount. The enhanced pressure effect can be derived by the increased molecule-solid interaction aided by a partial chemisorption effect.

### 2.5.1 Importance of Enhanced Intermolecular Interactions

Intermolecular interaction forms the so-called van der Waals molecules at lower temperature. The van der Waals molecules are not bound by the chemical bonding but mainly by dispersion and electrostatic interactions. The stabilization energies of van der Waals molecules are not so large except for water and water-associated dimers:  $(\text{H}_2)_2$ , 0.43 kJ/mol [26];  $(\text{N}_2)_2$ , 1.2 kJ/mol [26];  $\text{N}_2 \cdot \text{H}_2\text{O}$ , 7 kJ/mol [26];  $(\text{H}_2\text{O})_2$ , 29 kJ/mol [26];  $(\text{CO}_2)_2$ , 5.4 kJ/mol [27];  $(\text{O}_2)_2$ , 0.9–1.0 kJ/mol [9, 28];  $(\text{NO})_2$ , 6.7 kJ/mol [9]; and  $(\text{CH}_4)_2$ , 1.5 kJ/mol [29].

The stabilization energy depends on mutual orientation of molecules. For example, a  $\text{CO}_2$  dimer of a staggered side-by-side form is slightly stable compared with its T-shaped dimer [27]. The quadrupole moment plays an important role in the most stable dimer form (T-shaped configuration for  $(\text{N}_2)_2$  and parallel configuration for  $(\text{O}_2)_2$ ) [28]. When the stabilization energy of the dimer is close to or larger than the thermal energy at ambient temperature (2.5 kJ/mol), the dimerization can enhance the dimer-surface interaction. Hence  $\text{CO}_2$  and  $\text{NO}$  are quite promising to increase their adsorption on nanoporous materials at ambient temperature through the dimerization. Even  $\text{CH}_4$ ,  $\text{N}_2$ , and  $\text{O}_2$  have such possibility. The water-associated dimer will be discussed in Chap. 14. Here the dimerization-associated adsorption of supercritical  $\text{NO}$  and  $\text{N}_2$  will be discussed.

$\text{NO}$  is a paramagnetic molecule, and it forms its dimer in the liquid state at low temperature, exhibiting diamagnetism [30]; the dimer should be the vapor in the equilibrium with  $\text{NO}$  liquid. The critical temperature of  $\text{NO}$  is 180 K, and thereby it is quite difficult to adsorb enough supercritical  $\text{NO}$  at an ambient temperature. If we enhance the dimerization of  $\text{NO}$  molecules with the aid of the magnetic interaction,  $\text{NO}$  should lose the supercritical nature even at room temperature and behave as if it were a vapor. Once supercritical  $\text{NO}$  converts to “quasi-vapor” through dimerization, we can adsorb it easily on nanoporous materials. Kaneko et al. [31–33] dispersed iron oxide particles having a specific magnetism on the external

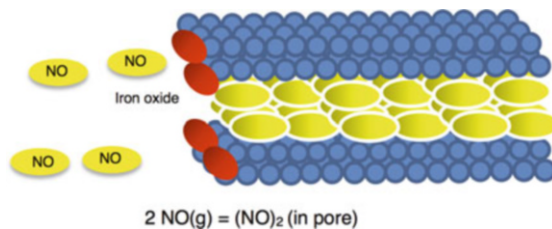
surface of activated carbon fibers. NO molecules were dimerized through the magnetic interaction between NO and the iron oxide, to be fully adsorbed in carbon nanopores, as illustrated in Fig. 2.12. The magnetic susceptibility measurement showed almost perfect dimerization for the adsorption of NO in carbon nanopores. The absolute adsorption amount of NO on the iron oxide dispersed activated carbon fiber at 303 K was more than 300 mg/g, and a marked adsorption hysteresis was observed. The strongly adsorbed NO in the carbon pores can be completely desorbed under ultrahigh vacuum at ambient temperature. Consequently, NO is not chemisorbed.

This anomalous dimerization of NO at ambient temperature was also evidenced in the case of single wall carbon nanotubes by infrared spectroscopy [34], indicating intensive high-pressure effect for NO molecules confined in nanopores [35]. Turner et al. [36] theoretically studied this high-pressure effect, and Srivastava et al. [37] revised it, considering that a weak chemical bond of NO with the carbon wall can explain the above experimental results.

High-pressure N<sub>2</sub> adsorption study on activated carbon fibers of different pore widths of 0.8–1.5 nm suggests the formation of (N<sub>2</sub>)<sub>2</sub> in carbon nanopores [38]. They obtained the cooperative energy of 4 kJ/mol between N<sub>2</sub> molecules inside carbon nanopores under compression by the external high pressure and intensive molecule-pore interaction; a cooperative interaction energy of 4 kJ/mol was larger than the dimerization energy of 1.2 kJ/mol, suggesting the presence of (N<sub>2</sub>)<sub>2</sub> in carbon nanopores even at ambient temperature. (N<sub>2</sub>)<sub>2</sub> inside nanopores of strong interaction potential may be regarded as a quasi-vapor [38]. The stabilized N<sub>2</sub> dimers should form the clusters in pores under the high pressure.

The density fluctuation of supercritical gas molecules, which is associated with the cluster formation, can be evaluated by use of in situ high-pressure small-angle X-ray scattering (SAXS). Ohba et al. [39] applied grand canonical Monte Carlo (GCMC) simulation-aided in situ high-pressure SAXS to supercritical CH<sub>4</sub> adsorption on ACFs. They analyzed the SAXS data with Ornstein-Zernike theory to determine an approximated scale of the heterogeneous structure of electron density, being the cluster size, and the density fluctuation of molecules which gives the cluster number; the cluster formation ratio is 0.6–0.8 and cluster size is 0.5 nm for CH<sub>4</sub> adsorbed in 0.6 nm pores below 10 MPa.

**Fig. 2.12** Enhanced NO dimerization model for iron-oxide-modified entrance of a carbon micropore



### 2.5.2 Simple Analysis of Quasi-vaporized Supercritical Gases

The adsorption isotherm of a vapor in nanopores can be well described by the phenomenological Dubinin-Radushkevich (DR) equation (Eq. 2.25):

$$W/W_0 = \exp \left[ - (A/E)^2 \right], \quad A = RT \ln(P_0/P), \quad E = \beta E_0 \quad (2.25)$$

Here  $W$  is the adsorbed amount at  $P/P_0$ ,  $W_0$  the limiting amount of adsorption, which often corresponds to the micropore volume,  $E_0$  the characteristic adsorption energy, and  $\beta$  the affinity coefficient.  $\beta E_0$  can be associated with the isosteric heat of adsorption,  $q_{st, \Phi=1/e}$ , at the fractional filling  $\Phi = e^{-1}$  (about 0.368) using the enthalpy of vaporization  $\Delta H_V$  at the boiling point.

$$q_{st, \Phi=1/e} = \Delta H_V + \beta E_0 \quad (2.26)$$

This DR plot analysis of the vapor adsorption isotherm is quite useful for evaluation of the limiting adsorption amount and isosteric heat of adsorption at intermediate fillings. To develop better nanoporous materials for a target supercritical gas, the description of the high-pressure gas adsorption isotherm through a simple adsorption equation and evaluation of isosteric heat of adsorption is indeed convenient. If the high-pressure gas adsorption isotherm can be described by the classical Langmuir equation, providing the saturated adsorption amount  $W_L$ , we can apply the quasi-vapor concept to the supercritical gas adsorption isotherm. Gas molecules strongly interact with pores to form a considerably dense structure through dimerization and/or cluster formation, as mentioned above. The higher-density adsorbed layer should be in equilibrium with the quasi-vapor in the pore. The maximum amount of the higher-density adsorbed layer of the supercritical gas is determined by the molecule-pore interaction whose details will be described in Chap. 3. The filling  $W/W_L$  of the pore spaces with supercritical gas at an equilibrium pressure depends on the molecule-pore interaction potential  $\Phi(H/2)_p$ , as given in Eq. 2.27 [40].

$$RT \cdot \ln(W_L/W) = \Phi(H/2)_p + U^{CO} \quad (2.27)$$

$W_L$  is the inherent micropore volume, which has enough strong interaction potential to adsorb a supercritical gas in the pore at the adsorption temperature through quasi-vaporization.  $H$  is the internuclear distance (physical width) of the opposite pore walls, and  $U^{CO}$  is the additional potential energy due to pre-adsorbed molecules. Then, supercritical gas in the in-pore potential field can be regarded as a vapor. Kaneko et al. [38] extended the DR equation for quasi-vaporized supercritical gases (Eq. 2.28).

$$\sqrt{\ln(W_L/W)} = \frac{RT}{\beta E_0} (\ln P_{0q} - \ln P) \quad (2.28)$$

Here,  $P_{0q}$  is the quasi-saturated vapor pressure which depends on the gas-pore interaction. It corresponds to the saturated vapor pressure  $P_0$  for a vapor, although the  $P_0$  of a real supercritical gas is not defined. A linear  $\sqrt{\ln(W_L/W)}$  vs.  $\ln P$  plot leads to  $P_{0q}$  and  $q_{st, \phi=1/e}$  through Eq. 2.26. Smaller  $P_{0q}$  indicates that the pores are fit for adsorption of a target supercritical gas. Thus, both  $P_{0q}$  and  $q_{st, \phi=1/e}$  are used to design better nanoporous materials for target gas storage [31, 38].

The importance of  $P_{0q}$  must be clarified. In the description of real gases, a reduced equation of state can be obtained with the aid of the reduced pressure ( $P_r = P/P_c$ ), reduced volume ( $V_r = V_m/V_c$ ), and reduced temperature ( $T_r = T/T_c$ ), where the  $r$  and  $c$  subscripts indicate reduced and critical, respectively [41]. If the concept of the  $P_{0q}$  is correct, we can obtain a reduced adsorption isotherm with the filling fraction  $W/W_L$  and  $P/P_{0q}$ .

This is illustrated in Fig. 2.13 for nanoporous carbon which have different methane adsorption isotherms (Fig. 2.13a). These isotherms were analyzed with the extended DR equation, providing the  $P_{0q}$  values. The reduced methane adsorption isotherm is plotted in Fig. 2.13b. All five reduced methane adsorption isotherms almost overlap each other, indicating the validity of the concept of  $P_{0q}$ ; supercritical methane should be converted to quasi-vaporized methane in the dispersion interaction-dominated potential field of nanopores.

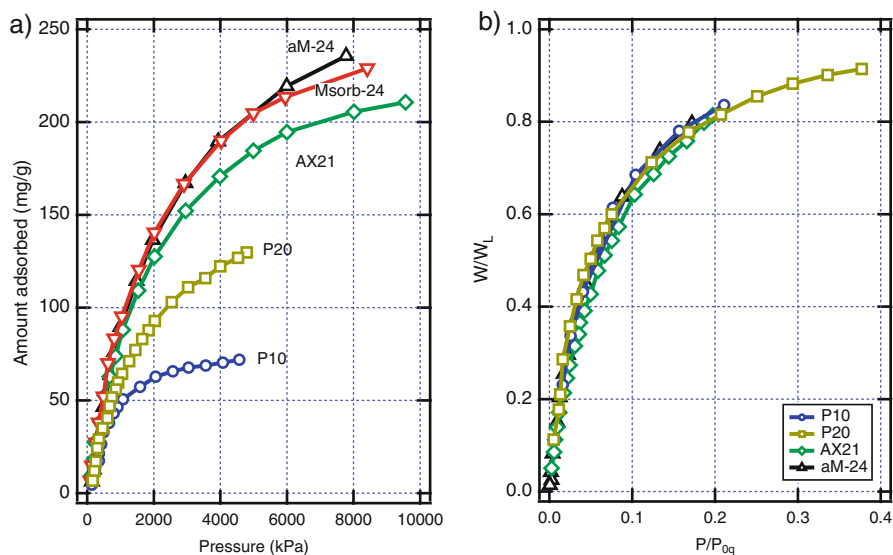


**Fig. 2.13** (a) Methane adsorption isotherms of nanoporous carbons whose pore width and surface area are in the range of 0.8–1.6 nm and 1140–2400  $\text{m}^2/\text{g}$  at 303 K and (b) their reduced adsorption isotherm. (Reproduced by permission from Springer Nature Terms and Conditions for RightsLink Permissions Springer Customer Service Centre GmbH: Springer Nature Adsorption [40], ©Kluwer Academic Publishers 1997)

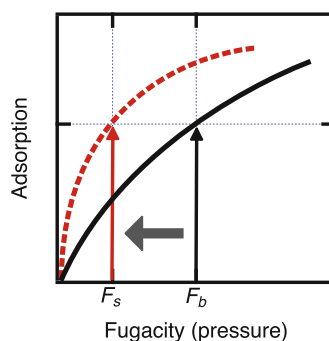
### 2.5.3 Surface Enrichment-Induced Enhancement of Supercritical Gas Adsorption

We can use inherent properties of a target gas molecule for its storage. If the molecules form the van der Waals molecule, we need to enhance the van der Waals molecule formation for better gas storage, as mentioned above. Another route for increasing the intermolecular interaction of target molecules relies on the enrichment of target molecules on the nanoporous materials.

The adsorbed amount increases with the gas pressure. The surface enrichment brings about the upward pressure shift of the gas. Figure 2.14 illustrates an effective equilibrium pressure shift by surface enrichment. If the surface-molecule interaction is enhanced, the concentration of gaseous molecules increases, and then effective pressure near solid surfaces becomes larger than that of bulk pressure: when the bulk pressure is  $F_b$ , the effective pressure near the solid surface is  $F_s$ , as shown in Fig. 2.14. Consequently, we can store more supercritical gas at a lower pressure  $F_s$  compared to storage without the surface enrichment effect.

Methane shows a weak acidity, and it is expected that methane molecules prefer basic surfaces. Kaneko et al. [42] dispersed fine MgO particles on the external surface of ACF, because the dispersion of MgO does not decrease the surface area, and the average pore width almost remains constant. Therefore, we can expect a marked enrichment of methane molecules near the basic MgO-dispersed carbon surface. The saturated methane adsorption of MgO-dispersed ACF is 1.5 times larger than that of ACF without MgO dispersion. The extended DR plots are linear, leading to similar  $q_{st, \phi=1/e}$  values (17.6 kJ/mol for MgO-dispersed ACF, 17.1 kJ/mol for ACF without MgO), which are larger than the heat of vaporization of bulk methane (8.2 kJ/mol). The difference of 9 kJ/mol between adsorbed methane and bulk methane is caused by the methane-pore dispersion interaction. Thus, dispersion of basic MgO nanoparticles is effective for enhancement of supercritical methane adsorption; this base-acid interaction-assisted micropore filling can be useful to increase the adsorptivity for supercritical gas.

**Fig. 2.14** Effective equilibrium pressure shift by surface enrichment.  $F_b$  and  $F_s$  are bulk and surface fugacities, respectively



### 2.5.4 Clathrate Formation-Mediated Adsorption of Supercritical Gas

Water molecules form hydrogen-bonding network mainly by electrostatic interactions, as mentioned above. Then the hydrogen-bonding network has collectively a neutral nature, which can form a clathrate compound with a neutral molecule such as Xe, H<sub>2</sub>, CO<sub>2</sub>, and CH<sub>4</sub>. Methane hydrates are the most representative, being a promising resource for clean energy. The detailed discussion will be given later in Chap. 14. Clathrate formation-associated adsorption can be induced without hydrogen-bonded network formation. A flexible crystal lattice can distort to accept gas molecules and form clathrates. This is a special case of thermodynamically confirmed absorption. The completion of the Clausius-Clapeyron equation assures the gas-liquid equilibrium of pure materials. van der Waals and Platteuw [43] showed that the Clausius-Clapeyron equation can be applied to binary systems. Cu-based MOF (ELM-11) shows the so-called gate adsorption for CO<sub>2</sub> and CH<sub>4</sub>, as mentioned above. The adsorption isotherms of supercritical CH<sub>4</sub> on ELM-11 at different temperatures are shown in Fig. 2.15 [18]. The adsorption and desorption isotherms both have sharp jumps at defined pressures. This gate absorption of CH<sub>4</sub> comes from clathrate formation between itself and ELM-11, described by the following chemical equilibrium (Eq. 2.29):

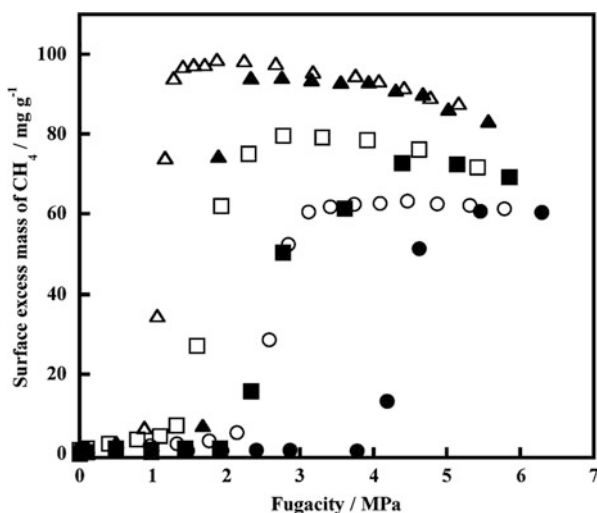
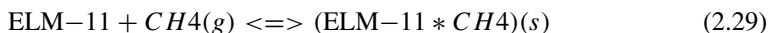


**Fig. 2.15** High-pressure adsorption isotherms of supercritical CH<sub>4</sub> on ELM-11: (●) 303 K, (■) 273 K, and (▲) 258 K. Closed symbol, adsorption; open symbol, desorption. (Reprinted with permission from Ref. [10]. Copyright ©2005 American Chemical Society)

Here, (ELM-11 \* CH<sub>4</sub>)(s) is a new clathrate compound of ELM-11 and CH<sub>4</sub>. We can apply the Clausius-Clapeyron equation after van der Waals and Platteeuw [43]. The gate pressure is assumed to be the vapor pressure of the clathrate compound (ELM-11 \* CH<sub>4</sub>)(s). Also, the volume change  $\Delta V$  can be approximated by  $\Delta V = V(CH_4) = zRT/P$ , where  $z$  is the compressibility factor. Then, the following Clausius-Clapeyron equation is obtained. Here,  $\Delta H_f$  is the enthalpy change of the clathrate formation. As to the desorption branch, the corresponding enthalpy change of the clathrate dissociation  $\Delta H_d$  is defined.

$$\frac{d \ln P}{d(1/T)} = \frac{-\Delta H_f}{zR} \quad (2.30)$$

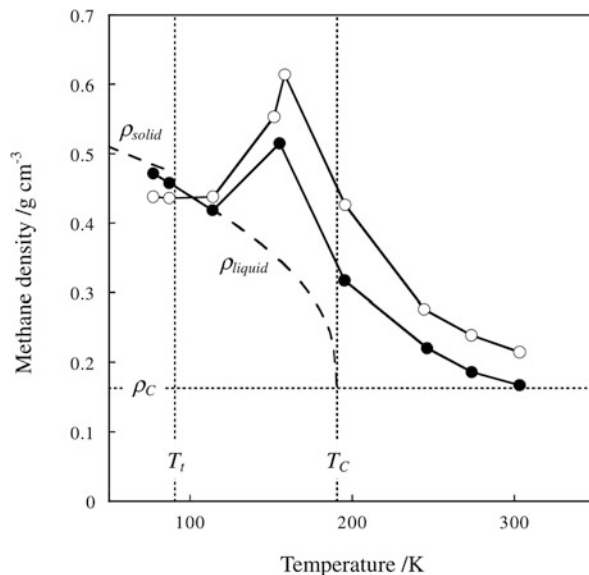
The slope of the logarithm of the gate pressure against the reciprocal temperature gives the linear relation. The calculation results in  $\Delta H_f = 13 \pm 1$  kJ/mol and  $\Delta H_d = 12.5 \pm 2$  kJ/mol. It is thus probable that absorption of supercritical gas on a flexible porous solid stems from the clathrate compound formation.

## 2.6 In-Pore Phase Diagram

The nature of supercritical gases inhibits their sufficient storage by physical adsorption. We show that even supercritical gas can be modified to have a vapor-like nature through enhanced intermolecular and/or molecule-surface interactions. Recent studies show that confinement of atoms, molecules, and ultrafine solids gives unique phase formation. High-pressure phase *KI* above 1.9 GPa is formed inside single wall carbon nanohorns (SWCNH) in vacuo [44]. In vacuo confinement of sulfur atoms inside single wall carbon nanotubes (SWCNT) or double wall carbon nanotubes produces an atomically 1D sulfur chain structure with metallic properties, which is only possible under intensive compression with >90 GPa for bulk sulfur [45]. These results support the presence of unique phase under highly confined situation even more evidently than the NO dimerization mentioned above. The formation of N<sub>2</sub> dimer and CH<sub>4</sub> clusters in nanopores under high-pressure conditions at ambient temperature also suggests the phase equilibrium between quasi-vapor and “adsorbed quasi-vapor” in nanopores. Thus, we can say that confinement of supercritical gases in nanopores phenomenologically induces the depression of the critical temperature. Miyawaki and Kaneko [46] examined the density change of methane adsorbed in slit-shaped carbon nanopores whose widths are 0.7 and 1.1 nm (see Fig. 2.16).

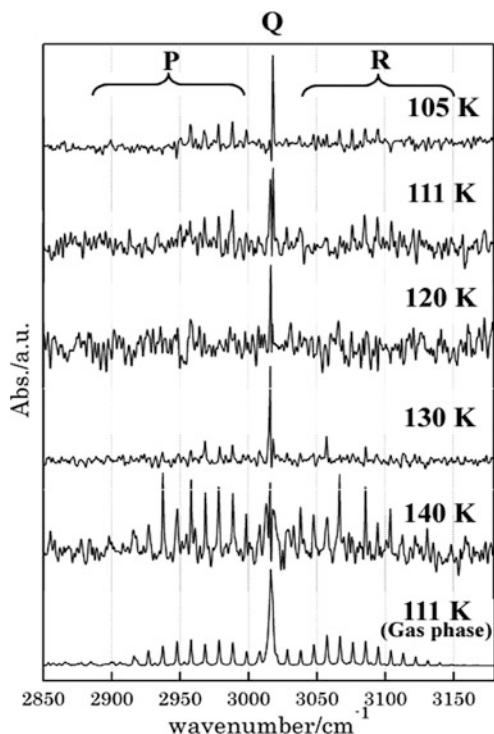
Figure 2.16 shows the temperature dependences of solid and liquid methane densities adsorbed in nanopores. The triple point  $T_{tr}$ , critical temperature  $T_c$  (190.5 K), and critical density  $\rho_c$  of bulk methane are shown in dotted lines in Fig. 2.16. The solid and liquid densities of bulk methane gradually decrease by

**Fig. 2.16** Temperature dependence of densities of solid, liquid, and methane adsorbed in slit-shaped carbon nanopores. Pore width:  $\circ$ , 0.7 nm;  $\bullet$ , 1.1 nm. (Reprinted from Ref. [46], Copyright (2001), with permission from Elsevier B.V.)



raising the temperature. On the contrary, the adsorbed methane density has a maximum around 156 K, below  $T_c$ , being much larger than the bulk liquid: the maximum density of methane adsorbed in the 0.7 nm pores is 1.8 times larger than the bulk liquid density, whereas that in the 1.2 nm pores is 1.5 times larger. Even the adsorbed methane density around  $T_c$  is 2 – 2.5 times larger than  $\rho_c$ , approaching to  $\rho_c$  above 300 K. In the critical state, methane adsorbed in the carbon pores must have the density same as  $\rho_c$ , and the critical temperature of adsorbed methane then shifts by more than 110 K, depending on the confinement in the pores. We can assume the presence of a quasi-vapor state of supercritical gas in nanopores, which is consistent with the previous discussion. In micropores having a deep interaction potential field for supercritical methane, there should be quasi-vapor of methane (quasi-vapor phase) and adsorbed methane (organized phase) in equilibrium with each other. Although phases must be described thermodynamically, molecular level understanding of gas molecules confined in pores is indispensable. Molecular spectroscopic methods cannot be applied to ordinary porous carbons due to strong absorption and scattering of light. However, light penetrates single wall carbon tubular structures and single wall carbon nanohorns due to their single graphene structure. The FT-IR measurement of methane adsorbed inside SWCNH is possible around melting temperature of bulk methane. SWCNH has a tubular structure of 2–6 nm width. We can use open and close SWCNH samples and calculate their difference spectrum which leads to the IR spectrum of methane inside the tubular spaces. Figure 2.17 shows the temperature dependence of IR spectra of methane adsorbed inside the tubular spaces of SWCNH at 120 K and  $P/P_0 = 0.1$ ; the tubular spaces are fully filled with methane at  $P/P_0 = 0.1$  at 120 K. Although the spectrum of bulk methane at 140 K exhibits a representative rotation-vibration structure of

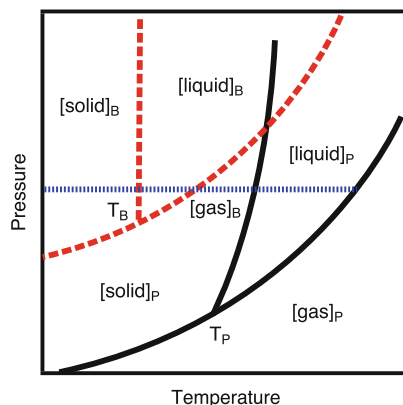
**Fig. 2.17** IR spectra of methane adsorbed inside SWCNH at  $P/P_0 = 0.1$  over the temperature range of 105–140 K. (Reprinted from Refs. [47], Copyright (2011) American Chemical Society)



P, Q, and R branches, the regular rotation-vibration structure is not observed for methane adsorbed inside SWCNH over the temperature range of 105–140 K. Consequently, the rotational motion of methane inside SWCNH is strongly perturbed below 140 K, although the irregular rotational structure is observed at 130 K and 140 K. The P and R branches of the spectrum at 120 K are almost nil, and only the Q branch is observed. Then, the rotational motion of methane molecules is highly restricted in nanoscale tubular spaces. The boiling point of the methane adsorbed inside SWCNH should be higher than 140 K [47]. The molecular-level information also suggests the upper shift of the phase transition temperature of the confined methane.

Miyahara and Gubbins [48] theoretically studied solid-liquid phase transition of Lennard-Jones methane in the slit-shaped pore by GCMC simulation. According to their study, the freezing points depend on the attractive interaction potential energy with the pore wall, inducing elevation of the freezing point for strong interaction and depression for weak interaction. The elevation of the freezing point of adsorbed molecules in micropores with surface force [49] and differential scanning calorimetry [50] measurements are reported, although adsorbed molecules were larger than methane. Thus, supercritical gas adsorbed in nanoscale pores has a phase diagram different from the bulk. Kanda et al. [51, 52] extended this approach

**Fig. 2.18** Qualitative illustration of phase diagram change with nanoconfinement. Subindexes B and P denote bulk and in-pore, respectively



to other phase boundaries, indicating the boundary shift of confined Lennard-Jones fluids. These studies suggest a downward shift of the phase boundaries of confined fluids in the pressure-temperature diagram (see Fig. 2.18). The molecule-pore interaction stabilizes molecular assembly structures inside the pores, and thereby, a bulk phase which is stable at high pressure can also be formed inside the pore at a lower pressure. This is associated with the discussed in-pore high-pressure effect. However, the discussion on phase boundary shift must be done carefully, since the phase stability must be rigorously described by statistical thermodynamics. In particular, a theoretical study on critical point of confined fluids is not easily concluded [53, 54].

**Acknowledgements** This is supported by the Grant-in-Aid for Scientific Research (B) (17H03039) and the OPERA project from JST.

## References

1. van der Waals JH (1873) Over de continuïteit van den gas- en vloeistofoestand. Ph.D. thesis, A.W. Sijthoff, Leiden. <https://trove.nla.gov.au/version/38392625>
2. Walton AJ (1976) Three phases of matter. McGraw-Hill, New York
3. Callen HB (1985) Thermodynamics and an introduction to thermostatistics. Wiley, New York. google-Books-ID: XJ0RAQAIAAJ
4. Potoff JJ, Siepmann JI (2001) Vapor-liquid equilibria of mixtures containing Alkanes, carbon dioxide, and nitrogen. *AIChE J* 47(7):1676–1682. <https://doi.org/10.1002/aic.690470719>
5. Dymond JH, Smith EB (1980) The virial coefficients of pure gases and mixtures: a critical compilation. Clarendon Press, Oxford. google-Books-ID: vAHwAAAAMAAJ
6. Barrie PJ (2005) Javascript programs to calculate thermodynamic properties using cubic equations of state. *J Chem Educ* 82(6):958. <https://doi.org/10.1021/ed082p958>
7. Peng DY, Robinson DB (1976) A new two-constant equation of state. *Ind Eng Chem Fundam* 15(1):59–64. <https://doi.org/10.1021/i160057a011>
8. Vallejos-Burgos F, Coudert FX, Kaneko K (2018) Air separation with graphene mediated by nanowindow-rim concerted motion. *Nat Commun* 9(1):1812. <https://doi.org/10.1038/s41467-018-04224-6>

9. Maitland GC (1981) Intermolecular forces: their origin and determination. Clarendon Press, Oxford. google-Books-ID: qhHwAAAAAAAJ
10. Noguchi H, Kondoh A, Hattori Y, Kanoh H, Kajiro H, Kaneko K (2005) Clathrate-formation mediated adsorption of methane on Cu-Complex crystals. *J Phys Chem B* 109(29):13851–13853. <https://doi.org/10.1021/jp052515o>
11. Hirschfelder JO, Curtiss CF, Bird RB, Laboratory UoWTC (1954) Molecular theory of gases and liquids. Wiley, Hoboken, google-Books-ID: HQtRAAAAMAAJ
12. Cho M, Silbey RJ (1996) Suppression and enhancement of van der Waals interactions. *J Chem Phys* 104(21):8730–8741. <https://doi.org/10.1063/1.471562>
13. Brunauer S (1943) The adsorption of gases and vapors: physical adsorption. Princeton University Press, Princeton
14. Rouquerol J, Rouquerol F, Llewellyn P, Maurin G, Sing KSW (2013) Adsorption by powders and porous solids: principles, methodology and applications, 2nd edn. Academic, New York
15. Hattori Y, Kaneko K, Ohba T (2013) 5.02 – Adsorption properties. In: Reedijk J, Poepelmeier K (eds) *Comprehensive inorganic chemistry II*, 2nd edn. Elsevier, pp. 25–44. <https://doi.org/10.1016/B978-0-08-097774-4.00502-7>. <http://www.sciencedirect.com/science/article/pii/B9780080977744005027>
16. Kaneko K, Matsumoto A (1989) The role of surface defects in the chemisorption of nitric oxide and sulfur dioxide on variable-sized crystalline  $\alpha$ -iron hydroxide oxide. *J Phys Chem* 93(24):8090–8095. <https://doi.org/10.1021/j100361a023>
17. Liu R, Gong T, Zhang K, Lee C (2017) Graphene oxide papers with high water adsorption capacity for air dehumidification. *Sci Rep* 7(1):9761. <https://doi.org/10.1038/s41598-017-09777-y>
18. Kondo A, Noguchi H, Ohnishi S, Kajiro H, Tohdoh A, Hattori Y, Xu WC, Tanaka H, Kanoh H, Kaneko K (2006) Novel expansion/shrinkage modulation of 2D layered MOF triggered by clathrate formation with CO<sub>2</sub> molecules. *Nano Lett* 6(11):2581–2584. <https://doi.org/10.1021/nl062032b>
19. Li D, Kaneko K (2001) Hydrogen bond-regulated microporous nature of copper complex-assembled microcrystals. *Chem Phys Lett* 335(1):50–56. [https://doi.org/10.1016/S0009-2614\(00\)01419-6](https://doi.org/10.1016/S0009-2614(00)01419-6)
20. Lototskyy MV, Yartys VA, Pollet BG, Bowman RC (2014) Metal hydride hydrogen compressors: a review. *Int J Hydrog Energy* 39(11):5818–5851. <https://doi.org/10.1016/j.ijhydene.2014.01.158>
21. Steele WA (1973) The physical interaction of gases with crystalline solids: I. Gas-solid energies and properties of isolated adsorbed atoms. *Surf Sci* 36(1):317–352. [https://doi.org/10.1016/0039-6028\(73\)90264-1](https://doi.org/10.1016/0039-6028(73)90264-1)
22. Ohba T, Takase A, Ohyama Y, Kanoh H (2013) Grand canonical monte carlo simulations of nitrogen adsorption on graphene materials with varying layer number. *Carbon* 61:40–46. <https://doi.org/10.1016/j.carbon.2013.04.061>
23. Kaneko K, Ishii C, Ruike M, Kuwabara H (1992) Origin of superhigh surface area and microcrystalline graphitic structures of activated carbons. *Carbon* 30(7):1075–1088. [https://doi.org/10.1016/0008-6223\(92\)90139-N](https://doi.org/10.1016/0008-6223(92)90139-N)
24. Kaneko K, Cracknell RF, Nicholson D (1994) Nitrogen adsorption in slit pores at ambient temperatures: comparison of simulation and experiment. *Langmuir* 10(12):4606–4609. <https://doi.org/10.1021/la00024a036>
25. Rejifu A, Noguchi H, Ohba T, Kanoh H, Rodriguez-Reinoso F, Kaneko K (2009) Adsorptivities of extremely high surface area activated carbon fibres for CH<sub>4</sub> and H<sub>2</sub>. *Adsorpt Sci Technol* 27(9):877–881. <https://doi.org/10.1260/0263-6174.27.9.877>
26. Hobza P, Zahradnk R (1988) Intermolecular complexes: the role of van der Waals systems in physical chemistry and in the biodisciplines. Elsevier, Amsterdam. google-Books-ID: kQjwAAAAAAAJ
27. Illies AJ, McKee ML, Schlegel HB (1987) Ab initio study of the carbon dioxide dimer and the carbon dioxide ion complexes [(CO<sub>2</sub>)<sup>2+</sup> and (CO<sub>2</sub>)<sup>3+</sup>]. *J Phys Chem* 91(13):3489–3494. <https://doi.org/10.1021/j100297a007>

28. Blaney BL, Ewing GE (1976) Van der Waals molecules. *Ann Rev Phys Chem* 27(1):553–584. <https://doi.org/10.1146/annurev.pc.27.100176.003005>
29. Rappé AK, Bernstein ER (2000) Ab initio calculation of nonbonded interactions: are we there yet? *J Phys Chem A* 104(26):6117–6128. <https://doi.org/10.1021/jp0008997>
30. Smith AL, Johnston HL (1952) The magnetic susceptibility of liquid nitric oxide and the heat of dissociation of (NO)<sub>2</sub>. *J Am Chem Soc* 74(18):4696–4698. <https://doi.org/10.1021/ja01138a073>
31. Kaneko K (1987) Anomalous micropore filling of nitric oxide on  $\alpha$ -iron hydroxide oxide-dispersed activated carbon fibers. *Langmuir* 3(3):357–363. <https://doi.org/10.1021/la00075a014>
32. Kaneko K, Fukuzaki N, Ozeki S (1987) The concentrated NO dimer in micropores above room temperature. *J Chem Phys* 87(1):776–777. <https://doi.org/10.1063/1.453579>
33. Kaneko K, Fukuzaki N, Kakei K, Suzuki T, Ozeki S (1989) Enhancement of nitric oxide dimerization by micropore fields of activated carbon fibers. *Langmuir* 5(4):960–965. <https://doi.org/10.1021/la00088a014>
34. Byl O, Kondratyuk P, Yates JT (2003) Adsorption and dimerization of NO inside single-walled carbon nanotubes infrared spectroscopic study. *J Phys Chem B* 107(18):4277–4279. <https://doi.org/10.1021/jp022565i>
35. Imai J, Souma M, Ozeki S, Suzuki T, Kaneko K (1991) Reaction of dimerized NO<sub>x</sub> (x = 1 or 2) with sulfur dioxide in a restricted slit-shaped micropore space. *J Phys Chem* 95(24):9955–9960. <https://doi.org/10.1021/j100177a064>
36. Turner CH, Johnson JK, Gubbins KE (2001) Effect of confinement on chemical reaction equilibria: the reactions 2NO=(NO)<sub>2</sub> and N<sub>2</sub>+3H<sub>2</sub>=2NH<sub>3</sub> in carbon micropores. *J Chem Phys* 114(4):1851–1859. <https://doi.org/10.1063/1.1328756>
37. Srivastava D, Turner CH, Santiso EE, Gubbins KE (2017) The nitric oxide dimer reaction in carbon nanopores. *J Phys Chem B*. <https://doi.org/10.1021/acs.jpcc.7b10876>
38. Kaneko K, Shimizu K, Suzuki T (1992) Intrapore field dependent micropore filling of supercritical N<sub>2</sub> in slit shaped micropores. *J Chem Phys* 97(11):8705–8711. <https://doi.org/10.1063/1.463389>
39. Ohba T, Omori T, Kanoh H, Kaneko K (2004) Cluster structures of supercritical CH<sub>4</sub> confined in carbon nanospaces with in situ high-pressure small-angle X-ray scattering and grand canonical monte carlo simulation. *J Phys Chem B* 108(1):27–30. <https://doi.org/10.1021/jp0363646>
40. Kaneko K, Murata K (1997) An analytical method of micropore filling of a supercritical gas. *Adsorption* 3(3):197–208. <https://doi.org/10.1007/BF01650131>
41. Atkins P, Paula Jd, Keeler J (2018) *Atkins physical chemistry*. Oxford University Press, Oxford. google-Books-ID: 3QpDDwAAQBAJ
42. Kaneko K, Murata K, Shimizu K, Camara S, Suzuki T (1993) Enhancement effect of micropore filling for supercritical methane by magnesia dispersion. *Langmuir* 9(5):1165–1167. <https://doi.org/10.1021/la00029a001>
43. van der Waals JH, Platteeuw JC (1958) *Clathrate solutions*. Wiley, pp 1–57. <https://doi.org/10.1002/9780470143483.ch1>, <http://onlinelibrary.wiley.com/doi/10.1002/9780470143483.ch1/summary>
44. Urita K, Shiga Y, Fujimori T, Iiyama T, Hattori Y, Kanoh H, Ohba T, Tanaka H, Yudasaka M, Iijima S et al (2011) Confinement in carbon nanospace-induced production of KI nanocrystals of high-pressure phase. *J Am Chem Soc* 133(27):10344–10347. <https://doi.org/10.1021/ja202565r>
45. Fujimori T, Morelos-Gomez A, Zhu Z, Muramatsu H, Futamura R, Urita K, Terrones M, Hayashi T, Endo M, Young Hong S et al (2013) Conducting linear chains of sulphur inside carbon nanotubes. *Nat Commun* 4:2162. <https://doi.org/10.1038/ncomms3162>
46. Miyawaki J, Kaneko K (2001) Pore width dependence of the temperature change of the confined methane density in slit-shaped micropores. *Chem Phys Lett* 337(4):243–247. [https://doi.org/10.1016/S0009-2614\(01\)00225-1](https://doi.org/10.1016/S0009-2614(01)00225-1)

47. Hashimoto S, Fujimori T, Tanaka H, Urita K, Ohba T, Kanoh H, Itoh T, Asai M, Sakamoto H, Niimura S et al (2011) Anomaly of CH<sub>4</sub> molecular assembly confined in single-wall carbon nanohorn spaces. *J Am Chem Soc* 133(7):2022–2024. <https://doi.org/10.1021/ja1086886>
48. Miyahara M, Gubbins KE (1997) Freezing/melting phenomena for Lennard-Jones methane in slit pores: a monte carlo study. *J Chem Phys* 106(7):2865–2880. <https://doi.org/10.1063/1.473415>
49. Klein J, Kumacheva E (1995) Confinement-induced phase transitions in simple liquids. *Science* 269(5225):816–819. <https://doi.org/10.1126/science.269.5225.816>
50. Kaneko K, Watanabe A, Iiyama T, Radhakrishnan R, Gubbins KE (1999) A remarkable elevation of freezing temperature of CCl<sub>4</sub> in graphitic micropores. *J Phys Chem B* 103(34):7061–7063. <https://doi.org/10.1021/jp9907692>
51. Kanda H, Miyahara M (2007) Sublimation phenomena of Lennard-Jones fluids in slit nanopores. *J Chem Phys* 126(5):054703. <https://doi.org/10.1063/1.2434152>
52. Kanda H, Miyahara M (2007) Freezing of Lennard-Jones fluid in cylindrical nanopores under tensile conditions. *Adsorption* 13(3–4):191–195. <https://doi.org/10.1007/s10450-007-9066-9>
53. Fisher ME, Nakanishi H (1981) Scaling theory for the criticality of fluids between plates. *J Chem Phys* 75(12):5857–5863. <https://doi.org/10.1063/1.442035>
54. Nakanishi H, Fisher ME (1983) Critical point shifts in films. *J Chem Phys* 78(6):3279–3293. <https://doi.org/10.1063/1.445087>

# Chapter 3

## Fundamental Science of Gas Storage



Tomonori Ohba, Fernando Vallejos-Burgos, and Katsumi Kaneko

### 3.1 Surface Excess Mass and Absolute Adsorption Amount

The interaction of supercritical gas with solid surface is not strong enough to induce predominant adsorption of the supercritical gas on solid surfaces, as mentioned in Chap. 2. Figure 3.1 shows schematically adsorbed structure and density of molecules for vapor and supercritical gas. Vapor molecules are strongly adsorbed on the surface even at low gas phase density, forming the stable adsorbed layer, whereas supercritical gas molecules are not strongly adsorbed, and their adsorbed density profile is diffuse even at a high gas phase density; we must apply high pressure gas to increase the adsorbed density. As the adsorbed density is not predominantly high compared with the bulk gas phase density, gaseous molecules are distributed near the surface. The adsorbed amount is determined from the difference between the adsorbed density and gas phase density, which is called “surface excess mass.” In the case of vapor adsorption, we can neglect the bulk gas phase density and easily measured the surface excess amount. However, the adsorbed density of supercritical gas cannot be neglected. We must take into account the bulk gas phase density in the adsorbed layer. Figure 3.2 shows the density profile of adsorbed layer with the relevance to the bulk gas phase density. Here, the thickness  $l$  of the adsorbed layer is defined by the distance from the outermost surface (Connolly surface [1]) to the point where the adsorbed density agrees with the bulk one. The area [ $A_{ex}$ ] corresponds to the surface excess amount. As the non-adsorbed gas within the adsorbed layer is regarded as concentrated on the surface, the sum of the

---

T. Ohba

Graduate School of Science, Chiba University, Inage, Chiba, Japan

e-mail: [ohba@chiba-u.jp](mailto:ohba@chiba-u.jp)

F. Vallejos-Burgos · K. Kaneko (✉)

Research Initiative for Supra-Materials, Shinshu University, Nagano, Japan

e-mail: [fvb@vallejos.cl](mailto:fvb@vallejos.cl); [kkaneko@shinshu-u.ac.jp](mailto:kkaneko@shinshu-u.ac.jp)

© Springer Nature Singapore Pte Ltd. 2019

K. Kaneko, F. Rodríguez-Reinoso (eds.), *Nanoporous Materials for Gas Storage*, Green Energy and Technology, [https://doi.org/10.1007/978-981-13-3504-4\\_3](https://doi.org/10.1007/978-981-13-3504-4_3)

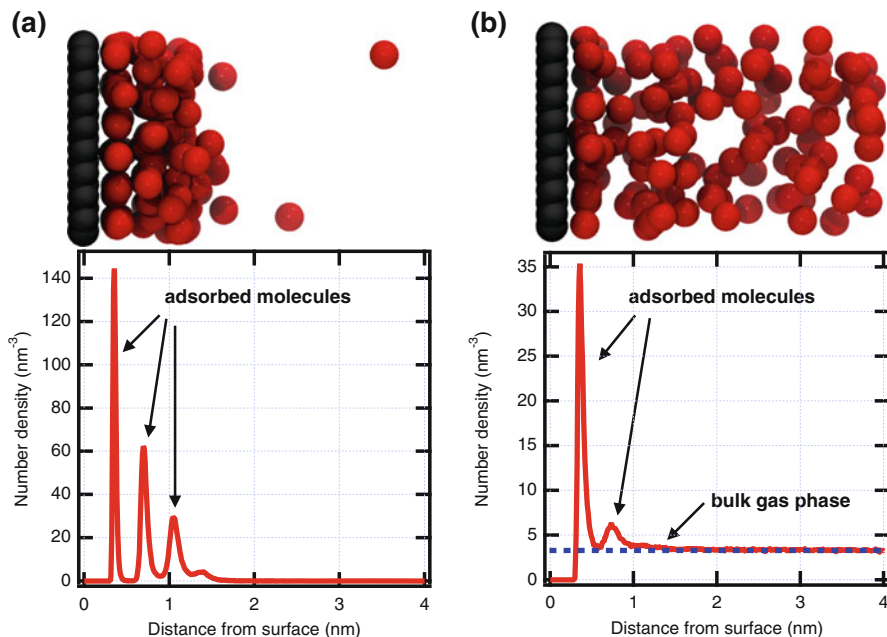
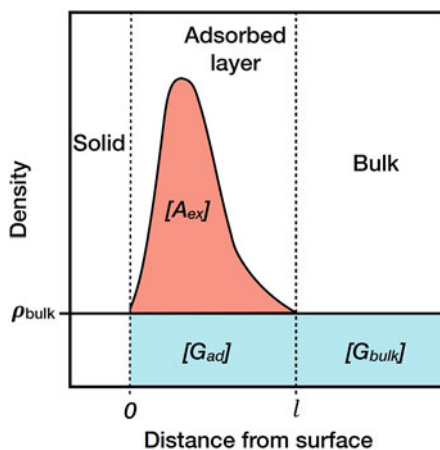


**Fig. 3.1** Adsorbed states and densities for vapor (a) and supercritical gas (b). Here bulk gas phase molecules mingle with adsorbed molecules in figure (b)

**Fig. 3.2** Density profile of supercritical gas on a surface. Areas  $[A_{ex}]$ ,  $[G_{ad}]$ , and  $[G_{bulk}]$  denote densities of adsorbed layer, of non-adsorbed gas on surface, and of bulk gas, respectively.  $l$  is the thickness of the adsorbed layer.  $A_{ex}$  is the surface excess amount. Here the origin of distance is on the Connolly surface, being different from that of Fig. 3.1



surface excess amount and amount of gas within the adsorbed layer is defined by absolute adsorption amount. The adsorbed layer thickness  $l$  can be rigorously defined, but it cannot be determined easily. Then, the direct measurement of the absolute adsorption amount is also difficult. Even nanoporous materials cannot form a distinct boundary between adsorbed layer on the solid surface and adsorptives due to insufficient attractive interaction. A careful analysis of high-pressure gas

adsorption isotherm provides a plausible thickness of adsorbed layers: 1 nm for Kr on graphite at 273 K [2] and 2 and 6 nm for methane on activated carbon and carbon black at 303 K, respectively [3]. The obtained layer thickness of adsorbed molecules above critical temperature suggests the diffuse adsorbed layer.

The absolute adsorption amount,  $n_{ab}$ , is mathematically expressed by Eq. 3.1:

$$n_{ab} = \int_{r=0}^l \rho_{ad}(r) dr = \int_{V_{ad}} \rho_{ad}(r) dr \quad (3.1)$$

where  $\rho_{ad}$  is the density of adsorbed layer and  $V_{ad}$  is the adsorbed layer volume which can be determined from surface area and  $l$ .  $n_{ab}$  is associated with the surface excess mass  $n_{ex}$  by Eq. 3.2:

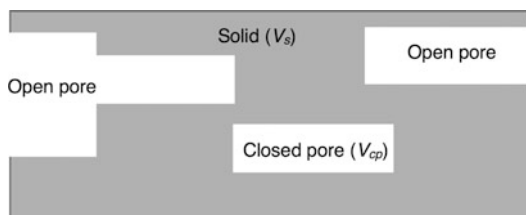
$$n_{ex} = n_{ab} - \rho_{bulk} V_{ad} \quad (3.2)$$

where  $\rho_{bulk}$  is the bulk gas density. We can determine directly  $n_{ex}$  and  $\rho_{bulk}$  by use of the adsorption measurement. On the contrary,  $n_{ab}$ ,  $V_{ad}$ ,  $l$ , and  $\rho_{ad}$  cannot be measured directly. An accurate information on adsorption mechanism needs an absolute adsorption isotherm. However, it is not easy to obtain the absolute adsorption isotherm reasonably. Nanopores, particularly micropores, have a relatively strong interaction potential with supercritical gases due to overlapping of the interaction potentials from pore walls, giving a maximum in the high-pressure adsorption isotherm in surface excess mass. Later derivation of the absolute adsorption isotherm from the high-pressure adsorption isotherm of a maximum will be shown. Chapter 4 gives a detailed description of physical chemistry on high-pressure adsorption isotherms.

## 3.2 Particle Density, High-Pressure Adsorption Isotherm of Supercritical Gas, and Absolute Adsorption

Vapor adsorption isotherms in the subatmospheric gas pressure range are measured volumetrically or gravimetrically. The volumetric method measures the gas pressure change with adsorption under a constant volume of the adsorption system, providing the equilibrium pressure and adsorption amount with the aid of the equation of state of gas. This volumetric method for vapor adsorption has been widely used owing to simple and concise instrumentation. However, we must be cautious for keeping the constancy of the dead space volume and temperature to avoid accumulation of the errors. The gravimetric method determines the adsorption amount and equilibrium pressure independently without accumulation of errors. However, the temperature of samples isolated from the walls of the adsorption equipment must be kept at the adsorption temperature. The volumetric measurement is more popular than the

**Fig. 3.3** Schematic model of a porous solid.  $V_s$  and  $V_{cp}$  are volumes of solid and closed pores



gravimetric one. Ordinary high-pressure adsorption isotherms are also measured volumetrically due to simplicity. However, the observed surface excess amount is often very small, and thereby we need to use an adsorption cell of small volume and highly pure gas (>99.99999% for adsorption of supercritical  $H_2$  [4]) under a rigorously controlled constant temperature; the temperature difference of 1 K between adsorptive gas and a pressure gauge induces a serious error of more than 100% for adsorption of supercritical hydrogen near room temperature. An accurate determination of the particle density must be carried out in order to evaluate the blank volume except for the sample volume. The gravimetric method for high-pressure adsorption isotherm has merits for an accurate determination of the surface excess amount and particle density from the buoyancy curve method using He gas [5]. Even the volumetric method needs the correct value of the volume of samples, which is evaluated from the accurate particle density; the well-known He replacement method does not provide the correct particle density and thereby the buoyancy curve method must be recommended.

Even the volumetric method needs the correct value of the sample volume, which is evaluated from the accurate particle density. In particular, adsorption amount of supercritical hydrogen on nanoporous materials is too small, and the accurate determination of the particle density of nanoporous samples is indispensable. The He replacement method at ambient conditions is widely used for evaluation of the particle density. However, nanoporous materials for hydrogen storage have ultramicropores where small amount of hydrogen molecules are adsorbed even at ambient temperature. Even the slight adsorption of He atoms gives a serious overestimation of the hydrogen adsorption amount. We need the accurate determination method of the particle density of nanoporous materials. The high-pressure He buoyancy method gives the reliable particle density together with the adsorption amount of He at ambient temperature.

Nanoporous materials have open and closed pores, as shown in Fig. 3.3. The closed pores are completely inaccessible for He atoms in the surroundings. There are several kinds of the density for porous solids depending on the accessibility of pores to atoms and molecules in the surroundings [6].

The determination of the surface excess amount needs the exclusion volume by nanoporous samples; the exclusion volume in the model structure is given by (solid volume ( $V_s$ ) + volume of closed pores ( $V_{cp}$ )). Consequently, the determination of the particle density defined by Eq. 3.3 is requested.

$$\rho_p = \frac{m_s}{V_s + V_{cp}} \quad (3.3)$$

where  $m_s$  is the mass of the nanoporous solid sample. If the adsorption amount of supercritical gas is not so predominant, the accurate value of the particle density is strongly requested. The buoyancy of the solid sample comes from the exclusion volume against the surrounding fluid (He), and then the buoyancy measurement of the nanoporous sample provides the particle density. We must measure the sample weight change with varying the He pressure with a gravimetric method. The larger the He pressure, the lighter the weight of the solid sample due to buoyancy. The experimentally observed weight,  $n_{obs}$ , of the solid sample is expressed by adsorbed amount of He,  $n(\text{He})_{ad}$ , and the buoyancy,  $W_{buoy}$  for the solid sample in the He media, as given by Eq. 3.4.

$$n_{obs} = n(\text{He})_{ad} + W_{buoy} \quad (3.4)$$

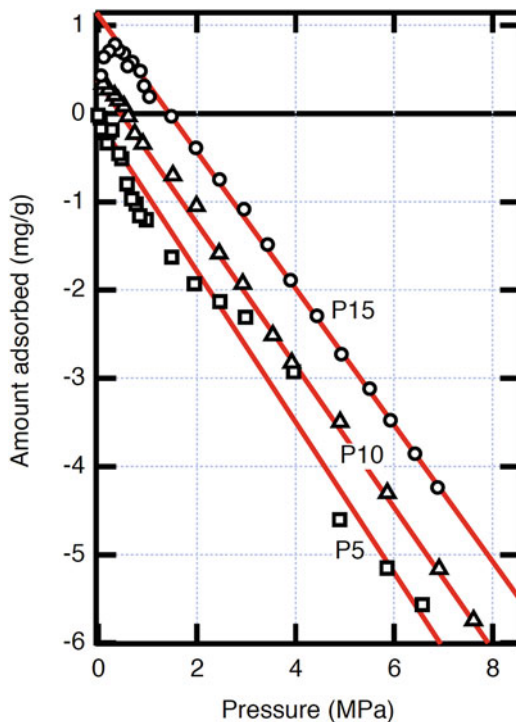
Here the  $W_{buoy}$ , depending on the gas phase He density, has a negative value, and the weight unit of mg per 1 g of the sample is convenient for this analysis. The He gas phase density is proportional to the He pressure, and then the buoyancy decreases linearly with the He pressure;  $n_{obs}$  decreases linearly with the He pressure. The state of He gas is approximated by the ideal gas law.  $n(\text{He})_{ad}$  is nil compared with  $W_{buoy}$  in the higher He pressure region. The slope of the linear relation gives the particle density of the solid sample according to Eq. 3.5.

$$\rho_s = -\frac{M_{\text{He}}}{RT} \frac{1}{dW_{buoy}/dP} \quad (3.5)$$

where the  $M_{\text{He}}$  is the molecular weight of He. Figure 3.4 shows high-pressure adsorption isotherms of He on activated carbon fiber at 303 K. The adsorption of He is observed below 2 MPa. However, the decrease in the sample weight is dominant due to the buoyancy effect, giving a linear relationship between the adsorption amount (observed sample weight) and He pressure. The particle densities of activated carbon fibers P5, P10, and P15 are 1.9, 1.95, and 2.04 g/mL, respectively, which are slightly smaller than the density of graphite (2.25 g/mL). Even the particle density from He buoyancy method is not necessary perfect. This is because the open porosity depends on the probe molecule [7]. The application of the particle density with the He buoyancy method to evaluation of hydrogen storage is recommended.

Figure 3.5 shows classification of adsorption isotherms of vapor recommended by IUPAC [1]. The vapor adsorption isotherms are classified into six types depending on the molecule-surface interaction; the types I and IV are subdivided into (a) and (b). Here the ordinate is adsorption amount (surface excess) and abscissa is the relative pressure ( $P/P_0$ ). The type I isotherm is observed for adsorption of vapor in micropores, because molecules interact strongly with micropores and the predominant adsorption begins from an extremely low relative pressure  $P/P_0$ . If the molecule-surface interaction is weak compared with the thermal energy, adsorption in the low  $P/P_0$  is nil, as type III and V. As storage of supercritical gases needs micropores which have deep interaction potential wells for the supercritical gas molecule, the nanoporous materials of IUPAC type I (Ia) adsorption isotherms of

**Fig. 3.4** He adsorption isotherms of activated carbon fiber at 303 K. The average pore widths of P5, P10, and P15 are 0.75, 0.8, and 1.0 nm, respectively. (Reprinted from Refs. [5], with the permission of AIP Publishing.)



$N_2$  at 77 K or Ar at 87 K with large pore volume are promising candidates for gas storage. The adsorption isotherm of  $N_2$  at 77 K or Ar at 87 K of promising applicants for gas storage should be of IUPAC type I (type Ia) with the large pore volume.

The adsorption isotherm of supercritical gas varies the shape depending on the intermolecular and molecule-surface interactions, and gas phase density. There are various types of high-pressure adsorption isotherms. Donohue and Aranovich [8] showed a variety of adsorption isotherms near and above the critical temperature with experimental and Ono-Kondo theoretical approaches. Figure 3.6 shows representative types of high-pressure adsorption isotherm of nanoporous materials for supercritical gas. The Henry type is observed for a weak interaction between gas and solid of wide porosity. The slight overlapping of the interaction potentials between a molecule and pore wall gives a Langmuir-type isotherm. If the surface excess does not increase so much with elevation of the gas pressure, the surface excess becomes smaller than that at a lower pressure owing to the high gas phase density. Accordingly the observed high-pressure adsorption isotherm exhibits a maximum, being completely different from vapor adsorption isotherm. This maximum type is observed for an intensive overlap of the interaction potentials. The nanoporous material giving the maximum type isotherm is promising for an efficient storage, as well as having the maximum at a lower pressure is preferable too.

The adsorption isotherm in terms of the absolute adsorption amount is indispensable to analyze the adsorption data thermodynamically [9]. Also the absolute adsorption amount gives a better measure of a real storage capacity than the

**Fig. 3.5** IUPAC classification of vapor adsorption isotherms. De Gruyter “Physisorption of gases, with special reference to the evaluation of surface area and pore size distribution (IUPAC Technical Report),” Walter De Gruyter GmbH Berlin Boston, 2015. (Copyright and all rights reserved. Material from this figure has been used with the permission of Walter De Gruyter GmbH.)

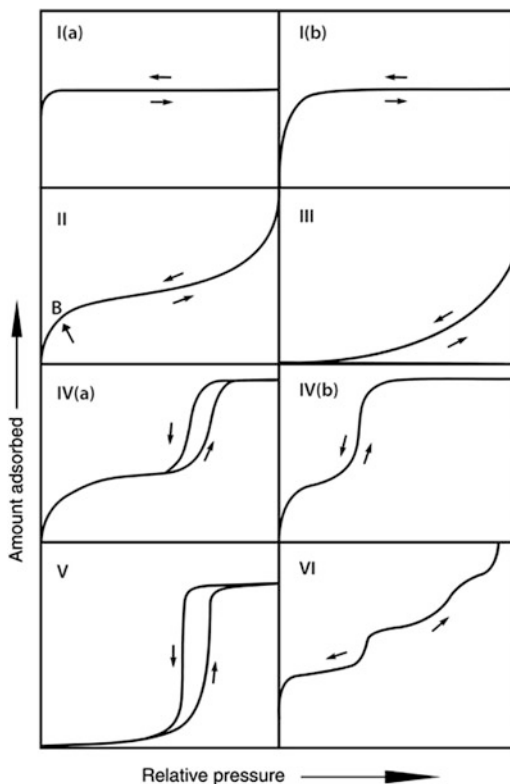
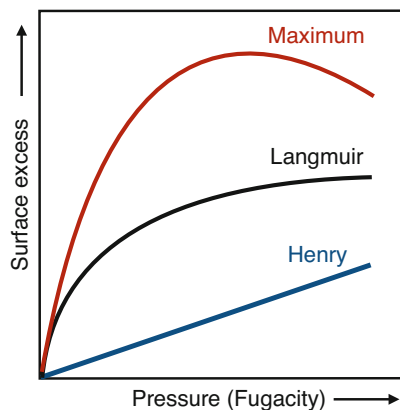


**Fig. 3.6** Types of high pressure adsorption isotherms for supercritical gas



surface excess amount. Molecular simulation can estimate the absolute adsorption amount according to a model pore structure. The experimental determination of absolute adsorption isotherm is a challenging research subject because of a serious difficulty in experimental measurement of the adsorbed layer volume or thickness of the adsorbed layer [10–13]. However, the detailed analysis of the high-pressure

adsorption isotherm by the DFT-assisted adsorbed volume mapping method [2] and buoyancy-mediated method [14] gives the plausible value of the absolute adsorption amount. Here, the buoyancy-mediated method is applied for high-pressure adsorption isotherm of a maximum type is shown below.

The gravimetrically observed value  $n_{obs}$  is given by Eq. 3.6:

$$n_{obs} = n_{tw} + \frac{B}{W_S} \quad (3.6)$$

Here  $n_{tw}$  is the total weight change per gram of adsorbent sample, and  $B$  and  $W_S$  are the blank of the weighing system and the sample adsorbent weight, respectively.  $n_{tw}$  contains the buoyancy term and Eqs. 3.7 and 3.8 are derived as follows.

$$n_{obs} = n_{ex} - \rho_{bulk} V_S + \frac{B}{W_S} \quad (3.7)$$

$$n_{obs} = n_{ab} - \rho_{bulk}(V_{ad} + V_S) + \frac{B}{W_S} \quad (3.8)$$

$\rho_{bulk} V_{ad}$  and  $\rho_{bulk} V_S$  denote the buoyancy for adsorbed layer and adsorbent sample, respectively. The particle density  $\rho_p$  is necessary for  $V_S$ . The  $n_{ab}$  becomes almost constant against the fugacity  $F$  near or beyond the maximum ( $dn_{ab}/dF \approx 0$ ), and then  $n_{tw}$  decreases with elevation of fugacity, giving almost linear decrease. The slope of the decreasing isotherm is expressed by  $V_{ad}$ , as shown by Eq. 3.9:

$$\frac{dn_{tw}}{dF} = -\frac{d}{dF} \rho_{bulk}(V_{ad} + V_S) = S_l \quad (3.9)$$

where  $S_l$  is the slope of the observed isotherm.

If the supercritical gas is not far from an ideal gas,  $V_{ad}$  is given by the Eq. 3.10:

$$V_{ad} = -\frac{RT}{M} S_l - \frac{1}{\rho_p} \quad (3.10)$$

Here  $M$  is the molecular weight of the gas. We can obtain the absolute adsorption isotherm using  $V_{ad}$ . Thus, high-pressure adsorption isotherm of supercritical gas has an essential issue for how to determine the absolute adsorption isotherm. The concept of net adsorption is also important for gas storage, and then it will be given later in Chap. 4.

Here, a simple classification using the compression factor of adsorbed gas is described, because the classification gives a qualitative information on the strength of molecule-surface interaction, being helpful to search better storage materials. In Chap. 2 the compression factor is defined by Eq. 2.4 which is given for the state of equation of real gases. Murata et al. [15] introduce the compression factor  $Z_{ad}$  of the adsorbed layer which is described by the average adsorbed layer density  $\langle \rho_{ad} \rangle$ , as given by Eq. (3.11).  $\langle \rho_{ad} \rangle$  is determined by

the adsorbed amount of supercritical gas and the pore volume which is independently determined by  $N_2$  adsorption at 77 K or Ar adsorption at 87 K for porous materials.

$$Z_{ad} = \frac{P}{\langle \rho_{ad} \rangle RT} \quad (3.11)$$

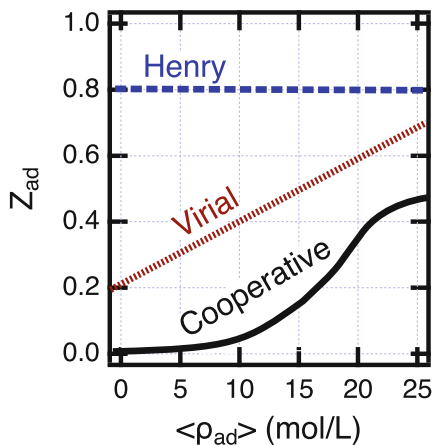
$P$  is the bulk gas phase pressure which equilibrates with adsorbed layer. The  $Z_{ad}$  vs.  $\langle \rho_{ad} \rangle$  plot just depends on the  $\langle \rho_{ad} \rangle$  which is determined by intermolecular and molecule-surface interactions, and thereby this plot leads to information on the adsorbed state of gas. Although there are many types of high-pressure adsorption isotherms, they are classified to only three types of the  $Z_{ad}$  vs.  $\langle \rho_{ad} \rangle$  plot, as shown in Fig. 3.7. The horizontal line, the linear increase, and the S-shaped curve in Fig. 3.7 correspond to Henry, virial, and cooperative transition types of supercritical gas adsorption, respectively. We will discuss the physical meaning of three types here. The simplest law on the gas-surface interaction is known as Henry law. When the gas phase density is too low to induce the intermolecular interaction, the  $\langle \rho_{ad} \rangle$  depends on the molecule-surface interaction, increasing linearly with the gas phase pressure (Eq. 3.12).

$$\langle \rho_{ad} \rangle RT = k_H P \quad (3.12)$$

$k_H$  is the Henry constant determined by the molecule-surface interaction. In the supercritical gas adsorption near ambient temperature, the  $\langle \rho_{ad} \rangle$  is often small, giving the Henry type of  $Z_{ad}$  vs  $\langle \rho_{ad} \rangle$  plot.  $Z_{ad}$  is constant at the constant temperature (Eq. 3.13); the adsorbed gas can be regarded as an ideal gas on solid surface.

$$Z_{ad} = \frac{1}{k_H RT} \quad (3.13)$$

**Fig. 3.7** Three types of  $Z_{ad}$  vs.  $\langle \rho_{ad} \rangle$  plot for classification of high-pressure adsorption isotherm of supercritical gas



The solid surface showing the Henry type is not promising for an efficient storage of a target gas. We can adsorb more supercritical gas on solids, when the intermolecular interaction is not negligible. The equation of state of the gas adsorbed on solid surface should be given by the virial equation for gases, which is discussed in Chap. 2 (2.1). If we take into account the second virial coefficient  $B_2$  for the gas adsorbed,  $Z_{ad}$  is expressed by Eq. 3.14.

$$Z_{ad} = \frac{1}{k_H RT} (1 - B_2 \langle \rho_{ad} \rangle) \quad (3.14)$$

Here  $B_2$  is negative and  $Z_{ad}$  increases with  $\langle \rho_{ad} \rangle$ . If the  $Z_{ad}$  vs.  $\langle \rho_{ad} \rangle$  plot deviates in a higher  $\langle \rho_{ad} \rangle$ , the higher-order terms of the virial equation must be taken into account. If the virial type of  $Z_{ad}$  vs.  $\langle \rho_{ad} \rangle$  plot with upward deviation in the higher  $\langle \rho_{ad} \rangle$  region is obtained, the solid surface is worthy of careful study as an applicant for gas storage. The S-shaped  $Z_{ad}$  vs.  $\langle \rho_{ad} \rangle$  plot is obtained for a high-pressure gas adsorption isotherm at relatively low temperature. When supercritical gas molecules are sufficiently adsorbed under high pressure, the intermolecular interaction transforms from the attractive interaction to repulsive one, providing the S-shaped  $Z_{ad}$  vs.  $\langle \rho_{ad} \rangle$  plot. The corresponding adsorption isotherm being Langmuirian is converted to Eq. 3.15. [16] Here  $A_S$ ,  $B_S$ ,  $C_S$ , and  $\rho_t$  are the fitting parameters that have physical meanings; the  $\rho_t$  is the adsorbed density of transition from attractive to repulsive intermolecular interactions.

$$Z_{ad} = A_S \tan^{-1} \left( B_S (\langle \rho_{ad} \rangle - \rho_t) \right) + C_S \quad (3.15)$$

The  $Z_{ad}$  vs.  $\langle \rho_{ad} \rangle$  plots of adsorption isotherms of supercritical hydrogen on single wall carbon nanohorn (SWCNH) at different temperatures are shown in Fig. 3.8 [15]. The adsorption isotherm at 303 K is of horizontal line, because the hydrogen-hydrogen interaction is smaller than the thermal energy at 303 K. The adsorption isotherm at 196 K is of Freundlich type, indicating the presence of non-negligible intermolecular interaction. We can observe Langmuir-type isotherm at

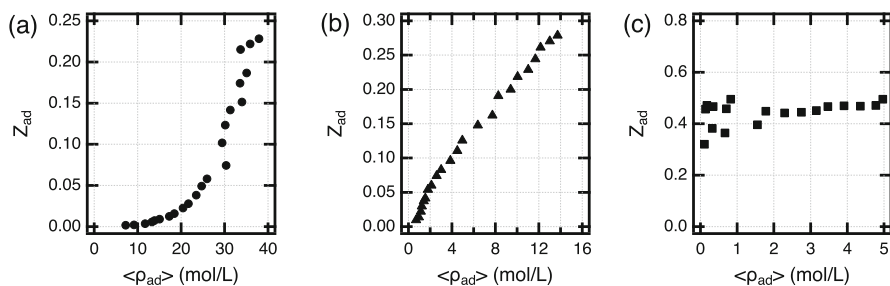


**Fig. 3.8**  $Z_{ad}$  vs.  $\langle \rho_{ad} \rangle$  from adsorption isotherms of supercritical hydrogen at (a) 77 K, (b) 196 K and (c) 303 K

77 K and the adsorbed density is large; the adsorbed density at 5 MPa coincides with the bulk liquid density at 20 K. As SWCNH has tubular inner spaces of 2–6 nm in diameter, hydrogen molecules are concentrated to form liquid-like dense adsorbed layer even at 77 K ( $>T_c = 33$  K). The adsorbed density at 20 K is higher than that of bulk liquid hydrogen, being close to the bulk solid density at the triple point [17]. The mass of a hydrogen molecule is only 2, showing quantum nature; the quantum hydrogen fluctuates more at lower temperature, which is evidenced theoretically and experimentally [17–20]. The de Broglie wave length  $\lambda_{dB}$  gives the fluctuation extent of the molecule, and thereby the lower the temperature, the larger the  $\lambda_{dB}$ ;  $\lambda_{dB}$  values of  $H_2$  at 20, 77, and 300 K are 0.30, 0.14, and 0.07 nm, respectively. The  $\lambda_{dB}$  of the  $H_2$  molecule at ambient temperature is still non-negligible in the adsorption in subnanoscale pores. It is noteworthy that the adsorbed hydrogen density is comparable to the bulk liquid density irrespective of the quantum fluctuation at 77 K.

### 3.3 Nanoporous Materials for Gas Storage

As physical adsorption of supercritical gases needs the strong interaction potential sites on a solid, we must design or produce optimum nanoporous materials for gas storage. The nanoporous materials for gas storage must fulfill required properties, as mentioned in Chap. 1. We have a variety of candidate materials such as porous carbons, metal organic frameworks, zeolites, silicas, and clay minerals. In this book, gas storage studies on porous carbons, MOFs, and zeolites are described. Active studies on gas storage on porous carbons and MOFs have been carried out, and the progresses must be shown in other chapters of this book. On the other hand, the adsorption study on zeolites has been carried out from the fundamental aspects, which give the important insight to design better storage materials even using porous carbons and MOFs. Also, zeolites have small micropores which are fit for concentration of diluted supercritical gases. Consequently, zeolited may have unique application potentials.

MOFs have unique pore structures which are introduced in Chap. 6; MOF does not consist of walls, but of pillars, being very different from the traditional nanoporous materials like porous carbons and zeolites. Figure 3.9 shows the model structures of single wall carbon nanotube (SWCNT) and MOF (ELM-11 [22, 23]). The pore space of SWCNT is completely embraced with a graphene layer. On the other hand, the MOF has no sheet-like walls, and the structure is composed of narrow belts or pillars.

Figure 3.9 shows explicitly the unique MOF structure. Then, we can divide nanoporous materials into pillar- and wall-frame structures. We will compare the pillar- and wall-frame structures from the interaction with a methane molecule using array of neutral carbon pillars. Recent science on nanoporous materials is going to challenge to design a customized pore structure for a specific application. This

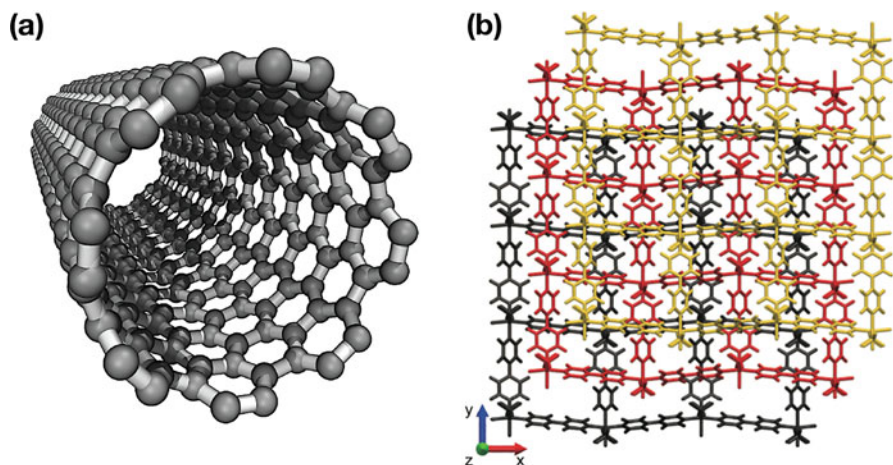


**Fig. 3.9** Structure of single wall carbon nanotube (a) and ELM11( $[\text{Cu}(\text{BF}_4)_2(\text{bpy})_2]$ ) (b). (Structure (b) is reproduced from Ref. [21] with permission of The Royal Society of Chemistry.)

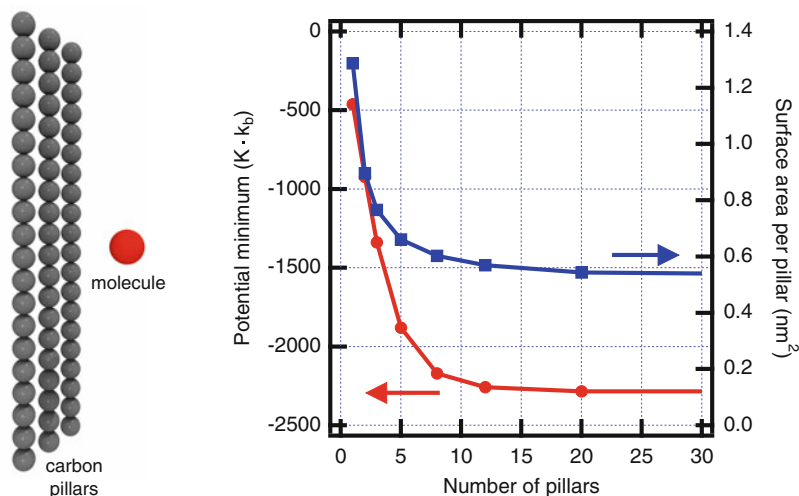
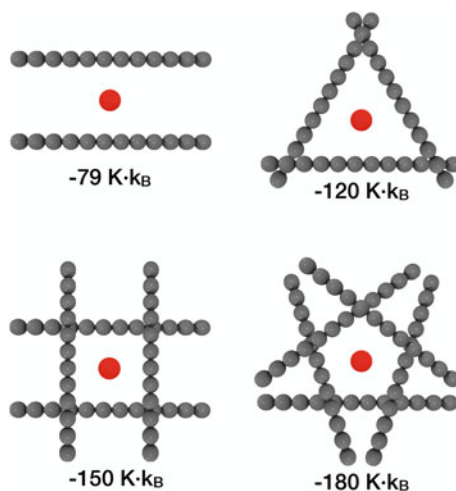


**Fig. 3.10** Interaction potential minimum and surface area per pillar for methane against carbon pillar number

comparison is useful for such pore structure designing. In this model, each carbon pillar consists of 20-carbon atoms which contact each other in the equilibrium distance of Lennard-Jones interaction.

A methane molecule is placed on the center of the pillar at the vertical distance. The dispersion interaction of methane with the pillar is obtained by the Lennard-Jones potential, providing the potential minimum value. The interaction potential becomes deeper as increasing the pillar number. Figure 3.10 shows the interaction potential minimum change of methane with the bundle of carbon pillars against the

**Fig. 3.11** Confinement of a methane molecule in different 2D geometries and the interaction potential depth



carbon pillar number. Also the relationship between the specific surface area and the pillar number is shown. The potential becomes rapidly deeper up to the five pillar number; the molecule-5 pillars interaction energy is five times larger than the molecule-single pillar interaction. The potential minimum is  $-1707 \text{ K} \cdot k_B$  for 12 pillars. The surface area decreases rapidly with the pillar number. If we need the high surface area, the number of pillars should be small. The single-pillar structure of the largest surface area cannot provide the strong interaction. Therefore, we need to choose an optimum wall width from the view points of the interaction strength and surface area.

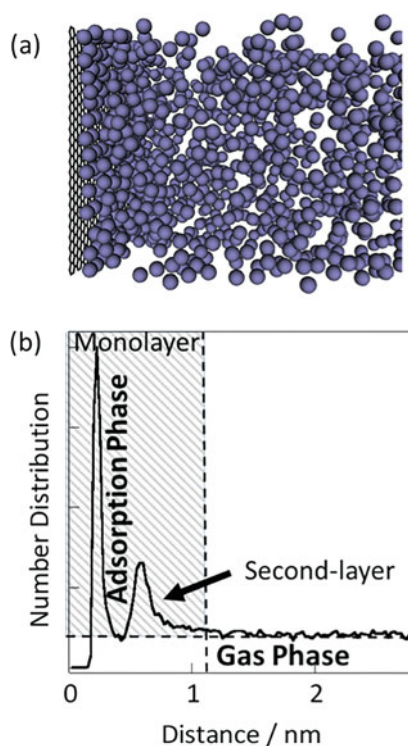
Another important factor is pore geometry. Here a schematic two-dimensional geometry for confinement of a molecule is considered, as shown in Fig. 3.11. A methane molecule is situated at the center of the geometry, and the vertical distance between the molecule and carbon pillar is kept to be  $2 \times \sigma_{\text{CH}_4}$ . Although the vertical distance is relatively large and the overlapping of the interaction potentials is not remarkable at the center, the effect of the geometry is explicit. The interaction potential depth depends on the pillar number of the geometry; the potential depths of the parallel arrangement (two pillars), triangle (three pillars), square (four pillars), and pentagon (five pillars) at the center are  $-79 \text{ K} \cdot k_B$  ( $0.66 \text{ kJ/mol}$ ),  $-120 \text{ K} \cdot k_B$  ( $1 \text{ kJ/mol}$ ),  $-150 \text{ K} \cdot k_B$  ( $1.2 \text{ kJ/mol}$ ), and  $-180 \text{ K} \cdot k_B$  ( $1.5 \text{ kJ/mol}$ ), respectively. In case of the pentagon, the potential depth at the monolayer inside position at the bottom is  $-580 \text{ K} \cdot k_B$  ( $4.8 \text{ kJ/mol}$ ) and that at the inner corner of the top is  $-815 \text{ K} \cdot k_B$  ( $6.8 \text{ kJ/mol}$ ). Thus the corner site akin to two pillars gives the deepest potential well. We need to take into account the confinement geometry to provide a deeper interaction potential well under the requirement of the larger confinement space for a larger adsorption capacity.

Molecular simulation has contributed to give structural understanding of molecules adsorbed in pores, although adsorbed structures of molecules inside pores cannot be studied by surface science tools. Experimental studies supported

by molecular simulation are powerful to elucidate the molecular structure confined in pores [24–26]. Experimental determination of the adsorbed layer thickness and absolute adsorption isotherm is quite difficult; molecular simulation gives clear images of intermolecular structure of supercritical gases on a solid. Molecular simulation views of supercritical methane adsorption on graphite surfaces, which are obtained using Lennard-Jones potential for methane molecules and 10 – 4 – 3 potential for methane-graphite interaction, are shown here; the Lennard-Jones parameters of methane are  $\sigma_{\text{CH}_4} = 0.3721 \text{ nm}$  and  $\epsilon_{\text{CH}_4} = 161.3 \text{ K} \cdot k_B$  [27].

An image of high-pressure adsorption of methane on graphite and density profile of methane are shown in Fig. 3.12. Methane molecules are densely adsorbed near graphite surface, and the adsorbed layer becomes diffusive with the vertical distance from the surface. As the methane-graphite surface interaction is considerably strong, relatively sharp monolayer and secondary layer peaks are observed. The adsorbed density becomes the bulk one at 1.3 nm, which is the thickness of the adsorbed layer,  $l$ . Molecular simulation can provide the  $l$  value regardless of the experimental difficulty of determining  $l$ . In this case, the bulk density is illustrated with a dashed line, which is not negligible. The hatched area corresponds to the surface excess amounts. The absolute adsorption amount can be obtained by summation of the

**Fig. 3.12** (a) Snapshot of methane molecules on graphite surface and (b) density profile of methane molecules. Conditions are 300 K and 8 MPa



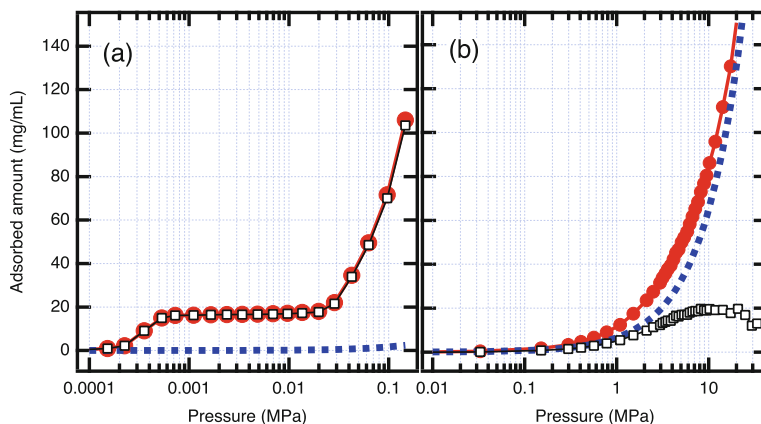


**Fig. 3.13** Absolute adsorption isotherms (filled symbols) and excess adsorption isotherms (open symbols) of methane on graphite at 120 K (a) and 300 K (b). Dashed curves represent bulk gas densities

hatched area and the rectangular area below the hatched area. Hence, molecular simulation can provide both of adsorption isotherms in the surface excess and absolute adsorption.

Accordingly the absolute adsorption isotherm of methane can be easily obtained by molecular simulation, as shown in Fig. 3.13; the absolute and excess adsorption isotherms of methane at 120 and 300 K are compared with each other. As the critical temperature of methane is 190 K, the adsorption isotherm at 120 K expresses the vapor adsorption isotherm. The bulk density for vapor adsorption at 120 K is negligibly small compared with the surface excess amount, leading to a considerably good agreement between the absolute and surface excess adsorption isotherms. We need to use highly pressurized methane for adsorption at 300 K up to 34 MPa in order to attain the sufficient filling. The bulk gas phase density increases markedly with the elevation of pressure. In this case, we do not use the fugacity in the high pressure range of Fig. 3.13b, and thereby the adsorption isotherms shift to left side in the expression of the fugacity. The great discrepancy between the absolute and surface excess adsorption isotherms is observed, and the absolute adsorption isotherm has a maximum. The simulated isotherms clearly indicate the importance of the absolute adsorption isotherm expression.

Molecular simulation can give an explicit structural information on molecules confined in nanopores under high pressure of the gas. The methane adsorption isotherms in a 2.0 nm graphite pore over the wide temperature range of 120–300 K are shown in Fig. 3.14. The adsorption isotherms at 120 and 150 K have two steps; the steps in the lower pressure and higher pressure come from the monolayer adsorption on the pore walls and filling of the residual pore space after completion of the monolayer formation, respectively. The first step almost disappears at 180 K, and a simple adsorption curve is observed above 210 K in the higher-pressure region.

**Fig. 3.14** Methane adsorption isotherms of graphitic slit pore of 2.0 nm in width at different temperatures. 120 (●), 150 (■), 180 (◆), 210 (○), 240 (□), 270 (◇), and 300 K (×). The second steps form a parabolic region depicted by the dashed curve

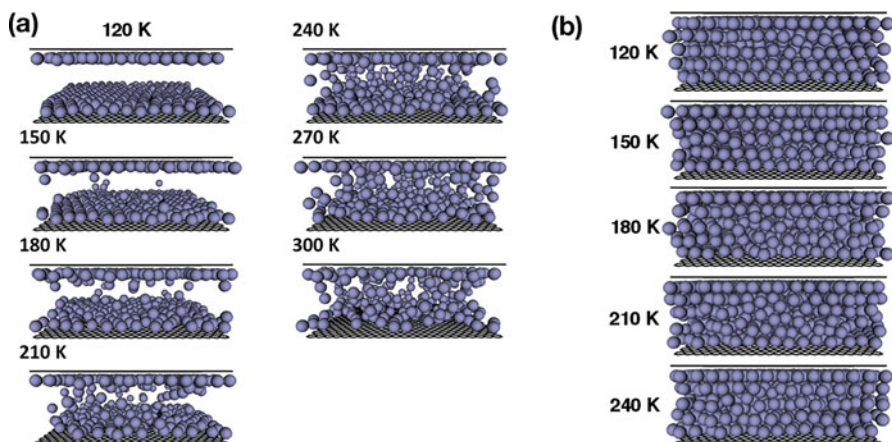
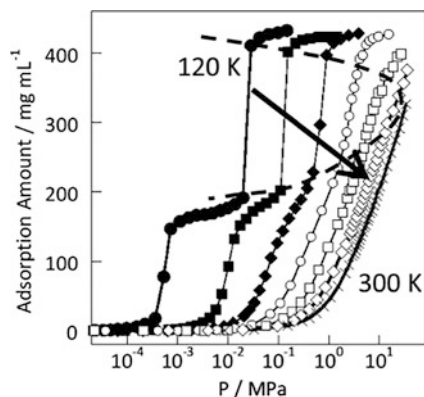


**Fig. 3.15** Snapshots of methane confined in a graphitic pore of 2 nm in width as a function of temperature at the adsorbed density of 150 mg/mL (a) and 400 mg/mL (b)

The parabolic area surrounded by the dashed curve indicates the coexistent region of gas-like and liquid-like phases. This behavior is similar to the coexistence of bulk gas and liquid below the critical temperature. Therefore, the effective critical temperature of methane adsorbed in the 2 nm pore is 300 K, being higher than that of bulk methane (190 K). In this case, the pressure is not corrected into the fugacity and the exact discussion must be avoided. We can say that the critical temperature is upper shifted by an intensive confinement, agreeing with the discussion in 2.6.

Accordingly methane in the 2 nm carbon pore below 300 K is not supercritical gas, being close to vapor. This coincides with the experimental results shown in Chap. 2. Figure 3.15 shows snapshots of adsorbed methane molecules of 150 mg/mL in the 2 nm pore at different temperatures. Ordered monolayer is formed at 120 K, whereas the monolayer is slightly disordered together with some molecules in the residual pore space at 150 and 180 K. Above 240 K the monolayer becomes diffuse

and molecules are more widely distributed in the pore space with elevation of the temperature; gaseous methane molecules increases at higher temperature. The appearance of snapshots of highly filled methane of 400 mg/mL sounds insensitive to the measuring temperature. Nevertheless, snapshots at 210 and 240 K suggest the disordered structure. The structure ordering can be understood more clearly from comparison of their radial distribution functions, as shown in Fig. 3.16. The radial distribution functions of monolayer methane at the adsorbed density of 150 mg/mL have a sharp nearest peak, regardless of different temperature. This is because methane molecules are adsorbed in the pore strongly, compared with their thermal energy. However, the radial distribution function at 120 K has clearly two peaks other than the nearest neighbor peak owing to a long-range ordering. The second nearest neighbor peak of the radial distribution function of the monolayer at 400 mg/mL and 120 K has the doublet structure, and even the third nearest neighbor peak is sharp; the monolayer at 120 K has a long-range order structure. Also the radial distribution function of the total adsorbed layer at 120 K has three peaks which are not as sharp as those of the monolayer. The radial distribution functions of the monolayer above 180 K are similar to each other, and their second nearest neighbor peak loses the doublet structure. It is noteworthy that the relatively ordered monolayer structure of 400 mg/mL at 180 K

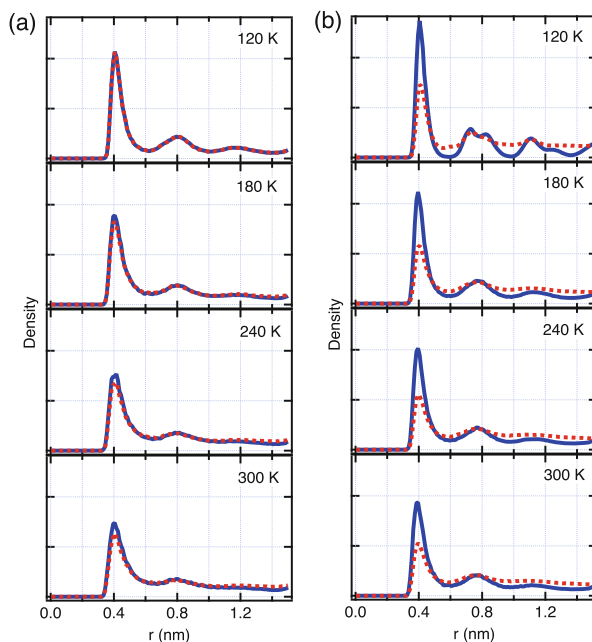


**Fig. 3.16** Radial distribution functions of methane adsorbed in a graphitic slit pore of 2 nm in width. Adsorbed density: (a) 150 mg/mL and (b) 400 mg/mL. Solid and dashed curves denote monolayer and total adsorbed molecules, respectively

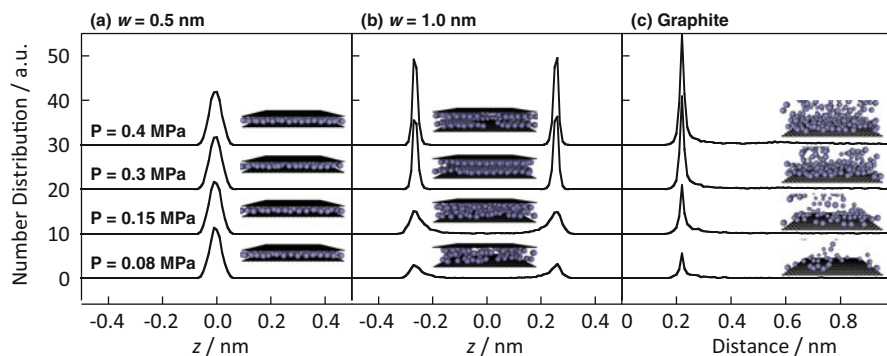


**Fig. 3.17** Density profiles and snapshots of methane molecules adsorbed in graphitic pores of 0.5 nm (a) and 1.0 nm (b) and on graphite (c) as a function of pressure at 300 K

is preserved even at 300 K due to the strong molecule-wall interaction. On the contrary, the first and second nearest neighbor peaks of the radial distribution function of the total adsorbed layer become more diffuse with elevation of the temperature.

Figure 3.17 shows the density profiles and snapshots of methane molecules adsorbed in graphitic slit pores of 0.5 and 1.0 nm and on the graphite surface as a function of methane pressure. The pore of 0.5 nm gives an intensive interaction potential field for methane molecules, and thereby methane molecules form a highly packed structure even at 300 K showing the importance of confinement of supercritical methane in small pores. The packing situation of the 1.0 nm pore is different from that of the 0.5 nm pore. Even the monolayer adsorption in the 1.0 nm pore is diffuse at a lower pressure compared with that in the 0.5 nm pore, although the monolayer adsorption peak becomes sharp at a higher pressure. In the case of adsorption on graphite, molecules are adsorbed at the monolayer position.

Figure 3.18 shows temperature dependence of adsorption isotherm of  $\text{CH}_4$  and two-dimensional distribution of methane molecules of the adsorbed density of 150 mg/mL in the graphitic slit pore of 1 nm in width. The adsorption isotherm at 120 K jumps almost vertically, being typical of vapor adsorption. However, the adsorption isotherm at 240 K above  $T_c$  loses the vertical uptake. The 2D distribution of molecules shows that methane molecules are associated with each other due to the intermolecular interaction at 120 K and the elevation of temperature destroys the intermolecular aggregate structure. This figure also shows the temperature sensitive structure of adsorbed molecules near the critical temperature. Consequently, nanoporous materials are indispensable to store a sufficient amount of supercritical methane. As the interaction between hydrogen molecules is much weaker than methane, quite small pore structures are necessary.

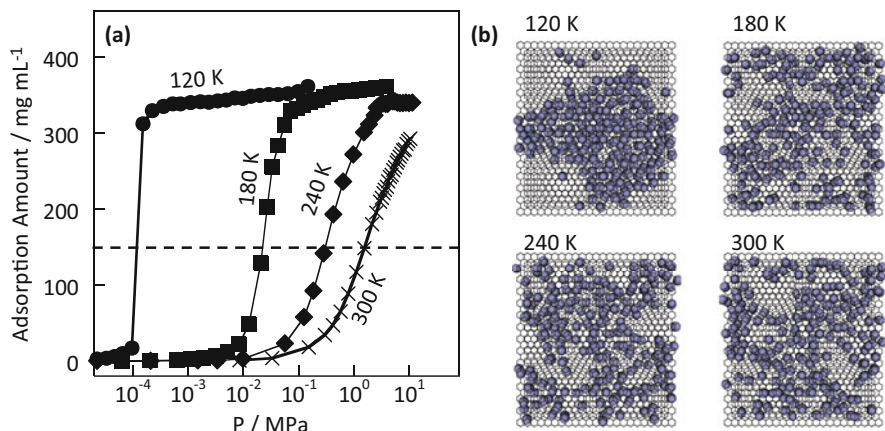


**Fig. 3.18** Temperature dependence of adsorption isotherm of  $\text{CH}_4$  and two-dimensional distribution of methane molecules in the graphitic slit pore of 1 nm in width. Here the two-dimensional snapshots are obtained for the adsorbed density of 150 mg/mL.

### 3.4 Effect of Adsorption Enthalpy on Gas Storage

Physical adsorption of gas decreases the entropy of the system consisting of a solid and gas, and then the enthalpy change on adsorption is always negative, being exothermic. Therefore, adsorption of gas on the solid emits the heat, accompanying with elevation of the system temperature. Maintaining the constant adsorption temperature is an essential key to guarantee the sufficient amount of storage of supercritical gas on nanoporous materials, and thereby an efficient release of the adsorption heat is requisite for the stable storage. Here, the basic thermodynamics on adsorption for experimental measurements is briefly given [9, 28, 29].

The experimental system on physical adsorption consists of adsorptives and gas-adsorbed solid (adsorbent), where the adsorptives (gas phase) and gas adsorbed (solid phase) are in equilibrium. Ordinary physical adsorption does not change the surface area for a given amount of adsorbent and the thermodynamic properties of the adsorbent by adsorbed gas. Then, we can obtain the following chemical potential expression.

$$\mu_g = f(T, P) \quad \mu_a = f'(T, P, n_a) \quad \mu_g = \mu_a \quad (3.16)$$

where  $\mu_g$  and  $\mu_a$  are the chemical potentials of the non-adsorbed and adsorbed gases, respectively, at temperature  $T$ , pressure  $P$ , and  $n_a$  moles of adsorbed gas. If the equilibrium is differentially displaced to a new temperature equilibrium, Eq. 3.17 is given.

$$-S_g dT + V_g dP = -\bar{S}_a dT + \bar{V}_a dP + \frac{\partial \mu_a}{\partial n_a} dn_a \quad (3.17)$$

Here,  $S_g$  and  $V_g$  are the molar entropy and molar volume of the non-adsorbed gas, respectively.  $\bar{S}_a$  and  $\bar{V}_a$  are the differential molar entropy and volume of adsorbed gas, respectively. When  $n_a$  does not change on the displacement, Eq. 3.18 is derived:

$$\left(\frac{\partial P}{\partial T}\right)_{n_a} = \frac{S_g - \bar{S}_a}{V_g - \bar{V}_a} \quad (3.18)$$

Noting that  $V_g \gg \bar{V}_a$  and the ideal gas equation  $V_g = \frac{RT}{P}$ , Eq. 3.19 is derived:

$$\left(\frac{\partial \ln P}{\partial T}\right)_{n_a} = \frac{S_g - \bar{S}_a}{RT} \quad , \quad -\Delta_a \bar{S} = \bar{S}_a - S_g \quad (3.19)$$

Since at adsorption equilibrium:

$$\Delta_a \bar{H} - T \Delta_a \bar{S} = 0 \quad (3.20)$$

$\Delta_a \bar{H}$  is the differential molar enthalpy of adsorption which gives the isosteric heat of adsorption  $q^{st}$ .

$$q^{st} = \Delta_a \bar{H} = \bar{H}_a - H_g \quad (3.21)$$

$\bar{H}_a$  and  $H_g$  are the differential molar enthalpy of the adsorbed gas and molar enthalpy of gas, respectively. Equation 3.19 is changed into a well-known formula in Eq. 3.22.:

$$\left(\frac{\partial \ln P}{\partial T}\right)_{n_a} = \frac{q^{st}}{RT^2} \quad (3.22)$$

When we have adsorption isotherms (absolute adsorption isotherms) at different temperature, the slope of the linear plot of  $\ln P$  against  $T^{-1}$  provides  $q^{st}$ . At least adsorption isotherms must be measured at two temperatures to determine the  $q^{st}$ . The quasi-vapor analysis shown in Chap. 2 is convenient to provide  $q^{st}$  at a fractional filling of about 0.4. The isosteric heat of adsorption is the heat which is transferred to the surroundings in the transfer of a differential quantity of gas from the gas phase to the adsorbed phase under isothermal and isobaric conditions. Various heats of adsorption other than the isosteric heat of adsorption are used in physical adsorption. The differential, adiabatic, isothermal, and integral heats of adsorption are associated with the experimental research; the different terminology comes from the different experimental procedure.

In this book, we discuss how the heat of adsorption influences the amount of adsorption using the simple model on methane adsorption instead of the detailed description of heat of adsorption. Since the interaction of methane with nanopores is considerably strong, the heat of adsorption effects significantly the effective adsorption amount. We will evaluate the effect of the exothermic heat of adsorption assuming an adiabatic process. Here we use the stabilized energy obtained from GCMC simulation as the approximated exothermic heat of adsorption. A model

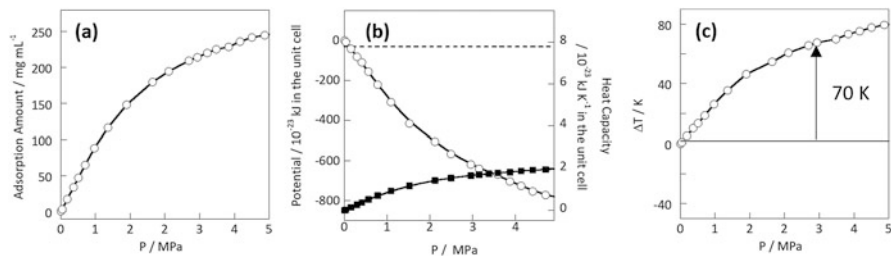


**Fig. 3.19** (a) Adsorption isotherm of supercritical methane in a graphitic pore of 1.0 nm width at 300 K. (b) Gained stabilized energy by methane adsorption (opened symbol) and heat capacity of adsorbed methane (filled symbol) and graphene walls (dashed line). (c) Temperature increase of methane-adsorbed carbon by heat of adsorption

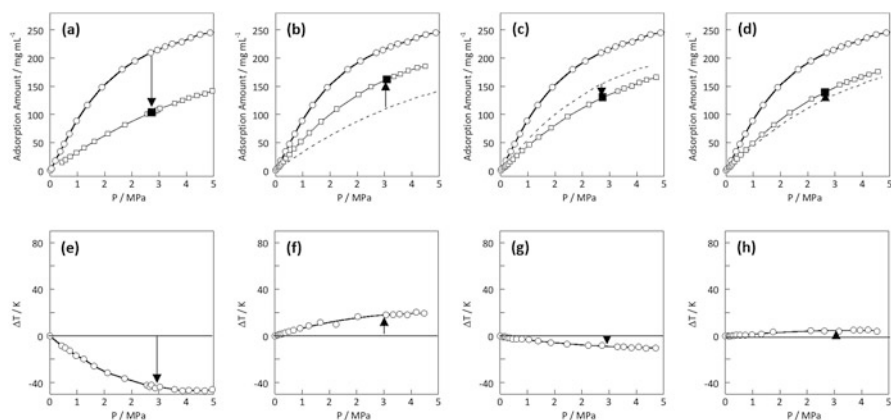


**Fig. 3.20** Adsorption isotherms of methane at 370 (a), 330 (b), 347 (c), and 338 K (d), which are depicted by squares. The adsorption isotherm at 300 K is shown by circles for comparison. Temperature changes by desorption (a), adsorption (b), desorption (c), and adsorption (d) are shown in (e), (f), (g), and (h), respectively

slit-shaped carbon pore of 1 nm in width, whose walls are composed of four graphene layers, is used for this simulation. This is a model of activated carbon. Figure 3.19 shows the GCMC-simulated adsorption isotherm of methane at 300 K (a), change in the total stabilized energy with the methane pressure (b) and the elevation of temperature with the methane pressure (c). The heat capacities of 35.31 and 8.527 J K<sup>-1</sup> mol<sup>-1</sup> are used for methane and graphite, respectively. The heat capacity of adsorbed methane is obtained from the adsorption amount. Thus, the elevation of the temperature of the model carbon and adsorbed methane is evaluated, as shown in Fig. 3.18c. The temperature increase is 70 K at 3 MPa, elevating the temperature of the methane adsorbed carbon model from 300 to 370 K. In the adiabatic system, the elevation of the temperature by 70 K decreases the adsorption amount. The adsorption isotherm at 370 K is shown in Fig. 3.20a. The adsorption amount at 3 MPa drops by about 50% at 370 K (an arrow in Fig. 3.20a), resulting in

the reduction of the temperature by 40 K due to desorption (see Fig. 3.20e). Then, the adsorption heat due to the increase of methane adsorption at 330 K (Fig. 3.20b) again elevates the temperature from 330 to 347 K (see Fig. 3.20f), giving rise to the corresponding desorption (Fig. 3.20c). The subsequent temperature drop from 347 K to 338 K (see Fig. 3.20g) through the desorption increases the adsorption slightly (see Fig. 3.20d), leading to the elevation of the temperature to 342 K, as shown in Fig. 3.20d. The converging temperature of the methane-model carbon is 342 K; the adsorption amount of 210 mg/mL at 3 MPa decreases to 140 mg/mL (more than 30% decrease) by the effect of heat of adsorption in the adiabatic conditions. This simple example intensively indicates the necessity of an efficient dissipation mechanism of the heat of adsorption. Thermal conductivities of graphite, carbon nanotube, and diamond are approximately 100–300, 3000–6000, and 1000–2000 W m<sup>-1</sup> K<sup>-1</sup>, respectively, and thereby addition of these materials of high thermal conductivity is promising in the storage of gas in nanoporous materials of low thermal conductivity.

We must take into account of the exothermic process on adsorption other than heat of adsorption. Hydrogen has nuclear spin isomers of parahydrogen and orthohydrogen whose two proton nuclear spins have antiparallel and parallel alignments, respectively. The contents of orthohydrogen and parahydrogen at ambient temperature are 0.75 and 0.25, respectively. The paraform is more stable than the orthoform, and then hydrogen at 20 K almost consists of parahydrogen (99.8%). The conversion of orthohydrogen into parahydrogen is quite slow, and the conversion heat from orthohydrogen to parahydrogen (523 J/g) is larger than heat of vaporization at 20 K (446 J/g) [30, 31]. Consequently, the orthohydrogen must be converted into parahydrogen in advance on liquefaction at low temperature. Similar attention must be paid for storage of hydrogen on nanoporous materials at low temperature.

**Acknowledgements** This is supported by the Grant-in-Aid for Scientific Research (B) (17H03039) and the OPERA project from JST.

## References

1. Thommes M, Kaneko K, Neimark AV, Olivier JP, Rodriguez-Reinoso F, Rouquerol J, Sing KS (2015) Physisorption of gases, with special reference to the evaluation of surface area and pore size distribution (IUPAC Technical Report). *Pure Appl Chem* 87(9–10):1051–1069. <https://doi.org/10.1515/pac-2014-1117>
2. Murata K, El-Merraoui M, Kaneko K (2001) A new determination method of absolute adsorption isotherm of supercritical gases under high pressure with a special relevance to density-functional theory study. *J Chem Phys* 114(9):4196–4205. <https://doi.org/10.1063/1.1344926>
3. Murata K, Kaneko K (2000) Nano-range interfacial layer upon high-pressure adsorption of supercritical gases. *Chem Phys Lett* 321(5):342–348. [https://doi.org/10.1016/S0009-2614\(00\)00367-5](https://doi.org/10.1016/S0009-2614(00)00367-5)
4. Murata K, Kaneko K, Kanoh H, Kasuya D, Takahashi K, Kokai F, Yudasaka M, Iijima S (2002) Adsorption mechanism of supercritical hydrogen in internal and interstitial nanospaces of single-wall carbon nanohorn assembly. *J Phys Chem B* 106(43):11132–11138. <https://doi.org/10.1021/jp020583u>

5. Kaneko K, Shimizu K, Suzuki T (1992) Intrapore field-dependent micropore filling of supercritical N<sub>2</sub> in slit-shaped micropores. *J Chem Phys* 97(11):8705–8711. <https://doi.org/10.1063/1.463389>
6. Ruike M, Kasu T, Setoyama N, Suzuki T, Kaneko K (1994) Inaccessible pore characterization of less-crystalline microporous solids. *J Phys Chem* 98(38):9594–9600. <https://doi.org/10.1021/j100089a038>
7. Noguchi H, Kondo A, Kajiro H, Kanoh H, Kaneko K (2006) Probe molecule-dependent particle density and its effect on the supercritical gas adsorption isotherm of nanoporous Cu complex crystals. *Adsorpt Sci Technol* 24(7):595–600. <https://doi.org/10.1260/026361706780810258>
8. Donohue M, Aranovich G (1999) A new classification of isotherms for Gibbs adsorption of gases on solids. *Fluid Phase Equilib* 158–160:557–563. [https://doi.org/10.1016/S0378-3812\(99\)00074-6](https://doi.org/10.1016/S0378-3812(99)00074-6)
9. Myers AL, Monson PA (2014) Physical adsorption of gases: the case for absolute adsorption as the basis for thermodynamic analysis. *Adsorption* 20(4):591–622. <https://doi.org/10.1007/s10450-014-9604-1>
10. Zhou L, Bai S, Su W, Yang J, Zhou Y (2003) Comparative study of the excess versus absolute adsorption of CO<sub>2</sub> on superactivated carbon for the near-critical region. *Langmuir* 19(7):2683–2690. <https://doi.org/10.1021/la020682z>
11. Keller JU, Zimmermann W, Schein E (2003) Determination of absolute gas adsorption isotherms by combined calorimetric and dielectric measurements. *Adsorption* 9(2):177–188. <https://doi.org/10.1023/A:1024249628239>
12. Phadungbut P, Fan C, Do DD, Nicholson D, Tangsathikulchai C (2015) Determination of absolute adsorption for argon on flat surfaces under sub- and supercritical conditions. *Colloids Surf A Physicochem Eng Asp* 480:19–27. <https://doi.org/10.1016/j.colsurfa.2015.04.011>
13. Brandani S, Mangano E, Sarkisov L (2016) Net, excess and absolute adsorption and adsorption of helium. *Adsorption* 22(2):261–276. <https://doi.org/10.1007/s10450-016-9766-0>
14. Murata K, Miyawaki J, Kaneko K (2002) A simple determination method of the absolute adsorbed amount for high pressure gas adsorption. *Carbon* 40(3):425–428. [https://doi.org/10.1016/S0008-6223\(01\)00126-9](https://doi.org/10.1016/S0008-6223(01)00126-9)
15. Murata K, Yudasaka M, Iijima S, El-Merraoui M, Kaneko K (2002) Classification of supercritical gas adsorption isotherms based on fluid-fluid interaction. *J Appl Phys* 91(12):10227–10229. <https://doi.org/10.1063/1.1479474>
16. Murata K, Kaneko K (2001) The general equation of supercritical gas adsorption isotherm. *J Phys Chem B* 105(36):8498–8503. <https://doi.org/10.1021/jp0107816>
17. Tanaka H, Kanoh H, El-Merraoui M, Steele WA, Yudasaka M, Iijima S, Kaneko K (2004) Quantum effects on hydrogen adsorption in internal nanospaces of single-wall carbon nanohorns. *J Phys Chem B* 108(45):17457–17465. <https://doi.org/10.1021/jp048603a>
18. Beenakker JJM, Borman VD, Krylov SY (1995) Molecular transport in subnanometer pores: zero-point energy, reduced dimensionality and quantum sieving. *Chem Phys Lett* 232(4):379–382. [https://doi.org/10.1016/0009-2614\(94\)01372-3](https://doi.org/10.1016/0009-2614(94)01372-3)
19. Wang Q, Challa SR, Sholl DS, Johnson JK (1999) Quantum sieving in carbon nanotubes and zeolites. *Phys Rev Lett* 82(5):956–959. <https://doi.org/10.1103/PhysRevLett.82.956>
20. Niimura S, Fujimori T, Minami D, Hattori Y, Abrams L, Corbin D, Hata K, Kaneko K (2012) Dynamic quantum molecular sieving separation of D<sub>2</sub> from H<sub>2</sub>-D<sub>2</sub> mixture with nanoporous materials. *J Am Chem Soc* 134(45):18483–18486. <https://doi.org/10.1021/ja305809u>
21. Hiraide S, Tanaka H, Miyahara MT (2016) Understanding gate adsorption behaviour of CO<sub>2</sub> on elastic layer-structured metal-organic framework-11. *Dalton Trans* 45(10):4193–4202. <https://doi.org/10.1039/C5DT03476K>
22. Kanoh H, Kondo A, Noguchi H, Kajiro H, Tohdoh A, Hattori Y, Xu WC, Inoue M, Sugiura T, Morita K et al (2009) Elastic layer-structured metal organic frameworks (ELMs). *J Colloid Interface Sci* 334(1):1–7. <https://doi.org/10.1016/j.jcis.2009.03.020>

23. Kondo A, Noguchi H, Ohnishi S, Kajiro H, Tohdoh A, Hattori Y, Xu WC, Tanaka H, Kanoh H, Kaneko K (2006) Novel expansion/shrinkage modulation of 2D layered MOF triggered by clathrate formation with CO<sub>2</sub> molecules. *Nano Lett* 6(11):2581–2584. <https://doi.org/10.1021/nl062032b>
24. Nicholson D, Parsonage NG (1982) *Computer simulation and the statistical mechanics of adsorption*. Academic Press, google-Books-ID: 7HInFGsTVFwC
25. Ohba T (2014) Size-dependent water structures in carbon nanotubes. *Angew Chem Int Ed* 53(31):8032–8036. <https://doi.org/10.1002/anie.201403839>
26. Futamura R, Iiyama T, Takasaki Y, Gogotsi Y, Biggs MJ, Salanne M, Sgalini J, Simon P, Kaneko K (2017) Partial breaking of the coulombic ordering of ionic liquids confined in carbon nanopores. *Nat Mater* 16(12):1225–1232. <https://doi.org/10.1038/nmat4974>
27. Rigby M (1986) *The forces between molecules*. Clarendon Press, google-Books-ID: ckd-CAQAIAAJ
28. Pace EL (1967) *Adsorption thermodynamics and experimental measurement*, vol 1, chap 4. Dekker, New York, pp 105–110
29. Ross S, Olivier JP (1964) *On physical adsorption*. Interscience Publishers, New York. google-Books-ID: DRBRAAAAMAAJ
30. Fowler (1967) *Statistical mechanics*. CUP Archive, google-Books-ID: qLE8AAAAIAAJ
31. Hartl M, Gillis RC, Daemen L, Olds DP, Page K, Carlson S, Cheng Y, Hügler T, Iverson EB, Ramirez-Cuesta AJ et al (2016) Hydrogen adsorption on two catalysts for the ortho-to parahydrogen conversion: Cr-doped silica and ferric oxide gel. *Phys Chem Chem Phys* 18(26):17281–17293. <https://doi.org/10.1039/C6CP01154C>

# Chapter 4

## Physical Chemistry and Engineering for Adsorptive Gas Storage in Nanoporous Solids



Orhan Talu

### 4.1 Introduction

This chapter (1) describes some of the common means to quantify adsorption equilibrium from a scientific viewpoint, (2) reviews common experimental techniques to measure adsorption and their correspondence to storage application performance, and (3) reviews some other critical engineering aspects of adsorptive gas storage. It is not intended to be an exhaustive review of scientific literature. Rather, it is intended to provide background and guidance to researchers developing systems on some critical issues involved in estimation and performance of adsorptive gas storage.

First noticed and documented in the 1700s, adsorption is simply the accumulation of fluid molecules at the immediate vicinity of an interface between two bulk phases. Accumulation occurs only within a few molecules thick layer of the interface. The accumulation can be caused by either (1) chemical bonds between the guest-host resulting in chemisorption or (2) physical intermolecular interaction forces between molecules/atoms of guest and host. Intermolecular forces, also responsible in condensation from vapor phase, involve electrostatic, induced electrostatic, and dispersion forces. Although adsorption occurs in between two immiscible liquids (i.e., spreading of oils on water) or on a liquid surface exposed to a gas/vapor, most practical applications of adsorption involve a solid phase. Adjoining fluid phase can be either a liquid or a gas (i.e.,  $T > T_{crit}$ ), or a vapor (i.e.,  $T < T_{crit}$ ).

Gas storage application involves a supercritical fluid (i.e., gas) and a nanoporous solid. At a molecular scale, the guest molecules are said to be on the solid surface, but when an entire solid particle is considered, guest molecules are in the solid

---

O. Talu (✉)

Chemical and Biomedical Engineering Department, Cleveland State University, Cleveland, OH, USA

e-mail: [o.talu@csuohio.edu](mailto:o.talu@csuohio.edu)

© Springer Nature Singapore Pte Ltd. 2019

K. Kaneko, F. Rodríguez-Reinoso (eds.), *Nanoporous Materials for Gas Storage*, Green Energy and Technology, [https://doi.org/10.1007/978-981-13-3504-4\\_4](https://doi.org/10.1007/978-981-13-3504-4_4)

65

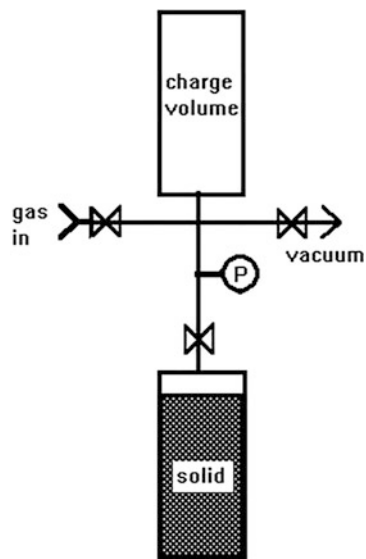
particle. This fact complicates the quantification of most fundamental thermodynamic property of adsorption as the amount adsorbed. These complications and its implication on gas storage application are discussed after description of simplest way to measure storage directly. The final sections of this chapter include some examples and brief review of important engineering aspects of adsorptive storage.

## 4.2 Direct Experimental Measurement of Adsorptive Gas Storage

From a practical viewpoint, the amount of gas stored in a container, or column, can be measured experimentally by using a simple apparatus similar to Fig. 4.1. The apparatus is kept isothermal at temperature  $T$  for simplicity in this example. The system has two containers connected by a valve. There is also vacuum-vent connection and an inlet connection for the subject gas. The inside volume of the containers,  $V^{\text{ch}}$  and  $V^{\text{col}}$ , is measured once as part of initial equipment calibration during commissioning of apparatus.

To perform experiments, a certain amount of solid adsorbent with vacuum mass of  $M$  is placed in the column. Initially, the solid is activated/regenerated by applying heat under vacuum. The column is then cooled, completely vacuumed, and the containers are isolated by closing the connecting valve. Subject gas is introduced to  $V^{\text{ch}}$  at pressure  $P^{\text{ch}}$  and temperature  $T$ . The gas is then introduced to the solid by opening the connecting valve. System  $P$  and  $T$  are monitored until they stabilize denoting phase equilibrium conditions have been reached between the gas phase

**Fig. 4.1** Apparatus for direct measurement of adsorptive gas storage. (Reprinted with permission from Langmuir 2010, 26(22), 17013–17023. Copyright 2010 American Chemical Society)



and adsorbed phase in the solid. Final values are noted as  $P^{eq}$  and  $T$ . The amount of gas stored and adsorbed can be calculated by material balances as follows:

Assuming ideal gas for simplicity, the amount of gas leaving the charge volume is calculated from initial and final conditions in the charge volume as

$$\Delta N^{ch} = \frac{P^{ch} V^{ch}}{RT} - \frac{P^{eq} V^{ch}}{RT} = N^{st} \quad (4.1)$$

This is the total amount of gas transferred to the solid container; it is also the *total amount stored* ( $N^{st}$ ) in the adsorbent packed column without making any distinction between gas and adsorbed phases.

Under the same conditions but without the solid phase present in the column, the amount of gas stored would be

$$N_{gas}^{st} = \frac{P^{eq} V^{col}}{RT} \quad (4.2)$$

Hence, the extra amount stored because of adsorption is given by

$$N_{ads}^{st} = N^{st} - N_{gas}^{st} \quad (4.3)$$

Thermodynamically this is an extensive property which needs to be reduced by a quantity describing the amount of solid in the system. Normally, the vacuum mass of solid is used for this purpose to provide mass-specific adsorbed storage amount as

$$n_{ads}^{st} = \frac{N_{ads}^{st}}{M} \quad (4.4)$$

Theoretically, any other extensive property of the solid such as solid volume or solid surface area can also be used in the denominator of Eq. (4.4) to indicate the extent of adsorption system, i.e., amount of solid. But mass is always preferred in adsorption studies since it is the most accurate, easy to measure, and readily available extensive property for any nanoporous solid. In practice mass is also almost exclusively used in laboratory experiments and in applications of adsorption. Combining the above equations one arrives at

$$n_{ads}^{st} = \frac{P^{ch} V^{ch}}{MRT} - \frac{P^{eq} (V^{ch} + V^{col})}{MRT} \quad (4.5)$$

If the mass-specific adsorbed storage amount is known, the total amount of gas stored in an application container can be calculated from its volume and mass of solid in it by

$$N^{\text{st}} = \frac{PV^{\text{col}}}{RT} + Mn_{\text{ads}}^{\text{st}} \quad (4.6)$$

The adsorbed storage amount defined here is particularly useful to compare different solids for a storage application, higher values indicating a better adsorbent for storage purposes. Unfortunately, almost all literature data on adsorption report surface excess amount adsorbed. Also molecular simulations normally yield absolute amount adsorbed. Therefore, it is important to understand how these different definitions of adsorption relate to adsorptive gas storage. Next few sections examine, in detail, how these different definitions are related to each other to enable estimation of adsorptive storage performance from literature and/or simulation data.

### 4.3 Quantification of Adsorption on Different Substrates

Adsorptive storage defined in previous section does not contain information about the microstructure of adsorbed gas-solid heterogeneous system. At the molecular scale, obviously part of the total volume in the container is occupied by the solid matrix where the gas density is zero. Also, part of the volume far from solid is simple compressed gas phase. Conceptually, there must be a 2D surface between these two 3D regions as solid and gas. Adsorbed molecules accumulate on/around this surface. The molecular level topology of this 2D surface has a profound impact on how adsorption occurs and quantified. Below the microstructure of the interface is first examined for a flat-open solid surface, as one extreme. Later the case of internal surface on pore walls of a nanoporous solid is examined. The two cases are similar in nature, but they represent two extreme cases of adsorption.

#### 4.3.1 Adsorption on a Flat, Open Solid Surface

Although an open surface is not particularly useful for storage purposes, adsorption on such is covered here to clearly delineate the differences between external and internal solid surfaces. In addition, historical development of adsorption science primarily originates from spreading on liquid surfaces which is similar to adsorption on open surfaces. Even publications by international organizations such as IUPAC utilize mental constructs of adsorption on open surfaces to explain adsorption [15], though there are no significant applications of adsorption which utilize open solid surfaces.

On an open surface, the density of a gas in the immediate vicinity of a solid may be depicted as in Fig. 4.2. There are three density profiles shown in the figure at three pressure levels in the adjoining gas phase at same temperature. Similar profiles result at different temperatures but same pressure.

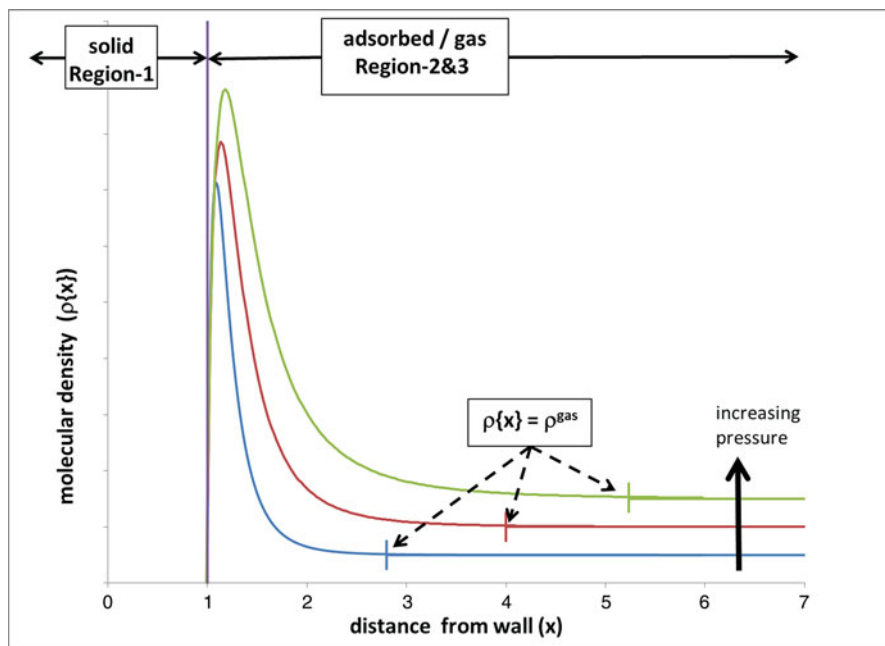


Fig. 4.2 Gas density profiles on a flat, open solid surface

In each case, the molecular density is zero in the solid matrix on the left in Region-1. An adsorbed layer of high gas density is formed next to the surface due to molecular interactions (Region-2). The density peaks close to the surface where the interactions are strongest because of short interaction distances. The density gradually decays to the gas density far away from the surface on the right of the figure in Region-3. The perturbed density region is the adsorbed phase. Amount adsorbed is simply a numerical quantification of this perturbation mathematically given as

$$\Gamma = \int_{\text{interfacial region}} \rho \{x\} . dx \quad (4.7)$$

Here,  $\Gamma$  is the area-specific amount adsorbed, area being perpendicular to the page. Area-specific amount adsorbed is the only scalable intensive property for adsorption on open surfaces. In direct extension to nanoporous solids traditionally, multiplying Eq. (4.7) with the specific surface area of solid as area per solid mass ( $\Sigma$ ) provides the amount adsorbed.

$$n = \Sigma.\Gamma \tag{4.8}$$

Equation (4.7) as primary description of adsorption on an open surface is simple and straight forward if the *interfacial region* is defined and somehow measured experimentally.

A very important feature to note is that the range of density perturbation depends on pressure; higher pressure causes a thicker surface layer. Small tick marks on density profiles in Fig. 4.2 show the thickness of surface layer. The impact of pressure on the peak density value is somewhat subdued since the first high-density layer (which is often called the monolayer) is already crowded at lowest pressure with molecules; additional adsorption can primarily occur by extending the adsorbed layer into the gas phase by forming other layers on an open surface. In essence, the adsorbed layer thickness depends on system properties (i.e., *P* and *T*) which complicate the definition and measurement of *interfacial region* necessary for Eq. (4.7) as was first recognized by J.W. Gibbs [1].

Under these circumstances, there are three ways to quantify the amount adsorbed for the system as depicted in Fig. 4.3. Only one density profile at some *T* and *P* is shown for the three definitions of adsorption.

First the description of *absolute* amount adsorbed is displayed in Fig. 4.3a. The integral in Eq. 4.7 is evaluated from solid surface to the end of density perturbation, denoted as *L* in the following equation.

$$\Gamma^{abs} = \int_1^L \rho \{x\} .dx \tag{4.9}$$

Absolute amount adsorbed needs knowledge of where solid starts (*x* = 1 location) and where perturbation ends (*x* = *L*). As discussed above, the thickness of adsorbed layer depends on *P* and *T* which renders absolute amount adsorbed mathematically

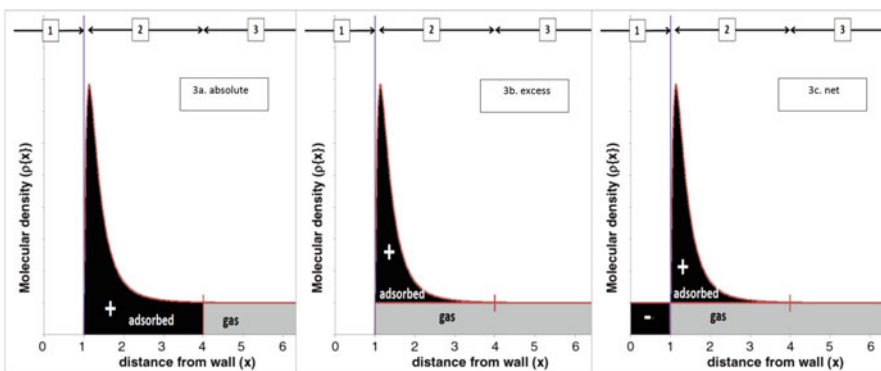


Fig. 4.3 Absolute, excess, and net adsorption on a flat, open surface

ill-defined, experimentally unmeasurable, and practically unusable for adsorption on an open surface.

Recognizing the ambiguity in defining a finite thickness of adsorbed layer, J.W. Gibbs [1] proposed to use a surface *excess* amount adsorbed description shown in Fig. 4.3b.

$$\Gamma^{\text{ex}} = \int_1^{\infty} (\rho\{x\} - \rho^g) .dx \quad (4.10)$$

In this equation,  $\rho^g$  is the gas density at  $P$  and  $T$  which can be determined from an appropriate equation of state. Notice the problematic upper integration limit is replaced with infinity circumventing the ambiguity of varying adsorbed layer thickness. Despite the infinity limit, the surface excess amount adsorbed is finite since the integrand vanishes at  $x$  values greater than  $L$ . The Gibbs' definition of adsorption mathematically transforms the inhomogeneous interfacial region to two homogeneous 3D phases as solid and gas with constant properties and a 2D surface phase with amount adsorbed given in Eq. (4.10). The Gibbs' dividing surface in essence locates the lower integration limit where  $x = 1$  in this example. Practically, use of surface excess adsorption depends on determining the location of Gibbs dividing surface experimentally.

Finally, *net* amount adsorbed is defined by Gumma and Talu [4, 5] following the original work by Coolidge [6] and McBain [7].

$$\Gamma^{\text{net}} = \int_0^{\infty} (\rho\{x\} - \rho^g) .dx \quad (4.11)$$

Here, the lower integration limit is extended into the entirety of the solid. The integrand has a negative value wherever there is solid, has a positive value through the adsorbed layer, and finally decays to zero in the gas phase depicted in Fig. 4.3c. Net adsorption completely circumvents the problem of locating where and how thick the adsorbed layer is. Only stipulation is that a 2D surface layer exists in the system.

It should be noted that the only unequivocal property to quantify adsorption on open surfaces is the area-specific excess amount adsorbed ( $\Gamma^{\text{ex}}$ ). Absolute and net adsorption, although can be defined conceptually for an open surface, cannot be uniquely measured in an experiment since the ratio of solid to gas volumes can be changed without changing the area in between them. Nevertheless, these illustrations are important to comprehend more complicated case of adsorption in nanopores where absolute and net adsorption can be defined and scaled in mass-specific terms, while excess adsorption becomes questionable.

### 4.3.2 Adsorption in Nanoporous Solids

Nanoporous solids are used in all practical applications of adsorption because of large surface area presented by the internal pores when pore diameters are comparable to dimensions of the guest molecule. Since vast majority of surface area is on the interior pore walls, often it is possible to completely ignore the adsorption on the open external surface of adsorbent particles. (Silica gel is a notable exception). The physical mechanisms involved in adsorption (i.e., intermolecular interactions) are same regardless of the nanoscale topology of the surface, be it on open like above figures or contained within a solid. The important practical difference is that the potential field imposed by the solid is significantly enhanced in small pores of a few (e.g., 1 to 4) molecular diameters because of the overlapping attractive potentials imposed by all walls surrounding a pore. Although the primary interactions are the same, there are important qualitative and quantitative differences between adsorption on open and internal pore surfaces which are worth noting:

1. Unlike an open surface, adsorption occurs in a nanoporous solid, not on surface.
2. With an open surface, the total area to solid volume ratio can be varied/changed independently. It is meaningless to quantify mass-specific surface area of an open surface solid, since the amount of solid can be varied without changing the exposed surface area (e.g., by extending the solid to negative values in Figs. 4.2 and 4.3).
3. For a nanoporous solid, many mass-specific properties must stay constant conceptually, such as surface area, pore volume, skeletal volume, etc. although these may be hard, if not impossible, to measure exactly.
4. With nanoporous solids, there is a chance that the guest molecules cannot enter some or all of the pores simply because the guest molecules are larger than the pore diameter (i.e., complete repulsion in molecular simulations). This is called molecular sieving which cannot occur on an open surface. This fact opens two possibilities:
  - (a). For crystalline solids with nanopores, either all the pore space is available to the guest molecule or the entire pore space is not available due to the regularity of crystalline solids.
  - (b). For amorphous nanoporous solids, the situation is more complicated since these materials (e.g., activated carbon) have a very wide pore-size distribution from sub-nanometers to micrometers. The pore space and surface area availability depends on the size of guest molecules in comparison to pore diameter. Mass-specific pore volume and surface area measured depend on the molecular size and pore-size distribution. The resulting mass-specific pore volume or surface area is no longer a thermodynamic property of the pure solid, but they become a pair property of solid and guest.
5. By virtue of items 3 and 4, the adsorption characterization may depend on if the nanoporous solid is crystalline or amorphous.

**Fig. 4.4** Amorphous solid pore structure relative to guest sizes

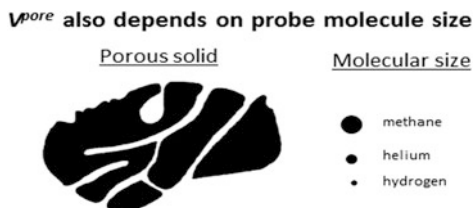


Figure 4.4 illustrates a cutaway cross section of an amorphous nanoporous solid such as an activated carbon particle and some different size molecules. The total pore volume in the micropores (i.e., cracks in 2D depiction in the figure) is needed to calculate absolute absorption. The volume occupied by the solid (dark areas in figure) is also necessary since the molecules cannot penetrate the solid matrix. Archimedes' displacement principle applied to a nanoporous solid gives different results for solid volume for different fluids used for displacement. Different number of helium, hydrogen, or methane molecules is necessary to fill the cracks in Fig. 4.4 which would result in different pore volume values. For example, notice the ink-bottle pore at the top of the particle. Hydrogen and helium molecules can enter this pore, while methane cannot. Hence, the solid cannot be said to have a constant pore volume as its own pure component physical property. The measured pore volume (or particle volume or solid skeletal volume) depends on the probe molecule used; hence, pore volume is a pair property of solid and guest molecule.

For crystalline solids such as zeolites on the other hand, the pore structure is regular and repeats in unit cells, which makes the situation more clearly tractable. But the basic fact still remains the same; pore volume, solid matrix volume, pore diameter, etc. are pair properties of solid-probe molecule system, rather than a pure property of the solid. Regardless of this complication, the fraction of pore and solid volume per mass of solid remains constant for a collection of nanoporous particles.

All three definitions of adsorption as absolute, surface excess, and net adsorption can be applied for a nanoporous solid. In fact, the difference between them is simply due to the definition of reference state in a thermodynamic sense. The details of experimental measurements determine which one is being reported. These definitions for nanoporous solids with relation to experimental techniques used in measuring gas adsorption are explained next.

#### 4.4 Experimental Measurements of Adsorption in Different Thermodynamic Frameworks

A pure component isotherm is the most fundamental and simplest characterization of the extent of adsorption. There are two common techniques [14] to measure the adsorption isotherm of a gas with a nanoporous solid: (1) volumetric and (2)

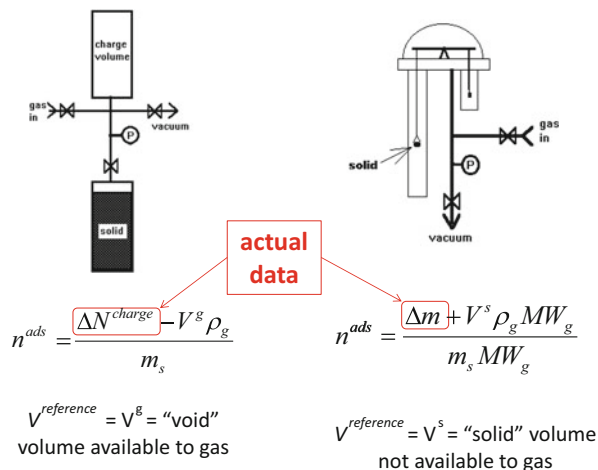


**Fig. 4.5** Common adsorption isotherm measurement apparatus. (Reprinted with permission from Langmuir 2010, 26(22), 17013–17023. Copyright 2010 American Chemical Society)

gravimetric. Many other approaches notably chromatographic techniques also exist but will not be discussed here. Simplified experimental apparatus schematics for the two common approaches are shown in Fig. 4.5.

#### 4.4.1 Volumetric Isotherm Measurement and Data Analysis

The procedure for volumetric measurement is exactly the same as the measurement of gas storage described in Sect. 4.1. The amount adsorbed can be written, in general, as

$$n = \frac{(P^{ch} - P^{eq}) V^{ch}}{MRT} - \frac{P^{eq} V^{ref}}{MRT} \quad (4.12)$$

where  $V^{ref}$  is the reference volume available for the gas molecules in the solid container below isolation valve in the figure. How  $V^{ref}$  is defined and measured determines which type of adsorption being reported as absolute, excess, or net.

As a first option, the empty column volume without any sample present ( $V^{col}$ ) can be easily and accurately measured with any gas as part of the initial equipment calibration which is necessary for charge volume also. It is the simplest option to use for  $V^{ref}$ . If that value is used in the above equation for reference volume, the result is *net* amount adsorbed.

$$n^{\text{net}} = \frac{(P^{\text{ch}} - P^{\text{eq}}) V^{\text{ch}}}{MRT} - \frac{P^{\text{eq}} V^{\text{col}}}{MRT} = n^{\text{st}}_{\text{ads}} \quad (4.13)$$

This is exactly equal to the adsorption storage amount given in Eq. 4.5. Hence, net adsorption directly shows the enhancement in gas storage caused by the existence of the solid in the container. Comparing two solids net adsorption amount directly compares their performance for storage of that gas at relevant conditions ( $T$  and  $P$ ).

The surface *excess* amount adsorbed ( $n^{\text{ex}}$ ) can be calculated from  $n^{\text{net}}$  by adding the amount of gas that would have been in the impenetrable solid volume. Resulting equation is

$$n^{\text{ex}} = \frac{(P^{\text{ch}} - P^{\text{eq}}) V^{\text{ch}}}{MRT} - \frac{P^{\text{eq}} (V^{\text{col}} - V^{\text{s}})}{MRT} \quad (4.14)$$

where  $V^{\text{s}}$  is the impenetrable solid volume where the gas density is zero. As discussed above, the measurement of  $V^{\text{s}}$  experimentally is problematic since it requires the use of probe molecules which surely is effected by the pore-size-distribution and attractive forces between the probe molecule and solid. This fact is somewhat obscured in literature since experimentally most researchers opt to measure the difference  $V^{\text{col}} - V^{\text{s}}$  directly using helium. This difference is back-calculated from Eq. (4.14) by assuming helium excess adsorption is zero. Commonly, helium at ambient temperature and low pressure is used to minimize the effect of actual adsorption on data though there is ample evidence for helium adsorption in literature [2]. One example is shown in Fig. 4.6 for helium adsorption in the zeolite, silicalite. If there was no helium adsorption, all the curves in the figure should collapse to a single straight line with the slope equal to  $-V^{\text{s}}$ . The curvatures and displacement are simply due to helium adsorption even in the nonpolar pores of silicalite. In this case, all pore space with about 0.6 nm diameter is available to helium; hence, there is not even the complicated effect of pore-size distribution and possible exclusion.

It is very important to realize that almost all data in literature on gas adsorption reports helium-surface-excess isotherm data. Unfortunately most of recent literature does not even describe how this critical measurement with helium is performed. Small differences in obtaining these correction factors (i.e., skeletal density, impenetrable solid volume, helium density, porosity, etc.) for data are not even reported which is the only means to compare/convert excess data to adsorptive storage capacity. To circumvent this shortcoming, most engineering applications assume numerous different properties such as porosity (at typically three levels as bed, particle, and crystal porosities), corresponding particle densities, solid skeletal density, etc.

The *absolute* amount adsorbed can be calculated from this experiment if both the solid and pore volume, or simply particle volume, is available. The equation is

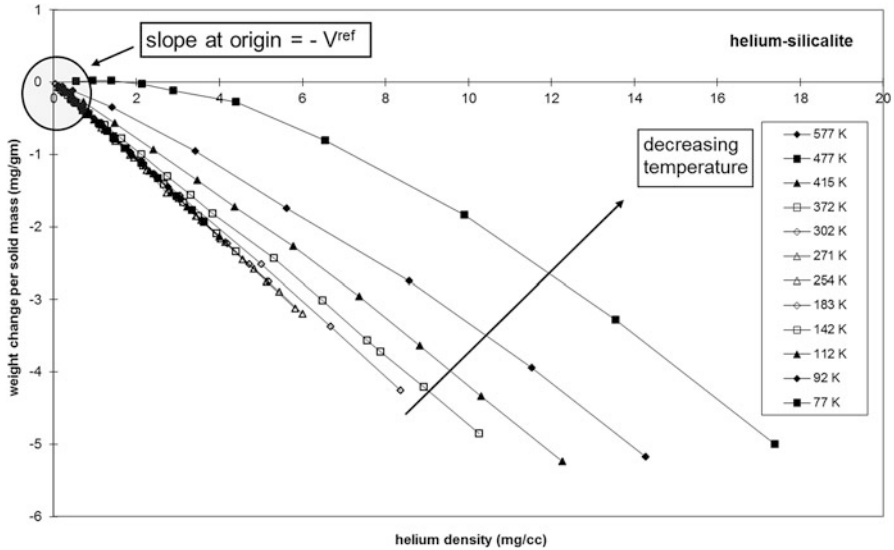


**Fig. 4.6** Helium data measured on gravimetric isotherm apparatus [2] (Reprinted by permission from Springer *Adsorption J.*, 2003, 9, 17–28. Copyright 2003)

$$n^{abs} = \frac{(P^{ch} - P^{eq}) V^{ch}}{MRT} - \frac{P^{eq} (V^{col} - V^s - V^p)}{MRT} \tag{4.15}$$

Here  $V^p$  is the pore volume which must be determined by some other means. There is no accurate experimental technique to directly measure  $V^{col} - V^s - V^p$  directly without invoking a secondary probe molecule, often a heavy vapor. Therefore, usually excess isotherm is measured using helium, and then the contribution for the pore space is back-calculated from saturation vapor adsorption by assuming the density in the pores is the same as the liquid at that temperature. This approximation gradually fails as pore-size approaches guest molecule size as has been shown numerous times by molecular simulations. The density of a few molecule thick adsorbed phases constrained in nanopores is not correlated with its bulk liquid density without the solid present. But lacking any better option, the approach is commonly used in literature to report the so-called absolute amount adsorbed.

It should be noted that  $V^p$  can be estimated by molecular simulations using helium as a probe gas; hence, absolute adsorption data from molecular simulations can be converted to excess adsorption fairly easily to be compared to experimental data. How to utilize molecular simulation data in adsorptive gas storage applications is revisited after this section.

### 4.4.2 Gravimetric Isotherm Measurement and Data Analysis

The procedures for gravimetric adsorption measurement are similar. The sample is placed in the bucket of a balance (see Fig. 4.5), initially activated by applying heat and vacuum. A base, zero mass ( $M$ ) of the solid is recorded after activation under vacuum. Subject gas is introduced. The final pressure and change in mass ( $\Delta m$ ) are recorded after equilibrium is reached indicated by stable weight and  $P$  and  $T$  readings. The amount adsorbed is calculated from the mass change by adding the buoyancy force exerted by the gas.

$$n = \frac{\Delta m}{MRT (MW_g)} + \frac{P^{eq} V^{ref}}{MRT} \quad (4.16)$$

where  $MW_g$  is the molecular weight of gas and  $V^{ref}$  is the effective buoyancy volume which includes the sample and any balance parts subject to buoyancy such as sample bucket. Once again, which adsorption value is reported depends on how  $V^{ref}$  is determined.

Simplest for reference buoyancy volume is using the volume of balance parts ( $V^{bal}$ ) effecting buoyancy force such as sample bucket, hang-down wires, etc. The total buoyancy effect of the balance can be easily and accurately measured with any gas without the sample in place as part of initial apparatus calibration. A high molecular weight inert gas (e.g., argon) rather than helium is preferred for these calibrations to increase accuracy of measurements. If only balance parts in buoyancy correction are included, the result is *net* amount adsorbed which is also equal to adsorptive storage amount:

$$n^{net} = \frac{\Delta m}{MRT (MW_g)} + \frac{P^{eq} V^{bal}}{MRT} = n_{ads}^{st} \quad (4.17)$$

*Excess* amount adsorbed requires inclusion of the volume occupied by the impenetrable solid phase in the buoyancy correction.

$$n^{ex} = \frac{\Delta m}{MRT (MW_g)} + \frac{P^{eq} (V^{bal} + V^s)}{MRT} \quad (4.18)$$

Similar to volumetric systems in usual practice, the total buoyancy volume as  $V^{bal} + V^s$  is back-calculated from Eq. (4.18) assuming helium does not adsorb ( $n^{ex}_{He} = 0$ ) at room temperature and low pressure. A helium experiment is performed following the same protocol with the sample in place which in effect makes the  $V^{ref}$  a property of both solid and helium. Care needs to be taken since helium is a very low weight gas and the balance response is low. Any inaccuracy during these measurements is magnified for the isotherm by the molecular weight ratio of subject gas to helium; e.g. impact of buoyancy force while measuring, for example, nitrogen isotherms, is sevenfold higher than helium!

## REFERENCE STATES WITH NANOOPOROUS SOLIDS

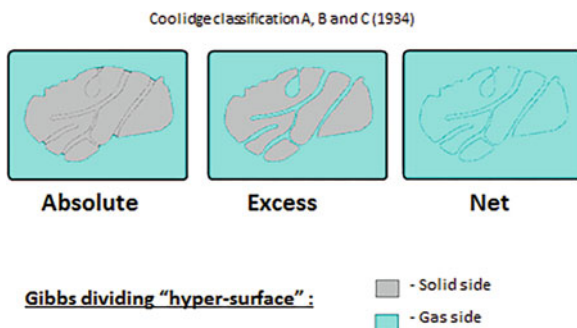


**Fig. 4.7** Reference states and Gibbs dividing surface for nanoporous solids. (Reprinted with permission from J. Phys. Chem. C 2013, *117*, 13059–13071. Copyright 2013 American Chemical Society)

Finally, *absolute* amount adsorbed requires inclusion of pore volume in the buoyancy compensation.

$$n^{\text{abs}} = \frac{\Delta m}{MRT (MW_g)} + \frac{P^{\text{eq}} (V^{\text{bal}} + V^s + V^p)}{MRT} \quad (4.19)$$

As discussed above, there is no single, unequivocal way to measure  $V^p$  (or the sum of the three volumes in second term).

Only molecular simulations performed on a computer can provide adsorbed phase properties without including the gas phase in the simulation. Experimentally, quantification of adsorption requires partitioning the volume between two 3D bulk phases since in physical measurements the gas phase always exists with the adsorbed phase. How this partitioning is defined and measured in experiments determines which thermodynamic framework is used to report the amount adsorbed. Figure 4.3 above illustrated solid-gas partitioning on an open surface. The solid-gas partitioning for the three reference states for an amorphous solid particle may be visualized as shown in Fig. 4.7.

### 4.4.3 Conversion of Data Between Net, Excess, and Absolute Adsorption

In summary, net adsorption is the easiest and the most accurate measurement for nanoporous materials. Excess and absolute amount adsorbed is obtained from net adsorption by compensating for impenetrable solid and pore volumes. The relation for adsorptive storage and the three definitions is given by

$$n_{\text{ads}}^{\text{st}} = n^{\text{net}} = \left[ n^{\text{ex}} - \frac{Pv^{\text{s}}}{RT} \right] = \left[ n^{\text{abs}} - \frac{P(v^{\text{s}} + v^{\text{p}})}{RT} \right] \quad (4.20)$$

where  $v^{\text{s}}$  and  $v^{\text{p}}$  are impenetrable solid volume and pore volume both in mass-specific terms. Thermodynamically, all three are equivalent in representing adsorption phenomena.

#### 4.4.4 Adsorption Isotherm Data from Molecular Simulations

With ever increasing power of computers, molecular simulations have become a powerful tool to study adsorption phenomena. The preferred approach is often Grand-Canonical-Monte-Carlo (GCMC) simulations performed at fixed temperature, volume, and chemical potential of the guest compound. The solid is often represented as a rigid body of atoms in the simulation box forming the fixed volume. The solid is taken as an inert species with fixed properties which only imposes a potential field in the pores for the guest molecules. The most important result of the simulations is number average ( $\langle N \rangle$ ) of the guest molecule in the simulation box. Absolute amount adsorbed is directly related to  $\langle N \rangle$  and total mass ( $m_{\text{box}}$ ) of solid atoms in the box with

$$n^{\text{abs}} = \frac{\langle N \rangle}{m_{\text{box}}} \quad (4.21)$$

The calculation of **net** adsorption and adsorptive storage is straightforward since the sum of  $v^{\text{s}}$  and  $v^{\text{p}}$  is the volume of the simulation box ( $V_{\text{box}}$ ) by definition in simulations:

$$n_{\text{ads}}^{\text{st}} = n^{\text{net}} = \left[ n^{\text{abs}} - \frac{P(v^{\text{s}} + v^{\text{p}})}{RT} \right] = \left[ \frac{\langle N \rangle}{m_{\text{box}}} - \frac{PV_{\text{box}}}{RT} \right] \quad (4.22)$$

Gas chemical potential provides  $P$  from an EOS. Molecular simulations of adsorption do not need an adjoining gas phase, thus eliminating the need to partition the available volume as gas-solid-adsorbed phases as in experiments.

Comparison of GCMC results to the common *excess* amount adsorbed requires pore volume  $v^{\text{s}}$  [3] which can only be determined from another set of molecular simulations for the probe gas (commonly helium). This approach exactly mimics the experimental technique used to determine  $V^{\text{ref}}$  with helium in experiments. The pore volume is easiest determined from the configurational integral of canonical ensemble simulations with helium as the guest molecule:

$$v^{\text{s}} = \frac{V_{\text{box}} - \int_{V_{\text{box}}} e^{-\frac{\phi}{kT}} .dV}{m_{\text{box}}} \quad (4.23)$$

where  $\phi$  is the helium-solid potential energy. Once  $\nu^s$  is known, the  $n^{\text{ex}}$  can be calculated from Eq. 4.20. This approach requires knowledge of helium-solid potential energy, and the extra simulations introduce additional computational burden.

## 4.5 Implications of Different Thermodynamic Frameworks on Adsorptive Gas Storage Characterization

The differences between net (i.e., stored), excess, and absolute amount adsorbed are usually substantial at high pressure with supercritical gases in nanoporous solids as indicated in Fig. 4.8 for methane adsorption in Norit R1 (an activated carbon) [9]. This dataset is quite unique in literature since it reports raw weight change measurements of the sample as well as helium buoyancy-corrected data directly providing net and excess amount adsorbed which in reality is very easy to do. Absolute adsorption in the figure is an approximation calculated using  $\nu^p = 0.462 \text{ cm}^3/\text{gm}$  estimate taken from another reference [10] for the same sample.

Simply looking at the net amount adsorbed (lowest curve) in Fig. 4.8, it can be stated that:

1. Adsorptive storage becomes negative beyond 21 MPa. At that pressure a container without the adsorbent stores same as a container with adsorbent. Beyond that pressure including nanoporous solid actually reduces amount of stored gas.
2. The adsorptive storage starts decreasing once pressure is above 5 MPa indicated by the maximum in net (stored) amount adsorbed. The increase in adsorptive

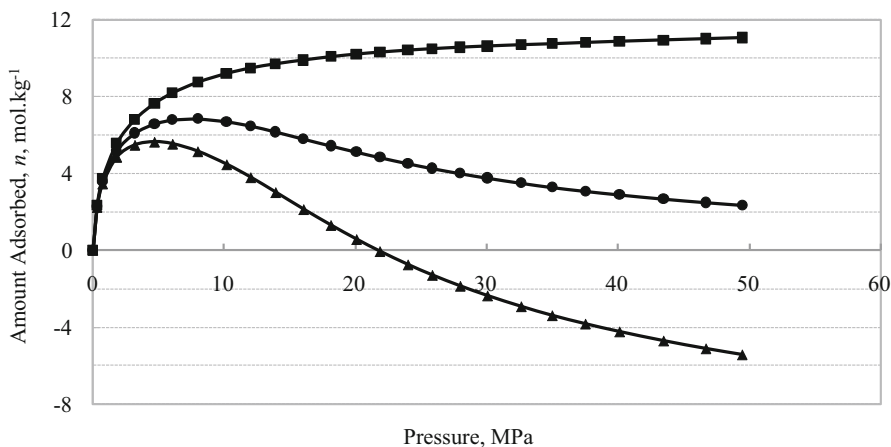


**Fig. 4.8** Absolute (squares), excess (circles), and net (triangles) adsorption isotherms for methane in Norit R1 activated carbon at 25 °C [9] (Reprinted with permission from Langmuir 2010, 26(22), 17, 013–17, 023. Copyright 2010 American Chemical Society)

storage by increasing pressure starts to diminish beyond that point. This fact, for example, has significant engineering implications.

These conclusions cannot be reached if only excess or absolute amount adsorbed was available. With excess adsorption, the impenetrable solid volume ( $v^s$ ) is necessary to determine where adsorptive storage is beneficial.  $V^s$  is necessary to compensate for the fact that gas density is zero within impenetrable solid matrix; hence, storage is even less than the gas phase. Further knowledge of pore volume ( $v^p$ ) is necessary with absolute adsorption in order not to double count for gas density in the pores.

Unlike other applications of adsorption involving vapors, volume of the solid and pore space is critically important for adsorptive gas storage applications since the density in gas phase is fairly high and adsorbed phase density is fairly low due to supercritical temperature. Simply having a high amount adsorbed on an isotherm is not sufficient to imply that the solid is a good material for adsorptive storage. The overall density of solid and the amount of space occupied by the impenetrable solid also play a crucial role. This fact is demonstrated in Fig. 4.9 for hydrogen adsorption in MOF-177 [11]. The reported storage amount is encouraging at 9 mol/kg at 100 bar. This is the total storage amount. But if the data is converted to net adsorption, it is evident that adsorptive storage is actually very low about 0.5 mol/kg. The subtle issue in this case is that majority of stored gas is simply in the gas phase between particles and in the large pores of the solid. The densified

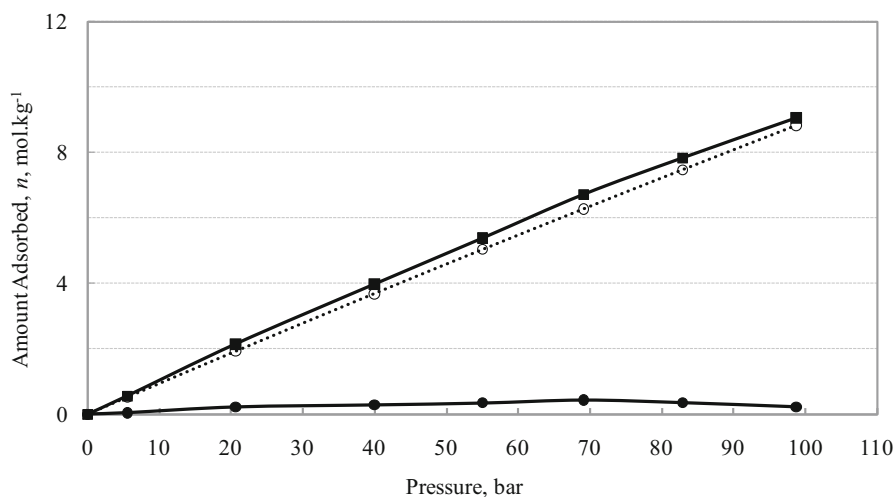


**Fig. 4.9** Contributions of adsorption to hydrogen storage at 298 K for MOF-177 calculated using experimental data of Li and Yang [11]. Total storage capacity (squares), net adsorption (filled circles), and the difference between the two quantities indicate the amount that would be stored in the same volume without the adsorbent when bulk gas is compressed to identical conditions (open circles). (Reprinted with permission from Langmuir 2010, 26(22), 17013–17023. Copyright 2010 American Chemical Society)

adsorbed layer right next to MOF-backbone can hardly overcome the space lost to the solid matrix as indicated by net amount adsorbed. This fact coupled with the inherently low packing density of MOF-177 makes this material not good for storage application despite the encouraging initial high-looking isotherm results.

## 4.6 Challenges in Measuring High-Pressure Adsorption for Gas Storage

Accurate measurement of pore and solid volumes is challenging for nanoporous solids. The impact of any inaccuracy can be very substantial especially for light gas adsorption in amorphous solids at high pressures; exactly the same situation where adsorptive storage is the most beneficial. To illustrate the significance of challenges faced by the scientific community, the results of a round-robin experiment are shown in Fig. 4.10 [9].

The study involves 11 different international laboratories worldwide. Excess hydrogen adsorption on the same sample of CMS4, an activated carbon, was measured at two temperatures. Several volumetric and gravimetric systems were used along with one open flow system. Figure 4.10 is a composite of relevant data at room temperature. Astonishing differences at high pressure is observed. At low pressure almost all data show Henry's law trend but with widely varying slopes. The researchers suggest numerous reasons for these discrepancies and make numerous excellent suggestions pointing to the challenges due to sensitivity of nanoporous materials and experimental protocols. At least one experimental uncertainty can be removed by using net adsorption for gas storage applications. We further strongly suggest, adsorption data should always be reported with enough information to convert particularly between net and excess adsorption since net adsorption, in

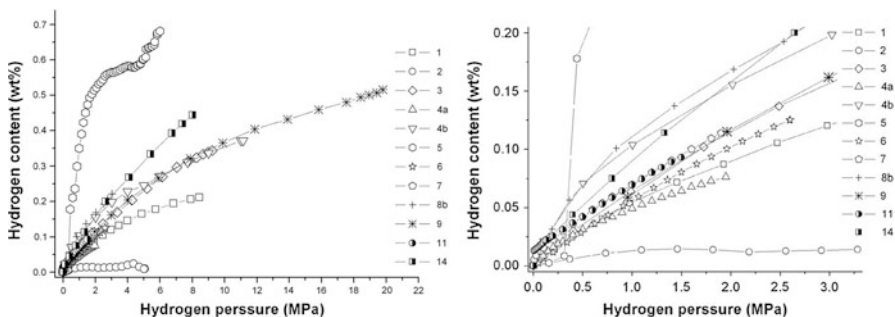


**Fig. 4.10** Hydrogen adsorption in the same sample of CMS 4 from 11 different laboratories at room temperature [8]. (Reprinted from *Int. J. Hydrogen Energy* 34 (2009) 3044–3057, Copyright 2009, with permission from Elsevier)

essence, is adsorbed storage amount. Simply reporting helium density along with isotherm data for nanoporous solids can alleviate numerous problems.

## 4.7 Other Engineering Considerations for Adsorptive Gas Storage

Three other engineering aspects of adsorptive gas storage heavily depend on physical chemistry of adsorption. These are (1) residual amount of gas left in container at depletion pressure, (2) temperature changes during charge/discharge of storage container due to heat of adsorption, and (3) impact of heavier compounds on long-term storage performance. These aspects are affected by the choice of solid and optimization of an overall engineering system. It is not our intention here to review the vast literature on these topics. Rather we will point out the essential issues with basic explanations with a few examples.

### 4.7.1 *Residual Gas Left in Adsorptive Storage Vessel at Depletion: Isothermal Storage Capacity*

An isotherm shows amount adsorbed against absolute pressure. In applications, a storage container operates between two finite pressure levels. A storage cylinder is practically depleted when the pressure approach atmospheric pressure. Vacuum application below atmospheric pressure is not feasible. Hence, the amount of gas delivered from an adsorptive storage container is effectively related to the difference in amount adsorbed at two pressure levels: a high charge pressure and a low (about atmospheric) depletion pressure. Substantial amount of gas is left in a container at depletion pressure when adsorption is involved simply due to the shape of type 1 isotherms which are concave to the pressure axis. A material having large capacity at charge pressure is only half of the issue. A good material should also have as low a capacity as possible at depletion pressure also. Often this point is not fully appreciated by material scientists trying to develop solids with highest affinity to the subject gas. The slope of isotherm at origin is as important as the plateau height of an isotherm when drawn on an engineering scale. This point is illustrated in Fig. 4.11 for two hypothetical materials [12] operating between a high and low pressure indicated with dashed lines. A cursory look at this figure may mislead scientists to thinking that material-10 is better than material-12 since it shows a higher isotherm throughout the range. But material-10 also has a very steep slope at origin, which indicates a strong affinity of solid for the gas, practically results in higher residual methane left in the container at depletion. The working isothermal gas storage capacity in this case is higher for material-12 although its isotherm is lower in the entire operational pressure range.

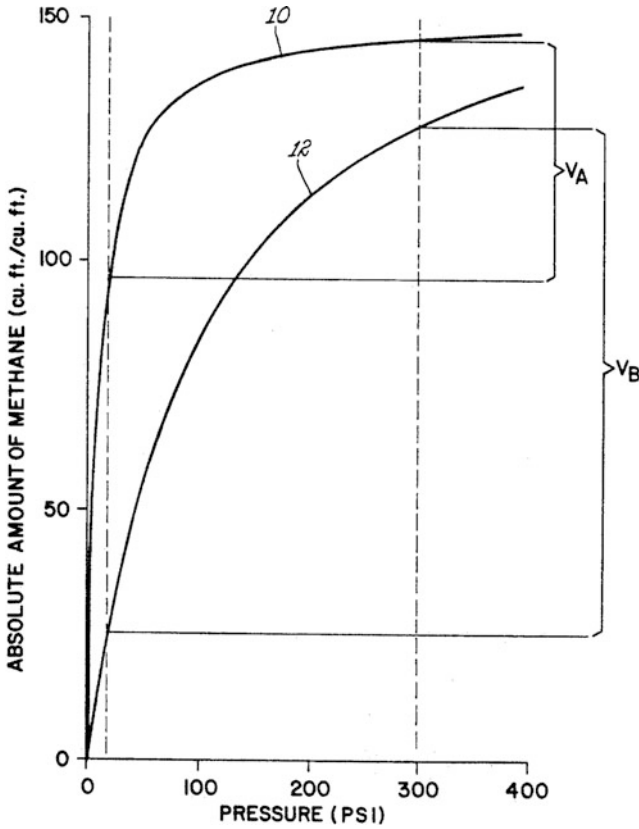
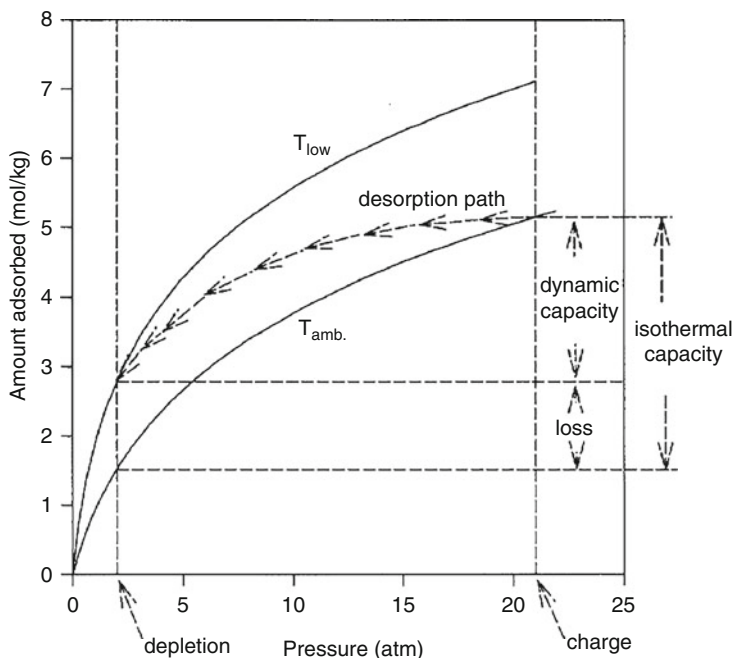


Fig. 4.11 Effect of residual left at depletion on storage capacity

#### 4.7.2 *Impact of Heat of Adsorption on Storage Performance: Dynamic Storage Capacity*

Adsorption is an exothermic process. Heat is released during charge increasing the temperature in a storage container. Conversely, the container cools down as the gas is discharged. These temperature excursions cause shifts in the adsorption isotherm effectively lowering the adsorptive gas storage performance below isothermal capacity. Figure 4.12 illustrates the phenomena for a container going through discharge operation [13]. This is a dynamic effect since the magnitude of temperature change depends on:

1. Heat of adsorption
2. Rate of charge/discharge operation
3. Geometric factors such as size and shape of storage container
4. Thermal properties of the stored gas and the container



**Fig. 4.12** Illustration for dynamic adsorptive storage gas storage capacity [13]. (Reprinted App. Thermal Eng., 1996, 16, 356–374, Copyright 1996, with permission from Elsevier)

#### 5. Surrounding conditions such as the temperature and existence of any external forced convection cooling/heating

All these are operational issues except the first item which is a physicochemical property of gas-nanoporous solid. Before giving some examples of these operational details, it is important to recognize the impact of heat of adsorption on dynamic performance. Heat of adsorption can be calculated from two or more isotherms at different temperatures [16]. Normally, a high interaction potential between the guest and nanoporous solid is thought to be desirable to increase adsorption hence storage amount. But high interaction energy also implies a higher heat of adsorption resulting in a larger temperature excursion hence reducing the dynamic capacity. There is a trade-off between the two effects pointing to a possibly optimal interaction potential, not necessarily the highest, to maximize actual dynamic performance of a storage system. Incidentally, a higher vertical interaction potential also signifies a high slope at origin which results in a larger residual amount left in a container at depletion. Both affect the residual amount not retrievable from the storage cylinder.

Other factors in the list involve operational aspects. As such it is not possible to make general statements about performance decrease beyond stating that there

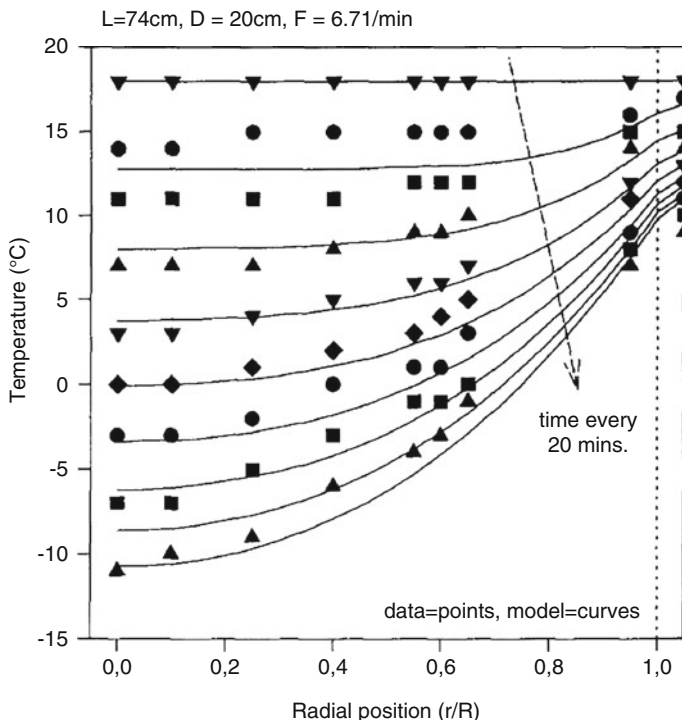


**Fig. 4.13** Radial temperature profiles with time for adsorptive methane storage tank [13] (Reprinted App. Thermal Eng., 1996, 16, 356–374, Copyright 1996, with permission from Elsevier)

will always be a loss, reduction from an isothermal performance. Here we show the results of one experimental study [13].

The temperature excursions are not small as shown in Fig. 4.13 for methane discharge from a reasonably sized container containing a common coconut shell-based activated carbon with about  $1100 \text{ m}^2/\text{gm}$  BET surface area. Experimental data shown in the figure mimics a subcompact car traveling at cruising speed with four cylindrical storage containers which last 3 h. The experiments were performed in lab environment; model assumes natural convection. The container initially at  $18^\circ\text{C}$  cools down to as low as  $-12^\circ\text{C}$  or  $30^\circ\text{C}$  temperature excursion in parts of the cylinder. As expected, the coldest location is at the center of the cylinder furthest away from the wall with high thermal mass and ambient air as the only heat source.

The capacity loss due to temperature excursion can be quantified as the amount of methane left in the cylinder when it is depleted. Figure 4.14 shows the impact of discharge rate and external thermal conditions on the residual amount left in the container by radial position. Isothermal operation is shown as a dashed line at 30%. At discharge rate of  $6.72 \text{ L/min}$ , the residual amount left varies from 50% to 40% of storage at charge pressure. The impact of external heat transfer conditions is shown

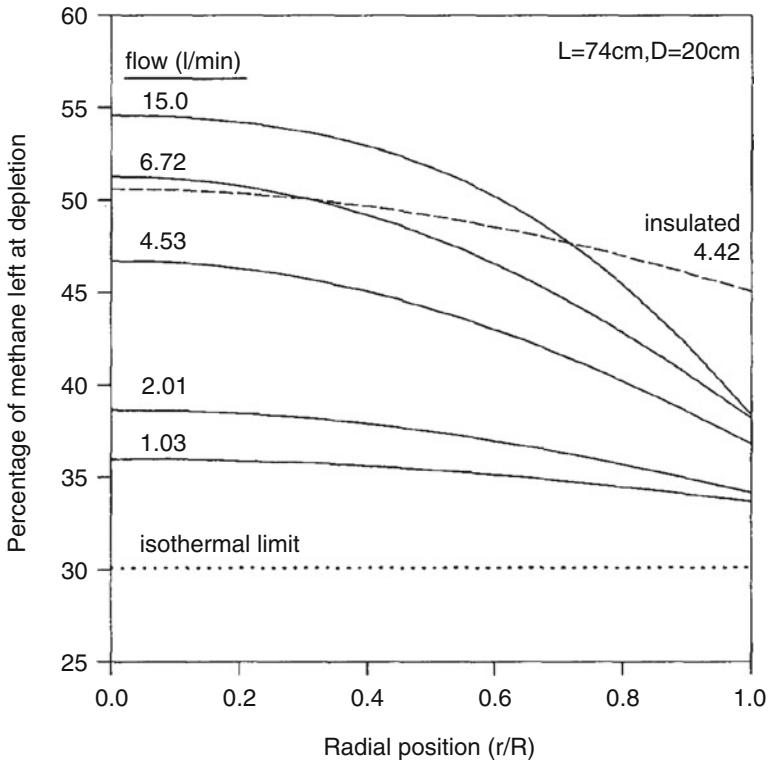
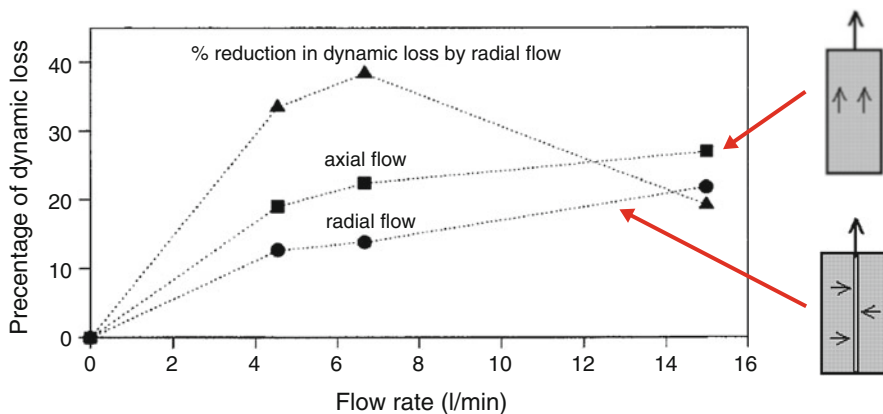


**Fig. 4.14** Radial distribution of residual methane left at depletion [13]. (Reprinted App. Thermal Eng., 1996, 16, 356–374, Copyright 1996, with permission from Elsevier)

for an insulated cylinder versus natural convection at about 4.4 and 4.53 L/min, respectively. These are very substantial losses for any engineering operation.

Some engineering systems can be designed to remedy the temperature excursions hence boost the dynamic storage capacity. Most of these engineering systems have been evaluated for the specific purpose of methane (i.e., natural gas) adsorptive storage in the 1980–1990s. It is generally agreed that inclusion of internal heat exchangers, common remedy by engineers, is not feasible for gas storage applications because of space, complexity, and weight especially in mobile applications. Other passive remedies have been evaluated also. For example, high heat capacity solids dispersed throughout the packing can act as thermal energy reservoirs. But the added weight and volume of these thermal reservoirs defeat the benefits, rendering the approach technically infeasible.

A simple passive remedy to reduce temperature excursions was proposed and tested by Chang and Talu [13] for the application used as an example here. Most of the energy available to compensate for temperature excursions is closer to the wall of the cylinder as evident in temperature profiles in Fig. 4.13. This is due to (1) high thermal mass of the vessel compared to packing and (2) heat transfer from surroundings. In addition, measured axial temperature profiles are almost flat



Experimental data for the effect of flow direction during discharge of ANG cylinders.

**Fig. 4.15** Effect of flow direction on dynamic losses [13]. (Reprinted App. Thermal Eng., 1996, 16, 356–374, Copyright 1996, with permission from Elsevier)

(not shown here) indicating substantial convective heat transfer in flow direction is possible. Hence, the proposed idea is to distribute energy from thermal reservoirs at the wall to the center of the cylinder by changing flow direction from axial to radial in the cylinder. A small perforated tube is inserted at the center of the cylinder and used to charge/discharge the cylinder, rather than just a valve at the top of packing. The tube has negligible impact on the weight of the cylinder and on the volume available for packing (both less than 1%). Figure 4.15 shows total dynamic loss for two different flow designs: (1) normal axial flow where the methane is retrieved from the top end of the cylinder and (2) radial flow where methane is retrieved from a perforated tube inserted at the center of the cylinder. This simple remedy alleviates almost 40% of the dynamic loss as shown in the figure.

### 4.7.3 Impact of Heavier Compounds on Storage Performance

Any real application of adsorptive storage will most likely involve impurities heavier than the subject gas in the feed stream. This is particularly the case for natural gas storage. Pipeline natural gas is predominantly methane (>92% depending on the region). The remaining portion contain light compounds, mostly nitrogen and oxygen/argon, and numerous heavy compounds such as carbon dioxide, natural gas liquids (C2–C5 range hydrocarbons) in fractional percentage range, and very heavy compounds such as sulfur species originating both from the NG well and intentionally added to odorize pipeline gas in parts-per-million concentrations. These heavy compounds are preferentially absorbed by nanoporous solids and

accumulate on the surface, if they can access the pores. In fact, nanoporous solids are commonly used in NG processing to remove/control these species.

In adsorptive natural gas storage, the accumulation of heavy species on the solid reduces capacity for methane storage; hence, the system performance decays at every charge-discharge cycle. In effect, the operation is governed with multicomponent adsorption rather than just methane adsorption. How fast the performance decays depends on the concentration of heavy compounds in the feed gas in relation to the characteristics of the nanoporous solid. The decay is slow especially for ppm-level impurities and very cumbersome to measure experimentally by simply cycling storage vessels tens of thousands of times. But the decay is not unbounded. The storage performance will stabilize over time after a certain number of cycles. This is similar to cyclic steady state in other applications of adsorption. When stability is reached, the total amount of a heavy compound introduced to the cylinder during charge step is the same as the total amount that leaves the cylinder during discharge step. These are also exactly same conditions when a column is equilibrated with a flowing gas; inlet and outlet flow rate of each species is equal. Hence, the ultimate impact of heavy impurities on adsorptive gas storage applications can be determined by simply measuring (or estimating) multicomponent adsorption equilibrium. The results will correspond to what will happen in an adsorptive storage system after infinite number of cycles or at cyclic steady state. Furthermore, the time (as number of cycles) it will take for maximum decay may be approximated by some simple model of the container. The resulting characteristic is an exponential decay to the final value, as would be expected.

Finally a safety note for adsorbed natural gas applications. Some of the heavy compounds are intentionally introduced into the system in commercial operations for safety reasons. The best example is odorants in pipeline and distribution NG. These are necessary for natural gas systems to alert in case of a leak since methane is odorless. Adsorptive gas storage operation effectively removes the odorants by preferential adsorption on the nanoporous material. If odorized NG is used during charge cycle, most likely non-odorized methane will be discharged from the cylinder. Engineering systems need to be designed to re-odorize desorbed natural gas.

## References

1. Gibbs JW (1928) The collected works of J. W. Gibbs. Longmans and Green, New York
2. Gumma S, Talu O (2003) Gibbs dividing surface and helium adsorption. *Adsorption* 9:17–28
3. Talu O, Myers AL (2001) Molecular simulation of adsorption: Gibbs dividing surface and comparison to experiment. *AIChE J* 47:1160–1168
4. Gumma S, Talu O (2010) Net adsorption: a thermodynamic framework for supercritical gas adsorption and storage in porous solids. *Langmuir* 26(22):17013–17023
5. Talu O (2013) Net adsorption of gas/vapor mixtures in microporous solids. *J Phys Chem C* 117:13059–13071
6. Coolidge AS (1934) Adsorption at high pressures. *J Am Chem Soc* 56:554–561

7. McBain JW, Britton GT (1930) The nature of sorption by charcoal of gases and vapors under great pressure. *J Am Chem Soc* 52:2198–2222
8. Zlotea C, Moretto P, Steriotis T (2009) A round Robin characterization of the hydrogen sorption properties of a carbon based material. *Int J Hydrog Energy* 34:3044–3057
9. Herbst A, Harting P (2002) Thermodynamic description of excess isotherms in high-pressure adsorption of methane, argon and nitrogen. *Adsorption J* 8:111–123
10. Ustinov EA, Do DD, Herbst A, Staudt R, Harting P (2002) Modelling of gas adsorption equilibrium over wide range of pressure: A thermodynamic approach based on equation of state. *J Colloid Interface Sci* 250:49–62
11. Li Y, Yang RT (2007) Gas adsorption and storage in metal-organic framework MOF-177. *Langmuir* 23:12937–12944
12. Talu O (1993) Gas storage process. US Patent 5,247,971
13. Chang KJ, Talu O (1996) Behavior and performance of adsorptive natural gas storage cylinders during discharge. *App Thermal Eng* 16:356–374
14. Talu O (2011) Measurement and analysis of mixture adsorption equilibrium in porous solids. *Chem Ing Tech* 83:67–82
15. Rouquerol J et al (1994) Recommendations for the characterization of porous solids. *Pure Appl Chem* 66(8):1739–1758
16. Talu O, Kabel RL (1987) Isotheric heat of adsorption and the vacancy solution model. *AIChE J* 33:510–514

# Chapter 5

## Nanoporous Carbons with Tuned Porosity



Conchi O. Ania and Encarnacion Raymundo-Piñero

### 5.1 Introduction

Nanoporous carbons (aka activated carbons) are unique materials that have been extensively used in many specialized applications from gas adsorption and separation, environmental remediation, catalysis, and energy storage [1–3]. Such variety of applications is mostly due to the flexible coordination chemistry of carbon atoms that allows almost infinite possibilities of three-dimensional structures and to their ability to react with other heteroatoms (e.g., oxygen, nitrogen, boron) to incorporate specific functionalities. From a structural point of view, nanoporous carbons are composed of distorted graphene-like layers of  $sp^2$  domains of carbon atoms also rich in defects (free edge sites), heteroatoms located at the edges (predominantly) or inserted in the basal planes, and carbon atoms in  $sp^3$  configurations [1, 4]. The distorted graphene layers are stacked by weak Van der Waals forces either in an ordered or turbostratic structure with different degrees of planarity depending on the graphitization extent of the materials. The free sites are associated with armchair (carbyne-like) and zigzag (carbene type) configuration carbon atoms (rather than H-terminated or free radicals as generally assumed for a long time) and account for the surface reactivity of carbons in gasification reactions or to chemisorb heteroatoms and create stable surface functionalities [5].

Nanoporous carbons can display a hierarchical pore structure and exist in 3D architectures reaching specific surface areas (SSA) over  $1000 \text{ m}^2/\text{g}$  [1, 2] and displaying a high fraction of pores of nanometric dimensions. The versatile surface chemistry of carbons also provides a useful tool to material's design, since small amounts of heteroatoms may control the physicochemical properties of the final

---

C. O. Ania (✉) · E. Raymundo-Piñero  
CEMHTI, CNRS (UPR 3079), University of Orléans, Orléans, France  
e-mail: [conchi.ania@cnrs-orleans.fr](mailto:conchi.ania@cnrs-orleans.fr)

carbons (e.g., self-organization, chemical stability, reactivity) [3]. The combination of an structural arrangement of graphene layers in varied pore architectures and an adequate surface chemistry makes nanoporous carbons successful adsorbents in many areas of adsorption, catalysis and so on [6], particularly when compared to direct competitor materials.

There are numerous studies in the literature on the preparation of nanoporous carbons with varied textural and chemical features [1, 2]. Hence, it is important to place this in the context of applications for gas storage. Indeed, the performance of an adsorbent in a specific application must (should) be modulated by selecting an adequate precursor and synthetic approach to control various characteristics such as structure, porosity, chemical composition, and morphology.

Among the large spectrum of materials with potential ability to selectively adsorb specific molecules of a gas mixture, activated carbons play an important role due to the versatility of forms, morphologies, and pore architectures. Indeed, numerous works in the literature describe that properly designed nanoporous carbons can achieve the target values for high-pressure gas storage of supercritical gases, when compared to other MOFs, zeolites, and so forth [7–9]. They do not only provide excellent adsorption capacities and selectivity for mixtures but also better mechanical stability under pressure (upon conforming), which is required for practical applications.

For practical gas-phase applications, an appropriate adsorbent must fit the requirements of high adsorption capacity at the operating conditions, fast adsorption kinetics, high selectivity toward the target gas molecule in a mixture of gases, easy regeneration, and high working or delivered capacity. These aspects should be achieved and controlled by tuning the porosity (i.e., high pore volume and uniform distribution of pore sizes, high density, and minimum interparticle space) and/or the surface chemistry to promote specific gas-adsorbent interactions. Hence, knowledge of the optimum the pore dimensions for high-pressure gas storage becomes critical.

Adsorption of supercritical gases takes place predominantly in pores that are less than 2 or 3 molecular diameters in width [9–11], where the adsorption potential is larger; on increasing the pore width, the forces responsible for the adsorption decrease rapidly. Thus, pores larger than 2 nm are typically not useful for the enhancement of gas storage, although they may be necessary for transport into and out of the micropores. The density of the adsorbed gas in large pores is low and similar to that of compressed gas, whereas it increases inside nanopores of adequate dimensions. Indeed, nanoporous carbons with extremely large SSAs usually have low packing densities.

For instance, for high-pressure hydrogen storage on nanoporous carbons, most experimental and theoretical studies fairly agree in the fact that the optimum pore size corresponds to pores that can hold two layers of adsorbed hydrogen (ca. 0.6–0.7 nm), whereas those larger than 1.5 nm contribute little to the storage and may be considered underused (Fig. 5.1) [10]. The volumetric storage capacity is also important; wide pores do not only adsorb H<sub>2</sub> less effectively but contribute to reducing the packing density of the adsorbent. Concerning CO<sub>2</sub> storage, the optimal

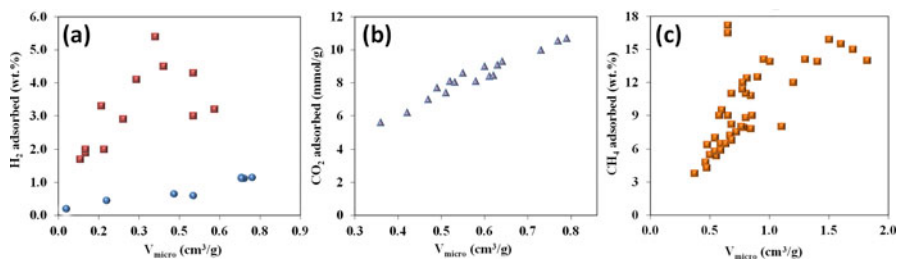


**Fig. 5.1** Correlation of the micropore volume of nanoporous carbons and the adsorption capacity of (a) H<sub>2</sub> at  $-196\text{ }^{\circ}\text{C}$  and 20 bar (squares, data from [17, 18]) and at  $25\text{ }^{\circ}\text{C}$  and 200 bar (circles, data from [19]); (b) CO<sub>2</sub> at  $25\text{ }^{\circ}\text{C}$  and 1.5 MPa. Data reproduced from [12]. Copyright 2014, with permission from Elsevier; (c) CH<sub>4</sub>. Data reproduced with permission from [9]. Copyright 2017 American Chemical Society

adsorption capacity and packing density have been reported for carbons with pores of ca.  $\sim 0.65\text{--}0.8\text{ nm}$  [11, 12]; on the other hand, selectivity toward the separation of CO<sub>2</sub> (kinetic diameter of 0.33 nm) from gases of similar dimensions such as CH<sub>4</sub> (0.39 nm) and N<sub>2</sub> (0.36 nm) requires pores around  $\sim 0.4\text{--}0.5\text{ nm}$ . Pores below these limits must be minimized to avoid kinetic restrictions [11, 12]. It has also been proposed that CO<sub>2</sub> capture under post-combustion conditions (1 bar and  $25\text{ }^{\circ}\text{C}$ ) involves exclusively the micropores below 0.6 nm, whereas for pre-combustion conditions (20 bar and  $25\text{ }^{\circ}\text{C}$ ), the entire microporosity plays a role with optimal performances in the 1.5–2 nm range. Thus, the design of the porosity of the carbon material should be conducted differently depending on their application [13]. For methane storage, an optimum pore size of ca. 0.76 nm has been reported to maximize the deliverability at ambient pressures [9, 14]. Other authors have indicated that the maximum methane storage at  $25\text{ }^{\circ}\text{C}$  and high pressure can be obtained in monolithic carbons with pore widths of 1.14 or 1.12 nm [15]. Another approach for methane storage is the adsorption of methane in the form of a gas hydrate (e.g., on activated carbons preloaded with water). As the methane hydrate is bulkier than the gas, the requirements of the adsorbent in terms of pore widths are different, and good performances have been reported for nanoporous carbons with micropores ca. 2–2.6 nm [16].

Besides dimensions, the shape of the pores is also important, due to its impact in the packing density of the adsorbed molecules. The microporous structure of activated carbons is dominated by slit-shaped pores, which favor a high packing density of adsorbed gas molecules, compared to cylindrical or spherical pores. This makes activated carbon most suitable adsorbents for the storage of small gases than zeolites or metal organic frameworks (MOFs) [7].

Most studies also agree on the best performance of monolithic or pelletized forms of carbon compared to granular or powdered adsorbents in order to comply with up-to-date requirements to achieve reasonable levels of gas storage [20–22].

The thermal management during cyclic operation in storage systems based on porous materials has to be considered as they may have a significant impact on

their performance. Compared to other adsorbents, AC usually have low heats of adsorption that prevent excessive heating or cooling of the storage vessel during the adsorption-desorption cycles [8–10].

Considering all this, it is clear that the understanding of the pore size/shape requirements of nanoporous carbons is essential for a rational design of carbon materials with increased gas storage capacity. While many theoretical studies may suggest optimal pore structures to maximize methane, hydrogen, or carbon dioxide storage, they give no indication or suggestion on how such materials might be produced. Thus, the aim of this chapter is to provide an overview on the synthetic approach for the preparation of activated carbons with adequate porosity and surface chemistry for the storage and separation of small gases of strategic interest (e.g., H<sub>2</sub>, CO<sub>2</sub>, and CH<sub>4</sub>). Even though numerous works exist on exploring approaches for the synthesis of mesoporous and macropores carbons with hierarchical and controlled architectures, we limit the discussion here to the control of the microporosity in carbons, since they exhibit the best performance in terms of gas storage, separation, and packing densities.

## 5.2 Conventional Activation Methods

Activated carbons are produced at industrial scale by so-called conventional activation methods (i.e., physical and chemical activation). Most processes start with a carbonization (pyrolysis) or an oxidation step of the precursor, followed by the exposure of the carbonized material to a reactive atmosphere in the presence of an activating agent that allows the development of a porous structure. The preparation of activated carbons from charcoals is an ancient artwork, and extensive work has been done to enhance the porosity of the resulting carbon adsorbents by the use of different activating agents, the choice of precursors, the optimization of the activation conditions (temperature, heating rate, gas flow), and the usage of various impregnation methods (soaking, stirring) [1]. The purpose of this chapter is to summarize the main differences of the conventional activation methods, considering both thermal (pyrolysis and gasification) and chemical activation.

### 5.2.1 Carbonization

Carbonization or pyrolysis involves the thermal transformation of a material to moderate/high temperatures in an inert atmosphere, with the purpose of eliminating most of the volatiles of the precursor. The residual solid obtained is a carbonaceous char, which is composed of carbon atoms arrangement in a cross-linked condensed aromatic structure in a random manner. The disorganized structure of the carbon atoms leaves interstices between the aromatic layers (incipient porosity, eventually filled with the tars formed during the carbonization). A subsequent activation of the char enlarges the incipient porosity and creates new pores.

Carbon chars are among the first synthetic materials manufactured by men; thus, knowledge of their production has been accumulated over a long time [23]. The use of pyrolysis as a thermal process to produce solids (chars), liquid fuels, and gaseous products that can be suitable for application in several fields (adsorbents, fertilizers, biofuels) has been largely investigated, as the yields of the gas/liquid/solid fractions depend on the thermal conditions (temperature, residence time, heating rate, atmosphere). For instance, carbonization at elevated pressure improves the yield of charcoal production and reduces the reaction time of the synthesis. This allows to extend the activation of the char over time and thus to obtain larger burn-offs while maintaining reasonable yields and densities [24]. Slow pyrolysis at low temperatures, heating rates, and long residence times favors the production of chars [23], as opposed to fast and flash pyrolysis (ca. moderate temperatures and short residence time) that favors the production of a liquid fraction [25].

Slow pyrolysis is typically carried out in an inert atmosphere, although the presence of oxidant agents such as steam can improve the SSA of the resulting chars [26–28]. This has been attributed to the ability of steam to penetrate more efficiently on the solid precursor during the slow pyrolysis, enhancing devolatilization [29] and gasification reactions – if the temperature is high enough [30]. The effect of steam also varies with the nature of the feedstock; SSA values ranging from 405 to 940 m<sup>2</sup>/g have been reported under steam-assisted slow pyrolysis of various biomass feedstocks [26–28]. Giudicianni et al. [27] found that the content in cellulose of the feedstock is determinant for the development of a microporous structure, with higher SSAs obtained for biomass precursors with cellulose content of 55 wt.%.

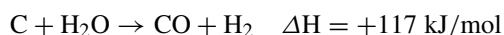
The temperature of the pyrolysis has an important effect in the development of the porosity. At low heating rates, the internal surface area development is strictly correlated to the degree of devolatilization and to the formation of cracks inside the matrix. Mild thermal conditions of ca. 400 °C favor the development of a macroporous structure due to the removal of large amounts of volatile matter. At about 500 °C, micropores and mesopores are created, leading to an increase in surface area and porosity; and at  $T > 800$  °C, the structure and micropore coalescence lead to low values of SSA [26, 31]. For certain precursors (e.g., high rank coals), a preoxidation step in air is needed for boosting the incipient porosity of the char [32].

It is important to highlight that carbon chars usually display a constricted pore network comprised of nanopores of small dimensions accessible through pore mouths or necks of narrow dimensions [1]. Thus, the low surface areas of these materials seen by N<sub>2</sub> at –196 °C might not be an indication of the lack of a microporous structure but rather due to the restricted diffusion of N<sub>2</sub> at cryogenic temperatures into pores smaller than 0.5 nm [33]. Following IUPAC recommendations [34], the analysis of the narrow microporosity of carbon materials with pore constrictions should be performed by CO<sub>2</sub> adsorption at 0 °C.

### 5.2.2 *Physical Activation*

The term thermal or physical activation refers to the development porosity in the gas phase, usually by reaction of a char with oxygen air, CO<sub>2</sub>, steam, or their mixtures. The reaction is generally at elevated temperatures (between 750 and 1100 °C) and proceeds through the formation of surface oxygen complexes. A detailed review on the understanding of the chemical reactions, thermodynamics, and kinetics of the physical activation with these gases can be found in [1]. We herein provide a comprehensive summary of the effect of various activation parameters on the development of a microporous network useful for gas storage applications.

The objective of the activation process is to enlarge and to open the incipient porosity developed during the carbonization. This is carried out under a reactive atmosphere in the presence of oxidants such as oxygen (or air), steam, and carbon dioxide, according to:



The gasification of chars under CO<sub>2</sub> and steam (and their mixtures) is preferred over the use of oxygen (air) due to the high exothermic enthalpy of the latter, which makes the reaction temperature difficult to control. As a result, oxygen does not penetrate inside the particles of the char, and a fast gasification occurs in the external surface, leading to the complete burn-out of the carbon material rather than to the formation of pores. In the case of CO<sub>2</sub> or steam, the reactions are endothermic; thus, an external heat supply is required, allowing an accurate control of the experimental conditions.

Physical activation is commonly carried out as a two-stage process, starting by the carbonization of the precursor and further activation of the obtained char. The use of a single-stage process is also possible, and it does not seem to have a significant impact in the porous features of the activated carbon in terms of micropore volume ( $V_{\text{micro}}$ ) and SSA [35].

Many experimental conditions can influence the final textural features of an activated carbon: the precursor origin and reactivity, the heating rate, the gas flow rate, the temperature and dwelling time of the activation, the activating agent, and so forth.

The choice of the gasification temperature is not arbitrary and depends on the reactivity of the precursor under CO<sub>2</sub> and steam. It is important to keep a moderate reactivity to assure a diffuse regime control of the reaction and prevent the fast gasification of the external surface of the materials (leading to a nonporous material). A simple approach to measure the gasification rate consists in carrying out a thermal profile of the char under CO<sub>2</sub> or steam atmosphere and evaluating

the rate of mass loss with the temperature. This test provides an idea of the onset temperature of the reactivity for the oxidizing gas chosen and allows comparing the reactivity rate of different precursors. Additionally, for certain precursors (e.g., coals), a preoxidation step is recommended to favor the formation of an incipient porosity in the char [36], as well as a well-developed microporosity after the gasification.

Among other parameters, the effect of the flow rate of the activating agent is also important. Slow rates (ca. below 10 ml/min) favor the development of microporosity due to a more uniform gasification through the whole carbon particle network [37]. At high CO<sub>2</sub> or steam flow rates, the gas does not penetrate deeper in the material, and the burn-off on the external surface of the carbon particle becomes more important than the generation of internal porosity. As a result, the carbon yield decreases and the activated carbons display low total pore volumes, and the porosity is mainly composed by macropores. This is an important difference with chemical activation, where fast rates favor the development of microporosity, as it will be addressed below. The particle size is also important, with smaller particle sizes leading to denser carbon materials and much more developed SSAs and narrow micropores.

Regarding the evolution of the porous features with the activation extent, as a general rule, burn-off degrees lower than ca. 50 wt.% render microporous activated carbons, with total pore volume and SSAs increasing with the burn-off, regardless the nature of the precursor (Fig. 5.2) [37–39]. The initial increase in the  $V_{\text{micro}}$  (particularly the narrow microporosity determined by CO<sub>2</sub> adsorption at 0 °C) during the gasification of the char becomes gradually smaller as the burn-off increases. Above 40–50 wt.% burn-off, a fall in the  $V_{\text{micro}}$  may be observed due to the widening of the pores, accompanied by the development of mesopores. Additionally, at high levels of burn-off, the ablation of the carbon particles becomes important; thus, the industrial gasification of chars rarely goes beyond 40–50 wt.% [1].

The activation under CO<sub>2</sub> and H<sub>2</sub>O renders materials with different porosity. Comparison is not straightforward since the chars present different reactivity to the oxidizing gases. Based on studies performed on the same precursor using CO<sub>2</sub> and steam at similar gasification rates, it may be concluded that CO<sub>2</sub> activation produces activated carbons with a narrow distribution of micropores, whereas steam activation generates carbons with wider micropore size distributions, a slightly larger development of mesopores [39]. Both gases produce activated carbons with a low functionalization due to the high temperatures of gasification, although CO<sub>2</sub> activation creates a slightly larger number of more stable oxygen groups than steam [41].

Gasification using water at supercritical conditions has also been studied for the preparation of activated carbons [42]. The gasification reaction using supercritical water is about 10 times faster than steam, favoring activated carbons with large  $V_{\text{micro}}$  and higher mechanical strength. As in the case of steam activation, increasing the activation temperature and time increases the SSA of the activated carbons,

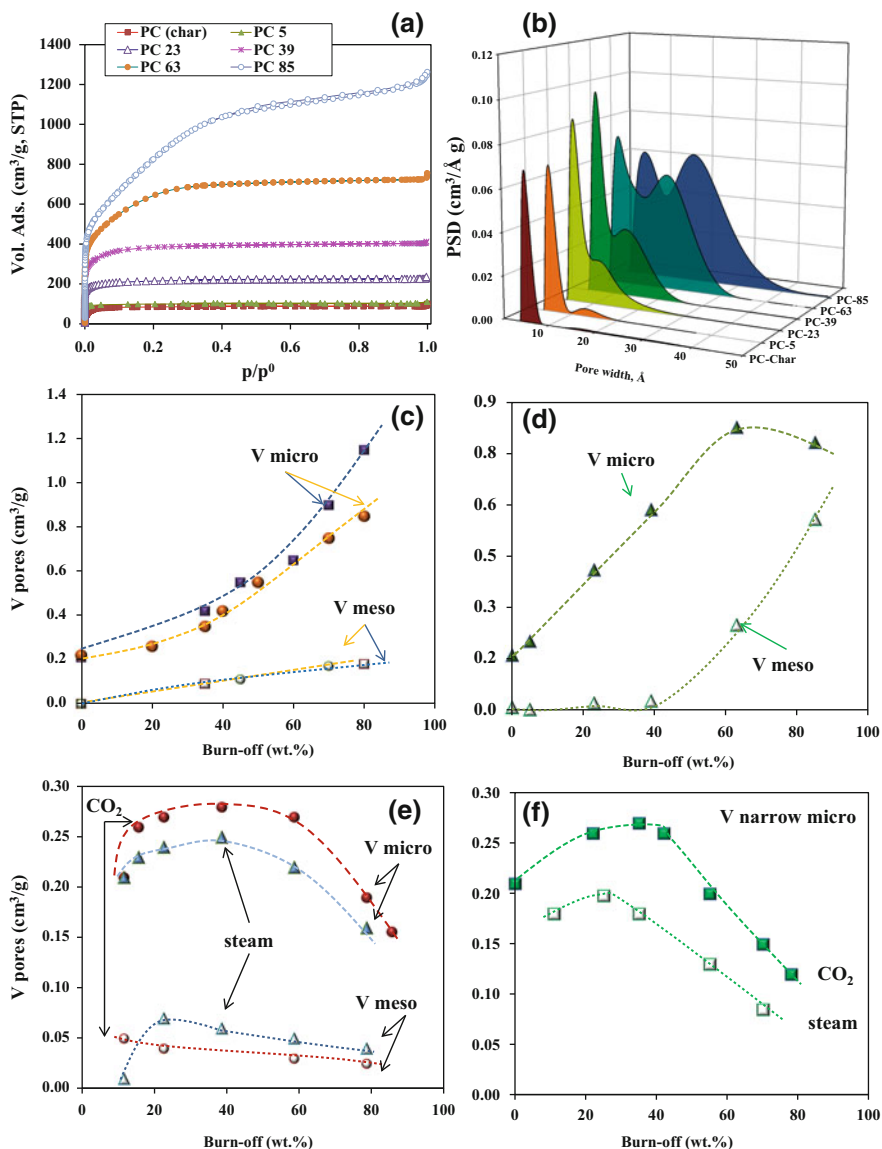


**Fig. 5.2** (a) Nitrogen adsorption isotherms at  $-196\text{ }^{\circ}\text{C}$  and (b) differential pore size distribution for a series of activated carbons prepared by CO<sub>2</sub> gasification of polyethylene-terephthalate wastes at various burn-off degrees. Reprinted from [40], Copyright 2015, with permission from Elsevier; (c,d) Evolution of the total micropore ( $V_{\text{micro}}$ ) and mesopores volumes ( $V_{\text{meso}}$ ) with the burn-off for activated carbons obtained from CO<sub>2</sub> gasification of almond shells (c, squares), olive stones (d, triangles); (c) redrawn from [1], Copyright 2006, with permission from Elsevier; (e) Evolution of total micropore ( $V_{\text{micro}}$ ), mesopores volumes ( $V_{\text{meso}}$ ) and (f) narrow microporosity as a function of burn-off for CO<sub>2</sub> (full symbols) and steam (empty symbols) gasification of olive stones. (e,f) Redrawn from [39], Copyright 1995, with permission from Elsevier

whereas the water flow rate favors the microporosity but has a subtle effect on the mesoporosity.

### 5.2.3 Chemical Activation

In general terms, chemical activation is considered as a reaction between a solid precursor and a chemical activating agent during the heating of the mixture in an inert atmosphere. The most studied precursors are lignocellulosic materials, coals, and chars; as activating agents, the most used are  $\text{ZnCl}_2$ ,  $\text{H}_3\text{PO}_4$ , and alkali hydroxides (e.g.,  $\text{KOH}$  and  $\text{NaOH}$ ).

Chemical activation has recognized advantages for the production of activated carbons with high developed porosity, as it leads to higher yields and allows the use of lower temperatures than physical activation. Additionally, the activation mechanisms are different in both processes, and so it is the porosity of the resulting activated carbons. A detailed review on the mechanism of the different chemical activation reactions for various activating agents can be found in [1]. It has been reported that differences on activation mechanisms when using  $\text{ZnCl}_2$ ,  $\text{H}_3\text{PO}_4$ , and  $\text{KOH}$  are clear when using lignocellulosic materials as precursors [43]. Although the three chemicals react with the precursor, some clear differences can be observed at the end of the impregnation step.  $\text{ZnCl}_2$  and  $\text{H}_3\text{PO}_4$  produce a dehydration of the precursor components yielding in a reduction in the dimensions of the particle. During the thermal treatment, the reactants remain inside the particles acting as a template for the creation of microporosity. The small size of the  $\text{ZnCl}_2$  molecule or its hydrates drives the creation of small and uniform size micropores, whereas the mixture of molecules produced during thermal treatment in  $\text{H}_3\text{PO}_4$  (e.g.,  $\text{H}_3\text{PO}_4$ ,  $\text{H}_4\text{P}_2\text{O}_5$ , or  $\text{H}_{13}\text{P}_{11}\text{O}_{34}$ ) leads to an heterogeneous microporosity. Therefore,  $\text{ZnCl}_2$  would act at temperatures below  $500\text{ }^\circ\text{C}$  and  $\text{H}_3\text{PO}_4$  below  $450\text{ }^\circ\text{C}$ .

$\text{KOH}$  does not act as a dehydrating agent on the precursor and starts to react above  $700\text{ }^\circ\text{C}$ , after the formation of the char. In such a case, activation initially consists of a redox reaction, where carbon is oxidized to  $\text{CO}$  or  $\text{CO}_2$ , thus, incidentally, creating some porosity and  $\text{K}_2\text{CO}_3$  as a by-product. As a result,  $\text{KOH}$  is reduced to metallic potassium. Potassium can be intercalated between the graphene layers of the carbon particles favoring the process by separating the layers, which generates micropores or even new high-energy sites for the redox reactions [44–46]. As  $\text{K}$  can be intercalated into graphite-like structures, whereas  $\text{Na}$  can be only intercalated/inserted in more disordered carbons [46], the development of porosity for precursors with low structural order (e.g., lignocellulosic and low rank coals) is better with  $\text{NaOH}$ , whereas  $\text{KOH}$  produce better results for highly ordered ones (e.g., high-range coals) [47]. As a consequence of such differences on activation mechanism, zinc chloride and phosphoric acid are activating agents usually used for

the activation of raw lignocellulosic materials, and alkaline metal hydroxides are mainly used for coal precursors or chars.

The main parameters of the preparation method affecting the porous texture characteristics of activated carbons (SSA, pore size, and pore size distribution) are impregnation ratio, activation temperature, activation time, and activating atmosphere. The impregnation ratio is the correlation between the weights of chemical agent and the precursor. The activating agent is generally in solution where concentration can be varied, but in some cases, as for NaOH, a direct mixing of the solid chemical and the precursor results more efficient for developing high SSA [48]. The impregnation ratio is a variable that highly affects not only the SSA but also the pore size distribution of the resulting activated carbon. A general trend is that increasing the impregnation ratio also increases the SSA of the activated carbon up to a maximum value. Regarding the pore size and volume (Fig. 5.3), there is

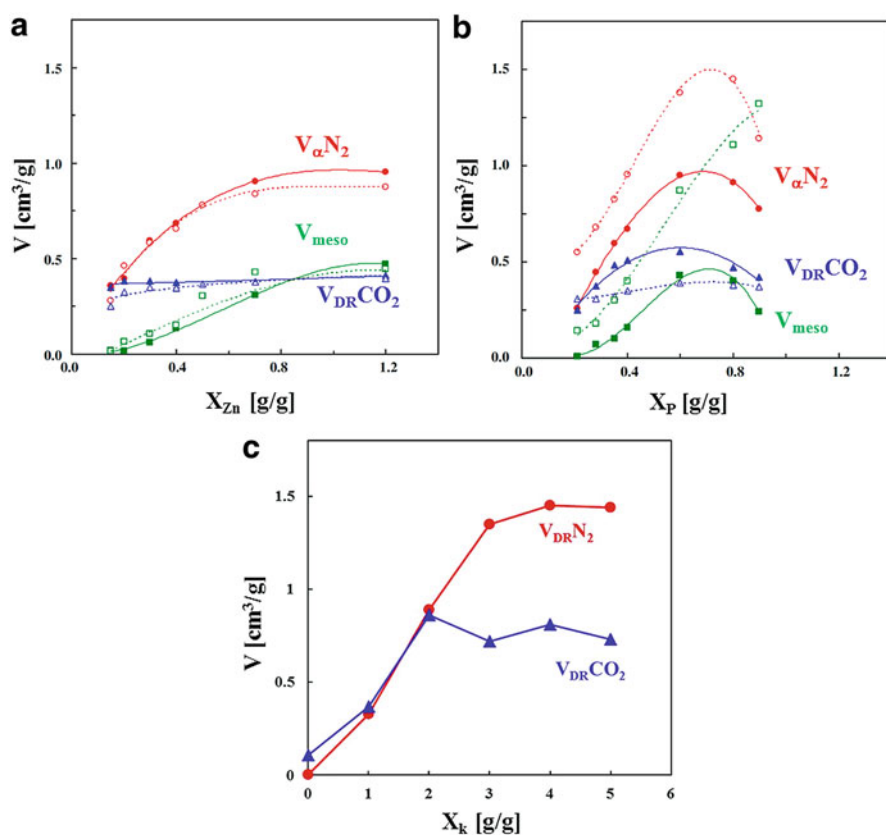


**Fig. 5.3** Evolution of different sets of pore volume along activation with (a) zinc chloride at 500 °C, (b) phosphoric acid at 450 °C of olive stones either in monolith (filled symbols) or powder (open symbols) (Reprinted from [49], Copyright 2007, with permission from Elsevier); and with (c) KOH at 700 °C of an anthracite (data redrawn from [50]). Symbols:  $V_{\text{N}_2}$  (circles);  $V_{\text{CO}_2}$  (triangles);  $V_{\text{meso}}$  (squares)

a strong development of porosity when increasing the impregnation ratio shows, whatever the activating agent. For low impregnation ratios, the increase in the SSA is related to the generation of micropores without an appreciable contribution of mesoporosity. For the particular example of KOH, the  $V_{\text{micro}}$  deduced from  $\text{CO}_2$  adsorption at  $0\text{ }^\circ\text{C}$  are quite similar to those deduced from  $\text{N}_2$  adsorption at  $-196\text{ }^\circ\text{C}$ , indicating the development of only narrow micropores. At higher impregnation ratios, there is a less pronounced increase in the porosity, and the pore size distribution becomes more heterogeneous, the differences among the effect of the chemicals becoming more clearly shown.  $\text{ZnCl}_2$  develops both wide micropores and small mesopores, whereas  $\text{H}_3\text{PO}_4$  also develops large mesopores and even macropores; KOH mostly produces the widening of the microporosity [43, 49, 50]. As a general rule, activation in NaOH renders similar results than KOH for a variety of carbon precursors [47, 48, 51].

Hence, the decrease in SSA generally observed at high impregnation ratios is due to the collapse of micropores due to weakness of pore walls after intensive dehydration for  $\text{ZnCl}_2$  and  $\text{H}_3\text{PO}_4$  and to an extensive gasification of pore walls for KOH or NaOH activation. Therefore, the differences in the activation mechanism of each activated agent drive to marked differences in the development of porosity when increasing the concentration of the chemical agent.

As a general trend, for a given impregnation ratio, an increase in the activation temperature leads to an increase in surface area due to the volatilization process and to a decrease in the carbon yield. Such effect cannot be dissociated from the effect of the activation time (i.e., the time that the sample is maintained at the fixed activation temperature), as for a given activation temperature, this should be long enough to allow the evolution of volatiles from the precursor in order to enable the pore development. However, too long activation times usually bring about the enlargement of the pores, causing a decrease in the SSA.

The combined effect of temperature and time for the activation of a lignocellulosic material (e.g., corncob) using  $\text{ZnCl}_2$  at a constant impregnation ratio of 1 is shown in Fig. 5.4a [52]. In the temperature range studied ( $400\text{--}800\text{ }^\circ\text{C}$ ), the SSA and the total pore volume increased with the pyrolysis temperature, reaching a maximum at about  $500\text{ }^\circ\text{C}$ . Raising the temperature from  $500$  to  $800\text{ }^\circ\text{C}$  resulted in a reduction in the SSA pore volume, likely due to a shrinkage of the carbon structure. The soaking time seems to play a less important role in the production of activated carbons (Fig. 5.4a); by increasing the soaking time from 0.5 to 1.0 h, the SSA and pore volume of the samples increased; longer soaking times reduced both textural parameters, which is most likely attributed to the further gasification of the micropore walls [52]. For temperatures higher than  $500\text{ }^\circ\text{C}$ , the carbon yield strongly decreases. Therefore in order to develop carbons with high SSA and  $V_{\text{micro}}$  with an acceptable carbon yield, by means of  $\text{ZnCl}_2$  activation of a variety of precursors and carbonization conditions, a temperature of  $500\text{ }^\circ\text{C}$  is recommended by several authors [53, 54].

Izquierdo et al. [55] applied a response surface to study the combined effect of activation temperature and time over the carbon porous texture characteristics when using  $\text{H}_3\text{PO}_4$  as activating agent and a lignocellulosic precursor. The authors

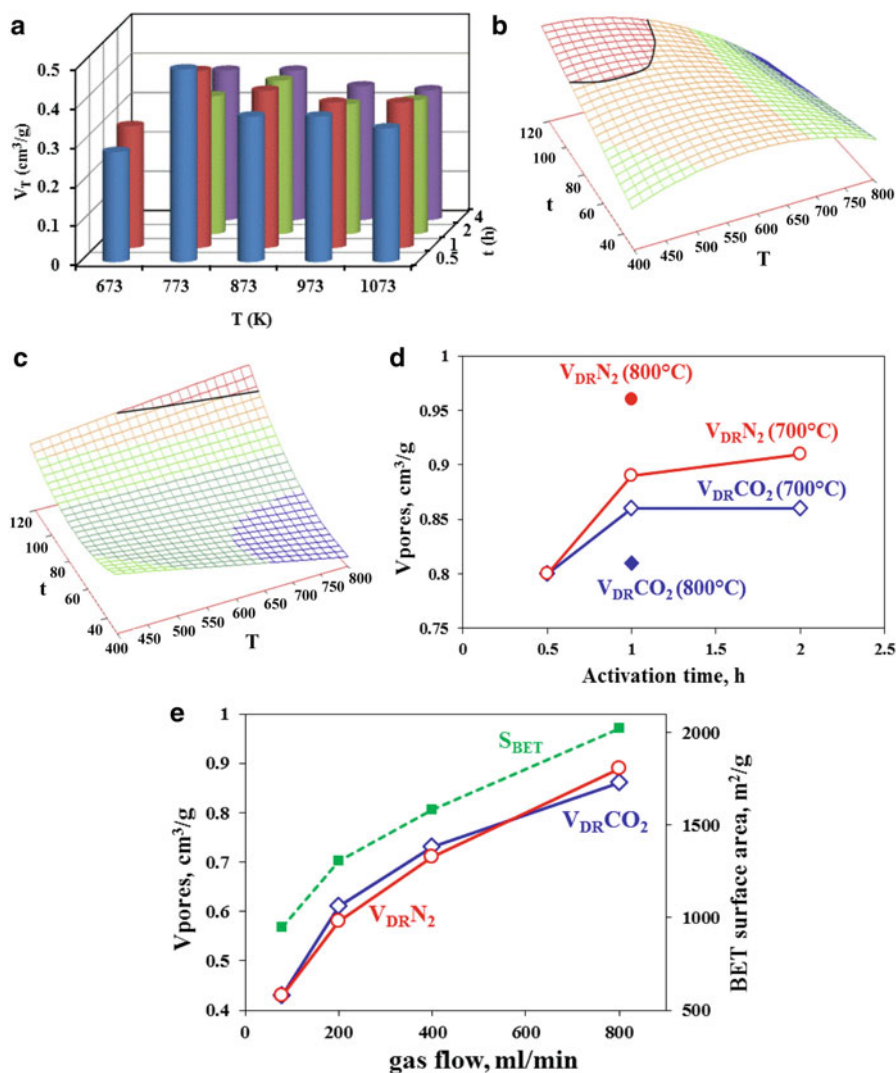


**Fig. 5.4** Effect of selected activation conditions on the texture of the activated carbons. **(a)** Effect of temperature and time on the total pore volume ( $V_T$ ) upon  $ZnCl_2$  activation of corn cob at an impregnation ratio of 1 (data from [52]). Response surface (temperature and time) for **(b)** mesopore and **(c)** micropore volumes upon  $H_3PO_4$  activation of almond shell at an impregnation ratio of 1.1 (data from [55], Copyright 2011, with permission from Elsevier). **(d)** Effect of activation temperature and time on total ( $V_{DR}N_2$ ) and narrow ( $V_{DR}CO_2$ ) micropore volumes upon KOH activation of an anthracite using an impregnation ratio of 2 (data from [50]). **(e)** Effect of the gas flow on  $V_{DR}N_2$ ,  $V_{DR}CO_2$  and the specific surface area ( $S_{BET}$ ) upon KOH activation at 700 °C of an anthracite using an impregnation ratio of 2 (data from [50])

found optimal activation temperatures in the range 400–550 °C and activation times between 85 and 120 min for obtaining carbons with high SSA. Figure 5.4b, c depicts the dependence of  $V_{\text{micro}}$  and mesopore volumes for an impregnation ratio of 1.1. The higher mesopore volume is obtained in similar range of activation temperature and time than that obtained for the higher values of SSA. However, maximum  $V_{\text{micro}}$  is obtained at higher activation temperatures in the same range of activation time. Thus, in order to obtain an activated carbon with high SSA, the response surface methodology indicates a wide temperature range of 400–550 °C and a wide activation time range between 90 and 120 min. However, for obtaining a microporous carbon, the range of temperature shifts to higher temperatures, and the range of activation time becomes narrower (600–800 °C, 112–120 min). However in such conditions, the carbon yield is too low.

In activation with alkali hydroxides, for temperatures below 700 °C, the initial redox reactions between the hydroxide and the carbon (starting at 375–475 °C for NaOH and at 250–375 °C for KOH, depending on the structural order of the precursor) [45] drive to a gasification of the carbon-producing gases such as CO, CO<sub>2</sub>, and H<sub>2</sub> and to a moderate development of porosity [56]. At temperatures above 700 °C, metallic potassium or sodium are produced and intercalate to the carbon matrix increasing the pore volume. Therefore, temperatures lower than 700 °C are not adapted for obtaining carbons with well-developed SSAs when using alkali hydroxides as activation agents. For temperatures above 700 °C, it has been reported that increasing the activation temperature results in higher SSAs and  $V_{\text{micro}}$  but also in a decrease in the carbon yield. Figure 5.4 shows for the same impregnation ratio and time of pyrolysis, increasing activation temperature from 700 to 800 °C results in a chemically activated carbon with higher total  $V_{\text{micro}}$  (calculated from the N<sub>2</sub> adsorption data) [50]. Nevertheless, as in the case of the effect of the KOH/carbon ratio, the higher temperature of pyrolysis produces a wider micropore size distribution as differences between the  $V_{\text{micro}}$  calculated from CO<sub>2</sub> and N<sub>2</sub> adsorption became larger. Moreover, an activation temperature higher than 800 °C is not recommended when narrow micropore size distributions are desired. This is attributed to the additional gasification due to the CO<sub>2</sub> formed upon the decomposition of the alkaline carbonate, causing the widening of the pores and a decrease in the overall reaction yield [57].

Little attention has been paid to the flow rate of the gas used during the heat treatment process. Lozano-Castello et al. showed the great impact of the gas flow on the porosity development of an anthracite coal activated with KOH [50]. During the hydroxide-carbon reaction, gases such as CO, CO<sub>2</sub>, and H<sub>2</sub> are evolved; hence, an increase in the gas flow improves the system purge, shifting the reaction toward the products and influencing the porous texture of the ACs. Figure 5.4 shows that changing the N<sub>2</sub> flow rate from 80 to 800 ml/min increases the microporosity development. Thereby, the  $V_{\text{micro}}$  and SSAs of the produced ACs are doubled; however, and interestingly, the micropore size distribution is not changed. It should be pointed out that the effect of the flow rate in the porous development using chemical activation is opposed to that of physical activation, as discussed above.

Regarding the nature of the inert gas, nitrogen, argon, and helium have been studied as purging atmospheres, using similar flow rates [57]. The main observation is that the sample porosity development increases with the efficiency of these three gases to remove the reaction products (i.e., their molecular weight), following the order  $\text{He} < \text{N}_2 < \text{Ar}$ , which confirms their role as purging gases.

### 5.3 Novel Approaches for Control of Microporosity

Conventional activation methods for the synthesis of nanoporous carbons do not allow a precise control of the pore size and volume. Furthermore, the formation of pores is usually accompanied by significant mass loss (hence low overall yield) and high energy consumption. Thus, introducing a rational design and new approaches that allow to control the porosity at a nanometric scale has received much attention. In the following sections, we will summarize most relevant methodologies to control the porosity in the synthesis of carbons, emphasizing on the generation of microporous carbons.

#### 5.3.1 Hydrothermal Carbonization

Just like natural renewable resources and sustainable chemical agents seem to be the key for the production environment-friendly nanoporous carbons with high SSA and controlled properties, alternative carbonization approaches are explored for lower energy consumption in the preparation of nanoporous carbons. A hydrothermal carbonization (HTC) is a thermochemical process in subcritical water for the conversion of wet/dry biomass to carbon materials. Typically, the yield of the solid fraction in HTC is higher than in hydrothermal gasification (e.g., above the supercritical temperature, with the gas fraction as primary product) and “hydrothermal liquefaction” (e.g., close to 400 °C, with the predominant production of liquid hydrocarbons). Thus, it has proven to be a powerful technique for the synthesis of carbons from biomass. The first studies reporting the hydrothermal transformation of biomass sources into coal-like materials were reported long ago, but the interest for the use of this technique as a simple method to obtain carbon materials (hydrochars) at mild conditions has growth much just in the last 20 years [58, 59].

During hydrothermal carbonization, water acts as a solvent and a catalyst, facilitating hydrolysis reactions and accelerating the decomposition of the biomass oligomers and monomers in smaller fragments, leading to the formation of a carbonaceous solid [60]. The choice of the hydrothermal carbonization conditions (temperature, residence time, pressure, and so forth) depends on the nature of the precursor and its thermal stability [61–63]. As a general rule, increasing the temperature and pressure of the hydrothermal conditions results in an increase in the conversion of the biomass feedstock into carbon particles. Both high-temperature

and low-temperature HTC processes can be applied for the preparation of carbon materials. The first one, typically between 300 and 800 °C, is beyond the stability of biomass components and other natural or organic precursors, and it has been mainly described for the synthesis of carbon filaments and graphitic carbons [64]. The low-temperature HTC process performs below 300 °C and is commonly used for the preparation of hydrochars and activated carbon derivatives, either based on direct solid conversion of biomass feedstocks [65] or the polymerization of the monomers generated upon the decomposition of biomass (carbohydrates/cellulose) [66].

The effect of the various operating parameters of HTC on the quality and yield of the products (solid char, liquid, and gas) has been extensively investigated [61, 62, 67]. It would seem that once the composition of the precursor is known, the hydrothermal conditions could be adapted in order to obtain carbon materials with optimized features.

Most hydrochars obtained from HTC using water as dispersion medium display poor textural parameters (e.g., SSAs seldom exceeding ca. 50 m<sup>2</sup>/g). A few examples are shown in Table 5.1. High surface areas hydrochars can be prepared by adjusting the salinity of the solution, as this modifies the cross-linking and growth of the primary carbon particles formed during the hydrothermal carbonization process. As an example, Fechner et al. [68] reported hydrochars with SSAs of 673 m<sup>2</sup>/g from the HTC of glucose under hypersaline conditions (Table 5.1). The nature of the salt system was found to be important, with high surface areas obtained for hygroscopic salt ions or eutectic salt melts (e.g., ZnCl<sub>2</sub>, LiCl, NaCl, KCl). Iron nanoparticles have also been used to accelerate the dehydration, condensation, and carbonization reactions occurring during HTC, thereby increasing the SSA of the resulting hydrochars [69].

Post-synthesis activation of the hydrochars is another alternative for producing activated carbons with high SSAs. In this regard, the reactivity of precursor and the oxygen content in the hydrochar are important indicators to predict the extent to which porosity will be developed in further chemical activation processes [61, 82].

Various authors have reported the production of high surface area activated carbons (ca. up to 3362 m<sup>2</sup>/g) upon chemical and physical activation of hydrochars prepared from various precursors (e.g., furfural, glucose, rice husks, starch, cellulose, eucalyptus sawdust). A summary of the porous features of selected hydrochar-derived activated carbons is presented in Table 5.1. In general, the yields of physical and chemical activation of hydrochars are similar, although the latter activated carbons display higher porous features [76, 80]. The temperature of the HTC step has a strong impact on the porosity of the activated carbons after post-synthesis activation. When the HTC is carried out from 180 to 240 °C, the higher density of carbonyl moieties and the low degree of aromatization favor the development of porosity after KOH activation [82]. Raising the temperature of the HTC process up to 280 °C enhances the chemical stability and structural order of the hydrochars; thus, activated carbons with lower porosity upon KOH activation are obtained. The structural order of the carbon precursor is also important [83]; as observed for the KOH activation of coals, a low porous development is obtained upon activation of hydrochars with high degree of aromatization and structural order [82].

**Table 5.1** Specific surface areas of hydrochars and activated hydrochars obtained from different starting raw materials and activation conditions. Reprinted from [61], Copyright 2016, with permission from Elsevier

Precursor	Synthesis parameters	S <sub>BET</sub> [m <sup>2</sup> /g]	Reference
Orange peels	Citric acid catalyst	0.2	[70]
Orange peels	CO <sub>2</sub> activation	618	[71]
Oak leaf	Citric acid catalyst	15.5	[70]
Pine cone	Citric acid catalyst	34	[70]
Glucose	LiCl/ZnCl <sub>2</sub>	673	[68]
Glucose	NaCl/ZnCl <sub>2</sub>	546	[68]
Glucose	KCl/ZnCl <sub>2</sub>	425	[68]
Glucose	NaCl	Not detected	[68]
Glucose	ZnCl <sub>2</sub>	477	[68]
Glucose	ZnCl <sub>2</sub>	Small	[68]
Glucose	Borax	233	[72]
Glucose	Borax	427	[73]
Starch	Fe (NH <sub>4</sub> ) <sub>2</sub> (SO <sub>4</sub> ) <sub>2</sub>	113	[69]
Starch	Fe <sub>2</sub> O <sub>3</sub>	402	[69]
Hazelnut shell	–	45	[74]
Hazelnut shell	KOH activation	1700	[75]
Glucose	NaOH activation	2120	[76]
Glucose	KOH activation	3152	[76]
Sucrose	H <sub>3</sub> PO <sub>4</sub> activation	2120	[76]
Sucrose	CO <sub>2</sub> activation	2555	[76]
Rice husk	HTC at 200 and 300 °C	14–25	[77]
Rice husk	KOH activation	3362	[78]
Rice husk	H <sub>3</sub> PO <sub>4</sub> activation	1498	[79]
Rice husk	CO <sub>2</sub> activation	446	[80]
Coconut shell	ZnCl <sub>2</sub> activation	1421	[81]
Coconut shell	ZnCl <sub>2</sub> activation	1775	[81]
Coconut shell	ZnCl <sub>2</sub> activation	1530	[81]

Less corrosive alternatives to KOH activation have proven to yield highly microporous materials when hydrochars are used as precursors, with textural properties matching those of optimized KOH-ACs. Activation using K<sub>2</sub>CO<sub>3</sub> resulted in better yields than KOH and in the retention morphology of the hydrochar [84]. Microporous materials with SSAs of ca. 3000 m<sup>2</sup>/g have also been obtained upon activation of hydrochars with KHCO<sub>3</sub> and a mixture of potassium oxalate and melamine [85, 86]. The materials also presented higher packing densities than superactivated carbons prepared upon KOH activation, due to a narrow distribution of micropores.

The incorporation of a catalyst (acid, oxidant, metallic salt) during the hydrothermal carbonization process also enhances the development of the pore structure in the subsequent activation step, due to the impact in the formation of hydrochars with

higher content in oxygen groups. The resulting hydrochars display more efficient features for their use as precursor in a subsequent chemical activation step [61, 69, 81]. For instance, the hydrothermal carbonization of coconut shell in the presence of  $\text{H}_2\text{O}_2$  and  $\text{ZnCl}_2$  led to the preparation of hydrochars with SSA of about 1753–2440  $\text{m}^2/\text{g}$ , with a large fraction of mesopores [81]. It was attributed to the better dehydration of the biomass by  $\text{ZnCl}_2$  at hydrothermal conditions.

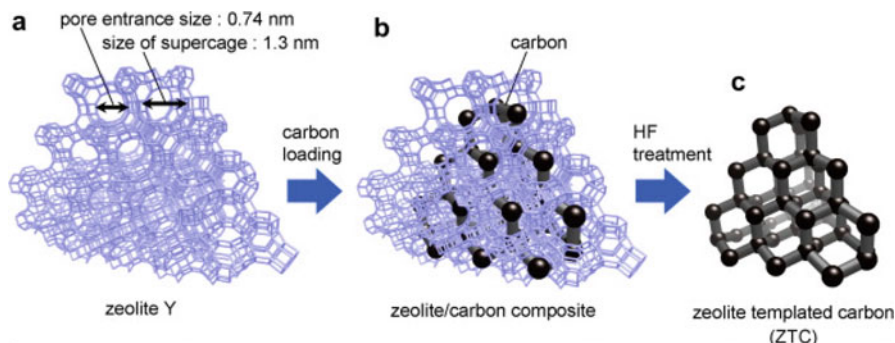
### 5.3.2 Nanocasting Techniques

Nanocasting techniques are classified into two categories depending on the template used: endo- and exo-templating routes, also called soft and hard templating, respectively. The concept soft templating refers to the preparation of porous material using an organic template (e.g., surfactants) that is self-assembled in a solvent in the presence of a polymerizable carbon precursor. The carbon material is obtained after a carbonization process, where the template is either consumed becoming a carbon precursor or sacrificed generating the final porous carbon [87]. It has been mainly used for obtaining mesoporous carbons through the self-assembly of block copolymers and precursors such as phenolic resins or resorcinol. The exo-templating approach consists on using a porous solid as sacrificial scaffold, so that the porous material obtained is an inverse replica of the template used. Zeolites of varied topology, mesoporous silica/oxides, and opals or colloidal silica templates have been used as scaffolds to obtain micro-, meso- and macroporous materials, respectively [88].

#### 5.3.2.1 Hard Templating

Hard-template techniques consist in the use of an appropriate porous material as sacrificial scaffold to replicate its porosity and structure through the infiltration of a carbon precursor followed by carbonization of the composite and removal of the template. The obtained carbon is a negative replica of the template, meaning that the carbon skeletal structure is related to the pores of the template, while the porosity of the carbon is related to the walls of the template after the chemical etching. Even though hard templating has marked a milestone in controlling the pore structure of carbons, the process is quite challenging and complex and still has to face a great disadvantage for scaling-up applications due to the need to remove the template.

Pioneering research studies on preparing microporous carbons via nanocasting methods were performed by Kyotani and co-workers using zeolites and layered clay minerals as templates [89, 90] and resulted to be particularly suitable for the synthesis of carbons with a desired structure of micropores of uniform sizes and shape. These materials are commonly referred to as zeolite-templated carbons (ZTC) and, due to the well-defined three-dimensional structure of most zeolites, very often present a periodic arrangement of micropores in the range of 1–2 nm (Fig. 5.5) [90–94].



Sample	Synthesis parameters	$S_{\text{BET}}$	$V_{\text{micro}}$	$V_{\text{meso}}$
		[ $\text{m}^2/\text{g}$ ]	[ $\text{cm}^3/\text{g}$ ]	[ $\text{cm}^3/\text{g}$ ]
b-P8(2)	Zeolite b, propylene CVD 800 °C, 2 h	1970	0.8	0.4
b-P8(4)	Zeolite b, propylene CVD 800 °C, 4 h	2050	0.9	0.4
b-PFA-P7(4)	Zeolite b, PFA carbonization, propylene CVD 700 °C, 4 h	1420	0.6	0.5
b-PFA-P8(2)	Zeolite b, PFA carbonization, propylene CVD 800 °C, 2 h	1640	0.6	0.5
b-PFA-P8(4)	Zeolite b, PFA carbonization, propylene CVD 800 °C, 4 h	1400	0.5	0.4
b-PFA-P7(4)-H	Zeolite b, PFA carbonization, propylene CVD 700 °C, 2 h	1270	0.8	0.4
b-PFA-P8(2)-H	Zeolite b, PFA carbonization, propylene CVD 800 °C, 2 h, heat treatment at 900 °C	2010	0.8	0.5
ZSM5-P8(4)	Zeolite ZSM-5, PFA carbonization, propylene CVD 800 °C, 4 h	110	0.0	0.1
M-P8(2)	Zeolite Mordenite, PFA carbonization, propylene CVD 800 °C, 2 h	180	0.1	0.3
L-P7(4)	Zeolite L, PFA carbonization, propylene CVD 700 °C, 2 h	570	0.2	0.4
L-P8(2)	Zeolite L, PFA carbonization, propylene CVD 800 °C, 2 h	360	0.1	0.6
d Y-PFA-P7(4)-H	Zeolite Y, PFA carbonization, propylene CVD 700 °C, 4 h, heat treatment at 900 °C	2750	1.5	0.0

**Fig. 5.5** (scheme) Synthesis procedure of the ZTC. (a) Crystal structure of the zeolite Y template, (b) illustration of zeolite/carbon composite. Impregnated carbon is shown by a black framework and (c) framework structure of the liberated ZTC after HF washing. Reprinted from [95], Copyright 2009, with permission from Elsevier. (table) Selected textural parameters of ZTC prepared from various zeolites. Adapted from [96], Copyright 2003, with permission from Elsevier

Unlike the preparation of mesoporous carbons, the nanocasting technique for the synthesis of microporous carbons with a uniform pore structure has important limitations, typically related to the infiltration of the carbon precursor within the

narrow channels of the zeolites, or the restricted polymerization in small pores that bring about a low carbon yields, and ultimately provokes the collapse of the carbon after the etching off the template [91].

The topology of the zeolite is important as it defines the size of the cavities and their connectivity; both parameters are critical to assure an efficient impregnation of the cavities to form robust carbon replica that retains the ordered structure of the zeolite after the removal of the scaffold. To obtain microporous carbons with high structural regularity, the pores in the zeolite template should be sufficiently large ( $>0.6\text{--}0.7$  nm) and three-dimensionally interconnected. As an example, zeolites Y (X), b, L, EMT and mordenite have been successfully used for this purpose. Whereas zeolites EMT and Y render porous ZTC with a high structural regularity, zeolites L and mordenite produce randomly oriented (nonporous in the case of zeolite L) carbons with no periodic order after dissolution of the template. This is due to the disconnected 1D or 2D pore system of the zeolite template [92, 96, 97].

The acidity of the zeolite also plays a role, as it affects the formation of the carbon layer when the infiltration is made by chemical vapor deposition (CVD), as the catalytic decomposition of a hydrocarbon gas is catalyzed by the acidic sites of the zeolite pores, avoiding the deposit of pyrolyzed carbon outside the zeolite particles. Thus, zeolites with poor acidic activity (such as silicalite-1) are not recommended as scaffolds. Similarly, zeolites with Si/Al ratio below 20 are preferred as they display higher acidity and greater heat stability [91, 98].

Regarding the carbon precursor, CVD of small hydrocarbon gases, polymer carbonization of organic monomers, and the combination of both have been mainly explored. The carbonization of polymeric organic monomers (e.g., furfuryl alcohol, acrylonitrile) starts with the loading of the precursor inside the pores of the zeolite, followed by the polymerization and carbonization. Although the method allows uniform carbon coverage of the pores, the obtained carbon replica usually do not present very high SSAs nor retains the ordered structure of the zeolite. This is due to the large fraction of volatiles decomposed during the carbonization of the polymerized monomer. On the other hand, the CVD method allows the incorporation of larger amounts of carbon inside the pores of the zeolites; thus, the carbons usually present a robust and ordered structure. Different hydrocarbons have been explored (acetylene, propylene, benzene) to obtain pure and doped ZTC. Better results in terms of higher surface area and micropores have been reported for acetylene due to its small size [97, 99]. It is also important to maintain the temperature of the CVD process lower than the temperature of the self-decomposition of the hydrocarbon, to avoid carbon deposition outside the zeolite particles. Other factors such as the concentration of the hydrocarbon feedstock and a thermal annealing of the zeolite/carbon composite before the removal of the template also allow obtaining carbons with high surface areas and an ordered structure.

The two-step method combines the advantages of both of them, allowing the uniform carbon deposition of the polymer carbonization and the formation of a robust carbon framework with an ordered structure and high SSA of the CVD method [17, 90, 92, 100]. As a result, ZTC with extremely high SSAs between 3600 and 4100  $\text{m}^2/\text{g}$  and micropore volumes of up to 1.5  $\text{cm}^3/\text{g}$  without detectable

mesopores have been reported after an annealing treatment at high temperature before removing the template (Fig. 5.5) [90, 93].

Although the SSA of some KOH-activated carbons is over 3000 m<sup>2</sup>/g, these carbons always suffer from the presence of some mesoporosity and have a broad pore distribution. Furthermore, ZTC prepared by a two-step method can also present high mechanical stability upon compaction, which is a desirable feature for gas storage applications [17].

Besides zeolites, the research has been extended to a wide variety of hard templates such as multilayered clays, colloid crystals, mesoporous silica, and several MOFs [101–103]. As an example, highly microporous carbons with large pore volumes (ca. 2.06 cm<sup>3</sup>/g) and SSA of up to 2872 m<sup>2</sup>/g have been obtained using various MOFs as templates (Liu 2008). The MOFs have a dual role providing the metal and carbon sources and acting as the sacrificial template [104]. Yang et al. [102] reported the synthesis of ultramicroporous MOF-derived carbons with hierarchical pore structures and high SSAs and total pore volumes. Due to the exceptional porosity, they exhibited better reversible H<sub>2</sub> storage capacity than those previously reported for other carbons and MOFs.

### 5.3.2.2 Soft Templating

Soft-templating approaches are based on the formation of supramolecular arrangements of precursor molecules (e.g., carbon precursor) with a template (e.g., surfactants), stabilization of the carbon matrix by polymerization, and the removal of the template. The microphase separation induced by the usually well-ordered phases of the templates is responsible for the ultimate structure of the resulting materials. One of the advantages of this approach is that the template is either destroyed or consumed as carbon precursor during the carbonization process, avoiding the need of a chemical etching off. However, the scaling-up is still economically and environmentally questionable, due to the synthetic origin of most of the templates.

The interest of soft-templating approaches has been mostly directed toward the preparation of carbon materials with hierarchical meso- and macroporosity [87], but it can also be extended to microporous carbons with high pore volumes and/or molecular sieving effects (thus of interest for gas storage applications) (Fig. 5.6). In this regard, the preparation of carbon materials with pores of different sizes is intimately related to the nature of the template. For instance, polyethylene oxide (PEO) blocks in block copolymeric surfactants tend to produce microporosity, and ionic surfactants produce micropores and small mesopores (2–4 nm), whereas nonionic surfactants (e.g., Brij and Pluronic) generate mesopores of up to 10 nm [105]. The morphology of the carbon materials can also be modulated by adjusting the concentration of the surfactant or block copolymer, the pH of the solution or the temperature of the reaction [106].

Precursor molecules typically employed in the resin formation that precedes the synthesis of soft-templated carbons are hydroxylated aromatic molecules

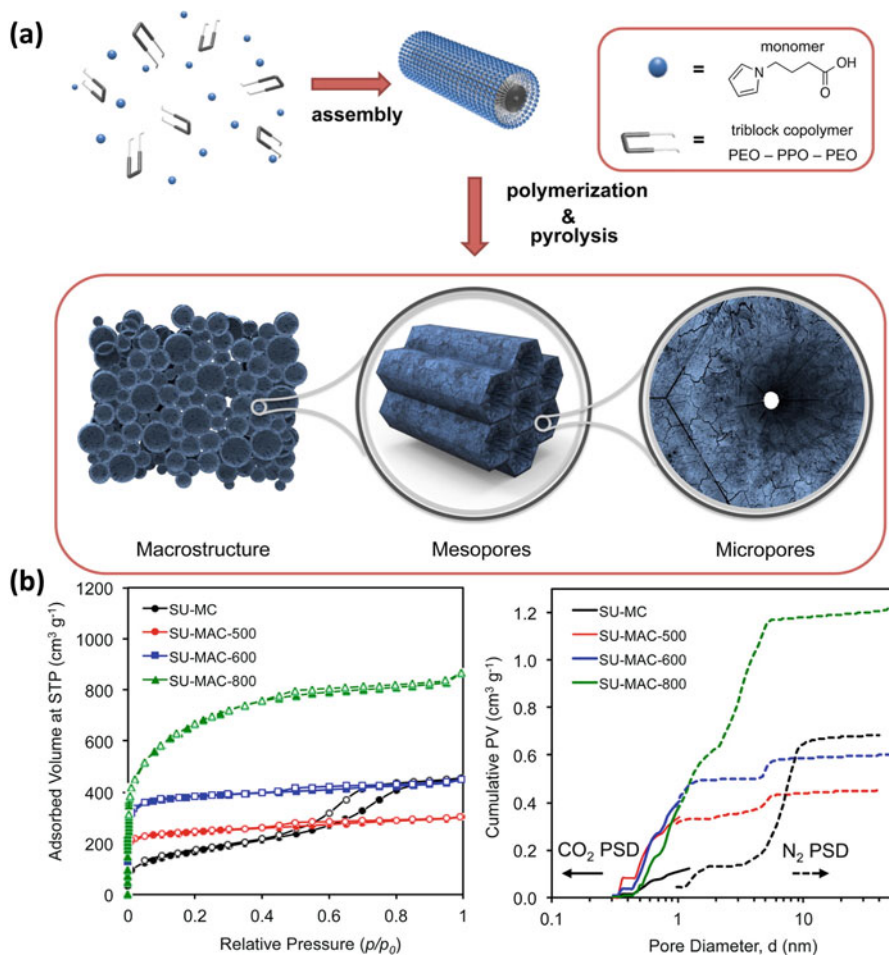


**Fig. 5.6** (a) Schematic illustration of the soft-templating synthesis of porous carbons with a hierarchical macro-, meso-, and microporous structure. (b)  $N_2$  adsorption isotherms at  $-196\text{ }^\circ\text{C}$  and cumulative pore volumes of selected carbons, where the solid and broken lines represent the results from the  $\text{CO}_2$  (0  $^\circ\text{C}$ ) and  $\text{N}_2$  ( $-196\text{ }^\circ\text{C}$ ) adsorption isotherms, respectively. Reprinted from [107], Copyright 2016, American Chemical Society

(e.g., phenol, resorcinol, phloroglucinol, resol) or functionalized compounds (e.g., melamine, pyrrole) if doped carbons are targeted. The chemical cross-linking of these molecules is often carried out in the presence of an aldehyde (formaldehyde, glyoxal) acting as a linker, to form the oligomer that co-assemble with the template micelles. The chemical composition of the polymeric carbon precursor controls the interaction strength with the template polymer and thus the degree of cross-linking that will define the porosity of the soft-templated carbon.

For instance, Liang et al. reported that phloroglucinol interacts more strongly than phenol-formaldehyde or resorcinol-formaldehyde complexes with Pluronic templates due to the formation of triple hydrogen bonds. As a result, soft-templated carbons prepared with phloroglucinol possessed a highly ordered 2-D hexagonal system, whereas those prepared using resorcinol and phenol rendered in poorly structured microporous carbons [108].

Since soft-templating routes are most often used for the preparation of mesoporous carbons, post-synthetic activation has been much explored to obtain microporous carbons [109–111]. In this regard, it is important to consider the stability of the material before the thermal activation. The pH conditions for polymerization of the carbon precursors and self-assembly strongly influence the thickness of the pore walls of the template carbon, which is determinant for its structural stability during the activation, particularly when using harsh activating agents such as KOH [112]. As a general rule, carbons synthesized under acidic conditions are more resistant to post-activation steps [109] than those obtained by using a basic synthesis route [109, 110, 113]. Another alternative for creating microporosity in mesoporous carbons involves the incorporation of TEOS during the soft-templating synthesis [114]; the dissolution of the silica precursor homogeneously distributed in the composite materials leads to the creation of micropores in the mesopore walls.

### 5.3.3 Sol-Gel Approaches

Sol-gel techniques are bottom-up approaches that enable a precise control over the synthesis parameters and thus over the final characteristics of the porous material. In 1989, Pekala et al. [115] reported the preparation of organic sol-gel-based materials through the polycondensation of resorcinol-formaldehyde (RF) mixtures in the presence of acid or base catalysts in aqueous media. The resulting materials contain abundant oxygen functionalities and thus are commonly referred to as organic gels or resins. A final carbonization step would convert them into carbon gels (Fig. 5.7).

The sol-gel process starts with the polymerization and condensation of the precursors (typically R and F), initially through an addition reaction to form hydroxymethyl derivatives that subsequently condensate to form methylene and

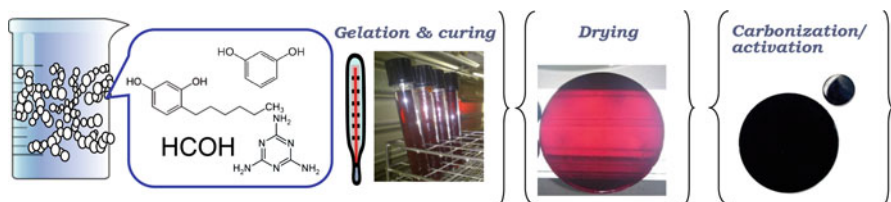


**Fig. 5.7** Steps and principles of the sol-gel approach for the preparation of nanoporous carbons

methylene ether bridged compound. When the reaction starts, polymer chains grow into aggregated clusters of a few nanometers in diameter; the cross-linking of these colloidal particles leads to the stiffening of an organic gel with an interconnected structure. To prepare the polymerization of the reactants, these are mixed with the catalyst and the solvent, stirred for form a homogenous mixture and allowed to gelate and polymerize at moderate temperatures in sealed vessels to minimize the solvent evaporation. Dynamic viscosity measurements have shown that the initial cluster formation and particle growth take about 1 h [116]; at this stage, the mixture constitutes a colloidal solution of clusters of monomeric particles. This general mechanism depends on the solution pH, the components molar ratios and the temperature, among others [117]. The next stage is the covalent cross-linking of the clusters until they become unstable and undergo spinodal decomposition leading to the solidification of the gel. The sol-gel polycondensation of R-F mixtures in the presence of a catalyst is endothermic, and then heating is required to provide the necessary energy for this reaction. The typical temperature for this reaction in aqueous medium is ca. 80 °C [117], although it may be decreased when longer gelation times [118] or alternative solvents to water are used [119]. The curing step is also important since it allows the polymeric clusters to cross-link and form the final shape of the gel. This is usually carried out at 80–90 °C for about a week to prevent the swelling during the drying stage [117, 120].

After the pioneering work of Pekala [115], much of the effort has focused on how different synthetic parameters affect the final organic gels and carbons, optimizing the porosity within the full nanometric scale. The nature of the catalyst and its concentration also affect the porosity of the carbon gel. The most widely used catalyst is  $\text{Na}_2\text{CO}_3$ ; as a general trend, low R/C molar ratio favors the formation of predominantly microporous carbon gels with low SSAs and poor mechanical properties. In contrast, for high R/C ratios, the resulting gels possess larger surface areas, a predominantly mesoporous structure and good mechanical strength [117, 121].

The pH of the initial solution also plays an important role on the properties of the final gel. Job et al. reported that it is possible to tailor the morphology and porosity of carbon gels by varying the initial pH of the precursor solution. For instance, in the case of resorcinol-formaldehyde carbon gels, on average increasing the pH decreases the pore size. More specifically, the carbon gels displayed a macroporous structure at pH between 2 and 4, mainly a micro-macroporous character at pH 5.00–5.45, a micro-mesoporous structure at pH 5.80–6.50, and quasi nonporous at pH 7.35 [122]. Rasines et al. [123] observed that both the pH and a pre-polymerization step were determinant for the preparation of carbon aerogels using melamine (M) as precursor. Attempts of preparing mechanically stable hydrogels at solution pH below 6 failed, regardless the M/R ratio used. Aerogels prepared at pH 8 and M/R = 0.5 ratio displayed low SSAs determined by  $\text{N}_2$  at  $-196\text{ °C}$  (ca. 70–90  $\text{m}^2/\text{g}$ ), but the analysis of the textural features by means of  $\text{CO}_2$  adsorption isotherms at 0 °C revealed the presence of a non-negligible narrow microporosity. This was attributed to the low cross-linking degree of the monomers at high pH values, yielding hydrogels that do not stand the supercritical drying and

carbonization steps. The formation of the microporosity was favored at higher M/R ratio, with samples showing  $700 \text{ m}^2/\text{g}$  and the micropores accounting for ca. 90% of total pore volume [123].

The molar ratio of the monomers defines the micro- to mesopore ratio. Usually, microporous gels are obtained at low R/C ratios; an increase in the R/C and R/W molar ratios provoke an enlargement of the mesopores, with a small impact on the microporosity [124, 125]. The temperature of the gelation/aging step mainly affects the mesopore network, whereas the microporosity is determined by the composition of the precursor's mixture [126].

The drying procedure of the organic gel defines the mechanical properties of the final carbon gel. Subcritical (solvent evaporation at atmospheric conditions), supercritical (the solvent is replaced by a fluid that is later removed at supercritical conditions), or freeze (the solvent is frozen and removed by sublimation) drying are the most commonly used methods, giving rise to xerogel, aerogels, or cryogels, respectively.

Subcritical drying is economically advantageous but produces carbon gels with rather low microporous structure, compared to supercritical drying. This is due to the surface tensions during the removal of the solvent. In contrast, supercritical drying minimizes the surface tensions and shrinkage giving rise to materials with higher pore volumes, although the pore size cannot be easily controlled [117, 120, 127, 128].

Carbonization of the organic gels under an inert atmosphere provokes the removal of the volatiles and the densification of the carbon gel. The carbonization of xerogels typically provokes a partial collapse of the mesoporosity, but it favors the formation of a microporous structure. This effect is generally more remarkable in gels prepared using low R/C ratio [117].

The carbonized gels can be further activated to enhance the porosity, in a similar pathway as that of any other carbon precursor. Carbon gels with SSA of 1800–1900  $\text{m}^2/\text{g}$  and micropore volumes of 0.6–0.7  $\text{cm}^3/\text{g}$ , with no contributions of mesopores, have been reported by activation using KOH at 800 °C (Fig. 5.8) [130]. Furthermore, chemical activation using wet-impregnation techniques can avoid the destruction of the mesoporosity while increasing the SSA and micropore volumes [130].

Other monomers have been used as alternative precursors to resorcinol, including catechol, hydroquinone, phloroglucinol, phenol, and other substituted phenolic rings, as well as heteroatom-containing monomers (e.g., urea, melamine, 3-hydroxypyridine) for the preparation of doped carbons [87, 123, 124]. The differences in the polycondensation reaction kinetics of these molecules define the features of the carbon gels. In this regard, phloroglucinol, being a more reactive molecule toward polycondensation reactions than resorcinol, promotes the formation of highly cross-linked polymers with a microporous structure. On the other hand, the presence of only one hydroxyl group in phenol makes its reactivity slower in compare to both phloroglucinol and resorcinol [87].

Low cost precursors (e.g., biomass, furfuryl alcohol) have also been explored as an economic alternative to the RF sol-gel process [128]. Antonietti and co-workers

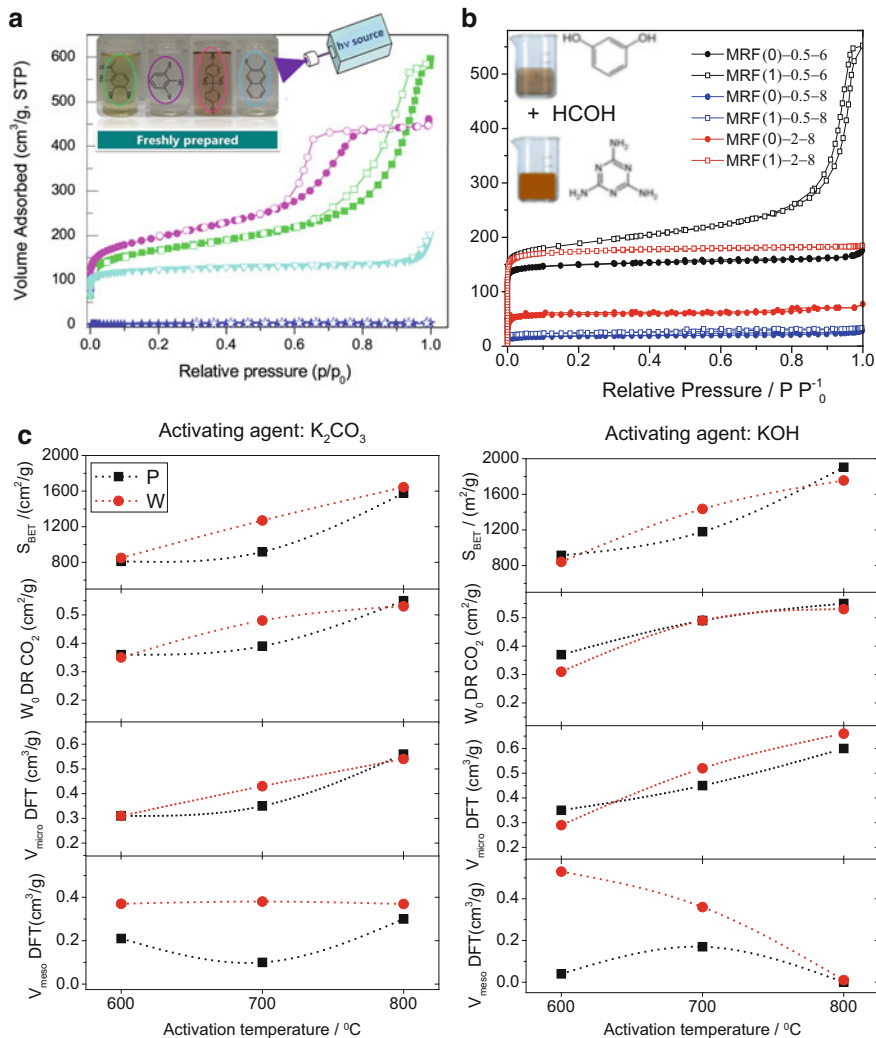


**Fig. 5.8**  $\text{N}_2$  adsorption isotherms at  $-196^\circ\text{C}$  of carbon gels prepared by (a) photo-assisted polycondensation of various organic molecules (Reprinted from [129], Copyright 2017, with permission from Elsevier 2017) and (b) melamine-resorcinol-formaldehyde mixtures using a pre-polymerization step (Reprinted from [123], Copyright 2015, with permission from Elsevier 2015); (c) correlation between the main textural parameters (SSA, micropore, and mesopore volumes) of activated xerogels as a function of activation temperature with (a) potassium carbonate and (b) potassium hydroxide for wet and powder impregnation. Reprinted from [130], with kind permission from Springer Science+Business Media Copyright 2017

reported that the general principles of sol-gel chemistry can be transferred to a sustainable preparation of carbon materials following a hydrothermal approach of low cost and available precursors such as carbohydrates, saccharides, or biowastes [131, 132].

Sol-gel routes carried out under controlled illumination conditions offer several advantages for the preparation of nanoporous carbons. The first one is much shorter time scale, since the aging time needed to induce the cross-linking of the polymeric precursor is significantly reduced due to the energy provided by light [129]. Other advantages are the versatility of organic precursors; by changing the chemistry of the organic precursor, carbons of varied morphology and with SSAs ranging between 10 and 720 m<sup>2</sup>/g and showing molecular sieving effects have been prepared. The degree of cross-linking, and thus the porosity of the final carbons, is defined by the structure and the number of reactive positions in the organic precursor. Linear dihydroxylated precursors formed dense porous carbon matrices mainly composed of narrow micropores, whereas trihydroxylated molecules assembled in large cross-linked clusters combining micro- and mesopores [129].

Another advantage of sol-gel routes is that they enable to produce carbon materials in the form of a monolith, which offers important advantages compared to powder or pellets (e.g., better diffusion and mass transfer rates of fluids, resistance to compression). Carbon monoliths are mostly hierarchical porous carbons, since their porosity is composed of interconnected pore networks of different sizes [133, 134]. Del Monte et al. have reported the synthesis of hierarchical carbon monoliths through a synthetic route based on using deep eutectic solvents (DES) composed of a phenol derivative as H-bond donor and an ammonium salt as H-bond acceptor as low cost and sustainable precursors [22, 135, 136]. Depending on the initial DES composition, the pore structure and chemical composition of the carbon monoliths can be modified. For instance, 4-hexylresorcinol favors the formation of hierarchical microporous carbon monoliths with enhanced molecular sieve features, while the presence of urea favors the formation of large mesopores [22, 135].

### 5.3.4 *Self-Activation*

Self-activation is the name that is generally given to a single-step pyrolysis of a carbon precursor resulting in porosity development without adding any activating agent. In this sense, self-activation of polymer-based precursors or biomass carbons has been reported if an alkali-rich precursor is carbonized under an inert gas flow or if the own gas products of the pyrolysis of the precursor are used as activating agents. For some particular precursors, the method is very efficient for producing highly microporous carbons for being used as gas adsorbents.

The carbonization of organic salts has recently been considered a sustainable synthetic strategy for the preparation of highly microporous carbons, when compared to chemical activation with harsh KOH. Highly porous carbons with

different textural properties have been obtained by direct carbonization of organic polymers and their salts (i.e., gluconates, alginates, citrates, sulfonates, maleic acid) as precursors. These compounds combine a carbon precursor (i.e., the organic moiety) and certain elements that during the heat treatment generate species capable of operating as activating agents. Sevilla et al. [137] reported the preparation of nanoporous carbons with SSAs ranging between 650 and 1960 m<sup>2</sup>/g and pore volumes of up to 2.6 cm<sup>3</sup>/g. The pore characteristics of the synthesized carbons can be modulated by selecting the appropriate organic salt, enabling the preparation of carbons which porosity would be exclusively made of micropores or mesopores. The high diapason of the inorganic elements acting as activating agents (e.g., Ca, K, Na) allowed to have high SSAs despite the low inorganic species content [137, 138]. The pore characteristics were tuned from a microporous to a mesoporous carbon by simply choosing the appropriate organic salt. For instance, the alkali K and Na salts favored the development of micropores, as it is well-known for other alkali-based activating agents, while calcium compounds gave rise to mesopores.

Following the same principle, Nakagawa et al. [139] and Bandosz et al. [140, 141] reported dynamic carbonization templating of a metal-loaded organic polymer (e.g., polystyrene sulfonic acid co-maleic acid-derived salts or polystyrene sulfonic acid co-divinylbenzene-derived salts), giving rise to polymer-derived carbons with a predominantly microporous structure due to the expansion of the matrix during carbonization in the presence of the metals undergoing reduction and oxidation reactions. The porosity of the material was deepening on the nature of the cation exchanged, with Na and Ni favoring the formation of microporous carbons and Cu, Fe, and Co mesoporous materials.

The direct pyrolysis of biomass materials containing naturally embedded alkaline or alkali earth elements at a molecular level (e.g., carbohydrates) has recently been demonstrated as a promising route to produce high surface area carbon without introducing extra activation agents. In particular, it has been shown that the pyrolysis of seaweeds rich in carrageenan (a potassium-rich biopolymer) or in sodium alginate results in carbon materials with high SSAs [142]. Due to the presence of Na or K polymers, which play the same role as additives in chemical activation processes, porosity can be developed without an additional activation step. A pyrolysis at temperature between 600 and 900 °C drives to carbon materials with SSAs up to 1400 m<sup>2</sup>/g. It has been also reported that one-step carbonization of other biomass materials including dead leaves [143], amaranthus waste [144], eggplant [145], or chicken eggshell membranes [146] can produce porous carbons with SSAs over 1000 m<sup>2</sup>/g.

Recently, Zhang et al. [147] reported the importance of physiologic function of plant organs in the microstructure and porosity of formed carbon nanomaterials from one-step pyrolysis of biomass. A disparity on porosity generation when pyrolyzing stems or leaves from lotus, asparagus lettuce, or celery has been shown. As an example, the lotus stem pyrolyzed carbon at 800 °C presents a SSA of 1610 m<sup>2</sup>/g, about 55% higher than the porous carbon from the leaves. Such results indicate that not only the alkali-rich polymer salts included in the biomass composition

act as activating agents but also the inorganic salts contained in the plant have an important role. The higher metal ion content in the stems, which plays the role of ion transportation for plants, would be on the origin of the extra porosity. Also, it has been shown that celery stem pyrolysis renders carbons with SSAs as high as 2194 m<sup>2</sup>/g without any extra activation process.

Self-activation of some polymers or biomass can be also performed by using the pyrolysis gases to prepare microporous activated carbons without any physical or chemical agent. Bommier et al. [148] synthesized high surface area nanoporous carbon from cellulose by using a very low Ar flow for increasing the residence time of evolving gases (e.g., H<sub>2</sub>O, CO<sub>2</sub>) in the reaction chamber. As a result, in situ activation reactions between the resulting carbon and the gases that are evolved during pyrolysis of cellulose are allowed to take place over a wide range of temperatures. A linear relationship was obtained between the flow rate of Argon during the reaction and several key properties of the nanoporous carbons, including SSA, pore volume, and short-range degree order. For a pyrolysis temperature of 1100 °C using a low flow rate of 10 mL/min, a SSA as high as 2600 m<sup>2</sup>/g and a pore volume of 2.1 cm<sup>3</sup>/g were obtained, as opposed to 98 m<sup>2</sup>/g and 0.06 cm<sup>3</sup>/g when a high flow rate of 200 mL/min was used.

Jeong et al. [149] also reported the synthesis of lignin-derived microporous carbons through direct carbonization in a tight closed reactor previously purged with Ar. The high amount of oxygen present in the lignin extracts (e.g., between 21 and 29 wt.%) is in the origin of a large amount of oxygen-containing gases during carbonization. It has been observed that the molecular weight of the lignin precursor plays an important role, where low-molecular-weight lignin precursors produce less defective and high SSA carbons. The highest surface area development was obtained when using Kraft lignin as precursor with a value of 1092 m<sup>2</sup>/g.

Self-activation has been also reported when biomass is pyrolyzed in a closed reactor in the presence of air. In such a case, air and moisture in the furnace are the responsible of the self-activation process of the materials. The oxygen may react with biomass-converted carbon to form CO<sub>2</sub> and together to the moisture and carbon dioxide in the air may serve as activating agents, under an auto-generated pressure, to directly activate the converted carbon.

The effect of the precursor and the pyrolysis conditions on the texture of the activated carbons when pyrolysis is carried out in a closed reactor without inert gas flowing has been described by Xia and Shi [150]. Regarding the precursor, the SSA reported for different biomass pyrolyzed at 1100 °C for 2 h were kenaf bast fiber 1280 m<sup>2</sup>/g, kenaf core 1148 m<sup>2</sup>/g, sugarcane bagasse 910 m<sup>2</sup>/g, sugarcane leaf 591 m<sup>2</sup>/g, coconut fiber 1413 m<sup>2</sup>/g, peanut shell 722 m<sup>2</sup>/g, and sawdust 1199 m<sup>2</sup>/g. The pyrolysis yield, the SSA, the pore volume, and the pore size distribution will depend on the pyrolysis temperature and the dwelling time as shown in Fig. 5.9 for the particular example of kenaf fibers as feedstock.

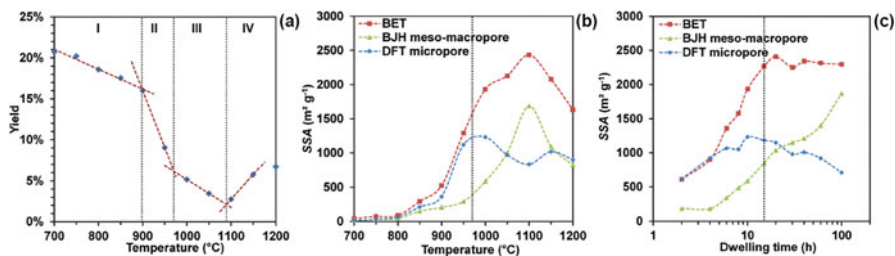


**Fig. 5.9** Pyrolysis of kenaf fibers in a closed reactor. (a) Temperature-dependent yield (pyrolysis time, 10 hours); (b) temperature-dependent surface area and pore volumes (pyrolysis time, 10 hours); (c) dwelling time-dependent surface area and pore volumes (pyrolysis temperature, 1000 °C) (Reproduced from [150] by permission of The Royal Society of Chemistry)

As the activation is produced by the reaction of  $\text{CO}_2$  and  $\text{H}_2\text{O}$  gas with the char, the development of porosity as a function of the temperature and the time follows the same tendencies than those shown in Sect. 5.2 for physical activation of lignocellulosic materials.

Sun et al. [151] selected other biomass feedstocks such as coconut shell, almond stone, walnut shell, and slash pine sawdust to verify the effectiveness of the self-activation with pyrolysis gases in a non-purged reactor for generating microporous carbons. The carbons prepared at temperatures ranging between 800 and 1000 °C presented SSAs from 700 to 1150  $\text{m}^2/\text{g}$  and pore volumes up to 0.61  $\text{cm}^3/\text{g}$  with around 80% micropores.

### 5.3.5 Carbon Molecular Sieves

Carbon molecular sieves (CMS) are carbonaceous materials with a narrow pore size distribution, with pores having several angstroms in diameter. Such unique pore structure of CMS can discriminate molecules on the basis of size and shape or on a difference in adsorption equilibrium or, even, in adsorption rate. Thus, microporous CMS require the presence of a specific porous network containing pore mouths of molecular dimensions, together with a relatively high micropore volume. These features will confer them with a high adsorption capacity and selectivity into a given application. Hence, a proper molecular sieve must exhibit high adsorption capacity and fast adsorption kinetics of certain components of a gas mixture which leads to high selectivity [152, 153].

Although some porous carbon obtained by standard processes as carbonization and activation can present molecular sieve properties by carefully selecting the precursors and conditions [154, 155], numerous procedures for specifically preparing CMS have been proposed. There are three major approaches to prepare CMS (Fig. 5.10): (i) the modification of existing porosity of a suitable porous carbon, mainly by CVD; (ii) the synthesis of CMS by the one-step pyrolysis of a carbon

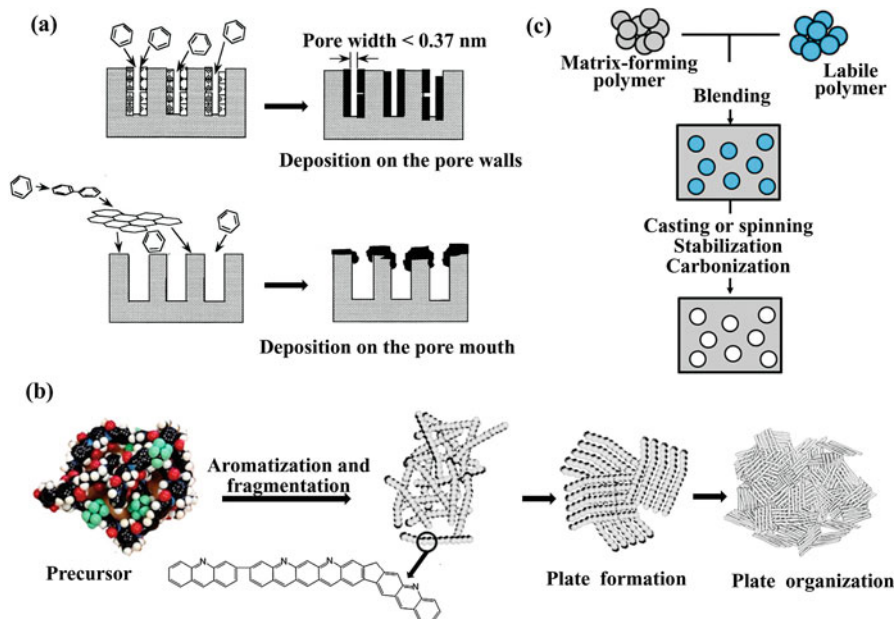


**Fig. 5.10** Schemes for CMS synthesis by different methodologies; (a) CVD (Adapted with the permission from [156], Copyright 1996 American Chemical Society); (b) polymer pyrolysis (adapted from [162], Copyright 2017, with permission from Elsevier); (c) polymer blend pyrolysis (Adapted from [163], Copyright 2017, with permission from Elsevier)

precursor; and (iii) the pyrolysis of polymer blends. The last two approaches are related to the direct pyrolysis of polymers or polymer blends and thus could be considered as self-activation methods. However, as they have been identified in the literature as procedures for specifically designing CMS, they will be described in the present section. Some other methods reported for preparing CMS, such as the pyrolysis of ion exchange resins containing different types of cations, have been already described in Sect. 5.3.4.

The most extended method for modifying the existent porosity of a porous carbon is CVD, which is based on the deposition of pyrolytic carbon at the mouth of the pores to reduce the pore entrance. This method is particularly effective if performed over microporous carbons [156, 157]. CMS can be prepared from a wide variety of porous carbons, e.g., lignocellulosic biomass [158], coal [159], or porous-activated carbon fibers [156, 160]. However, CVD conditions such as temperature, duration of deposition, vapor flow rate, and composition must be accurately optimized for avoiding the excess of carbon deposition driving to a complete pore blocking.

Although pyrolytic carbon or pyrocarbon can be obtained from thermal decomposition of a number of volatile unsaturated hydrocarbons such as benzene [156, 157], methylpentane [161], or methane [160], considerable attention has been paid

to benzene, as it does not generate intermediate compounds during the cracking process, making the deposition process controllable.

It has been reported that the deposition mechanism of carbon from benzene depends mainly on the temperature. Up to 700 °C, benzene diffusion through the pores is faster than its decomposition, and the carbon deposits uniformly over the entire pore surface, thereby reducing the pore size and the pore volume of the pristine material. At temperatures between 700–800 °C, the kinetics of benzene decomposition is faster than the diffusion, thus provoking strong pore diffusion limitations. As a result, the reactant does not reach the inner pore surfaces, and the carbon deposition occurs mainly at the pore entrances, reducing the accessible pore size but not the pore volume of the material. Finally, at temperatures above 800 °C, the kinetics is controlled by the mass transfer (external diffusion), and carbon deposition occurs on the external surface of the particles, thereby blocking all the pores. Thus, in order to reach the desired effect for a CMS, carbon deposition must be carried out in the kinetic regime corresponding to strong pore diffusion limitations (Fig. 5.10). Such conditions must be determined in each case, since they depend on the type of hydrocarbon and on the texture of the pristine activated carbon [157].

Other approach for modulating the porosity of a porous carbon for conferring molecular sieve properties consists in pyrolyzing a mixture of coal and organic additives such as pitch, phenol, and formaldehyde [164–166]. Miura et al. [164] reported the possibility of control the micropore diameter with accuracy at a sub-angstrom level. They found that the pore size of the resultant carbons was controllable with changing the relative amount of the additives. It has been shown that with increasing the amount of a coal-tar pitch over a coal, the pore diameter shifts from 0.43 to 0.37 nm, without modifying the total micropore volume.

The synthesis of CMS has been also reported by direct pyrolysis of organic precursors as polymers or resins. The use of organic compounds with well-known structure might open up the possibility for the design of MSC formation at molecular level [152]. In practice, commercial microporous CMS are mainly produced by CVD, but it has been reported that some commercial MSC from polymer precursors (e.g., C-1012 from Supelco Corp.) can be purely microporous (pore diameter below 0.56 nm) with high specific surface areas and micropore volumes (2000 m<sup>2</sup>/g and 0.73 cm<sup>3</sup>/g, respectively) [153]. Such materials are on a granular (spherical) form, but the main research effort during the last years on synthesis of CMS from polymers has been done to obtain materials with a filmy shape for being applied as membranes for gas separation/adsorption.

Koresh and Soffer [167] first shown that carbon molecular sieve membranes can be easily obtained by pyrolysis of thermosetting polymer membranes such as polyacrylonitrile (PAN), poly(vinylidene chloride) (PVDC), PFA, cellulose, or saran copolymer, able to keep the morphology of the parent materials. They described that the pore dimensions of carbon were dependent on the morphology of the organic precursor and on the pyrolysis conditions. According to their results, by appropriately choosing a sequence of thermal treatments, membrane pore size can be continuously tuned. Research development after that initial work has shown that

the choice of the polymeric precursor is important because pyrolysis of different precursors may yield different kinds of carbon membranes having completely different porous textures from microporous to macroporous, and adsorption/separation behaviors [168]. Mainly microporous carbon membranes have been synthesized from several precursors, including polyimides [169, 170], coal-tar pitch [171], furfuryl alcohol [172], PVDC copolymer [173], or phenolic resin [174].

The pyrolysis of polyimides is one of the most investigated methods, as it allows to prepare either amorphous or graphitic carbons or nanoporous or dense (nonporous) materials, by simply selecting the molecular structure of the precursor and the pyrolysis conditions. As an example, Ohta et al. [170] reported the use of polyimides with repeating units containing pendant groups of  $-\text{CH}_3$  and  $-\text{CF}_3$ . The authors found that varying the amount of F content in repeating unit from 5 to 31 wt.%, the microporous surface area after a pyrolysis at 600 °C went from 856 to 1342  $\text{m}^2/\text{g}$  and the micropore volume from 0.28 to 0.44  $\text{cm}^3/\text{g}$ . In both conditions, the average micropore diameter was around 0.55 nm.

The effect of PI film pyrolysis temperature and atmosphere of CMS porous texture has been shown by Lua and Su [175]. The authors reported that increasing the pyrolysis temperature simultaneously created new pores and narrowed the existing ones. The carbon membranes prepared at 1000 °C under vacuum displayed the highest micropore volume (detected by  $\text{CO}_2$  adsorption), while the membranes prepared at 800 °C under vacuum had the highest characteristic adsorption energy.

As recently reviewed by Yang et al. [163], polymer blend technique is an efficient method for the preparation of microporous carbon materials having controlled structure and textures. The carbonization behavior depends predominantly on the precursor (matrix-forming polymer), but pore structure of the final carbons can be controlled by the selection of blended polymers, which can be either vaporized or decomposed into gases to leave pore in the matrix (labile polymer). Various polymers have been employed as the matrix-forming ones, such as polyimides (PI), phenol resins (FR), polyacrylonitrile (PAN), poly(phenylene oxide) (PPO), and pitches, and as the labile ones, such as polyvinylpyrrolidone (PVP), polystyrene, polyethylene, poly(ethylene glycol) (PEG), polyurethane, and polybenzimidazole. After blending two polymers either as solids or in a liquid, either membranes or fibers are formed by casting and spinning, respectively, followed by carbonization after stabilization if necessary (as depicted in Schema Xc). The pores formed in the resulting carbon membranes and fibers are due to the decomposition or removal of the labile polymer of the blend, that acts as a sacrificial template.

As an example, pore control in carbon membranes derived from polyimide is successfully performed by blending polyvinylpyrrolidone (PVP) with different molecular weights. As exposed above, the pyrolysis of PI membranes results in porous carbons, but Kim et al. [176] have shown that the micropore volume when blending with PVP increases with increasing the amount of PVP but also with increasing the  $M_w$  of PVP. Other blends that effectively work to increase micropores in the carbon films are PPO/PVP [177] or PF/PEG [178].

### 5.3.6 Carbide-Derived Carbons

Carbide-derived carbons, CDC, previously named « mineral carbons » [179] have caught increasing attention during the last decades due to the possibility of tuning their textural properties for applications in energy and gas storage [180–184]. CDCs are produced by selective etching of metals from crystalline metal carbides. In such a way, the metal carbide lattice has the role of template as metal is extracted layer by layer. The transformation is conformal, and an atomic level control can be achieved at the same time that the carbide sample size and shape is maintained. Depending on the carbide used as precursor and the synthesis conditions, different carbon allotropes can be produced ranging from amorphous carbon to graphite or even nanocrystalline diamond [185].

Several methods have been reported for selective removal of metal or metalloid atoms from carbides such as hydrothermal leaching, thermal decomposition, etching at high temperatures in molten salts, halogenation, or electrochemical etching at room temperature. Among them, hydrothermal leaching, thermal decomposition, and electro-chemical etching at high temperatures typically produce nonporous or low porosity carbons. On the other hand, halogenation and electrochemical etching at room temperature are the most suitable routes for obtaining nanoporous carbons, as it will be detailed below.

Electrochemical etching by oxidation of carbides has proven to be efficient for producing CDCs at room temperature from binary metal carbides (such as VC and V<sub>2</sub>C), [186] or MAX phase metal carbides (with M = early transition metal; A = Al or Si, and X = C or N; e.g. Ti<sub>3</sub>AlC<sub>2</sub>, Ti<sub>2</sub>AlC, and Ti<sub>3</sub>SiC<sub>2</sub>) [187]. In particular, the CDC films obtained by electrochemical oxidation of Ti<sub>3</sub>AlC<sub>2</sub> in HF present a very narrow pore size distribution with pores smaller than 2 nm diameter. Such a promising synthesis pathway of nanoporous CDC has been not much explored even if in a recent work Messner et al. [188] demonstrated that many metal carbides (NbC, Nb<sub>2</sub>C, TaC, Ta<sub>2</sub>C, VC, VCrC, TiC, and TiCrC) having a cubic or hexagonal structure can be oxidized electrochemically producing soluble metal ions in the solutions and carbon.

Halogenation is the most suitable for obtaining nanoporous carbons. The general reaction involved in the synthesis of carbon from metal carbides by halogenation can be written as  $M_xC_y(s) + (z/2) X_2(g) \rightarrow x MeXz(g) + y C(s)$  where Me represents metal and X the halogen.

The most commonly used etching agent is Cl<sub>2</sub>, but other halogens such as F<sub>2</sub> and XeF<sub>2</sub> can be used instead of Cl<sub>2</sub> [189]. The chlorination process for obtaining CDCs has been first reported by Hutchins in 1918 [190]. At that time, the carbon was considered just as a subproduct of the reaction of SiC with chlorine for obtaining SiCl<sub>4</sub>. Some decades later, in 1959, Mohun et al. [191] showed that carbons obtained at various chlorination temperatures through a slightly modified method had interesting adsorption capacities of some vapors. However, the first detailed study of the porous texture of the CDC carbons by N<sub>2</sub> and CO<sub>2</sub> adsorption was performed by Boehm et al. in 1975 [192] over carbons produced by chlorination of SiC and TaC.

The factors controlling the porous textures of the carbons produced by chlorination of carbides are related to the initial carbide chemistry and porosity, some processing parameters as gas mixtures or chlorination temperature, and post-halogen treatment.

At low chlorination temperatures, the crystal structure of the carbide templates the pore size distribution of the final CDC. As different carbides have different spatial distributions of carbon atoms in their lattice, halogenation for removing metals will lead to different carbon pore size distributions [193]. It has been reported that binary carbides with würtzite/zinc blend (hexagonal/cubic) structure such as SiC or with NaCl (cubic) ones such as 3C-SiC, TiC, VC, or ZrC yield small micropores with narrow pore size distribution as the first neighbor separation is uniform. In contrast, binary carbides with rhombohedral (e.g. B<sub>4</sub>C) or orthorhombic (e.g. Mo<sub>2</sub>C) structures, and layered hexagonal ternary carbides with a MAX phase (e.g. Ti<sub>2</sub>AlC, Ti<sub>3</sub>SiC<sub>2</sub>) that display a large non-uniform nearest neighbor separation, give rise to CDC of larger pores and wide pore size distributions having a great contribution of mesoporosity (Fig. 5.11) [194–198].

Overall, increasing the chlorination temperature also increases the average micropore size of the CDC, regardless the carbide used as precursor (see Fig. 5.11a). As exposed above, at low chlorination temperatures, the parent carbide controls the initial pore size, but increasing the chlorination temperature from 400 °C to 1200 °C can result in a tenfold increase in the pore width. Higher chlorine treatment temperatures increase the mobility of carbon atoms and facilitate the formation of larger-sized graphene fragments and graphene layers stacking, which results in the formation of larger pores [199]. Larger and straighter pores facilitate the removal of trapped metal chlorides produced during the chlorination reaction. In addition, the chlorides rapidly produced at high temperatures may cause expansion of CDC particles, particularly those produced from layered carbides [196–198]. These phenomena contribute to increase the total pore volume and size in CDC. In general,

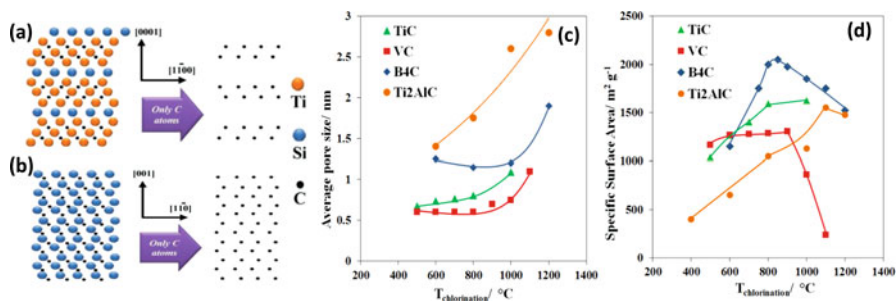


**Fig. 5.11** (a) [11–20] Projection of Ti<sub>3</sub>SiC<sub>2</sub> with removal of all Ti and Si atoms (Reprinted from [198], Copyright 2005, with permission from Elsevier), (b) [110] projection of 3C-SiC with removal of all Si atoms (Reprinted from [201], Copyright 2006, with permission from Elsevier). Effect of chlorination temperature over average pore size (c) and BET surface area (d) for porous carbons obtained from TiC (data depicted from [202]); VC (data depicted from [203]); B<sub>4</sub>C (data depicted from [202, 204]); Ti<sub>2</sub>AlC (data depicted from [196, 202])

at low chlorination temperatures, N<sub>2</sub> or Ar adsorption isotherms of the resultant carbons are of type I since they become of type IV when increasing temperature indicating the presence of mesopores [200]. At the same time, specific surface area was reported to have a bell-shaped temperature dependence independently of the parent carbide (see Fig. 5.11b).

In sum, limiting factors for the specific surface area include, at low temperature, clogging of pores with chlorides and chlorine residues and, at high temperature, graphitization and structure collapsing. Therefore, in order to obtain only micropores with pore sizes adapted to the adsorption of small gases such as CO<sub>2</sub>, CH<sub>4</sub>, or H<sub>2</sub>, a moderate chlorination temperature should be used. As an example, gas separation analysis shows that CDCs obtained at temperatures lower than 1000 °C from binary carbides have an important specific surface area and a narrow pore size distribution being excellent materials for the complex CO<sub>2</sub> separation from N<sub>2</sub>, i.e., nitrogen accessibility at room temperature and atmospheric pressure is inhibited compared to larger molecules (e.g., CH<sub>4</sub>) probably due to specific interactions at the pore mouth [183].

A strategy for obtaining microporous carbons with high micropore volume, narrow pore size distribution, and high surface area would be to perform chlorination at low temperature and to add a posttreatment step. It has been reported from one side that a heat treatment under H<sub>2</sub> at temperatures around 200–600 °C is effective for opening the clogged pores and to increase the pore volume, and from the other, a chemical or physical activation can be performed over the CDC for increasing the pore volume and specific surface area [182, 184, 205, 206].

## 5.4 Conclusions

Among the large spectrum of materials with potential ability to selectively adsorb specific molecules of a gas mixture, nanoporous carbons play an important role due to the versatility of forms, morphologies, and pore architectures. They do not only display excellent adsorption capacities and selectivity for gas mixtures but also better mechanical stability under pressure, which is required for practical applications. Such features make them successful materials for gas storage applications, when compared to direct competitor materials such as zeolites and metal organic frameworks. For practical gas-phase applications, an appropriate adsorbent must present a high adsorption capacity at the operating conditions, which can be achieved and modulated by tuning the porosity, for which the preparation of carbon materials with optimum textural features (in terms of specific surface area and adequate pore dimensions) becomes critical for gas storage. Nanoporous carbons are traditionally manufactured by the so-called conventional activation methods based on the thermal or chemical gasification of a carbon precursor under carbon dioxide or steam atmospheres. This process is used at industrial scale for over a century, and thus knowledge on the optimized operating conditions depending on the nature and reactivity of the precursor has been accumulated over the years. In

the last years, these classical approaches are being revisited from new perspectives, trying to increase carbon yields and use renewable sources and wastes as precursors, to modulate the textural features of the resulting carbons by more sustainable and less energy-demanding processes. However, a small control over the porous features is obtained with conventional activation methods, for which the design and development of new approaches that allow a precise control of the porosity (in terms of pore size and volume) of the carbon materials have received much attention in the last decades. The combination of hydrothermal carbonization of various precursors with post-synthesis activation, the use of nanocasting approaches with adequate templates, or microporous carbons obtained from carbides are among the most promising approaches to obtain porous carbons with adequate porosity for gas storage. The critical issue to be solved in the near future would be to demonstrate whether if the performance of such highly featured carbons with ad hoc porous features can overcome the cost associated with the synthesis for a scale-up, hence granting their practical application.

**Acknowledgments** The authors thank financial support of the European Research Council through an ERC-Consolidator Grant (ERC-CoG 648161, PHOROSOL).

## References

1. Marsh H, Rodriguez-Reinoso F (2006) Activated carbon. Elsevier, Oxford
2. Tascon JMD (ed) (2012) Novel carbon adsorbents, 1st edn. Elsevier, Amsterdam
3. Bandosz TJ (ed) (2006) Activated carbon surfaces for environmental remediation. Elsevier, Boston
4. Guo J, Morris JR, Ihm Y et al (2012) Topological defects: origin of nanopores and enhanced adsorption performance in nanoporous carbon. *Small* 8:3283–3288
5. Radovic LR, Bockrath B (2005) On the chemical nature of graphene edges: origin of stability and potential for magnetism in carbon materials. *J Am Chem Soc* 127:5917–5927
6. Roskill Report, The Economics of Activated Carbon, The Roskill Report, 6th Edition, Roskill Information Services Ltd. 2, Clapham Road, London SW9 0JA, UK
7. Casco ME, Martínez-Escandell M, Gadea-Ramos E et al (2015) High-pressure methane storage in porous materials: are carbon materials in the pole position? *Chem Mater* 27:959–964
8. van den Berg AWC, Otero-Areán C (2008) Materials for hydrogen storage: current research trends and perspectives. *Chem Commun* 6:668–681
9. Kumar KV, Preuss K, Titirici MM et al (2017) Nanoporous materials for the onboard storage of natural gas. *Chem Rev* 117:1796–1825
10. Berenguer-Murcia A, Marco-Lozar JP, Cazorla-Amorós D (2018) Hydrogen storage in porous materials: status, milestones, and challenges. *Chem Rev.* <https://doi.org/10.1002/tcr.201700067>
11. Hornbostel MD, Bao J, Krishnan G et al (2013) Characteristics of an advanced carbon sorbent for CO<sub>2</sub> capture. *Carbon* 56:77–85
12. Marco-Lozar JP, Kunowsky M, Suarez-Garcia F et al (2014) Sorbent design for CO<sub>2</sub> capture under different flue gas conditions. *Carbon* 72:125–134
13. Martin CF, Plaza MG, Pis JJ et al (2010) On the limits of CO<sub>2</sub> capture capacity of carbons. *Sep Purif Methods* 74:225–229

14. Wu K, Chen Z, Li X et al (2016) Methane storage in nanoporous material at supercritical temperature over a wide range of pressures. *Sci Rep*. <https://doi.org/10.1038/srep33461>
15. Tan Z, Gubbins KE (1992) Adsorption in carbon micropores at supercritical temperatures. *J Phys Chem* 94:6061–6069
16. Zhou Y, Wang Y, Chen H et al (2007) Methane storage in wet activated carbon: studies on the charging/discharging process. *Carbon* 43:2007–2012
17. Masika E, Mokaya R (2013) Preparation of ultrahigh surface area porous carbons templated using zeolite 13X for enhanced hydrogen storage. *Prog Nat Sci Mater Int* 23:308–316
18. Sevilla M, Sangchoom W, Balahmar N et al (2016) Highly porous renewable carbons for enhanced storage of energy-related gases (H<sub>2</sub> and CO<sub>2</sub>) at high pressures. *ACS Sust Chem Eng* 4:4710–4716
19. Jorda-Beneyto M, Suarez-Garcia F, Lozano-Castello D et al (2007) Hydrogen storage on chemically activated carbons and carbon nanomaterials at high pressures. *Carbon* 45:293–303
20. Molina-Sabio M, Almansa C, Rodríguez-Reinoso F (2003) Phosphoric acid activated carbon discs for methane adsorption. *Carbon* 41:2113–2119
21. Almansa C, Molina-Sabio M, Rodríguez-Reinoso F (2004) Adsorption of methane into ZnCl<sub>2</sub>-activated carbon derived discs. *Microporous Mesoporous Mater* 76:185–191
22. López-Salas N, Jardim EO, Silvestre-Albero A et al (2014) Use of eutectic mixtures for preparation of monolithic carbons with CO<sub>2</sub> adsorption and gas-separation capabilities. *Langmuir* 30:12220–12228
23. Antal MJ, Grønli M (2003) The art, science and technology of charcoal production. *Ind Eng Chem Res* 42:1619–1640
24. Inagaki M, Park KC, Endo M (2010) Carbonization under pressure. *New Carbon Mater* 25:409–420
25. Bridgewater AV (1999) *Handbook on fast pyrolysis of biomass*. CPL Press, Newbury
26. Ragucci R, Giudicianni P, Cavalierebet A et al (2013) Cellulose slow pyrolysis products in a pressurized steam flow reactor. *Fuel* 107:122–130
27. Giudicianni P, Pindozzi S, Grottole CM et al (2017) Pyrolysis for exploitation of biomasses selected for soil phytoremediation: characterization of gaseous and solid products. *Waste Manag* 61:288–299
28. Cyganiuk A, Gorska O, Olejniczak A et al (2012) Pyrolytic production of microporous charcoals from different wood resources. *J Anal Appl Pyrol* 98:15–21
29. Minkova V, Razvigorova M, Bjornbom E (2001) Effect of water vapour and biomass nature on the yield and quality of the pyrolysis products from biomass. *Fuel Process Technol* 70:53–61
30. Khezami L, Chetouani A, Taouk B et al (2005) Production and characterisation of activated carbon from wood components in powder: cellulose, lignin, xylan. *Powder Technol* 157:48–56
31. Andrade M, Parra JB, Haro M et al (2012) Characterization of the different fractions obtained from the pyrolysis of rope industry waste. *J Anal Appl Pyrol* 95:31–37
32. Ruiz B, Parra JB, Pajares JA et al (2006) Effect of coal pre-oxidation on the optical texture and porosity of pyrolysis chars. *J Anal Appl Pyrolysis* 75:27–32
33. Garrido J, Linares-Solano A, Martín-Martínez JM et al (1987) Use of nitrogen vs. carbon dioxide in the characterization of activated carbons. *Langmuir* 3(1):76–81
34. Thommes M, Kaneko K, Neimark A et al (2015) Physisorption of gases, with special reference to the evaluation of surface area and pore size distribution (IUPAC Technical Report). *Pure Appl Chem*. <https://doi.org/10.1515/pac-2014-1117>
35. Rodríguez-Reinoso F, Linares-Solano A, Molina-Sabio M et al (1984) The two-stage air-CO<sub>2</sub> activation in the preparation of activated carbons. Characterization by gas adsorption. *Adsorpt Sci Technol* 1:211–222
36. Parra JB, Pis JJ, de Sousa JC et al (1996) Effect of coal preoxidation on the development of microporosity in activated carbons. *Carbon* 34:783–787
37. Pis JJ, Mahamuda M, Pajares JA et al (1998) Preparation of active carbons from coal: Part III: Activation of char. *Fuel Process Technol* 57:149–161

38. Rodríguez-Reinoso F (1991) Controlled gasification of carbon and pore structure development. In: Lahaye J, Ehrburger P (eds) *Fundamental issues in control of carbon gasification reactivity*. Kluwer Academic Publishers, Amsterdam, pp 533–571
39. Rodríguez-Reinoso F, Molina-Sabio M, Gonzalez MT (1995) The use of steam and CO<sub>2</sub> as activating agents in the preparation of activated carbons. *Carbon* 33(1):15–23
40. Jagiello J, Ania CO, Parra JB et al (2015) Dual gas analysis of microporous carbons using 2D-NLDFT heterogeneous pore surface model and combined adsorption data of N<sub>2</sub> and CO<sub>2</sub>. *Carbon* 91:330–337
41. Molina-Sabio M, Gonzalez MT, Rodríguez-Reinoso F et al (1996) Effect of steam and carbon dioxide activation in the micropore size distribution of activated carbon. *Carbon* 34(4):505–510
42. Cai Q, Huang Z-H, Fang F et al (2004) Preparation of activated carbon microspheres from phenol-resin by supercritical water activation. *Carbon* 42(4):775–783
43. Molina-Sabio M, Rodríguez-Reinoso F (2004) Role of chemical activation in the development of carbon porosity. *Colloids Surf A Physicochem Eng Asp* 241:15–25
44. Marsh H, Yan DS, O'Grady TM et al (1984) Formation of active carbons from cokes using potassium hydroxide. *Carbon* 22:603–611
45. Lillo-Ródenas MA, Cazorla-Amorós D, Linares-Solano A (2003) Understanding chemical reactions between carbons and NaOH and KOH: an insight into the chemical activation mechanism. *Carbon* 41:267–275
46. Raymundo-Piñero E, Azais P, Cacciaguerra T et al (2005) KOH and NaOH activation mechanisms of multiwalled carbon nanotubes with different structural organisation. *Carbon* 43:786–795
47. Lillo-Ródenas MA, Marco-Lozar JP, Cazorla-Amorós D et al (2007) Activated carbons prepared by pyrolysis of mixtures of carbon precursor/alkaline hydroxide. *Anal Appl Pyrol* 80:166–174
48. Lillo-Ródenas MA, Lozano-Castelló D, Cazorla-Amorós D et al (2001) Preparation of activated carbons from Spanish anthracite: II. Activation by NaOH. *Carbon* 39:751–759
49. Nakagawa Y, Molina-Sabio M, Rodríguez-Reinoso F (2007) Modification of the porous structure along the preparation of activated carbon monoliths with H<sub>3</sub>PO<sub>4</sub> and ZnCl<sub>2</sub>. *Microporous Mesoporous Mater* 103:29–34
50. Lozano-Castelló D, Lillo-Ródenas MA, Cazorla-Amorós D et al (2001) Preparation of activated carbons from Spanish anthracite I. Activation by KOH. *Carbon* 39:741–749
51. Fierro V, Torné-Fernandez V, Celzard A (2007) Methodical study of the chemical activation of Kraft lignin with KOH and NaOH. *Microporous Mesoporous Mater* 101:419–431
52. Tsai WT, Chang CY, Lee SL (1997) Preparation and characterization of activated carbons from corn cob. *Carbon* 35:1198–2000
53. Ahmadpour A, Do DD (1996) The preparation of active carbons from coal by chemical and physical activation. *Carbon* 34:471–479
54. Caturla F, Molina-Sabio M, Rodríguez-Reinoso F (1991) Preparation of activated carbon by chemical activation with ZnCl<sub>2</sub>. *Carbon* 29:999–1007
55. Izquierdo MT, Martínez de Yuso A, Rubio B et al (2011) Conversion of almond shell to activated carbons: methodical study of the chemical activation based on an experimental design and relationship with their characteristics. *Biomass Bioenergy* 35:1235–1244
56. Ahmadpour A, Do DD (1997) The preparation of activated carbon experimental from macadamia nutshell by chemical activation. *Carbon* 35:1723–1732
57. Linares-Solano A, Lillo-Ródenas MA, Marco-Lozar JP et al (2012) NaOH and KOH for preparing activated carbons used in energy and environmental applications. *Int J Energy, Environ Econ* 20:59–91
58. Bergius F (1913) In: Knapp W (ed) *Die Anwendung hoher Drücke bei chemischen Vorgängen und eine Nachbildung des Entstehungsprozesses der Steinkohle*. Wilhelm Knapp, Halle a. d. Saale, pp 41–58
59. Berl E, Schmidt A, Koch H (1932) The development of carbon. *Angew Chem* 45:0517–0519

60. Demir-Cakan R, Baccile N, Antonietti M et al (2009) Carboxylate-rich carbonaceous materials via one-step hydrothermal carbonization of glucose in the presence of acrylic acid. *Chem Mater* 21:484–490
61. Jain A, Balasubramanian R, Srinivasan MP (2016) Hydrothermal conversion of biomass waste to activated carbon with high porosity: a review. *Chem Eng J* 283:789–805
62. Titirici MM, Antonietti M (2010) Chemistry and materials options of sustainable carbon materials made by hydrothermal carbonization. *Chem Soc Rev* 39:103–116
63. Liu Z, Quek A, Parshetti G et al (2013) A study of nitrogen conversion and polycyclic aromatic hydrocarbon (PAH) emissions during hydrochar–lignite co-pyrolysis. *Appl Energy* 108:74–81
64. Fujino T, Calderon-Moreno JM, Swamy S et al (2002) Phase and structural change of carbonized wood materials by hydrothermal treatment. *Solid State Ionics* 151:197–203
65. Dinjus E, Kruse A, Troeger N (2011) Hydrothermal carbonization. Influence of lignin in lignocelluloses. *Chem Eng Technol* 34:2037–2043
66. Sevilla M, Fuertes AB (2009) Chemical and structural properties of carbonaceous products obtained by hydrothermal carbonization of saccharides. *Chem Eur J* 15:4195–4203
67. Libra JA, Ro KS, Kammann C (2011) Hydrothermal carbonization of biomass residuals: a comparative review of the chemistry, processes and applications of wet and dry pyrolysis. *Biofuels* 2:71–106
68. Fechler N, Wohlgemuth SA, Jäker P et al (2013) Salt and sugar: direct synthesis of high surface area carbon materials at low temperatures via hydrothermal carbonization of glucose under hypersaline conditions. *J Mater Chem A* 1:9418–9421
69. Cui X, Antonietti M, Yu SH (2006) Structural effects of iron oxide nanoparticles and iron ions on the hydrothermal carbonization of starch and rice carbohydrates. *Small* 2:756–759
70. Titirici MM, Thomas A, Yu SH et al (2007) A direct synthesis of mesoporous carbons with bicontinuous pore morphology from crude plant material by hydrothermal carbonization. *Chem Mater* 19:4205–4212
71. Fernandez M, Ledesma B, Román S et al (2015) Development and characterization of activated hydrochars from orange peels as potential adsorbents for emerging organic contaminants. *Bioresour Technol* 183:221–228
72. Fellingner T-P, White RJ, Titirici MM et al (2021) Borax-mediated formation of carbon aerogels from glucose. *Adv Funct Mater* 22:3254–3260
73. Wohlgemuth SA, Fellingner T-P, Jäker P et al (2013) Tunable nitrogen doped carbon aerogels as sustainable electrocatalysis in the oxygen reduction reaction. *J Mater Chem A* 1:4002–4009
74. Aydınçak K, Yumak T, Sinag A et al (2012) Synthesis and characterization of carbonaceous materials from saccharides (glucose and lactose) and two waste biomasses by waste biomasses by hydrothermal carbonization. *Ind Eng Chem Res* 51:9145–9152
75. Unur E, Brutti S, Panero S et al (2013) Nanoporous carbons from hydrothermally treated biomass as anode materials for lithium ion batteries. *Microporous Mesoporous Mater* 174:25–33
76. Romero-Anaya A, Ouzzine M, Lillo-Ródenas M (2014) Spherical carbons: synthesis, characterization and activation processes. *Carbon* 68:296–307
77. Kalderis D, Kotti MS, Méndez A et al (2014) Characterization of hydrochars produced by hydrothermal carbonization of rice husk. *Solid Earth* 5:477–483
78. Zhang Z, Qu Y, Guo Y et al (2014) A novel route for preparation of high-performance porous carbons from hydrochars by KOH activation. *Colloids Surf A Physicochem Eng Asp* 447:183–187
79. Ding L, Zou B, Li Y et al (2013) The production of hydrochar-based hierarchical porous carbons for use as electrochemical supercapacitor electrode materials. *Colloids Surf A Physicochem Eng Asp* 423:104–111
80. Liu Z, Zhang FS (2011) Removal of copper(II) and phenol from aqueous solution using porous carbons derived from hydrothermal chars. *Desalination* 267:101–106
81. Jain A, Balasubramanian R, Srinivasan MP (2014) Hydrothermal pretreatment for mesoporous carbon synthesis: enhancement of chemical activation. *J Mater Chem A* 2:520–528

82. Falco C, Marco-Lozar J, Salinas-Torres D et al (2013) Tailoring the porosity of chemically activated hydrothermal carbons: influence of the precursor and hydrothermal carbonization temperature. *Carbon* 62:346–355
83. Linares-Solano A, Lozano-Castelló D, Lillo-Ródenas M et al (2007) Carbon activation by alkaline hydroxides, chemistry & physics of carbon. In: Radovic L (ed) *Chemistry and physics of carbon*, vol 1. CRC Press, Boca Raton, pp 1–62
84. Mestre AS, Freire C, Pires J et al (2014) High performance microspherical activated carbons for methane storage and landfill gas or biogas upgrade. *J Mater Chem A* 2:15337–15344
85. Sevilla M, Ferrero GA, Fuertes AB (2017) Beyond KOH activation for the synthesis of superactivated carbons from hydrochar. *Carbon* 114:50–58
86. Sevilla M, Fuertes AB (2016) A green approach to high-performance supercapacitor electrodes: the chemical activation of hydrochar with potassium bicarbonate. *ChemSusChem* 9:1880–1888
87. Chuenchom L, Kraehnert R, Smarsly BM (2012) Recent progress in soft-templating of porous carbon materials. *Soft Matter* 8:10801–10812
88. Lu AH, Schuth F (2006) Nanocasting: a versatile strategy for creating nanostructured porous materials. *Adv Mater* 18:1793–1805
89. Kyotani T, Sonobe N, Tomita A (1988) Formation of highly orientated graphite from polyacrylonitrile by using a two-dimensional space between montmorillonite lamellae. *Nature* 331:331–333
90. Kyotani T, Nagai T, Inoue S et al (1997) Formation of new type of porous carbon by carbonization in zeolite nanochannels. *Chem Mater* 9:609–615
91. Nishihara H, Kyotani T (2012) Zeolite-templated carbon – its unique characteristics and applications. In: Tascon JMD (ed) *Novel carbon adsorbents*, 1st edn. Elsevier, Amsterdam, pp 295–322
92. Ma Z, Kyotani T, Tomita A (2000) Preparation of a high surface area microporous carbon having the structural regularity of Y zeolite. *Chem Commun* 0:2365–2366
93. Ma Z, Kyotani T, Liu Z et al (2001) Very high surface area microporous carbon with a three-dimensional nano-array structure: synthesis and its molecular structure. *Chem Mater* 13:4413–4415
94. Ma Z, Kyotani T, Tomita A (2002) Synthesis methods for preparing microporous carbons with a structural regularity of zeolite Y. *Carbon* 40:2367–2374
95. Nishihara H, Yang QH, Hou HX et al (2009) A possible buckybowllike structure of zeolite templated carbon. *Carbon* 47:1220–1230
96. Kyotani T, Ma ZX, Tomita A (2003) Template synthesis of novel porous carbons using various types of zeolites. *Carbon* 41:1451–1459
97. Yang ZX, Xia YD, Mokaya R (2007) Enhanced hydrogen storage capacity of high surface area zeolite-like carbon materials. *J Am Chem Soc* 129:1673–1679
98. Chen L, Singh RK, Webley P (2007) Synthesis, characterization and hydrogen storage properties of microporous carbons templated by cation exchanged forms of zeolite Y with propylene and butylene as carbon precursors. *Microporous Mesoporous Mater* 102:159–170
99. Yang ZX, Xia YD, Sun XZ et al (2006) Preparation and hydrogen storage properties of zeolite-templated carbon materials nanocast via chemical vapor deposition: effect of the zeolite template and nitrogen doping. *J Phys Chem B* 110:18424–18431
100. Matsuoka K, Yamagishi Y, Yamazaki T et al (2005) Extremely high microporosity and sharp pore size distribution of a large surface area carbon prepared in the nanochannels of zeolite Y. *Carbon* 43:876–879
101. Xia Y, Yang Z, Mokaya R (2010) Templated nanoscale porous carbons. *Nanoscale* 2:639–659
102. Yang SJ, Kim T, Im JH et al (2012) MOF-derived hierarchically porous carbon with exceptional porosity and hydrogen storage capacity. *Chem Mater* 24:464–470
103. Sonobe N, Kyotani T, Tomita A (1991) Formation of graphite thin film from polyfurfuryl alcohol and polyvinyl acetate carbons prepared between the lamellae of montmorillonite. *Carbon* 29:61–67

104. Liu B, Shioyama H, Akita T et al (2008) Metal-organic framework as a template for porous carbon synthesis. *J Am Chem Soc* 30:5390–5391
105. Petkovich N, Stein A (2013) Controlling macro- and mesostructures with hierarchical porosity through combined hard and soft templating. *Chem Soc Rev* 42:3721–3739
106. Mai Y, Eisenberg A (2012) Self-assembly of block copolymers. *Chem Soc Rev* 41:5969–5985
107. To JWF, Je J, Mei J et al (2016) Hierarchical N-doped carbon as CO<sub>2</sub> adsorbent with high CO<sub>2</sub> selectivity from rationally designed polypyrrole precursor. *J Am Chem Soc* 138:1001–1009
108. Liang CD, Dai S (2006) Synthesis of mesoporous carbon materials via enhanced hydrogen-bonding interaction. *J Am Chem Soc* 128:5316–5317
109. Xing W, Zhuo SP, Gao XL (2009) Preparation of hierarchical porous carbon by post activation. *Mater Lett* 63:1311–1313
110. Yan Y, Wei J, Zhang FQ et al (2008) The pore structure evolution and stability of mesoporous carbon FDU-15 under CO<sub>2</sub>, O<sub>2</sub> or water vapor atmospheres. *Microporous Mesoporous Mater* 113:305–314
111. Gorka J, Zawislak A, Choma J et al (2008) KOH activation of mesoporous carbons obtained by soft-templating synthesis. *Carbon* 46:1159–1161
112. Meng Y, Gu D, Zhang F et al (2006) A family of highly ordered mesoporous polymer resin and carbon structures from organic-organic self-assembly. *Chem Mater* 18:4447–4464
113. Gorka J, Jaroniec M (2011) Hierarchically porous phenolic resin-based carbons obtained by block copolymer-colloidal silica templating and post-synthesis activation with carbon dioxide and water vapor. *Carbon* 49:154–160
114. Liu R, Shi Y, Wan Y et al (2006) Triconstituent co-assembly to ordered mesostructured polymer silica and carbon silica nanocomposites and large-pore mesoporous carbons with high surface areas. *J Am Chem Soc* 128:11652–11662
115. Pekala RW (1989) Organic aerogels from the polycondensation of resorcinol with formaldehyde. *J Mater Sci* 24:3221–3227
116. Job N, Panariello F, Crine M et al (2007) Rheological determination of the sol–gel transition during the aqueous synthesis of resorcinol-formaldehyde resins. *Colloids Surf A Physicochem Eng Asp* 293:224–228
117. Al-Muhtaseb SA, Ritter JA (2003) Preparation and properties of resorcinol–formaldehyde organic and carbon gels. *Adv Mater* 15:101–114
118. Pröbstle H, Schmitt C, Fricke J (2002) Button cell supercapacitors with monolithic carbon aerogels. *J Power Sources* 105:189–194
119. Berthon S, Barbieri O, Ehrburger-Dolle F et al (2001) DLS and SAXS investigations of organic gels and aerogels. *J Non-Cryst Solids* 285:154–161
120. Job N, They A, Pirard R, Marien J et al (2005) Carbon aerogels, cryogels and xerogels: influence of the drying method on the textural properties of porous carbon materials. *Carbon* 43:2481–2494
121. Macias C, Rasines G, Garcia TE et al (2016) Synthesis of porous and mechanically compliant carbon aerogels using conductive and structural additives. *Gels* 2:4
122. Job N, Pirard R, Marien J et al (2004) Porous carbon xerogels with texture tailored by pH control during sol–gel process. *Carbon* 42:619–628
123. Rasines G, Lavela P, Macias C et al (2015) N-doped monolithic carbon aerogel electrodes with optimized features for the electrosorption of ions. *Carbon* 83(2015):262–274
124. Rasines G, Lavela P, Macias C et al (2015) Mesoporous carbon black-aerogel composites with optimized properties for the electro-assisted removal of sodium chloride from brackish water. *J Electroanal Chem* 741:42–50
125. Rasines G, Lavela P, Macias C et al (2015) Mesoporous carbon black-aerogel composites with optimized properties for the electro-assisted removal of sodium chloride from brackish water. *J Electroanal Chem* 741:42–50
126. Isaacs Páez E, Haro M, Juárez-Pérez EJ et al (2015) Fast synthesis of micro/mesoporous xerogels: textural and energetic assessment. *Microporous Mesoporous Mater* 209:2–9
127. Szczurek A, Amaral-Labat G, Fierro V et al (2011) Bimodal activated carbons derived from resorcinol-formaldehyde cryogels. *Sci Technol Adv Mater* 12:035001 (12pp)

128. Szczurek A, Amaral-Labat G, Fierro V et al (2011) The use of tannin to prepare carbon gels. Part I: carbon aerogels. *Carbon* 49:2773–2784
129. Balan L, Fernandez de Cordoba MC, Zaier M et al (2017) A green and fast approach to nanoporous carbons with tuned porosity: UV-assisted condensation of organic compounds at room temperature. *Carbon* 116:264–274
130. Gomis-Berenguer A, Garcia-Gonzalez R, Mestre AS et al (2017) Designing micro- and mesoporous carbon networks by chemical activation of organic resins. *Adsorption* 23:303–312
131. Titirici MM, Antonietti M, Baccile N (2008) Hydrothermal carbon from biomass: a comparison of the local structure from poly- to monosaccharides and pentoses/hexoses. *Green Chem* 10:1204–1212
132. Hu B, Wang K, Wu L et al (2010) Engineering carbon materials from the hydrothermal carbonization process of biomass. *Adv Mater* 22:813–828
133. Feinle A, Elsaesser MS, Husing N (2016) Sol-gel synthesis of monolithic materials with hierarchical porosity. *Chem Soc Rev* 45:3377–3399
134. Antonietti M, Fehler N, Fellingner TP (2014) Carbon aerogels and monoliths: control of porosity and nanoarchitecture via sol-gel routes. *Chem Mater* 26:196–210
135. Lopez-Salas N, Carriazo D, Gutierrez MC et al (2016) Tailoring the textural properties of hierarchical porous carbons using DESs. *J Mater Chem A* 4:478–489
136. Carriazo D, Gutiérrez MC, Ferrer ML et al (2010) Resorcinol-based deep eutectic solvents as both carbonaceous precursors and templating agents in the synthesis of hierarchical porous carbon monoliths. *Chem Mater* 22:6146–6152
137. Sevilla M, Fuertes AB (2013) A general and facile synthesis strategy towards highly porous carbons: carbonization of organic salts. *J Mater Chem A* 1:13738–13741
138. Raymundo-Piñero E, Leroux F, Béguin F (2006) A high performance carbon for supercapacitors obtained by carbonization of a seaweed biopolymer. *Adv Mater* 18:1877–1882
139. Nakagawa H, Watanabe K, Harada Y et al (1999) Control of micropore formation in the carbonized ion exchange resin by utilizing pillar effect. *Carbon* 37:1455–1461
140. Hines D, Bagreev A, Bandosz TJ (2006) Surface properties of porous carbon obtained from polystyrene sulfonic acid-based organic salts. *Langmuir* 20:3388–3397
141. Ania CO, Bandosz TJ (2006) Metal-loaded polystyrene-based activated carbons as dibenzothiophene removal media via reactive adsorption. *Carbon* 44:2404–2412
142. Raymundo-Piñero E, Cadek M, Béguin F (2009) Tuning carbon materials for supercapacitors by direct pyrolysis of seaweeds. *Adv Funct Mater* 19:1032–1039
143. Biswal M, Banerjee A, Deo M et al (2013) From dead leaves to high energy density supercapacitors. *Energy Environ Sci* 6:1249–1259
144. Gao SY, Geng KR, Liu HY et al (2015) Transforming organic-rich amaranthus waste into nitrogen-doped carbon with superior performance of the oxygen reduction reaction. *Energy Environ Sci* 8:221–229
145. Li ZJ, Lv W, Zhang C et al (2015) A sheet-like porous carbon for high-rate supercapacitors produced by the carbonization of an eggplant. *Carbon* 92:11–14
146. Li Z, Zhang L, Amirkhiz BS et al (2012) Carbonized chicken eggshell membranes with 3D architectures as high-performance electrode materials for supercapacitors. *Adv Energy Mater* 2:431–437
147. Zhang Y, Liu S, Zheng X et al (2017) Biomass organs control the porosity of their Pyrolyzed carbon. *Adv Funct Mater* 27:1604687–1604695
148. Bommier C, Xu R, Wang W et al (2015) Self-activation of cellulose: a new preparation methodology for activated carbon electrodes in electrochemical capacitors. *Nano Energy* 13:709–717
149. Jeon JW, Zhang L, Lutkenhaus JL et al (2015) Controlling porosity in lignin-derived nanoporous carbon for supercapacitor applications. *ChemSusChem* 8:428–432
150. Xia C, Shi SQ (2016) Self-activation for activated carbon from biomass: theory and parameters. *Green Chem* 8:2063–2071

151. Sun K, Leng C, Jiang J et al (2017) Microporous activated carbons from coconut shells produced by self-activation using the pyrolysis gases produced from them, that have an excellent electric double layer performance. *New Carbon Mater* 32:451–459
152. Kyotani T (2000) Control of pore structure in carbon. *Carbon* 38:269–286
153. Wahby A, Silvestre-Albero J, Sepúlveda-Escribano A (2012) CO<sub>2</sub> adsorption on carbon molecular sieves. *Microporous Mesoporous Mater* 164:280–287
154. De la Casa-Lillo MA, Alcañiz-Monge J, Raymundo-Piñero E et al (1998) Molecular sieve properties of general-purpose carbon fibres. *Carbon* 36:1353–1360
155. Manso R, Pajares JA, Guil JM et al (2000) Activated carbons with molecular sieve properties. *Bol Soc Española Cerámica y Vidrio* 39:556–559
156. Kawabuchi Y, Kishino M, Kawano S et al (1996) Carbon deposition from benzene and cyclohexane onto active carbon fiber to control its pore size. *Langmuir* 12:4281–4285
157. Freitas MMA, Figueiredo JL (2001) Preparation of carbon molecular sieves for gas separations by modification of the pore sizes of activated carbons. *Fuel* 80:1–6
158. Mohamed AR, Mohammadi M, Darzi GN (2010) Preparation of carbon molecular sieve from lignocellulosic biomass: a review. *Renew Sustain Energ Rev* 14:1591–1599
159. Vyas SN, Patwardhan SR, Gangadhar B (1993) Synthesis of carbon molecular sieves by activation and coke deposition. *Fuel* 72:551–555
160. De la Casa-Lillo MA, Moore BC, Cazorla-Amoros D et al (2002) Molecular sieve properties obtained by cracking of methane on activated carbon fibers. *Carbon* 40:2489–2494
161. Hu H, Vansant EF (1995) Carbon molecular sieves produced from walnut Shell. *Carbon* 33:561–567
162. Rungta M, Wenz GB, Zhang C et al (2017) Carbon molecular sieve structure development and membrane performance relationships. *Carbon* 115:237–248
163. Yang Y, Le T, Kang F et al (2017) Polymer blend techniques for designing carbon materials. *Carbon* 111:546–568
164. Miura K, Hayashi J, Hashimoto K (1991) Production of molecular sieving carbon through carbonization of coal modified by organic additives. *Carbon* 29:653–660
165. Bello G, García R, Arriagada R (2002) Carbon molecular sieves from Eucalyptus globulus charcoal. *Microporous Mesoporous Mater* 56:139–145
166. Alcañiz-Monge J, Marco-Lozar JP, Lozano-Castelló D (2012) Monolithic carbon molecular sieves from activated bituminous coal impregnated with a slurry of coal tar pitch. *Fuel Process Technol* 95:67–72
167. Koresh JE, Soffer A (1983) Molecular sieve carbon permselective membrane. Part I. Presentation of a new device for gas mixture separation. *Sep Sci Technol* 18(1983):723–734
168. Salleh WNW, Ismail AF, Matsuura T et al (2011) Precursor selection and process conditions in the preparation of carbon membrane for gas separation: a review. *Sep Purif Rev* 40:261–311
169. Steel KM, Koros WJ (2005) An investigation of the effects of pyrolysis parameters on gas separation properties of carbon materials. *Carbon* 43:1843–1856
170. Ohta N, Nishi Y, Morishita T et al (2008) Preparation of microporous carbon films from fluorinated aromatic polyimides. *Carbon* 46:1350–1357
171. Liang C, Sha G, Guo S (1999) Carbon membrane for gas separation derived from coal tar pitch. *Carbon* 37:1391–1397
172. Hirota Y, Nishiyama N (2016) Pore size control of microporous carbon membranes and application to H<sub>2</sub> separation. *J Jpn Pet Inst* 59:266–275
173. Liu J, Calverley EM, McAdon MH et al (2017) Newcarbon molecular sieves for propylene/propane separation with high working capacity and separation factor. *Carbon* 123:273–282
174. Fuertes AB, Menendez I (2002) Separation of hydrocarbon gas mixtures using phenolic resin-based carbon membranes. *Sep Purif Technol* 28:29–41
175. Lua AC, Su J (2006) Effects of carbonisation on pore evolution and gas permeation properties of carbon membranes from Kapton polyimide. *Carbon* 44:2964–2972

176. Kim YK, Park HB, Lee YM (2005) Gas separation properties of carbon molecular sieve membranes derived from polyimide/polyvinylpyrrolidone blends: effect of the molecular weight of polyvinylpyrrolidone. *J Membr Sci* 251:159–167
177. Itta AK, Tseng HH, Wey MY (2011) Fabrication and characterization of PPO/PVP blend carbon molecular sieve membranes for H<sub>2</sub>/N<sub>2</sub> and H<sub>2</sub>/CH<sub>4</sub> separation. *J Membr Sci* 372:387–395
178. Zhang XY, Hu HQ, Zhu YD et al (2007) Carbon molecular sieve membranes derived from phenol formaldehyde novolac resin blended with poly (ethylene glycol). *J Membr Sci* 289:86–91
179. Mohun WA (1962) Mineral active carbon and process for producing same. US Patent 3,066,099
180. Chmiola G, Yushin Y, Gogotsi C et al (2006) Anomalous increase in carbon capacitance at pore sizes less than 1 nanometer. *Science* 313:1760–1763
181. Yushin G, Dash R, Jagiello J (2006) Enhanced hydrogen uptake by carbide-derived carbons with optimized pore structure. *Adv Funct Mater* 16:2288–2293
182. Presser V, McDonough J, Yeon SH et al (2011) Effect of pore size on carbon dioxide sorption by carbide derived carbon. *Energy Environ Sci* 4:3059–3066
183. Silvestre-Albero A, Rico-Frances S, Rodriguez-Reinoso F et al (2013) High selectivity of TiC-CDC for CO<sub>2</sub>/N<sub>2</sub> separation. *Carbon* 59:221–228
184. Yeon SH, Osswald S, Gogotsi Y et al (2009) Enhanced methane storage of chemically and physically activated carbide-derived carbon. *J Power Sources* 191:560–567
185. Yushin G, Nikitin A, Gogotsi Y (2006) Carbide derived carbon. In: Gogotsi Y (ed) *Nanomaterials handbook*. CRC Press, Boca Raton, pp 237–280
186. Camargo LGB, Palazzo BG, Taylor G et al (2015) Carbide-derived carbon by electrochemical etching of vanadium carbides. *J Electrochem Soc* 162:H811–H815
187. Lukatskaya MR, Halim J, Dyatkin B et al (2014) Room-temperature carbide-derived carbon synthesis by electrochemical etching of MAX phases. *Angew Chem Int Ed* 53:4877–4880
188. Messner M, Walczyk DJ, Palazzo BG et al (2018) Electrochemical oxidation of metal carbides in aqueous solutions. *J Electrochem Soc* 165:H3107–H3114
189. Batisse N, Guérin K, Dubois M et al (2010) Fluorination of silicon carbide thin films using pure F<sub>2</sub> gas or XeF<sub>2</sub>. *Thin Solid Films* 518:6746–6751
190. Hutchins O (1918) Method for the production of silicon tetrachloride, US Patent 1271713
191. Mohun WA (1959) A novel amorphous carbon. In: *Proceedings of the 4th biennial conference on carbon*. Pergamon, Oxford, pp 443–453
192. Boehm HP, Warnecke HH (1975) Structural parameters and molecular sieve properties of carbons prepared from metal carbides. In: *Proceedings of the 12th biennial conference on carbon*. Pergamon, Oxford, pp 149–150
193. Presser V, Heon M, Gogotsi Y (2011) Carbide-derived carbons- from porous networks to nanotubes and graphene. *Adv Funct Mater* 21:810–833
194. Thomberg T, Janes A, Lust E (2010) Energy and power performance of electrochemical double-layer capacitors based on molybdenum carbide derived carbon. *Electrochim Acta* 55:3138–3143
195. Dash RK, Nikitin A, Gogotsi Y (2004) Microporous carbon derived from boron carbide. *Microporous Mesoporous Mater* 72:203–208
196. Hoffman EN, Yushin GN, Barsoum BM et al (2005) Synthesis of nanoporous carbide-derived carbon by chlorination of titanium aluminum carbide. *Chem Mater* 17:2317–2322
197. Hoffman EN, Yushin GN, El-Raghy T et al (2008) Micro and mesoporosity of carbon derived from ternary and binary metal carbides. *Microporous Mesoporous Mater* 112:526–532
198. Yushin GB, Hoffman EN, Nikitin A et al (2005) Synthesis of nanoporous carbide-derived carbon by chlorination of titanium silicon carbide. *Carbon* 44:2075–2082
199. Gogotsi Y, Nikitin A, Ye H et al (2003) Nanoporous carbide-derived carbon with tunable pore size. *Nat Mater* 2:591–594
200. Urbonaitė S, Juarez-Galan JM, Leis J et al (2008) Porosity development along the synthesis of carbons from metal carbides. *Microporous Mesoporous Mater* 113:14–21

201. Welza S, McNallana MJ, Gogotsi Y (2006) Carbon structures in silicon carbide derived carbon. *J Mater Process Technol* 179:11–22
202. Chmiola J, Yushin G, Dash RK et al (2005) Double-layer capacitance of carbide-derived carbons in sulfuric acid. *Electrochem Solid-State Lett* 8:A357–A360
203. Janes A (2007) Synthesis and characterisation of nanoporous carbide-derived carbon by chlorination of vanadium carbide. *Carbon* 45:2717–2722
204. Gogotsi Y, Dash RK, Yushin G et al (2005) Tailoring of nanoscale porosity in carbide-derived carbons for hydrogen storage. *J Am Chem Soc* 127:16006–16007
205. Sevilla M, Mokaya R (2011) Activation of carbide-derived carbons: a route to materials with enhanced gas and energy storage properties. *J Mater Chem* 21:4727–4732
206. Dash R, Chmiola J, Yushin G et al (2006) Titanium carbide derived nanoporous carbon for energy related applications. *Carbon* 44:2489–2249

# Chapter 6

## Metal-Organic Frameworks



V. Bon, I. Senkowska, and S. Kaskel

### 6.1 Metal-Organic Frameworks: Construction Principles and Topology

Metal-organic frameworks (MOFs), also called porous coordination polymers (PCPs), are coordination networks of metal complexes, often multinuclear species, with multifunctional organic ligands (linkers). According to IUPAC recommendations, one of the criteria a MOF needs to fulfill is that it contains potential voids, but no physical measurements of porosity or other properties are required per se [1]. However, for gas storage applications, not only the potential voids available in the crystal structure but especially the gas-accessible porosity is of paramount importance, and thus we only consider MOFs in this chapter showing experimentally proven porosity, e.g., by physisorption methods.

Coordination networks represent a huge class of materials. They extend through repeating coordination entities in 1, 2, or 3 dimensions [1]. The repeating coordination entities are usually metals or metal ions (clusters, multinuclear complexes) and organic multidentate ligands (linkers). The role of the cluster is to direct the coordinating linkers into predefined directions in space. Thus, they are often regarded as the “nodes” of the network. The bi-, tri-, or multifunctional ligands connect the nodes into stable network architecture (Fig. 6.1). The basic design principles of MOFs date back to the concept introduced by Robson [2, 3], which relies on building block concept. The term “reticular chemistry,” which means net-like, was proposed in the early 2000s by Omar Yaghi, one of the pioneers of the MOF research. In his review article, reticular synthesis is defined as follows:

---

V. Bon · I. Senkowska (✉) · S. Kaskel  
Technische Universität Dresden, Dresden, Germany  
e-mail: [irena.senkowska@chemie.tu-dresden.de](mailto:irena.senkowska@chemie.tu-dresden.de)

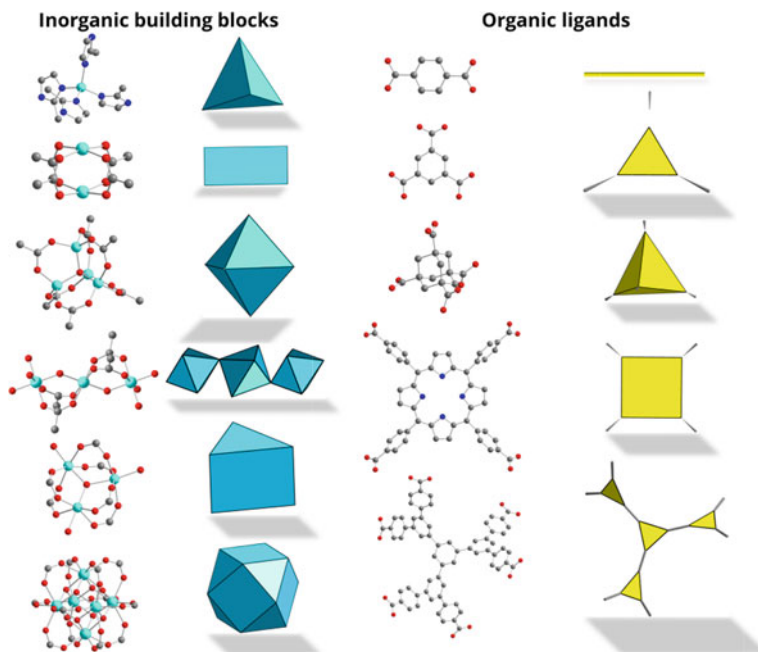


**Fig. 6.1** Prototypical examples of the inorganic building blocks and organic ligands, often used for the construction of MOFs

In essence, reticular synthesis can be described as the process of assembling judiciously designed rigid molecular building blocks into predetermined ordered structures (networks), which are held together by strong bonding.

Construction of MOFs can be directly compared with a children's building kit, namely, combination of bricks with different geometry will lead to a well-defined 3D architecture. Yaghi and co-workers successfully extrapolated this principle to the MOF chemistry calling it modular chemistry, meaning the combination of inorganic units or secondary building units (SBU) with organic units or ligands with certain geometries into networks [4]. However, a combination of dozens of known metal clusters with thousands of organic ligands of different connectivity could lead to formation of different kinds of compounds: molecular 0D complexes, 1D chains, 2D sheets, and 3D frameworks. In order to rationalize the selection process and with that enable the design of targeted frameworks, mathematical graph theory was involved for better explanation, representation, and classification of the frameworks. Thus, initially multidimensional structures were simplified in a manner that usually metal ions or clusters and organic ligands were represented as vertices of a net, interconnected to each other [5]. Such kind of simplification allowed to classify the underlying topologies of the MOFs, which were often identical to those of simple inorganic solids [6]. Application of a reverse approach allows constructing complicated 3D frameworks with target crystal structure and porosity. Following

this strategy, the correct choice of the building blocks may lead to a formation of open 3D frameworks with various pore systems [7–9]. However experimentally, in some cases utilization of the same building units in the synthesis can lead to the formation of MOFs with different framework topologies, so-called polymorphs, differing only by orientation of the ligand in framework [10]. In summary, the use of the modular approach in the MOF synthesis allows to synthesize open frameworks with various pore sizes, shapes, and connectivities, which is extremely important for diverse applications including gas storage. Since the majority of porous compounds are three-dimensional networks, this type of coordination networks (3D) will be mostly discussed below.

This approach allows building crystalline frameworks by combining inorganic and organic building blocks of geometry predefined by deliberate synthesis. The geometry of the building units usually determines the underlying framework topology; however, there are more than 100 possible network topologies for tetrahedral nodes. Therefore, the isorecticular approach is sometimes also called topological. However, in many cases it is not straightforward to predict the topology with a high probability. In some particular cases, the framework topology is strongly dependent on synthesis conditions, reagent concentration, etc. Therefore, O’Keeffe and co-workers performed an extended analysis of the Cambridge Structural Database (CSD) in order to analyze the frequency of occurrence of defined uninodal nets for the same building blocks. They showed the majority of MOF structures, submitted into the CSD at that time to have tetrahedral geometry [11]. These are followed by octahedral, trigonal, and all others. Another interesting statistical trend, observed in this study, is experimental occurrence of high-symmetrical structures while much higher theoretical possibilities of the low-symmetry topologies. Tilings and nets are consolidated in EPINET and RCSR databases [12–14]. Since periodic nets are nothing else but special kind of graphs, graph theory is widely used for generating and describing of nets. Each net in the RCSR database is labeled by a unique three-letter code, which can be abbreviation of the mineral (*dia*, diamond; *qtz*, quartz) or centering and symmetry (*bct*, body-centered tetragonal; *fcu*, face-centered cubic). The main rules for deconstructing the crystal structures into their underlying nets as well as comprehensive state-of-the-art analysis of the existing structures can be found in the recent reviews by Yaghi and O’Keeffe [6, 7].

Nowadays, most of the new MOF structures are synthesized using isorecticular or topological approach. However, there are very special cases, in which direct synthesis is not possible for different reasons. In such cases different approaches have to be used.

## 6.2 Historical Aspects of Discovery and Development of MOFs

In Japan, Susumu Kitagawa was among the early pioneers to explore the field of coordination polymers in the early 1990s starting with the synthesis and character-

ization of Cu- and Ag-based 1D coordination polymers [15]. Later, he succeeded in the synthesis of open 3D framework materials with composition  $[M_2(4,4'\text{-bpy})_3(\text{NO}_3)_4] \cdot x\text{H}_2\text{O}_n$  ( $M=\text{Co}, \text{Ni}, \text{Zn}$ ) showing open pore systems, accessible for gas molecules [16]. In 2004, Kitagawa and co-workers published a review article “Functional Porous Coordination Polymers,” promoting intensive MOF research worldwide [17].

In parallel in another part of the world, Omar Yaghi used squarates in the combination with  $\text{Mn}^{2+}$  and  $\text{Zn}^{2+}$  ions in the synthesis, resulting in compounds with hydrogen-bonded chains, sheets, and even 3D frameworks [18]. Further development of the strategy to combine organic polycarboxylates with metal ions led to the synthesis of  $\text{Zn}_3[(\text{CTC})(\text{C}_5\text{H}_5\text{N})_2]$  (CTC, *cis,cis*-1,3,5-cyclohexanetricarboxylate) possessing one-dimensional channels with an aperture of nearly 6 Å, proven by crystallographic analysis [19]. Later, the synthetic strategies for the construction of the porous modular solids were highlighted [20]. Applying a modular approach to a number of organic ligands and metal clusters resulted in numerous porous solids involving archetypical MOF-5 (Fig. 6.2b), at that time an absolute record holder in terms of porosity [4]. High gas storage capacity of MOF-5 was confirmed soon experimentally in cryogenic hydrogen physisorption experiment at 77 K, resulting in a record of 7.1 wt.% excess uptake at 40 bar [21].

It is worth to mention that simultaneously with Yaghi, Choi and co-workers synthesized  $\text{Cu}_3(\text{btc})_2$  (btc, 1,3,5-benzenetricarboxylate) MOF, also known as HKUST-1 (HKUST, *Hong Kong University of Science and Technology*, Fig. 6.2a) [22], which combines low-cost initial reagents, good stability, and one of the highest volumetric methane capacities among all known MOFs [23] and with that is among best and prospective materials for methane storage applications [24].

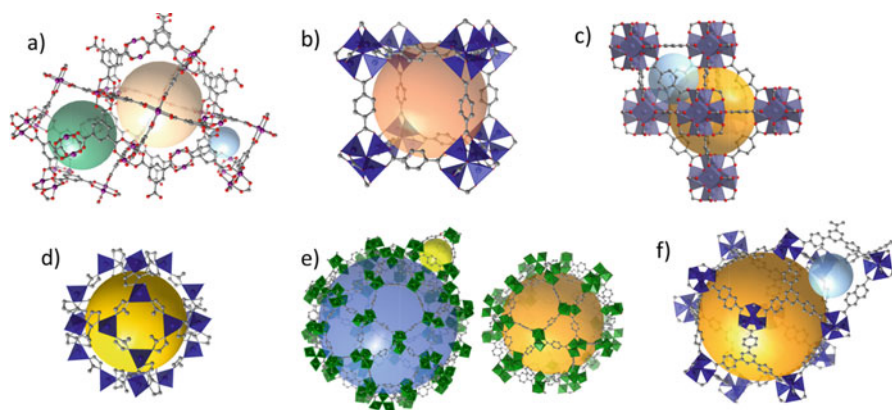


**Fig. 6.2** Pore structure in HKUST-1 (a), MOF-5 (b), UiO-66 (c), ZIF-8 (d), MIL-101 (e), and DUT-6 (f)

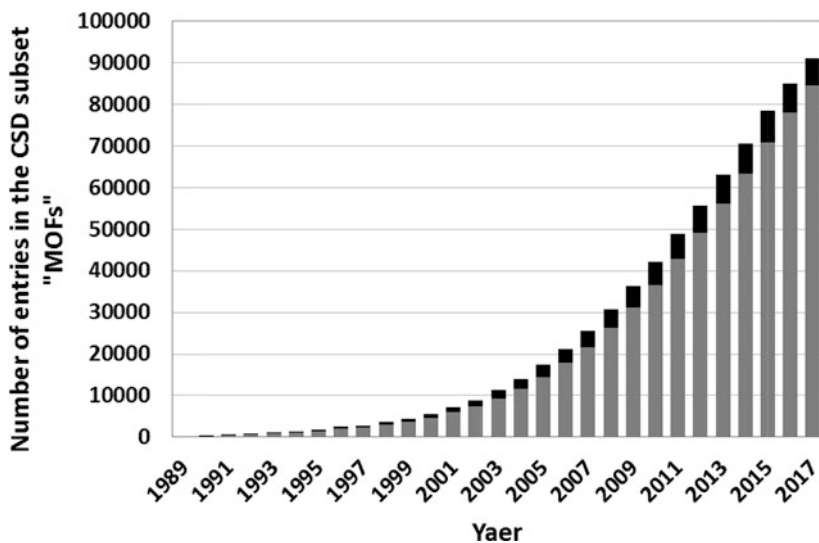


Fig. 6.3 MOF entries in the Cambridge Structural Database (CSD) [33] over the years

In Europe, Tony Cheetham and Gérard Férey studied the formation of the inorganic clusters and open framework inorganic materials [25] and with that established a MIL (MIL, Matériaux de l'Institut Lavoisier) series, which started with mono- and diphosphonate frameworks [26]. Later polycarboxylate ligands were used as organic components, leading to a first porous solid MIL-47 [27], followed by the prominent series of MIL-53, MIL-88, MIL-100, MIL-101 (Fig. 6.2e), MIL-125, and MIL-140, which are chemically more stable than the zinc-based networks discussed above.

The prominent breakthroughs reporting higher and higher specific surface areas ( $>3000 \text{ m}^2 \text{ g}^{-1}$ ) surpassing activated carbons significantly motivated the initiation of MOF research worldwide. Our group succeeded in the synthesis of highly porous, mesoporous compounds such as DUT-6 [28] (Fig. 6.2f), DUT-32 [29], and DUT-76 [30] (DUT, Dresden University of Technology) reaching the surface areas up to  $6400 \text{ m}^2 \text{ g}^{-1}$ . DUT-32 has excellent hydrogen storage properties, and the excess maximum capacity is achieved at 53 bar and reaches  $85 \text{ mg g}^{-1}$  ( $7.8 \text{ wt\%}$ ;  $22.9 \text{ mg cm}^{-3}$ ) which is only surpassed by MOF-210 ( $86 \text{ mg g}^{-1}$ ) [31] and NU-100 ( $99.5 \text{ mg g}^{-1}$ ) [32].

The lively interest to the MOF research is reflected in the constantly growing international MOF community, as well as permanently growing number of new MOF structures in the CSD database reaching 85,200 entries in the CSD v.5.39 from February 2018 (Fig. 6.3) and more and more applications in various other areas being developed today.

### 6.3 Determination of the Crystal Structure and Crystallographic Porosity (Void Fraction)

Since one of the main advantages of MOFs is their crystallinity, the determination of the crystal structure is indispensable in the MOF research. Often MOFs can be obtained as single crystals, which allows for *ab initio* structure determination by single crystal X-ray diffraction. However, typically single crystals of MOFs consist only of 10–50% of ordered framework and consequently scatter rather weakly if X-rays from ordinary laboratory source are used. Thus, data collection on the single crystals of highly porous structures is recommended at synchrotron beamlines, providing a brilliant monochromatic radiation with high photon flux and sensitive detectors. The pores of MOFs are filled with disordered guest molecules, which indeed significantly contribute to the reflections intensities, but usually cannot be localized and modelled unambiguously [34]. Consequently, the SQUEEZE procedure is often used to subtract the contribution of the guest molecules from reflection dataset. If single crystals of sufficient size and quality are difficult to obtain, the structure determination is much more challenging. In case the structure is targeted from PXRD data, the correct indexing of the powder pattern, especially for structures crystallizing in low-symmetry space groups, is ambiguous and cannot be considered as a routine procedure [34, 35]. Structure modelling is a valuable supplement to predict a reasonable starting structural model for a refinement. If the correct unit cell and space group is found, diverse characterization techniques such as TG, elemental analysis, NMR, IR, physisorption experiments, etc. are used to support the assumption of the starting model. Moreover, direct space methods like simulated annealing or parallel tempering are used in order to obtain an initial model for the Rietveld refinement. For example, crystal structures of mesoporous MIL-100(M) and MIL-101(Cr) were solved using computational structure simulation and simultaneous Rietveld refinement [36].

The crystalline structure of MOFs allows the calculation of the pore size distribution without any porosity measurements using a geometrical approach. For this purpose, several programs were developed in recent years. Sarkisov and Harrison developed a useful code named Poreblazer, which allows to calculate textural properties such as geometrical surface area, pore volume, and pore size distribution [37]. At the same time, Haranczyk and co-authors published a Zeo++ program, which additionally allows to analyze other structural features like distance grids and Voronoi networks [38]. Another, more sophisticated way for theoretical estimation of the textural properties of MOFs is the simulation of the adsorption isotherms using Grand Canonical Monte Carlo Simulations (GCMC). Using software codes like MUSIC [39] or RASPA [40], one can calculate the nitrogen adsorption isotherm at 77 K, and afterward by applying classical BET theory, Gurvich rule and suitable DFT models derive the BET area, pore volume, and pore size distribution. Such methods may be also extended to predict high-pressure adsorption isotherms as they are relevant to gas storage applications described in this book. The value of modern simulation methods cannot be emphasized enough. In many cases

the isotherms predicted reflect well the total uptake and the relative pressures at which characteristic steps, reflecting pore filling mechanism, should occur. With that in hand, a direct comparison with experimental data gives important insights, in particular into the phase purity of the MOF materials used, the completeness of solvent removal, and potential degradation mechanisms. However, isotherm simulation so far is still limited to rigid frameworks (see Sect. 6.6 Flexibility).

## 6.4 Stability of MOFs

The chemical, thermal, hydrothermal, and mechanical stabilities (resistance of the structure to degradation) of MOFs have been typically perceived as problematic, but this is an outdated perception [41]. In recent years, many chemically stable and thermally stable MOFs were discovered, enabling an exciting expansion of their application. For gas storage applications, chemical (more specifically hydrolytic) and mechanical stability play the most important role, since compacted forms of MOFs, such as pellets or extrudates, are usually required. A critical aspect for natural gas storage is also the degradation by H<sub>2</sub>S.

### 6.4.1 Hydrolytic Stability

The greatest concerns for the improvement of MOF chemical stability have been largely related to water vapor [42]. A metal-ligand coordination bond is a weak point in the structure. Hydrolysis produces a protonated linker and a hydroxyl group (or water) [41]. The strength of this bond can be a strong indicator of the hydrolytic stability [43].

In 2014, K. Walton and co-workers have assigned a stability classification for MOFs experimentally characterized after water exposure [43]: (i) thermodynamically stable MOFs, (ii) MOFs with high kinetic stability, (iii) MOFs of low kinetic stability, and (iv) unstable. The MOFs of group (i) are stable after long-term exposure to aqueous solutions and have strong potential for a wide range of applications. For example, JUC-110 and Ni<sub>3</sub>(BTP)<sub>2</sub> belong to this group, demonstrating stability in boiling water but also MIL-96(Al), MIL-101(Cr), ZIF-8 (Fig. 6.2d), and NOTT-300 which are stable under steaming conditions (for more examples see ref. [43, 44]).

Group (ii) is stable after exposure to high humidity and has strong potential for industrial applications with high humidity conditions. There is a wide range of MOFs in this category including well-studied structures such as UiO-66, DUT-67, and several members of the MIL family of materials. MOFs of low kinetic stability (e.g., MIL-110(Al), MIL-125(Ti), CPO-27) are stable only at low humidity and have potential for applications with pre-dried gas conditions.

Some MOFs are not only highly hydrostable but also capable of retaining their structural integrity on repeated exposure to subsequent water vapor adsorption/desorption cycles [45]. For example, amine-modified  $H_2N$ -MIL-125-Ti remains virtually unaltered during the short non-equilibrium multi-cycle ad-/desorption experiments [44].

### 6.4.2 Mechanical Stability

In typical industrial processing, hydrostatic compressions and shear forces are the two most common mechanical loadings that would be encountered by MOF powders for shaping and in high adsorber columns. Thus the corresponding Young's modulus or elastic moduli ( $E$ , measure how the substance resistance to being deformed elastically), bulk modulus ( $K$ , how resistant is the substance to compressibility), and shear modulus ( $G$ , the material's response to shear stress) are the most relevant mechanical properties. They can be calculated and used to estimate MOF resistance to mechanical degradation.

Due to the high void fraction of MOFs, they are expected to be of low mechanical stability, whereas solvated materials are more mechanically stable than desolvated [46, 47]. The mechanical instability of MOFs usually manifest itself as phase changes, partial collapse of pores, or even amorphization, in response to mechanical loading [41]. High porosity and mechanical stability are intrinsically two competing properties; therefore usually longer linker leads to lower mechanical stability [48], as it was shown by studies on MOF-5 analogues [49, 50] and UiO-66 and UiO-67 structures [51]. The bulk moduli of typical MOFs are in the range of 5–30 GPa

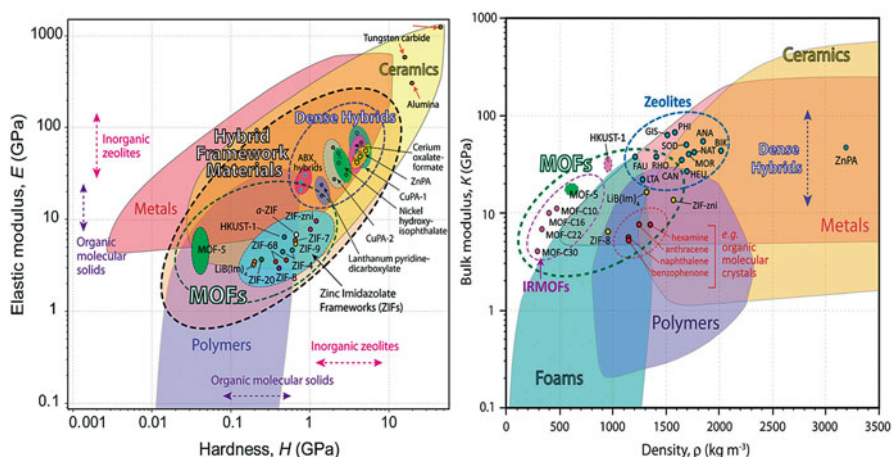


**Fig. 6.4** Left: Elastic modulus versus hardness material property map for coordination networks, encompassing both dense and porous framework structures presented with other major classes of materials. Right: Bulk modulus versus physical density material property map for MOFs, plotted alongside other major classes of materials. Reproduced from Ref. [48] with permission from The Royal Society of Chemistry

(Fig. 6.4). The  $K$  values of inorganic zeolites fall in the range of 15–70 GPa, [52] which are generally higher compared with MOFs. For instance, the bulk modulus of a zeolite with the *sod* topology is about five times higher than that of its ZIF counterpart (ZIF-8).

The Young's modulus of ZIF-8 measured on a single crystal is 3.2 GPa. The cubic symmetry of ZIF-8 also exhibits elastic anisotropy, where elastic modulus ( $E$ )  $E_{\max} \approx 3.8$  GPa and  $E_{\min} \approx 2.8$  GPa corresponding to the Young's moduli of the (100)- and (111)-oriented crystal facets, respectively [53]. The measured values of  $E$  and hardness ( $H$ ) for the ZIF-8 powder were reported to be 2.25 GPa and 343 MPa, respectively [54]. One possible way to enhance the mechanical robustness of MOFs is the preparation of MOF-based composites to exploit the synergistic interactions between them and inorganic nanomaterials [55], as was demonstrated on example on ZIF-8/boron nitride composite [54]. The composite containing ZIF-8/BN in the mole ratio 1:2 shows a remarkable improvement of elastic modulus and hardness, with  $E$  nearly double that of the bare ZIF-8, while  $H$  is 30% higher. However, it should be pointed out that the “fillers” in general will lower the overall gas adsorption capacity.

Computational investigations have shown that 12-connected Hf-UiO-66 has one of the highest shear and bulk moduli of all MOF structures, which are similar to values typical for zeolites, rendering it among the most mechanically stable MOFs [51, 56].

## 6.5 Targeted Design of MOFs for Gas Storage

The potential of MOFs as gas storage materials was recognized quite early. The first methane adsorption was reported by Kitagawa and co-workers in 1997–2000 [16, 57, 58], and in 2003 Yaghi et al. reported the first measurement of hydrogen storage in MOFs performed on two isoreticular compounds MOF-5 and IRMOF-8 [59]. These pioneering studies initiated great interest in MOFs as gas storage materials based on physisorption.

The main reason for the success story of MOFs as adsorbents is that they fulfill an initial requirement for high gravimetric gas storage density – high specific surface area – as adsorption relies on surface upon which gas molecules can adsorb. Highly porous MOFs indeed are the record holder in terms of gravimetric storage capacities for gases and vapors [29, 30, 32, 60, 61].

It has been quickly recognized that also other factors, besides the surface area, are important for high uptake. First of all, dimensions of the pores in the framework have a strong influence on the gas storage at low and high pressures. Indeed, in pores possessing a diameter close to the size of few gas molecules, van der Waals potentials of the pore walls can overlap more effectively than in larger pores, thus enhancing the strength of interaction and magnitude of adsorption enthalpy. As a consequence MOFs with similar building units and network topology show a higher

storage capacity for frameworks with smaller pores at low pressures [62], especially for hydrogen [63, 64]. MOFs with smaller pores show also higher heat of adsorption for hydrogen [65]. If the pores are large, the increased hydrogen density at low loadings appears primarily at the “pockets” presented in the framework [66].

At higher pressure, the specific pore volume is dominating the gravimetric storage capacity of isoreticular MOFs, so the interpenetration and small pores become disadvantageous, and the mesoporous materials (in mesoporous MOFs the pores are typically 2–4 nm and thus still relatively small as compared to ordered mesoporous oxides) show higher uptake because of higher density of the gas compressed inside the pores.

Chen and co-worker, for example, have demonstrated for isoreticular NOTT-100 – NOTT-103 MOFs the gravimetric methane uptake systematically to increase with increasing porosity, while their methane storage pore occupancy decreases with increasing pore size [67]. Similar observations were reported also for other isoreticular series. Among record holders in terms of gravimetric uptake at room temperature and 65 bar are MOF-210 [31], Al-soc-MOF-1 [62], and DUT-49 [68] showing all an excess uptake of ca.  $0.41 \text{ g g}^{-1}$ . To date, the highest volumetric methane storage and working capacities (at 65 bar and room temperature) were determined for HKUST-1 (about 270 and 200  $\text{cm}^3(\text{STP}) \text{ cm}^{-3}$ , respectively) [23, 69]. The effective release from the tank filled with HKUST-1 powder operated at room temperature between 65 and 5 bar is ca. 130 v/v [24] (Fig. 6.5).

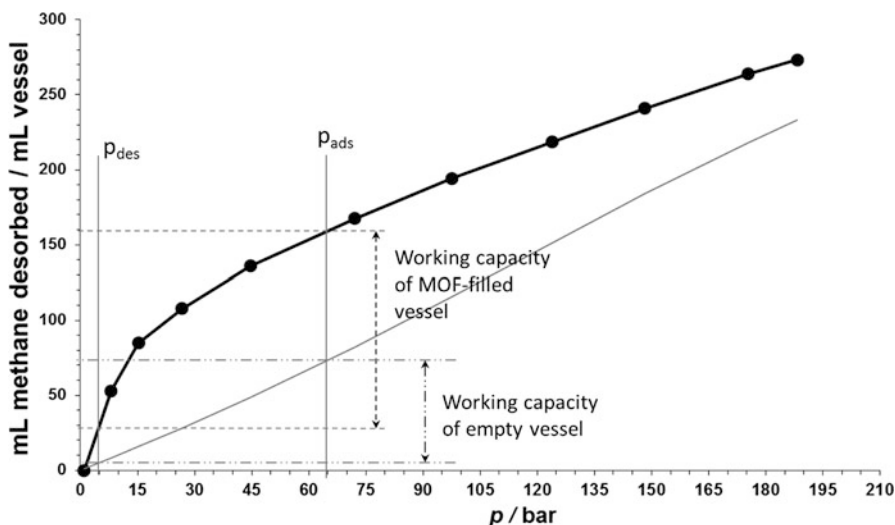


**Fig. 6.5** Desorption isotherm at 293 K obtained from a vessel filled with HKUST-1 powder (black circles) [24]. The gray line presents the amount of gas delivered from the empty vessel under same conditions. The working capacities between 5 and 65 bar are indicated. As zero point, the atmospheric pressure is taken

### 6.5.1 Pore Size

The easiest way to control the pore size is the use of isorecticular chemistry, namely, varying ligand lengths within the same topological type of network. As a simple example, the isorecticular series of IRMOFs (IRMOF states for isorecticular metal-organic framework) can be considered (Fig. 6.6) [59]. All materials of IRMOF series are constructed from octahedral inorganic SBU  $Zn_4O^{6+}$ , which are interconnected by linear dicarboxylate ligands into 3D frameworks with **pcu** (primitive cubic) underlying topology. Varying the distance between the carboxylates by use of terephthalic, 2,6-naphthalenedicarboxylic, 4,4'-biphenyldicarboxylic, and terphenyldicarboxylic acid, respectively, in the synthesis yields IRMOF-1, IRMOF-8, IRMOF-12, and IRMOF-16 frameworks with increasing pore sizes (Fig. 6.6). Increasing distance between carboxylates from 5.75 Å in IRMOF-1 to 14.22 Å in IRMOF-16 leads to the increase in the pore apertures from 12.2 Å and 15.0 Å in IRMOF-1 to 24.5 Å in IRMOF-16.

Another more versatile approach to control the pore size distribution in MOFs while maintaining the building blocks is based on the control of the underlying topology of the framework [12]. One of the most versatile examples of this approach is the combination of the  $Zr_6O_8$  SBU with bent 2,5-thiophenedicarboxylate [10, 70]. In this particular case, the modulation of the cluster connectivity combined with different potential orientations of the bent ligand result in the formation of a plenty of “polymorphs.” This can be controlled by the type and amount of modulator (monocarboxylic acid) added in the MOF synthesis. For instance, the use of 50

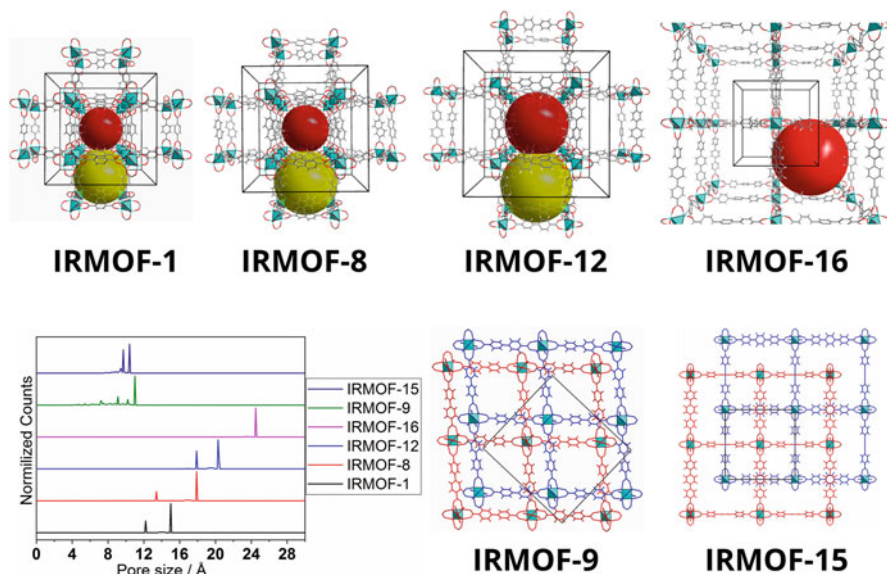


**Fig. 6.6** Crystal structure and pore size distribution for selected IRMOF materials

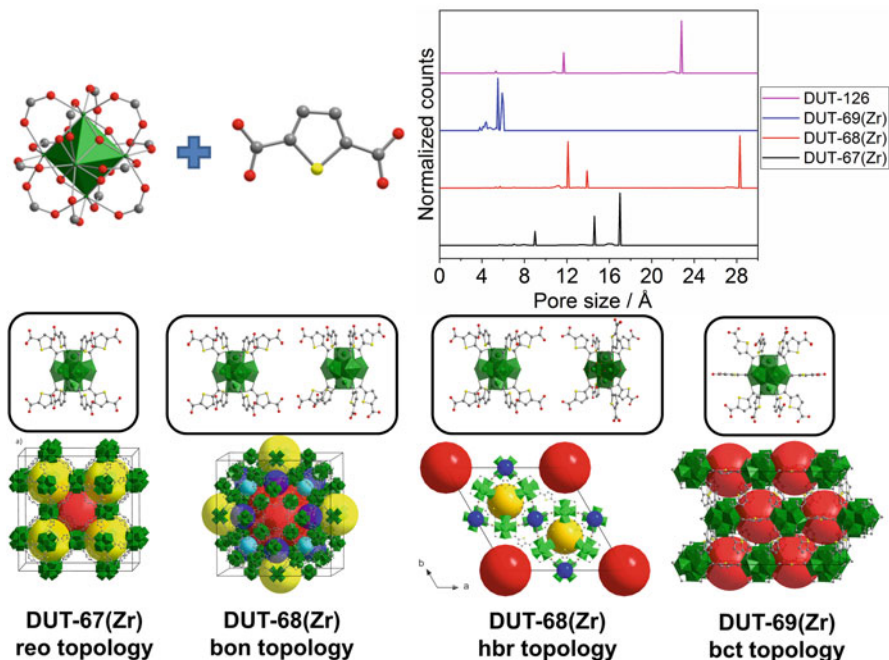


**Fig. 6.7** Building units, cluster connectivity, crystal structures, and pore size distribution of Zr-based polymorphic MOF materials containing 2,5-thiophenedicarboxylate as linker

equivalents of acetic acid in proportion to the ligand leads to formation of DUT-69, possessing 10-connected framework with **bct** underlying topology. If the amount is increased to 120 equivalents, DUT-67, a unimodal 8-connected framework with **reo** topology, is formed. Further increase of modulator amount to 180x leads to the formation of binodal 8,8-connected framework DUT-68. If trifluoroacetic acid is used as a modulator, DUT-126 is formed, having also a binodal 8,8-connected framework, but due to another orientation of the ligands around one of the SBUs, the hexagonal structure with **hbr** topology is formed (Fig. 6.7).

In this way, having the same building units and often same connectivity, one can construct different frameworks with various underlying network topologies and, consequently, completely different pore systems and pore size distribution. As expected, the smallest pores 3–6 Å are observed in the 10-connected framework. For DUT-67(Zr) three different micropores are observed in the size range of 9–17 Å. In the case of DUT-68(Zr) and DUT-126(Zr), the small mesopores with diameter of 28 Å and 22 Å, respectively, are present.

Using the same modulating strategy, it is also possible to disturb the connectivity of the cluster in an irregular way, creating the missing linker defects, not necessarily detectable by X-ray diffraction. Wu et al. demonstrated the controlled introduction of linker vacancy defects in UiO-66, and so the gas adsorption capacities in the high-pressure regime could be improved significantly (i.e., up to 30% for CH<sub>4</sub> at 60 bar

and 50% for CO<sub>2</sub> at 35 bar, both at 300 K) [71]. This enhancement in gas adsorption was attributed to the presence of numerous mesopores.

The mesoporosity and ultrahigh pore volume are advantageous for the gas storage at higher pressures. Yildirim et al. [23] claimed that a hypothetical MOF with optimal methane storage properties should have a pore volume of 3.2 cm<sup>3</sup> g<sup>-1</sup>, a density of 0.27 g cm<sup>-3</sup>, and a surface area of 7500 m<sup>2</sup> g<sup>-1</sup> to be able to adsorb 0.5 g methane per gram of MOF (195 cm<sup>3</sup>(STP) cm<sup>-3</sup>) at 65 bar. For example, DUT-32 has the porosity characteristics which are very close to those of the desired hypothetical MOF: pore volume of 3.16 cm<sup>3</sup> g<sup>-1</sup> and density of 0.27 g cm<sup>-3</sup>. DUT-32's maximum excess methane capacity at 298 K is reached with 0.24 g g<sup>-1</sup> at 105 bar (corresponding to 65 mg cm<sup>-3</sup>). Due to the large pore volume, DUT-32 achieves a total CH<sub>4</sub> storage capacity of 0.55 g g<sup>-1</sup> (149 g L<sup>-1</sup>, 210 cm<sup>3</sup> (STP) cm<sup>-3</sup>) at 130 bar [29].

But the mesoporosity often involves some complexity [72]. So, the collapse of the framework upon solvent removal became a major issue but also the interpenetration and formation of dense polymorphs [72]. There are several approaches proposed for stabilizing the framework against collapse and enhancement of network robustness. One of them uses the insertion of linear cross-linking neutral ligands between the inorganic clusters possessing open metal sites. An illustration of the strengthening of a framework was reported by Klein et al. A very fragile framework with **pto** topology (DUT-34) that could not be desolvated while retaining its porosity, even by supercritical CO<sub>2</sub> drying, was stabilized by incorporation of a neutral 4,4-bipyridine cross-linker (Fig. 6.8). After supercritical drying, a material (DUT-23) with permanent porosity and a remarkable BET surface area of 4850 m<sup>2</sup> g<sup>-1</sup> was obtained [73].

The compound based on Co has remarkably high maximum gravimetric excess methane (0.27 g g<sup>-1</sup> at 100 bar at 298 K) and hydrogen (74 mg g<sup>-1</sup> at 77 K) storage capacities. The general applicability of this strategy was demonstrated also for other

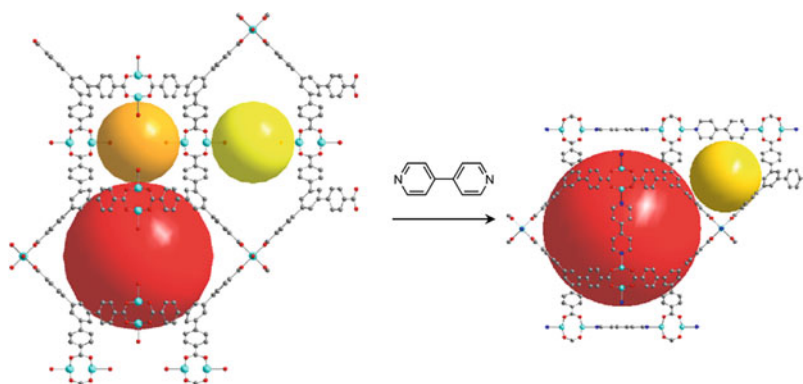


**Fig. 6.8** The fragile framework of DUT-34 (left) stabilized by 4,4-bipyridine to give robust DUT-23 (right)

MOFs [74–76]. It has been shown by Zhou and co-workers that the same strategy can be also applied for dicarboxylate cross-linkers in a flexible Zr-MOF (PCN-700), where the linkers of different lengths could be installed between  $Zr_6$  clusters [77].

The MOFs with the largest pore aperture, accessible also in desolvated form, could be synthesized by Yaghi and co-workers, by the systematic expansion of a well-known MOF structure, MOF-74 (also known as CPO-27), from its original link of 1 phenylene ring to 11 affording an isorecticular series with pore apertures and pore volume ranging from 14 to 98 angstroms and 0.6 to 3.41  $\text{cm}^3 \text{g}^{-1}$ , respectively (Fig. 6.9) [78].

One novel elegant approach to vary the pore size within the same topology is solvent-assisted ligand exchange (SALE). Hupp, Farha, and co-workers demonstrated on the example of the pillared layer MOF the possibility to replace the pillar post-synthetically by a longer one (Fig. 6.10). Such stepwise substitution of pillars allows to obtain MOFs with variable pore size that cannot be synthesized directly [79]. Rosi and co-workers demonstrated an equal effectiveness of the technique also for carboxylate ligands [80]. The technique gives opportunities to exchange ligands with similar but also different lengths as well as introduce functionalized ligands post-synthetically.

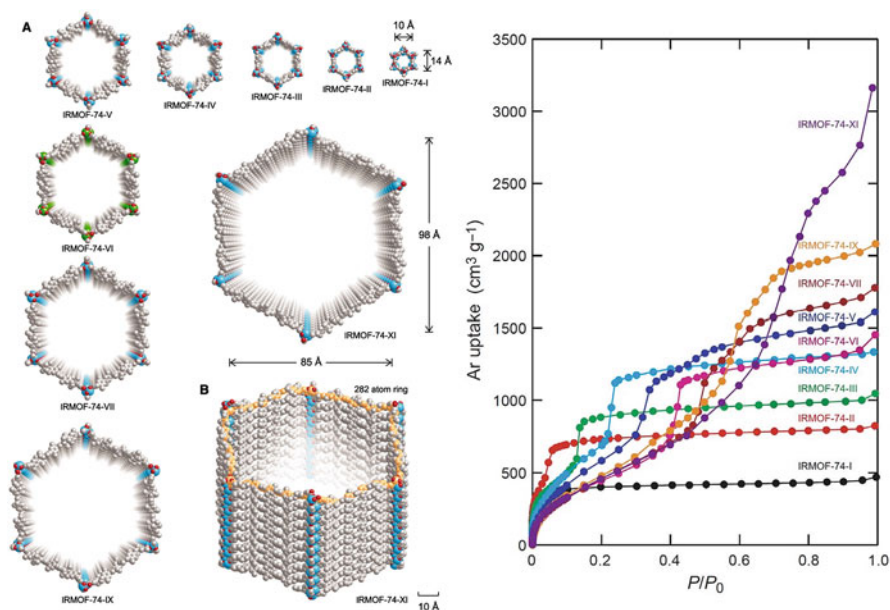


**Fig. 6.9** Left: Crystal structures of IRMOF-74 series. (a) Single one-dimensional channel shown for each member of IRMOF series, starting from the smallest (top right). C atoms are shown in gray, O atoms in red, Mg atoms in blue, and Zn atoms in green. (b) Perspective side view on the hexagonal channel of the largest member of the series. Right: Ar adsorption isotherm of all IRMOF-74 series at 87 K. Reprinted with permission from [78]. Copyright (2012) American Association for the Advancement of Science

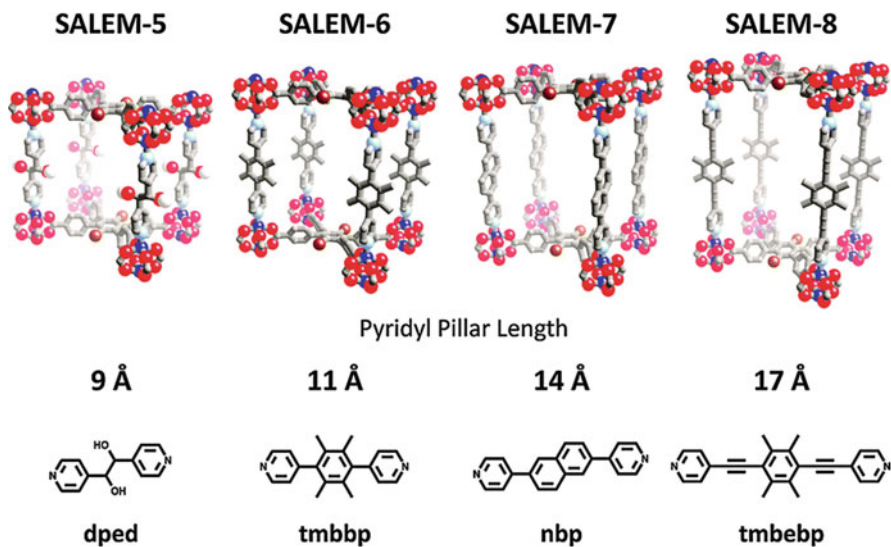


**Fig. 6.10** Increasing pore sizes in an isoreticular series of pillared, paddle wheel-based MOFs synthesized via SALE. Reprinted from [81]. Published by the Royal Society of Chemistry

One proposed way to decrease the pore size of MOFs is the targeted synthesis of interpenetrated frameworks. Interpenetration is defined as occurring when the voids associated with one framework are occupied by one or more independent frameworks which are not chemically bound to each other but can be disentangled only by breaking internal connections (bonds) [82].

For example, hydrogen uptake has been carefully studied for PCN-6 and their interpenetration isomer PCN-6' [83]. PCN-6 exhibits 133% enhancement in volumetric and 29% in gravimetric hydrogen uptake compared to PCN-6' due to the structural interpenetration.

Successful approaches for control of interpenetration in MOFs are mostly reaction parameters (such as synthesis temperature and concentration of reactants) or more rational approaches based on the linker design [84, 85]. The most efficient way to increase the degree of interpenetration is to extend the length of the linker in an appropriate topology, since longer linkers lead to larger void space and to increase in total entropy of the system, interpenetration occurs.

For example, it has been found that longer organic linkers readily lead to twofold interpenetrating structures during the synthesis of the IRMOF series (IRMOF, isoreticular MOF). However, more dilute reaction solutions are prone to afford non-interpenetrating MOFs with larger pores. Along with this research strategy, pairs of interpenetration isomers for IRMOF-10, IRMOF-12, IRMOF-14, and IRMOF-16 were obtained (Fig. 6.6), each pair composed of one non-interpenetrated and the other with twofold interpenetrated structure [84]. Telfer and co-workers recently reported even a family of MOFs in which one sub-lattice

is fully occupied and the occupancy level of the other can be controlled during synthesis to produce frameworks with variable levels of partial interpenetration [86]. Interconversion of non-interpenetrated 3D metal-organic MOFs to doubly interpenetrated analogues by thermal treatment even in the absence of solvent was also reported [87].

To avoid the interpenetration, consequently, the short linkers are advantageous, as well as topologies making the interpenetration difficult. It is probably obvious that some nets will be easier to interpenetrate than others, even if it is not proven that self-dual nets actually have a higher ratio of interpenetration than other nets [88], so this is a major concern when designing (non)interpenetrated MOFs [89].

The next level of IRMOF design was achieved applying the supermolecular building blocks (SBB) or metal-organic polyhedra (MOPs). In this case, an MOP is used instead of classical inorganic SBU for the construction of the 3D frameworks. The concept of MOPs or “nanoballs” was introduced in the early 2000s simultaneously by groups of Yaghi [90] and Zaworotko [91], who reported molecular compounds with overall composition  $[(L)(S)Cu_2(bdc)_2]_{12}$  (L, pyridine; S, methanol; bdc, 1,3-benzenedicarboxylate), which depending on the synthesis conditions crystallize in different polymorphic modifications. The crystal structure of MOP-1 is composed of 12 paddle wheel units which are interconnected by 24  $bdc^{2-}$  linkers and can be described in the simplified way as truncated cuboctahedron (Fig. 6.11).

MOP-1 has eight triangular and six square windows that are 8 and 12 Å across forming a spherical cavity of 15 Å in diameter and 1766 Å<sup>3</sup> in volume. Later the isostructural MOP was constructed with Mo<sub>2</sub> units [92]. A first attempt to design the porous framework out of the “nanoballs” was reported by Zaworotko and co-workers by introducing the flexible spacer between two isophthalate moieties. The resulting framework crystallizes in tetragonal symmetry and exhibits twofold interpenetration [93]. As a further development, Ni- and Co-based SBUs were

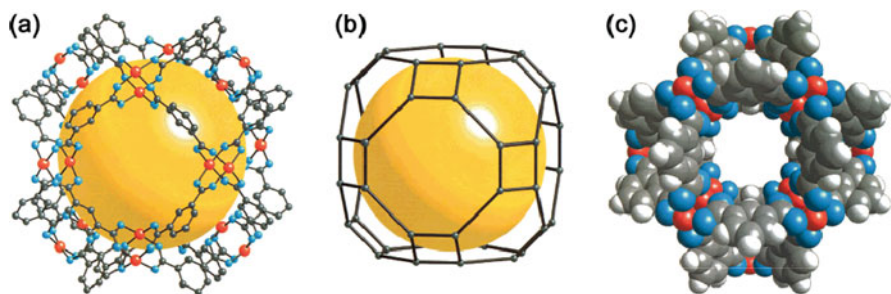


**Fig. 6.11** Crystal structure of MOP-1: (a) 12 paddle wheel units (Cu, red; O, blue; C, gray) linked by (*m*-BDC) to form a (b) large truncated cuboctahedron of 15 Å diameter void (yellow sphere); the gray spheres represent the polyhedron constructed by linking together only the carboxylate C atoms in (a) to form linked square SBUs, an arrangement that provides for a (c) large porous polyhedron with triangular and square windows. Reprinted with permission from [90]. Copyright (2001) American Chemical Society

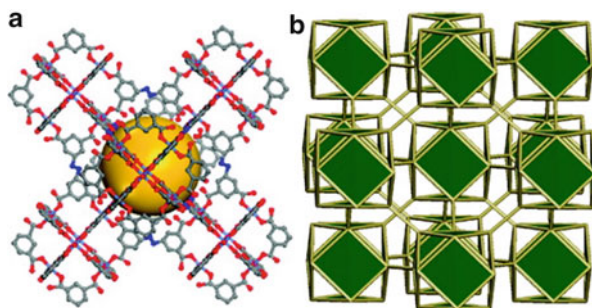


**Fig. 6.12** Crystal structure of  $[\text{Ni}_2(\text{L}_1)(\text{H}_2\text{O})_3]_n$ : (a) atomic structure, (b) topological representation. Reprinted with permission from [94]. Copyright (2008) American Chemical Society

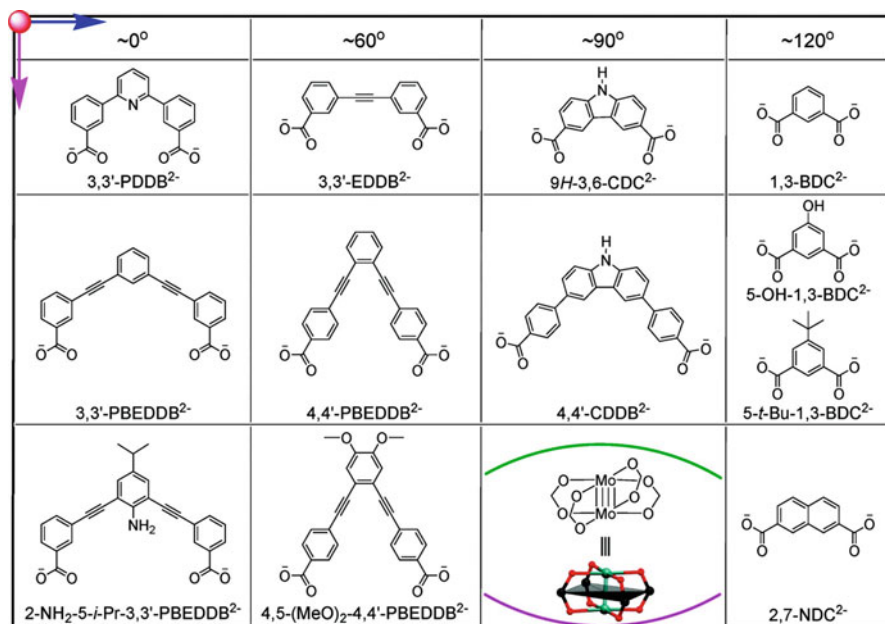


**Fig. 6.13** Mo<sub>2</sub>(O<sub>2</sub>C-)<sub>4</sub> cluster and bridging dicarboxylate ligands with different bridging angles, sizes, and non-bridging functional groups. Reprinted with permission from [95]. Copyright (2010) American Chemical Society

interconnected by 3,5-dicarboxyl-(3',5'-dicarboxylazophenyl)benzene forming another type of MBB, cubohemioctahedra, which are interconnected into the 12-connected **fcu** net (Fig. 6.12).

Later on, MOPs based on the Mo-Mo cluster and ligands with various geometry having intercarboxylate angles ranging from 0 to 120° were described by Zhou and co-workers [95] (Fig. 6.13).

The same group even showed the possibility of the ligand substitution within the MOPs [96].

Using MOPs as building blocks to design MOFs provides a high degree of control over the resulting structure and topology. MOPs provide plenty of open metal sites [97], determining the size and geometry of the micropore and providing sites for further connection. Furthermore the choice of shape, size, and symmetry of the molecular entity connecting the SBBs can control the number of pores as well as their shape and size. In recent years it was successfully applied to the synthesis of several (i.e., mesoporous) MOFs [98].

Lah and co-workers obtained an extended MOF with **rht** topology from MOP-1 by utilizing covalent bonding [99]. This MOF contains octahedral and tetrahedral cavities of 18.8 Å and 13.7 Å in diameter, respectively. Eddaoudi and Zaworotko also reported the MOF with a **rht**-like network based on MOP-1 unit ( $\text{Cu}_6\text{O}(\text{TZI})_3(\text{H}_2\text{O})_9(\text{NO}_3)$ ), TZI, 5-tetrazolylisophthalate), consisting of three different types of open cages with the largest 20.2 Å in diameter [100].

Kaskel and co-workers [30, 68] and the group of H-C Zhou [101] succeeded in synthesizing highly porous MOFs from cuboctahedral MOPs based on copper paddle wheels and carbazole-3,6-dicarboxylate (9H-3,6-CDC). The MOP cuboctahedra can be interconnected in two different ways: (i) interconnection of the paddle wheels by a neutral diamine ligand results in a framework with primitive cubic **pcu** topology [102], and (ii) interconnection of two carbazole moieties yields the close cubic packing of the MOPs or **fcu** underlying topology (Fig. 6.14). The framework obtained by route (i) could not be activated for porosity tests, while in the second case, a highly porous, gas-accessible framework with the record gravimetric methane uptake could be isolated.

Recently Eddaoudi and co-workers reviewed the SBB approach and defined the main edge-transitive polyhedrons and corresponding MOPs for the design of MOF structures with target hierarchical pore system (Fig. 6.15) [103].

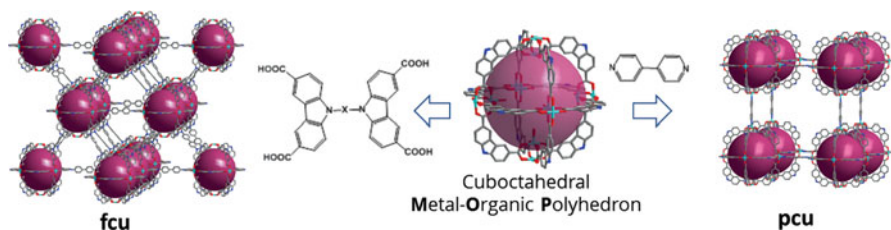


**Fig. 6.14** Two different way of interconnection of 3,6-carbazoledicarboxylate-based cuboctahedral MOPs

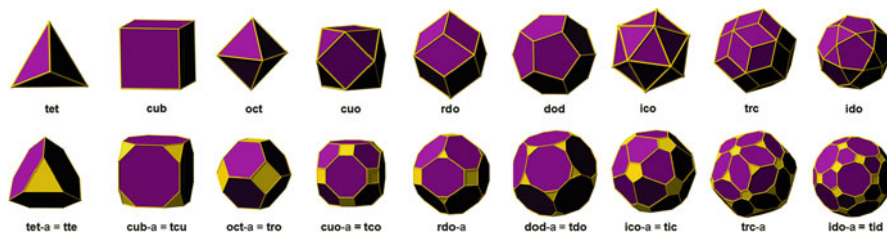


**Fig. 6.15** Nine edge-transitive polyhedra and their augmented equivalents. Reprinted from [103]. Published by the Royal Society of Chemistry

## 6.5.2 Chemical Composition of the Surface

Besides pore size, the chemical composition of the surface is an important characteristic influencing the interaction strength between the adsorptive and surface, because of electrostatic and dispersive interactions, which depend on the polarizability, dipole, and quadrupole moment of the adsorbed molecules.

### 6.5.2.1 Open Metal Sites

The finding that metal centers influence the gas uptake led to the intensive research on MOFs with coordinatively unsaturated metals or so-called open metal sites (OMSs) [104]. These can be obtained by removal of terminal ligands from the metal. Open metal sites are supposed to strongly polarize the gas molecules and, therefore, be responsible for high storage capacities already at low pressures [105].

In some MOFs the potential OMSs are available directly after the synthesis, if the metals in the cluster are coordinated by additional ligands (usually solvent molecules) in addition to the linkers. As prime examples HKUST-1 [22], MIL-101 [106], or CPO-27 [107] (MOF-74) can be named. The interaction and adsorption sites of adsorbed gas in these MOFs were, amongst others, investigated by *in situ* neutron diffraction. For HKUST-1 up to nine D<sub>2</sub> adsorption sites were localized within the nanopore structure, whereat the primary site is located at the coordinatively unsaturated Cu atoms [108, 109]. It provides direct structural evidence of the potential importance of such metal sites to hydrogen storage. Similar observations were made for MFM-101 (MFM, Manchester Framework Material, replacing the NOTT designation), where the first adsorption site was located at the axial position of the Cu paddle wheel with a Cu-D<sub>2</sub> (centroid) distance of 2.50(3) Å, slightly longer than that observed in HKUST-1 (2.40 Å) [110].

Similarly, the CD<sub>4</sub> molecules in HKUST-1 were found to be located much closer to the copper ion than half the mixed Lennard-Jones parameter for methane and copper is [111]. It can be caused by the high Lewis acidity of the open metal center, which might result in a polarization of the CD<sub>4</sub> molecules. Neutron powder

diffraction studies reveal the significant contribution of open Cu(II) sites in HKUST-1 also for acetylene binding [112]. Similar values have been observed for methane adsorption on other MOFs with open metal sites [113].

Studies exploiting vibrational spectroscopies, EXAFS, *in silico* calculations, neutron experiments, NMR, and gas adsorption have examined in depth the interactions of CO<sub>2</sub>, CO, CH<sub>4</sub>, and H<sub>2</sub>O with the MOF-74/CPO-27 frameworks pointing on the importance of open metal sites ([114] and references therein).

As mentioned before, the paddle wheels and even more MOPs are ideal building blocks for the design of highly porous MOFs containing a high number of open metal sites. For example, DUT-49, an interconnected **fcu** network of MOPs, contains 2.5 mmol Cu per gram of framework and is one of the world record holders in terms of gravimetric methane excess adsorption capacity [68].

In order to assemble highly porous structures while increasing the density of open metal sites, the paddle wheels and MOPs were used as connectors to create a **ftw** topology. As a consequence, DUT-75 and an isorecticular system, DUT-76, have 3.2 and 2.8 mmol Cu per gram of framework, respectively [30].

But the OMSs can be also introduced in addition to those present in the cluster, using metalloligands, bearing, for example, 2,2'-bipyridine, salen, or porphyrin moiety [115]. Several reviews address porphyrinic coordination polymers ([116] and references therein). Many authors demonstrated the possibility to vary the metal inside metalloligand, in such a way modifying the open metal sites nature without altering the overall topology [117, 118]. A comprehensive study on the influence of the metal coordinated by the salen ligand on the gas adsorption capacity (hydrogen at 77 K, methane at 298 K, and carbon dioxide at 298 K) was reported by us for DUT-117(M) MOF. DUT-117(M) series with the overall composition Cu<sub>4</sub>(mbpatb)<sub>2</sub>(M(salen))<sub>0.5</sub>(dabco)<sub>2.5</sub> (mbpatb, 4,4',4'',4'''-1,3-phenylenebis-(azanetriyl)tetrabenzoate, 1,4-diazabicyclo[2.2.2]octane) contains Cu, Ni, or Pd as metal of salen. In this series DUT-117(Ni) stands out as the best material for adsorptive methane storage with a high working capacity of 171 cm<sup>3</sup> cm<sup>-3</sup> between 5 and 65 bar [119].

A relatively new strategy to enhance the amount of open metal centers in MOFs is called “defect engineering” [120]. Jiang and co-workers reported on USTC-253-TFA (TFA, trifluoroacetic acid), exhibiting a much higher CO<sub>2</sub> uptake capacity (167%) than the parent USTC-253 MOF. The introduction of TFA during the synthesis of USTC-253 creates defects in USTC-253-TFA with exposed metal centers [121].

### 6.5.2.2 Organic Functional Groups

Due to the organic nature of the linker, the inner surface of the MOF can be easily functionalized on demand using the powerful tools of organic synthesis. There are several reports in the literature, pointing on the importance of the surface functionality for adsorbate-adsorptive interaction and consequently for the adsorption capacity [114].

For example, it is widely accepted that MOFs containing amine functional groups can have specific binding to CO<sub>2</sub> molecules, thus improving the selectivity and uptake capacity because of their potential to form carbamates via H<sub>2</sub>N(δ<sup>-</sup>)...C(δ<sup>+</sup>)O<sub>2</sub> interactions [122]. The attachment of alkyldiamines to coordinatively unsaturated metal sites has been demonstrated as an effective strategy for increasing low-pressure CO<sub>2</sub> adsorption selectivity and capacity [123]. Functionalization of Mg<sub>2</sub>(dobpdc) (dobpdc, 4,4'-dioxidobiphenyl-3,3'-dicarboxylate), adopting an expanded MOF-74 structure type (IRMOF-74\_III), with N,N'-dimethylethylenediamine (mmen), generated an adsorbent with exceptional CO<sub>2</sub> capacity under flue gas conditions and step-shaped adsorption isotherms [124], which could be explained by the cooperative nature of the CO<sub>2</sub> adsorption mechanism [125].

The use of two primary alkylamine functionalities covalently tethered to the linkers of IRMOF-74-III resulted in a material that can adsorb CO<sub>2</sub> at low pressures through a chemisorption mechanism [126]. In contrast to other primary amine-functionalized solid adsorbents binding CO<sub>2</sub> primarily as ammonium carbamates, the major chemisorption product for this material is carbamic acid. The equilibrium of reaction products also shifts to ammonium carbamate when water vapor is present.

Schröder and co-worker used a combination of powder diffraction and inelastic neutron scattering to show that the primary binding site for CO<sub>2</sub> in NOTT-300 is a pocket containing hydrogen bonds from a OH group with an additional weak cooperative hydrogen bond from an aromatic CH group [127].

Density functional theory calculations show that the CO<sub>2</sub>-sulfonate interaction can enhance the adsorption capacity. It was also observed experimentally. Thus, Cu(bpy)<sub>2</sub>(EDS) (TMOF-1; bpy, 4,4'-bipyridine; EDS, 1,2-ethanedisulfonate) adsorbs 40% more CO<sub>2</sub> than MOF-508b(Cu), which contains the same N-donor ligand and a prototypical primitive cubic topology, as well [128]. Also sulfone-functionalized metal-organic frameworks, such as USTC-253, exhibit a much higher CO<sub>2</sub> uptake capacity (168–182%) than the corresponding unfunctionalized MOFs [121].

### 6.5.3 *Post-synthetic Modification as Strategy for Surface Design*

A number of MOF structures cannot be synthesized directly mainly because of the low tolerance of the functional groups to the relatively harsh solvothermal reaction conditions or, in the case of inorganic part, difficulties in the formation of the targeted SBU in the solution. In the first review article, devoted to post-synthetic modification (PSM) in MOFs, Cohen distinguished for post-synthetic modifications three classes: (i) covalent PSM, (ii) dative PSM, and (iii) post-synthetic deprotection (Fig. 6.16).

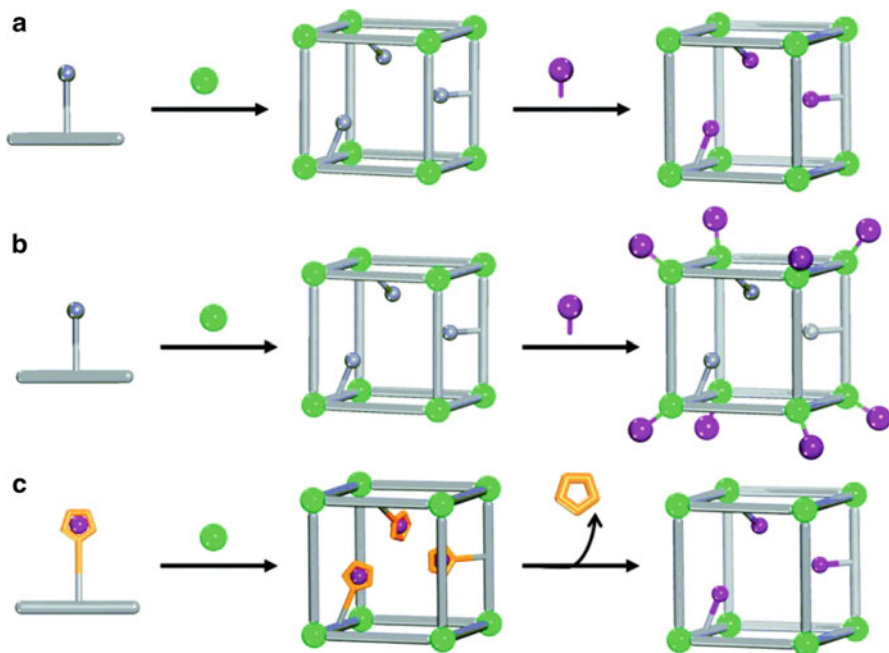


**Fig. 6.16** Generic schemes for (a) covalent PSM, (b) dative PSM, and (c) post-synthetic deprotection. Reprinted with permission from [129]. Copyright (2012) American Chemical Society

Covalent PSM is a frequent type of modification and is based on the condensation or “click” reactions of the organic ligands, incorporated in MOFs, namely, formation of the new covalent bonds inside the MOF. Usually amine- or aldehyde-tagged MOFs are used for this type of reactions. The most archetypical example of the covalent PSM was reported by Cohen and co-workers. MOFs containing aminobenzenedicarboxylates were selected because of the availability of the ligand. In the first step, corresponding amino-substituted DMOF-1, IRMOF-3, and UMCM-1 were synthesized (Fig. 6.17). Further all materials were subjected to PSM using anhydrides with alkyl chains involving 1–19 carbon atoms. Expectedly, increasing the reaction temperature from room temperature to 328 K leads to higher conversion for most materials [130]. Another popular covalent PSM approach, so-called click chemistry, is usually based on the cycloaddition reactions between azide and alkyne groups. Using IRMOF-16 with azide functionalized ligand, click reaction with a number of alkyne substrates was achieved [131].

Dative PSM is based on the cleavage and formation of dative bonds from ligand to the metal center. HKUST-1 could be considered as a very first example of such PSM, offering the possibility to remove the terminal water molecule from the paddle wheel and coordinate different organic species. The main condition for such type of PSM is the presence of open metal sites in MOFs. This strategy allows to coordinate the ligands post-synthetically, which are not stable under solvothermal conditions

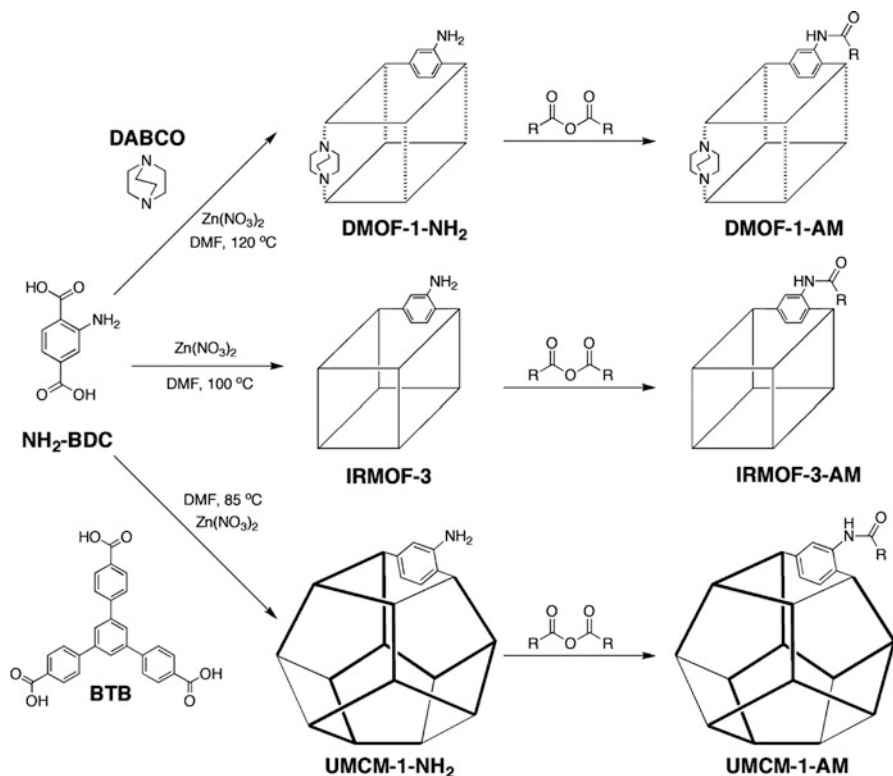


**Fig. 6.17** Synthesis and covalent PSM of DMOF-1, IRMOF-1, and UMCM-1. Reprinted with permission from [130]. Copyright (2009) American Chemical Society

[129]. Thus, the possibility of amine coordination to the  $\text{Cr}_3\text{O}^{7+}$  metal cluster of MIL-101(Cr) was shown by Chang and co-workers [132]. Recently, Zr-based MOFs with reduced connectivity were reported by several groups. Reducing of the maximal connectivity from 12 (as it is the case in UiO-66-related structures) to 10, 8, or even 6 creates additional coordination places on cluster, which can be used for PSM. We used this approach in DUT-67(Zr), to control the hydrophobicity of the framework by introducing long-chain monocarboxylates as well as fluorinated carboxylic acids [133]. Water vapor adsorption isotherms point on the changes in the water adsorption mechanism and change in the pore-filling sequence with increasing hydrophobicity of the pore surface. Even chiral substituents could be introduced using dative PSM, and catalytic activity of the resulting frameworks could be proved in Michael addition reaction [134].

Hybridization of approaches (i) and (ii) allows introducing additional coordination sites, which further are able to coordinate additional metal ions and in such a way create additional OMSs. Yaghi and co-workers modified amino-UMCM-1 with 2-pyridinecarboxylaldehyde with further chelate coordination of palladium (Fig. 6.18) [135].

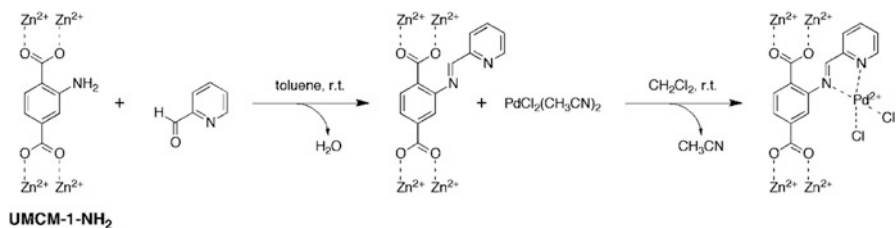


**Fig. 6.18** Scheme of combined covalent and dative PSM of NH<sub>2</sub>-UMCM-1. Reprinted with permission from [129]. Copyright (2012) American Chemical Society

The last approach of post-synthetic deprotection (iii), introduced by Cohen, allows to synthesize MOFs with sensitive protective groups. These groups can be later removed thermally in the post-synthetic step, which in the case of MOFs often can be combined with desolvation. This approach was for the first time introduced by H. Kitagawa and called “protection-complexation-deprotection.” In this particular case, hydroxyl groups of dihydroxyterephthalic acid were protected by acetylation. During the synthesis of MOF, protection groups were removed [136]. Another more elegant and controlled approach was introduced by Telfer and co-workers on example of non-interpenetrated version of IRMOF-10. A bulky *tert*-butylcarbamate (Boc) group was used to protect the amino group of 2-aminobiphenyl-4,40-dicarboxylate. After successful synthesis of MOF, Boc groups were removed by thermal treatment in DMF at 423 K [137]. This approach was also used to introduce the catalytic proline sites into the stable Zr-based UiO-67 and UiO-68 frameworks [138]. More details on PSM in MOFs are reviewed by Cohen ([129] and references therein). All mentioned approaches are based on the modification of the side chains or coordination to the cluster, while the crystal structure of MOF itself stays intact during the whole modification process. In many cases exchange of cations and even ligands is also possible. Brozek and Dincă reviewed the existing literature on metal exchange in SBU and conclude that even in highly connected metal clusters with strong M-O bonds, such as Al-O-Al chains of MIL-53(Al) or Zr-based UiO-67, partial metal exchange is possible to the ions with same charge and similar size [139]. Further post-synthetic metalation techniques are elaborately described by Evans et al. [140]. For low-connected clusters, such as paddle wheels, nearly complete metal exchange is possible. Indeed, the metal exchange in the cluster is strongly dependent on the MOF and is often not or not completely reversible.

## 6.6 Flexibility and Adsorption

In the very early age of the MOF development, Susumu Kitagawa and co-workers recognized a subgroup of frameworks, which reversibly change their crystal

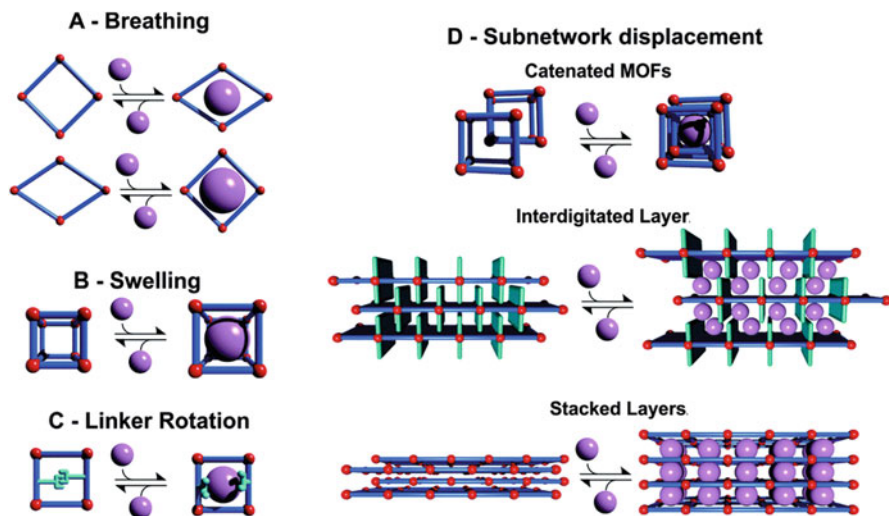


**Fig. 6.19** Various structural features can support flexible behavior in MOFs. Reprinted from [145]. Published by the Royal Society of Chemistry

structure upon adsorption and desorption of guest molecules, nowadays declared as a unique feature of MOFs. Further, he proposed a classification in which all frameworks are divided into three generations [141]:

1. Coordination polymers, which irreversibly collapse upon solvent removal.
2. MOFs, which retain their structure, upon solvent removal.
3. Frameworks, which reversibly change their crystal structure, while guest molecules are removed or adsorbed. The mechanism of the flexibility, however, can be of different origin (Fig. 6.19).

One of the first materials of this class is a 2D MOF with the composition  $\text{Cu}(4,4'\text{-bipyridine})_2(\text{BF}_4)_2$ , nowadays recognized as ELM-11 (ELM stands for elastic layer material) [142]. The crystal structure is composed of 2D  $\text{Cu}(4,4'\text{-bipy})_2$ -layers which are packed in A-B-A-B manner. The 2D coordination polymer is dense with no accessible porosity, but introducing certain guest molecules ( $\text{CO}_2$ , *n*-butane, alcohols) at a strictly defined threshold concentration initiates the phase transition of the material: the distance between layers is expanded with creation of accessible porosity. This type of transformation was further called “gate opening,” and flexible MOFs, showing this effect, are now denoted as “gate pressure” MOFs. Shortly hereafter Kitagawa and co-workers discovered further flexible materials with similar flexibility mechanism [143, 144].

Serre et al. reacted Cr(III) salt with terephthalic acid in a hydrothermal synthesis and obtained a microporous material, further denoted as MIL-53(Cr), with a crystal structure, based on infinite Cr-OH-Cr chains, interconnected by linear 1,4-benzenedicarboxylates to form infinite rectangular channels, very similar to

a wine-rack motive. A first sign of flexibility of the structure was observed in the thermo-PXRD experiment, showing reversible structural transition from “high temperature” (more porous) to “low temperature” (less porous) form [146]. Further, a similar effect was observed in the CO<sub>2</sub> adsorption experiments and was further denoted as “breathing.” The complex mechanism of the phase transition in this case was studied by synchrotron *in situ* PXRD/adsorption. MIL-53 shows two transitions during the adsorption: (1) transition from “large pore” (lp) form to the “narrow pore” (np) form at low pressures and (2) reopening of the structure (np to lp transformation) by reaching the threshold pressure. The flexibility mechanism in this case is based on the changes of dihedral angles between carboxylate group and phenyl ring or deformation of so-called carboxylate hinges. Later on, isostructural materials, showing similar properties, were synthesized with nearly all three-valent metal ions [145].

Another type of flexing, so-called swelling or uniform expansion of the structure, was observed in MIL-88 materials, constructed from Fe<sub>3</sub>OFe<sup>6+</sup> inorganic bricks and linear dicarboxylates [147]. Although MIL-88d is still a record holder in the sense of unit cell expansion showing 333% of unit cell change during the transition, all these materials show flexibility exclusively in the liquid phase. DUT-8(Ni), a representative of pillared layer MOFs, switches between the dense, close pore phase and porous, open pore phase upon adsorption of gases, accompanied by the unit cell volume change of 240% [148, 149].

Much smaller change in the unit cell volume and adsorption capacity is observed for the cases of network displacements within the interpenetrated pillared layer structures [150] and linker rotation in ZIF-8 [151].

One of the unique adsorption phenomena, closely connected with flexibility, is “negative gas adsorption” (NGA) [152]. The fundamental thermodynamics and underlying mechanism of this counterintuitive gas pushout during external pressure increase are summarized in the several manuscripts [145, 153, 154].

Although the phenomena of flexibility or switchability are not entirely understood yet from both experimental and theoretical points of view, several prospective applications were proposed. Matsuda et al. demonstrated the selective adsorption of CO against nitrogen in a flexible framework [155]. Sensor applications are also considered as promising applications for switchable solids [156].

For the application of MOFs as adsorbents for adsorptive gas storage, the working (usable) capacity is crucial, which represents the difference in adsorption capacity at maximum storage pressure ( $P_{\text{ads}}$ ) and the residual amount of gas at the lowest pressure allowed into the storage tank ( $P_{\text{des}}$ ). The microporous MOFs show excellent overall uptakes of gas, but quite low pressure (usually below 5 or even 1 bar) should be applied to remove the gas from the MOF completely. The gate pressure MOFs with the stepped isotherms and “gate closing pressure” in the right pressure region (above 1 bar) should help to overcome this problem [145] (Fig. 6.20a, b). Long and co-workers highlighted an advantage of “gate pressure” MOF for high-pressure gas storage applications using M(bdp)

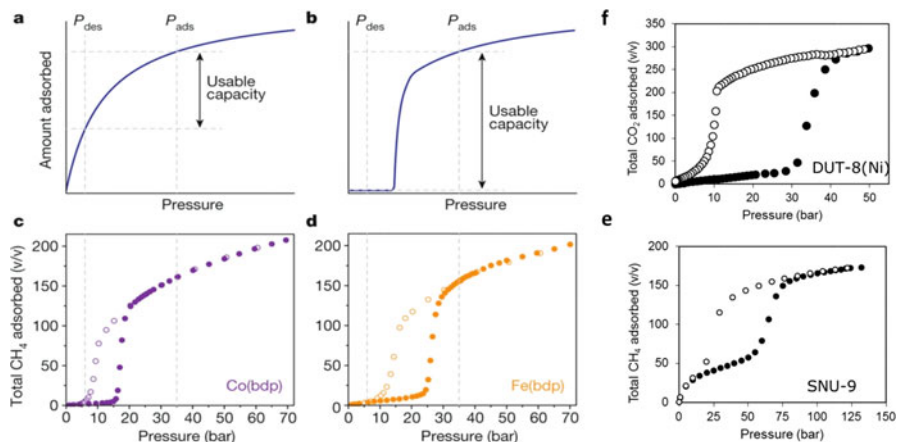


**Fig. 6.20** High-pressure  $\text{CH}_4$  adsorption isotherms: The usable capacity is compared for an idealized adsorbent exhibiting a classical Langmuir-type adsorption isotherm (a) and an “S-shaped” or “stepped” adsorption isotherm (b), with the minimum desorption pressure  $P_{\text{des}}$  and the maximum adsorption pressure  $P_{\text{ads}}$  indicated by the vertical dashed gray lines. Total  $\text{CH}_4$  adsorption isotherms for Co(bdp) (c) and Fe(bdp) (d) at 298 K. Here  $P_{\text{des}} = 5.8$  bar and  $P_{\text{ads}} = 35$  bar are indicated by dashed gray lines. (e) Total  $\text{CH}_4$  adsorption isotherms for SNU-9 at 298 K. (f) Total  $\text{CO}_2$  adsorption isotherms for DUT-8(Ni) at 298 K. Filled circles represent adsorption; open circles represent desorption. Figures (a–d) reprinted with permission from [157]. Copyright (2015) Springer Nature

(M, Co, Fe; bdp, 1,4-benzenedipyrazolate) [157] (Fig. 6.20). SNU-9 [158, 159] shows flexible behavior in the room temperature  $\text{CH}_4$  adsorption isotherm as well (Fig. 6.20e).

Similar to M(bdp), high gate closing pressure in the  $\text{CO}_2$  adsorption isotherm of DUT-8(Ni) at 298 K makes it attractive for  $\text{CO}_2$  storage (Fig. 6.20f) [148].

## References

- Batten SR et al (2013) Terminology of metal-organic frameworks and coordination polymers (IUPAC recommendations 2013). *Pure Appl Chem* 85:1715–1724. <https://doi.org/10.1351/pac-rec-12-11-20>
- Hoskins BF, Robson R (1990) Design and construction of a new class of scaffolding-like materials comprising infinite polymeric frameworks of 3D-linked molecular rods. A reappraisal of the zinc cyanide and cadmium cyanide structures and the synthesis and structure of the diamond-related frameworks  $[\text{N}(\text{CH}_3)_4][\text{CuI}Zn\text{II}(\text{CN})_4]$  and  $\text{CuI}[4,4',4'',4''']\text{-tetracyanotetraphenylmethane}]\text{BF}_4 \cdot x\text{C}_6\text{H}_5\text{NO}_2$ . *J Am Chem Soc* 112:1546. <https://doi.org/10.1021/ja00160a038>
- Hoskins BF, Robson R (1989) Infinite polymeric frameworks consisting of three dimensionally linked rod-like segments. *J Am Chem Soc* 111:5962. <https://doi.org/10.1021/ja00197a079>

- Eddaoudi M, Moler DB, Li H, Chen B, Reineke TM, O’Keeffe M, Yaghi OM (2001) Modular chemistry: secondary building units as a basis for the design of highly porous and robust metal–organic carboxylate frameworks. *Acc Chem Res* 34:319–330. <https://doi.org/10.1021/ar000034b>
- Yaghi OM, O’Keeffe M, Ockwig NW, Chae HK, Eddaoudi M, Kim J (2003) Reticular synthesis and the design of new materials. *Nature* 423:705–714. <https://doi.org/10.1038/nature01650>
- O’Keeffe M, Yaghi OM (2012) Deconstructing the crystal structures of metal–organic frameworks and related materials into their underlying nets. *Chem Rev* 112:675–702. <https://doi.org/10.1021/cr200205j>
- Li M, Li D, O’Keeffe M, Yaghi OM (2014) Topological analysis of metal–organic frameworks with Polytopic linkers and/or multiple building units and the minimal transitivity principle. *Chem Rev* 114:1343–1370. <https://doi.org/10.1021/cr400392k>
- Inge AK et al (2016) Unprecedented topological complexity in a metal–organic framework constructed from simple building units. *J Am Chem Soc* 138:1970–1976. <https://doi.org/10.1021/jacs.5b12484>
- Howarth AJ, Li P, Farha OK, O’Keeffe M (2018) Bottom-up design and generation of complex structures: a new twist in reticular chemistry. *Cryst Growth Des* 18:449–455. <https://doi.org/10.1021/acs.cgd.7b01434>
- Bon V, Senkowska I, Baburin IA, Kaskel S (2013) Zr- and Hf-based metal–organic frameworks: tracking down the polymorphism. *Cryst Growth Des* 13:1231–1237. <https://doi.org/10.1021/cg301691d>
- Ockwig NW, Delgado-Friedrichs O, O’Keeffe M, Yaghi OM (2005) Reticular chemistry: occurrence and taxonomy of nets and grammar for the Design of Frameworks. *Acc Chem Res* 38:176–182. <https://doi.org/10.1021/ar0200221>
- Furukawa H, Kim J, Ockwig NW, O’Keeffe M, Yaghi OM (2008) Control of vertex geometry, structure dimensionality, functionality, and pore metrics in the reticular synthesis of crystalline metal–organic frameworks and Polyhedra. *J Am Chem Soc* 130:11650–11661. <https://doi.org/10.1021/ja803783c>
- Hyde ST, Delgado Friedrichs O, Ramsden SJ, Robins V (2006) Towards enumeration of crystalline frameworks: the 2D hyperbolic approach. *Solid State Sci* 8:740–752. <https://doi.org/10.1016/j.solidstatesciences.2006.04.001>
- O’Keeffe M, Peskov MA, Ramsden SJ, Yaghi OM (2008) The Reticular Chemistry Structure Resource (RCSR) database of, and symbols for, crystal nets. *Acc Chem Res* 41:1782–1789. <https://doi.org/10.1021/ar800124u>
- Kitagawa S, Munakata M, Tanimura T (1991) Tetranuclear copper(I)-based infinite one-dimensional chain complex. Synthesis and X-Ray crystal structure of  $\{[\text{Cu}_2(\mu\text{-}3\text{-methylpyridazine})_2(\mu\text{-pyrazine})_3](\text{ClO}_4)_2\}_\infty$ . *Chem Lett* 20:623–626. <https://doi.org/10.1246/cl.1991.623>
- Kondo M, Yoshitomi T, Matsuzaka H, Kitagawa S, Seki K (1997) Three-dimensional framework with channeling cavities for small molecules:  $\{[\text{M}_2(4,4'\text{-bpy})_3(\text{NO}_3)_4] \cdot x\text{H}_2\text{O}\}_n$  (M=Co, Ni, Zn). *Angew Chem Int Ed* 36:1725–1727. <https://doi.org/10.1002/anie.199717251>
- Kitagawa S, Kitaura R, S-i N (2004) Functional porous coordination polymers. *Angew Chem Int Ed* 43:2334–2375. <https://doi.org/10.1002/anie.200300610>
- Yaghi OM, Li G, Groy TL (1995) Conversion of hydrogen-bonded manganese(II) and zinc(II) squarate ( $\text{C}_4\text{O}_{42^-}$ ) molecules, chains and sheets to three-dimensional cage networks. *Dalton Trans*:727–732. <https://doi.org/10.1039/DT9950000727>
- Yaghi OM, Jernigan R, Li H, Davis EC, Groy TL (1997) Construction of a new open-framework solid from 1,3,5-cyclohexanetricarboxylate and zinc(II) building blocks. *Dalton Trans*:2383–2384. <https://doi.org/10.1039/A702287E>
- Yaghi OM, Li H, Davis C, Richardson D, Groy TL (1998) Synthetic strategies, structure patterns, and emerging properties in the chemistry of modular porous solids. *Acc Chem Res* 31:474–484. <https://doi.org/10.1021/ar970151f>

21. Kaye SS, Dailly A, Yaghi OM, Long JR (2007) Impact of preparation and handling on the hydrogen storage properties of  $\text{Zn}_4\text{O}(\text{1,4-benzenedicarboxylate})_3$  (MOF-5). *J Am Chem Soc* 129:14176–14177. <https://doi.org/10.1021/ja076877g>
22. Chui SS-Y, Lo SM-F, Charmant JPH, Orpen AG, Williams ID (1999) A chemically functionalizable Nanoporous material  $\text{Cu}_3(\text{TMA})_2(\text{H}_2\text{O})_3$ . *Science* 283:1148–1150. <https://doi.org/10.1126/science.283.5405.1148>
23. Peng Y, Krungleviciute V, Eryazici I, Hupp JT, Farha OK, Yildirim T (2013) Methane storage in metal–organic frameworks: current records, surprise findings, and challenges. *J Am Chem Soc* 135:11887–11894. <https://doi.org/10.1021/ja4045289>
24. Senkovska I, Kaskel S (2008) High pressure methane adsorption in the metal-organic frameworks  $\text{Cu}_3(\text{btc})_2$ ,  $\text{Zn}_2(\text{bdc})_2\text{dabco}$ , and  $\text{Cr}_3\text{F}(\text{H}_2\text{O})_2\text{O}(\text{bdc})_3$ . *Microporous Mesoporous Mater* 112:108–115. <https://doi.org/10.1016/j.micromeso.2007.09.016>
25. Cheetham AK, Férey G, Loiseau T (1999) Open-framework inorganic materials. *Angew Chem Int Ed* 38:3268–3292. [https://doi.org/10.1002/\(SICI\)1521-3773\(19991115\)38:22<3268::AID-ANIE3268>3.0.CO;2-U](https://doi.org/10.1002/(SICI)1521-3773(19991115)38:22<3268::AID-ANIE3268>3.0.CO;2-U)
26. Barthelet K, Riou D, Férey G (2001) Hydrothermal synthesis and structure determination of  $\text{Ag}_3(\text{VVO}_2)\{\text{O}_3\text{P-CH}_2\text{-PO}_3\}$  or MIL-42: a new vanadium(V) methylenediphosphonate inserting silver cations. *Solid State Sci* 3:203–209. [https://doi.org/10.1016/S1293-2558\(00\)01132-8](https://doi.org/10.1016/S1293-2558(00)01132-8)
27. Barthelet K, Marrot J, Riou D, Férey G (2002) A breathing hybrid organic–inorganic solid with very large pores and high magnetic characteristics. *Angew Chem Int Ed* 41:281–284. [https://doi.org/10.1002/1521-3773\(20020118\)41:2<281::AID-ANIE281>3.0.CO;2-Y](https://doi.org/10.1002/1521-3773(20020118)41:2<281::AID-ANIE281>3.0.CO;2-Y)
28. Klein N, Senkovska I, Gedrich K, Stoeck U, Henschel A, Mueller U, Kaskel S (2009) A mesoporous metal-organic framework. *Angew Chem Int Ed* 48:9954–9957. <https://doi.org/10.1002/anie.200904599>
29. Grüner R et al (2014) A new metal-organic framework with ultra-high surface area. *Chem Commun* 50:3450–3452. <https://doi.org/10.1039/c4cc00113c>
30. Stoeck U, Senkovska I, Bon V, Krause S, Kaskel S (2015) Assembly of metal-organic polyhedra into highly porous frameworks for ethene delivery. *Chem Commun* 51:1046–1049. <https://doi.org/10.1039/c4cc07920e>
31. Furukawa H et al (2010) Ultrahigh porosity in metal-organic frameworks. *Science* 329:424–428. <https://doi.org/10.1126/science.1192160>
32. Farha OK et al (2010) De novo synthesis of a metal-organic framework material featuring ultrahigh surface area and gas storage capacities. *Nat Chem* 2:944–948. <https://doi.org/10.1038/nchem.834>
33. Groom CR, Bruno IJ, Lightfoot MP, Ward SC (2016) The Cambridge structural database. *Acta Cryst B* 72:171–179. <https://doi.org/10.1107/S2052520616003954>
34. Oien-Odegaard S, Shearer GC, Wragg DS, Lillerud KP (2017) Pitfalls in metal-organic framework crystallography: towards more accurate crystal structures. *Chem Soc Rev* 46:4867–4876. <https://doi.org/10.1039/C6CS00533K>
35. Gandara F, Bennett TD (2014) Crystallography of metal-organic frameworks. *IUCrJ* 1:563–570. <https://doi.org/10.1107/S2052252514020351>
36. Férey G, Mellot-Draznieks C, Serre C, Millange F, Dutour J, Surble S, Margiolaki I (2005) A chromium terephthalate-based solid with unusually large pore volumes and surface area. *Science* 309:2040–2042. <https://doi.org/10.1126/science.1116275>
37. Sarkisov L, Harrison A (2011) Computational structure characterisation tools in application to ordered and disordered porous materials. *Mol Sim* 37:1248–1257. <https://doi.org/10.1080/08927022.2011.592832>
38. Willems TF, Rycroft CH, Kazi M, Meza JC, Haranczyk M (2012) Algorithms and tools for high-throughput geometry-based analysis of crystalline porous materials. *Microporous Mesoporous Mater* 149:134–141. <https://doi.org/10.1016/j.micromeso.2011.08.020>
39. Chempath S, Düren T, Sarkisov L, Snurr RQ (2013) Experiences with the publicly available multipurpose simulation code, Music. *Mol Sim* 39:1223–1232. <https://doi.org/10.1080/08927022.2013.819103>

40. Dubbeldam D, Calero S, Ellis DE, Snurr RQ (2016) RASPA: molecular simulation software for adsorption and diffusion in flexible nanoporous materials. *Mol Sim* 42:81–101. <https://doi.org/10.1080/08927022.2015.1010082>
41. Howarth AJ, Liu Y, Li P, Li Z, Wang TC, Hupp JT, Farha OK (2016) Chemical, thermal and mechanical stabilities of metal–organic frameworks. *Nat Rev Mater* 1:15018. <https://doi.org/10.1038/natrevmats.2015.18>
42. Gelfand BS, Shimizu GKH (2016) Parameterizing and grading hydrolytic stability in metal–organic frameworks. *Dalton Trans* 45:3668–3678. <https://doi.org/10.1039/C5DT04049C>
43. Burtch NC, Jasuja H, Walton KS (2014) Water stability and adsorption in metal–organic frameworks. *Chem Rev* 114:10575–10612. <https://doi.org/10.1021/cr5002589>
44. Jeremias F, Lozan V, Henninger SK, Janiak C (2013) Programming MOFs for water sorption: amino-functionalized MIL-125 and UiO-66 for heat transformation and heat storage applications. *Dalton Trans* 42:15967–15973. <https://doi.org/10.1039/C3DT51471D>
45. Qadir N, Said SAM, Bahaidarah HM (2015) Structural stability of metal organic frameworks in aqueous media – controlling factors and methods to improve hydrostability and hydrothermal cyclic stability. *Microporous Mesoporous Mater* 201:61–90. <https://doi.org/10.1016/j.micromeso.2014.09.034>
46. Chapman KW, Halder GJ, Chupas PJ (2008) Guest-dependent high pressure phenomena in a Nanoporous metal–organic framework material. *J Am Chem Soc* 130:10524–10526. <https://doi.org/10.1021/ja804079z>
47. Graham AJ, Tan J-C, Allan DR, Moggach SA (2012) The effect of pressure on Cu-btc: framework compression vs. guest inclusion. *Chem Commun* 48:1535–1537. <https://doi.org/10.1039/C1CC16045A>
48. Tan JC, Cheetham AK (2011) Mechanical properties of hybrid inorganic-organic framework materials: establishing fundamental structure-property relationships. *Chem Soc Rev* 40:1059–1080. <https://doi.org/10.1039/C0CS00163E>
49. Bahr DF et al (2007) Mechanical properties of cubic zinc carboxylate IRMOF-1 metal-organic framework crystals. *Phys Rev B* 76:184106. <https://doi.org/10.1103/PhysRevB.76.184106>
50. Kuc A, Enyashin A, Seifert G (2007) Metal–organic frameworks: structural, energetic, electronic, and mechanical properties. *J Phys Chem B* 111:8179–8186. <https://doi.org/10.1021/jp072085x>
51. Wu H, Yildirim T, Zhou W (2013) Exceptional mechanical stability of highly porous zirconium metal–organic framework UiO-66 and its important implications. *J Phys Chem Lett* 4:925–930. <https://doi.org/10.1021/jz4002345>
52. Gatta GD, Lee Y (2014) Zeolites at high pressure: a review. *Mineral Mag* 78:267–291. <https://doi.org/10.1180/minmag.2014.078.2.04>
53. Tan JC, Bennett TD, Cheetham AK (2010) Chemical structure, network topology, and porosity effects on the mechanical properties of Zeolitic Imidazolate frameworks. *PNAS* 107:9938–9943. <https://doi.org/10.1073/pnas.1003205107>
54. Kumar R, Raut D, Ahmad I, Ramamurty U, Maji TK, Rao CNR (2014) Functionality preservation with enhanced mechanical integrity in the nanocomposites of the metal-organic framework, ZIF-8, with BN nanosheets. *Mater Horiz* 1:513–517. <https://doi.org/10.1039/C4MH00065J>
55. Li W, Henke S, Cheetham AK (2014) Research update: mechanical properties of metal-organic frameworks – influence of structure and chemical bonding. *APL Mater* 2:123902. <https://doi.org/10.1063/1.4904966>
56. Boyd PG, Moosavi SM, Witman M, Smit B (2017) Force-field prediction of materials properties in metal-organic frameworks. *J Phys Chem Lett* 8:357–363. <https://doi.org/10.1021/acs.jpcclett.6b02532>
57. Kondo M et al (1999) Rational synthesis of stable channel-like cavities with methane gas adsorption properties: {Cu-2(pzdc)(2(L))<sub>n</sub>} (pzdc = pyrazine-2,3-dicarboxylate; L = a pillar ligand). *Angew Chem Int Ed* 38:140–143. [https://doi.org/10.1002/\(SICI\)1521-3773\(19990115\)38:1/2<140::AID-ANIE140>3.0.CO;2-9](https://doi.org/10.1002/(SICI)1521-3773(19990115)38:1/2<140::AID-ANIE140>3.0.CO;2-9)

58. Noro S-I, Kitagawa S, Kondo M, Seki K (2000) A new, methane adsorbent, porous coordination polymer  $[\{\text{CuSiF}_6(4,4'\text{-bipyridine})_2\}_n]$ . *Angew Chem Int Ed* 39:2082–2084
59. Rosi NL, Eckert J, Eddaoudi M, Vodak DT, Kim J, O’Keeffe M, Yaghi OM (2003) Hydrogen storage in microporous metal-organic frameworks. *Science* 300:1127–1129. <https://doi.org/10.1126/science.1083440>
60. Furukawa H et al (2010) Ultrahigh porosity in metal-organic frameworks. *Science* 329:424–428. <https://doi.org/10.1126/science.1192160>
61. Hu YH, Zhang L (2010) Hydrogen storage in metal-organic frameworks. *Adv Mater* 22:E117–E130. <https://doi.org/10.1002/adma.200902096>
62. Alezi D et al (2015) MOF crystal chemistry paving the way to gas storage needs: aluminum-based soc-MOF for  $\text{CH}_4$ ,  $\text{O}_2$ , and  $\text{CO}_2$  storage. *J Am Chem Soc* 137:13308–13318. <https://doi.org/10.1021/jacs.5b07053>
63. Lin X et al (2006) High  $\text{H}_2$  adsorption by coordination-framework materials. *Angew Chem Int Ed* 45:7358–7364. <https://doi.org/10.1002/anie.200601991>
64. Lin X, Jia JH, Hubberstey P, Schroder M, Champness NR (2007) Hydrogen storage in metal-organic frameworks. *CrystEngComm* 9:438–448. <https://doi.org/10.1039/b706207a>
65. Schmitz B, Müller U, Trukhan N, Schubert M, Férey G, Hirscher M (2008) Heat of adsorption for hydrogen in microporous high-surface-area materials. *ChemPhysChem* 9:2181–2184. <https://doi.org/10.1002/cphc.200800463>
66. Gómez-Gualdrón DA et al (2017) Understanding volumetric and gravimetric hydrogen adsorption trade-off in metal-organic frameworks. *ACS Appl Mater Interfaces* 9:33419–33428. <https://doi.org/10.1021/acsami.7b01190>
67. He Y, Zhou W, Yildirim T, Chen B (2013) A series of metal-organic frameworks with high methane uptake and an empirical equation for predicting methane storage capacity. *Energy Environ Sci* 6:2735–2744. <https://doi.org/10.1039/C3EE41166D>
68. Stoeck U, Krause S, Bon V, Senkovska I, Kaskel S (2012) A highly porous metal-organic framework, constructed from a cuboctahedral super-molecular building block, with exceptionally high methane uptake. *Chem Commun* 48:10841–10843. <https://doi.org/10.1039/c2cc34840c>
69. Li B, Wen H-M, Zhou W, Xu Jeff Q, Chen B (2016) Porous metal-organic frameworks: promising materials for methane storage. *Chem* 1:557–580. <https://doi.org/10.1016/j.chempr.2016.09.009>
70. Drache F, Bon V, Senkovska I, Getzschmann J, Kaskel S (2017) The modulator driven polymorphism of Zr(IV) based metal-organic frameworks. *Philos Trans R Soc A* 375. <https://doi.org/10.1098/rsta.2016.0027>
71. Wu H, Chua YS, Krungleviciute V, Tyagi M, Chen P, Yildirim T, Zhou W (2013) Unusual and highly tunable missing-linker defects in zirconium metal-organic framework UiO-66 and their important effects on gas adsorption. *J Am Chem Soc* 135:10525–10532. <https://doi.org/10.1021/ja404514r>
72. Senkovska I, Kaskel S (2014) Ultrahigh porosity in mesoporous MOFs: promises and limitations. *Chem Commun* 50:7089–7098. <https://doi.org/10.1039/c4cc00524d>
73. Klein N et al (2011) Route to a family of robust, non-interpenetrated metal-organic frameworks with pto-like topology. *Chem Eur J* 17:13007–13016. <https://doi.org/10.1002/chem.201101383>
74. Müller P, Wisser FM, Bon V, Grünker R, Senkovska I, Kaskel S (2015) Postsynthetic paddle-wheel cross-linking and functionalization of 1,3-Phenylenebis(azanetriyl)tetrabenzoate-based MOFs. *Chem Mater* 27:2460–2467. <https://doi.org/10.1021/cm504573z>
75. Burnett BJ, Choe W (2012) Stepwise pillar insertion into metal-organic frameworks: a sequential self-assembly approach. *CrystEngComm* 14:6129–6131. <https://doi.org/10.1039/C2CE25545F>
76. Jeong S, Kim D, Shin S, Moon D, Cho SJ, Lah MS (2014) Combinational synthetic approaches for Isorecticular and polymorphic metal-organic frameworks with tuned pore geometries and surface properties. *Chem Mater* 26:1711–1719. <https://doi.org/10.1021/cm404239s>

77. Yuan S et al (2016) Flexible zirconium metal-organic frameworks as bioinspired switchable catalysts. *Angew Chem Int Ed* 55:10776–10780. <https://doi.org/10.1002/anie.201604313>
78. Deng H et al (2012) Large-pore apertures in a series of metal-organic frameworks. *Science* 336:1018–1023. <https://doi.org/10.1126/science.1220131>
79. Bury W, Fairen-Jimenez D, Lalonde MB, Snurr RQ, Farha OK, Hupp JT (2013) Control over catenation in pillared paddlewheel metal-organic framework materials via solvent-assisted linker exchange. *Chem Mater* 25:739–744. <https://doi.org/10.1021/cm303749m>
80. Li T, Kozłowski MT, Doud EA, Blakely MN, Rosi NL (2013) Stepwise ligand exchange for the preparation of a family of mesoporous MOFs. *J Am Chem Soc* 135:11688–11691. <https://doi.org/10.1021/ja403810k>
81. Deria P, Mondloch JE, Karagiari O, Bury W, Hupp JT, Farha OK (2014) Beyond post-synthesis modification: evolution of metal-organic frameworks via building block replacement. *Chem Soc Rev* 43:5896–5912. <https://doi.org/10.1039/C4CS00067F>
82. Batten SR, Robson R (1998) Interpenetrating nets: ordered, periodic entanglement. *Angew Chem Int Ed* 37:1460–1494. [https://doi.org/10.1002/\(SICI\)1521-3773\(19980619\)37:11<1460::AID-ANIE1460>3.0.CO;2-Z](https://doi.org/10.1002/(SICI)1521-3773(19980619)37:11<1460::AID-ANIE1460>3.0.CO;2-Z)
83. Ma S, Sun D, Ambrogio M, Fillinger JA, Parkin S, Zhou H-C (2007) Framework-catenation isomerism in metal-organic frameworks and its impact on hydrogen uptake. *J Am Chem Soc* 129:1858–1859. <https://doi.org/10.1021/ja067435s>
84. Jiang H-L, Makal TA, Zhou H-C (2013) Interpenetration control in metal-organic frameworks for functional applications. *Coord Chem Rev* 257:2232–2249. <https://doi.org/10.1016/j.ccr.2013.03.017>
85. Haldar R, Sikdar N, Maji TK (2015) Interpenetration in coordination polymers: structural diversities toward porous functional materials. *Mater Today* 18:97–116. <https://doi.org/10.1016/j.mattod.2014.10.038>
86. Ferguson A et al (2016) Controlled partial interpenetration in metal-organic frameworks. *Nat Chem* 8:250. <https://doi.org/10.1038/nchem.2430>
87. Jeong S et al (2017) Topology conversions of non-interpenetrated metal-organic frameworks to doubly interpenetrated metal-organic frameworks. *Chem Mater* 29:3899–3907. <https://doi.org/10.1021/acs.chemmater.6b05277>
88. Alexandrov E, Blatov V, Proserpio D (2014) Interpenetration of three-periodic networks in crystal structures: description and classification methods, geometrical-topological conditions of implementation. *J Struct Chem* 55:1308–1325. <https://doi.org/10.1134/S0022476614070130>
89. Öhrström L (2015) Let's talk about MOFs—topology and terminology of metal-organic frameworks and why we need them. *Crystals* 5:154–162. <https://doi.org/10.3390/cryst5010154>
90. Eddaoudi M, Kim J, Wachter JB, Chae HK, O'Keeffe M, Yaghi OM (2001) Porous metal-organic Polyhedra: 25 Å cuboctahedron constructed from 12 Cu<sub>2</sub>(CO<sub>2</sub>)<sub>4</sub> paddle-wheel building blocks. *J Am Chem Soc* 123:4368–4369. <https://doi.org/10.1021/ja0104352>
91. Moulton B, Lu J, Mondal A, Zaworotko MJ (2001) Nanoballs: nanoscale faceted polyhedra with large windows and cavities. *Chem Commun*:863–864. <https://doi.org/10.1039/B102714J>
92. Ke Y, Collins DJ, Zhou H-C (2005) Synthesis and structure of Cuboctahedral and Anticuboctahedral cages containing 12 Quadruply bonded Dimolybdenum units. *Inorg Chem* 44:4154–4156. <https://doi.org/10.1021/ic050460z>
93. Perry JJ, Kravtsov VC, McManus GJ, Zaworotko MJ (2007) Bottom up synthesis that does not start at the bottom: quadruple covalent cross-linking of nanoscale faceted Polyhedra. *J Am Chem Soc* 129:10076–10077. <https://doi.org/10.1021/ja0734952>
94. Cairns AJ, Perman JA, Wojtas L, Kravtsov VC, Alkordi MH, Eddaoudi M, Zaworotko MJ (2008) Supermolecular Building Blocks (SBBs) and Crystal Design: 12-connected open frameworks based on a molecular Cubohemioctahedron. *J Am Chem Soc* 130:1560–1561. <https://doi.org/10.1021/ja078060t>

95. Li J-R, Yakovenko AA, Lu W, Timmons DJ, Zhuang W, Yuan D, Zhou H-C (2010) Ligand bridging-angle-driven assembly of molecular architectures based on Quadruply bonded Mo–Mo dimers. *J Am Chem Soc* 132:17599–17610. <https://doi.org/10.1021/ja1080794>
96. Jian-Rong L, Hong-Cai Z (2010) Bridging-ligand-substitution strategy for the preparation of metal-organic polyhedra. *Nat Chem* 2:893–898. <https://doi.org/10.1038/nchem.803>
97. Lopez-Olvera A, Sanchez-Gonzalez E, Campos-Reales-Pineda A, Aguilar-Granda A, Ibarra IA, Rodriguez-Molina B (2017) CO<sub>2</sub> capture in a carbazole-based supramolecular polyhedron structure: the significance of Cu(ii) open metal sites. *Inorg Chem Front* 4:56–64. <https://doi.org/10.1039/C6QI00342G>
98. Perry Iv JJ, Perman JA, Zaworotko MJ (2009) Design and synthesis of metal-organic frameworks using metal-organic polyhedra as supermolecular building blocks. *Chem Soc Rev* 38:1400–1417. <https://doi.org/10.1039/b807086p>
99. Zou Y, Park M, Hong S, Lah MS (2008) A designed metal-organic framework based on a metal-organic polyhedron. *Chem Commun*:2340–2342. <https://doi.org/10.1039/B801103F>
100. Nouar F, Eubank JF, Bousquet T, Wojtas L, Zaworotko MJ, Eddaoudi M (2008) Supermolecular Building Blocks (SBBs) for the design and synthesis of highly porous metal-organic frameworks. *J Am Chem Soc* 130:1833–1835. <https://doi.org/10.1021/ja710123s>
101. Lu W, Yuan D, Makal TA, Wei Z, Li J-R, Zhou H-C (2013) Highly porous metal-organic framework sustained with 12-connected nanoscopic octahedra. *Dalton Trans* 42:1708–1714. <https://doi.org/10.1039/c2dt32479b>
102. Li J-R, Timmons DJ, Zhou H-C (2009) Interconversion between molecular Polyhedra and metal–organic frameworks. *J Am Chem Soc* 131:6368–6369. <https://doi.org/10.1021/ja901731z>
103. Guillerm V et al (2014) A supermolecular building approach for the design and construction of metal-organic frameworks. *Chem Soc Rev*. <https://doi.org/10.1039/c4cs00135d>
104. He Y, Chen B (2011) Metal–organic frameworks: frameworks containing open sites. In: *Encyclopedia of inorganic and bioinorganic chemistry*. Wiley. <https://doi.org/10.1002/9781119951438.eibc2213>
105. Panella B, Hirscher M (2010) Physisorption in porous materials. In: *Handbook of hydrogen storage*. Wiley-VCH Verlag, pp 39–62. <https://doi.org/10.1002/9783527629800.ch2>
106. Lebedev OI, Millange F, Serre C, Van Tendeloo G, Ferey G (2005) First direct imaging of Giant pores of the metal-organic framework MIL-101. *Chem Mater* 17:6525–6527. <https://doi.org/10.1021/cm051870o>
107. Bonino F et al (2008) Local structure of CPO-27-Ni metallorganic framework upon dehydration and coordination of NO. *Chem Mater* 20:4957–4968. <https://doi.org/10.1021/cm800686k>
108. Peterson VK, Liu Y, Brown CM, Kepert CJ (2006) Neutron powder diffraction study of D<sub>2</sub> sorption in Cu<sub>3</sub>(1,3,5-benzenetricarboxylate)<sub>2</sub>. *J Am Chem Soc* 128:15578–15579. <https://doi.org/10.1021/ja0660857>
109. Peterson VK, Brown CM, Liu Y, Kepert CJ (2011) Structural study of D<sub>2</sub> within the Trimodal pore system of a metal organic framework. *J Phys Chem C* 115:8851–8857. <https://doi.org/10.1021/jp2010937>
110. Lin X et al (2009) High capacity hydrogen adsorption in Cu(II) Tetracarboxylate framework materials: the role of pore size, ligand functionalization, and exposed metal sites. *J Am Chem Soc* 131:2159–2171. <https://doi.org/10.1021/ja806624j>
111. Getzschmann J et al (2010) Methane storage mechanism in the metal-organic framework Cu<sub>3</sub>(btc)<sub>2</sub>: an in situ neutron diffraction study. *Microporous Mesoporous Mater* 136:50–58. <https://doi.org/10.1016/j.micromeso.2010.07.020>
112. Xiang S, Zhou W, Gallegos JM, Liu Y, Chen B (2009) Exceptionally high acetylene uptake in a microporous metal–organic framework with open metal sites. *J Am Chem Soc* 131:12415–12419. <https://doi.org/10.1021/ja904782h>
113. Wu H, Zhou W, Yildirim T (2009) High-capacity methane storage in metal–organic frameworks M<sub>2</sub>(dhtp): the important role of open metal sites. *J Am Chem Soc* 131:4995–5000. <https://doi.org/10.1021/ja900258t>

114. Easun TL, Moreau F, Yan Y, Yang S, Schroder M (2017) Structural and dynamic studies of substrate binding in porous metal-organic frameworks. *Chem Soc Rev* 46:239–274. <https://doi.org/10.1039/C6CS00603E>
115. The use of metallogligands in metal-organic frameworks. In: *Progress in inorganic chemistry*. <https://doi.org/10.1002/9780470440124.ch4>
116. Zou C, Wu C-D (2012) Functional porphyrinic metal-organic frameworks: crystal engineering and applications. *Dalton Trans* 41:3879–3888. <https://doi.org/10.1039/C2DT11989G>
117. Kitaura R, Onoyama G, Sakamoto H, Matsuda R, Noro SI, Kitagawa S (2004) Immobilization of a Metallo Schiff Base into a microporous coordination polymer. *Angew Chem Int Ed* 43:2684–2687. <https://doi.org/10.1002/anie.200352596>
118. Choi E-Y, Wray CA, Hu C, Choe W (2009) Highly tunable metal-organic frameworks with open metal centers. *CrystEngComm* 11:553–555. <https://doi.org/10.1039/B819707P>
119. Müller P, Bon V, Senkovska I, Getzschmann J, Weiss MS, Kaskel S (2017) Crystal engineering of Phenylenebis(azanetriyl)tetrabenzoate based metal-organic frameworks for gas storage applications. *Cryst Growth Des* 17:3221–3228. <https://doi.org/10.1021/acs.cgd.7b00184>
120. Chong S, Thiele G, Kim J (2017) Excavating hidden adsorption sites in metal-organic frameworks using rational defect engineering. *Nat Commun* 8:1539. <https://doi.org/10.1038/s41467-017-01478-4>
121. Jiang ZR, Wang H, Hu Y, Lu J, Jiang HL (2015) Polar group and defect engineering in a metal-organic framework: synergistic promotion of carbon dioxide sorption and conversion. *ChemSusChem* 8:878–885. <https://doi.org/10.1002/cssc.201403230>
122. Lin Y, Kong C, Chen L (2016) Amine-functionalized metal-organic frameworks: structure, synthesis and applications. *RSC Adv* 6:32598–32614. <https://doi.org/10.1039/C6RA01536K>
123. Demessence A, D’Alessandro DM, Foo ML, Long JR (2009) Strong CO<sub>2</sub> binding in a water-stable, Triazolate-bridged metal-organic framework functionalized with Ethylenediamine. *J Am Chem Soc* 131:8784–8786. <https://doi.org/10.1021/ja903411w>
124. McDonald TM, Lee WR, Mason JA, Wiers BM, Hong CS, Long JR (2012) Capture of carbon dioxide from air and flue gas in the alkylamine-appended metal-organic framework mmen-Mg<sub>2</sub>(dobpdc). *J Am Chem Soc* 134:7056–7065. <https://doi.org/10.1021/ja300034j>
125. McDonald TM et al (2015) Cooperative insertion of CO<sub>2</sub> in diamine-appended metal-organic frameworks. *Nature* 519:303. <https://doi.org/10.1038/nature14327>
126. Flaig RW et al (2017) The chemistry of CO<sub>2</sub> capture in an amine-functionalized metal-organic framework under dry and humid conditions. *J Am Chem Soc* 139:12125–12128. <https://doi.org/10.1021/jacs.7b06382>
127. Yang S et al (2012) Selectivity and direct visualization of carbon dioxide and sulfur dioxide in a decorated porous host. *Nat Chem* 4:887. <https://doi.org/10.1038/nchem.1457>
128. Zhang G, Wei G, Liu Z, Oliver SRJ, Fei H (2016) A robust sulfonate-based metal-organic framework with permanent porosity for efficient CO<sub>2</sub> capture and conversion. *Chem Mater* 28:6276–6281. <https://doi.org/10.1021/acs.chemmater.6b02511>
129. Cohen SM (2012) Postsynthetic methods for the functionalization of metal-organic frameworks. *Chem Rev* 112:970–1000. <https://doi.org/10.1021/cr200179u>
130. Wang Z, Tanabe KK, Cohen SM (2009) Accessing postsynthetic modification in a series of metal-organic frameworks and the influence of framework topology on reactivity. *Inorg Chem* 48:296–306. <https://doi.org/10.1021/ic801837t>
131. Goto Y, Sato H, Shinkai S, Sada K (2008) “Clickable” metal-organic framework. *J Am Chem Soc* 130:14354–14355. <https://doi.org/10.1021/ja7114053>
132. Hwang YK et al (2008) Amine grafting on coordinatively unsaturated metal centers of MOFs: consequences for catalysis and metal encapsulation. *Angew Chem Int Ed* 47:4144–4148. <https://doi.org/10.1002/anie.200705998>
133. Drache F, Bon V, Senkovska I, Marschelke C, Synytska A, Kaskel S (2016) Postsynthetic inner-surface functionalization of the highly stable zirconium-based metal-organic framework DUT-67. *Inorg Chem* 55:7206–7213. <https://doi.org/10.1021/acs.inorgchem.6b00829>
134. Nguyen KD, Kutzscher C, Drache F, Senkovska I, Kaskel S (2018) Chiral functionalization of a zirconium metal-organic framework (DUT-67) as a heteroge-

- neous catalyst in asymmetric Michael addition reaction. *Inorg Chem* 57:1483–1489. <https://doi.org/10.1021/acs.inorgchem.7b02854>
135. Doonan CJ, Morris W, Furukawa H, Yaghi OM (2009) Isoreticular metal–organic frameworks. *J Am Chem Soc* 131:9492–9493. <https://doi.org/10.1021/ja903251e>
136. Yamada T, Kitagawa H (2009) Protection and deprotection approach for the introduction of functional groups into metal–organic frameworks. *J Am Chem Soc* 131:6312–6313. <https://doi.org/10.1021/ja809352y>
137. Deshpande RK, Minnaar JL, Telfer SG (2010) Thermolabile groups in metal–organic frameworks: suppression of network interpenetration, post-synthetic cavity expansion, and protection of reactive functional groups. *Angew Chem Int Ed* 49:4598–4602. <https://doi.org/10.1002/anie.200905960>
138. Kutzscher C, Nickerl G, Senkovska I, Bon V, Kaskel S (2016) Proline functionalized UiO-67 and UiO-68 type metal–organic frameworks showing reversed diastereoselectivity in aldol addition reactions. *Chem Mater* 28:2573–2580. <https://doi.org/10.1021/acs.chemmater.5b04575>
139. Brozek CK, Dinca M (2014) Cation exchange at the secondary building units of metal-organic frameworks. *Chem Soc Rev* 43:5456–5467. <https://doi.org/10.1039/C4CS00002A>
140. Evans JD, Sumbly CJ, Doonan CJ (2014) Post-synthetic metalation of metal-organic frameworks. *Chem Soc Rev* 43:5933–5951. <https://doi.org/10.1039/C4CS00076E>
141. Horike S, Shimomura S, Kitagawa S (2009) Soft porous crystals. *Nat Chem* 1:695–704. <https://doi.org/10.1038/nchem.444>
142. Blake JA, Hill JS, Hubberstey P, Li W-S (1997) Rectangular grid two-dimensional sheets of copper(II) bridged by both co-ordinated and hydrogen bonded 4,4[prime or minute]-bipyridine (4,4[prime or minute]-bipy) in [Cu({small micro}-4,4[prime or minute]-bipy)(H<sub>2</sub>O)<sub>2</sub>(FBF<sub>3</sub>)<sub>2</sub>][middle dot]4,4[prime or minute]-bipy. *Dalton Trans*:913–914. <https://doi.org/10.1039/A700036G>
143. Kitaura R, Fujimoto K, Noro S-i, Kondo M, Kitagawa S (2002) A pillared-layer coordination polymer network displaying hysteretic sorption: [Cu<sub>2</sub>(pzdc)<sub>2</sub>(dpyg)]<sub>n</sub> (pzdc = Pyrazine-2,3-dicarboxylate; dpyg = 1,2-Di(4-pyridyl)glycol). *Angew Chem Int Ed* 41:133–135. [https://doi.org/10.1002/1521-3773\(20020104\)41:1<133::aid-anie133>3.0.co;2-r](https://doi.org/10.1002/1521-3773(20020104)41:1<133::aid-anie133>3.0.co;2-r)
144. Li D, Kaneko K (2001) Hydrogen bond-regulated microporous nature of copper complex-assembled microcrystals. *Chem Phys Lett* 335:50–56. [https://doi.org/10.1016/S0009-2614\(00\)01419-6](https://doi.org/10.1016/S0009-2614(00)01419-6)
145. Schneemann A, Bon V, Schwedler I, Senkovska I, Kaskel S, Fischer RA (2014) Flexible metal-organic frameworks. *Chem Soc Rev* 43:6062–6096. <https://doi.org/10.1039/c4cs00101j>
146. Serre C, Millange F, Thouvenot C, Noguès M, Marsolier G, Louër D, Férey G (2002) Very large breathing effect in the first Nanoporous chromium(III)-based solids: MIL-53 or CrIII(OH)·{O<sub>2</sub>C–C<sub>6</sub>H<sub>4</sub>–CO<sub>2</sub>}·{HO<sub>2</sub>C–C<sub>6</sub>H<sub>4</sub>–CO<sub>2</sub>H}<sub>x</sub>·H<sub>2</sub>O<sub>y</sub>. *J Am Chem Soc* 124:13519–13526. <https://doi.org/10.1021/ja0276974>
147. Mellot-Draznieks C, Serre C, Surblé S, Audebrand N, Férey G (2005) Very large swelling in hybrid frameworks: a combined computational and powder diffraction study. *J Am Chem Soc* 127:16273–16278. <https://doi.org/10.1021/ja054900x>
148. Klein N et al (2010) Monitoring adsorption-induced switching by (129)Xe NMR spectroscopy in a new metal-organic framework Ni<sub>2</sub>(2,6-ndc)<sub>2</sub>(dabco). *Phys Chem Chem Phys* 12:11778–11784. <https://doi.org/10.1039/c003835k>
149. Bon V et al (2015) Exceptional adsorption-induced cluster and network deformation in the flexible metal-organic framework DUT-8(Ni) observed by in situ X-ray diffraction and EXAFS. *Phys Chem Chem Phys* 17:17471–17479. <https://doi.org/10.1039/C5CP02180D>
150. Bureekaew S et al (2010) Control of interpenetration for tuning structural flexibility influences sorption properties. *Angew Chem Int Ed* 49:7660–7664. <https://doi.org/10.1002/anie.201002259>

151. Fairen-Jimenez D, Moggach SA, Wharmby MT, Wright PA, Parsons S, Düren T (2011) Opening the gate: framework flexibility in ZIF-8 explored by experiments and simulations. *J Am Chem Soc* 133:8900–8902. <https://doi.org/10.1021/ja202154j>
152. Krause S et al (2016) A pressure-amplifying framework material with negative gas adsorption transitions. *Nature* 532:348–352. <https://doi.org/10.1038/nature17430>
153. Coudert F-X (2015) Responsive metal–organic frameworks and framework materials: under pressure, taking the heat, in the spotlight, with friends. *Chem Mater* 27:1905–1916. <https://doi.org/10.1021/acs.chemmater.5b00046>
154. Chang Z, Yang D-H, Xu J, Hu T-L, Bu X-H (2015) Flexible metal–organic frameworks: recent advances and potential applications. *Adv Mater* 27:5432–5441. <https://doi.org/10.1002/adma.201501523>
155. Sato H et al (2014) Self-accelerating CO sorption in a soft Nanoporous crystal. *Science* 343:167–170. <https://doi.org/10.1126/science.1246423>
156. Freund P, Senkowska I, Kaskel S (2017) Switchable conductive MOF–Nanocarbon composite coatings as threshold sensing architectures. *ACS Appl Mater Interfaces* 9:43782–43789. <https://doi.org/10.1021/acsami.7b13924>
157. Mason JA et al (2015) Methane storage in flexible metal–organic frameworks with intrinsic thermal management. *Nature* 527:357–361. <https://doi.org/10.1038/nature15732>
158. Bon V et al (2014) In situ observation of gating phenomena in the flexible porous coordination polymer  $\text{Zn}_2(\text{BPnDC})_2(\text{bpy})$  (SNU-9) in a combined diffraction and gas adsorption experiment. *Inorg Chem* 53:1513–1520. <https://doi.org/10.1021/ic4024844>
159. Park HJ, Suh MP (2010) Stepwise and hysteretic sorption of  $\text{N}_2$ ,  $\text{O}_2$ ,  $\text{CO}_2$ , and  $\text{H}_2$  gases in a porous metal-organic framework  $[\text{Zn}_2(\text{BPnDC})_2(\text{bpy})]$ . *Chem Commun* 46:610–612. <https://doi.org/10.1039/B913067E>

# Chapter 7

## Zeolites and Other Adsorbents



Eduardo Pérez-Botella, Miguel Palomino, Susana Valencia, and Fernando Rey

### 7.1 Historical Review of Zeolites in Adsorption Processes

The first report on the presence of adsorbed molecules in zeolites was at the very origin of its discovery. Indeed, the term “zeolite” was coined by the reputed Swedish mineralogist Axel F. Cronstedt in 1756 [1] when he observed that a particular natural zeolite, probably stellerite [2], formed a kind of froth at the surface of the solid when heated by a blow-pipe flame. The mineral was apparently “boiling”, and consequently, Cronstedt named these minerals as “zeolites” from the Greek word *zein* “to boil” and *lithos* “stone”. The observed froth on the outer surface of the stone was water that is desorbed upon heating. At ambient temperatures, water remains adsorbed on the cations placed inside the cavities of the zeolite having stilbite/stellerite structure as it is shown in Fig. 7.1.

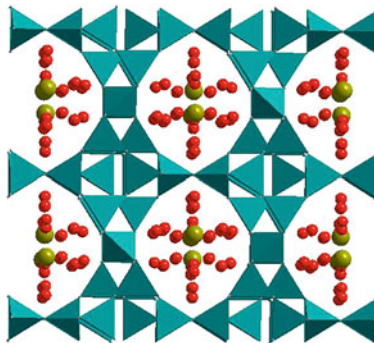
Since Cronstedt’s discovery, zeolites remained largely ignored by chemists and were mostly anecdotic samples for mineralogists. Cronstedt showed that zeolites retain water in 1756, but it wasn’t until 1857 that these materials were demonstrated to reversibly adsorb and desorb water for an indefinite number of cycles [4]. The first report on synthesis of zeolites appeared in 1846 describing the synthesis of Levynne [5]. Previously, the cation exchange properties of zeolites had been described [6] opening the path for the first industrial application of zeolites as water softeners for laundry compositions [7–9]. The use of zeolite for laundry powders is still one of the major applications of zeolites nowadays.

In this scenario, it is not surprising that also the adsorption properties of zeolites were studied. Indeed, the hypothesis that zeolites behave as porous sponges able to adsorb a large variety of liquids and/or gases was postulated in 1896 [10].

---

E. Pérez-Botella (✉) · M. Palomino · S. Valencia · F. Rey  
The A-Team of the Instituto de Tecnología Química (Universitat Politècnica de València – Consejo Superior de Investigaciones Científicas), Valencia, Spain  
e-mail: [frey@itq.upv.es](mailto:frey@itq.upv.es)

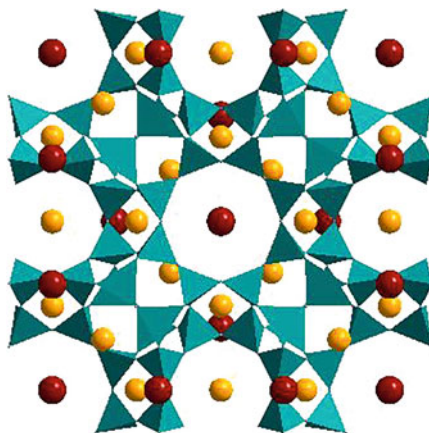
**Fig. 7.1** Stellerite structure [3]. Cyan tetrahedra, Si-O framework; yellow balls,  $\text{Ca}^{2+}$  cations; red balls, water molecules



Later, Grandjean described the adsorption of ammonia, air and hydrogen amongst other molecules in dehydrated chabazite in 1909 [11]. The first time when the molecular sieve effect was described using zeolites was in 1925 by Weigel and Steinhoff, who observed that dehydrated chabazite adsorbs water, methanol, ethanol and formic acid, while acetone, diethyl ether or benzene were excluded [12]. The molecular sieve effect was not fully understood until the first structural elucidations of zeolites reporting the presence of structural porosity were described [13–15]. McBain coined the term “Molecular Sieves” in 1932 referring to the intrinsically very high selective adsorption processes that can be carried out using zeolites as adsorbents [16]. McBain’s publication was a turning point in the science of zeolites, since it caught the attention of a young researcher, Richard M. Barrer, who at that time was studying the adsorption of gases on activated carbon. As mentioned in the excellent biography of R. M. Barrer written by L.R.C. Rees [17], R. M. Barrer realised about the extraordinary potential of zeolites for gas separation processes, but he also envisaged the need of being able to produce synthetic zeolites for controlled investigations. He developed synthetic methods for producing zeolites by mimicking the crystallization conditions of natural zeolites. That is, he successfully attempted the crystallization of zeolites under alkaline conditions at temperatures above 200 °C (i.e. hydrothermal conditions). Following this approach, Prof. Barrer discovered some synthetic analogues of natural zeolites, such as chabazite and mordenite [18–20], and provided the synthesis route for new zeolites that do not have any natural counterpart, such as zeolites P and Q [21–24]. The structure of these two zeolites was found to be identical to that of a zeolite named as ZK-5 (Fig. 7.2).

Furthermore, Prof. R. M. Barrer conducted the first synthesis using tetraalkylammonium cations [26, 27], and he also carried out the alkaline-ammonium exchange in low-silica/alumina zeolites providing a new route for obtaining zeolites in its proton-exchanged form by subsequent calcination [28]. Barrer’s main contributions to zeolite synthesis and their uses in adsorption are reviewed in one of the most famous books in zeolite science, *Zeolites and Clay Minerals as Sorbents and*

**Fig. 7.2** Structure of Cs-K-ZK-5 [25]. Cyan tetrahedra, Si-O framework; orange balls,  $K^+$  cations; red balls,  $Cs^+$



*Molecular Sieves*, published in 1978 [29], which is still widely used by most scientists working in this field.

The seminal research of R. M. Barrer boosted further investigation in industry that resulted in the development of the most important applications of zeolites, i.e. as catalysts for refining processes. These contributions were particularly relevant at Union Carbide in the USA. Indeed, a research programme was initiated at Union Carbide in 1949. That year, R. M. Milton was enrolled in this programme for attempting the separation of  $N_2$  and  $O_2$  from air by separation methods instead of using cryogenic distillation. Milton learnt about the work on molecular sieving of Barrer and McBain and attempted this separation using chabazite. Afterwards, he tried the synthesis of chabazite at lower temperatures and used higher alkalinity in the crystallization media. During the course of this research, he identified two new zeolites: zeolite A and zeolite X, which are of colossal importance in chemistry even today. Also, Milton was involved in the scaling up of zeolite production from lab to industry [30–33]. In 1951, D. W. Breck joined Milton's team, and he was able to obtain a low Al content zeolite X, renaming this new material as zeolite Y. The team led by Milton and Breck in the period 1949–1954 discovered about 24 zeolites, some of them with natural analogous zeolites but some others without natural counterparts. In 1954, the first zeolite was commercialized, and in 1959, zeolite Y was produced as an acid catalyst for many processes in refinery. Particularly, Milton and Rabo described the use of acidic zeolite Y for cracking vacuum gas oil, which over time turned into the most profitable catalyst in refinery ever reported [30, 34–36].

As presented above, a small number of extremely active and productive teams were able to open a new field of research. Zeolites were rapidly implemented at industrial scale for chemical productions taking advantage of their molecular-sieve properties, which allow very highly selective separations and their use as acid catalysts in refineries.

## 7.2 Main Features of Zeolites as Adsorbents

Zeolite structures are built by  $[TO_4]$  tetrahedra (where T is typically Si or Al) that are sharing O atoms with four  $[TO_4]$  at their neighbourhood. These tetrahedra are perfectly ordered forming well-defined pores with apertures of molecular dimensions. The chemical composition of any dry silico-aluminate zeolite is as follows:  $[SiAl_xO_2]^{x-} M^+_x$ . The incorporation of trivalent Al atoms in the zeolite framework produces a negative framework charge that is compensated by cations ( $M^+$ ), which are located within the pores and cavities of zeolites. Charge compensation in zeolites is schematized in Fig. 7.3 [37–39].

The cation  $M^+$  is located inside the pores and cavities of zeolites in the dehydrated state, and it remains at well-defined positions but without belonging to the zeolite structure. Typically, these materials adsorb a large quantity of water, which coordinates the cations and increases their mobility. The amount of water adsorbed by a zeolite depends on the Si/Al (i.e. Al content) and on the compensating cations [40, 41].

Typically, high Al-content zeolites (also called low-silica zeolites) adsorb larger amounts of water than low Al-content zeolites (high silica). Even more important than the total water adsorption capacity is the shape of their isotherms that shows, in the case of high Al containing zeolites, that most of the adsorption occurs at very low partial pressures. This is attributed to the presence of very high electrostatic fields due to the large concentration of cations inside zeolites, thus resulting in very hydrophilic adsorbents [29, 42, 43]. On the contrary, pure silica zeolites (i.e. Al-free zeolites) do not contain any cations inside their inner spaces and are much less prone to adsorb water than Al-containing zeolites, thus allowing for the control of the hydrophilicity-hydrophobicity of the zeolitic adsorbent [44–46].

Similarly to water, other polar molecules are strongly adsorbed on low-silica molecular sieves, while non-polar molecules are preferentially adsorbed on high- and pure-silica zeolites. The selective adsorption of water in low-silica zeolites is widely used for drying applications, where the zeolite is exposed to a wet stream that needs to be purified [47]. At one point, the total water adsorption capacity of the zeolite is reached, and then the adsorbent must be regenerated. A strong adsorbent-adsorbent interaction implies that either high temperature or very low pressure will be needed to recover the full adsorption capacity of the zeolite for further cycles [43, 48].

**Fig. 7.3** Charge compensation in silico-aluminate zeolites

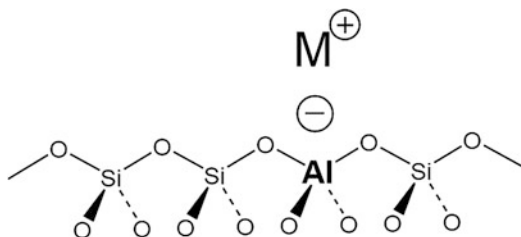




**Fig. 7.4** Classification of zeolites by their pore aperture. Left, small-pore zeolite; middle, medium-pore zeolite; right, large-pore zeolite, corresponding to LTA, EUO and FAU structures, respectively [49, 51]

However, the most important parameter in the study of zeolites as adsorbents is the presence of structural microporosity with pore apertures in the range of many molecules of industrial interest. In this sense, a clear classification has been established depending on the number of tetrahedra of the zeolite ring that gives access to its channels and cavities. Consequently, zeolites having pores accessible through rings formed by 8, 10 and 12 tetrahedra are named “small, medium and large pore zeolites”, respectively [49, 50]. Figure 7.4 shows the pore aperture of three different zeolites belonging to each class of this classification. Other zeolites having pore apertures larger than 12 tetrahedra are known as extra-large-pore zeolites.

As presented above, the main features of zeolites are polarity and pore size. These two properties can be tuned for achieving a preferential adsorption of a component of a given mixture, thus resulting in the use of zeolites as very selective adsorbents for separations of mixtures in the gas or liquid phase.

For a given separation, polarities and kinetic diameters of the different components of the mixture need to be studied for choosing the most appropriate zeolite. Separations on zeolites can be performed based on the thermodynamics or on the kinetics of the adsorption and, additionally, on the characteristic molecular-sieving effect of these microporous materials.

The most obvious selective separation is that of molecules that possess very different kinetic diameters. For instance, linear and branched hydrocarbons can be successfully separated by using small-pore zeolites as true molecular sieves. These materials allow the entrance of linear molecules into their inner space while excluding branched hydrocarbons [29, 52, 53].

Thermodynamic separations, i.e. separations of molecules with different polarities and similar kinetic diameters, have been reported on zeolites. For these separations, the tuning of the chemical composition of the zeolite is the keystone for finding the right adsorbent. As previously discussed, high-silica zeolites selectively adsorb the non-polar component of a mixture, while the polar molecule is not adsorbed; oppositely, by employing high-Al zeolites, the polar component will be

preferentially adsorbed, while the non-polar component will be less retained on the zeolite. These approaches have been successfully used for separation of CO<sub>2</sub>/CH<sub>4</sub>, water/hydrocarbons, N<sub>2</sub>/O<sub>2</sub>, etc. [19, 47, 48, 54–59].

Kinetic separations require the most subtle zeolite selection, as minor differences in the pore size can result in huge differences in diffusion. This is the case of separation of molecules that have very similar kinetic diameters and do not significantly differ in their polarities. For these separations, a precise adjustment of the pore opening must be done by controlling atom substitution in framework positions [60–63]. Other less common compositions different than aluminosilicate zeolites, such as aluminophosphate, gallophosphate, etc., provide isostructural materials with slightly different lattice parameters [64–66]. For instance, industrially relevant olefin/paraffin separations can be performed this way.

Crystal size of the zeolite has been described as a paramount parameter for controlling the final selectivity and efficiency of the process, especially in the case of separations under kinetic control [67–70]. On this regard, the influence of crystal size of MFI type of zeolites (ZSM-5 or silicalite) has been studied for different adsorbates [71].

### ***7.2.1 Swing Adsorption Processes and Working Capacity***

Zeolites were early recognized as selective adsorbents. Since the commercialization of the first synthetic zeolites by members of the Union Carbide in the 1950s [32, 72, 73], these materials have been applied to a wide variety of separation and purification processes, of which several have found their way to industrial implementation [43, 59, 74, 75]. As has been discussed before, the specific chemical and physical properties of the zeolites greatly influence their adsorptive behaviour.

The industrial use of zeolites as adsorbents was made possible by the development of pressure swing adsorption (PSA) technology in the 1960s [76], which meant a great breakthrough, as it stimulated research on adsorption processes and on new and improved adsorbents [74]. Conceptually, swing adsorption cycles are simple. A minimum number of two parallel adsorbent beds are needed. The stream to be purified or fractionated is passed through a bed of “clean” adsorbent (by clean meaning adsorbate-free and active). Once the first bed is saturated, it needs to be regenerated, and the feed stream is transferred to the second adsorbent bed. While one bed is at the desorption/regeneration step, the other is adsorbing, thus permitting a continuous operation of the process as a whole. There are different ways in which the regeneration step is carried out, which give name to the type of swing adsorption process [74]:

- Vacuum or pressure swing adsorption (VSA, PSA or VPSA) essentially exploit differences in pressure between the adsorption and the desorption steps. More specifically, in PSA processes, adsorption occurs at pressures above ambient, while regeneration is achieved by reducing pressure to ambient or slightly under

ambient. In VSA processes, the adsorption step is carried out at ambient pressure, and the regeneration is done by pulling vacuum. VPSA processes combine high-adsorption and low-desorption operational pressures.

- In temperature swing adsorption (TSA) processes, regeneration is mainly performed by heating the adsorbent bed in order to desorb the adsorbed species.

It is as well common to use purge streams or displacement adsorbates to enhance desorption [43, 74, 77, 78]. Also important to note is that there is a strong interplay between adsorbent characteristics and process design, i.e. substantially different adsorbents can be used for the same purpose if the process is well designed for the specific application [43].

One of the fundamental parameters in swing adsorption processes is the working capacity of the adsorbent, which is not only related to its maximum loading/storage capacity but also to the shape of the adsorption isotherms. The working capacity is defined as the difference between the amount adsorbed during the adsorption step and the amount that remains adsorbed at the conditions of the desorption step (see Fig. 7.5). High maximum loadings are desired, as they improve the productivity of the industrial process by minimizing the size of the adsorbent bed/column or the cycle time. However, too steep (also called square) isotherms (strong adsorbate-adsorbent interactions) may require very low pressures or high temperatures in order to achieve acceptable working capacities.

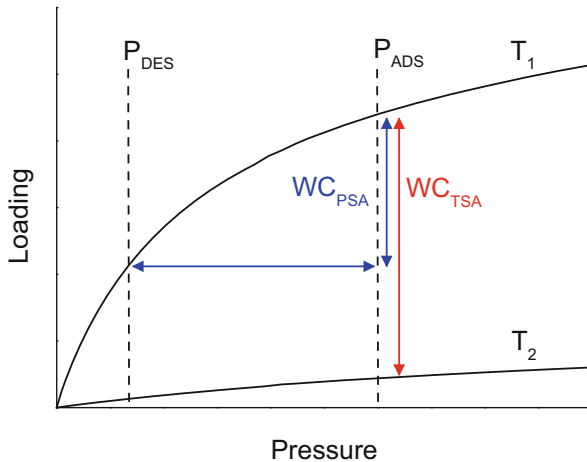


**Fig. 7.5** Example of adsorption isotherms at two different temperatures ( $T_1 < T_2$ ).  $P_{ADS}$  and  $P_{DES}$  are the adsorption and desorption step pressures of the PSA process, respectively.  $T_1$  and  $T_2$  are the adsorption and desorption step temperatures of the TSA process, respectively. The working capacity in a PSA process  $WC_{PSA}$  is the difference between the loadings at  $P_{ADS}$  and  $P_{DES}$  at working temperature. The working capacity in a TSA process  $WC_{TSA}$  would be the difference between the loadings at  $T_1$  and  $T_2$  at working pressure

## 7.3 Tailored Zeolites for Adsorption Processes

In the subsections below, we will go through some examples of zeolite-based adsorption processes that are or can be used to separate/purify commonly used chemicals, which are as follows [43, 59, 74, 75, 79]:

- Drying applications: water removal from gas streams or from liquid mixtures
- Separation of the components of air, mainly oxygen and nitrogen
- Carbon dioxide recovery from flue gases
- Methane separation and purification. Methane storage
- Separation of olefins from paraffins
- Separation of linear and ramified hydrocarbons
- Miscellaneous separation and purification applications

### 7.3.1 Drying Applications: Water Removal

As mentioned in Sect. 7.1, the Swedish mineralogist Cronstedt coined the term “zeolites” in 1756 after heating one type of these minerals (probably stellerite) and noticing its water release [80]. This is representative of the fact that these materials show high affinity towards the adsorption of water. Both natural and the first synthetic zeolites with low-silica content (i.e. high extra-framework cation content) are significantly hydrophilic [81].

Adsorbents used for drying applications need to possess a highly polar surface to which the water molecules are attracted strongly via dipole or quadrupole interactions [47]. After their commercial breakthrough in the 1950s, synthetic A and X zeolites rapidly replaced the previously used adsorbents such as silica gel and activated alumina, due to their improved capacities and selectivities at low water contents and temperatures above ambient. As a matter of fact, the first adsorption processes in which zeolites were implemented were drying operations, i.e. water removal from natural gas and air [81, 82]. The removal of water, along with CO<sub>2</sub> and sulphur compounds in the case of natural gas, prior to these processes is important to avoid plugging of heat exchangers and corrosion of the conductions [37, 43, 74]. Some examples of multiple adsorbate removal will be given throughout this chapter.

Several patents in the 1960s claimed the use of zeolites X and A for drying of gas currents. Milton proposed zeolite 4A for drying natural gas [83], as well as zeolites 5A and 13X, with larger pore sizes, for both drying and sweetening of natural gas [84]. He also showed that type X zeolites were useful for water separation from vapour mixtures [42], and shortly after he proposed type A zeolites for the same purpose [85]. Since then, the range of zeolite-based drying applications has grown markedly.

Zeolite 3A has been used for drying unsaturated hydrocarbon streams [37, 82] due to its selective size exclusion of molecules bigger than 2.9 Å, i.e. the size of water molecules. In this way, olefins will not enter the zeolite, and the possibility

of oligomerization inside the pores is avoided. This zeolite has been used as well for drying polar liquids, such as ethanol, amines, H<sub>2</sub>S or even the ethanol/water azeotrope [86–88]. Zeolite 3A has also been implemented recently in natural gas drying applications, due to its improved applicability in rapid swing adsorption processes [89]. The drying of acidic gases, such as HCl, HNO<sub>3</sub>, SO<sub>2</sub> or NO<sub>2</sub>, has been achieved with high-silica mordenite and chabazite, which remain stable in harsh environments [43]. Zeolites 3A and 4A have found a non-regenerative use in solvent drying at a laboratory scale [90].

As can be understood from the examples mentioned above, even though the use of zeolites for drying applications is not a novelty, it is also not in any way obsolete. A summary of the characteristics that have led zeolites to success in this field of application is found below.

- Both natural and the low-silica synthetic zeolites are highly hydrophilic. They show high selectivities and capacities for water.
- Chemical properties that are relevant for particular drying processes, such as stability of the material or specific interactions, can be modified in zeolites by varying the Si/Al ratio or by ion exchange.
- The pore size of these materials can be finely tuned as well, by choosing amongst the different available structures (of which zeolites A, X, mordenite and chabazite are the most popular for drying applications) and by further ion exchange [59].

### 7.3.2 *Oxygen and Nitrogen Separation*

Oxygen and nitrogen production from air at a medium and small scale can be performed using pressure-vacuum swing adsorption processes, in which the main adsorbent is a zeolite [59, 74, 81, 91, 92]. Along with the development of the commercial synthesis procedures of zeolites A and X and the possibility of pore-size tuning by cation exchange, Milton already envisaged the potential applicability of these materials in the separation of oxygen from nitrogen [73]. He proposed size exclusion of nitrogen at cryogenic temperatures by proper adjusting the pore size as the approach to this separation. However, exploiting the differences in the strength of the interactions between the cations and the adsorbates turned out to be a more effective way of achieving this separation for most applications [81, 91].

Since the 1960s, a number of patents has been published, in which zeolites, mainly type X, exchanged with different cations were compared in terms of their performance in PSA processes for air separation, focused on oxygen recovery. In the year 1964, members of the Union Carbide Corporation issued three patents entitled “Separation of an oxygen-nitrogen mixture”. In the first one, the inventor claimed the use of zeolites with pore size smaller than 4.6 Å for this application at subambient temperatures [93]. In the second one, the use of type X zeolites exchanged with divalent cations at ambient temperature was claimed, of which Sr<sup>2+</sup>-, Ba<sup>2+</sup>- and Ni<sup>2+</sup>-exchanged X zeolites were the most promising [94]. In

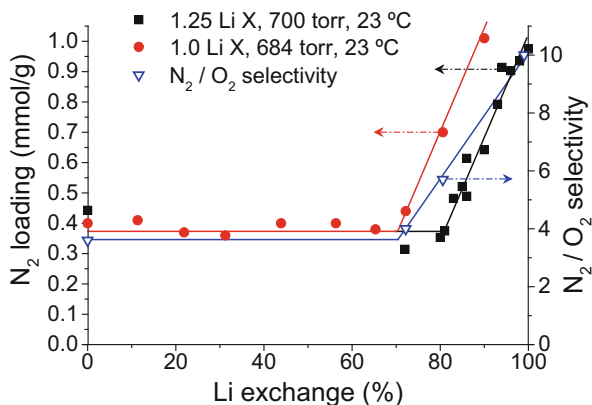


**Fig. 7.6** Nitrogen loading of zeolites Li(1.25)X and Li(1.0)X and selectivity of Li(1.0)X vs lithium ion exchange [92, 99]

the third patent, the inventor claimed the use of type X zeolites exchanged with monovalent cations at ambient temperatures, of which the  $\text{Li}^{2+}$ -exchanged material showed the best performance in terms of capacity and separation factor [91]. These three patents highlight the importance of the minimum pore size ( $>4 \text{ \AA}$ ) in this separation, in order to avoid kinetic hindrances. McKee also implied that the improved performance of some of these materials was because of the specific interactions of the exchanged cations with the quadrupole moment of the  $\text{N}_2$  molecule.

The search for an optimal adsorbent for this purpose was continued by many in the following years, mostly still considering type X zeolites exchanged with alkali or earth-alkali metal cations [95–97]. More than a few zeolite-based adsorption processes for the separation of oxygen and nitrogen from air have been developed and commercialized since then by companies such as Union Carbide Corporation, Esso Research and Engineering, Air Liquide, Praxair Technology or Air Products and Chemicals [77, 82]. The greatest breakthrough was achieved in 1989 by Chao of UOP with the discovery of LiLSX zeolite (Lithium Low Silica X) [92], which remains the preferred adsorbent for this application at the present time and has been implemented in many of the existing processes [98]. Chao based on the previously mentioned patents and the observation that there was a “loophole” with respect to the lithium-exchanged X zeolites. After carrying out a systematic study, in which both the Si/Al ratio and the extent of lithium exchange were modified, he concluded that the lowest possible Si/Al ratios and the highest lithium contents led to optimal nitrogen capacities and selectivities over oxygen (see Fig. 7.6).

As can be seen in Fig. 7.6, upon increasing the portion of Li exchange (the remaining portion being Na ions), the nitrogen loading remains approximately constant around 0.4 mmol/g up to a threshold of around 80% Li exchange for Chao’s Li(1.25)X. After this threshold is surpassed, the  $\text{N}_2$  loading increases linearly with

**Fig. 7.7** Zeolite X cell (FAU structure) and cation sites [40]

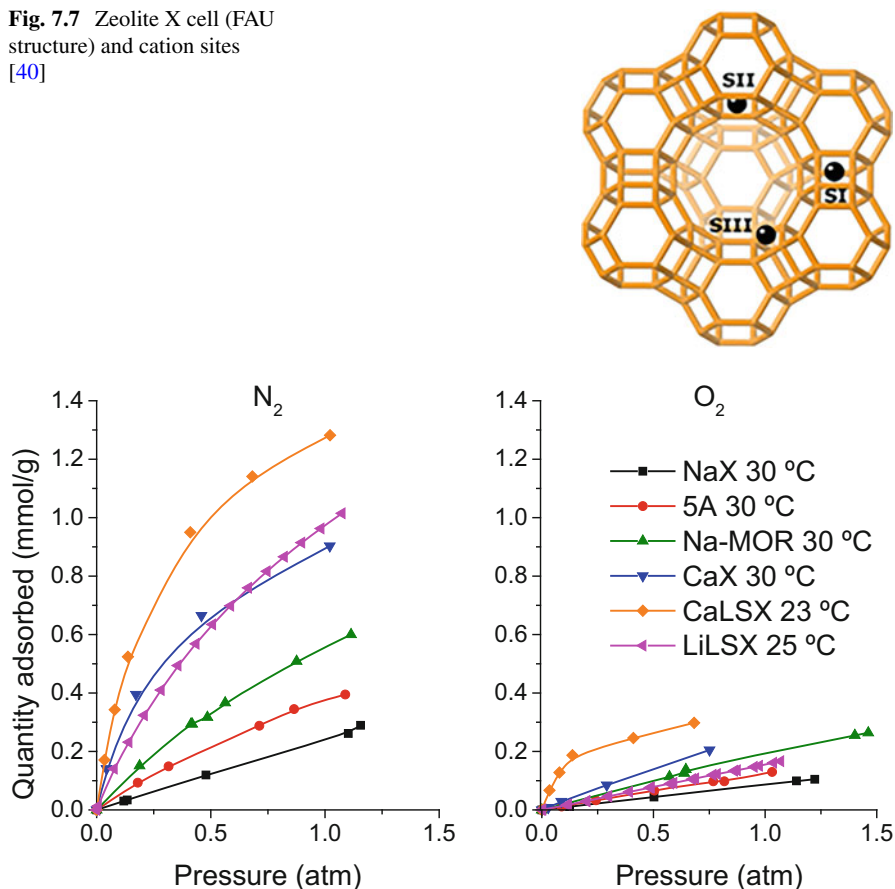


**Fig. 7.8** Adsorption isotherms of  $N_2$  and  $O_2$  on different X-type zeolites at ambient temperatures [43, 77, 102]

the increase in lithium exchange. Later works have reduced this threshold to 70% by further reducing the Si/Al ratio to 1 in Li(1.0)X. The  $N_2/O_2$  selectivity follows a very similar trend [99].

This is related to the three different types of positions that lithium ions can occupy inside zeolite cavities at each exchange extent (see Fig. 7.7). Below the aforesaid threshold, the lithium cations only substitute the sodium cations occupying the SI and SII positions. This, jointly with the fact that Li cations are available for adsorption only if they occupy SIII positions, leads to the observed trends of nitrogen capacity and selectivity with lithium exchange extent [59].

Another reason for the suitability of this material for its implementation in the separation process is the shape of its nitrogen adsorption isotherms, which present low loadings at low pressures and high loadings at high pressures (see Fig. 7.8), thus maximizing the working capacity and facilitating the desorption step in a VSA process [74, 98].

Engelhard titanosilicates, which are zeolite-related nanoporous materials with a mixed octahedral-tetrahedral framework, have been used as well for this separation. More concretely, contracted titanosilicate CTS-1 (Na,Sr-containing ETS-4 dehydrated at 300–340 °C) has been used for air separation by exploiting its molecular-sieve effect [100, 101]. This material discriminates nitrogen and oxygen by size, adsorbing O<sub>2</sub> but excluding N<sub>2</sub> at room temperature, hence recovering Milton's original idea of achieving this separation using molecular sieves.

The versatility of zeolites and other related materials as adsorbents can be appreciated in their application to the separation of the main components of air, i.e. oxygen and nitrogen. The development of the optimal adsorbent LiLSX is a beautiful example of how the adsorption properties of a zeolite can be tailored. In summary:

- A molecular sieving process with N<sub>2</sub> size exclusion was ruled out, but a minimum pore size (ca. 4 Å) for avoiding kinetic hindrances was established. The separation would be based on equilibrium adsorption, due to the specific interactions between N<sub>2</sub> and the zeolite cations.
- Type X zeolites exchanged with different cations were tested, but no striking discovery was made until LiLSX was patented by Chao.
- Maximizing the degree of exchange of Na<sup>+</sup> by Li<sup>+</sup> led to an unexpected increase in nitrogen capacity. This increase was linear above a certain threshold value. The specific interaction of N<sub>2</sub> with Li<sup>+</sup> cations led to a much higher N<sub>2</sub>/O<sub>2</sub> selectivity that had not been observed at lower exchange degrees and to an optimal isotherm shape as well.
- Further lowering the Si/Al ratio resulted in a framework with an increased number of negative charges and thus more extra-framework cations that could be exchanged by lithium. This as well decreased the lithium exchange threshold value, allowing for higher N<sub>2</sub> capacities at lower Li contents and thus lowering the cost of the adsorbent.

### ***7.3.3 Carbon Dioxide Separation and Capture***

Atmospheric CO<sub>2</sub> levels are known to be rising, and this leads to global warming due to its greenhouse effect. The consensus attained by many countries is to reduce the anthropogenic CO<sub>2</sub> emissions in order to prevent global warming to the greatest possible extent [103]. Carbon dioxide is produced in great amounts in any fossil fuel-driven process, such as transportation or energy production, and in natural gas treatment and steam reforming. The rate at which it is released is much faster than the rate at which it can be “reabsorbed” by the biosphere; thus, there is an increasing need for finding (improved) ways of consuming or sequestering and storing this carbon dioxide [104].

The relevant gas mixtures from which carbon dioxide needs to be separated at the present time are as follows:

- Pre-combustion gases from steam reforming of fossil fuels ( $\text{CO}_2/\text{H}_2$  with presence of water, CO and  $\text{CH}_4$ )
- Post-combustion gases, also called flue gases ( $\text{CO}_2/\text{N}_2$  with presence of  $\text{H}_2\text{O}$ )
- Natural gas ( $\text{CH}_4/\text{CO}_2$ , with presence of  $\text{H}_2\text{O}$ ,  $\text{H}_2\text{S}$  and light hydrocarbons)
- Landfill gas and biogas ( $\text{CH}_4/\text{CO}_2/\text{N}_2$  with considerable amounts of  $\text{H}_2\text{O}$ )

Carbon dioxide capture from pre-combustion gases is related to hydrogen purification, which will be discussed in the last section of this chapter; however, zeolites have not received much attention as adsorbents for the  $\text{CO}_2/\text{H}_2$  separation. Thus, a review on pre-combustion capture will not be presented here. The cases of natural gas and landfill gas will be presented in the next section, where the emphasis is on methane upgrading from the mentioned mixtures. In this section, we will focus on post-combustion  $\text{CO}_2$  separation.

The currently more mature technology for carbon dioxide capture from flue gases is amine scrubbing, but the associated high regeneration costs of the liquid sorbent and the corrosion of process equipment have stimulated the search of alternative methods to separate  $\text{CO}_2$  from  $\text{N}_2$  [105–108]. PSA processes based on physisorption and chemisorption of  $\text{CO}_2$  are being investigated, which use solid adsorbents like zeolites and zeolite-like materials like aluminophosphates (AlPOs) or silicoaluminophosphates (SAPOs), amine-grafted zeolites and mesoporous silicas, metal organic frameworks (MOFs), metal oxides and carbonates and carbonaceous materials [105, 109–112]. Carbon dioxide adsorbs preferentially on these materials due to its larger polarizability compared to nitrogen.

“Traditional” zeolites show a high  $\text{CO}_2$  selectivity and capacity in the presence of  $\text{N}_2$  at low pressures and moderate temperatures. Most studies of zeolite adsorbents for carbon dioxide capture from flue gases have focused on types A and X zeolites, of which 13X is considered the best candidate for post-combustion PSA [105, 109, 110, 113, 114]. However, post-combustion streams inherently contain water produced along with carbon dioxide in the combustion reaction of fossil fuels, and the same reasons which make zeolites good  $\text{CO}_2$  adsorbents yield them hydrophilic as well. Consequently, competitive adsorption of water is one of the main drawbacks of PSA processes for  $\text{CO}_2$  separation using zeolites [115]. The highly polar surface of these materials also leads to high heats of adsorption of  $\text{CO}_2$ , which can result in a difficult regeneration of the zeolite adsorbent bed, and to the formation of strongly bound carbonate-like species [116]. Furthermore, water presence can favour chemisorption of  $\text{CO}_2$  and formation of bicarbonate-like species [117, 118].

Therefore, later research, both in simulations and experimental studies, has been directed to the examination of materials with less polar surfaces which still maintain high  $\text{CO}_2/\text{N}_2$  selectivity while facilitating the desorption step (high- and pure-silica zeolites, aluminophosphates or silicoaluminophosphates) [110, 119–122]. The possibility of kinetic separations, using PSA or membrane processes, has been explored as well [108, 120, 123].

These “new-generation” zeolite-related adsorbents maintain the chemical stability of traditional zeolites and most of their structural diversity, although not all the possible compositional analogues are available for every structure [110]. The lower

heats of adsorption of CO<sub>2</sub> in these materials lead to higher working capacities at normal PSA working conditions (>5 bar) and easier regeneration steps if compared with traditional type X and A zeolites, which are already saturated with CO<sub>2</sub> at pressures below ambient due to their high affinity towards CO<sub>2</sub> [122].

Amongst the mentioned adsorbents, we can find high- and pure-silica zeolites with CHA, LTA, RHO, MFI, DDR and other structures [54, 55, 120, 121, 124–127] and aluminophosphates and silicoaluminophosphates with analogous and different structures [119, 128–130]. Titanosilicates like ETS-4 have been developed as well for CO<sub>2</sub> capture [119, 131]. It is quite noticeable that most of the cited materials, whether used for thermodynamic- or kinetic-based separation, have structures with small pore sizes (between ca. 3.5 and 4.5 Å), corresponding to eight-membered rings (8MRs). Although some of these adsorbents have been developed for CO<sub>2</sub> removal from natural gas streams, their application to carbon dioxide capture is quite related, because of the similar behaviour of nitrogen and methane when adsorbed on low-polarity materials [119, 127].

Other strategies that have been explored in CO<sub>2</sub> capture are trapdoor mechanisms and water-facilitated adsorption. Trapdoor mechanisms have been identified for Cs- and K-exchanged CHA (Si/Al = 1.9) [132, 133] and Na-, K- and Cs-exchanged RHO (Si/Al = 4.5) materials [134], which show extraordinary selectivities towards CO<sub>2</sub>. However, the regenerability of these adsorbents in process-relevant conditions has not been addressed in these works, and from the isotherm shapes, it can be seen that they will present similar problems to traditional zeolites (low working capacities in PSA due to high CO<sub>2</sub> affinity). Water-facilitated adsorption of CO<sub>2</sub> has been studied for carbon capture technology, in an attempt to turn the mentioned problematic competitive adsorption of water into something beneficial. It is inspired in the biological mechanisms of CO<sub>2</sub> transport in aqueous environments, and some zeolites have been proposed for this application [135, 136]. Nevertheless, this is still a relatively immature technology, and many practical aspects need to be considered.

As can be seen above, carbon dioxide capture is a research field still under active development, and the search of a feasible method to achieve it at a large scale has put it in the spotlight of industry and academy researchers. Separation of CO<sub>2</sub> by adsorption has been tested on different solid adsorbents, like carbons, MOFs and zeolite-like materials. Amongst these, zeolites show the greatest thermal and chemical stabilities [105, 122] and a high CO<sub>2</sub> capacity and selectivity over N<sub>2</sub>. If properly modified, the adsorption properties of these materials can be optimized for CO<sub>2</sub> capture from N<sub>2</sub>-rich streams in the presence of water:

- Compositional variants of zeolites with low-polarity surfaces, such as pure- and high-silica zeolites, AIPOs and SAPOs, circumvent or minimize problems related to traditional type X and A zeolites, like high energetic demand for regeneration, carbonate-like species formation or competitive water adsorption, which drastically reduces CO<sub>2</sub> capacity of the adsorbents.
- Furthermore, the lower heats of adsorption on these materials yield isotherms with closer to linear shapes at pressures relevant to PSA processes, thus maximizing the working capacity.

- It has been observed that most of these materials have what in zeolite science are called small pores, i.e. with sizes between ca. 3.5 and 4.5 Å, corresponding to 8MRs, as opposed to the most popular traditional 13X zeolite.
- The higher synthesis cost of tailor-made materials has probably led to the disregard of their promising characteristics in many of the existing reviews on CO<sub>2</sub> capture by adsorption [105, 109, 111–114, 122].

### 7.3.4 Methane Purification and Storage

#### 7.3.4.1 Methane Purification

Methane is a compound primarily obtained from natural gas, which is used as a fuel for energy production. In 2014, 22% of the world's electricity was produced by natural gas, and this dependence on natural gas is expected to grow in the coming years [137].

Natural gas is extracted from underground deposits, where it can be found along with oil. The composition of natural gas is variable (see Table 7.1) [138–140].

Coalbed methane and landfill gas or biogas are other possible methane sources [141, 142]. Coalbed methane is found along with coal deposits and is mainly made up of methane (50–99%, typically >80%), with minor amounts of nitrogen, CO<sub>2</sub>, light hydrocarbons, H<sub>2</sub>S and SO<sub>2</sub>. However, its composition varies largely depending on the specific coalfield [142–145]. Landfill gas and biogas are produced from human activity-derived waste decomposition. Both are produced in anaerobic digestion processes that take place in landfills (solid waste) or sewage plants (waste water). The composition of landfill gas is variable as well (see Table 7.1), the main components being methane, CO<sub>2</sub> and nitrogen.

**Table 7.1** Composition of natural gas and landfill gas [138, 139, 141]; note that these values may vary depending on the deposit or the kind of waste anaerobically digested, respectively

Component	Natural gas, volume fraction (%)	Landfill gas, volume fraction (%)
Methane	55–98%	35–60%
Carbon dioxide	0.2–30%	35–55%
Ethane	0.1–20%	200–14000 ppmv
Propane	0.05–12%	
Other light hydrocarbons	0.1–7%	
Nitrogen	0.1–0.5%	0–20%
Oxygen	0.09–0.3%	0–2.5%
Hydrogen sulphide	Traces–28%	1–1700 ppmv
Helium	Traces–4%	–
Carbon monoxide	Traces	–
Water	NA <sup>a</sup>	1–10%

<sup>a</sup>Although water levels are not given in these references, natural gas contains water that has to be removed prior to its transport and processing [140]

These methane-rich gas mixtures have to meet several requirements before being used or transported as liquefied natural gas (LNG) or over pipelines. Gases with no heating value that are major contaminants in these mixtures (mainly  $N_2$  and  $CO_2$ ) have to be kept below specific levels in order to improve the heating value of the mixture. Water,  $CO_2$  and other impurities, such as  $H_2S$ , have to be removed to avoid corrosion and plugging of the equipment used for the processing and transportation. Hydrocarbons with chains of more than three carbon atoms ( $C_{3+}$ ) can cause plugging problems as well and need to be separated, even though they increase the heating value of the mixture [48, 140, 146]. The specifications for contaminants in the feed for LNG production are far more stringent than those for natural gas pipelines [140, 147].

Depending on the source (main contaminants), the production scale and the transport method (as LNG or over pipelines), the processes used for methane upgrading may vary. The usual processing order starts with acid gas removal and then drying and, finally,  $C_{3+}$  hydrocarbon and nitrogen separation. Large-scale production, especially of LNG, accounts for the use of techniques with high operational cost such as cryogenic distillation for nitrogen, helium and  $C_{3+}$  hydrocarbon rejection, aqueous amine scrubbing for simultaneous  $CO_2$  and  $H_2S$  removal or scrubbing with triethylene glycol for water removal [147]. However, middle- and small-scale production along with methane upgrading from highly contaminated gas streams embody notable opportunities for adsorption-based processes (mostly PSA) to be implemented, due to their great operational flexibility [48, 146, 148]. Zeolites have been reportedly used for the removal of all of these contaminants from methane-rich gas mixtures. Drying of gas mixtures on zeolites has been already discussed in Sect. 7.3.1. Below,  $CO_2/CH_4$ ,  $N_2/CH_4$  separations and sulphur-containing compound and  $C_{3+}$  hydrocarbon removal by adsorption on zeolites will be discussed.

Carbon dioxide separation from methane has been performed in PSA processes on a wide range of zeolitic materials, such as traditional A, X and Y zeolites [57, 58]; other synthetic zeolites, such as silicalite or mordenite [149]; natural zeolites, such as clinoptilolite [150]; or titanosilicate materials, such as ETS-4 [48, 131]. This separation has been studied and rationalized as well in many academic works, and analogous to the case of  $CO_2$  capture from  $N_2$ -rich streams, tailor-made materials are promising. Medium-, high- and pure-silica zeolites with RHO [55], LTA [54], CHA [151], AEI, STT, RRO [152] and FAU [148] structures, along with SAPOs and AlPOs with analogous and different structures [153, 154], have been found having promising  $CO_2/CH_4$  selectivities and optimal  $CO_2$  heats of adsorption (27–32 kJ/mol) [148]. Computational studies have been carried out, which also focus on screening of materials with low-polarity surfaces and optimization of PSA processes using them [155]. As in the case of  $CO_2$  capture from flue gas, medium- and small-pore zeolites are most frequently addressed.

Nitrogen separation from methane-rich mixtures by adsorptive methods is problematic because of the fact that essentially all known adsorbents present a higher affinity towards methane. This stronger interaction with the solid is due to the higher polarizability of methane, if compared to nitrogen [43, 48, 156]. Swing adsorption processes in which methane is preferentially adsorbed over nitrogen seem less

practical, because of the larger bed size required. However, the  $N_2$  molecule (3.64 Å) is slightly smaller than the  $CH_4$  molecule (3.80 Å) [37], which makes it possible to find an adsorbent with appropriate pore size, so that either molecular sieving takes place or a sufficiently high difference in the adsorption rates of both species allows for their separation [156].

Kinetic separation of a  $CH_4/N_2$  mixture over zeolite 4A was studied and patented by Habgood shortly before this material's synthesis was patented [157, 158]; still, the regeneration step rendered the process unviable. Natural clinoptilolites have been proposed as kinetically selective sorbents by Frankiewicz and Donnelly [159] in their "raw" and Ca-exchanged forms. Chao patented their Mg-exchanged form for their use in a PSA process, although no process details are given [160]. Titanosilicates like ETS-4 and thereof derived materials (CTS-1, Ba-ETS-4, Sr-ETS-4) have proven to be very well suited for nitrogen removal in PSA units [100, 156] and have been implemented, as a part of the Molecular Gate™ technology, developed by Engelhard Corporation (now BASF) [48, 161]. These materials consist of an octahedral-tetrahedral framework with narrow 8MR openings, whose size can be tuned by ion exchange or thermal treatment. Controlled thermal treatment results in their contraction, thus yielding "contracted" titanosilicates, such as CTS-1.

Hydrogen sulphide and organosulfur compounds are present in many natural gas and oil deposits. Natural gas sweetening is of high importance to prevent corrosion of pipelines and materials used in processing and transportation. Furthermore,  $H_2S$  is highly toxic, and its emissions to the atmosphere are regulated; thus, it has to be removed from natural gas and properly eliminated or recovered for sulphur production [140]. Zeolites 4A and 5A have been used for  $H_2S$  removal, presenting problems such as competitive  $CO_2$  and water adsorption and high regeneration energy requirements [140]. Zeolites of the types X and Y have been evaluated for  $H_2S$  and organosulfur compound removal as well [162–164]. However, all these materials not only do readily adsorb  $H_2S$ ,  $CO_2$  and  $H_2O$  but favour the formation of carbonyl sulphide (COS) if both hydrogen sulphide and carbon dioxide are present at usual bed regeneration temperatures ( $CO_2 + H_2S \rightarrow COS + H_2O$ ) by adsorbing the water formed in the reaction, thus displacing the equilibrium towards COS formation [140, 165, 166]. Hydrophobic materials such as high-silica and pure-silica zeolites have been studied both in simulation and experiments, and they seem promising in this sense. Furthermore, the  $H_2S$  heat of adsorption is reduced in comparison with traditional zeolites while maintaining high  $H_2S/CH_4$  selectivities, thus making regeneration easier. Suitable candidates from these studies are Si-CHA and silicalite [167–169]. Titanosilicates, especially ETS-2, have been as well proposed as highly selective  $H_2S$  sorbents [170, 171]; however, no mention to regeneration is made in these works.

There is only a limited amount of works in the open literature on separation of hydrocarbons other than methane (and especially  $C_{3+}$  fractions) from natural gas streams using zeolites. However, a recent systematic study [146] presents zeolites KY, KX and 5A as suitable candidates for this application. Titanosilicate material ETS-10 has been studied for ethane extraction from natural gas [172]; however, this

may be desirable only in limited cases, as ethane increases the heating value of the gas mixture. The possibility of using a silicalite membrane for the separation has been addressed as well [173].

### 7.3.4.2 Methane Storage

With the fast development of the worldwide economies, energy consumption and its impact on the environment have become important concerns. The strong dependence on crude oil and oil depletion on the midterm horizon and its effect on the global warming have boosted the efforts to develop alternative and cleaner fuels. Natural gas, mainly constituted by methane, has been pointed out as an alternative fuel due to its natural abundancy, high octane number (RON = 107) and low CO<sub>2</sub> emissions related to its H/C ratio, the highest amongst the hydrocarbons. However, one of the key points to overcome is the low energy density of methane gas under ambient conditions, compared to conventional liquid fuels. For this reason, it is much more desirable to transport and use natural gas as liquefied (LNG) or compressed (CNG), as an alternative to traditional liquid fuels, like gasoline or diesel in the automotive industry. In this context, LNG at -161 °C has a density around 600 times greater than that of natural gas, with an energy density of approximately 72% of that of gasoline. On the other hand, CNG at 200 bar (3000 psi) and room temperature has a density 230 times greater than that of natural gas and an energy density of 26% with respect to that of gasoline [174]. The main drawbacks of LNG and CNG are the use of cryogenic temperatures and the high-energy demand for compressing the gas, respectively. Also, safety concerns for light-duty vehicles must be taken into account for CNG. Thus, the use of adsorbed natural gas (ANG) has been widely studied as an efficient and safer alternative to transport and storage of natural gas on porous materials.

The US Department of Energy (DOE) raised the threshold adsorption capacity for a suitable methane adsorbent to 315 cm<sup>3</sup> (STP)/cm<sup>3</sup> at 298 K and 65 bar and a gravimetric capacity of 50 wt% [175], encouraging research groups in academia and industry to develop adsorbents that fulfil these ambitious requirements.

When ANG technologies started to arise as an alternative to conventional fuels, zeolites belonged to the materials firstly studied [176] due to its high thermal and chemical stability, well-developed synthesis routes and narrow and tuneable pore size distribution. The acquired knowledge in methane adsorption opened the door to new families of adsorbents, comprising advanced carbonaceous materials, metal-organic frameworks (MOFs), zeolitic imidazolate frameworks (ZIFs), porous polymer networks (PPNs) and covalent organic frameworks (COFs) [177–183].

Key points in the storage of methane are the specific surface area and the micropore volume of the adsorbent. As a rule of thumb, the higher the micropore volume, the larger the methane storage capacity. Most of the known microporous adsorbents lie on a relatively narrow band of data points in a plot of adsorption capacity at 35 bar and 298 K as a function of the surface area, as shown in Fig. 7.9.

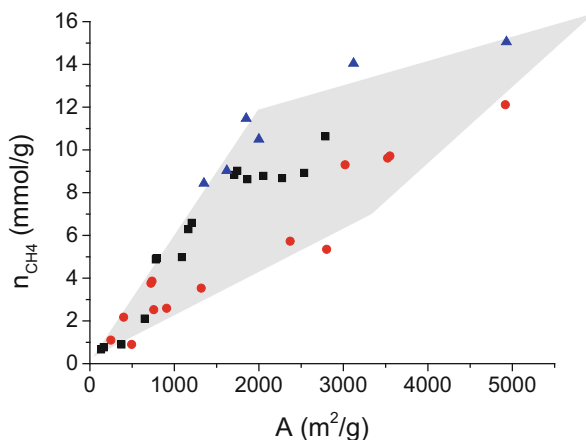


**Fig. 7.9** Methane adsorbed amount at 35 bar and 298 K as a function of the accessible surface area. Black squares [184]; red circles [178]; green triangles [185]

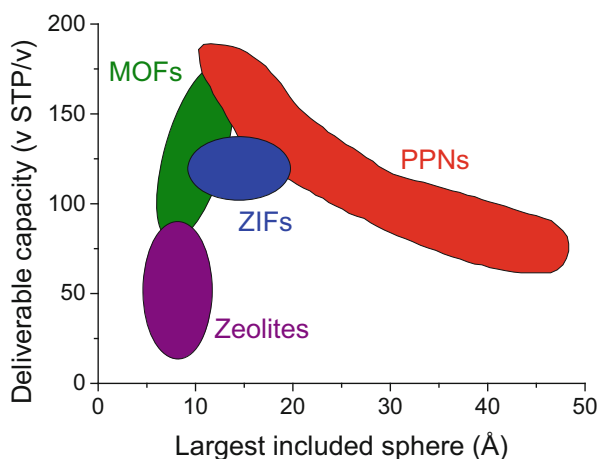


**Fig. 7.10** Deliverable methane capacity and the largest included sphere diameter. Adapted from [186]

However, theoretical calculations indicate that a maximum in the working capacity for methane is found in materials with a pore diameter of 11 Å [186], as seen in Fig. 7.10, as the interaction between methane and the solid adsorbent is enhanced due to the confinement effect [187].

Methane has no permanent dipole or quadrupole moment. For this reason, its adsorption strength or heat of adsorption is very little influenced by the polarity of the zeolite or the nature of the compensating cations. For a series of ion-exchanged Y and X zeolites, the initial heat of adsorption only varies from 18.2 to 24.58 kJ/mol [188, 189]. In fact, the high hydrophilicity of cationic zeolites is detrimental for

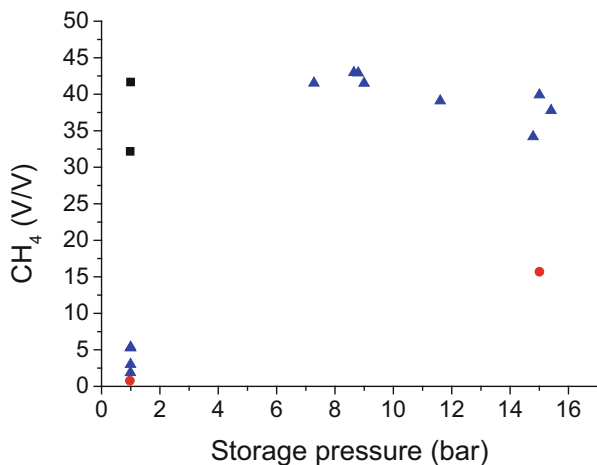


**Fig. 7.11** Black squares, nanovalved MCM-48-5A; green triangles, MOFs; red circles, bulk methane. (See Ref. [191] for additional information)

methane storage due to the preferential adsorption of water and polar species, with the consequent loss in storage capacity with cycling. Thus, the use of pure- or high-silica zeolites is highly desirable, thus increasing the regenerability of the adsorbent [190].

Unconventional novel materials based on zeolites have also been studied for methane storage. For instance, zeolite 5A beads are coated with a mesoporous amorphous silica layer of MCM-48 [191], in which the outer layer acts as a nanovalve that can be closed by adsorbing 2,2-dimethylbutane. The coated beads adsorb 200% more methane than the bare 5A zeolite beads, reaching adsorption capacities similar to those reported for MOFs (see Fig. 7.11).

As can be concluded from the above, the main challenge to be overcome in the use of zeolites for methane storage is their low adsorption capacity if compared with other adsorbents (MOFs, carbons). Other issues relevant to methane storage on zeolites are the conformation of the final adsorbent and hereto related the zeolite-binder interaction and cumulative adsorption of high  $C_n$  hydrocarbons during consecutive adsorption/desorption cycles and heat transfer.

### 7.3.5 Olefins from Paraffins

Light olefins constitute a highly demanded feedstock in industry for obtaining many chemicals and value-added products, as well as high octane number fuels. The required separation of olefins from paraffins is one of the most energy-consuming processes in the petrochemical industry, as it is currently carried out by cryogenic distillation due to the close kinetic diameters and boiling points of the molecules

[192]. The total energy used during ethylene and propylene separations has been recently reported to account for more than 0.3% of the global energy consumption [79]. Therefore, alternative separation procedures aiming to reduce the economic cost and increase energy savings are highly desirable.

In this sense, the use of zeolites as selective adsorbents able to separate olefins from paraffins constitutes a convenient approach. Cationic aluminosilicate zeolites [65, 193–196] and exchanged with Cu and/or Ag cations [197–200], silicoaluminophosphates [70, 201], neutral aluminophosphates [65, 66, 202] and purely siliceous zeolites [62, 70, 203–207] have been reported as selective adsorbents for the separation of olefins from paraffins, in particular propylene from propane. The use of neutral molecular sieves instead of aluminosilicate zeolites has the benefit of avoiding the blockage of the porosity due to oligomerization of the olefins on the acid sites, which are absent in these zeolites. This also leads to an increase of the lifetime of the adsorbent and the robustness of the process as a whole. The absence of acidity also contributes to the hydrophobicity of these materials, thus avoiding problems due to competitive water adsorption in case the adsorbate stream is not entirely dry. From the above, it seems that uncharged molecular sieves (i.e. pure-silica zeolites and aluminophosphates) are the most promising materials for carrying out the separation of olefins from paraffins.

Zeolitic materials can separate olefins from paraffins based on kinetic effects or by taking benefit of their molecular sieve nature as differences in polarity are not significant. In this sense, amongst the existing zeolites, those having small-pore aperture possess the adequate pore size and therefore are very useful for this separation. Pure-silica small-pore zeolites, such as chabazite, ITQ-12, decadodecasil DD3R and ITQ-32, have shown encouraging results in the kinetic separation of propylene from propane [62, 70, 204–208]. In addition, the separation of linear butenes from butane has also been reported for CHA structure in the purely siliceous and aluminophosphate compositions, in ITQ-32 and RUB-41 zeolites [62, 64, 209].

Regardless of the promising results reported for kinetic separations of light olefins from paraffins using pure-silica zeolites [70], to the best of our knowledge, none of these materials are currently applied in industry. This is possibly due to the increased costs in the preparation of these materials when compared to conventional aluminosilicates and the necessity of increasing the adsorption rates for achieving faster separation processes.

Moreover, the pore opening of the zeolites can be controlled with a resolution better than 0.1 nm allowing the separation of molecules with close kinetic diameters, and these materials have been traditionally considered as essentially rigid solids when compared to other microporous materials such as MOFs. However, this is not completely true as was already reported for several zeolites that undergo structural changes during dehydration, such as rho, chabazite and silicalite [210–215]. Interestingly, the structural flexibility can play a significant role on the separation, as occurs in the case of aluminosilicate zeolite Rho for the CO<sub>2</sub>/CH<sub>4</sub> separation, in which a unit cell expansion and cation movement take place during adsorption of CO<sub>2</sub> increasing the uptake [55, 134, 216, 217]. However, the effect of zeolite framework flexibility on olefin/paraffin separation has been scarcely reported [63, 218].

For instance, it has been observed that Si-ITQ-29 (LTA structure) is able to kinetically separate propane from propylene, while Ge-ITQ-29 is not. The structural analysis of both materials indicates that there is practically no difference in the pore opening of the windows that give access to the cavities of zeolites ITQ-29. Also, crystal sizes of both materials were very close to each other. By applying advanced computational techniques including framework vibration to the study of molecular diffusion, it was possible to understand this unusual behaviour. The results showed that Ge incorporation into the zeolite framework increases the structural flexibility of the zeolite, resulting in a broader range of pore aperture during thermal vibration. Therefore, Ge-ITQ-29 allows the entrance of propane and propene inside its porosity, while Si-ITQ-29 hinders the entrance of propane but not propene due to its lower flexibility [63].

A very similar approach has been applied to understand the unusual behaviour of the very challenging ethylene/ethane separation on a new zeolite, named ITQ-55. In this case, the tortuosity of the channel system combined with the right flexibility of the ITQ-55 framework allows the very effective separation of ethylene from ethane with the highest selectivity ever reported for a non-ionic porous material [219].

As a consequence, it can be concluded that besides the adequate pore aperture and properties of the zeolite adsorbent, the structural flexibility may affect also the adsorption behaviour in separation processes of molecules with very close kinetic diameters by taking advantage of the thermal vibration of the framework which could act as a “molecular trapdoor” mechanism.

### 7.3.6 *Linear from Branched Hydrocarbons*

The separation of linear from branched hydrocarbons (or normal from isoparaffins) was one of the first major industrial successes of zeolites as molecular sieves [75, 82]. The main purpose of this separation is gasoline upgrading, i.e. increasing the octane number by (partly) removing n-paraffins. The separated n-paraffins can be used as raw materials for manufacturing diverse chemicals, such as detergents.

The critical diameter of these species is around 4.5 Å for linear and >5.5 Å for branched paraffins [220], which means that size exclusion of the latter can be exploited for the separation of mixtures if a suitable adsorbent is found. The first time that this separation was attempted on a zeolite was by Barrer [221, 222]. He used natural and synthetic chabazite and recognized some of the limitations of his system, such as difficult thermal regeneration without the use of a displacement adsorbate or oligomerization if olefins were present. He, as well, rationalized the dependences of the diffusion ( $\text{CH}_4 \approx \text{C}_2\text{H}_6 > \text{C}_3\text{H}_8 > \text{C}_4\text{H}_{10}$ , etc.) and the adsorption affinity of the linear paraffins in the zeolite with their chain length. These trends were opposing, thus indicating the possibility of obtaining different products depending on the process arrangement. Similar observations were made later on different type X and Y zeolites [223] and on 5A zeolite [224]. The effects of material polarity (Si/Al ratio) and pore size on adsorption have been studied as well on a range of materials [52, 225].

At an industrial level, this separation has been achieved on zeolite 5A (window size around 4.4 Å) by different processes, each of them optimized for a certain fraction. Union Carbide's IsoSiv process is a VSA process designed for the separation of light fractions (C<sub>5</sub>–C<sub>12</sub>) [75, 226]. For heavier fractions (C<sub>10+</sub>), vacuum pulling is not enough to desorb the linear paraffins adsorbed, and normal TSA would cause cracking of the adsorbed species at usual regeneration temperatures. Thus, processes, such as Exxon's Ensorb process, have been developed, in which desorption is carried out at lower temperatures (260–370 °C) and aided by a displacer species, such as NH<sub>3</sub> [75, 78, 227]. UOP's Molex process also separates the paraffin C<sub>10</sub>–C<sub>14</sub> fraction from the non-paraffins [228]. Further examples of processes for this separation include Texaco's T.S.F process, Shell's process, BP's process and VEB Leuna-Werke's process [82]. Other adsorbents that have been patented for this separation are type X and Y zeolites and silicalite [229–232].

### 7.3.7 Diverse Separation and Purification Applications

This section includes some interesting applications which are not as extended as the ones explained above but which are worth mentioning, as the versatility of zeolites and related materials is clearly shown.

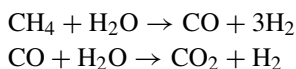
#### 7.3.7.1 Non-polar Molecules from Aqueous Mixtures

It may sound surprising to attempt to selectively adsorb non-polar molecules from aqueous mixtures using zeolites, whose first and most characteristic application was in drying, but the development of high- and pure-silica zeolites with hydrophobic surfaces opened up this attractive possibility [44].

Production of alcohols from fermentation broths requires their separation from water and the other components of the mixture. Distillation, which is the traditional way of performing this separation, is an energy-intensive technique, and due to that, alternative methods have been proposed, such as solvent extraction, adsorption, membrane processes or combinations of these with distillation [233–235]. Silicalite was discovered as one of the first pure-silica molecular sieves, and its hydrophobicity was inexorably recognized as useful for the mentioned separation applications [44]. In particular, separation of 1-butanol and ethanol from water was achieved using this material [236, 237], and further modifications, such as synthesis in fluoride media (to lower the concentration of hydrophilic silanol groups) or synthesis as membranes, have improved their original selectivity [238, 239]. On the other hand, the combination of ITQ-29 and SAPO-34 materials (pure-silica LTA and SAPO-CHA, respectively) in consecutive beds has permitted to isolate butanol from the ABE fermentation (acetone-butanol-ethanol) vapours with excellent purity and recovery [240].

### 7.3.7.2 Hydrogen Purification

Hydrogen is mainly produced in refineries in reforming processes of fossil fuels, especially steam methane reforming [241]. The reactions that usually take place are the steam-reforming reaction itself and the water-gas shift reaction [242]:



The process off-gas is a stream that typically contains 70–80% H<sub>2</sub>, 15–25% CO<sub>2</sub>, 3–6% CH<sub>4</sub>, 1–3% CO and trace N<sub>2</sub> and is saturated with water [243]. This hydrogen-rich stream is the feed of a multicolumn PSA process from which a 99.999% pure H<sub>2</sub> product gas can be obtained with a recovery of 86% [243, 244]. This PSA uses two adsorbents in each bed, arranged in two layers. The first layer consists of activated carbon, which removes the water, carbon dioxide and most of the methane impurities. The second layer consists of zeolite 5A and selectively separates CO and N<sub>2</sub> from the gas. Even though zeolite 5A could selectively adsorb CO<sub>2</sub> and H<sub>2</sub>O from the stream as well, the regeneration of the zeolite would require by far more energy than that of the activated carbon. The high N<sub>2</sub>/H<sub>2</sub> selectivity on the zeolite is another reason for the success of this process [43]. If CO<sub>2</sub> is to be recovered (pre-combustion carbon capture), the most usual approach is absorption in a physical solvent [106], although multibed PSA methods for the simultaneous production of H<sub>2</sub> and CO<sub>2</sub> have as well been reported using combinations of carbons and zeolite 5A as the adsorbents [245].

### 7.3.7.3 Trace Carbon Monoxide Removal from Air

Zeolites can be modified by ion exchange in order to modify the interaction strength with specific adsorbates. If a suitable cation is exchanged, even chemisorption can take place. Chemisorption infrequently is the choice because of the strong and specific interaction that is established between the adsorbate and the adsorbent, which yields high regeneration costs. In fact, the vast majority of the above-presented applications are driven by physisorption. Nonetheless, some products of high added value account for higher production costs if required.

The use of ultrahigh purity gases in many industries and especially the electronic industry requires that the levels of some contaminants, such as carbon monoxide or hydrogen, are reduced to low ppb levels [59]. Silver-exchanged X zeolites have been applied for the removal of CO, H<sub>2</sub> and light olefins from air, as a prepurifying stage in the production of ultrahigh purity nitrogen [246]. In this case, the interaction is specific between the Ag<sup>+</sup> cations and the molecules and can be explained as a  $\pi$ -complexation. Gold and copper cations were initially considered as well, but Au<sup>+</sup> was rejected for cost reasons, and Cu<sup>+</sup> did not disperse well on the zeolite and could present oxidation problems at the regeneration step. Commercial samples of 13X, LiLSX and clinoptilolite zeolites were tested as well, but immediate breakthrough

of the contaminants was observed. The exchange, washing, drying and thermal activation procedures of the AgX materials were optimized for large-scale operation as well. Si/Al ratios lower than 10, exchanges above 80% and minimal excess of Ag are the optimal characteristics. The thermal activation procedure has to be controlled in order to keep at least 85% of micropore volume. The resulting materials achieve large breakthrough times and high working capacities [59].

## 7.4 Conclusions and Perspectives

The trajectory of zeolites in their use as adsorbents and some of their industrially established and other applications under development have been reviewed. Zeolites and other related materials have been presented as very efficient and selective adsorbents, whose properties can be finely tuned and even tailored for specific purposes. In several of the applications presented, pure-silica zeolites and other less polar zeolitic materials appear as the most promising. Nonetheless, traditional separation technologies and processes are firmly settled and optimized, and unless there is an opportunity of significant improvement with high chances of success, no risks are taken by the industry.

In relationship with this, we consider that efforts should be made in order to lower the manufacture costs of zeolites and especially pure-silica zeolites and other hydrophobic zeolitic materials, whose production is not affordable by current methods at an industrial scale. Another focus of research should be to increase the thermal conductivity of these adsorbents, as this would enhance efficiency in both adsorption and regeneration steps and open up a way of further lowering operation costs.

Moreover, improvements in the rate of diffusion of the adsorbates in certain applications, while maintaining selectivity, are highly desirable. For instance, the kinetic separation of olefins from paraffins ( $C_2$  and  $C_3$  fractions) using pure-silica zeolites would be much less expensive if diffusion of the olefin were faster. In this sense, the synthesis of nanocrystalline zeolites, i.e. zeolites with crystals with sizes in the nanometre scale, could lead to a better pore accessibility and faster adsorption kinetics. One foreseeable problem of this approach is a drop in the selectivity of the adsorbent, as a larger portion of its adsorbing surface would be external and not derived from its structural porosity. A way to overcome this decrease in selectivity while still improving the kinetics of the process is the use of zeolitic membranes, in which only certain adsorbates would permeate the membrane in significant amounts in the relevant process times. Again, disadvantages related to the use of zeolitic membranes are their challenging and expensive manufacture.

Additionally, we have reasons to believe that a number of truly striking separations, such as hydrogen isotope separation, ethylene/acetylene and the  $C_4$  and  $C_5$  fraction separation, particularly aimed towards butadiene and isoprene production, show potential for their feasibility using zeolitic adsorbents.

**Acknowledgements** The authors thank the Spanish Ministry of Economy, Industry and Competitiveness for its funding by means of the projects (MAT2015-71842-P MINECO/FEDER and Severo Ochoa SEV-2016-0683). EPB acknowledges the Spanish Ministry of Education, Culture and Sport for the FPU grant FPU15/01602.

## References

1. Cronstedt AF (1756) Om en obekant bärg art, fom kallas Zeolites. Kongl Vetenskaps Acad Handl 17:120–123
2. Colella C, Gualtieri AF (2007) Cronstedt's zeolite. Microporous Mesoporous Mater 105:213–221. <https://doi.org/10.1016/j.micromeso.2007.04.056>
3. Galli E, Alberti A (1975) The crystal structure of stellerite. Bull Soc Fr Minéral Cristallogr 98:11–18
4. Damour MA (1840) Sur quelques minéraux connus sous le nom de quartz résinite. Ann Min 17:202
5. Sainte-Claire-Deville MH (1862) Reproduction de la Lévyne. C R Acad Sci 54:324–327
6. Eichhorn H (1858) Ueber die Einwirkung verdünnter Salzlösungen auf Silicate. Ann Phys Chem 181:126–133. <https://doi.org/10.1002/andp.18581810907>
7. Gans R (1905) Zeolithe und ähnliche Verbindungen, ihre Konstitution und Bedeutung für Technik und Landwirtschaft. Jahrb der Königlich Preuss Geol Landesanstalt 26:179–211
8. Gans R (1909) Alumino-silicate or artificial zeolite. US Patent 943,535
9. Gans R (1906) Konstitution der Zeolithe, ihre Herstellung und technische Verwendung. Jahrb der Königlich Preuss Geol Landesanstalt 27:63–94
10. Friedel G (1896) Sur quelques propriétés nouvelles des zéolithes. Bull la Société Française Minéralogie 19:94–118
11. Grandjean MF (1909) Étude optique de l'absorption des vapeurs lourdes par certaines zéolithes. C R Acad Sci 149:866–868
12. Weigel O, Steinhoff E (1924) IX. Die Aufnahme organischer Flüssigkeitsdämpfe durch Chabasit. Zeitschrift für Krist - Cryst Mater:61. <https://doi.org/10.1524/zkri.1924.61.1.125>
13. Pauling L (1930) XXII. The Structure of Sodalite and Helvite. Zeitschrift für Krist - Cryst Mater 74:213–225. <https://doi.org/10.1524/zkri.1930.74.1.213>
14. Pauling L (1930) The structure of some sodium and calcium aluminosilicates. Proc Natl Acad Sci 16:453–459. <https://doi.org/10.1073/pnas.16.7.453>
15. Taylor WH (1930) I. The structure of analcite (NaAlSi<sub>2</sub>O<sub>6</sub> · H<sub>2</sub>O). Zeitschrift für Krist - Cryst Mater 74:1–19. <https://doi.org/10.1524/zkri.1930.74.1.1>
16. McBain JW (1932) V. Sorption by chabasite, other zeolites and permeable crystals. In: The sorption of gases and vapors by solids. G. Routledge & Sons, London
17. Rees LVC (1998) Richard Maling Barrer. Biogr Mem Fellows R Soc 44:37–49. <https://doi.org/10.1098/rsbm.1998.0003>
18. Barrer RM, White EAD (1952) 286. The hydrothermal chemistry of silicates. Part II. Synthetic crystalline sodium aluminosilicates. J Chem Soc:1561–1571. <https://doi.org/10.1039/jr9520001561>
19. Barrer RM (1938) The sorption of polar and non-polar gases by zeolites. Proc R Soc A Math Phys Eng Sci 167:392–420. <https://doi.org/10.1098/rspa.1938.0138>
20. Barrer RM (1941) Migration in crystal lattices. Trans Faraday Soc 37:590. <https://doi.org/10.1039/TF9413700590>
21. Barrer RM (1948) 33. Synthesis of a zeolitic mineral with chabazite-like sorptive properties. J Chem Soc 127. <https://doi.org/10.1039/jr9480000127>
22. Barrer RM, Riley DW (1948) 34. Sorptive and molecular-sieve properties of a new zeolitic mineral. J Chem Soc 133. <https://doi.org/10.1039/jr9480000133>

23. Barrer RM, Robinson DJ (1972) The structures of the salt-bearing aluminosilicates, Species P and Q. *Z Krist* 135:374–390
24. Meier WM, Kokotailo GT (1965) The crystal structure of synthetic zeolite ZK-5. *Z Krist* 121:211–219
25. Parise JB, Shannon RD, Prince E, Cox DE (1983) The crystal structures of the synthetic zeolites (Cs, K)-ZK5 and (Cs, D)-ZK5 determined from neutron powder diffraction data. *Z Krist* 165:175–190. <https://doi.org/10.1524/zkri.1983.165.1-4.175>
26. Barrer RM, Denny PJ, Flanigen EM (1967) Molecular sieve adsorbents. US Patent 3,306,922
27. Barrer RM, Villiger H (1969) Probable structure of zeolite Omega. *J Chem Soc D Chem Commun* 659. <https://doi.org/10.1039/c29690000659>
28. Barrer RM (1949) Preparation of some crystalline hydrogen zeolites. *Nature* 164:112–113. <https://doi.org/10.1038/164112a0>
29. Barrer RM (1978) Zeolites and clay minerals as sorbents and molecular sieves. Academic, London
30. Flanigen EM, Rabo JA (2001) A tribute to Robert Mitchell Milton, zeolite pioneer (1920–2000). *Microporous Mesoporous Mater* 47:119–123. [https://doi.org/10.1016/S1387-1811\(01\)00301-8](https://doi.org/10.1016/S1387-1811(01)00301-8)
31. Breck DW, Eversole WG, Milton RM et al (1956) Crystalline zeolites. i. The properties of a new synthetic zeolite, type A. *J Am Chem Soc* 78:5963–5972. <https://doi.org/10.1021/ja01604a001>
32. Breck DW, Eversole WG, Milton RM (1956) New synthetic crystalline zeolites. *J Am Chem Soc* 78:2338–2339. <https://doi.org/10.1021/ja01591a082>
33. Reed TB, Breck DW (1956) Crystalline zeolites. II. Crystal structure of synthetic zeolite, type A. *J Am Chem Soc* 78:5972–5977. <https://doi.org/10.1021/ja01604a002>
34. Rabo JA, Pickert PE, Boyle JE (1968) Hydrocarbon conversion catalysts. US Patent 3,367,885
35. Rabo JA, Pickert PE, Boyle JE (1966) Hydrocarbon conversion process with the use of a Y type crystalline zeolite. US Patent 3,236,762
36. Rabo JA, Pickert PE, Boyle JE (1964) Decationized molecular sieve compositions. US Patent 3,130,006
37. Breck DW (1974) Zeolite molecular sieves: structure, chemistry and use, Wiley, New York
38. Cundy CS, Cox PA (2003) The hydrothermal synthesis of zeolites: history and development from the earliest days to the present time. *Chem Rev* 103:663–701. <https://doi.org/10.1021/cr020060i>
39. Cundy CS, Cox PA (2005) The hydrothermal synthesis of zeolites: precursors, intermediates and reaction mechanism. *Microporous Mesoporous Mater* 82:1–78. <https://doi.org/10.1016/j.micromeso.2005.02.016>
40. Mortier WJ (1982) Compilation of extra framework sites in zeolites. Butterworth Scientific Limited, Guildford
41. Wright PA, Connor JA (2008) Families of microporous framework solids. In: *Microporous framework solids*. Royal Society of Chemistry, Cambridge, pp 8–78
42. Milton RM (1963) Water separation from a vapor mixture. US Patent 3,078,635
43. Sircar S, Myers A (2003) Gas separation by Zeolites. In: *Handbook of zeolite science and technology*. Marcker Dekker, Inc, New York/Basel
44. Flanigen EM, Bennett JM, Grose RW et al (1978) Silicalite, a new hydrophobic crystalline silica molecular sieve. *Nature* 271:512–516. <https://doi.org/10.1038/271512a0>
45. Blasco T, Cambor MA, Corma A et al (1998) Direct synthesis and characterization of hydrophobic aluminum-free Ti–beta zeolite. *J Phys Chem B* 102:75–88. <https://doi.org/10.1021/jp973288w>
46. Lew CM, Sun M, Liu Y et al (2009) Pure-silica-zeolite low-dielectric constant materials. *Ordered Porous Solids*:335–364. <https://doi.org/10.1016/B978-0-444-53189-6.00013-5>
47. Sircar S (2002) Drying processes. In: *Handbook of porous solids*. Wiley-VCH Verlag GmbH, Weinheim, pp 2533–2567

48. Tagliabue M, Farrusseng D, Valencia S et al (2009) Natural gas treating by selective adsorption: material science and chemical engineering interplay. *Chem Eng J* 155:553–566. <https://doi.org/10.1016/j.cej.2009.09.010>
49. McCusker LB, Liebau F, Engelhardt G (2001) Nomenclature of structural and compositional characteristics of ordered microporous and mesoporous materials with inorganic hosts. *Pure Appl Chem* 73:381–394
50. Flanigen EM, Broach RW, Wilson ST (2010) Introduction. In: Kulprathipanja S (ed) *Zeolites in industrial separation and catalysis*. Wiley-VCH Verlag GmbH & Co. KGaA, Weinheim, pp 1–26
51. IZA Structure Commission (2018) IZA Structure Commission. <http://www.iza-structure.org/>
52. Denayer JF, Baron GV, Martens JA, Jacobs PA (1998) Chromatographic study of adsorption of n-alkanes on zeolites at high temperatures. *J Phys Chem B* 102:3077–3081. <https://doi.org/10.1021/jp972328t>
53. Daems I, Singh R, Baron G, Denayer J (2007) Length exclusion in the adsorption of chain molecules on chabazite type zeolites. *Chem Commun* 1316. <https://doi.org/10.1039/b615661d>
54. Palomino M, Corma A, Rey F, Valencia S (2010) New insights on CO<sub>2</sub>–methane separation using LTA zeolites with different Si/Al ratios and a first comparison with MOFS. *Langmuir* 26:1910–1917. <https://doi.org/10.1021/la9026656>
55. Palomino M, Corma A, Jordá JL et al (2012) Zeolite Rho: a highly selective adsorbent for CO<sub>2</sub>/CH<sub>4</sub> separation induced by a structural phase modification. *Chem Commun* 48:215–217. <https://doi.org/10.1039/c1cc16320e>
56. Grajciar L, Čejka J, Zukal A et al (2012) Controlling the adsorption enthalpy of CO<sub>2</sub> in zeolites by framework topology and composition. *ChemSusChem* 5:2011–2022. <https://doi.org/10.1002/cssc.201200270>
57. Collins JJ (1973) Bulk separation of carbon dioxide from natural gas. US Patent 3,751,878
58. Kumar R (1991) Adsorptive process for producing two gas streams from a gas mixture. US Patent 5,026,406
59. Barrett P a, Stephenson NA (2011) Adsorption properties of zeolites. In: Martínez Sánchez C, Pérez Pariente J (eds) *Zeolites and ordered porous solids: fundamentals and applications*. Editorial Universitat Politècnica de Valencia, Valencia, pp 149–180
60. Zhu W, Kapteijn F, Moulijn JA (2001) A novel adsorbent for the separation of propane/propene mixtures. *Stud Surf Sci Catal* 135:144. [https://doi.org/10.1016/S0167-2991\(01\)81227-1](https://doi.org/10.1016/S0167-2991(01)81227-1)
61. Zhu W, Kapteijn F, Moulijn JA et al (2000) Shape selectivity in adsorption on the all-silica DD3R. *Langmuir* 16:3322–3329. <https://doi.org/10.1021/la9914007>
62. Palomino M, Cantón A, Corma A et al (2007) Pure silica ITQ-32 zeolite allows separation of linear olefins from paraffins. *Chem Commun* 24:1233–1235. <https://doi.org/10.1039/B700358G>
63. Gutiérrez-Sevillano JJ, Calero S, Hamad S et al (2016) Critical role of dynamic flexibility in Ge-containing zeolites: impact on diffusion. *Chem – A Eur J* 22:10036–10043. <https://doi.org/10.1002/chem.201600983>
64. Casty GL, Hall RB, Reyes SC, et al (2004) Separation of 1-butene from C4 feed streams. US Patent App. 2004/0260138 A1
65. Padin J, Rege SU, Yang RT, Cheng LS (2000) Molecular sieve sorbents for kinetic separation of propane/propylene. *Chem Eng Sci* 55:4525–4535. [https://doi.org/10.1016/S0009-2509\(00\)00099-3](https://doi.org/10.1016/S0009-2509(00)00099-3)
66. Cheng LS, Wilson ST (2001) Process for separating propylene from propane. US Patent 6,293,999 B1
67. Hedin N, DeMartin GJ, Roth WJ et al (2008) PFG NMR self-diffusion of small hydrocarbons in high silica DDR, CHA and LTA structures. *Microporous Mesoporous Mater* 109:327–334. <https://doi.org/10.1016/j.micromeso.2007.05.007>
68. Kärger J, Ruthven DM, Theodorou DN (2012) *Diffusion in nanoporous materials*. Wiley-VCH Verlag & Co. KGaA, Weinheim

69. Burton A (2017) Recent trends in the synthesis of high-silica zeolites. *Catal Rev Sci Eng* 00:1–44. <https://doi.org/10.1080/01614940.2017.1389112>
70. Ruthven DM, Reyes SC (2007) Adsorptive separation of light olefins from paraffins. *Microporous Mesoporous Mater* 104:59–66. <https://doi.org/10.1016/j.micromeso.2007.01.005>
71. Voogd P, Van Bekkum H (1989) Diffusion of n-hexane and 3-methylpentane in H-ZSM-5 crystals of various sizes. *Stud Surf Sci Catal* 46:519–531. [https://doi.org/10.1016/S0167-2991\(08\)61007-1](https://doi.org/10.1016/S0167-2991(08)61007-1)
72. Milton RM (1959) Molecular sieve adsorbents. US Patent 2,882,244
73. Milton RM (1959) Molecular sieve adsorbents. US Patent 2,882,243
74. Yang R (2003) Adsorbents: fundamentals and applications. Wiley, Hoboken
75. Ruthven DM (2011) Molecular sieve separations. *Chemie-Ingenieur-Technik* 83:44–52. <https://doi.org/10.1002/cite.201000145>
76. Skarstrom CW (1960) Method and apparatus for fractionating gaseous mixtures by adsorption. US Patent 2,944,627
77. Sircar S, Rao MB, Golden TC (1999) Fractionation of air by zeolites. In: Dabrowski A (ed) Adsorption and its applications in industry and environmental protection, Vol I: applications in industry, Elsevier Science B.V., Amsterdam, pp 395–423
78. Asher WJ, Campbell ML, Epperly WR, Robertson JL (1969) Desorb n-paraffins with ammonia. *Hydrocarb Process* 48:134–138
79. Sholl DS, Lively RP (2016) Seven chemical separations to change the world. *Nature* 532:435–437. <https://doi.org/10.1038/532435a>
80. Breck DW, Smith JV (1959) Molecular sieves. *Sci Am* 200:85–96
81. Flanigen EM (1980) Molecular sieve zeolite technology: the first 25 years. *Pure Appl Chem* 52:2191–2211
82. Anderson RA (1977) Molecular sieve adsorbent applications state of the art. In: Katzer JR (ed) Molecular sieves – II. American Chemical Society, Washington, DC, pp 637–649
83. Milton RM (1962) Drying of natural gas by adsorption. US Patent 3,024,867
84. Milton RM (1963) Sweetening and drying of natural gas. US Patent 3,078,634
85. Milton RM (1965) Water removal from gas mixtures. US Patent 3,164,453
86. Sowerby B, Crittenden BD (1988) An experimental comparison of type A molecular sieves for drying the ethanol-water azeotrope. *Gas Sep Purif* 2:77–83. [https://doi.org/10.1016/0950-4214\(88\)80016-1](https://doi.org/10.1016/0950-4214(88)80016-1)
87. Teo WK, Ruthven DM (1986) Adsorption of water from aqueous ethanol using 3-A molecular sieves. *Ind Eng Chem Process Des Dev* 25:17–21. <https://doi.org/10.1021/i200032a003>
88. Ausikaitis JP, Garg DR (1983) Adsorption separation cycle. US Patent 4,373,935
89. Wang Y, Deckman HW, Wittrig AM, et al (2018) Swing adsorption processes using zeolite structures. US Patent App. 2018/0056235 A1
90. Burfield DR, Lee KH, Smithers RH (1977) Desiccant efficiency in solvent drying. A reappraisal by application of a novel method for solvent water assay. *J Organomet Chem* 42:3060–3065. <https://doi.org/10.1021/jo00438a024>
91. McKee DW (1964) Separation of an oxygen-nitrogen mixture. US Patent 3,140,933
92. Chao CC (1989) Process for separating nitrogen from mixtures thereof with less polar substances. US Patent 4,859,217
93. McRobbie H (1964) Separation of an oxygen-nitrogen mixture. US Patent 3,140,931
94. McKee DW (1964) Separation of an oxygen-nitrogen mixture. US Patent 3,140,932
95. Berlin NH (1967) Vacuum cycle adsorption. US Patent 3,313,091
96. Coe CG, Kuznicki SM (1984) Polyvalent ion exchanged adsorbent for air separation. US Patent 4,481,018
97. Sircar S, Conrad RR, William J. Am (1985) Binary ion exchanged type X zeolite adsorbent. US Patent 4,557,736
98. Wu C-W, Kothare MV, Sircar S (2014) Equilibrium adsorption isotherms of pure N<sub>2</sub> and O<sub>2</sub> and their binary mixtures on LiLSX zeolite: experimental data and thermodynamic analysis. *Ind Eng Chem Res* 53:7195–7201. <https://doi.org/10.1021/ie500268s>

99. Kirner JF (1993) Nitrogen adsorption with highly Li exchanged X-zeolites with low Si/Al ratio. US Patent 5,268,023
100. Kuznicki SM, Bell VA, Petrovic I, Desai BT (2000) Small-pored crystalline titanium molecular sieve zeolites and their use in gas separation processes. US Patent 6,068,682
101. Kuznicki SM, Bell VA, Nair S et al (2001) A titanosilicate molecular sieve with adjustable pores for size-selective adsorption of molecules. *Nature* 412:720–724. <https://doi.org/10.1038/35089052>
102. Hirano S, Yoshida S, Harada A et al (2001) Dynamic adsorption properties of Li ion exchanged zeolite adsorbents. In: Kaneko K, Kanoh H, Hanzawa Y (eds) *Fundamentals of adsorption*, vol 7. IK International, pp 872–879
103. IPCC (2014) IPCC 2014: Climate change 2014: synthesis report. Switzerland, Geneva
104. Lincoln SF (2005) Fossil fuels in the 21st century. *Ambio* 34:621–627
105. Riboldi L, Bolland O (2017) Overview on pressure swing adsorption (PSA) as CO<sub>2</sub> capture technology: state-of-the-art, limits and potentials. *Energy Procedia* 114:2390–2400. <https://doi.org/10.1016/j.egypro.2017.03.1385>
106. Rubin ES, Davison JE, Herzog HJ (2015) The cost of CO<sub>2</sub> capture and storage. *Int J Greenh Gas Control* 40:378–400. <https://doi.org/10.1016/j.ijggc.2015.05.018>
107. U.S. National Coal Council (2015) *Fossil Forward : Revitalizing CCS*
108. Li B, Duan Y, Luebke D, Morreale B (2013) Advances in CO<sub>2</sub> capture technology: a patent review. *Appl Energy* 102:1439–1447. <https://doi.org/10.1016/j.apenergy.2012.09.009>
109. Lee SY, Park SJ (2015) A review on solid adsorbents for carbon dioxide capture. *J Ind Eng Chem* 23:1–11. <https://doi.org/10.1016/j.jiec.2014.09.001>
110. Hedin N, Chen L, Laaksonen A (2010) Sorbents for CO<sub>2</sub> capture from flue gas – aspects from materials and theoretical chemistry. *Nanoscale* 2:1819. <https://doi.org/10.1039/c0nr00042f>
111. Wang Q, Luo J, Zhong Z, Borgna A (2011) CO<sub>2</sub> capture by solid adsorbents and their applications: current status and new trends. *Energy Environ Sci* 4:42–55. <https://doi.org/10.1039/C0EE00064G>
112. Choi S, Drese JH, Jones CW (2009) Adsorbent materials for carbon dioxide capture from large anthropogenic point sources. *ChemSusChem* 2:796–854. <https://doi.org/10.1002/cssc.200900036>
113. Boot-Handford ME, Abanades JC, Anthony EJ et al (2014) Carbon capture and storage update. *Energy Environ Sci* 7:130–189. <https://doi.org/10.1039/C3EE42350F>
114. Chang F, Zhou J, Chen P et al (2013) Microporous and mesoporous materials for gas storage and separation: a review. *Asia Pac J Chem Eng* 8:618–626. <https://doi.org/10.1002/apj.1717>
115. Brandani F, Ruthven DM (2004) The effect of water on the adsorption of CO<sub>2</sub> and C<sub>3</sub>H<sub>8</sub> on type X zeolites. *Ind Eng Chem Res* 43:8339–8344. <https://doi.org/10.1021/ie040183o>
116. Martín-Calvo A, Parra JB, Ania CO, Calero S (2014) Insights on the anomalous adsorption of carbon dioxide in LTA zeolites. *J Phys Chem C* 118:25460–25467. <https://doi.org/10.1021/jp507431c>
117. Montanari T, Finocchio E, Salvatore E et al (2011) CO<sub>2</sub> separation and landfill biogas upgrading: a comparison of 4A and 13X zeolite adsorbents. *Energy* 36:314–319. <https://doi.org/10.1016/j.energy.2010.10.038>
118. Wang Y, LeVan MD (2010) Adsorption equilibrium of binary mixtures of carbon dioxide and water vapor on zeolites 5A and 13X. *J Chem Eng Data* 55:3189–3195. <https://doi.org/10.1021/je100053g>
119. Cheung O, Hedin N (2014) Zeolites and related sorbents with narrow pores for CO<sub>2</sub> separation from flue gas. *RSC Adv* 4:14480–14494. <https://doi.org/10.1039/C3RA48052F>
120. Gómez-Álvarez P, Calero S (2016) Highly selective zeolite topologies for flue gas separation. *Chem – A Eur J* 22:18705–18708. <https://doi.org/10.1002/chem.201604009>
121. Pham TD, Hudson MR, Brown CM, Lobo RF (2014) Molecular basis for the high CO<sub>2</sub> adsorption capacity of chabazite zeolites. *ChemSusChem* 7:3031–3038. <https://doi.org/10.1002/cssc.201402555>
122. Pham TD, Xiong R, Sandler SI, Lobo RF (2014) Experimental and computational studies on the adsorption of CO<sub>2</sub> and N<sub>2</sub> on pure silica zeolites. *Microporous Mesoporous Mater* 185:157–166. <https://doi.org/10.1016/j.micromeso.2013.10.030>

123. Kim J, Abouelnasr M, Lin LC, Smit B (2013) Large-scale screening of zeolite structures for CO<sub>2</sub> membrane separations. *J Am Chem Soc* 135:7545–7552. <https://doi.org/10.1021/ja400267g>
124. Pham TD, Liu Q, Lobo RF (2013) Carbon dioxide and nitrogen adsorption on cation-exchanged SSZ-13 zeolites. *Langmuir* 29:832–839. <https://doi.org/10.1021/la304138z>
125. Miyamoto M, Fujioka Y, Yogo K (2012) Pure silica CHA type zeolite for CO<sub>2</sub> separation using pressure swing adsorption at high pressure. *J Mater Chem* 22:20186. <https://doi.org/10.1039/c2jm34597h>
126. Himeno S, Tomita T, Suzuki K et al (2007) Synthesis and permeation properties of a DDR-type zeolite membrane for separation of CO<sub>2</sub>/CH<sub>4</sub> gaseous mixtures. *Ind Eng Chem Res* 46:6989–6997. <https://doi.org/10.1021/ie061682n>
127. Couck S, Lefevere J, Mullens S et al (2017) CO<sub>2</sub>, CH<sub>4</sub> and N<sub>2</sub> separation with a 3DFD-printed ZSM-5 monolith. *Chem Eng J* 308:719–726. <https://doi.org/10.1016/j.cej.2016.09.046>
128. Fischer M (2017) Computational evaluation of aluminophosphate zeotypes for CO<sub>2</sub>/N<sub>2</sub> separation. *Phys Chem Chem Phys* 19:22801–22812. <https://doi.org/10.1039/C7CP03841K>
129. Liu Q, Cheung NCO, Garcia-Bennett AE, Hedin N (2011) Aluminophosphates for CO<sub>2</sub> separation. *ChemSusChem* 4:91–97. <https://doi.org/10.1002/cssc.201000256>
130. Cheung O, Liu Q, Bacsik Z, Hedin N (2012) Silicoaluminophosphates as CO<sub>2</sub> sorbents. *Microporous Mesoporous Mater* 156:90–96. <https://doi.org/10.1016/j.micromeso.2012.02.003>
131. MolecularGate (2018) Molecular Gate<sup>®</sup> Adsorption Technology. <http://www.moleculargate.com/>
132. Du T, Fang X, Liu L et al (2018) An optimal trapdoor zeolite for exclusive admission of CO<sub>2</sub> at industrial carbon capture operating temperatures. *Chem Commun* 54:3134–3137. <https://doi.org/10.1039/C8CC00634B>
133. Shang J, Li G, Singh R et al (2012) Discriminative separation of gases by a “molecular trapdoor” mechanism in chabazite zeolites. *J Am Chem Soc* 134:19246–19253. <https://doi.org/10.1021/ja309274y>
134. Lozinska MM, Mowat JPS, Wright PA et al (2014) Cation gating and relocation during the highly selective “trapdoor” adsorption of CO<sub>2</sub> on univalent cation forms of zeolite Rho. *Chem Mater* 26:2052–2061. <https://doi.org/10.1021/cm404028f>
135. Wang J, Wang S, Xin Q, Li Y (2017) Perspectives on water-facilitated CO<sub>2</sub> capture materials. *J Mater Chem A* 5:6794–6816. <https://doi.org/10.1039/C7TA01297G>
136. Jeong W, Kim J (2016) Understanding the mechanisms of CO<sub>2</sub> adsorption enhancement in pure silica zeolites under humid conditions. *J Phys Chem C* 120:23500–23510. <https://doi.org/10.1021/acs.jpcc.6b06571>
137. World Energy Council (2017) Full report: the role of natural gas (Perspective from the 2016 world energy scenarios)
138. Saha D, Grappe HA, Chakraborty A, Orkoulas G (2016) Postextraction separation, on-board storage, and catalytic conversion of methane in natural gas: a review. *Chem Rev*. <https://doi.org/10.1021/acs.chemrev.5b00745>
139. Solar C, Blanco A, Vallone A, Sapag K (2010) Adsorption of methane in porous materials as the basis for the storage of natural gas. *Nat Gas*:205–245. <https://doi.org/10.5772/9846>
140. Kidnay AJ, Parrish WR (2006) Fundamentals of natural gas processing. Taylor & Francis Group, Boca Raton/London/New York
141. Energy Information Administration (1997) Renewable energy annual 1996
142. Flores RM (1998) Coalbed methane: from hazard to resource. *Int J Coal Geol* 35:3–26. [https://doi.org/10.1016/S0166-5162\(97\)00043-8](https://doi.org/10.1016/S0166-5162(97)00043-8)
143. Kim AG (1973) The composition of coalbed gas (Report of investigations 7762)
144. Ripepi N, Louk K, Amante J et al (2017) Determining coalbed methane production and composition from individual stacked coal seams in a multi-zone completed gas well. *Energies* 10:1533. <https://doi.org/10.3390/en10101533>
145. Li Q, Ju Y, Bao Y et al (2015) Composition, origin, and distribution of coalbed methane in the Huaibei Coalfield, China. *Energy Fuel* 29:546–555. <https://doi.org/10.1021/ef502132u>

146. Yang Y, Burke N, Ali S et al (2017) Experimental studies of hydrocarbon separation on zeolites, activated carbons and MOFs for applications in natural gas processing. *RSC Adv* 7:12629–12638. <https://doi.org/10.1039/C6RA25509D>
147. Rufford TE, Smart S, Watson GCY et al (2012) The removal of CO<sub>2</sub> and N<sub>2</sub> from natural gas: a review of conventional and emerging process technologies. *J Pet Sci Eng* 94–95:123–154. <https://doi.org/10.1016/j.petrol.2012.06.016>
148. García EJ, Pérez-Pellitero J, Pirngruber GD et al (2014) Tuning the adsorption properties of zeolites as adsorbents for CO<sub>2</sub> separation: Best compromise between the working capacity and selectivity. *Ind Eng Chem Res* 53:9860–9874. <https://doi.org/10.1021/ie500207s>
149. Sircar S, Kumar R, Koch WR, VanSloun J (1988) Recovery of methane from land fill gas. US Patent 4,770,676
150. Seery MW (1999) Bulk separation of carbon dioxide from methane using natural clinoptilolite. US Patent 5,938,819
151. Pourmahdi Z, Maghsoudi H (2017) Adsorption isotherms of carbon dioxide and methane on CHA-type zeolite synthesized in fluoride medium. *Adsorption* 23:799–807. <https://doi.org/10.1007/s10450-017-9894-1>
152. Pham TD, Lobo RF (2016) Adsorption equilibria of CO<sub>2</sub> and small hydrocarbons in AEI-, CHA-, STT-, and RRO-type siliceous zeolites. *Microporous Mesoporous Mater* 236:100–108. <https://doi.org/10.1016/j.micromeso.2016.08.025>
153. Su X, Tian P, Fan D et al (2013) Synthesis of DNL-6 with a high concentration of Si (4 Al) environments and its application in CO<sub>2</sub> separation. *ChemSusChem* 6:911–918. <https://doi.org/10.1002/cssc.201200907>
154. Bacsik Z, Cheung O, Vasiliev P, Hedin N (2016) Selective separation of CO<sub>2</sub> and CH<sub>4</sub> for biogas upgrading on zeolite NaKA and SAPO-56. *Appl Energy* 162:613–621. <https://doi.org/10.1016/j.apenergy.2015.10.109>
155. First EL, Hasan MMF, Floudas CA (2014) Discovery of novel zeolites for natural gas purification through combined material screening and process optimization. *AIChE J* 60:1767–1785. <https://doi.org/10.1002/aic.14441>
156. Dolan WB, Butwell KF (2002) Selective removal of nitrogen from natural gas by pressure swing adsorption. US Patent 6,444,012 B1
157. Habgood HW (1958) The kinetics of molecular sieve action. sorption of nitrogen–methane mixtures by linde molecular sieve 4A. *Can J Chem* 36:1384–1397. <https://doi.org/10.1139/v58-204>
158. Habgood HW (1958) Removal of nitrogen from natural gas. US Patent 2,843,219
159. Frankiewicz TC, Donnelly RG (1983) Methane/nitrogen gas separation over the zeolite clinoptilolite by the selective adsorption. In: *Industrial gas separations*. American Chemical Society, Washington, DC, pp 213–233
160. Chao CC (1990) Selective adsorption on magnesium-containing clinoptilolites. US Patent 4,964,889
161. Mitariten M (2001) New technology improves nitrogen-removal economics. *Oil Gas J* 99:42–44
162. Melo DMA, De Souza JR, Melo MAF et al (2006) Evaluation of the zinox and zeolite materials as adsorbents to remove H<sub>2</sub>S from natural gas. *Colloids Surfaces A Physicochem Eng Asp* 272:32–36. <https://doi.org/10.1016/j.colsurfa.2005.07.005>
163. Ryzhikov A, Hulea V, Tichit D et al (2011) Methyl mercaptan and carbonyl sulfide traces removal through adsorption and catalysis on zeolites and layered double hydroxides. *Appl Catal A Gen* 397:218–224. <https://doi.org/10.1016/j.apcata.2011.03.002>
164. dos Santos JPL, de Carvalho Lima Lobato AK, Moraes C et al (2016) Comparison of different processes for preventing deposition of elemental sulfur in natural gas pipelines: a review. *J Nat Gas Sci Eng* 32:364–372. <https://doi.org/10.1016/j.jngse.2016.04.045>
165. Bülow M (2016) Comments on the publication Use of zeolites for the removal of H<sub>2</sub>S: A mini-review by Mehtap Ozekmekci, Gozde Salkic and Mehmet Ferdi Fellah, *Fuel Processing Technology*, 139, 49–60, November 2015. *Fuel Process Technol* 142:396. <https://doi.org/10.1016/j.fuproc.2015.10.031>

166. Aitani AM (1993) Sour natural gas drying. *Hydrocarb Process* 72:67–73
167. Shah MS, Tsapatsis M, Siepmann JI (2015) Monte Carlo simulations probing the adsorptive separation of hydrogen sulfide/methane mixtures using all-silica zeolites. *Langmuir* 31:12268–12278. <https://doi.org/10.1021/acs.langmuir.5b03015>
168. Shah MS, Tsapatsis M, Siepmann JI (2016) Identifying optimal zeolitic sorbents for sweetening of highly sour natural gas. *Angew Chem Int Ed* 55:5938–5942. <https://doi.org/10.1002/anie.201600612>
169. Maghsoudi H, Soltanieh M, Bozorgzadeh H, Mohamadizadeh A (2013) Adsorption isotherms and ideal selectivities of hydrogen sulfide and carbon dioxide over methane for the Si-CHA zeolite: Comparison of carbon dioxide and methane adsorption with the all-silica DD3R zeolite. *Adsorption* 19:1045–1053. <https://doi.org/10.1007/s10450-013-9528-1>
170. Rezaei S, Tavana A, Sawada JA et al (2012) Novel copper-exchanged titanasilicate adsorbent for low temperature H<sub>2</sub>S removal. *Ind Eng Chem Res* 51:12430–12434. <https://doi.org/10.1021/ie300244y>
171. Rezaei S, Jarligo MOD, Wu L, Kuznicki SM (2015) Breakthrough performances of metal-exchanged nanotitanate ETS-2 adsorbents for room temperature desulfurization. *Chem Eng Sci* 123:444–449. <https://doi.org/10.1016/j.ces.2014.11.041>
172. Magnowski NBK, Avila AM, Lin CCH et al (2011) Extraction of ethane from natural gas by adsorption on modified ETS-10. *Chem Eng Sci* 66:1697–1701. <https://doi.org/10.1016/j.ces.2011.01.005>
173. Arruebo M, Coronas J, Menéndez M, Santamaría J (2001) Separation of hydrocarbons from natural gas using silicalite membranes. *Sep Purif Technol* 25:275–286. [https://doi.org/10.1016/S1383-5866\(01\)00054-5](https://doi.org/10.1016/S1383-5866(01)00054-5)
174. U.S. Department of Energy (2018) Alternative Fuels Data Center. Fuel properties comparison. [https://www.afdc.energy.gov/fuels/fuel\\_properties.php](https://www.afdc.energy.gov/fuels/fuel_properties.php)
175. ARPA-E (2012) DE-FOA-0000672: methane opportunities for vehicular energy. <https://arpa-e-foa.energy.gov/Default.aspx?Search=DE-FOA-0000672>
176. Munson RA, Clifton RA, States United, Center. CPMR (1971) Natural gas storage with zeolites. 9p.
177. Makal TA, Li J-R, Lu W, Zhou H-C (2012) Methane storage in advanced porous materials. *Chem Soc Rev* 41:7761. <https://doi.org/10.1039/c2cs35251f>
178. Düren T, Sarkisov L, Yaghi OM, Snurr RQ (2004) Design of new materials for methane storage. *Langmuir* 20:2683–2689. <https://doi.org/10.1021/la0355500>
179. Zhang M, Li H, Perry Z, Zhou H-C (2014) Gas storage in metal-organic frameworks. *Encycl Inorg Bioinorg Chem*:1–19. <https://doi.org/10.1002/9781119951438.eibc2210>
180. Ahmed DS, El-hiti GA, Yousif E et al (2018) Design and synthesis of porous polymeric materials and their applications in gas capture and storage: a review. *J Polym Res* 25(75):1–21
181. Alcañiz-Monge J, De La Casa-Lillo MA, Cazorla-Amorós D, Linares-Solano A (1997) Methane storage in activated carbon fibres. *Carbon* 35:291–297. doi: [https://doi.org/10.1016/S0008-6223\(96\)00156-X](https://doi.org/10.1016/S0008-6223(96)00156-X)
182. Rejifu A, Noguchi H, Ohba T et al (2009) Adsorptivities of extremely high surface area activated carbon fibres for CH<sub>4</sub> and H<sub>2</sub>. *Adsorpt Sci Technol* 27:877–882. <https://doi.org/10.1260/0263-6174.27.9.877>
183. Yuguo W, Cemal E, Anwar K, Rashid O (2011) Experimental and theoretical study of methane adsorption on granular activated carbons. *AIChE J* 58:782–788. <https://doi.org/10.1002/aic.12611>
184. Sun Y, Liu C, Su W et al (2009) Principles of methane adsorption and natural gas storage. *Adsorption* 15:133–137. <https://doi.org/10.1007/s10450-009-9157-x>
185. Peng Y, Krungleviciute V, Eryazici I et al (2013) Methane storage in metal-organic frameworks: current records, surprise findings, and challenges. *J Am Chem Soc* 135:11887–11894. <https://doi.org/10.1021/ja4045289>
186. Simon CM, Kim J, Gomez-Gualdrón DA et al (2015) The materials genome in action: identifying the performance limits for methane storage. *Energy Environ Sci* 8:1190–1199. <https://doi.org/10.1039/C4EE03515A>

187. Kishima M, Mizuhata H, Okubo T (2006) Effects of confinement on the adsorption behavior of methane in high-silica zeolites. *J Phys Chem B* 110:13889–13896. <https://doi.org/10.1021/jp0621981>
188. Zhang SY, Talu O, Hayhurst DT (1991) High-pressure adsorption of methane in zeolites NaX, MgX, CaX, SrX and BaX. *J Phys Chem* 95:1722–1726. <https://doi.org/10.1021/j100157a044>
189. Talu O, Zhang SY, Hayhurst DT (1993) Effect of cations on methane adsorption by NaY, MgY, CaY, SrY, and BaY zeolites. *J Phys Chem* 97:12894–12898. <https://doi.org/10.1021/j100151a043>
190. Tagliabue M, Rizzo C, Onorati NB et al (2012) Regenerability of zeolites as adsorbents for natural gas sweetening: a case-study. *Fuel* 93:238–244. <https://doi.org/10.1016/j.fuel.2011.08.051>
191. Song Z, Nambo A, Tate KL et al (2016) Nanovalved adsorbents for CH<sub>4</sub> storage. *Nano Lett* 16:3309–3313. <https://doi.org/10.1021/acs.nanolett.6b00919>
192. Eldridge RB (1993) Olefin/paraffin separation technology: a review. *Ind Eng Chem Res* 32:2208–2212. <https://doi.org/10.1021/ie00022a002>
193. Grande CA, Gigola C, Rodrigues AE (2003) Propane-propylene binary adsorption on zeolite 4A. *Adsorption* 9:321–329. <https://doi.org/10.1023/A:1026223914143>
194. Granato MA, Vlught TJH, Rodrigues AE (2007) Molecular simulation of propane-propylene binary adsorption equilibrium in zeolite 13X. *Ind Eng Chem Res* 46:7239–7245. <https://doi.org/10.1021/ie0705655>
195. Mofarahi M, Salehi SM (2013) Pure and binary adsorption isotherms of ethylene and ethane on zeolite 5A. *Adsorption* 19:101–110. <https://doi.org/10.1007/s10450-012-9423-1>
196. Reyes SC, Olson DH, Liu H, et al (2005) Light hydrocarbon separation using 8-member ring zeolites. US Patent App. 2005/0096494 A1
197. Yang RT, Kikkides ES (1995) New sorbents for olefin/paraffin separations by adsorption via  $\pi$ -complexation. *AIChE J* 41:509–517
198. Aguado S, Bergeret G, Daniel C, Farrusseng D (2012) Absolute molecular sieve separation of ethylene/ethane mixtures with silver zeolite A. *J Am Chem Soc* 134:14635–14637. <https://doi.org/10.1021/ja305663k>
199. Van Miltenburg A, Zhu W, Kapteijn F, Moulijn JA (2006) Adsorptive separation of light olefin/paraffin mixtures. *Chem Eng Res Des* 84:350–354. <https://doi.org/10.1205/cherd05021>
200. Cen PL (1990) Adsorption uptake curves of ethylene on Cu(I)-NaY zeolite. *AIChE J* 36:789–793. <https://doi.org/10.1002/aic.690360518>
201. Richter M, Roost U, Lohse U (1993) Molecular sieving of n-butenes by microporous silicoaluminophosphates. *J Chem Soc Chem Commun* 17:1616–1617. <https://doi.org/10.1039/c39930001616>
202. Rege SU, Yang RT (2002) Propane/propylene separation by pressure swing adsorption: sorbent comparison and multiplicity of cyclic steady states. *Chem Eng Sci* 57:1139–1149. [https://doi.org/10.1016/S0009-2509\(01\)00440-7](https://doi.org/10.1016/S0009-2509(01)00440-7)
203. Zhu W, Kapteijn F, Moulijn JA (1999) Shape selectivity in the adsorption of propane / propene on the all-silica DD3R. *Chem Commun* 24:2453–2454
204. Olson DH, Cambor MA, Villaescusa LA, Kuehl GH (2004) Light hydrocarbon sorption properties of pure silica Si-CHA and ITQ-3 and high silica ZSM-58. *Microporous Mesoporous Mater* 67:27–33. <https://doi.org/10.1016/j.micromeso.2003.09.025>
205. Olson DH (2002) Light hydrocarbon separation using 8-member ring zeolites. US Patent 6,488,741 B2
206. Barrett PA, Boix T, Puche M et al (2003) ITQ-12: a new microporous silica polymorph potentially useful for light hydrocarbon separations. *Chem Commun* 17:2114–2115. <https://doi.org/10.1039/B306440A>
207. Gutierrez-Sevillano JJ, Dubbeldam D, Rey F et al (2010) Analysis of the ITQ-12 zeolite performance in propane-propylene separations using a combination of experiments and molecular simulations. *J Phys Chem C* 114:14907–14914. <https://doi.org/10.1021/Jp101744k>

208. Zhu W, Kapteijn F, Moulijn JA (1999) Shape selectivity in the adsorption of propane / propene on the all-silica DD3R. *Chem Commun*:2453–2454. <https://doi.org/10.1039/a906465f>
209. Tijsebaert B, Varszegi C, Gies H et al (2008) Liquid phase separation of 1-butene from 2-butenes on all-silica zeolite RUB-41. *Chem Commun*:2480–2482. <https://doi.org/10.1039/b719463c>
210. Corbin DR, Abrams L, Jones GA et al (1990) Flexibility of the zeolite RHO framework. In situ X-ray and neutron powder structural characterization of divalent cation-exchanged zeolite RHO. *J Am Chem Soc* 112:4821–4830. <https://doi.org/10.1021/ja00168a029>
211. Calligaris M, Mezzetti A, Nardin G, Randaccio L (1984) Cation sites and framework deformations in dehydrated chabazites. Crystal structure of a fully silver-exchanged chabazite. *Zeolites* 4:323–328. [https://doi.org/10.1016/0144-2449\(84\)90007-1](https://doi.org/10.1016/0144-2449(84)90007-1)
212. Fischer RX, Kahlenberg V, Lengauer CL, Tillmanns E (2008) Thermal behavior and structural transformation in the chabazite-type zeolite willhendersonite,  $\text{KCaAl}_3\text{Si}_3\text{O}_{12}\cdot 5\text{H}_2\text{O}$ . *Am Mineral* 93:1317–1325. <https://doi.org/10.2138/am.2008.2745>
213. Müller JA, Conner WC (1993) Cyclohexane in ZSM-5. 1. FTIR and X-ray studies. *J Phys Chem* 97:1451–1454. <https://doi.org/10.1021/j100109a033>
214. García-Pérez E, Parra JB, Ania CO et al (2008) Unraveling the argon adsorption processes in MFI-type zeolite. *J Phys Chem C* 112:9976–9979. <https://doi.org/10.1021/jp803753h>
215. Hay DG, Jaeger H, West GW (1985) Examination of the monoclinic/orthorhombic transition in silicalite using XRD and silicon NMR. *J Phys Chem* 89:1070–1072. <https://doi.org/10.1021/j100253a005>
216. Pera-Titus M, Palomino M, Valencia S, Rey F (2014) Thermodynamic analysis of framework deformation in Na, Cs-RHO zeolite upon  $\text{CO}_2$  adsorption. *Phys Chem Chem Phys* 16:24391–24400. <https://doi.org/10.1039/C4CP03409K>
217. Balestra SRG, Hamad S, Ruiz-Salvador AR et al (2015) Understanding nanopore window distortions in the reversible molecular valve zeolite RHO. *Chem Mater* 27:5657–5667. <https://doi.org/10.1021/acs.chemmater.5b02103>
218. Min JG, Luna-Triguero A, Byun Y et al (2018) Stepped propane adsorption in pure-silica ITW zeolite. *Langmuir* 34:4774–4779. <https://doi.org/10.1021/acs.langmuir.8b00628>
219. Bereciartua PJ, Cantín Á, Corma A, et al (2017) Control of zeolite framework flexibility and pore topology for separation of ethane and ethylene. *Science* (80- ) 358:1068–1071. <https://doi.org/10.1126/science.aao0092>
220. Jiménez-Cruz F, Laredo GC (2004) Molecular size evaluation of linear and branched paraffins from the gasoline pool by DFT quantum chemical calculations. *Fuel* 83:2183–2188. <https://doi.org/10.1016/j.fuel.2004.06.010>
221. Barrer RM (1942) Fractionation of mixtures of hydrocarbons. US Patent 2,306,610
222. Barrer RM, Belchetz L (1945) Separation of mixtures using zeolites as molecular sieves. Parts I, II and III. *J Soc Chem Ind* 64:130–135. <https://doi.org/10.1002/jctb.5000630501>
223. Denayer JFM, Baron GV (1997) Adsorption of normal and branched paraffins in faujasite zeolites NaY, HY, Pt/NaY and USY. *Adsorption* 3:251–265. <https://doi.org/10.1007/BF01653628>
224. Águeda VI, Uguina MA, Delgado JA et al (2017) Equilibrium and kinetics of adsorption of high molecular weight n-paraffins on a calcium LTA molecular sieve. *Adsorption* 23:257–269. <https://doi.org/10.1007/s10450-016-9846-1>
225. Daems I, Lefflaive P, Méthivier A et al (2006) Influence of Si:Al-ratio of faujasites on the adsorption of alkanes, alkenes and aromatics. *Microporous Mesoporous Mater* 96:149–156. <https://doi.org/10.1016/j.micromeso.2006.06.029>
226. IsoSiv (1962) IsoSiv process operates commercially. *Chem Eng News* 40:59–63. <https://doi.org/10.1021/cen-v040n017.p059>
227. Asher WJ, Epperly WR (1962) Hydrocarbon separation process. US Patent 3,070,542
228. Kulprathipanja S, Johnson JA (2002) Liquid separations. In: *Handbook of porous solids*. Wiley-VCH Verlag GmbH, Weinheim, pp 2568–2622
229. Kulprathipanja S, Neuzil RW (1983) Process for separating normal paraffins using silicalite adsorbent. US Patent 4,367,364

230. Kulprathipanja S, Neuzil RW (1984) Low temperature process for separating hydrocarbons. US Patent 4,455,444
231. Neuzil RW (1972) Selectively adsorbing multibranched paraffins. US Patent 3,706,813
232. Owaysi FA, Al-Ameeri RS (1985) Purification of liquid paraffins. EP 0 164 905 A1
233. Hartline FF (1979) Lowering the cost of alcohol. *Science* (80-) 206:41–42. <https://doi.org/10.1126/science.206.4414.41>
234. Kumar S, Singh N, Prasad R (2010) Anhydrous ethanol: a renewable source of energy. *Renew Sust Energy Rev* 14:1830–1844. <https://doi.org/10.1016/j.rser.2010.03.015>
235. Harvey AP, Lee JGM (2012) Intensification of biofuel production. In: *Comprehensive renewable energy*. Elsevier Ltd, Oxford, pp 205–215
236. Milestone NB, Bibby DM (1981) Concentration of alcohols by adsorption on silicalite. *J Chem Technol Biotechnol* 31:732–736. <https://doi.org/10.1002/jctb.503310198>
237. Maddox IS (1982) Use of silicalite for the adsorption of n-butanol from fermentation liquors. *Biotechnol Lett* 4:759–760. <https://doi.org/10.1007/BF00134673>
238. Zhang K, Lively RP, Noel JD et al (2012) Adsorption of water and ethanol in MFI-type zeolites. *Langmuir* 28:8664–8673. <https://doi.org/10.1021/la301122h>
239. Farzaneh A, Zhou M, Antzutkin ON et al (2016) Adsorption of butanol and water vapors in silicalite-1 films with a low defect density. *Langmuir* 32:11789–11798. <https://doi.org/10.1021/acs.langmuir.6b03326>
240. Van der Perre S, Gelin P, Claessens B et al (2017) Intensified biobutanol recovery by using zeolites with complementary selectivity. *ChemSusChem* 10:2968–2977. <https://doi.org/10.1002/cssc.201700667>
241. Dagdougui H, Sacile R, Bersani C, Ouammi A (2018) Hydrogen production and current technologies. In: *Hydrogen infrastructure for energy applications*. Elsevier, London, pp 7–21
242. Ogden JM (1999) Prospects for building a hydrogen energy infrastructure. *Annu Rev Energy Environ* 24:227–279. <https://doi.org/10.1146/annurev.energy.24.1.227>
243. Sircar S, Golden TC (2000) Purification of hydrogen by pressure swing adsorption. *Sep Sci Technol* 35:667–687. <https://doi.org/10.1081/SS-100100183>
244. Fuderer A, Rudelstorfer E (1976) Selective adsorption process. US Patent 3,986,849
245. Sircar S (1979) Separation of multicomponent gas mixtures. US Patent 4,171,206
246. Ackley MW, Barrett PA (2008) Silver-exchanged zeolites and methods of manufacture therefor. US Patent 7,455,718 B2

# Chapter 8

## Methane Storage on Nanoporous Carbons



Francisco Rodríguez-Reinoso and Joaquín Silvestre-Albero

### 8.1 Introduction

The high-energy demand worldwide and the associated global warming due to the large CO<sub>2</sub> emissions to the atmosphere are renovating the interest in natural gas as a vehicular fuel. Compared to the other fossil fuels (such as gasoline and diesel), natural gas exhibits certain economic (lower cost), environmental (less CO<sub>2</sub>, CO, and NO<sub>x</sub> emitted in a vehicle running with natural gas), and trade balance benefits [1]. One of the main limitations of methane to be scaled-up as a fuel is the low volumetric energy density in STP conditions (0.038 MJ/L) and the associated limited mileage in vehicles. Actual approaches to increase fuel density are based either in compressed natural gas (CNG) or liquefied natural gas (LNG). In the first approach, natural gas is compressed at 20–25 MPa under ambient temperature, the final volumetric energy density increasing up to 9.2 MJ/L. Although this approach is widely used in many countries, there are some disadvantages either (i) economical (necessity to use expensive multistage compressors not affordable for domestic use), (ii) technical problems (associated safety risk when using onboard high pressure), or (iii) technological issues (onboard tanks must be made from thick metals, with the associated large weight, and the high pressure limits the versatility in their design). Under these conditions, three to four compressed cylinders will be necessary to achieve the same driving range as actual gasoline tank does (energy density of gasoline 34.2 MJ/L). Concerning liquefaction, due to the low critical temperature of methane (the main component of natural gas), natural gas cannot be condensed by simply applying pressure, and temperatures below 191 K are required for condensation. Liquefied natural gas is usually stored as a boiling liquid at about

---

F. Rodríguez-Reinoso · J. Silvestre-Albero (✉)

Laboratorio de Materiales Avanzados, Departamento de Química Inorgánica-Instituto Universitario de Materiales, Universidad de Alicante, Alicante, Spain  
e-mail: [joaquin.silvestre@ua.es](mailto:joaquin.silvestre@ua.es)

© Springer Nature Singapore Pte Ltd. 2019

K. Kaneko, F. Rodríguez-Reinoso (eds.), *Nanoporous Materials for Gas Storage*, Green Energy and Technology, [https://doi.org/10.1007/978-981-13-3504-4\\_8](https://doi.org/10.1007/978-981-13-3504-4_8)

209

112 K in a cryogenic tank at a pressure of 0.1 MPa. Volumetric energy density of LNG is around 22.2 MJ/L, that is, 64% that of gasoline. Furthermore, LNG has some drawbacks associated with the high economical cost of the liquefaction unit (not suitable for domestic use), high risk due to overpressure in the vessel after prolonged storage periods, and difficulty to handle cryogenic liquids by nonspecialized people.

One of the most promising alternatives to widen the applicability of natural gas as a vehicular fuel consists in the concentration of natural gas in the cavities of nanoporous materials. By taking advantage of the strong adsorption potential in small cavities, natural gas can be concentrated to similar values of CNG at 25 MPa but at a much lower pressure (around 3.5 MPa). The adsorbed natural gas (ANG) technology exhibits a number of advantages, such as lower cost (natural gas can be filled from a domestic pipeline using a single-step compressor), less safety concerns (onboard natural gas is stored at a lower pressure, e.g., 3.5 MPa or perhaps as high as 6.5 MPa), and an important issue, that is, the design and construction of the high-pressure vessel. Pressures above 20 MPa require thick and expensive metallic containers with a mandatory cylindrical or spherical shape. However, the possibility to store natural gas at lower pressures opens the gate toward the design of lighter and more versatile containers able to adapt to the interior of the car, thus minimizing unnecessary space losses and cost requirements.

Despite the promising advantages of ANG, one of the main limitations at the moment concerns the design of a proper porous material able to store natural gas or methane with a high energy density and inside the minimum volume. The Advanced Research Projects Agency-Energy (ARPA-E) of the US Department of Energy (DOE) has been the main institution defining the requirements of a porous material to be applied in onboard storage applications [2]. In 1993 the DOE defined the storage target at 150 v/v for a final pressure of 3.5 MPa. This target was revised a few years later up to 180 v/v at the same pressure conditions, and since 2012 it is defined at 263 v/v (pressure and temperature not being defined), for adsorbent or packed bed systems, or a gravimetric capacity above 0.5 kg/kg. These values are equivalent to compressed natural gas at 25 MPa and 298 K. As described above, natural gas is mainly constituted by methane (>95%), the remaining 5% being constituted by light hydrocarbons (ethane, ethylene, propane), nitrogen, carbon dioxide, and hydrogen sulfide. Although a proper porous material must be able to work under real conditions, i.e., in the presence of these concomitant species (unless a guard bed is installed), in the next sections, we will concentrate in methane as the principal component of natural gas. However, it is important to highlight that the presence of some of these contaminants in the onboard storage system will give rise to preferential and stronger adsorption in narrow pores, thus decreasing the storage capacity after subsequent refueling.

Adsorption in a porous material offers the possibility of storing methane at a high density while keeping moderate physical conditions for the bulk phase. At the moment, the most widely investigated nanoporous materials for methane adsorption/storage are carbon materials, zeolites, and metal-organic frameworks

(MOFs) [3–5]. Previous studies described in the literature have shown that all these materials exhibit advantages and disadvantages, without a clear candidate able to fulfill all the requirements from the point of view of the DOE target. However, carbon materials have some advantages that must be emphasized [6]:

1. Porous structure, pore size and shape, and pore volume, among other parameters, can be tailored through the synthesis process. As it will be discussed later, these parameters are crucial to control the methane adsorption and storage/delivery capacity.
2. Most carbon materials (for instance, activated carbons from biomass residues) exhibit a slit-shaped pore geometry, while zeolites and MOFs exhibit preferentially spherical or cylindrical shapes. As it will be discussed later, the morphology of the pore entrance and cavity will be of paramount importance to define the adsorption and storage performance.
3. Surface chemistry in carbon materials can be easily designed through pre- and post-synthesis treatments. Although the presence of surface functionalities is a priori a noncritical parameter for methane adsorption (a nonpolar molecule), there are already some studies that denote a beneficial effect in the methane storage capacity [7].
4. Carbon materials do not contain metal species (contrary to zeolites or MOFs), and consequently the adsorbate-adsorbent interactions in carbon materials are rather low (in the specific case of methane, the dispersive van der Waals interactions with the carbon surface are rather weak), thus favoring any regeneration step needed for refueling.
5. Carbon materials are in general hydrophobic with the associated benefits for methane adsorption in humid environments.
6. Compared to other sorbents, carbon materials exhibit a large versatility in terms of thermal conductivity (over five orders of magnitude) from the lowest values in amorphous carbon ( $\sim 0.01$  W/m·K) to the highest in graphene ( $\sim 2000$  W/m·K) and carbon nanotubes ( $\sim 3000$ – $3500$  W/m·K) [8]. As it will be described later, the ability of carbon materials to conduct heat will be highly important to minimize losses in the adsorption/desorption capacity due to thermal effects during charging and discharging steps.
7. In general carbon materials and zeolites exhibit very good mechanical properties, thus facilitating a subsequent conforming step under pressure to make pellets or monoliths to reduce the volume occupied by the adsorbent. On the contrary, MOFs are in general more fragile, and several of them lose partially or totally the textural properties and adsorption properties after a conforming step under pressure [9, 10].

While zeolites and MOFs will be covered in the subsequent chapters, here we will evaluate the state of the art for nanoporous carbon materials in methane storage, from the theoretical predictions about the optimum nanoporous network to the best gravimetric and volumetric values achieved and reported to date.

## 8.2 Initial Requirements for a Carbon Material and Theoretical Predictions

Methane is a highly volatile molecule with a spherical morphology and without any dipolar or quadrupole moment. These characteristics inhibit the presence of large specific intermolecular interactions so that at room temperature methane is a gas under supercritical conditions (critical temperature is as low as 191 K). The nature of the methane molecule also affects the adsorbent-adsorbate interactions, so that a strong adsorption potential is required to concentrate the methane molecules to reach the DOE targets. From these premises, it is mandatory to design carbon materials with a highly developed microporosity (pores below 2 nm), so that the proximity of both walls will give rise to an enhanced trapping ability.

Theoretical predictions can provide tools to screen beforehand suitable adsorbents for methane storage in terms of porous structure, pore size and shape, wall thickness, and carbon wall density, among others. Nonlocal density functional theory and grand canonical Monte Carlo simulations have been applied to study methane adsorption in model porous carbons for a wide range of pore sizes and supercritical temperatures [11]. Simulations predict an optimum pore size that maximizes the excess adsorption at a given temperature and pressure. Matranga et al. have determined the optimum pore size for methane storage at a pressure of 3.4 MPa to be around 0.8 nm (H value is equal to 1.14 nm; H is the distance between the centers of the carbon atoms in the opposing graphite layers), considering a slit-shaped pore model [12]. Cracknell et al. obtained a similar value using Grand canonical ensemble Monte Carlo simulations [13]. According to these data, at 274 K the optimal material to store a large amount of methane is a porous carbon with a pore size able to accommodate two adsorbed layers of methane, for low-pressure applications, and three-four layers for high-pressure applications. This can be clearly observed in Fig. 8.1 where the density of adsorbed methane is calculated for different pore sizes and up to high pressure. At this point it is important to highlight that narrower pores ( $H = 0.74$  nm or pore width around 0.4 nm), able to hold only one layer of methane molecules, will provide a theoretical maximum in the adsorbed methane density, although the storage capacity will be limited in these narrow pores [14]. Furthermore, these narrow pores must be minimized to avoid losses due to methane left in the adsorbent during the desorption step, i.e., to maximize the delivery capacity.

Despite the benefits of the carbon cavities to improve the adsorption capacity of methane, these simulations predict a maximum energy density at 3.4 MPa and 274 K of a quarter that of gasoline, i.e., such an ideal system would not deliver more than 139 g/L of methane (209 v/v) [12] or even a slightly larger quantity, i.e., 166 g/L (249 v/v), as reported by Cracknell et al. [13].

These results clearly anticipate that the design of the carbon material is one of the critical steps to achieve an optimized storage system. A priori the material must contain the proper porous structure so that the adsorption capacity at the highest pressure is maximum, whereas the amount retained within the porosity upon

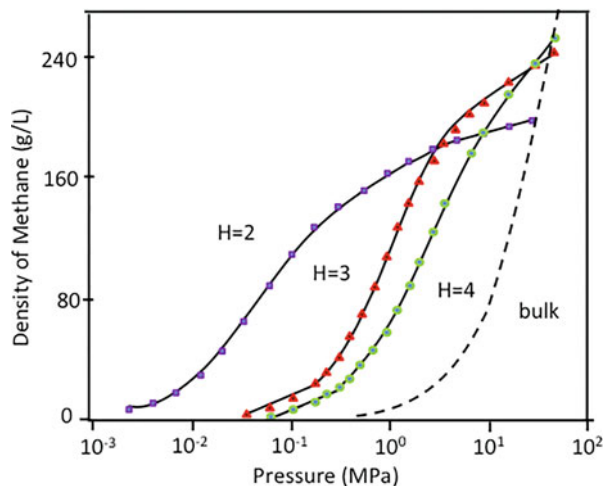


**Fig. 8.1** Adsorption isotherms at 274 K from the simulation of methane on model carbon adsorbents for different pore sizes  $H = 2 \sigma_{ff}$  (pore width around 0.8 nm),  $H = 3 \sigma_{ff}$  (pore width around 1.2 nm), and  $H = 4 \sigma_{ff}$  (pore width around 1.6 nm). Reprinted with permission from Ref. [13]. Copyright (1993) American Chemical Society

released (usually 0.5–0.1 MPa) is minimum, i.e., the amount delivered upon request must reach a maximum. Despite having a highly developed microporous structure, the pore shape is an inherent property of the solid adsorbent with an important effect in the adsorption properties. Whereas cylindrical and spherical pores dominate in zeolites and MOFs, slit-shaped morphology is most widely accepted for carbon materials. Simulation results using Grand canonical Monte Carlo anticipate that more methane can be adsorbed in slit-shaped pores, followed by hexagonal and cylindrical ones [13]. Indeed, at 274 K and 3.4 MPa, the best model zeolite will yield only 53.1 g/L or 79.65 v/v, a value much lower than the one predicted for carbon materials, i.e., carbon material can be anticipated *a priori* as an optimum system to store methane. Another important parameter to consider in the carbon material is the density of the system, i.e., the space taken by the atoms and the space waste by poor packing of the crystallites must be minimum (sometimes up to 85% of the space in the container is nonmicroporous volume due to the poor packing of the carbon crystallites) [15]. Similar grand canonical ensemble Monte Carlo (GCEMC) simulations using model slit-shaped carbon pores have shown that other potential variables with an influence in the adsorbed methane density are the density of carbon atoms in the pore wall and the pore width, while variations in the interlayer spacing and the number of layer planes in the pore wall have little effect [14]. For the evaluated storage conditions (3.4 MPa and 298 K), the maximum volumetric methane capacity is found for carbons whose pores can accommodate two layers of methane molecules ( $H \sim 1.12$  nm or pore width around 0.78 nm), rather than carbons with narrower pores ( $H = 0.74$  nm), in close agreement with

previous studies [13, 14]. Furthermore, an increase in the amount of methane adsorbed ( $\sim 12\%$ ) was anticipated after an increase in the carbon atom density from 31.90 to 38.18 atoms/nm<sup>2</sup> (skeletal density from 1.90 to 2.27 g/cm<sup>3</sup>), i.e., a larger adsorption capacity is predicted for perfect graphite compared to normal activated carbons.

The majority of the theoretical predictions described in the literature for methane storage in carbon materials are performed under static and isothermal conditions, i.e., the accompanied heat and mass transfer limitations during adsorption and desorption are not considered. Taking into account that adsorption is an exothermic process, the dynamic filling of the storage media and the subsequent delivery or desorption are unavoidably related to thermal and mass transfer effects. Biloé et al. nicely addressed these limitations using a Dubinin-Astakhov (DA) based model [16]. In the specific case of a model carbon material under ideal charging and discharging conditions, i.e., free from heat and mass transfer limitations, DA equation predicts a maximum delivery capacity of 208 v/v at 3.5 MPa and 298 K. This can be considered as the upper limit that can be achieved assuming a void-free carbon monolith with a micropore width of 1.6 nm, a micropore volume of 1 cm<sup>3</sup>/g, and a narrow pore size distribution ( $n$  coefficient in the DA equation = 2). However, this scenario changes drastically under dynamic conditions. Experimental studies described in the literature for storage vessels containing activated carbon have shown that under dynamic conditions (fast filling), the temperature inside the vessel can go from room temperature up to temperatures above 353 K [17]. Dynamic charging/discharging processes require also the knowledge of the mass transfer limitations. Indeed, experimental studies using a composite of the superactivated carbon Maxsorb and expanded natural graphite have described a pressure drop as high as 0.3 MPa for high discharge flow rates or even larger (above 0.7 MPa) for highly packed sorbents [18]. DA-based calculations under adiabatic conditions show that the charging process is more sensitive to the heat transfer limitations with a 50% loss in storage capacity for a 80 K temperature increase [16, 19]. The highest storage capacity for methane during the charging step under adiabatic conditions is achieved in slit-shaped micropores of 1.5 nm, whatever the heat transfer and mass transfer limitations are, this value being close to 153 v/v (for  $\Delta T \sim 0$ ) [16]. Contrary to the charging process, the delivery is highly sensitive to the mass transfer limitations so that a pressure drop of 1 MPa can give rise to 46.5% loss in the storage capacity for a 2.5 nm slit-pore, this pore size being the optimum for the delivery process [16].

In summary, these simulations clearly anticipate that a proper carbon material for ANG must combine a proper porous structure with narrow micropores, a proper pore size and shape (slit-shaped pores with a narrow pore size distribution centered at around 0.8 nm (or  $H = 1.14$  nm)), among others [20]. However, even when these requirements can be fulfilled, there are other parameters that must be taken into consideration, such as heat and mass transfer limitations that, a priori, will limit drastically the final performance of the carbon material. At this point it is important to highlight that there are already several studies in the literature dealing with the modification of the storage vessel or the adsorbent to mitigate the heat

transfer limitations [16, 18, 19]. Among the different possibilities, there is the option to (a) introduce heat exchangers within or around the vessel (e.g., a water annular wrapping and a gas diffuser in the center of the vessel or recirculation of air condition within the car), (b) modify the adsorbent with a highly conductive medium (e.g., expanded natural graphite), (c) incorporation of an encapsulated phase change material with a high heat of fusion at ambient temperature (e.g.,  $\text{Na}_2\text{HPO}_4 \cdot 12\text{H}_2\text{O}$  would be capable to adsorb the heat released during the charging step and resupply it during the discharge step), etc.

Last but not least, if theoretical predictions are correct, storage values above 200 v/v will be hard to be achieved using carbon materials under static conditions, while under adiabatic conditions, these values will not exceed 160 v/v (at 3.5 MPa and 298 K). Therefore, conventional strategies will no longer work to reach the new DOE target under the currently proposed storage conditions, and new strategies will need to be developed such as working at higher pressures (up to 6.5 or perhaps 10 MPa, if an easily conformed deposit can be built to withstand these working pressures) or lower temperatures (e.g., 270 K).

### 8.3 Density of the Adsorbed Phase

As described above, methane is a spherical molecule that exhibits small intermolecular interactions, thus defining a low critical temperature (191 K). Under the industrially relevant conditions for methane storage, i.e., adsorption at room temperature and high pressure, methane is a fluid in supercritical conditions. Compared to vapor adsorption studies or subcritical adsorption measurements (for instance,  $\text{N}_2$  at 77 K), the adsorbate will not be able to condense in the cavities of the carbon material under supercritical conditions, i.e., the adsorbed molecules constitute a thermodynamically distinct phase to a typical saturated liquid. One of the first consequences of these properties is the presence of a characteristic maximum in the excess methane adsorption isotherms at high pressure. As it can be observed in Fig. 8.2, the maximum depends not only on the nature of the adsorbent (porous structure) but also on the adsorption temperature.

This maximum in the excess adsorption isotherm takes place when the bulk density starts to rise faster than the adsorbed methane density. Another consequence of supercritical physisorption is the presence of a different adsorption mechanism compared to vapors or gases in subcritical conditions (pore filling must be different) and the difficulty to estimate the adsorbed phase density ( $\rho_{\text{ads}}$ ) and the volume of the adsorbed phase ( $V_{\text{ads}}$ ), both variables being necessarily known to estimate the absolute or storage capacity from the excess adsorption isotherms. In the case of condensable probes, the adsorbed phase density is assumed to be equal to the density of the adsorptive in its liquid state [22]. However, this is still an open question for probe molecules under supercritical conditions. Kaneko et al. evaluated the state of nitrogen at supercritical conditions on the slit-shaped micropores (0.7–1.4 nm) of micrographitic carbon fibers and presumed a transformation of supercritical

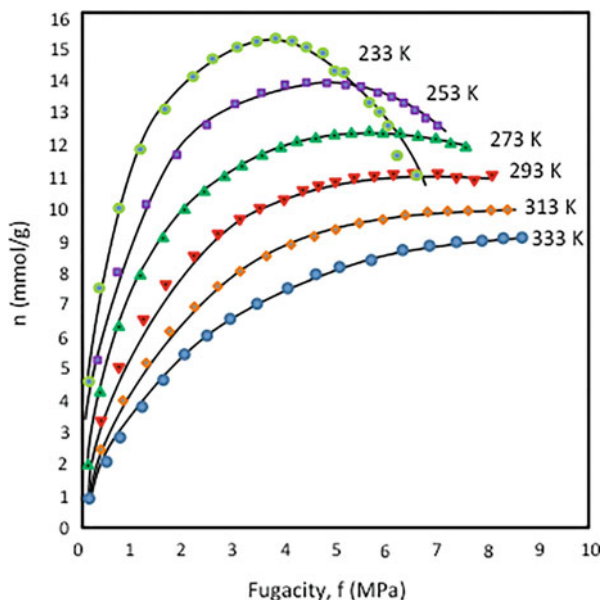


**Fig. 8.2** Excess methane adsorption isotherms for a KOH-activated coconut shell carbon material. Reprinted with permission from Ref. [21]. Copyright (2000) American Chemical Society

nitrogen into quasivapor due to the strong adsorption potential in micropores [23]. Langmuir-Freundlich equations by Zhou et al. were used to model the high-pressure methane adsorption isotherms on a KOH-activated carbon from coconut shells [21]. Intermolecular distances of the adsorbed methane molecules were evaluated from the model parameters, and the obtained values were different to the ones present in the liquid state.

Analyzing the values described in the literature, it is clear that at temperatures above 273 K, the adsorbed methane densities ( $\rho_{\text{ads}}$ ) are quite below the density of liquid methane ( $0.47 \text{ g/cm}^3$ ). Rodríguez-Reinoso et al. reported the use of the characteristic curve of adsorption derived from the Dubinin's theory of volume filling of micropores to estimate the density of methane adsorbed in activated carbons at 298 K. By adjusting the characteristic curve for  $\text{CH}_4$  at 298 K,  $\text{N}_2$  at 77 K and  $\text{CO}_2$  at 273 K for a series of 35 activated carbon materials, the authors achieved a very good fitting for the three probe molecules with a density of adsorbed methane ranging from 0.21 to  $0.27 \text{ g/cm}^3$  [24]. Taking into account that the density of the adsorbed methane depends on the micropore size, these authors estimated the adsorbed density in narrow and wide micropores, these values being around  $0.21 \text{ g/cm}^3$  and  $0.09 \text{ g/cm}^3$ , respectively.

Simulation studies on model microporous carbon materials have shown that the density of adsorbed methane increases with pressure, the estimated value being around  $0.27 \text{ g/cm}^3$  for pores accommodating two adsorbed layers at 3 MPa [14]. A similar approach using the characteristic curve was applied by García-Blanco et

al. to estimate the density of methane in a series of nanoporous materials, including carbons, zeolites, and MOFs. The final density estimated was around  $0.16 \text{ g/cm}^3$  for activated carbon Maxsorb and slightly larger ( $0.20\text{--}0.25 \text{ g/cm}^3$ ) for zeolites and MOFs [25]. Slightly lower density values ( $0.13\text{--}0.18 \text{ g/cm}^3$ ) were described in the literature for activated carbon fibers and powdered activated carbons at 4 MPa and 298 K [26]. Small-angle neutron scattering (SANS) in these samples confirmed the dependence of the adsorbed phase density with the pore size. In summary, experimental results clearly show that the density of adsorbed methane in supercritical conditions is around 32–60% that of liquid methane, i.e., the presence of a strong adsorption potential in narrow micropores is not sufficient to overcome the large intermolecular distance of the methane molecules in the gas phase. These experimental values are in good agreement with theoretical predictions described above.

#### 8.4 Adsorption/Storage Capacity in Carbon Materials

The methane uptake in a nanoporous carbon material can be expressed in two different ways, gravimetrically and volumetrically. The gravimetric uptake represents the mass of methane adsorbed per unit mass of adsorbent, whereas the volumetric uptake is the volume of methane adsorbed under standard temperature and pressure conditions per unit volume of the adsorbent. The results obtained in any conventional manometric or gravimetric adsorption equipment are usually given in a gravimetric basis (e.g., mg/g or  $\text{cm}^3/\text{g}$ ). However, for vehicular applications the volumetric adsorption capacity is more useful due to the limited space in any passenger's vehicle. Consequently, the volumetric uptake must be calculated from the gravimetric value using the density of the adsorbent. Unfortunately, the calculation of the density of the adsorbent is not straightforward due to the different morphology of the adsorbents (powder, grains, monoliths, pellets, etc.) and the different kind of density that can be used (e.g., crystallographic, bulk, skeleton, and apparent density). Nowadays the ideal crystallographic density is widely accepted, mainly for metal-organic frameworks, since this is easily calculated and it represents the maximum possible volumetric uptake. Also in the case of carbon materials, although being amorphous, some authors have suggested the "crystallographic density" from the sum of skeletal volume and pore volume. However, filling the onboard storage tank with a single monolith is an unrealistic approach from a technological point of view (together with the difficulty to synthesize such a crystal). Consequently, the use of the crystallographic density for nanoporous materials is not correct since it gives rise to overestimated storage values. Bulk density after conforming of the adsorbent into monoliths or pellets seems to be a more appropriate approach to provide more reliable volumetric data. In any case, volumetric uptakes must always be reported with the specification of the procedure used to measure the density.

### 8.4.1 Gravimetric Methane Uptake

As described above, the Advanced Research Projects Agency-Energy (ARPA-E) of the US Department of Energy (DOE) has defined a new storage gravimetric target of 0.5 g (CH<sub>4</sub>)/g [2]. Doing some basic calculations, it is clear that to achieve this objective for an ideal carbon material with a pore volume of 1 cm<sup>3</sup>/g, the density of the adsorbed methane would need to approach 0.5 g/cm<sup>3</sup>. The potential use of high-surface area porous materials to adsorb methane in onboard gas storage systems dates back to 1971 when Ronald A. Munson and Robert A. Clifton suggested the incorporation of this kind of materials to increase the amount of methane stored at low pressures [27]. These documents were followed by others from Ford Motor Company researchers about the potential application of carbon materials and zeolites for onboard methane storage [28]. In 1985 Engel and Turko patented one of the first methane storage systems working with activated carbon as a sorbent at a maximum pressure of 3.4 MPa [29]. Since these pioneering studies, the search for a suitable carbon adsorbent to improve the adsorption capacity and lower the final cost of the material has been an active area of research. Systematic studies using carbon materials with a ranging degree of activation have shown that the methane adsorption capacity at 298 K and 3.4 MPa exhibits a good correlation with the total micropore volume ( $V_{N_2}$ ) deduced from the N<sub>2</sub> adsorption data at 77 K, whereas this correlation failed when using the narrow micropore volume ( $V_{CO_2}$ ) deduced from the CO<sub>2</sub> adsorption isotherm at 273 K [24]. These results confirm that at 3.4 MPa, pores above 0.8 nm (those reflected by  $V_{N_2}$ ) participate in the adsorption process, in close agreement with theoretical predictions described above. An even better correlation was observed by Rodríguez-Reinoso et al. for the excess methane adsorption capacity at 3.5 MPa with the surface area accessible to a small molecule such as dichloromethane (kinetic diameter 0.33 nm) and the BET surface area of the synthesized carbon materials [30]. Tailoring the porous network through chemical and physical activation of olive stones, Rodríguez-Reinoso et al. achieved carbon materials with a gravimetric excess uptake ranging from 0.107 to 0.143 g/g [24]. The methane adsorption capacity not only depends on the activation conditions used (and indirectly in the pore size and pore size distribution) but also in the kind of carbon material evaluated. By comparing powdered activated carbons and activated carbon fibers, Lozano-Castelló et al. demonstrated that the excess methane adsorption capacity for these materials exhibits also a linear relationship with the total micropore volume, although the pore size distribution also had an important effect [26]. Powdered activated carbons exhibited a slightly larger adsorption capacity compared to activated carbon fibers with a similar micropore volume due to the presence of a narrower pore size distribution in the former samples. The best performing carbon materials in a gravimetric basis were a CO<sub>2</sub>-activated carbon fiber with a high activation degree (up to 0.154 g/g) and a KOH-activated anthracite (up to 0.191 g/g). Similar experiments using the superactivated carbon Maxsorb (Kansai Coke Corp.) gave even a larger value (0.197 g/g at 4 MPa and 298 K).

Carbon materials derived from metallic carbides after an appropriate chlorination treatment have also been described in the literature as promising candidates for methane adsorption in gravimetric basis. Kockrick et al. reported the adsorption performance of ordered mesoporous carbide-derived carbons (OM-CDC) obtained at low and high chlorination temperatures, with a total excess amount adsorbed as high as 0.173 g/g and 0.191 g/g, respectively (at 298 K and 10 MPa) [31]. These excellent results could even be improved up to 0.206 g/g after a post-reductive hydrogen treatment of the OM-CDC. This excellent performance was attributed to the high content of micropores with optimal size and the large total pore volume caused by mesoscopic structuring of the OM-CDC. An enhanced methane adsorption capacity was also described for carbide-derived carbons after a subsequent physical or chemical activation [32]. Whereas the original TiC-CDC had an excess adsorption capacity slightly below 0.12 g/g, a subsequent activation with CO<sub>2</sub> at 1243 K gave rise to an increase in the adsorption capacity up to 0.185 g/g, both values measured at 6 MPa and 298 K.

Chemical activation with KOH of cokes and petroleum pitches is probably the most appropriate synthesis route at the moment to achieve high-surface area activated carbons with excellent adsorption properties for methane. This is for instance the case of the Maxsorb carbon described above. Amoco licensed this recipe in 1984 to the Anderson Development Company, and later on to Kansai Coke and Chemicals in Japan. As described above, Maxsorb carbon is able to achieve an excess uptake close to 0.18–0.19 g/g at 4.8 MPa and 298 K [26, 33].

From all the data described above, it is clear that 0.2 g CH<sub>4</sub>/g carbon looks a priori as an upper limit for the gravimetric excess methane adsorption capacity in carbon materials at 298 K and moderate pressures (below 6.0 MPa), this limit being quite far from the gravimetric DOE target. Consequently, the excess methane adsorption capacity must be increased using different approaches (further activation is not a proper approach since, as will be discussed in the next section, it would give rise to a decrease in the sorbent density) such as using higher pressure (at the expenses of a higher cost due to the necessity for a multistage compressor and high-pressure metering equipment) or lower temperatures. For instance, Casco et al. reported excess values above 0.25 g/g for petroleum-pitch derived high-surface area carbon materials at pressures of 10 MPa [9].

As it can be observed in Fig. 8.3, the adsorption isotherms reported by Casco et al. for high-pressure methane are fully reversible over the whole pressure range evaluated for all kind of carbon materials evaluated, thus anticipating the potential of these carbon materials for pressure-swing adsorption (PSA) units. The best results were obtained for an activated carbon prepared from a PY petroleum residue and a 8:1 chemical activation ratio with KOH, i.e., a sample with an extremely large activation degree (BET surface area above 3200 m<sup>2</sup>/g). Samples with narrower pores (for instance F400) become useless for high-pressure applications since they become saturated already at 3–4 MPa, i.e., larger pores are required to keep growing the adsorption capacity at higher pressure values. The role of the different pore sizes in the methane adsorption process under real experimental conditions can be clearly

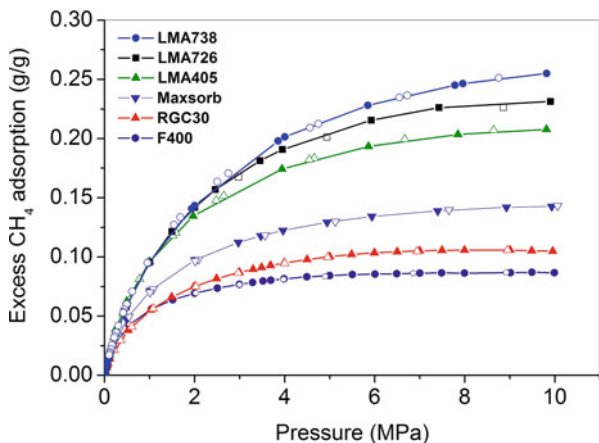


**Fig. 8.3** Excess methane adsorption isotherms for different activated carbon materials (petroleum-pitch derived carbons and commercial samples). Adapted with permission from ref. [9]. Copyright (2015) American Chemical Society

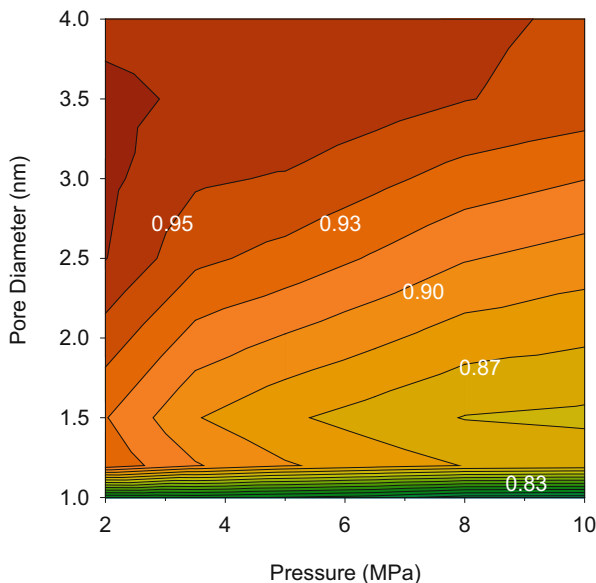


**Fig. 8.4** Coefficient of determination for  $\text{CH}_4$  uptake in gravimetric basis (mmol/g) at 298 K and up to 10 MPa, and the volume of pores smaller to the threshold size (y-axis). Reprinted with permission from ref. [9]. Copyright (2015) American Chemical Society

appreciated in Fig. 8.4. As it can be observed, for applications dealing with moderate pressures (e.g., 2 MPa), pores around 2.5–3.8 nm govern the adsorption behavior, whereas larger pores are required for higher pressures.

At this point it is important to highlight that these values correspond to an excess adsorption capacity, i.e., the amount adsorbed obtained from the high-pressure manometric or gravimetric equipment. However, to evaluate the potential of these carbon materials for an onboard storage device, it is necessary to estimate also the compressed methane contained in large pores (not considered as excess) and the methane in the interparticle space. The so-called total storage capacity can be obtained from the excess adsorption data, the density of the fluid in the bulk ( $\rho_{\text{bulk}}$ ) and the volume of the adsorbed phase ( $V_{\text{ads}}$ ) [9]. Consequently, these values must be increased by 20–30% to get the final storage uptake. In the specific case of activated carbon LMA738 the gravimetric storage capacity is as high as 0.3 g/g at 10 MPa and 298 K. A similar value but surprisingly at a lower pressure (3.5 MPa) was reported by Celzard et al. in 2005 for an anthracite-derived activated carbon prepared by chemical activation with NaOH (using a low activation ratio; NaOH/carbon mass = 3) [34].

Last but not least, it is important to emphasize that although the storage or adsorption capacity at high pressure is an important parameter to evaluate the potential of a given adsorbent for onboard applications, not all this capacity is usable when natural gas is delivered to the engine due to the necessity of a minimum inlet pressure. Consequently, not only the total adsorption capacity is important but also the delivery capacity, i.e., the amount of methane released between the maximum charging pressure and the minimum engine inlet pressure. Although it is widely accepted in the literature to use 0.1 MPa as the minimum pressure to calculate the delivery capacity, the DOE has defined a minimum value for the real engine of 0.48 MPa [2]. Consequently, to maximize the methane delivered or working capacity, it is necessary to design carbon materials with a minimum adsorption at these pressures, i.e., the presence of narrow micropores (below 0.8 nm) must be kept to a minimum [15]. Furthermore, as described before the working capacity in vehicular applications under adiabatic conditions is largely dependent to intrinsic thermal and mass transfer effects during charging and discharging steps [16].

#### 8.4.2 Volumetric Methane Uptake

The suitability of natural gas to be used in vehicular applications highly depends on the ability to store a sufficient amount of methane in the onboard fuel tank using a proper nanoporous material and a minimum volume, i.e., with minimum interference with usable space. Consequently, in addition to design a nanoporous material with a large micropore surface area and hence a high storage capacity, the adsorbent under consideration must have a high packing density, i.e., the methane must be stored in the minimum volume. Activated carbon materials are characterized by a low packing density in powder form (for instance Maxsorb carbon has a packing density of 0.37 g/cm<sup>3</sup>). The low packing density of carbon materials becomes detrimental for the total volumetric storage capacity. As it can be

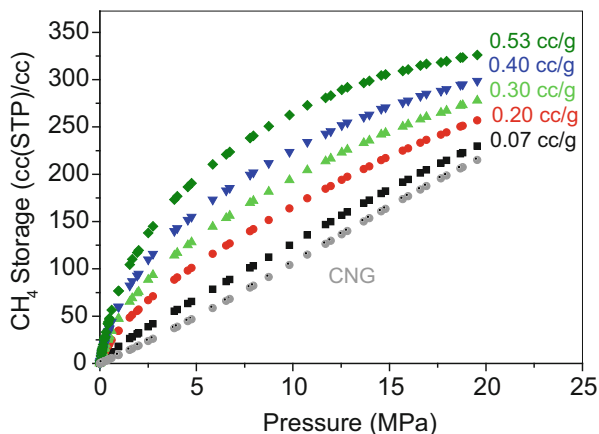


**Fig. 8.5** Methane storage capacity at 298 K and up to 25 MPa for a petroleum-pitch derived activated carbon (LMA 738) as a function of the packing density. CNG stands for compressed natural gas at 298 K. Reprinted with permission from ref. [9]. Copyright (2015) American Chemical Society

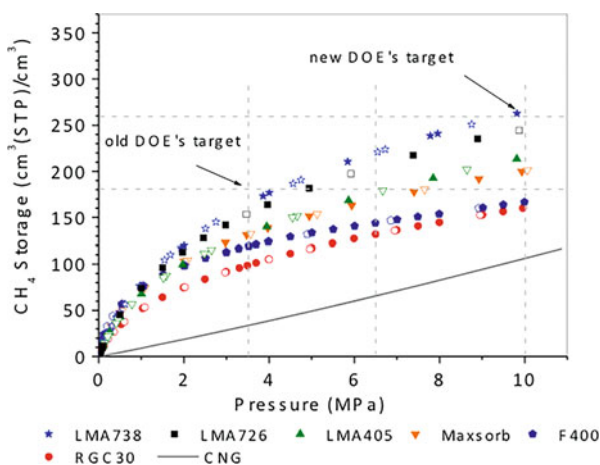


**Fig. 8.6** Methane storage capacity ( $\text{cm}^3/\text{cm}^3$ ) for different activated carbon materials. Solid line represents CNG. Adapted with permission from ref. [9]. Copyright (2015) American Chemical Society

appreciated in Fig. 8.5, a packing density above  $0.4\text{--}0.5\text{ g/cm}^3$  is crucial to achieve a sufficient concave isotherm (preferentially below 10 MPa) to justify the benefit of ANG versus CNG.

In the specific case of sample LMA 738 (see Fig. 8.6), this sample prepared by chemical activation with KOH of a petroleum-pitch residue achieved a storage capacity as high as 265 v/v at 298 K and 10 MPa. At this point it is important to highlight that this is one of the few carbon materials described

in the literature able to reach the actual volumetric DOE target of 263 v/v, although at 10 MPa. However, as described above this high pressure will require an expensive compressor (not affordable for domestic use) and will limit the capacity to design an adaptable storage vessel. At a more convenient pressure (6.5 MPa), the delivery capacity (down to 0.5 MPa) for a binderless monolith of sample LMA738 prepared at 753 kg/cm<sup>2</sup> is as high as 174 v/v [9]. To our knowledge this is one of the best delivery values described in the literature until now. Another point to highlight is the large versatility of these petroleum pitches to produce carbon materials with an excellent adsorption performance and the improved thermal conductivity (around 0.1–0.2 W/m·K) of these carbon materials compared to conventional carbons [35]. Furthermore, recent studies by Casco et al. have shown that these carbons can be prepared from different residues with an excellent performance for methane storage independently of the residue (it is not a single value obtained for a single carbon material, as reported frequently in the literature) [36]. One of the main advantages of the petroleum-derived carbon is the self-sintering ability of the carbon precursor that allows preparing monoliths without the use of a binder, thus preventing the partial blocking of the porosity. However, the use of a binder is the main approach described in the literature to densify the carbon adsorbent. Saran, humic acid derived sodium salt (HAS), polyvinyl alcohol (PVA), phenolic resins (PR), carboxy-methyl cellulose (CMC) and Teflon (TF) are among the most widely applied binders to conform the carbon adsorbents.

MacDonald et al. developed monoliths of activated carbon AX-21 (Maxsorb) with polyvinylidene copolymer (Saran) as a binder [33]. The incorporation of the binder is reflected in a slight decrease in the gravimetric adsorption capacity, whereas the volumetric capacity remained mainly unchanged. The composite with a 37% of Saran 159 latex gives a delivery capacity of 140 v/v ( $\rho_{\text{carbon}} = 0.8 \text{ g/cm}^3$ ) at 3.5 MPa and 298 K. Bose et al. studied the same activated carbon AX-21 after incorporation of PVA as a binder [37]. Disk shape tablets made by composites of PVA and AX-21 were developed with an improved storage capacity from 109 v/v up to 185 v/v, due to the increased packing density of the composite (0.7 g/cm<sup>3</sup> versus 0.3 g/cm<sup>3</sup> of the original carbon powder). Rash et al. have recently reported an excellent delivery value (up to 151 v/v in between 3.5 MPa and 0.1 MPa) for the commercial WV-A 1100 Nuchar activated carbon after a subsequent chemical activation step and using polyvinylidene chloride (PVDC) as a binder [17]. A rather similar delivery capacity in volumetric basis was reported for anthracite-derived activated carbons monoliths [26]. While the original activated carbon (in powder form after a packing step) had a delivery capacity of 145 v/v, the incorporation of a binder gave rise to a certain decrease in the storage capacity. In this sense, a binder propriety of Waterlink Sutcliffe Carbon (WSC) was the best performing material (delivery capacity of the composite 126 v/v), while polyvinyl alcohol (PVA) was the worse one due to the complete blocking of the porosity (down to 29 v/v). A slightly larger methane uptake (162 v/v) was obtained for Mongolian anthracite based porous carbon monoliths using carboxy-methyl cellulose as a binder [38].

Another approach to increase the packing density of powder activated carbons is to minimize the interparticle void space by packing different particle sizes. According to Greenbank et al. when the largest particles are less than one-third the size of the smallest large particles, and 60% of the adsorbent particles have a size greater than 60 mesh, the adsorbent particles are oriented in such a way that the packing density achieved is 130% larger than the particle's apparent density [39]. Mixing grains of well-chosen different sizes and subsequent compaction at  $100 \text{ kg/cm}^2$  allowed Celzard et al. to achieve among the best carbon materials for methane storage in volumetric basis [34]. An storage capacity of 193 v/v and a delivery of 163 v/v were reported at 3.5 MPa and 298 K for NaOH activated anthracites. Those are among the best results described in the literature until now.

## 8.5 Conclusions

This chapter summarizes the main achievements in the preparation of carbon adsorbents for high-pressure methane storage. Theoretical predictions clearly anticipate the importance of a proper porous structure, i.e., pore size, shape and pore size distribution. GCMC simulations anticipate that the optimum pore size for methane storage is 0.8 nm (or  $H = 1.14 \text{ nm}$ ), the slit-shaped morphology exhibiting a larger adsorbed methane density compared to other geometries (for instance cylindrical or spherical pores). However, a small fraction of larger pores must be necessary (according to theoretical predictions micropore width of 1.5 nm for optimized charge and 2.5 nm for optimized discharge steps) to minimize heat and mass transfer limitations under dynamic conditions. Theoretically, the maximum storage capacity in a volumetric basis must be around 200 v/v for a static system, while this number must decrease to 155 v/v or below under adiabatic conditions, depending on nature of the adsorbent and the heat and mass transfer limitations [40]. Experimental results clearly show that excess gravimetric uptake in carbon materials exhibits an upper limit at around 0.2 g/g at 3.5 MPa and 298 K, independently of the carbon material and the activation conditions used. Although those are excess values, the gravimetric storage capacity (ca. 0.3 g/g) is still quite far from the actual DOE target (0.5 g/g). From a volumetric basis, carbon materials exhibit a better performance provided that proper monoliths with a high packing density can be prepared. The best adsorption results show that carbon materials are able to reach the volumetric DOE target (263 v/v), but only at inconveniently high-pressures (10 MPa). Concerning the delivery capacity, an upper limit at around 160 v/v (at 3.5 MPa) and 170 v/v (at 6.5 MPa) seems to be the actual record values for an onboard storage system filled with activated carbon. Recent calculations for a 110 L tank filled to 5 MPa with a proper activated carbon estimate a driving range of up to 225 km, a value very competitive with actual pure electric vehicles [41].

## References

1. Cai H, Burnham A, Chen R, Wang M (2017) Wheels to wheels: environmental implications of natural gas as a transportation fuel. *Energy Policy* 109:565–578
2. See the DOE MOVE program at <http://arpa-e.energy.gov/?q=arpa-e-programs/move>. Accessed Jan 2018
3. Menon V, Komarneni S (1998) Porous adsorbents for vehicular natural gas storage: a review. *J Porous Mater* 5:43–48
4. Li B, Wen H-M, Zhou W, Xu JQ, Chen B (2016) Porous metal-organic frameworks: promising materials for methane storage. *Chem* 1:557–580
5. Vasanth Kumar K, Preuss K, Titirici MM, Rodríguez-Reinoso F (2017) Nanoporous materials for onboard storage of natural gas. *Chem Rev* 117:1796–1825
6. Marsh H, Rodríguez-Reinoso F (2006) *Activated carbon*. Elsevier, Amsterdam
7. Greinke RA, Bretz L, Mullhaupt JT (1994) Method for storing methane using a halogenating agent treated activated carbon. US Patent 5,372,619
8. Balandin AA (2011) Thermal properties of graphene and nanostructured carbon materials. *Nat Mater* 10:569–581
9. Casco ME, Martínez-Escandell M, Gadea-Ramos E, Kaneko K, Silvestre-Albero J, Rodríguez-Reinoso F (2015) High-pressure methane storage in porous materials: are carbon materials in the pole position? *Chem Mater* 27:959–964
10. Peng Y, Krungleviciute V, Eryazici I, Hupp JT, Farha OK, Yildirim T (2013) Methane storage in metal-organic frameworks: current records, surprise findings and challenges. *J Am Chem Soc* 135:11887–11894
11. Tan Z, Gubbins KE (1990) Adsorption in carbon micropores at supercritical temperatures. *J Phys Chem* 94:6061–6069
12. Matranga KR, Myers AL, Glandt ED (1992) Storage of natural gas by adsorption on activated carbon. *Chem Eng Sci* 47:1569–1579
13. Cracknell RF, Gordon P, Gubbins KE (1993) Influence of pore geometry on the design of microporous materials for methane storage. *J Phys Chem* 97:494–499
14. Chen XS, McEnaney B, Mays TJ, Alcañiz-Monge J, Cazorla-Amoros D, Linares-Solano A (1997) Theoretical and experimental studies of methane adsorption on microporous carbons. *Carbon* 35:1251–1258
15. Quinn DF, MacDonald JA (1992) Natural gas storage. *Carbon* 30:1097–1103
16. Biloe S, Goetz V, Guillot A (2002) Optimal design of an activated carbon for an adsorbed natural gas storage system. *Carbon* 40:1295–1308
17. Rash TA, Gillespie A, Holbrook BP, Hiltzik LH, Romanos J, Soo YC, Sweany S, Pfeifer P (2017) Microporous carbon monolith synthesis and production for methane storage. *Fuel* 200:371–379
18. Biloe S, Goetz V, Mauran S (2001) Dynamic discharge and performance of a new adsorbent for natural gas storage. *AIChE J* 47:2819–2830
19. Barbosa Mota JP, Rodrigues AE, Saatdjian E, Tondeur D (1997) Dynamics of natural gas adsorption storage systems employing activated carbon. *Carbon* 35:1259–1270
20. Shen J, Dailly A, Beckner M (2016) Natural gas sorption evaluation on microporous materials. *Microp Mesop Mater* 235:170–177
21. Zhou L, Zhou Y, Li M, Chen P, Wang Y (2000) Experimental and modeling study of the adsorption of supercritical methane on a high surface activated carbon. *Langmuir* 16:5955–5959
22. Rouquerol F, Rouquerol J, Sing K (1999) *Adsorption by powders and porous solids*. Academic Press, London
23. Kaneko K, Shimizu K, Suzuki T (1992) Intrapore field-dependent micropore filling of supercritical N<sub>2</sub> in slit-shaped micropores. *J Chem Phys* 97:8705–8711
24. Rodríguez-Reinoso F, Almansa C, Molina-Sabio M (2005) Contribution to the evaluation of the density of methane adsorbed on activated carbon. *J Phys Chem B* 109:20227–20231

25. García-Blanco AA, Vallone AF, Korili SA, Gil A, Sapag K (2016) A comparative study of several microporous materials to store methane by adsorption. *Microp Mesop Mater* 224:323–331
26. Lozano-Castelló D, Alcañiz-Monge J, de la Casa-Lillo MA, Cazorla-Amoros D, Linares-Solano A (2002) Advances in the study of methane storage in porous carbonaceous materials. *Fuel* 81:1777–1803
27. Munson RA, Clifton RA (1971) Natural gas storage with zeolites. Bureau of Mines Nonmetallic Minerals Program. Technical progress report-38
28. Otto K (1981) Adsorption of methane on activated carbons and zeolites. Ford Motor Company report, Michigan
29. Engel LJ, Turko JW (1985) Gaseous hydrocarbon fuel storage system and power plant for vehicles and associated refueling apparatus. US Patent 4,522,159
30. Rodríguez-Reinoso F, Nakagawa Y, Silvestre-Albero J, Juárez-Galán JM, Molina-Sabio M (2008) Correlation of methane uptake with microporosity and surface area of chemically activated carbons. *Microp Mesop Mater* 115:603–608
31. Kockrick E, Schrage C, Borchardt L, Klein N, Rose M, Senkowska I, Kaskel S (2010) Ordered mesoporous carbide derived carbons for high pressure gas storage. *Carbon* 48:1707–1717
32. Yeon SH, Osswald S, Gogotsi Y, Singer JP, Simmons JM, Fischer JE, Lillo-Rodenas MA, Linares-Solano A (2009) Enhanced methane storage of chemically and physically activated carbide-derived carbon. *J Power Sour* 191:560–567
33. McDonald JAF, Quinn DF (1998) Carbon adsorbents for natural gas storage. *Fuel* 77:61–64
34. Celzard A, Fierro V (2005) Preparing a suitable material designed for methane storage: a comprehensive report. *Energy Fuel* 19:573–583
35. Kubo T, Sakamoto H, Fujimori T, Itoh T, Ohba T, Kanoh H, Martínez-Escandell M, Ramos-Fernández JM, Casco M, Rodríguez-Reinoso F, Urita K, Moriguchi I, Endo M, Kaneko K (2012) Diffusion-barrier-free porous carbon monoliths as a new form of activated carbon. *ChemSusChem* 5:2271–2277
36. Casco ME, Martínez-Escandell M, Kaneko K, Silvestre-Albero J, Rodríguez-Reinoso F (2015) Very high methane uptake on activated carbons prepared from mesophase pitch: a compromise between microporosity and bulk density. *Carbon* 93:11–21
37. Bose TK, Chachine R, St-Arnaud JM (1991) High-density adsorbent and method of producing same. US Patent 4,999,330
38. Byamba-Ochir N, Shim WG, Balathanigaimani MS, Moon H (2017) High density Mongolian anthracite based porous carbon monoliths for methane storage by adsorption. *Appl Energy* 190:257–265
39. Greenbank M (1988) Preparation of a dense pack particulate gas adsorbent. US Patent 4,972,658
40. Beckner M, Dailly A (2016) A pilot study of activated carbon and metal-organic frameworks for methane storage. *Appl Energy* 162:506–514
41. Beckner M, Dailly A (2015) Adsorbed methane storage for vehicular applications. *Appl Energy* 149:69–74

# Chapter 9

## Methane Storage on Metal-Organic Frameworks



Anne Dailly and Matthew Beckner

### 9.1 Introduction

According to Omar Yaghi, a pioneer of reticular chemistry, “Metal-organic frameworks (MOFs) are the fastest growing class of materials in chemistry today” [1]. Consisting of interchangeable metal-containing nodes and carbon-based struts, MOFs have stimulated much interest and research in many applications, including methane storage.

High surface area and high porosity microporous materials, such as MOFs, are an attractive option to store methane at ambient temperature and low pressure (50 bar) [2–4]. Indeed, when such materials are exposed to pressurized methane, a van der Waals-type interaction between the gas and the material causes a high-density film to adsorb on the surface of the material. This high-density film allows adsorbents to potentially store more methane at lower pressures than pure gas compression. Because the methane-adsorbent interaction is weak, simply depressurizing the gas is sufficient to desorb the methane from the surface.

The challenges with using adsorbents for methane storage are numerous. Mainly, the thermodynamics of physisorption works against gas storage and delivery performances. When filling a material bed with an adsorbate, adsorption, being exothermic, can greatly increase the temperature of the bed and further reduce the quantity of gas stored within the material. Conversely, the bed temperature’s decrease upon depressurization leads to adsorbate retention within the material. Although MOFs and more conventional adsorbents, such as activated carbons, have

---

A. Dailly (✉)

General Motors Global Research and Development, Energy Storage Material Laboratory, Warren, MI, USA

e-mail: [anne.dailly@gm.com](mailto:anne.dailly@gm.com)

M. Beckner

General Motors Global Fuel Cell Business, Hydrogen Storage System, Pontiac, MI, USA

© Springer Nature Singapore Pte Ltd. 2019

K. Kaneko, F. Rodríguez-Reinoso (eds.), *Nanoporous Materials for Gas Storage*, Green Energy and Technology, [https://doi.org/10.1007/978-981-13-3504-4\\_9](https://doi.org/10.1007/978-981-13-3504-4_9)

227

a large number of pores that afford a vast amount of free space, these materials have a high tortuosity on the macroscale so that any straight pathway for a gas molecule within the material is much shorter than the mean free path of the bulk gas. This impacts storage and delivery kinetics by slowing diffusion. Adsorbents will also add cost and weight to any storage system and efforts shall be made to minimize both. Nevertheless, increased storage capacity at lower pressures still makes adsorbed methane storage an attractive advanced storage solution.

The main catalyst for research in methane storage is due to a renewed interest in natural gas (NG), a fossil fuel extracted from numerous regions in United States (US) and around the world [5, 6]. Introducing low-carbon fuels like NG has been one of the strategies to reduce transportation greenhouse gas (GHG) emissions, which account for 27% of the US's total GHG emissions [7]. In terms of infrastructure, more than one million miles of underground NG pipelines already exist across the United States. Compressed natural gas (CNG) can substitute either gasoline or diesel in vehicles ranging from passenger vehicles to Class 8 vehicles. Because of its lower energy density compared to gasoline (the heating value of NG at 250 bar is about  $11.1 \text{ MJ} \cdot \text{L}^{-1}$  compared to  $32 \text{ MJ} \cdot \text{L}^{-1}$  for gasoline), NG tanks occupy approximately three times more space on a vehicle to store an equivalent energy of gasoline. Because of this lower energy density, longer driving ranges come at the expense of cargo space, which is where the bulk cylindrical pressure vessels are usually positioned. Adsorbed natural gas could allow for lower service pressures resulting in tanks that could be shaped to efficiently fit within the vehicle with minimal loss of cargo space and enabling home refueling options.

Natural gas has a wide variety of mixtures containing high molecular weight hydrocarbons, carbon dioxide, nitrogen, oxygen, and hydrogen sulfide; the main constituent is methane (70–90% [8–10]). For materials development and screening, it is most useful to try to simplify experiments as much as possible. As a result, the vast majority of research into adsorbed natural gas research is focused on methane adsorption with only a few researches focusing on gas mixtures [8–11]. For that reason, this chapter will focus on methane adsorption only.

In this chapter, the reviews of methane storage in MOFs are contextualized to the specific application in vehicular transportation. Fundamentals of methane storage and important sorption concepts are presented. Best means of evaluating storage performance parameters have been canvassed, and results are detailed and discussed. First, we present the relationships between methane excess adsorption, measured quantities, and MOFs' textural properties. We demonstrate how the choice of certain parameters can affect the calculated total gas storage values. We show how MOFs' structure and chemistry affect the methane storage uptake, particularly the influence of surface area, pore sizes, and open metal sites. Then the temperature dependence of adsorption is exemplified as it plays a key role along with the shape of the adsorption isotherm on useable gas. Finally, we study the impact of densification of the MOFs on the methane storage. A pilot study on about 1–2 kg benchmark MOFs allow for better understanding on what to expect in terms of diffusion kinetics at production-size scale.

## 9.2 Physical Adsorption, Methane Storage Quantities, and Material Densities

The classic picture of adsorption is of a sheet of material immersed in a gas. van der Waals-type interactions cause a higher density film to form on the surface of the material (Fig. 9.1). The gas-solid interaction is quantified by a potential energy that is corrugated, dependent upon the atomic positions in the solid sheet. This corrugated potential results in a number of adsorption sites at the potential minima. Depending upon the temperature, adsorbed molecules can be locally adsorbed, where adsorbed molecules oscillate within the potential well, or mobile, where adsorbed molecules are free to move between adsorption sites [12].

In MOFs, studies have shown that metal-oxygen clusters are preferential adsorption sites for the gas, and the effect of the organic linkers becomes evident with increasing pressure [13, 14]. The ligands adsorb to a lesser extent, and they primarily provide the structure of the material. Additionally, since methane is supercritical above  $-82.3\text{ }^{\circ}\text{C}$ , most applications will allow only monolayer adsorption of methane, meaning that the adsorbing gas will not condense into a liquid. Although the structure of MOFs is not a flat sheet as an adsorbing system is often imagined, the underlying equations for calculating total storage from adsorption are the same.

Under given pressure and temperature ( $p, T$ ) conditions, excess adsorption is defined as the total amount of gas at the surface less the amount that would be present if there were no gas-solid interactions. The excess adsorption is the only quantity associated to the adsorbed phase readily accessible to measurements such as macroscopic volumetric methods used for the data presented through this chapter. However, the total amount of methane that a material can store, which accounts for all the gas molecules present in the pores, voids, and defects, is more relevant for practical applications and must be computed. There are two ways to represent the total amount of gas stored in the material: the total mass of gas stored in an adsorbent system per mass of adsorbent, gravimetric storage  $m_{\text{st}}$ , or per volume of adsorbent, volumetric storage  $v_{\text{st}}$ . Gravimetric storage may be calculated from the excess adsorption  $m_{\text{exc}}$  (per mass of adsorbent) using:

$$m_{\text{st}} = m_{\text{exc}} + \rho_{\text{gas}} v_{\text{pore}} \quad (9.1)$$



**Fig. 9.1** The gas density along the long axis of the tank shows the excess adsorption (blue) compared to the normal gas density (red) (left). For comparison, the density profile of an empty tank is also shown (right)

where  $\rho_{\text{gas}}$  is the gas density and  $v_{\text{pore}}$  is the total pore volume accessible to the gas per mass of adsorbent. This is simply the excess adsorption plus the amount of gas in the gas phase. This formula can easily be deduced from examination of Fig. 9.1. Technically, all quantities here except for the pore volume are pressure and temperature dependent, but in practice they are expressed as a function of pressure or temperature only, depending on the experimental measurement. The volumetric storage may be calculated from the gravimetric storage if the bulk density of the material  $\rho_b$  is known

$$v_{\text{st}} = m_{\text{st}}\rho_b \quad (9.2)$$

and

$$v_{\text{st}} = m_{\text{exc}}\rho_b + \rho_{\text{gas}}v_{\text{pore}}\rho_b \quad (9.3)$$

We can rewrite both the gravimetric and volumetric storage by using that the pore volume is  $v_{\text{pore}} = \rho_b^{-1} - \rho_s^{-1}$ ,

$$m_{\text{st}} = m_{\text{exc}} + \rho_{\text{gas}} \left( \frac{1}{\rho_b} - \frac{1}{\rho_s} \right) \quad (9.4)$$

and

$$v_{\text{st}} = m_{\text{exc}}\rho_b + \rho_{\text{gas}} \left( 1 - \frac{\rho_b}{\rho_s} \right) \quad (9.5)$$

A critical consequence of Eq. (9.5) is seen by comparing the volumetric storage to the storage of an empty tank (i.e., the gas density). If we want the volumetric storage to be greater than the storage in an empty tank, from Eq. (9.5) one readily obtains that this is true if and only if

$$m_{\text{exc}} > \frac{\rho_{\text{gas}}}{\rho_s} \quad (9.6)$$

which is independent of the adsorbent's pore volume. There is, therefore, some pressure  $p_c$  above which an empty system will perform better than an adsorbent system (Fig. 9.2)

$$\rho_{\text{gas}}(p_c, T) = m_{\text{exc}}\rho_s \quad (9.7)$$

Since the gas density is a monotonically increasing function of temperature, we can increase  $p_c$  by either increasing the excess adsorption in the  $(p, T)$  region of interest or by increasing the skeletal density of the material. For methane storage applications, we are therefore concerned with increasing excess adsorption to maximize this critical pressure. The physics of methane physisorption, however, makes this task difficult.

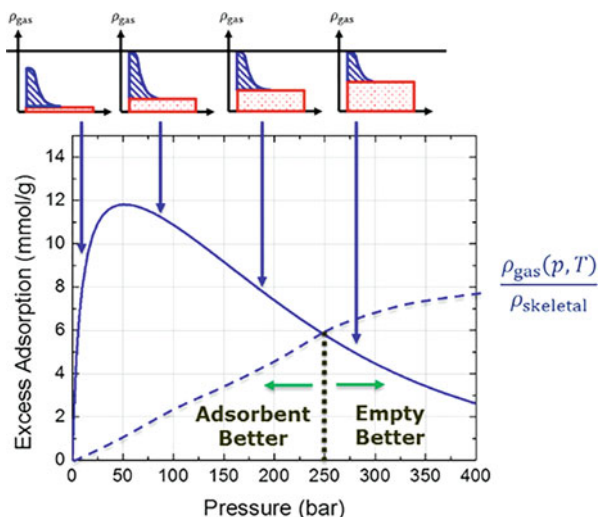


**Fig. 9.2** Hypothetical excess methane adsorption (solid line) compared to  $\rho_{\text{gas}}(p, T)/\rho_s$  (dashed line). Schematics of excess adsorbed molecules (blue) and gas density molecules (red) evolution with increasing gas pressure

Because methane is supercritical in the temperature range of most methane storage applications, only monolayer adsorption is possible, meaning that there is only one methane molecule per adsorption site. Consequently, the excess adsorption isotherm will reach a maximum and begin to decrease after a certain pressure. As pressure increases, the gas density at the adsorbent surface starts to saturate, while the bulk gas density keeps increasing. The isotherm's maximum and following rollover occur when the density of the coexistent bulk phase increases faster than the adsorbed phase. When graphed, the pressure  $p_c$  becomes apparent (Fig. 9.2).

Although the pressure at which an empty system begins to outperform an adsorbent-based system is independent of the pore volume, the actual value of gravimetric or volumetric storage is not. The critical step here is the pore volume determination. Figure 9.3 shows a schematic of an adsorbent powder grain. There are four important volumes defined in Fig. 9.3: the skeletal volume  $V_s$ , the apparent volume  $V_a$ , the crystal volume  $V_c$ , and the bulk volume  $V_b$ . Each volume has a corresponding density calculated by dividing the sample mass by the appropriate volume. The volume that is available to the gas is the open pore volume and the intergranular void volume. So, the pore volume is  $V_{\text{pore}} = V_{\text{bulk}} - V_s$ . Since we will refer to the pore volume normalized to the sample mass, we have  $v_{\text{pore}} = \rho_b^{-1} - \rho_s^{-1}$  as was used to arrive at Eq. (9.6). In this way, Eq. (9.6) reflects the way the adsorbent material is packed in a system.

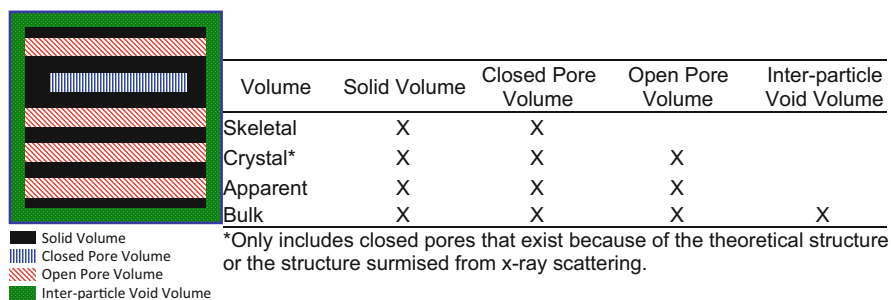


**Fig. 9.3** Diagram showing a 2-D cross-section of a MOF particle containing channel-like pores and the definitions of different derived volumes from their basic definitions

In MOF literature, the crystal density is given in lieu of the bulk density because it is easily obtained from X-ray diffraction and allows for easier comparison between publications. It has been, therefore, common to use the crystal density instead of the bulk density when calculating storage in MOFs. However, the crystal density is a microscopic quantity which does not take into account pores blocked due to crystal defects or the relative packing of adsorbent particles. When considering applications, it is critical to use the bulk density for storage calculations. Since the crystal density is larger than the bulk density, using the crystal density leads to idealized “best case scenario” values for storage capacity.

### 9.3 Experimental Details

All results presented in this chapter were obtained using experimental characterization methods as follows. Most gas adsorption-desorption measurements were performed at ambient temperature using an automated volumetric adsorption apparatus (PCT-Pro 2000 from Hy-Energy LLC) over the pressure range of 0–70 bar. The excess methane adsorption isotherms were calculated from successive gas expansions using the volumetric method (i.e., Sieverts’ method) and equations detailed in references [15, 16]. The dead space volumes were determined at 298 K using helium treated as a negligibly adsorbing gas. Pure compressed methane (99.999% CH<sub>4</sub>) was used for the sorption measurements. All gases were obtained from Airgas, Inc. In the case where higher pressures were required (e.g., Fig. 9.5), a custom-built volumetric adsorption instrument was used [17, 18]. The dead space volumes and methane purity were the same as the lower pressure measurements. For the application-scale measurements in Sect. 9.4.5, a custom-built instrument with a sample chamber volume of 3 L was used. This was also a volumetric type instrument. The sample chamber had 11 resistance thermometers evenly spaced down the long access of the cylindrical chamber to measure the temperature evolution at different point in the sample.

Most MOFs were available at lab scale or larger scale as mentioned previously. A minimum quantity of 150 mg was required for our specific Sieverts' type instrument and measurements to avoid background noise and uncertainty errors.

The porous texture analysis of the MOFs adsorbents was carried out using N<sub>2</sub> and Ar adsorption measurements at 77 K and 87 K, respectively, using a Quantachrome Autosorb-1 gas sorption apparatus. The specific surface area (SSA) was determined from N<sub>2</sub> at 77 K using the Brunauer-Emmett-Teller (BET) equation. It should be noted that the SSA was calculated over a range of P/P<sub>0</sub><sup>-1</sup> of 5 × 10<sup>-2</sup>-1.0 × 10<sup>-1</sup>, as these conditions can influence the value of the resulting area. The pore size distributions were determined using a standard nonlocal density function theory (NLDFT) method from the Ar sorption data. The total pore volume V<sub>p</sub> was obtained from the saturation value of the Ar adsorption isotherms (0.995 P/P<sub>0</sub><sup>-1</sup>) using the liquid density.

The air- and moisture-sensitive samples were handled, loaded, and weighed in an argon atmosphere on a precision balance (±1 mg). The remaining samples were loaded and weighed in a room temperature atmosphere on a precision balance (±0.1 mg). Additionally, all materials were outgassed in the sample holder at various temperatures<sup>1</sup> and a 10<sup>-5</sup> torr vacuum overnight prior to any sorption measurements.

All the MOFs which have been considered as potential methane storage materials share the same attributes. In addition to being three-dimensional crystalline hybrid inorganic-organic frameworks, they exhibit high porosity and high specific surface area. The variety of available metals and bridging ligands combined in the framework yields an extensive range of structures with diverse pore sizes and functionalities. Extensive sets of MOFs have been synthesized at laboratory scale, and limited ones have been scaled up. MOFs have been evaluated as methane adsorbents not only in order to down select the most promising adsorbent for selected (p,T) operating conditions but also to understand the mechanisms and interplay between the material's properties and its storage capacity. The adsorbents reported in this chapter were either synthesized in house, obtained from numerous collaborations with universities (Texas A&M University; University of Nottingham, UK; University of California, Berkeley; and University of Michigan), or bought from suppliers. Materials were provided along with their crystalline characterization.

A substantial number of studied MOFs were based on aromatic carboxylate ligands. IRMOF-1 and MIL-53 are both constructed from H<sub>2</sub>BDC (1,4-benzenedicarboxylic acid) [19, 20]. Amino-MOF-177 is based on H<sub>3</sub>BTB (4,4',4''-benzene-1,3,5-triyl-tri-benzoic acid) [21]. This latter is used in conjunction with H<sub>2</sub>TDC (2,5-Thiophenedicarboxylic acid) in the synthesis

---

<sup>1</sup>High temperatures are desired to drive moisture and volatiles from the MOF surface. However, each MOF will degrade if heated to too high a temperature. The degas temperature was therefore chosen for each MOF to be high enough to remove unwanted guest molecules but low enough to ensure the MOF would not decompose.

of UMCM-3 [21]. UMCM-4 is prepared with H<sub>3</sub>TCTA (4,4',4'' tricarboxyl-triphenylamine) [22]. HKUST-1 and MOF-74 (Co, Ni) are synthesized using H<sub>3</sub>BTC (1,3,5 benzenetricarboxylic acid) [23] and H<sub>2</sub>DOBDC (2,5-dihydroxy-1,4-benzenedicarboxylic acid) [24], respectively. PCN-14 is constructed from H<sub>4</sub>ADIP (5,5'-(9,10-anthracenediyl) diisophthalate) [25]. H<sub>4</sub>ABTC (3,3',5,5'-azobenzenetetracarboxylic acid) is used in PCN-250 (Ca, Co, NiCo, and Mg) [26]. PCN-6' is synthesized with H<sub>3</sub>TATB (4,4',4''-s-triazine-2,4,6-triyl-tribenzoic acid) [27], PCN-11 with H<sub>4</sub>SBTC (trans-stilbene-3,3',5,5'-tetracarboxylic acid), Zr-ABDC with H<sub>2</sub>ABDC (4,4'-azobenzenedicarboxylic acid) [28–30], and UTSA-20 with H<sub>6</sub>BHB (3,3',3'',5,5',5''-benzene-1,3,5-triyl-hexabenzoic acid) [31]. H<sub>4</sub>TCPB (1,2,4,5-tetrakis(4-carboxyphenyl)benzene) is used for the synthesis of PCN-320, while H<sub>8</sub>ETTB (4',4''',4''''',4''''''-ethene-1,1,2,2-tetrayltetrakis{([1,1'-biphenyl]-3,5-dicarboxylic acid) is used for PCN-922 [32]. PCN-66 is constructed from H<sub>6</sub>btei (5,5',5''-benzene-1,3,5-triyltris(1-ethynyl-2-isophthalic acid), while PCN-61 is constructed from H<sub>6</sub>ntei (5,5',5''-(4,4',4''-nitrilotris(benzene-4,1-diyl)tris(ethyne-2,1-diyl))triiisophthalic acid) [33]. H<sub>4</sub>TPTA (terphenyl-3,2'',5'',3'-tetracarboxylic acid) is used in the synthesis of PCN-306, H<sub>4</sub>PDDA (5,50-(pyridine-3,5-diyl)diisophthalic acid) in the synthesis of PCN-305, H<sub>4</sub>FTPTA (fluoro functionalized terphenyl-3,2'',5'',3'-tetracarboxylic acid) in the synthesis of PCN-308, and H<sub>4</sub>MTPTA (methyl functionalized terphenyl-3,2'',5'',3'-tetracarboxylic acid) in the preparation of PCN-307 [34]. PCN-56, PCN-57, and PCN-70 are constructed from H<sub>2</sub>TPDC-2CH<sub>3</sub>, H<sub>2</sub>TPDC-4CH<sub>3</sub> (methyl functionalized 4,5,9,10-tetrahydropyrene-2,7-dicarboxylic acid), and H<sub>2</sub>TPDC-nC<sub>6</sub>H<sub>13</sub> (dimethylbutyl functionalized 4,5,9,10-tetrahydropyrene-2,7-dicarboxylic acid), respectively [35]. NOTT-107 is prepared using H<sub>4</sub>TPTC-4CH<sub>3</sub> (methyl functionalized [1,1',4',1'']Terphenyl- 3,3'',5,5''-tetracarboxylic acid) [36, 37]. PCN-26 is synthesized with H<sub>8</sub>TDM (10.4.6.5 5,5'-((2,2-Bis((3,5-dicarboxyphenoxy)methyl)propane-1,3-diyl)bis(oxy))diisophthalic acid) [38]. NOTT-119 is based on H<sub>6</sub>BTTI (5,5',5''-(4,4',4''-(benzene-1,3,5-triyl)tris(1H-1,2,3-triazole-4,1-diyl))triiisophthalic acid) [39] and UMCM-300 based on H<sub>6</sub>BTPI (1,3,5-tris(3',5'-dicarboxy[1,1'-biphenyl]-4-yl)benzene) [39]. PCN-124 is synthesized with H<sub>4</sub>PDAI (5,50-((pyridine-3,5-dicarbonyl)bis-(azanediyl))diisophthalic acid) [40, 41]. H<sub>4</sub>TCPB (tetrakis (4-carboxyphenyl) porphyrin) is used in the preparation of PCN-223 and PCN-224 [42, 43].

Nitrogen-based bridging ligands were also examined such as H<sub>2</sub>BDP (1,3 benzenedi(4'-pyrazolyl) and TTPM tetrakis(4-tetrazolylphenyl)methane in the construction of Zn(1,3 BDP) [44] and MD6-128 [45], respectively. Ligands used in the construction of the studied MOFs are displayed on Fig. 9.4.

The versatility of organic ligands has provided many possibilities for the construction of porous MOFs with various topologies. This allows us to establish the key physical properties (chemistry, structure, surface area, etc.) that influence the methane storage behavior of various microporous MOFs materials.

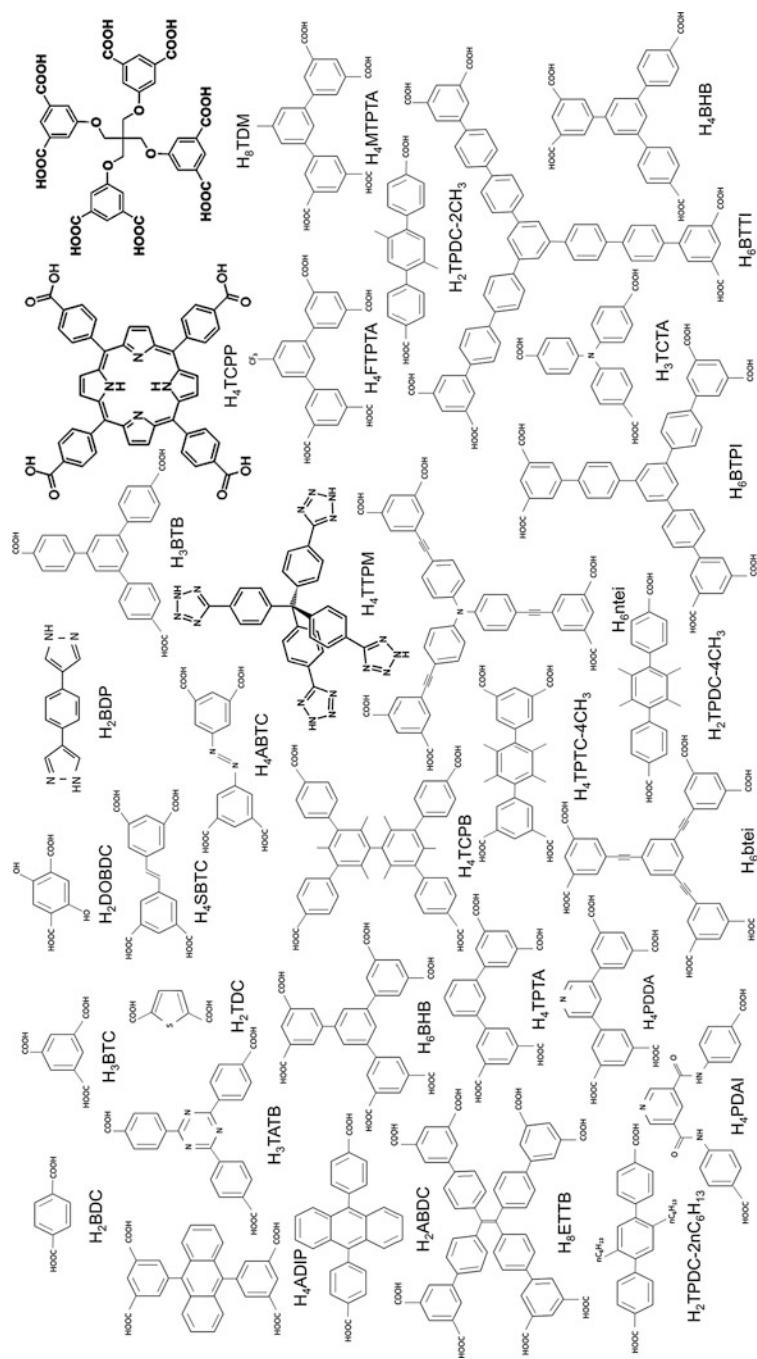


**Fig. 9.4** Ligands used in the construction of studied MOFs

## 9.4 Review and Analysis of Methane Storage Trends in MOFs

### 9.4.1 Excess Adsorption and MOF Porous Texture

Figure 9.5 displays typical excess methane adsorption isotherms at 295 K measured on several MOFs up to 300 bar:  $\text{Cu}_3(\text{btc})_2$ ,  $\text{Al}(\text{Fumarate})$ , and  $\text{Zn MOF-74}$ . The experimentally measured methane adsorption isotherms were found to belong to type 1 of the International Union of Pure and Applied Chemistry (IUPAC) classification [46]. As pressure increases, the difference between the bulk phase density and the adsorbed phase becomes smaller. Methane uptake increases with increasing pressure until, at high pressure, a stage is reached when all the sites are occupied and further increasing the pressure does not cause any additional methane to adsorb. The presence in the isotherm of a maximum is a typical feature of excess adsorption isotherms as mentioned previously. All measured MOFs show excess methane isotherms of similar shape with maximum uptakes in proportion to the sites available for the adsorbate molecules.

A summary of MOFs' maximum excess methane adsorption as a function of their BET-specific surface areas is shown in Fig. 9.6. The existence of a reliable correlation between the excess methane adsorption uptakes and the porous texture of the MOFs is of interest as it would enable the storage capacity of a given material to be estimated when measurements are not available and thereby easily check its suitability for methane storage applications. Unlike the linear correlation observed

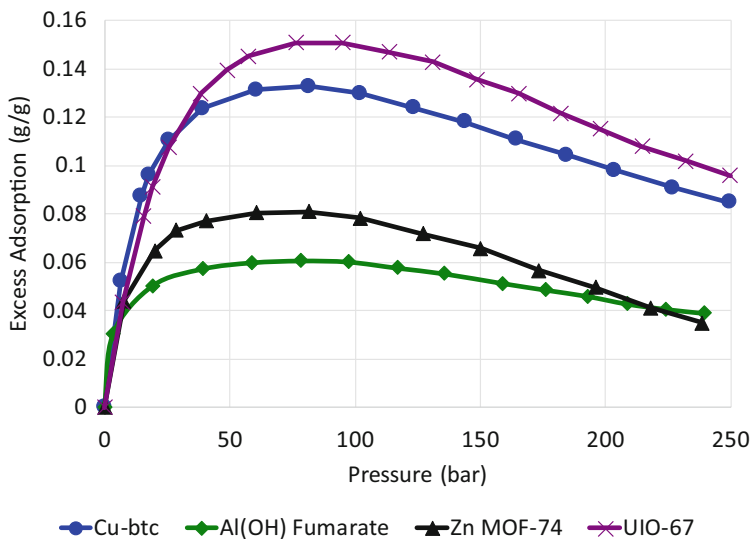
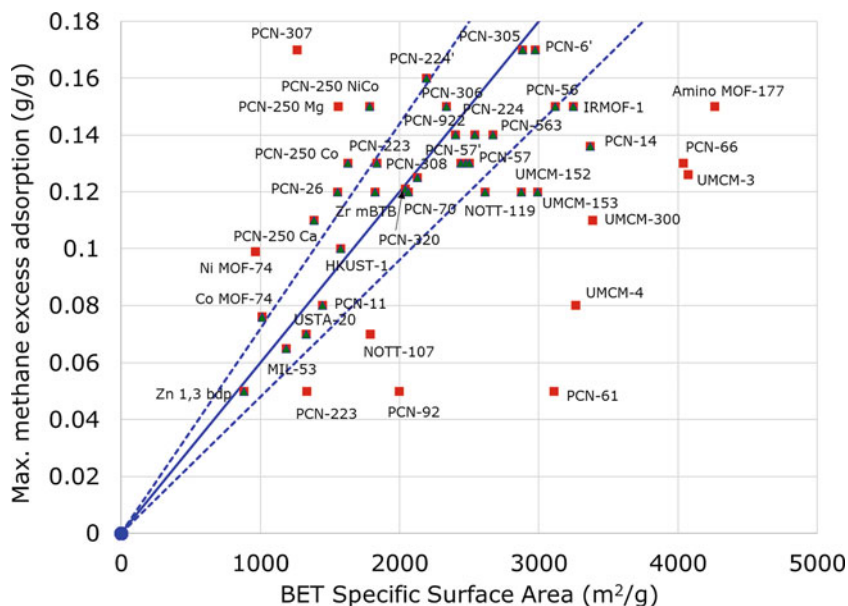


Fig. 9.5 Excess methane adsorption isotherms at 295 K and pressure range up to 250 bar



**Fig. 9.6** Measured maximum excess methane adsorptions at ambient temperature on MOFs vs. MOFs BET-specific surface areas ( $N_2$ )

between hydrogen excess maximum adsorption at 77 K and the BET-specific surface areas of the adsorbents, where 1 wt% excess uptake could be expected every  $500 \text{ m}^2 \cdot \text{g}^{-1}$  [47–49], the linear trend between the methane maximum excess uptakes and the MOFs porous texture is more blurred. An overall linear tendency between maximum excess methane adsorption and the BET-specific surface areas can be drawn, but it is not as straightforward as what was found for hydrogen cryo-adsorption. In Fig. 9.6 the blue line shows that for every  $1000 \text{ m}^2/\text{g}$  of specific surface area, one can expect  $0.06 \text{ g/g}$  of maximum methane excess adsorption. Accounting for uncertainty in the measurement, 75% of the MOFs data fall within 20% of this line. The dashed blue lines represent the 20% boundary. MOFs' data marked with green triangles are data falling within 20% of the fit line including uncertainty (10% in excess and 10% in surface area). A trend between the maximum methane excess uptakes and micropores volumes was investigated, but no better correlation was found than the one obtained versus surface areas. Overall, the chemistry of the MOFs has little impact on the maximum uptakes. The correlation between the BET-specific surface areas and maximum excess methane uptakes seems fairly independent of the chemical composition and structure of the MOFs. Present data were indeed obtained on various porous frameworks built from the linking of different building blocks and organic units with different functionalities. Surface area of the solid adsorbent is one of the key factors which affect the adsorption. The extent of adsorption depends directly upon the surface area of the

MOF, i.e., the larger the surface area of the adsorbent, the greater is the extent of adsorption.

Although there is a general trend, it's important to understand what makes materials fall outside of this latter. Another key parameter which affects the methane uptake is the pore size distribution. The hydrocarbon molecules, adsorbates, adhere to the surface by weak attractive interactions known as van der Waals forces. Adsorption occurs in pores whose diameter is close to twice the molecular diameter of the molecule being adsorbed which is why pore size distribution within the adsorbent is a determining factor. A few studies tried to determine the pore sizes required within the adsorbent for the adsorption of methane. For instance, Poirier studied methane adsorption on nanoscale carbon slit pores and showed that the lowest potential energy of guest molecule such as methane was found for pore size about 7 Å [50]. Wilmer et al. used high-throughput computational simulations to predict useful structure-property relationships for MOFs and came to a similar conclusion. For volumetric methane uptakes, they found optimal pore sizes to be 4 and 8 Å, exactly big enough for one or two methane molecules [36]. Indeed, the Lennard-Jones molecule size of methane reported by Kurniawan et al. is 3.75 Å [51]. It can be seen from Fig. 9.6 that the drawn linear correlation between the maximum excess uptakes and the specific surface areas fails for those MOFs with either narrow microporosity or porosity tending toward mesopores. For instance, MOF adsorbents UMCM-3 and PCN-307 were not expected to display maximum excess methane uptakes, given their BET-specific surface areas. PCN-307 and UMCM-3 are exceeding and falling behind expectations, respectively. The reason can be deduced from their corresponding pore size distributions displayed on Fig. 9.7.

PCN-307 predictably displays narrower pore width distribution than UMCM-3, which shows pores in both micropores and mesopores ranges (micropores defined as pore diameters of less than 2 nm and mesopores as pore diameters between 2 nm and 50 nm). As mentioned above, the larger pores constituting UMCM-3 are less effective for adsorption of methane molecules.

Another material characteristic which may affect the methane adsorption uptake is the presence of open metal sites. Among the MOFs out of the trend in Fig. 9.6 are Ni MOF-74 and Co MOF-74, with the latter displaying lesser maximum excess adsorption uptake for an almost identical BET SSA than the former. In that particular case, the difference in pores sizes cannot be the explanation because the two MOFs are isostructural, constructed with the same organic linker but different metal constituting the building unit. MOF-74's, or  $M_2(\text{DOBDC})$ , resulting framework consists of honeycomb-like structure with pore diameter of about 12 Å. Metal centers are bonded in a square-pyramid coordination environment leaving the  $M^{2+}$  cation in the center of the square plane open and accessible to the adsorbed gas molecules. Unsaturated metal sites have been shown to enhance methane affinities compared to non-open metals [24, 52–54]. The origin of the enhancement is believed to be due to unscreened electrostatic interaction between  $\text{CH}_4$  and the coordinately unsaturated metal ion. When different metals ( $M = \text{Ni}, \text{Co}, \text{Zn}$  and  $\text{Mg}$ ) are compared through calculations and experiments, data suggest that the overall variation of binding strength of methane with the metal species

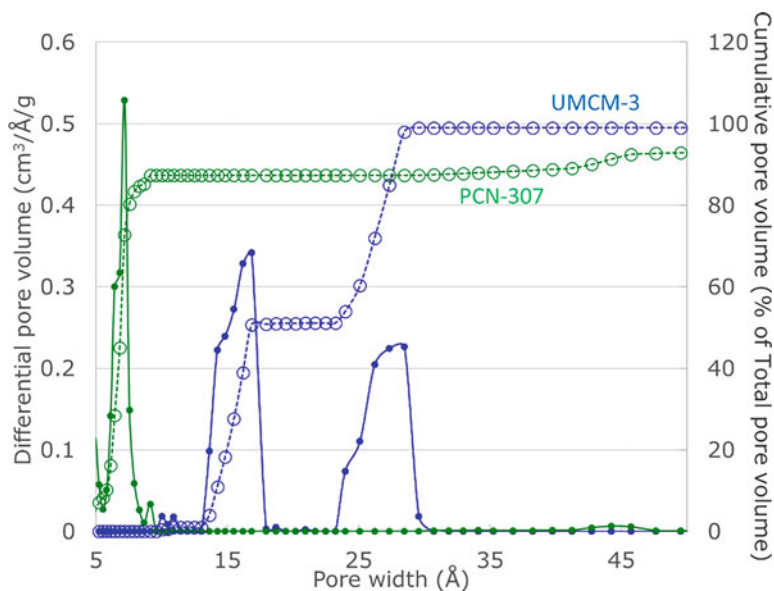


**Fig. 9.7** Differential pore volume and cumulative pore volume expressed as a function of pore width for PCN-307 and UMCM-3 MOFs samples

is small and slightly stronger with Ni than the others. This is evidenced not only in Fig. 9.6 but also on the methane excess adsorption isotherms collected on the four  $M_2(\text{DOBDC})$  ( $M = \text{Mg}, \text{Co}, \text{Ni}$  and  $\text{Zn}$ ) samples at 298 K up to 250 bar as displayed in Fig. 9.8. Among the different MOFs,  $\text{Ni}_2(\text{DOBDC})$  exhibits indeed the highest excess methane adsorption uptake. The studied samples have BET-specific surface areas, ( $\text{Mg}$ )  $1079 \text{ m}^2 \cdot \text{g}^{-1}$ , ( $\text{Ni}$ )  $966 \text{ m}^2 \cdot \text{g}^{-1}$ , ( $\text{Zn}$ )  $771 \text{ m}^2 \cdot \text{g}^{-1}$ , and ( $\text{Co}$ )  $1013 \text{ m}^2 \cdot \text{g}^{-1}$ , very similar to those of samples presented in the study conducted by Wu et al. on the important role of open metal sites on methane storage capacity in  $M_2(\text{DOBDC})$  [52].

From the measured high-pressure isotherms, one may conclude that the relative strength of methane bonding follows the trend  $\text{Zn}^{2+} < \text{Co}^{2+} < \text{Mg}^{2+} < \text{Ni}^{2+}$  which coincidentally relates to the ionic radii of the cations:  $0.68 \text{ \AA}$  ( $\text{Zn}^{2+}$ )  $>$   $0.67 \text{ \AA}$  ( $\text{Co}^{2+}$ ). While the hydrogen adsorption at 77 K on  $M_2(\text{DOBDC})$  has been shown to depend on the  $M\text{-H}_2$  distances, i.e., on metal radius, this is not the case for methane, which is a larger molecule with different geometry. Actually, the measurement errors for high-pressure isotherms are relatively large for Co and Zn based MOF-74, as evidenced by the error bars, so caution must be made when giving potential order on binding enhancement effect. Furthermore, MOF properties and resulting adsorption can differ due to synthesis process parameters and activation of the porosity conditions: reactant materials proportion, crystallization/drying time, solvent exchange, synthesis/activation temperature, etc. In any rate, open metal sites

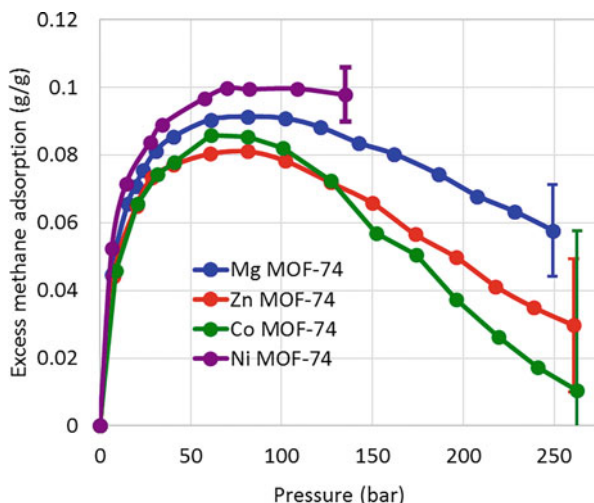


**Fig. 9.8** High-pressure excess methane isotherms on  $M_2(\text{DOBDC})$  series ( $M = \text{Zn, Ni, Co, Mg}$ )

in  $M_2(\text{DOBDC})$  series have been evidenced to exhibit binding strength for methane gas and can be used as MOF design strategy to increase methane storage.

### 9.4.2 Methane Adsorption and Thermodynamics

Porosity and open metal sites are not the only factors affecting the extent of adsorption. As adsorption is accompanied by the evolution of heat, as per Le Chatelier's principle, the magnitude of adsorption should decrease with rise in temperature. Conversely, excess adsorption is greater at lower temperatures. The nature of adsorption and desorption, being exothermic and endothermic processes respectively, means that the thermodynamics are not favorable for storing and releasing methane. A good understanding of the behavior of the adsorbent with temperature is crucial for any applications. Figure 9.9 illustrates the measurements of the excess adsorption isotherms on IRMOF-1 over the temperature range of 213–298 k and for pressures of up to 70 bar. An increase of pressure of the adsorbate gas increases the extent of adsorption. The adsorption increases more rapidly with pressure at lower temperature.

The methane excess adsorption exhibits a strong dependence on temperature. Variation of the excess adsorption with temperature and pressure must be understood for the design and use of efficient adsorption-based storage systems such as gas storage, gas separation, and adsorption-based heating pumps, to name only a few. An analytical representation of the measured adsorption data over a range of pressure and temperature swing of the system can allow to estimate excess storage at specific ( $p, T$ ) operating conditions and further compute the total storage

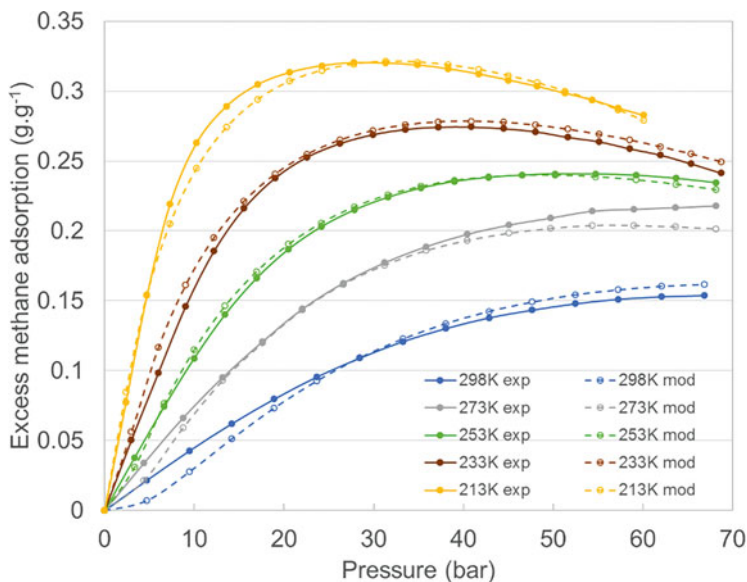


**Fig. 9.9** Experimental (plain) and modelled (dash) excess methane adsorption isotherms on IRMOF-1 between 213 and 298 K and up to 70 bar

capacity. In this example, the modified Dubinin-Astakhov (DA) model has been used to fit the experimental data. The accuracy of the fit of the experimental data over the whole  $(p, T)$  range has to be considered in conjunction with the physical significance of the parameters to make a proper assessment of the system's performance. Otherwise, conclusions about the material's performances, such as its usable methane capacities, may not correspond to reality.

The experimental methane excess adsorption isotherms have been fitted using a modified DA model presented by Richard et al. [55]. The equation

$$n_{ex} = n_{max} \exp \left[ - \left( \frac{RT}{\alpha + \beta T} \right)^m \ln^m \left( \frac{p_s}{p} \right) \right] - \rho_g V_a \quad (9.8)$$

was applied where  $n_{max}$  is the limiting adsorption (per unit mass of adsorbent), which relates to the maximum filling of the entire volume of adsorption space.  $P_0$  is a pseudo-saturation pressure corresponding to the limiting adsorption.  $\alpha$  and  $\beta$  are the enthalpic and entropic factors, respectively, of the free energy of adsorption.  $V_a$  is the adsorption volume,  $\rho_g$  is the methane gas phase density,  $R$  is the universal constant, and  $T$  is the absolute equilibrium temperature. The five parameters,  $P_0$ ,  $n_{max}$ ,  $\alpha$ ,  $\beta$ , and  $V_a$ , were determined by a simultaneous fit to all the experimental adsorption isotherms over the studied  $(p, T)$  range. The modified DA model (Eq. 9.8) was used successfully to describe the measured excess methane adsorption

isotherms over the whole  $(p, T)$  range. The modeled methane excess adsorption isotherms are presented in Fig. 9.9 as dashed lines. These curves visibly fit the experimental data accurately over the whole studied  $(p, T)$  range. Some deviations between measured and modeled curves are visible. Nevertheless, the modified DA model leads to results that are essentially within the measurement uncertainties. The deviation noticeable at low pressure and high temperature is a consequence from the empirical DA model not satisfying Henry's law at low pressure.

Simulations of the thermal effects and impacts during adsorption and desorption cycles are valuable tools, especially when model validated against experiments, since it allows for the estimation of the material's behavior toward the adsorbate at specific  $(p, T)$  conditions.

### 9.4.3 Total Storage and Usable Capacity

Gas storage capacity is contingent on excess adsorption and bulk density measurements as explained in Sect. 9.2. The bulk density includes the contribution of the particle volume, the interparticle void volume, and the internal pore volume. The bulk density is not an intrinsic property of the material but is contingent upon the way the material is packed. The total uptake depends on excess gravimetric uptake and bulk density (Eqs. (9.4) and (9.5)) which may vary considerably depending on the processing of the material. Unlike amorphous materials such as activated carbons, the well-defined crystal structure of MOFs allows for the approximation of the total storage. An oversimplified estimate of a MOF's total storage capacity can be made from its excess gravimetric methane uptake and the material's crystallographic density as previously discussed. Contrary to the bulk density, the crystallographic density is an intrinsic property of the material.

Figure 9.10 evidences the impact of the density, crystallographic versus bulk, into the calculation of the total storage capacity. The example is given for two MOFs,  $\text{Cu}_3\text{btc}_2$  and DUT-6, for which excess methane adsorption isotherms at 298 K clearly show an advantage of DUT-6 over  $\text{Cu}_3\text{btc}_2$  if considering maximum uptakes. The shape of the excess isotherms at low filling (pressures) vary for the two samples, most likely as a result of variations in methane affinity due to chemical differences in the building units. The higher affinity for methane in materials such as Cu-based MOFs can cause the adsorption to increase more rapidly as a function of pressure [56]. The differences in chemical compositions but also in structure (e.g., pore size) of the adsorbents were found to affect mainly how adsorption isotherms increase as a function of pressure. When computing the total methane uptake using the crystallographic densities of the materials,  $\text{Cu}_3\text{btc}_2$  surpasses DUT-6 for most of the studied pressure range. Total methane uptakes are also much higher for both MOFs than those obtained using the measured bulk densities. In that later case, the total methane uptakes calculated for both materials are very comparable. This clearly evidences the impact of density on the calculation of the total storage.

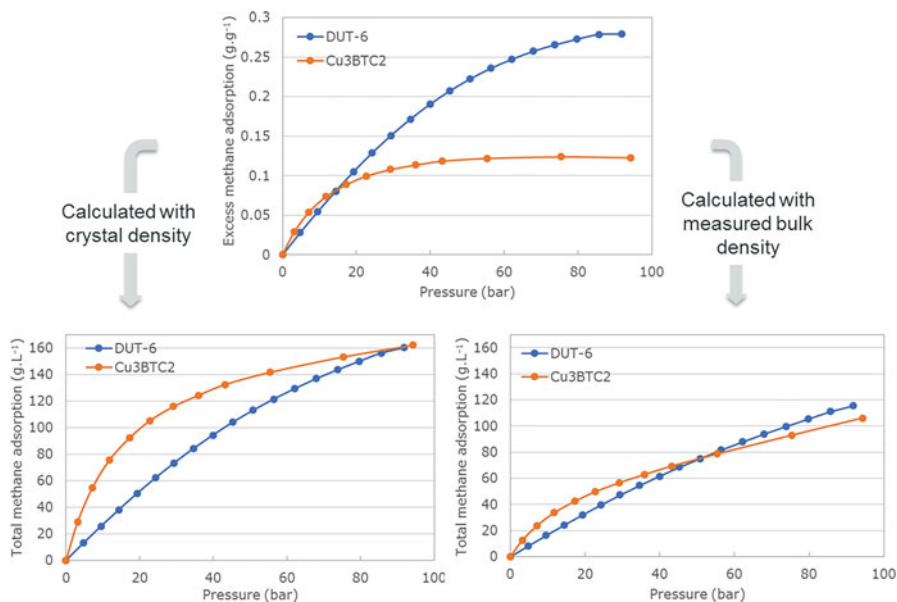


**Fig. 9.10** Total methane uptakes calculated from the corresponding excess methane adsorption isotherms and either crystallographic density of the MOF or its measured bulk density

Measurements of the bulk density can also greatly impact the storage calculations. In principle, the bulk density can be any value less than or equal to the crystal density. Consider the MOF Cu<sub>3</sub>btc<sub>2</sub>, for example, in Fig. 9.11. The resulting calculation varies immensely with the value used for the bulk density. Using the crystal density in place of the bulk density causes the gravimetric storage to be undercalculated. Since the bulk density has a larger open pore volume, it accounts for more gas per mass adsorbent, evident from Eq. (9.1). If, in the extreme high density, one uses the skeletal density, then the gravimetric storage is equal to the excess adsorption. Conversely, using the crystal density overestimates the volumetric storage by as much as a factor of two for the same reason. Note that the volumetric storage intersects the line of the gas density at the same pressure  $p_c \approx 240$  bar regardless of the density used. This is expected since the gas density represents the volumetric storage of an empty tank, and we know, from Eq. (9.6), that the pressure  $p_c$  must be independent of material packing.

Calculations of the total storage capacities will impact the evaluation of not only the overall storage but also the gas delivery for potential applications. While the storage capacity of a storage system is a crucial parameter, the usable capacity, or quantity of gas which can be delivered on desorption, is more important for applications. The storage capacity of an adsorbed methane system is always greater than the usable capacity. This is due to the thermodynamics of physical adsorption and desorption of methane in the porous media.

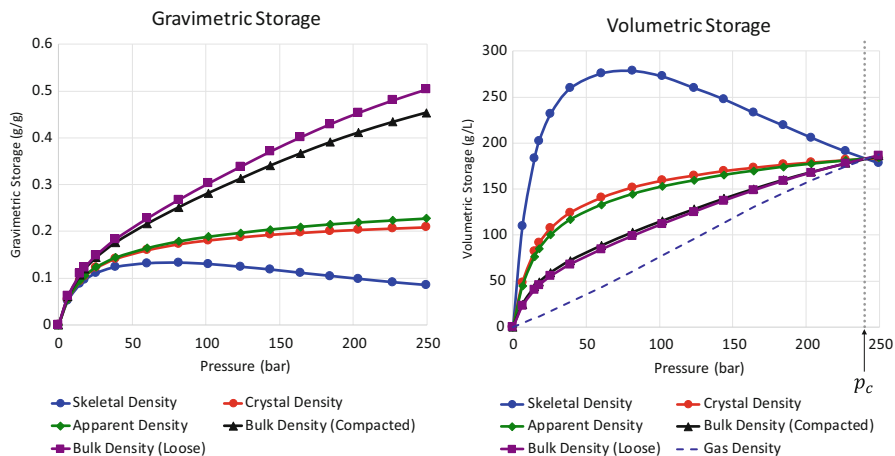


**Fig. 9.11** The gravimetric storage (left) and volumetric storage (right) calculated using Eqs. (9.2) and (9.5) with different densities substituted for the bulk density

Because physisorption is always an exothermic process, it is accompanied by the release of heat. When the concentration of the adsorbate increases at a rate faster than the adsorbent bed can dissipate the heat of adsorption, then the bed's temperature may increase significantly with time. The warming of the system is likely to lead to reduced uptake because the process of physisorption decreases as the temperature increases. A similar analysis can be done when the cooling effect of desorption is considered. When the concentration of the adsorbate decreases at a faster rate than the bed can warm, then bed temperatures may drop significantly thus slowing the rate of desorption and hampering the ease of gas delivery. These considerations support the necessity to understand and evaluate the thermodynamics of the gas-adsorbent system with  $(p, T)$  operating conditions as discussed earlier.

Temperatures fluctuations can be mitigated during fueling based on the type of fueling. There are usually two types: fast-fill and time-fill (or slow-fill). They differ by the amount of gas dispensed and the time it takes for it to be delivered. In a fast-fill-type situation, the gas is dispensed to the vessel quickly from fuel stored at high pressures. Time-fill fueling dispenses the gas directly from the compressor, slowly building up to the desired pressure. For this reason, a time-fill fueling usually allows to get more gas into the vessel than a fast-fill approach. As the fueling rate increases, the temperature of the gas also increases dramatically. The gas molecules warm up, expand more, and become less dense therefore containing less energy by volume than if it were filled slowly over time to reach the rated pressure.

The evaluation of the usable capacities for the two MOFs, DUT-6 and  $\text{Cu}_3\text{btc}_2$ , which have been reviewed previously, can be conducted assuming an isothermal discharge. Practical reality is likely to be different. As for fueling, temperature variations are also expected during gas delivery, i.e., desorption. Isothermal discharge is less likely to occur as it implies extremely slow desorption process. Typical

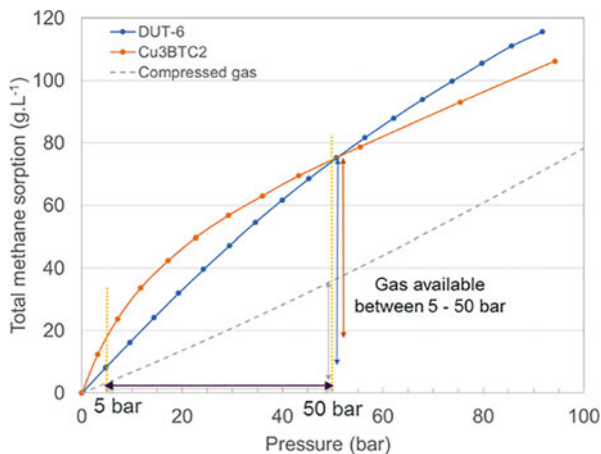


**Fig. 9.12** Total methane uptakes for DUT-6 (blue) and Cu<sub>3</sub>btc<sub>2</sub> (orange) at 295 K and amount of methane to be delivered isothermally between 50 bar and 5 bar. Methane density as a function of pressure plotted for comparison (dashed line)

desorption leads to cooling down of the adsorbent bed temperatures and therefore less gas molecules to desorb. Utmost discharge can be achieved by heating up the adsorbent bed, but this engineering solution is not always recommended as it can cost energy and add complication to the storage system.

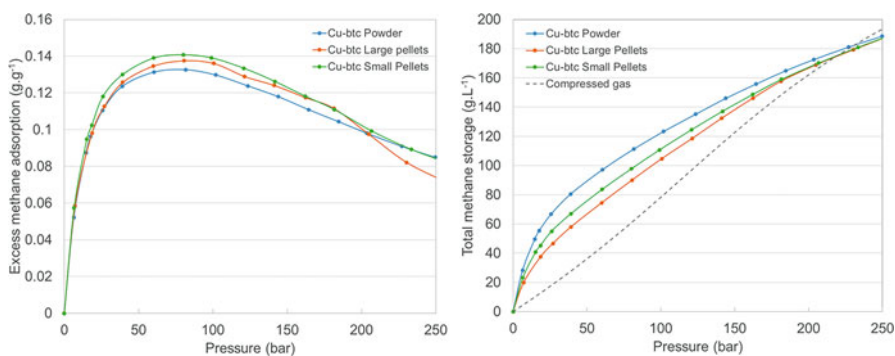
The usable capacities measured for DUT-6 and Cu<sub>3</sub>btc<sub>2</sub>, i.e., gas available between 50 bar and 5 bar selected pressures, are shown on Fig. 9.12. The density of pure methane as a function of pressure is also plotted for comparison. As foreseen from their textural properties, both MOFs show volumetric storage gains over purely compressed gas especially at low pressures around 50 bar. Even though DUT-6 and Cu<sub>3</sub>btc<sub>2</sub> have the same total volumetric methane uptakes at 50 bar, DUT-6 has the highest usable methane capacity, assuming isothermal delivery. This is due to the fact that Cu<sub>3</sub>btc<sub>2</sub> with open metal sites has stronger interaction with methane than DUT-6, which results in more methane retained by the Cu-based MOF at 5 bar.

#### 9.4.4 Influence of MOF Shaping and Densification

From Eq. (9.5), it is clear that increasing the bulk density of the material is one strategy for increasing the storage capacity. The impact of adsorbent material densification must also be taken into account. An example is given through the study of Cu<sub>3</sub>btc<sub>2</sub> powder and extruded pellets provided by MOF Technologies. Textural characterizations of the studied materials batches are given in Table 9.1. Powder compaction and densification result in a slight decrease of the BET-specific surface area from powder to pellets. Shaping has little effect on porosity and thus

**Table 9.1** Density and porosity measurements summary for  $\text{Cu}_3\text{btc}_2$  and Al-fumarate powders at laboratory scale and pilot scale

	Al(OH) fumarate		Cu-btc powder		Cu-btc small pellets		Activated carbon	
	Lab scale	Pilot scale	Lab scale	Pilot scale	Lab scale	Pilot scale	Lab scale	Pilot scale
Skeletal density [ $\text{g}/\text{cm}^3$ ]	1.7	1.7	2.5	2.1	2.2	1.8	2.2	2.3
Bulk density [ $\text{g}/\text{cm}^3$ ]	0.57	0.56	0.37	0.41	0.34	0.33	0.54	0.56
Sample mass [g]	0.891	1715	0.876	1256	0.626	1013	1.139	1721
Max. $\Delta T$ [K]	–	15.5	–	18.4	–	22.5	–	27.8
Max. $\Delta T/m$ [K/kg]	–	9.0	–	14.6	–	22.2	–	16.2
Gas permeability [ $10^{-10} \text{ cm}^2$ ]	–	8	–	24	–	Ind.	–	1.7

**Fig. 9.13** Excess methane adsorption and total methane adsorption obtained on MOF Technologies  $\text{Cu}_3\text{btc}_2$  powder and pellets

excess methane gravimetric adsorption measured for all samples fall within the same range and measurements errors (Fig. 9.13). The densification also increases the bulk density of the individual pellet but the overall bed densities diminish with compaction. The  $\text{Cu}_3\text{btc}_2$  powder packed denser than the  $\text{Cu}_3\text{btc}_2$  small pellets (about 2 mm diameter and 10 mm long) which in turn packed denser than the  $\text{Cu}_3\text{btc}_2$  large pellets (about 4 mm diameter and 10 mm long). In this way, the measured tapped densities decreased when increasing the pellet size.

The total storage capacity of the adsorbent is influenced by the amount of macropores and interparticular voids present in the material. Therefore, it can vary considerably depending on the processing of the powder, leading to significant

variations in the storage capacities of the system. In fact, one of the challenges for the industrial use of MOFs is to deliver them in a suitable form which minimizes the number of large pores and interparticular voids, which are inefficient for adsorption. Furthermore, large voids reduce the materials density and thereby the corresponding volumetric capacity.

As a common industrial practice, adsorbent powders are compacted under external pressure into pellets or monoliths to increase their packing density. Compaction is critical for gas storage applications as the space available for the storage tank is limited and MOF powders have usually very low bulk density, in the range of  $0.1\text{--}0.4\text{ g}\cdot\text{cm}^{-3}$  [57, 58]. These low bulk densities are a downside of their highly developed porosity and fluffy powder form. One objective of the compaction is for the adsorbent to occupy the container volume more efficiently by shaping the monolith or pellet under a proper form and density with minimal reduction of porosity and gas adsorption uptake.

Given that excess methane adsorption uptakes are very similar for  $\text{Cu}_3\text{btc}_2$  powder and small and large pellets, the associated total methane storage uptakes depend for the most part on the tapped densities. Total methane storage uptakes decrease from  $\text{Cu}_3\text{btc}_2$  powder to small pellets and to further large pellets in agreement with bed densities values.

#### 9.4.5 Scaling Up Material Synthesis: Can Laboratory Results Predict Performance at Applications Scale?

When scaling up materials, the first priority is to ensure that the material properties are the same for larger synthesis batches. The key material properties for storage, evident from Eqs. (9.4) and (9.5), are the skeletal density, bulk density, and excess adsorption. Three MOFs were investigated for scaled-up synthesis:  $\text{Al}(\text{OH})$  fumarate, powdered  $\text{Cu-btc}$ , and small pellets of  $\text{Cu-btc}$ . Firstly, the excess adsorption values agreed well within uncertainty for the pilot and lab scale for all three materials (Fig. 9.14 left). There was also good agreement for volumetric

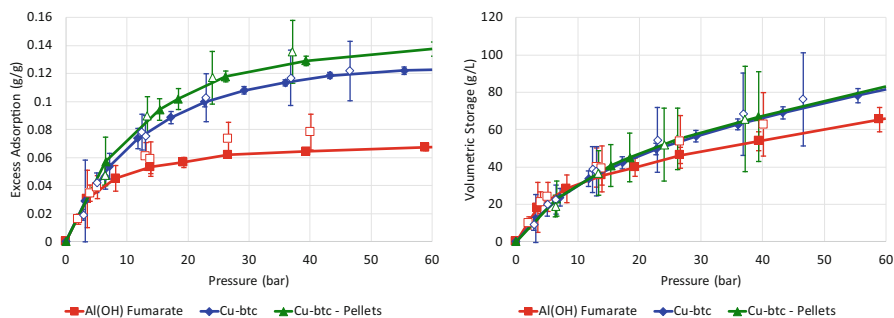


**Fig. 9.14** Adsorption isotherms for  $\text{Cu}_3\text{btc}_2$  and  $\text{Al}$ -fumarate. The solid symbols are the lab-scale measurements, and the open symbols are the pilot-scale measurements (3 L)

adsorption (Fig. 9.14 right). The bulk and skeletal densities also agreed within uncertainty (Table 9.1). Note that there is a higher uncertainty in the densities for the pilot-scale measurements because of the large volumes used. The data here indicates that there is little difference between the lab-scale and pilot-scale synthesis batches. In particular, the agreement in excess adsorption data indicates that the activation process (desolvation and porosity activation) is successful regardless of scale.

Working with larger sample sizes, on the order of a kilogram, has two main advantages. The first is in evaluating thermodynamic characteristics. A large sample size will behave more closely to the actual application size. The second is in evaluating gas kinetics. Given the proper instrumentation, the diffusion properties of the materials can be observed during the adsorption experiment [17].

Beginning with the thermodynamic characteristics, each data point in the adsorption isotherm is a gas expansion from a reference volume (empty chamber) into the sample chamber (with material). As the gas adsorbs, the temperature of the system increases because the adsorption process is exothermic. The evolution of the temperature of the system as a function of time can be observed as shown in Fig. 9.15 left, in which the reference volume was pressurized to 20 bar and allowed to expand into the sample chamber under vacuum. Here, an activated carbon has been included as a reference material.

The activated carbon has the largest temperature increase. This could indicate that heat of adsorption is lower for the MOFs. However, one must consider that there are differences in the masses used in each experiment and that the total temperature change is proportional to the total heat released upon adsorption, which is in turn proportional to the mass of adsorbent. Taking mass into account, the Cu-btc pellets have the highest  $\Delta T/m$  (Table 9.1).

Additionally, the time at which the material reaches a maximum temperature is also higher for the MOFs. This is an indication that the MOFs have a lower thermal conductivity than the benchmark carbon, meaning it takes longer to transfer

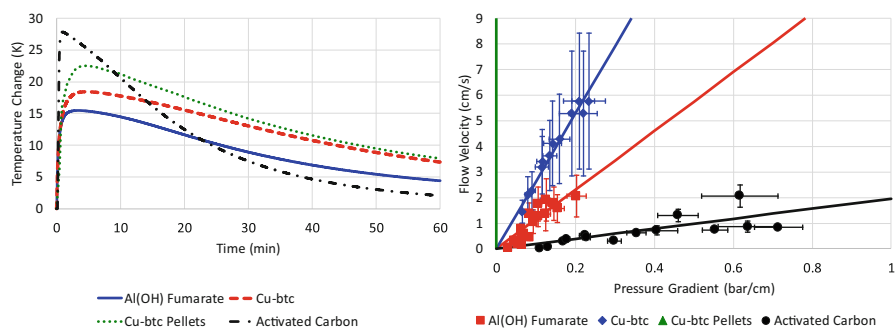


**Fig. 9.15** (Left) A comparison of the sample temperature change upon adsorption. For each sample, the reservoir was pressurized to 20 bar and allowed to expand into the sample cell under vacuum. (Right) Darcy's law plot for each material. The Cu-btc pellets' flow velocity was above the measurement limit and is represented here by a vertical line at 0 pressure gradient

the heat from the material to the temperature sensors. Indeed, if the temperature vs. time curves are fit with an exponential decay curve, such as in Newton's law of cooling, the time constant is largest for the activated carbon ( $2.96 \text{ s}^{-1}$ ) followed by Al(OH) Fumarate ( $1.30 \text{ s}^{-1}$ ), the Cu-btc pellets ( $1.17 \text{ s}^{-1}$ ), and the Cu-btc powder ( $1.06 \text{ s}^{-1}$ ). It's noteworthy that there is a 10% increase in the time constant by pelletizing the Cu-btc, an indication that thermal conductivity is improved by pelletizing either by increasing the thermal conductivity of the material or by allowing more gaseous methane between pellets to exchange heat with the outside environment. It is also possible that the temperature peaks are shifted in time because the diffusion kinetics are slower. Using the method of Burress et al. [17], we find a characteristic adsorption time on the order of 0.1 ns for methane,<sup>2</sup> so the actual process of adsorbing a methane molecule is essentially instantaneous. However, if diffusion kinetics are slow, then it will be taking more time to get the gas through the material. This becomes a huge issue in gas storage applications because slow diffusion will affect the gas delivery rate and can limit the usable amount of methane in the system.

Using the 3 L system, a method for determining the permeation coefficient for porous materials can be used [17]. The 3 L system has evenly spaced thermocouples positioned down the long axis of the sample chamber. By monitoring the pressure and sample temperature at different points during the gas expansion, the flow velocity vs. pressure gradient can be determined.

In Fig. 9.15 right, the slope  $m$  of the fit line of the flow velocity vs. pressure gradient data is related to the gas permeability  $\kappa$  in Darcy's law by

$$m = \frac{\kappa}{\phi\eta} \quad (9.9)$$

where  $\phi = 1 - \rho_b/\rho_s$  is the total porosity of the material in the tank and  $\eta$  is the viscosity of methane ( $\sim 1.1 \times 10^{-5} \text{ Pa s}$ ). The higher the slope, the faster gas will flow through the materials for a given pressure gradient. The adsorption kinetics is much slower for the activated carbon than the MOFs meaning that when using these materials, the MOFs will be able to deliver the methane at a much faster rate.

The MOF pellets, which have a relatively large volume between pellets due to packing, have the fastest adsorption kinetics. The gas flowed so swiftly through the pellets that this method could not accurately determine the flow velocity and is thus represented by a vertical line in Fig. 9.15 right. This is a key observation because the volumetric capacity of the pellets and the powder is identical. Thus, by pelletizing the material, the adsorption kinetics and thermal properties have been improved without sacrificing storage performance.

<sup>2</sup>Note: For this calculation, the area per adsorption site was assumed to be  $33 \text{ \AA}^2$ . This was based on the critical density of methane  $\alpha(T) = (1/\rho_{\text{critical}})^{2/3}$  at 293 K and pressures greater than 1 bar.

## 9.5 Conclusion

Results and analysis from extensive experimental methane storage studies on metal-organic frameworks have been reviewed. Distinct factors influencing excess, total, and usable methane capacities in MOFs have been discussed. Crystalline MOFs offer an ideal platform to gain understanding on the interplay between the materials' properties and the methane storage performances. MOF adsorbents, as an alternative methane storage technology, seek to bypass the pressure and thermal challenges of traditional compressed gas technology by utilizing their chemical and physical properties to store the gas.

The studies presented in this chapter provide insights on which key properties to adjust to maximize methane storage and delivery: optimized pore sizes, high surface area, slow take off on isotherm to favor high usable capacity, and optimized MOFs bulk density to compromise between gas uptake and diffusion kinetics. However, they also show some challenges such as limited maximum excess methane uptake due to the material's porosity and thermodynamics, inherent to physisorption, playing against storage and delivery performances. Overall MOFs' potential for methane storage has been demonstrated and comes on par, if not better, than what observed with activated carbon materials.

Outcomes of application scale study evidence that laboratory scale results, when appropriate parameters are chosen, such as bulk density instead of crystallographic density, temperatures and pressures variations considered as well, can be used to predict accurately the behavior of the storage system at larger scale, i.e. vehicle level. In particular, pilot-scale experiments show an increase in Darcy's law permeability over an activated carbon benchmark. Pelletization also increases the permeability and improves the thermal properties for  $\text{Cu}_3\text{btc}_2$ .

With that said, Fig. 9.16 summarizes the actual status of MOFs in terms of methane storage at 50 bar compared to existing technologies. Adsorbed methane on MOFs provides density advantages over pure methane compression at 50 bar but still has some way to go to match the benchmark 200 bar compressed gas technology. In the past decade, there has been an explosion in the number of newly synthesized MOFs with the total number reaching tens of thousands. Only a small

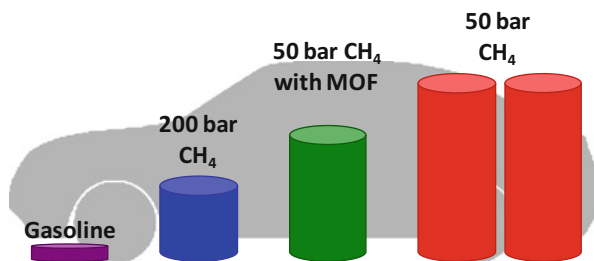


**Fig. 9.16** Comparison of the densities of 10 gallons of gasoline with equivalent total energies of methane in several storage options. A standard-size passenger vehicle is included for scale.

fraction of them have been investigated for methane storage, and there is still a lot to discover from the properties of these versatile materials.

## References

1. Peplow M (2015) Materials Science: the holy story. *Nature* 520(7546):148–150
2. Eddaoudi M, Kim J, Rosi N et al (2002) Systematic design of pore size and functionality in isorecticular MOFs and their application in methane storage. *Science* 295:469–472
3. Lozano-Castelló D, Alcaniz-Monge J, de la Casa-Lillo M et al (2002) Advances in the study of methane storage in porous carbonaceous materials. *Fuel* 81:1777–1803
4. Wegrzyn J, Gurevitch M (1999) Adsorbent storage of natural gas. *Appl Energy* 55:71–83
5. Menon VC, Komarneni S (1998) Porous adsorbents for vehicular natural gas storage: a review. *J Porous Mater* 5:43–58
6. Elliott D, Topaloglu T (1986) The development of new adsorbent materials for the storage of natural gas on-board vehicles. *Conf Proc Gaseous Fuels Transp I*:489–504
7. US Department of Energy. Transportation Energy Data Book 2014
8. Tagliabue M, Farrusseng D, Valencia S et al (2009) Natural gas treating by selective adsorption: material science and chemical engineering interplay. *Chem Eng J* 155:553–566
9. Dialyzed S, Tyke M, Dialyzed F (1967) Adsorption equilibria in the methane-propane-silica gel system at high pressures. *Ind Eng Chem Fundam* 6:546–554
10. Grant RJ, Manes M (1966) Adsorption of binary hydrocarbon gas mixtures on activated carbon. *Ind Eng Chem Fundam* 5:490–498
11. Shen J, Dailly A, Beckner M (2016) Natural Gas sorption evaluation on microporous materials. *Microporous Mesoporous Mater* 235:170–177
12. Burress J, Kraus M, Beckner M et al (2009) Hydrogen storage in engineered carbon nanospaces. *Nanotechnology* 20(20):204026
13. He Y, Zhou W, Qian G, Chen B (2014) Methane storage in metal–organic frameworks. *Chem Soc Rev* 43:5657–5678
14. Koh HS, Rana MK, Wong-Foy AG, Siegel DJ (2015) Predicting methane storage in open-metal-site metal–organic frameworks. *J Phys Chem C* 119(24):13451–13458
15. Broom DP (2011) Hydrogen storage materials: the characterization of their storage properties. Springer-Verlag, London
16. Beckner M, Dailly A (2016) A pilot study of activated carbon and metal-organic frameworks for methane storage. *Appl Energy* 162:306–514
17. Voskuilen T, Zhang Y, Pourpoint T (2010) Development of a Sievert apparatus for characterization of high pressure hydrogen sorption materials. *Int J Hydrog Energy* 35:10387–10395
18. Beckner M, Dailly A (2015) Adsorbed methane storage for vehicular applications. *Appl Energy* 149:69–74
19. Rosi NL, Eckert J, Eddaoudi M et al (2003) Hydrogen storage in microporous metal-organic frameworks. *Science* 300(5622):1127–1129
20. Loiseau T, Serre C, Huguénard C et al (2004) A rationale for the large breathing of the porous aluminum terephthalate (MIL-53) upon hydration. *Chem Eur J* 10:1373–1382
21. Chae H, Siberio-Perez D, Kim J et al (2004) A route to high surface area, porosity and inclusion of large molecules in crystals. *Nature* 427(6974):523–527
22. Koh K, Wong-Foy AG, Matzger AJ (2010) Coordination copolymerization mediated by  $Zn_4O(CO_2R)_6$  metal clusters: a balancing act between statistics and geometry. *J Am Chem Soc* 132(42):15005–15010
23. Chui SS, Lo SM, Charmant JP et al (1999) A chemically functionalizable nanoporous material. *Science* 283(5405):1148–1150

24. Zhou W, Wu H, Yildirim T (2008) Enhanced H<sub>2</sub> adsorption in isostructural metal-organic frameworks with open metal sites: strong dependence of the binding strength on metal ions. *J Am Chem Soc* 130:15268–15269
25. Ma S, Sun D, Simmons JM et al (2008) Metal-organic framework from an anthracene derivative containing nanoscopic cages exhibiting high methane uptake. *J Am Chem Soc* 130:1012–1016
26. Feng D, Wang K, Wei Z et al (2014) Kinetically tuned dimensional augmentation as a versatile synthetic route towards robust metal–organic frameworks. *Nat Commun* 5:5723
27. Kim J, Yang ST, Choi SB et al (2011) Control of catenation in CuTATB-n metal-organic frameworks by sonochemical synthesis and its effect on CO<sub>2</sub> adsorption. *J Mater Chem* 21(9):3070–3076
28. Wang XS, Ma S, Rauch K et al (2008) Metal–organic frameworks based on double-bond-coupled di-isophthalate linkers with high hydrogen and methane uptakes. *Chem Mater* 20(9):3145–3152
29. Wu H, Simmons JM, Liu Y et al (2010) Metal-organic frameworks with exceptionally high methane uptake: where and how is methane stored? *Chem-Eur J* 16(17):5205–5214
30. Schaate A, Dühnen S, Platz G et al (2012) A novel Zr-based porous coordination polymer containing azobenzenedicarboxylate as a linker. *Eur J Inorg Chem* 5:790–796
31. Guo Z, Wu H, Srinivas G et al (2011) A metal–organic framework with optimized open metal sites and pore spaces for high methane storage at room temperature. *Angew Chem Int Ed* 50(14):3178–3181
32. Wei Z, Lu W, Jiang HL, Zhou HC (2013) A route to metal–organic frameworks through framework templating. *Inorg Chem* 52:1164–1166
33. Zhao D, Timmons DJ, Yuan D, Zhou HC (2010) Tuning the topology and functionality of metal-organic frameworks by ligand design. *Acc Chem Res* 44(2):123–133
34. Liu Y, Li JR, Verdegaal WM et al (2013) Isostructural metal–organic frameworks assembled from functionalized diisophthalate ligands through a ligand-truncation strategy. *Chem Eur J* 19:5637–5643
35. Jiang HL, Feng D, Liu TF et al (2012) Pore surface engineering with controlled loadings of functional groups via click chemistry in highly stable metal–organic frameworks. *J Am Chem Soc* 134:14690–14693
36. Wilmer CE, Leaf M, Lee CY et al (2012) Large-scale screening of hypothetical metal–organic frameworks. *Nat Chem* 4:83–89
37. Yan Y, Yang S, Blake AJ, Schröder M (2014) Studies on metal-organic frameworks of Cu(II) with isophthalate linkers for hydrogen storage. *Acc Chem Res* 47(2):296–307
38. Zhuang W, Yuan D, Liu D et al (2012) Robust metal–organic framework with an octatopic ligand for gas adsorption and separation: combined characterization by experiments and molecular simulation. *Chem Mater* 24:18–25
39. Yan Y, Yang S, Blake AJ et al (2011) A mesoporous metal–organic framework constructed from a nanosized C<sub>3</sub>-symmetric linker and [Cu<sub>24</sub>(isophthalate)<sub>24</sub>] cuboctahedra. *Chem Commun* 47(36):9995–9997
40. Yan Y, Lin X, Yang S et al (2009) Exceptionally high H<sub>2</sub> storage by a metal–organic polyhedral framework. *Chem Commun* 9(0):1025–1027
41. Park J, Li JR, Chen YP et al (2012) A versatile metal–organic framework for carbon dioxide capture and cooperative catalysis. *Chem Commun* 80(48):9995–9997
42. Feng D, Gu ZY, Chen YP et al (2014) A highly stable porphyrinic zirconium metal–organic framework with shp-a topology. *J Am Chem Soc* 136(51):17714–17717
43. Feng D, Chung WC, Wei Z et al (2013) Construction of ultrastable porphyrin Zr metal–organic frameworks through linker elimination. *J Am Chem Soc* 135:17105–17110
44. Choi HJ, Dinca M, Dailly A, Long JR (2010) Hydrogen storage in water-stable metal–organic frameworks incorporating 1,3- and 1,4-benzenedipyrazolate. *Energy Environ Sci* 3:17–123
45. Dinca M, Dailly A, Long JR (2008) Structure and charge control in metal–organic frameworks based on the tetrahedral ligand tetrakis(4-tetrazolylphenyl)methane. *Chem-Eur J* 14(33):10280–10285

46. Thommes M, Kaneko K, Neimark AV et al (2015) Physisorption of gases, with special reference to the evaluation of surface area and pore size distribution (IUPAC Technical Report). *Pure Appl Chem* 87(9–10):1051–1069
47. Chahine R, Bose TK (1996) Hydrogen energy progress XI. T N Veziroglu et al Editors 1259
48. Chahine R, Benard B (1998) *Advances in cryogenics engineering*, vol 43. Plenum Press, New York, p 1257
49. Hirscher M, Panella B, Schmidt B (2010) Metal organic frameworks for hydrogen storage. *Microporous Mesoporous Mater* 129:335–339
50. Poirier E (2014) Ultimate H<sub>2</sub> and CH<sub>4</sub> adsorption in slit-like carbon nanopores at 298 K: a molecular dynamics study. *RSC Adv* 4(44):22848–22855
51. Kurniawan Y, Bathia SK, Rudolph V (2006) Simulation of binary mixture adsorption of methane and CO<sub>2</sub> at supercritical conditions in carbons. *AIChE J* 52(3):957–967
52. Wu H, Zhou W, Yildirim T (2009) High capacity storage in metal-organic frameworks M<sub>2</sub>(dhtp): the important role of open metal sites. *J Am Chem Soc* 131:4995–5000
53. He Y, Zhou W, Qian G, Chen B (2014) Methane storage in metal organic frameworks. *Chem Soc Rev* 16(43):5657–5678
54. Dietzel PDC, Panella B, Hirscher M et al (2006) Hydrogen adsorption in a nickel based coordination polymer with open metal sites in the cylindrical cavities of the desolvated framework. *Chem Commun* 9:959–961
55. Richard MA, Benard B, Chahine R (2009) Gas adsorption process in activated carbon over a wide temperature range above the critical point. Part 1: modified Dubinin-Astakhov model. *Adsorption* 15(1):43–51
56. Rowsell JLC, Millward AR, Park KS, Yaghi OM (2004) Hydrogen sorption in functionalized metal-organic frameworks. *J Am Chem Soc* 126(18):5666–5667
57. Purewal J, Liu D, Sudik A et al (2012) Improved hydrogen storage and thermal conductivity in high-density MOF-5 composites. *J Phys Chem* 116(38):20199–20212
58. Ming Y, Purewal J, Liu D et al (2014) Thermophysical properties of MOF-5 powder. *Microporous Mesoporous Mater* 185:235–244

# Chapter 10

## Storage of Hydrogen on Nanoporous Adsorbents



Philip L. Llewellyn

### 10.1 Introduction

Hydrogen is an important energy vector. As described in Chap. 1, its use as a fuel in combustion or its use in fuel cells is of interest due to its very high energy density of the order of 120–142 MJ/kg, which can be compared to around 46 MJ/kg for gasoline. Hydrogen is a renewable energy source and readily available. The other interest of hydrogen in the aforementioned processes is that it is *clean*. Indeed, water is the product, and with the desire to move away from carbon-based technologies, using hydrogen can be a vital game changer. With these arguments in terms of sustainable growth and hydrogen as a clean fuel, the International Energy Agency has been promoting hydrogen as an energy vector since the end of the 1970s through the “Production and Utilization of Hydrogen Program” [1].

Hydrogen can be produced by different methods. The vast majority of hydrogen today is produced via steam reforming with sources such as coal, natural gas, and naphtha/oil [2]. Thermal gasification or pyrolysis can be used with sources including biomass. Finally, water can be split via electrolysis or photolysis. Hydrogen is currently used in several chemical processes. These include the production of ammonia via the Haber process and for the removal of sulfur during oil refinery. It is equally used to make other molecules such as cyclohexane and methanol which are intermediates in the production of pharmaceuticals and plastics. Hydrogenation is used to form fats from oils, as in the preparation of margarine. Hydrogen acts as a protective atmosphere during the production of flat glass sheets and is also used as a flushing gas during the manufacture of silicon wafers.

---

P. L. Llewellyn (✉)

Aix-Marseille University, CNRS, Laboratoire MADIREL (UMR 7246), Marseille, France  
e-mail: [philip.llewellyn@univ-amu.fr](mailto:philip.llewellyn@univ-amu.fr)

Much academic work is focused on the use of hydrogen for vehicular use. Several arguments are given as to why to develop “hydrogen cars” with respect to other non-CO<sub>2</sub>-emitting vehicles such as electric-powered vehicles. The main ones are of refueling time and range. An electric car requires a minimum of 30 min to recharge, whereas hydrogen refueling can take 3–5 min. The average range of an electric car is around 150–200 km, whereas a hydrogen-fueled car can have the same range as a petrol-fueled car. A general rule of thumb estimate suggests that to cover 500 km, around 5 kg of hydrogen would be required which, in gaseous form, corresponds to a volume of around 55 m<sup>3</sup>. Any means to decrease this volume for storage is of interest with solutions using compression, absorption, and adsorption.

For the storage of hydrogen, as with other gases, several desirable characteristics are required. These include:

- Storage and release temperatures as close to ambient or the actual process temperature
- Rapid uptake and release rates
- Full reversibility
- High volumetric/gravimetric storage densities
- As inexpensive as possible in order to render these technologies as affordable as possible and to compete with current energy use

Hydrogen can be stored in a compressed state. Most often, this can be carried out at up to 200–300 bars in metallic cylinders. However, it is possible to store hydrogen at up to 700 bars in more lightweight carbon fiber composite vessels. Over time, hydrogen can embrittle metals (especially steel), and this can lead to a degradation of the mechanical properties of the storage vessel. When using carbon fiber composite vessels, the inner container can be made of a polymer. This polymer can leach solvents with time, and water has been identified as a problem for polyamide-based plastics, for example. Furthermore, permeation of hydrogen through the polymer liner can also be an issue. Finally, the polymer liner can be subject to structural deformations.

Cryogenic storage of hydrogen is possible with the liquefaction of hydrogen occurring at around –253 °C (20 K) where high hydrogen densities can be obtained. However, this process is both energy intensive and time consuming. Long-term storage can be problematic due to significant evaporation. As such, this approach may not be of interest for vehicular use but can be of interest for land or sea transport.

Cryo-compressed storage combines a storage at low temperatures (20 K) inside a pressurized vessel (up to 300 bar), leading to high storage densities (up to 80 g/L). Indeed, such a vessel can withstand much higher pressure before evaporation/boiling occurs also leading to greater autonomy.

In view of avoiding high pressures or very low temperatures, alternative storage methods can be envisaged. Chemical storage of hydrogen can be envisaged via the formation of hydride structures. Covalent and complex metal hydrides are formed with light metals from groups 1, 2, and 3 such as Li, Mg, B, and Al. These can be contrasted with interstitial metal hydrides with elements such as Sc and Yt as well as

the lanthanides and actinides. The drawbacks of these types of “chemical” bonding approaches can lie in terms of kinetics of uptake and release, reversibility, and heat management.

An alternative approach to store hydrogen is to use physisorption with nanoporous materials. With respect to the chemical storage of hydrogen, physisorption has the advantage of inherently fast adsorption/desorption kinetics and complete reversibility. Furthermore, with the suitable associated technology, adsorption-based processes can equally be of interest in terms of safety and cost with respect to gas compression and can equally be of interest when considering the significant losses of cryogenic liquid that occur with hydrogen liquefaction. A nice comparison between cryo-compression and cryo-adsorption hydrogen storage methods has been proposed by Petitpas et al. [3].

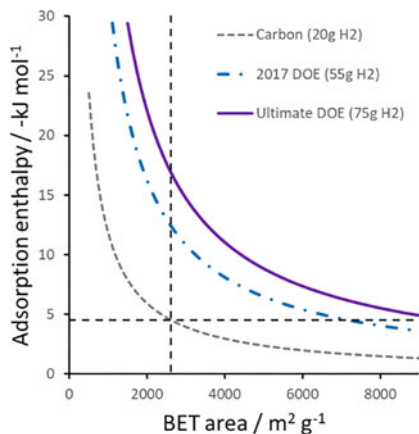
When considering hydrogen storage using adsorption, the hurdles that have to be overcome include the requirement to reach a high gas density inside the nanopores and a need to improve the nominally weak interactions between hydrogen and the surface of most porous materials studied so far. Indeed, a key study by Bhatia and Myers [4] suggested that for the optimal adsorptive storage of hydrogen at ambient temperature, between a lower working pressure of 1.5 bars and an upper working pressure of 30 bars, then the enthalpy change should be in the order of  $15 \text{ kJ mol}^{-1}$ . As will be discussed below, many materials show adsorption enthalpies of around  $5\text{--}6 \text{ kJ mol}^{-1}$ , and this study predicts that for an enthalpy change of  $5.6 \text{ kJ mol}^{-1}$ , then an optimal operating temperature should be 115 K (i.e.,  $-158 \text{ }^\circ\text{C}$ ). Interestingly, this study also predicts that the adsorbent should be homogeneous and that the introduction of heterogeneity can only lead to small increases in the storage capacity of hydrogen via physisorption. Indeed, the introduction of strong adsorption sites will probably affect the adsorption below the lower working pressure of 1.5 bars. This study has been extended by Garrone et al. [5] using data from zeolites to conclude that maybe energies in the range  $22\text{--}25 \text{ kJ mol}^{-1}$  could be required and that there is a relationship between enthalpy and entropy for the zeolites investigated. Bae and Snurr [6] using molecular modeling on MOFs equally concluded that energies in the range  $18.5$  to  $22\text{--}25 \text{ kJ mol}^{-1}$  could be optimal for storage in the range  $1.5\text{--}100$  bars and  $298 \text{ K}$ . The range in energies proposed arises from the variety of MOF structures considered.

This problem is neatly proposed by Roszak et al. [7] and illustrated in Fig. 10.1. The authors give a means to calculate a given gravimetric capacity for hydrogen with a relationship between average adsorption energy and available surface area with the inclusion of a factor to consider the material topology. The vertical and horizontal lines in this figure represent the maximum BET surface and average adsorption energy observed with a graphite surface. The clear take-home message from this proposition is that, in order to reach any of the DOE goals for hydrogen storage, considerable increases in surface area and/or binding energy are required.

There thus seem to be two main parameters to follow when evaluating porous materials for hydrogen storage: *uptakes* and *adsorption energies*. In terms of uptakes, many studies evaluate these at 1 bar which can be considered as a minimum

**Fig. 10.1**

Iso-weight-capacity curves for constant gravimetric capacity, adapted from that proposed by Roszak et al. [7]. The dashed lines indicate the surfaces (horizontal line) and average binding energy (vertical line) required for an adsorbent with typical graphene characteristics to achieve different gravimetric capacities



pressure with respect to a storage/delivery application. Thus, it is equally important to follow the uptakes at higher pressures, at around 15 bars as suggested by Bhatia and Myers [4], for example. In terms of energy, one should aim for an adsorption enthalpy of at least  $15 \text{ kJ mol}^{-1}$  for a room temperature type application, and this should be relatively constant throughout the pore filling thus requiring a certain homogeneity of the adsorbent.

Of the various forms of porous material, one can distinguish three main families that have been studied for hydrogen storage: (i) zeolites, (ii) active carbons, and (iii) metal-organic frameworks. The remaining pages of this chapter will discuss these families with some comparison made with respect to the aforementioned constraints in the final conclusions.

In viewing the literature concerning hydrogen sorption in nanoporous materials, several issues have arisen. The first concerns the conditions used in measuring the hydrogen uptake. Indeed, it is relatively simple to use commercial apparatus to measure hydrogen sorption at 77 K and up to 1 bar. However, for use one could expect that pressures up to around 100 bars could be used for automotive storage, with a lower working pressure at around 5 bars. Secondly, one would hope for storage at around ambient temperatures, although a study by Bénard et al. [8] strongly suggests that vehicular storage at such temperatures may not be feasible. Thus, the studies to 1 bar at 77 K can give an indication of the materials characteristics toward hydrogen, but not of their final interest in any hydrogen storage application. When possible, results will be discussed for data at 1 bar/77 K, as well as at higher pressures and/or temperatures.

The further problem concerns a comparison of results of excess or total (absolute) adsorption values [9]. Most commercial equipment will render the excess value as a result, and one can often observe excess isotherms which pass through a maximum at a given pressure, depending on the temperature. An example of this is given in Fig. 10.2 concerning the adsorption of hydrogen at 77 K on MOF-5 (data from Bastos-Netto et al. [10]).

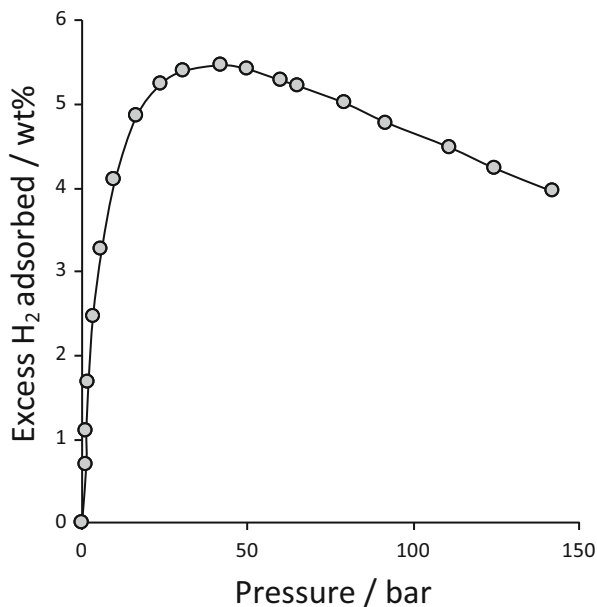


**Fig. 10.2** Excess hydrogen uptakes at 77 K as a function of pressure obtained with the metal-organic frameworks, MOF-5. A clear maximum in the isotherm is visible. Data obtained from the article by Bastos-Neto et al. [10]

The decrease in values above the maximum can be used to assess the compressibility of H<sub>2</sub> within the material and evaluate the total uptake. The absolute value requires a knowledge of the volume in which the adsorption occurs, i.e., it is an estimation of both the surface-adsorbed H<sub>2</sub> and the H<sub>2</sub> gas compressed within the adsorbed volume. For highly nanoporous materials, this adsorbed volume can be equated to the micropore volume in a first instance. Importantly, knowledge of the total uptake enables determination of the volumetric storage density within the compound, which is one of the considerations in selecting a hydrogen storage material. In many cases at 77 K and 1 bar, the difference in excess and absolute uptakes can be small; however this is not the case at higher pressures and temperatures. In many articles, the precision as to whether the values given are excess or absolute is not given, and this makes comparison all the more difficult.

Finally, it has been noted that there can be problems in terms of irreproducibility in hydrogen storage research as summarized by Broom and Hirscher [11]. This is especially the case here, as hydrogen measurements themselves are quite sensitive to error. Furthermore, with some of the more novel samples, there may also be problems in terms of sample purity and/or activation.

## 10.2 Hydrogen Adsorption with Zeolites and Related Materials

Zeolites are ordered tectosilicates constructed of a three-dimensional network of tetrahedral oxy-metal centers ( $\text{MO}_4$ ). The term zeolite was originally coined in 1756 by Swedish mineralogist Axel Fredrik Cronstedt, who observed that rapidly heating the material, believed to have been stilbite, produced large amounts of steam from water that had been adsorbed by the material. Based on this, he called the material zeolite, from the Greek ζέω (zēō), meaning “to boil,” and λίθος (líthos), meaning “stone.” The large majority of zeolites contain micropores which can be accessible to hydrogen.

The interest of zeolites and zeolite-like materials, for hydrogen adsorption, lies in several points:

- There are over 230 different ordered zeolite structures [12]. Indeed, natural zeolites are aluminosilicates with a general formula of  $\text{M}_{2/n}\text{O} \cdot \text{Al}_2\text{O}_3 \cdot x\text{SiO}_2 \cdot y\text{H}_2\text{O}$ , where M is any alkali or alkaline earth atom, n is the charge on that atom, x is the number of Si tetrahedron varying from 2 to 10, and y is the number of water molecules varying from 2 to 7. The aluminum and silica tetrahedra can be arranged in a large number of structures with around 30 natural zeolite structures known. However, it is possible to substitute the Si and/or Al for a large number of other framework species including P, Ge, Ga, etc., and this leads to a much greater flexibility in the number of different frameworks accessible and leads to the value of 230 mentioned above. Among this variety of structures, there may be several of interest to store small molecules such as hydrogen.
- It is possible to modulate the chemistry of zeolites further to the framework compositions. Indeed, the introduction of trivalent atoms (e.g., Al) is compensated by the inclusion of cations. Indeed, cations such as  $\text{Na}^+$ ,  $\text{Ca}^{2+}$ , and  $\text{NH}_4^+$  can be found. This therefore gives a further opportunity to modulate the interaction of specific molecules, such as hydrogen, with respect to these materials.
- The pore apertures of zeolites are relatively small, in the range of around 0.2–1 nm. Further to the choice between different structures, the pore size can be “engineered” by the exchange of compensation cations in the structure which can sit in these apertures. Thus, for example, the Linde A zeolite, the exchange of  $\text{Na}^+$  for  $\text{Ca}^{2+}$  or  $\text{K}^+$  can lead to a modulation of the pore apertures in the range from 0.3 to 0.5 nm. This again is an opportunity to tailor the characteristics of these materials for hydrogen storage. Small pore materials may indeed seem to be of interest if one considers the kinetic diameter of hydrogen, of around 0.29 nm.
- The order of the structures, pore networks, and surface chemistries, as described above, can be of interest for the storage of a challenging molecule such as hydrogen. Indeed, if a fine-tuned material can be optimized, then the order that can be procured is certainly an advantage over less ordered adsorbents.

- Zeolites are nicely adapted to the use of molecular modeling. Indeed, the various levels of order, as described above, can easily be described computationally. Thus, molecular simulation can be used as a tool to (i) understand the adsorption mechanisms in play, (ii) screen various materials for hydrogen storage, and (iii) predict the storage properties of materials that have so far not been synthesized. Indeed, there is a conundrum where an estimate of over 100,000 unique zeolite framework types should be stable if they could be synthesized [13] and the actual number of materials so far synthesized. This gives an opportunity for molecular modeling to identify a structure of potential interest prior to effort in the synthesis.
- Finally, the majority of zeolites are stable to temperature, humidity, and many other chemicals. This explains their use in many applications in gas separation, gas storage, ion exchange, and catalysis. Thus, if a material is found of interest for hydrogen storage, then one can benefit from this prior experience for upscale and use.

There seem to be very few studies that have systematically explored any single one of the parameters described above. In terms of exploring different structure types, Weitkamp et al. [14] studied the uptake of hydrogen at 300 °C and pressure of 100 bars with NaA and SAPO-42 of LTA structure, sodalite (SOD), NaX and NaY (with FAU structure), zeolite Rho (RHO), ZK-5 (KFI), and sigma-1 (DDR). They concluded that under these conditions, the hydrogen could enter the sodalite cages in materials that contain such units and found an uptake of 9.2 cm<sup>3</sup>/g at the abovementioned conditions in the sodalite sample, which corresponds to around 0.17 H<sub>2</sub> per sodalite cage. Such a result was confirmed in another comparative study by Dong et al. [15].

The sodalite cage is formed from four-membered and six-membered rings and has an internal diameter of approximately 0.6 nm which are only accessible to very small molecules. Joining the cages via the four-membered rings leads to the zeolite sodalite (SOD structure). By bridging the four-membered rings, zeolite A (LTA structure) is formed, and bridging via the six-membered rings leads to the formation zeolite X or Y (FAU structure) is formed. The difference between the X and Y pertains to the Si/Al ratio.

It is then interesting to compare the uptakes with NaA and SAPO-42 which both have the LTA structure. While NaA contains Na<sup>+</sup> as the compensation cation, the SAPO-42 material does not contain any compensation cations and is thus a more “neutral” structure. The hydrogen uptake is around 0.25 0.17 H<sub>2</sub> per sodalite cage in the NaA structure and only 0.1 0.17 H<sub>2</sub> per sodalite cage in SAPO-34. This highlights the chemistry that can play a role in the storage of hydrogen. To further explore the pore field gradient on hydrogen uptake, the authors explored the effect of exchanging the Na<sup>+</sup> cation with K<sup>+</sup>, Rb<sup>+</sup>, and Cs<sup>+</sup>, in a study that mirrored previous work by Fraenkel and Shabtai [16]. The aim of these studies was to study the influence of the size of the compensation cation (Na<sup>+</sup>, 0.102 nm; K<sup>+</sup>, 0.138 nm; Rb<sup>+</sup>, 0.152 nm; Cs<sup>+</sup>, 0.167 nm) as it is believed that its position in the zeolite cages can influence (i) the size of the window leading to increased interactions and

then (ii) to the volume of the cages leading to a decrease in the volume available for H<sub>2</sub> uptake. In both studies it was found that substitution of the Na<sup>+</sup> with K<sup>+</sup> seemed to give higher uptakes although to differing extents, and this may be related to the amount of substitution. However, further substitution with Rb<sup>+</sup> and Cs<sup>+</sup> leads to decreases in H<sub>2</sub> uptake with the study by Weitkamp even evidencing negligible values [14].

Another zeolite containing sodalite units is faujasite with FAU structure [12]. This structure can equally be prepared with different cations and varying quantities of these. The Weitkamp study showed that the two Na<sup>+</sup> containing versions of FAU, NaX, and NaY adsorbed similar quantities of H<sub>2</sub> per sodalite cage [14]. The study by Efstathiou et al. [17] studied a series of cation exchanged X zeolites, replacing the Na<sup>+</sup> with the larger cations, Cs<sup>+</sup>, Ni<sup>+</sup>, and Eu<sup>+</sup>. Langmi et al. [18, 19] also studied both X and Y zeolites exchanged with several cations. The general trend in each of these studies with the LTA structure highlights that the use of overly large cations leads to significant decreases in H<sub>2</sub> uptake. Li and Yang [20] studied a series of low silica X samples and suggested that the strongest adsorption sites should be in the order of Li<sup>+</sup> > Na<sup>+</sup> > K<sup>+</sup> as predicted by the ionic radii of the cations. They also suggested that the oxygen sites of zeolite framework are minor sites for hydrogen adsorption.

The studies on the zeolites containing sodalite units show that very small pore materials could be of interest. Another small pore zeolite which has been studied for hydrogen storage is chabazite. The chabazite (CHA) structure can be described by layers of double six-rings that are interconnected by four-rings giving windows with eight-membered rings with pore of around 0.38 × 0.38 nm in dimension [12]. In a comparison with the sodalite containing structure, Zecchina et al. [21] suggested that the high silica analogue of chabazite, SSZ-13 (Si/Al > 5), may be of interest for hydrogen storage at 77 K. To understand the mechanisms related to the hydrogen adsorption, IR spectroscopy is a powerful tool. This study suggested that the H<sub>2</sub> was in relatively strong interaction with -OH groups that could be found at the eight-rings, followed by interactions with OH groups located on the six-membered rings with increasing coverage. Finally, condensation of hydrogen in the nanovoids was observed. Variable temperature IR spectroscopy can be used to estimate an interaction energy with a value of around 9.7 kJ mol<sup>-1</sup> estimated, which is well above the values estimated for graphite (around 4 kJ mol<sup>-1</sup>). In order to follow the role of the surface chemistry on the hydrogen interactions, the authors compared three different CHA materials (H-SSZ-13, H-SAPO-34, and H-CHA) [22]. These materials can be shown to have different Brønsted acid site strengths and densities. The conclusions of this study suggest that the hydrogen uptake is improved with an increase in acid site strength whereas a large increase in acid site density seems to lead to a decrease in hydrogen uptake. This latter result can be explained by the mutual interactions via H-bonds between the additional Brønsted sites inside the chabazite cages which would seem to require an energetic cost to displace the adjacent OH ligand which is higher than the adsorption enthalpy of the OH- H<sub>2</sub> adduct.

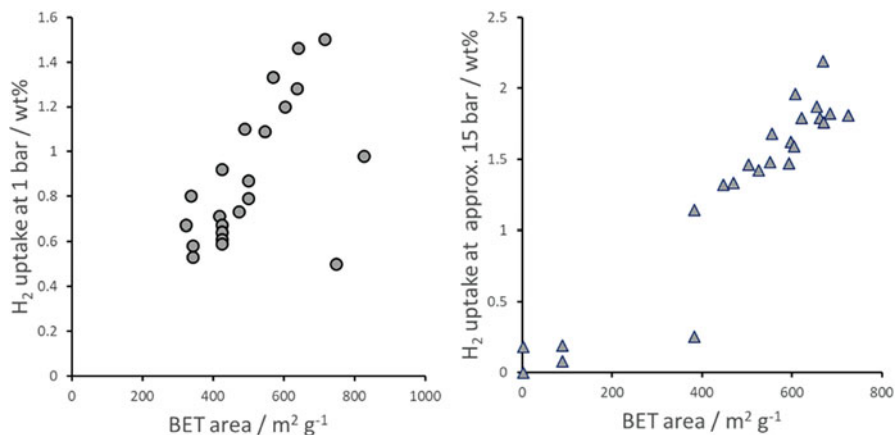


**Fig. 10.3** Hydrogen uptakes as a function of BET area for various zeolites at 1 bar (left) and approximately 15 bars (right)

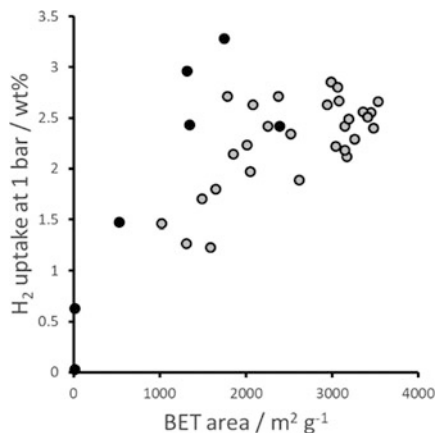
This is in correlation with the work of Kazansky et al. [23], who studying FAU-type zeolites suggested that the hydrogen interactions are high when the faujasite has a low Si/Al ratio because there are more basic sites and stronger perturbation of the H-H bond.

When comparing these different studies with the different zeolites, it is difficult to find clear trends. Langmi et al. [18, 19] show a general trend of hydrogen uptake, at 77 K and 15 bars, with respect to available surface area. Figure 10.3 plots the uptakes of hydrogen with respect to surface area under two different conditions: (i) at 77 K and around 1 bar and (ii) at 15 bars at various temperatures between 77 K and room temperature. There are only a few outliers which would seem to confirm that it would seem that the uptakes can be related to BET area. This suggests that the pore chemistry of the zeolites chosen has a limited impact on hydrogen uptake for this family of material.

A number of the aforementioned studies suggested that the extra-framework cations in the different zeolite structures can play a role on the uptake as they present sites of various sorption strengths. However, the above correlation strongly suggests that hydrogen adsorption occurs on the whole of the available surface. In an attempt to induce other sorption mechanisms, Li and Yang [20] studied hydrogen uptake with zeolite materials which have been bridged with carbon containing 5% Pt, and this has been suggested as a means to increase the storage capacity via spillover-type effects. Indeed, these authors suggested that such a hybrid material showed a  $2.6\times$  higher uptake than that of parent Li-LSX zeolite under the same conditions (77 K and 1 bar). Importantly, this uptake was shown to be reversible.

In general, as can be observed in Fig. 10.4, quite moderate hydrogen uptakes have been observed with zeolites. Uptakes above 2 wt% at 77 K are rare. Nevertheless, the fact that doping with metals shows increased uptakes is encouraging, and this approach can be used with other porous hosts. Furthermore, the idea that a given

**Fig. 10.4** Hydrogen uptakes at 77 K and 1 bar of various carbon-based materials as a function of BET area. Data obtained with the pure carbon materials are represented by circles and that obtained with doped materials are represented by squares



pore size can be optimal for hydrogen storage at a given temperature is equally of interest when designing hydrogen storage adsorbents which have larger pore size distributions such as active carbons, described below.

### 10.3 Hydrogen Adsorption with Carbon-Based Materials

Carbons are probably the first known adsorbents, having been used as far back as ancient Egyptian times for olive oil purification, for example. It is fascinating to note that this vast family of materials is one of the stalwarts in adsorption science. Initial work on the adsorption of hydrogen on carbon-based materials suggested great promise [24].

In its most simple form, a carbon adsorbent can be considered as a graphene sheet. The maximum surface area of such a sheet is around 2608 m<sup>2</sup> g<sup>-1</sup>. If one considers that hydrogen adsorption is purely a surface phenomenon, then an uptake of around 1%wt per 500 m<sup>2</sup> g<sup>-1</sup>, the Chahine rule [8, 25], can be expected. This is equivalent to a hydrogen density of 10 μmol H<sub>2</sub>/m<sup>2</sup>. Thus, with graphene, one can expect a maximum uptake of around 5–6%wt. However, there is a vast range of different carbon materials in which the surface area and other characteristics can vary immensely. Activated carbon can be made from different natural (coconut, olive stones, corncob, etc.) or synthetic (polymers) sources, and their synthesis mode in terms of pyrolysis and activation can impart a wide range of properties. These materials have a wider pore size distribution than, say, zeolites or MOFs, but there are methods to control these pore sizes and pore size distributions. Other more ordered carbons include nanotubes, nanohorns, and templated carbon materials. Carbons can be doped with heteroatoms and can be grafted with organic moieties, and nanoparticles can be occluded inside the porosity. This huge spectrum of possibilities in terms of physical and chemical characteristics makes these materials

of interest to explore for many applications, including hydrogen storage. More information concerning this fascinating family of material can be found in the following monographs [26–28] and reviews [29, 30].

### 10.3.1 Hydrogen Adsorption on High Surface Area Carbons

When looking to the use of carbons and carbon-based materials for hydrogen storage, a first avenue to explore is the surface area as it has been argued that this is one crucial parameter [31]. Indeed, the study by Jin et al. [32] strongly suggests that hydrogen adsorption capacities are linear function of surface area but also of parameters such as micropore surface area, total pore volume, and micropore volume. Furthermore, the abovementioned Chahine rule [8, 25] is based on the observation that hydrogen uptake is a function of surface area. Scattering in any of the reported linear relationships (ignoring any eventual measurement errors) can be due to influences of pore size heterogeneity and pore chemistry, although, as we will see below, smaller pore sizes can also lead to increases in H<sub>2</sub> uptake. From an experimental standpoint, it is possible to distinguish studies carried out (i) to 1 bar at 77 K and (ii) to higher pressures, for example, 20 bars, also at 77 K. These two limits will be discussed below.

Of the studies at 1 bar and 77 K, Wang et al. [33] prepared a doubly activated carbon with a surface area of 3530 m<sup>2</sup> g<sup>-1</sup> showing an uptake of around 2.49 wt%. Zhang et al. [34] prepared a series of KOH-activated carbons from corncob and observed an uptake of 2.66 wt% for the highest surface area material (3530 m<sup>2</sup> g<sup>-1</sup>). A KOH-activated carbon with a surface area of 2376 m<sup>2</sup> g<sup>-1</sup> and average pore size of 0.55 nm has shown an uptake of 2.71 wt% [35].

From the studies at 77 K and 20 bars, several authors note capacities above 6 wt%. Tellez-Juárez et al. [36] prepared carbons from bituminous coals (max. BET area = 3530 m<sup>2</sup> g<sup>-1</sup>) that showed uptakes above 6 wt% with only slightly further uptake with increasing pressure. Sevilla et al. [37] prepared a polypyrrole-based activated carbon with a surface area of 3450 m<sup>2</sup> g<sup>-1</sup> and hydrogen uptake capacity of 7.03 wt%. Wang et al. [33] reported hydrogen uptake of 7.08 wt% for a doubly activated carbon with a surface area of 3190 m<sup>2</sup> g<sup>-1</sup>. Higher capacities have been attained for zeolite-templated carbon materials (a) templated from zeolite beta with a surface area of 3332 m<sup>2</sup> g<sup>-1</sup> and a hydrogen uptake of 7.3 wt% [38] and (b) templated from zeolite beta with a lower surface area of 3150 m<sup>2</sup> g<sup>-1</sup> but a hydrogen uptake of 8.33 wt% [39]. In many of these studies, it was noted that saturation was not obtained indicating that higher uptakes could be possible at higher pressures. It has equally been suggested that the zeolite-like structural ordering of the carbon can be one reason for the enhanced hydrogen sorption capacity.

Few studies have concentrated on the energies of adsorption in these relatively pure carbon materials. Zhao et al. [40] measured isotherms in the temperature range 77–114 K and calculated isosteric enthalpies in the order of 4 kJ mol<sup>-1</sup>. The abovementioned work by Yang et al. [39] with a zeolite-templated carbon calculated

an adsorption energy which varied in the range from  $8 \text{ kJ mol}^{-1}$  at low loading to around  $4 \text{ kJ mol}^{-1}$  at higher uptakes. The energy distribution was heterogeneous suggesting a range of sorption sites and with the high energy sites at loadings below 1 wt%.

The main conclusion from this initial series of results is that one can relate the hydrogen uptakes at higher pressures, with the examples given here at 20 bar, to the extent of the surface area as calculated by the BET method. This is in spite of the problems noted in the use of BET approach for the calculation of areas of samples with micropores [9]. A second general conclusion is that the uptake at 1 bar and 77 K cannot simply be related to the BET area. The arguments given in the literature pertain to the enhanced interactions of hydrogen inside the micropores of these materials. A further point to note is that hydrogen may be able to access porosity that is not available to nitrogen at 77 K [41]. This can further lead to the non-correlation of the adsorption results obtained with hydrogen and nitrogen at 77 K. The argument that microporosity can play a beneficial role in hydrogen uptake will be discussed below.

The experimental results given above highlight the difficulty to prepare carbon-based materials with surface areas above  $3600 \text{ m}^2 \text{ g}^{-1}$ . Theoretical modeling has suggested, however, that it can be possible to exceed this limit by decreasing the size of the graphene sheets and thus make use of edge sites. Indeed, experimental work has hinted that an important role can be played by these sites on  $\text{H}_2$  sorption [42]. The work by Kuchta et al. [43–45] has suggested that graphene fragments can be of interest as long as they are not too small as this leads to low energy of adsorption and decreasing uptake. Graphene fragments which are too large will lose the ratio of edge contributions to  $\text{H}_2$  uptake. Their work has thus concentrated on the coronene unit ( $\text{C}_{24}\text{H}_{12}$ ) which could be assembled in a disordered fashion. Their optimized structure thus had a theoretical surface area of around  $6500 \text{ m}^2 \text{ g}^{-1}$ , a 30–50% increase compared to pure graphene-based materials. However, as with other carbon-rich adsorbents, the calculated adsorption energy in these systems is in the region of  $4 \text{ kJ mol}^{-1}$ . This therefore suggests that in order to maximize the  $\text{H}_2$  sorption under the desired conditions of temperature and pressure, then one needs not only to maximize the number of adsorption sites per unit mass and volume of the solid (potentially proportional to the surface area) but also tune the  $\text{H}_2$ -solid interaction energy that would allow more sites to adsorb  $\text{H}_2$  molecules.

### ***10.3.2 Varying the Pore Size of Carbon Materials***

As explained above, under the majority of adsorption conditions, poorly polarizable hydrogen will generally form a monolayer via relatively by weak van der Waals forces. It is therefore expected that the uptake will be related to the extent of available surface to this probe. However, as the pore size is decreased, the hydrogen-

to-surface interactions should increase due to an overlapping of potential fields from both sides of the pore, and this can lead to an increase in the adsorption capacity. Indeed, with respect to microporous samples, many mesoporous materials show moderate hydrogen uptakes. For example, Pang et al. [46] evidenced an uptake of 1.78 wt% at 77 K and 1 bar for a mesoporous carbon with a surface area of  $2314 \text{ m}^2 \text{ g}^{-1}$ , and Gadiou et al. [47] evidenced an uptake of around 3.5 wt% at 77 K and 10 bars for a templated mesoporous carbon. It thus follows that an optimal pore size should be attainable as a means to increase the hydrogen storage capacity under a given set of experimental conditions. From a theoretical standpoint, it is clearly possible to predict which pore sizes can be of interest for hydrogen at a given pressure and temperature, using Monte Carlo simulation, for example [48].

Experimentally, a number of authors have evidenced the effect of microporosity on hydrogen uptake at pressures up to 1 bar. Indeed, among others, Yushin et al. [49] suggested that surface area alone cannot be responsible for hydrogen uptake and that one should not ignore the effect of pore size and especially pores smaller than 1 nm. Further work by Zhang et al. [34] equally suggested that the micropore volume between 0.65 nm and 1.5 nm could be more important than BET area and total pore volume for hydrogen uptakes at 1 bar and 77 K. As an example, a hydrogen capacity of 2.85 wt% was observed at 1 bar/77 K for a material with a surface area of  $2988 \text{ m}^2 \text{ g}^{-1}$  which was almost 20% higher than the material with the highest surface area ( $3530 \text{ m}^2 \text{ g}^{-1}/2.66 \text{ wt\% H}_2$ ). However, the micropore volume for pores between 0.65 and 0.85 nm was almost twice as high for the former material suggesting that these pores could be influential for uptake under these conditions. Further studies concentrated on nitrogen-doped activated carbons which were prepared with different pore sizes [50] and suggested that pore with diameters in the range 0.56–0.70 nm could be optimal for hydrogen uptake, again at 1 bar and 77 K. This is in line with other studies with carbide-derived carbons known to have a high surface areas and tunable pore volume, which also suggested that a pore size of around 0.6 nm could be optimal [40, 51, 52].

Many authors suggest that the role of microporosity is diminished for the adsorption of hydrogen up to higher pressures. However, some studies suggest that pore sizes below 1 nm still impact this adsorption. A plot of hydrogen storage normalized to surface area vs. pore size seems to show that a porosity below 0.8 nm is of importance [53]. Theoretical studies suggest that a lower limit for porosity should be 0.56 nm for hydrogen storage at 77 K [54]. This study further investigated  $\text{H}_2$  uptakes at 300 K and 10 MPa and suggested an optimal pore width of 0.6 nm. However, under either of these conditions, the maximum uptake evidenced was below 4 wt%. This suggests pore size alone cannot give an adequate answer to increase the hydrogen storage capacity.

In terms of calculating the influence of pore size on the energy of sorption, Garcia Blanco et al. [55] used Monte Carlo simulation to highlight the decrease in hydrogen adsorption enthalpy with an increase in pore size. Further work by Rogacka et al. [7] suggested that as the pore width decreases from 1.2 nm to 0.6 nm, then the

adsorption energy for hydrogen effectively doubles. While these studies show the stronger attractive contributions of gas-gas interactions in the smaller pores where a denser adsorbate structure can be formed, the highest sorption energies were below  $10 \text{ kJ mol}^{-1}$  showing the limit in this approach pore size engineering of activated carbon-based materials.

An alternative family of carbon-based materials that could be used to engineer  $\text{H}_2$  uptake are single-walled carbon nanotubes and nanohorns. The curved surface of these materials can thus show different sorption sites in the interior of the structures and on the outer surface, with the pore curvature showing a significant role [56]. Indeed, Murata et al. [57] studied the hydrogen adsorption on single-walled nanohorns. The authors measured the isotherms at three different temperatures (77, 196, and 303 K) and suggest that the internal and interstitial spaces correspond to two different sorption sites. The adsorbed density of hydrogen in the interstitial spaces was shown to be lower than that in the internal volume. This was explained by self-stabilization effects which arise from the cluster formation by hydrogen molecules around more strongly adsorbed molecules in the interstitial spaces. The maximum uptake, obtained with an oxidized single-walled nanohorn, was 2.5 wt% at 77 K and around 50 bars. Average adsorption energies were of the order of  $5 \text{ kJ mol}^{-1}$ .

Hydrogen adsorption has been extensively studied on carbon nanotubes. An early study of  $\text{H}_2$  uptake on bunches (or ropes) of carbon single-walled nanotubes (SWNTs) was found to exceed 8 wt.%, at 80 K at around 100 bars [58]. It was suggested that the hydrogen is first adsorbed on the outer surfaces of the NTs. At above around 40 bars, an upswing in the isotherm was interpreted as a phase transition occurs where there is a separation of the individual SWNTs, and hydrogen is physisorbed on their exposed surfaces. Nevertheless, if one would like to compare with some of the other data in this section, the uptake at 20 bars on this material is in the order of 1.6 wt%. Increasing the temperature does not seem favorable as uptakes in the order of 0.4 wt% have been obtained with SWNTs at 298 K and 80 bars [59]. Further experimental studies confirmed this value with 1.58 wt %  $\text{H}_2$  uptake at 77 K and initial adsorption energies in the order of  $7\text{--}7.5 \text{ kJ mol}^{-1}$  [60]. Theoretical work has investigated the effect of SWNT bundles and their separation distance with the aim to optimize uptake in the interstices of the bundles [61]. It was found that a 0.6 nm distance was optimal for adsorption at 298 K and 0.9 nm at 77 K. Adsorption energies up to  $7.2 \text{ kJ mol}^{-1}$  were calculated. Interestingly, a theoretical study by the same authors [62] suggests that although the adsorption potential for hydrogen in SWNTs is enhanced relative to slit pores of the same size, the storage capacity of an array of tubes is less than that for idealized slit pore geometries, except at very low pressures. Experimental studies further suggest that the voids between the bundles may not be accessible [63].

Further work has followed hydrogen uptake on multiwall nanotubes (MWNTs). The study by Hou et al. [42] concerned a series of MWNTs mean outer diameters in the range of 13–53 nm and internal diameters below 5 nm. The highest uptake (4.6 wt% at 293 K/131 bars) was obtained for the largest diameter material (55 nm). An interesting conclusion from this study is that the hydrogen storage capacity

of the MWNTs was seen to be proportional to their diameter in the range of 13–53 nm but inversely proportional to their surface area. This strongly suggests a strong role is played by the interplanar spacing between the adjacent platelets in MWNTs. Nevertheless, other studies conclude that MWNTs may not be of interest with respect to activated carbons [64]. This all goes to show the probable effect of sample preparation and the difficulty in finding clear conclusions for these different forms of carbon-based adsorbents. Indeed, it has been shown that ball milling can increase the hydrogen sorption uptakes, probably through the creation of defects [65].

Figure 10.4 shows a collection of hydrogen uptake data at 77 K and 1 bar for a series of carbon-based materials. While no perfect trend is observed for the pure carbon materials, the data does suggest that even for the highest surface area materials, the uptakes flatten out and rarely surpass 3 wt%. It is clear, however, from the few data points obtained with materials whose carbon walls have been doped with heteroatoms, that these show slightly higher uptakes at the expense of BET area. This is described further below.

### 10.3.3 Doping the Carbon Walls with Heteroatoms

An alternative idea to enhance interactions of hydrogen with carbon-based materials is to substitute the carbon itself with other light elements such as Ca, N, P, B, and Be. This energetic *corrugation* of the surface can thus lead to increases in hydrogen interactions and thus uptakes. Furthermore, if very light elements are used, then the overall system weight could also decrease, ideally making such materials of great interest.

Maybe the simplest heteroatom to follow is oxygen, and the work by Zhao et al. [40] showed little influence in the adsorption enthalpies ranging from 3.9 to 5.2 kJ mol<sup>-1</sup> depending on the oxygen content. In a similar vein, molecular modeling has equally shown that functionalizing graphene with hydrogen does not lead to strong effects [66]. However, it was noted that other heteroatoms may be of interest.

Firlej et al. [67] used theoretical approaches to understand the effect of a 5–10% substitution of boron of atoms in a nanoporous carbon. The hydrogen uptake and energies seem to be greatly improved, with calculated energies in the range of 10–14 kJ mol<sup>-1</sup> at low coverage and uptakes around 5% at 298 K/100 bars. Further theoretical work by Roszak et al. [68] proposed to use Be either single atom substitution or with the inclusion of Be<sub>2</sub> dimers. The latter seemed to lead to calculated hydrogen binding energies of 23 kJ mol<sup>-1</sup> for the first hydrogen atom and 8 kJ mol<sup>-1</sup> for the second thus showing the relevance of this approach.

Experimentally, several studies can be reported. 10 atomic% boron has been successfully substituted into a material prepared from resorcinol and triethyl borate [69]. This material showed a sixfold increase in H<sub>2</sub> uptake at 100 bars and 77 K (0.18 → 1.1 wt%) and a quite remarkable H<sub>2</sub> uptake of 5.9 wt% at 298 K and 100 bars.

### 10.3.4 Doping Porous Carbons with Metals

A number of groups have studied the influence of doping various types of carbon with metals. The aim of this is to enhance the hydrogen uptake with the formation of side on bonded hydrogen ligands, also known as Kubas interactions [70]. Indeed, doping with metals, such as nickel, has been shown to enhance hydrogen uptake [71]. Some of the first studies of hydrogen adsorption on single-walled nanotubes evidenced adsorption energies as high as  $19.6 \text{ kJ mol}^{-1}$  [72], and while the authors did not retain this possibility, the sample contained up to 20% of cobalt nanoparticles, and one cannot eliminate the supposition that these may also affect hydrogen sorption. A more complete study, this time with ordered mesoporous carbons doped with Pt, Pd, Ni, and Ru (loadings of 1, 5, and 10% were investigated), showed increases in uptake, with respect to the parent carbon, in the range of 2.7 to 5.4, at around 1 bar [73]. However, in this study the effect of change in material density was not considered thus making it difficult to evaluate the additional effect of the metal with respect to the initial mass of the carbon. Nevertheless, it was found that the lowest loading 1% of Ni was shown to give the highest uptake at this lower pressure. The authors equally studied the uptake at 300 bars and again evidenced that it was the 1% Ni-ordered mesoporous carbon which gave the highest uptake (2.14 wt%). However, the results given almost scale with BET area suggesting that the carbon itself plays an important, if not dominant, role for the adsorption of hydrogen at this high pressure.

Several groups have investigated the use of metals such as platinum in order to induce spillover effects. Indeed, the doping of SWNTs with Pt has shown increases in the order of 25% for  $\text{H}_2$  uptake at 298 K and 100 bars (almost to 0.5 wt% [59]), and small 8% increase in  $\text{H}_2$  uptake was observed with Pt-loaded zeolite-templated carbon when compared to the parent materials [74]. Inelastic neutron scattering has been used to evidence the formation of atomic hydrogen [75]. In this study using Pd-doped activated carbon fibers, new C-H bonds were observed after  $\text{H}_2$  sorption at 293 K and 16 bars which was given as proof of this phenomenon. Elsewhere, Takagi et al. [76] who studied the adsorption of hydrogen on Pt- and Pd-activated carbon fibers concluded that the increases in uptakes on these materials with respect to the parent carbon were due to (i) hydrogen chemisorption on the Pt particles and (ii) formation of Pd hydride. However, at 303 K it was evidenced that the hydrogen adsorption was reversible.

The results obtained with metal-doped materials generally highlight the strong role of enhancement of  $\text{H}_2$  uptake at relatively low pressures, with an increasingly important role of the remaining carbon substrate as the adsorption pressure increases. This has to be considered when considering real operating pressures.

As mentioned above, the interaction of hydrogen with a pure carbon surface is quite moderate to low ( $4\text{--}5 \text{ kJ mol}^{-1}$ ) which implies that in use, almost any contaminant will displace the hydrogen leading to loss of efficiency. Doping samples with metals has shown to lead to enhancement of adsorption uptakes and adsorption interactions at low pressures (i.e., low loadings) with the effect diminishing with

higher pressures implying that the surface of the carbon substrate is playing a more significant role. Furthermore, the additional weight of the metal could be a significant barrier if vehicular storage of hydrogen is considered.

### ***10.3.5 Conclusions with Respect to Carbon Materials***

The most mature research into hydrogen storage in porous materials concerns carbon-based adsorbents. As mentioned at the start of this section, the range of carbon-based materials is extremely broad. Many of the materials are heterogeneous and highly depend on the preparation method employed. It is thus quite logical to find a huge variety of results of which some seem to be contradictory, and it is difficult to find universal trends. Nevertheless, it would seem that hydrogen adsorption on pure carbon-based materials depends on both available surface area and micropore size. Depending on the temperature and pressure conditions considered, relationships between surface area and/or micropore volume have been obtained. However, the study by Zhao et al. [40] showed some very nice relationships between hydrogen uptake and the second virial coefficient. Importantly, while the first virial coefficient reflects adsorbate-adsorbent interactions, the second virial coefficient is a function of adsorbate-adsorbate interactions, and this should be food for thought.

It is possible to prepare active carbons with surface areas in the region of  $3600 \text{ m}^2 \text{ g}^{-1}$ , but the interaction energies on such surfaces are quite low ( $4\text{--}5 \text{ kJ mol}^{-1}$ ). Molecular modeling has suggested that decreasing the graphene domain size can increase the available surface area as there will be an increase in edge sites. It is possible to increase the hydrogen-adsorbent interactions by decreasing the pore size. Indeed, for the adsorption of hydrogen at 1 bar and 77 K, it has been suggested by several authors that pores in the range of 0.6 nm may be optimal. However, at ambient temperatures and high pressures, slightly larger pores have been suggested of more interest ( $\sim 0.8 \text{ nm}$ ). Nevertheless, the increase in the adsorption enthalpy in these smallest pores only remains in the region of  $9\text{--}10 \text{ kJ mol}^{-1}$  which is probably not optimal for practical use.

Effort has thus been made to increase the attractivity of the carbon surface or pores for hydrogen. The introduction of light elements into the carbon lattice has been carried out in order to induce some form of energetic corrugation. Porous carbons have been doped with metals, and this has resulted in increased interactions and higher uptakes.

Looking toward applications, process modeling has been made in view of the use of active carbons in a sorbent-based cryogenic compressed hydrogen system [77]. Interestingly, only a 4.5 wt% gravimetric capacity was considered, although pressures of 100 bar and a temperature of 10 K were used. A second study considered a higher-pressure range (350 bars) and a temperature range of 60–298 K and using a Maxsorb MSC-30 sample [78]. Here it was concluded that both cryogenic temperatures are required for storage and heating required to recover the maximum amount of hydrogen.

## 10.4 Hydrogen Adsorption with Metal-Organic Frameworks

Metal-organic frameworks (MOFs) and related materials are the most recent family of porous materials that has been used in hydrogen adsorption research. Metal-organic frameworks (MOFs) or porous coordination polymers (PCPs) [79, 81] is a generic term given to a very wide range of materials that have found considerable interest since the pioneering work of Hoskins and Robson [81]. This family of MOFs and PCPs encompass a very wide range of materials of which subsets can be known as ZIFs (zeolite imidazole frameworks) [82], COFs (covalent organic frameworks) [83], MOP (microporous organic polymers) [84], and others.

Metal-organic frameworks (or MOFs) are constructed from metals or metal cluster nodes which are linked together through organic moieties. The metals that can be used are divalent (Cu, Zn, Mg...), trivalent (Al, Cr, Ga, Fe, In...), or tetravalent (V, Zr, Ti, Hf...) with almost every metal in the periodic table having been incorporated in one MOF structure or another. A very large number of organic linker moieties have equally been introduced with the carboxylate, imidazolate, phosphonate, and pyrazolate families of note. The coordination of both node and linker can be varied to give different structure geometries [79, 85–87]. The linker can be modified in length to tailor the available pore volume [80]. The metals can be partially unsaturated to give specific adsorption sites. Furthermore, the nodes and linkers can each be functionalized with groups of varying degrees of polarity. With this wide variety of chemistry available, it can be appreciated that many thousands of different MOF structures have been reported so far. The possibility to further modulate the chemistry leads to an almost infinite spectrum of materials able to be prepared with an equally infinite variation of physical and chemical properties.

Some MOFs are of quite low density and thus have been reported to have remarkable specific pore volumes and BET-specific areas. Recent interest in MOFs dates from the mid-1990s [81, 88–90] where porosity and significant gas uptakes were reported. This seeded the interest in these materials for adsorption-based applications [91], and it is not surprising that probably the first domain where these materials were researched for was for hydrogen storage [92], with notably the initial work of the group of Yaghi on MOF-5 [93].

In view of hydrogen storage, this family of materials can thus be considered as one which can combine the order of zeolites with the high surface areas available in carbons. In addition, as with these aforementioned materials, one can hope to increase the interaction for hydrogen with several strategies for functionalization. A further interest of this family of materials equally lies in the ability to easily model the interactions of H<sub>2</sub> with different MOFs which can lead to an improved understanding of the mechanisms in play [94].

One of the potential drawbacks traditionally associated with MOFs concerns the variation of values observed in the literature, and this can be due to materials preparation or their stability toward contaminants and notably water. Indeed, as mentioned previously, one of the first MOFs to come to attention in terms of hydrogen storage was MOF-5 or IRMOF-1 [93]. However, it was shown that

the preparation, activation, and storage conditions of this material are critical to the hydrogen uptake performance [95]. Indeed, this can often be the case with this family of materials and can be due to factors such as starting reactants, solvent, synthesis temperature, and time as well as activation conditions. Indeed, the synthesis of MOFs can, at first, seem quite simple, but subtle changes in the recipe followed can give rise to differences in properties. As such, verified recipes, such as those gathered for zeolites [96], will be essential in the future. A second factor which can lead to differences in sorption performance with MOFs is the instability to contaminants, such as water [97]. This seems especially the case with MOF-5 [95] but has also been shown for other well-known MOFs such as HKUST-1 [98]. However, as the chemistry of these materials can be so vast, then there are many MOFs which are very stable and these include, among others, MIL-100(Cr) [99] and UiO-66(Zr) [100].

As with the other materials treated in this chapter, the first direction one can investigate to increase hydrogen storage capacity is to increase the available surface for adsorption. MOFs have been prepared with reported surface areas above  $7000 \text{ m}^2 \text{ g}^{-1}$ , and a theoretical MOF with a surface area limit of  $14,600 \text{ m}^2 \text{ g}^{-1}$  has equally been proposed [101].

A second direction that can be taken is to increase the energy of interaction for hydrogen. Indeed, many MOF materials show interaction energies in the range  $3\text{--}6 \text{ kJ mol}^{-1}$  (e.g., [102]), and it has been shown that the amount of hydrogen adsorbed is directly related to this interaction [103].

#### 10.4.1 *H<sub>2</sub> Uptakes with Reference MOFs*

As mentioned above, one of the first MOFs to be studied for hydrogen sorption is known was MOF-5. The benchmark value obtained for excess H<sub>2</sub> uptake on MOF-5(Zn) is 7.1 wt% at 77 K and around 40 bars, which was calculated to be around 10 wt% absolute (or total) H<sub>2</sub> uptake [95]. It has been suggested that the hydrogen is preferentially located close to the metal oxide nodes of MOF-5 with secondary sites close to the phenylene linker [104, 105]. Similar uptakes have been observed with a second material; NOTT-112 with a BET area of  $3800 \text{ m}^2 \text{ g}^{-1}$  shows an excess H<sub>2</sub> uptake of 7.07 wt% at around 35–40 bars at 77 K and a total H<sub>2</sub> uptake of 10 wt% at 77 bars and 77 K [106].

One of the possibilities to vary the adsorption properties of MOFs is to change the length of the organic linker unit. This possibility was initially shown by Yaghi and co-workers [79] for the case of the IRMOF series. Indeed, increasing the linker length leads to an increase in pore size and pore volume. This phenomenon can also be observed in other MOF series with different ligands such as the NOTT materials, although this has not been experimentally confirmed at present [107].

Thus, changing the linker length resulting in a change in available surface area leads to a proportional increase in excess gravimetric H<sub>2</sub> uptake at 77 K [108]. Interestingly in this work, a comparison of volumetric uptake showed much smaller

differences, thus suggesting the importance of this metric for practical applications. This does however highlight the critical role of the organic linker on the hydrogen uptake. This is in contrast and seemingly inconsistent with models where the metal oxide nodes dominate sorption behavior. Indeed, one example is IRMOF-20 which has a relatively low ratio of metal oxide to organic linker but an uptake of 9.1 wt% at 100 bars and 77 K [109]. Indeed, this MOF combines extremely high surface area ( $> 4000 \text{ m}^2 \text{ g}^{-1}$ ) with moderate density. This suggests that volumetric storage density even in materials with extremely high porosity can be excellent.

Molecular modeling is a tool that can help identify MOFs with the most optimal  $\text{H}_2$  storage performances. The tools that have been used have often considered the topological aspects of many materials with, in the case of MOFs, the use of the CoRE database [110]. From such studies, Ahmed et al. [109], as mentioned above, suggest the interest in IRMOF-20, whereas Gómez-Gualdrón et al. [111] argue that NU-1103 can also be of interest with a  $\text{H}_2$  capacity of around 12.6 wt% at 100 bars and 77 K.

#### 10.4.2 Location of Hydrogen in MOFs

While high surface area is a significant performance parameter, one can then aim to understand the adsorption a little more and in particular where the hydrogen molecules prefer to sit. As described above in the case of MOF-5, it was suggested that the corners of the pores are the preferential adsorption sites with secondary sites close to the phenylene linker [104, 105, 112]. Variable temperature infrared (VTIR) spectroscopy measurements suggest that hydrogen placed in this corner site represents a binding energy of around  $7.4 \text{ kJ mol}^{-1}$  with a secondary site with a lower binding energy of around  $3.5 \text{ kJ mol}^{-1}$  [113].

In a copper-based material, CPL-1, the hydrogen equally seems to be located in the corner or pocket of the pore channel which are again close to the metal oxide nodes [114]. VTIR has been used to locate the hydrogen adsorbed in the UiO-66/UiO-67 family of materials with, again, preferential interactions with -OH and O- centers located at the oxy-zirconium node, with the hydroxyl groups being the most preferred site [115]. The question then arises as to whether it is the more confined pore space that is important or the proximity to an electron rich zone in proximity of the metal.

With the MOFs mentioned above, the interaction energies are relatively low and in the range  $3\text{--}6 \text{ kJ mol}^{-1}$ . As it would seem that the hydrogen prefers the most sterically confined areas available in the MOF porosity, one could exploit the possibility to decrease the pore size to increase  $\text{H}_2$ -surface interactions, as discussed by Chun et al. [116]. As an example, this has been demonstrated with a MOF with molecular formula  $\text{Mg}_3(\text{O}_2\text{C-C}_{10}\text{H}_6\text{-CO}_2)_3$  [117] which has been suggested to have a pore size in the region  $3.46\text{--}3.64 \text{ nm}$  and a  $\text{H}_2$  sorption energy up to  $9.5 \text{ kJ mol}^{-1}$ . However, when compared to the energies that have been suggested as requirements

in the introduction, it seems clear that just decreasing the pore size is not sufficient to obtain the interactions required for any application. Thus, other strategies have been explored as described below.

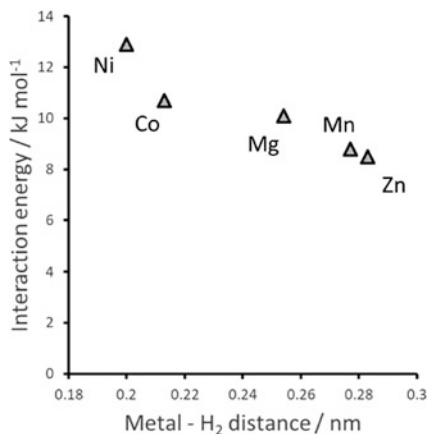
### 10.4.3 Increasing H<sub>2</sub>-MOF Interactions by Varying the Metal Node

As described so far in this chapter, in many MOFs the metal itself is quite shielded, and thus it has a limited influence on H<sub>2</sub> uptake. Nevertheless, it has been suggested using molecular simulation that changing the metal – even if shielded – may affect the hydrogen sorption properties [118].

However, in some cases, the metal can be available as an adsorption site and thus can be a strong binding center [119, 120]. One example was demonstrated by Dinca et al. [121] with a manganese-based compound with formula Mn<sub>3</sub>(Mn<sub>4</sub>Cl)<sub>3</sub>(btt)<sub>8</sub>(CH<sub>3</sub>OH)<sub>10</sub>]<sub>2</sub> (btt<sup>3-</sup> = 1,3,5-benzenetristetrazolate). Upon evacuation, part of the methanol is able to be evacuated, and a fraction of the Mn<sup>2+</sup> ions are disposed as open coordination sites. The hydrogen uptake is around 2.2 wt % at 77 K and 1.2 bars with an initial hydrogen energy calculated to be around 10 kJ mol<sup>-1</sup>. However, it would seem that the fraction of exposed metal sites is quite low which leads to energies which decrease significantly with increasing uptake. Further work, exploring different metal centers did not show improved behavior [122]. Similar behavior is observed with MIL-101(Cr) with an initial enthalpy of around 9.5–10 kJ mol<sup>-1</sup> which strongly decreases with uptake [123, 124], whereas HKUST-1 (Cu<sub>2</sub>btc<sub>3</sub>) showed zero-coverage H<sub>2</sub> sorption energies of 6.8 kJ mol<sup>-1</sup> [125], although VTIR [126] suggests that energies up to 10 kJ mol<sup>-1</sup> could be obtained with this same material. Probably the highest interaction energy was calculated, using periodic DFT combined with GCMC, as around 13.4 kJ mol<sup>-1</sup> at the open Cu<sup>2+</sup> sites in MOF-505 [127]. All of these systems show the promise of using open coordination sites but with the need to increase their density.

One MOF material where there is a high density of open coordination sites is CPO-27 [128, 129] or MOF-74 [130, 131]. Indeed, metals such as Mg, Mn, Co, Ni, and Zn can be used in the preparation of these materials, and the open coordination sites can be found in six linear metal oxy chains along the length of the cylindrical pores. A 2.2 wt% has been found for the Ni and Co materials, whereas a 2.5 wt% H<sub>2</sub> uptake has been found for the Mg compound [132]. The authors have suggested that approximately 1 H<sub>2</sub> molecule is adsorbed per metal coordination site with average adsorption energies of 13, 11.5, and 10.9 kJ mol<sup>-1</sup> for the Ni, Co, and Mg compounds, respectively [132, 133]. One could expect higher energies, compared to cases where the H<sub>2</sub> molecule could be actually coordinated to the metal center. Indeed, the adsorbed H<sub>2</sub> molecule is found at a distance of around 0.28 nm from the Zn in this material, whereas the Zn-O distance (i.e., metal to ligand) is around 0.212 nm [134]. The reason for this longer distance can be explained by

**Fig. 10.5** Energy of adsorption as a function of metal-H<sub>2</sub> distances in a series of MOF-74/CPO-27 materials. Data from Zhou et al. [131]



steric limitations for the H<sub>2</sub> molecule within the spherical pores, compared to a flat surface, for example. However, one can relate the interaction energy with the metal-H<sub>2</sub> distance as shown in Fig. 10.5. Thus, it would seem that the relative strength of interaction of M-H<sub>2</sub> may be empirically predicted by the ionic radius of the cations in same coordination environment, and this could provide an avenue for the design of MOFs with unsaturated metal sites.

#### 10.4.4 Increasing H<sub>2</sub>-MOF Interactions by Occlusion of Species Inside the Porosity

Doping with metals or other species can be of interest [135]. Indeed, as with the other porous host discussed in this chapter, it has been argued that doping with some metals can lead to hydrogen spillover [136–138]. As an example, Liu et al. [139] doped MIL-53 and MIL-101 with a 20 wt% Pt/C mixture, and these have shown to give higher uptakes at 298 K with notably a doubling of uptake in the case of the MIL-101 system. Excellent spillover enhancement factors of 3.3 and 3.1 were found for MOF-5 and IRMOF-8, respectively [136]. However, there are doubts concerning the reversibility of the phenomena with the possible formation of hydrides, for example, with MOF-177/Pt [140]. In addition, in the case of a MIL-100(Al)/Pt material, the formation of a Pd β-hydride is clearly evidenced [141].

It is also possible to dope the pores with clusters in order to increase the interaction with hydrogen. One example that was shown was with the fluorinated cluster Mo<sub>6</sub>Br<sub>8</sub>F<sub>6</sub> which was incorporated into MIL-101(Cr) [124]. The initial enthalpies that were measured for this system were at around 13.5 kJ mol<sup>-1</sup> which strongly drop off. The strong interactions can be related to the strong ionic character of the Mo-F bond, especially when compared to Mo-Cl, Mo-Br, or Mo-I bonds.

In analogy with zeolites, cations have been used as doping species. From a theoretical standpoint, the effect of lithium occluded in MOF-5 has been studied which suggested that a 2 wt% uptake can be achieved at 300 K [142]. Two lithium cations seemed to be placed on each side of the organic ring, and it is suggested that clustering would not occur. Each  $\text{Li}^+$  could then bind to three  $\text{H}_2$  molecules with a binding interaction over twice that of on the organic linker alone. Experimentally, it has been more difficult to reach the targets suggested by modeling. Indeed, the hydrogen adsorption energy was shown to only increase from 7.7 to 8.1  $\text{kJ mol}^{-1}$  in a lithium-doped polymer [143], and a lower enthalpy of adsorption was noted for a lithium exchanged indium MOF [144], and in this study it was suggested that the lithium exchange leads to an increased pore size.

### ***10.4.5 Increasing $\text{H}_2$ -MOF Interactions Using Pore Flexibility and/or Catenation***

Catenation has been suggested as a means to decrease the pore size but equally permitting an increase in pore opening flexibility and thus potentially to an interesting means to increase hydrogen storage capacity [145].

Indeed, catenation isomers in the HKUST-1 structural analogue PCN-6 have been suggested as a means to significantly increase the hydrogen uptake [146]. Furthermore, a comparison between the non-catenated PCN-6' and catenated PCN-6 shows differences in interactions. At low loading the interactions are similar where the first  $\text{H}_2$  molecules are found to be close to the Cu-centers. At higher loadings there are differences in which in the catenated sample, there are three sites close to the Cu-center, whereas in the non-catenated sample, there is only one. This leads to stronger interactions with loading.

It is equally possible to use the inherent flexible nature of a MOF structure to enhance  $\text{H}_2$  storage capacity. One study proposed the use of a material based on units of  $\text{Ni}_2(\text{bipy})_3(\text{NO}_3)_4$ , to allow  $\text{H}_2$  to enter the pores and then be trapped inside the porosity [147]. Indeed, the dynamics of the bridging bipy molecules (where bipy = 4,4-bipyridyl) would seem to confer a certain flexibility to the framework and allow probes that appear oversized from a static view of the structure to pass through the windows and access the pores via a gating type effect.

### ***10.4.6 Conclusions Concerning MOFs***

A glimpse of the hydrogen uptakes at 1 bar and 77 K on various MOFs (Fig. 10.6 left) paints a similar picture to the carbon-based materials (Fig. 10.4). Indeed, under these conditions, uptakes above 3 wt% are rare. It is thus clear that much higher

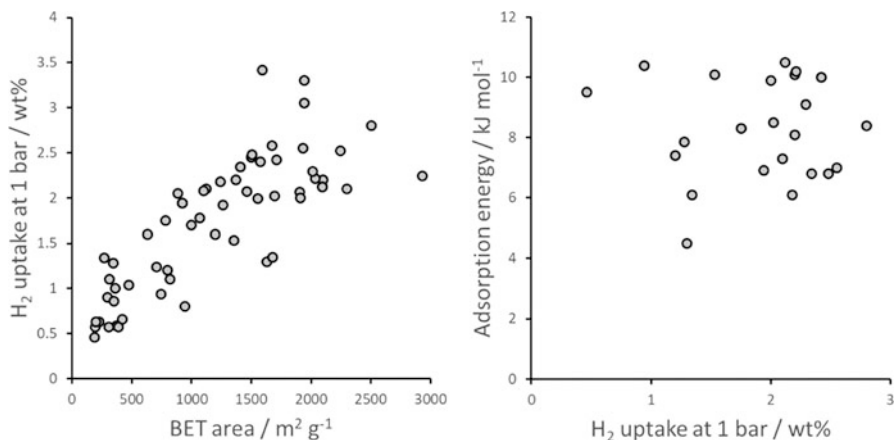


**Fig. 10.6** (left) Excess H<sub>2</sub> uptakes with various MOFs at 77 K and 1 bar as a function of BET area. (right) Energy of adsorption of H<sub>2</sub> as a function of excess uptake

pressures will be required for any application and that even varying the metal node does not have a very strong effect on the uptakes themselves. The other thing that is clear from this summary is that no strong correlation between BET area and H<sub>2</sub> uptake can be made. Figure 10.6 (right) plots the energies of adsorption as a function of uptake at 1 bar at 77 K for various studies that have been cited in this chapter. Surprisingly, there again seems to be no specific correlation. This could be due to the heterogeneity of the samples studied and/or the calculation method used to estimate the adsorption energies. However, this plot also highlights the need to increase the rather weak interactions between the MOF framework and the hydrogen as has been noted previously [148]. This all highlights the difficulties in using experimental data to obtain correlations, and thus one can turn to molecular simulation to gain further insights.

Using molecular simulation, Frost et al. [149] suggested that (i) the low-pressure hydrogen uptake is directly correlated to the interaction energy of hydrogen with the surface, (ii) the medium-pressure uptake is related to the extent of available surface, and (iii) the high-pressure uptake is related to the pore volume. The review of K. M. Thomas [150] concerning a limited number of MOF materials equally seems to show a poor correlation between the amount of H<sub>2</sub> adsorbed at 77 K and 1 bar with the BET area which agrees with Fig. 10.6 (left). However, this work also showed that the high-pressure H<sub>2</sub> uptake at 77 K relates well to the BET area. This therefore further suggests that it is relatively difficult to define exact pressure domains (i.e., low, medium, high), as this equally depends on the temperature. However, the general findings suggested by Frost et al. [103] could act as guidelines for the design of any porous material for gas storage.

In terms of MOF materials design, one can turn to molecular modeling for guidance [149]. Indeed, the effect of metal has been studied in several cases as well as the effect of organic ligand. Maybe one general trend that has come from many

studies (e.g., [118]) is that increasing the aromatic content of the organic linkers can have a positive effect on uptake. As such, one path forward is to design other framework materials such as PAFs (porous aromatic frameworks). In the case of PAF-3, for example, uptakes in the region of 6 wt% have been measured [151].

## 10.5 Overall Conclusions

Over the last 30 years or so, there has been intense research into the storage properties of hydrogen with nanoporous adsorbents. The interest arises from the ease of use and full recovery of the stored gas. However, the drawback of the use of nanoporous materials is the lack of capacity for any practical vehicular H<sub>2</sub> storage. Hydrogen capacities above 10 wt% have been observed for materials under high pressure but also under cryogenic conditions. The best result found by the author was for the MOF NU-1103: 12.6 wt%/77 K/100 bars [111].

Decorating the various nanoporous materials with functions (e.g., use of heteroatoms with carbons or changing metal centers in MOFs) leads to slight increases in uptakes at low pressure. However, it would seem that the effects of this decoration are less significant for high pressure H<sub>2</sub> storage. Thus, from the above discussions, the highest uptakes will generally be obtained for materials with the largest specific surface per unit volume. This is confirmed both experimentally for MOF adsorbents and in hydrogen sorption simulations on carbon nanostructures. However, in terms of adsorption energy, no materials have evidenced constant hydrogen interactions above 15–20 kJ mol<sup>-1</sup> which is the design requirement set out by several authors.

Nevertheless, there are huge possibilities for the design of carbon-based structures and in the realm of metal-organic frameworks. Features of interest which have been highlighted from carbon materials seem to include pores in the range of 0.5–0.7 nm. Molecular simulation can be used further as a design tool and has been used to suggest that surface areas above 7000 m<sup>2</sup> g<sup>-1</sup> could be obtained for both carbons and MOFs. The work is cut out for future work in this domain.

## References

1. Elam CC, Gregoire Padró CE, Sandrock G, Luzzi A, Lindblad P, Fjermestad Hagen E (2003) Realizing the hydrogen future: the international energy agency's efforts to advance hydrogen energy technologies. *Int J Hydrog Energy* 28(6):601–607
2. Banerjee S, Musa MN, Jaafar AB (2017) Economic assessment and prospect of hydrogen generated by OTEC as future fuel. *Int J Hydrog Energy* 42(1):26–37
3. Petitpas G, Bénard P, Klebanoff LE, Aceves XS (2014) A comparative analysis of the cryo-compression and cryo-adsorption hydrogen storage methods. *Int J Hydrog Energy* 39(20):10564–10584
4. Bhatia SK, Myers AL (2006) Optimum conditions for adsorptive storage. *Langmuir* 22(4):1688–1700

5. Garrone E, Bonelli B, Areán CO (2008) Enthalpy–entropy correlation for hydrogen adsorption on zeolites. *Chem Phys Lett* 456(1–3):68–70
6. Bae Y-S, Snurr RQ (2010) Optimal isosteric heat of adsorption for hydrogen storage and delivery using metal-organic frameworks. *Micro Meso Mater* 132(1–2):300–303
7. Rogacka J, Firllej L, Kuchta B (2017) Modeling of low temperature adsorption of hydrogen in carbon nanopores. *J Mol Model* 23(1):20
8. Bénard P, Chahine R (2007) Storage of hydrogen by physisorption on carbon and nanostructured materials. *Scr Mater* 56(10):803–808
9. Rouquerol J, Rouquerol F, Llewellyn P, Maurin G, Sing KSW (2013) Adsorption by powders and porous solids: principles, methodology and applications. Academic Press, Oxford
10. Bastos-Neto M, Patzschke C, Lange M, Möllmer J, Möller A, Fichtner S, Schrage C, Lässig D, Lincke J, Staudt R, Krautscheide H, Gläser (2012) Assessment of hydrogen storage by physisorption in porous materials. *Energy Environ Sci* 5(8):8294–8303
11. Broom DP, Hirscher M (2016) Irreproducibility in hydrogen storage material research. *Energy Environ Sci* 9(11):3368–3380
12. Baerlocher C, McCusker LB, Olson DH (2007) Atlas of zeolite framework types. Elsevier, Amsterdam
13. Treacy MMJ, Rivin I, Balkovsky E, Randall KH, Foster MD (2004) Enumeration of periodic tetrahedral frameworks. II Polynodal graphs. *Micro Meso Mater* 74(1–3):121–132
14. Weitkamp J, Fritz M, Ernst S (1995) Zeolites as media for hydrogen storage. *Int J Hydrog Energy* 20(12):967–970
15. Dong J, Wang X, Xu H, Zhao Q, Li J (2007) Hydrogen storage in several microporous zeolites. *Int J Hydrog Energy* 32(18):4998–5004
16. Fraenkel D, Shabtai J (1977) Encapsulation of hydrogen in molecular sieve zeolites. *J Am Chem Soc* 99(21):7074–7076
17. Efstathiou AM, Siub SL, Bennett CO (1990) Encapsulation of molecular hydrogen in zeolites at 1 atm. *J Catal* 123(2):456–462
18. Langmi HW, Walton A, Al-Mamouri MM, Johnson SR, Book D, Speight JD, Edwards PP, Gameson I, Anderson PA, Harris IR (2003) Hydrogen adsorption in zeolites A, X, Y and RHO. *J Alloys Compd* 356–357:710–715
19. Langmi HW, Book D, Walton A, Johnson SR, Al-Mamouri MM, Speight JD, Edwards PP, Harris IR, Anderson PA (2005) Hydrogen storage in ion-exchanged zeolites. *J. Alloys Compd* 404–406:637–642
20. Li Y, Yang RT (2006) Hydrogen storage in low silica type X zeolites. *J Phys Chem B* 110(34):17175–17181
21. Zecchina A, Bordiga S, Vitillo JG, Ricchiardi G, Lamberti C, Spoto G, Bjørgen M, Lillerud KP (2005) Liquid hydrogen in protonic Chabazite. *J Am Chem Soc* 127(17):6361–6366
22. Regli L, Zecchina A, Vitillo JG, Cocina D, Spoto G, Lamberti C, Lillerud KP, Olsbye U, Bordiga S (2005) *Phys Chem Chem Phys* 7(17):3197–3203
23. Kazansky VB, Borovkov VY, Serich A, Karge HG (1998) Low temperature hydrogen adsorption on sodium forms of faujasites: barometric measurements and drift spectra. *Micro Meso Mater* 22(1–3):251–259
24. Chahine R, Bose TK (1994) Low-pressure adsorption storage of hydrogen. *Int J Hydrog Energy* 19(2):161–164
25. Poirier E, Chahine R, Bose TK (2001) Hydrogen adsorption in carbon nanostructures. *Int J Hydrog Energy* 26(8):831–835
26. Marsh H, Rodriguez-Reinoso F (2006) Activated carbon. Elsevier, Amsterdam
27. Bottani EJ, Tascon JMD (2011) Adsorption by carbons. Elsevier, Amsterdam
28. Tascon JMD (2012) Novel carbon adsorbents. Elsevier, Amsterdam
29. Thomas KM (2007) Hydrogen adsorption and storage on porous materials. *Catal Today* 120(3–4):389–398
30. Sevilla M, Mokaya R (2014) Energy storage applications of activated carbons: supercapacitors and hydrogen storage. *Energy Environ Sci* 7(4):1250–1280

31. Panella B, Hirscher M, Roth S (2005) Hydrogen adsorption in different carbon nanostructures. *Carbon* 43(10):2209–2214
32. Jin H, Lee YS, Hong I (2007) Hydrogen adsorption characteristics of activated carbon. *Catal Today* 120(3–4):399–406
33. Wang H, Gao Q, Hu J (2009) High hydrogen storage capacity of porous carbons prepared by using activated carbon. *J Am Chem Soc* 131(20):7016–7022
34. Zhang C, Geng Z, Cai M, Zhang J, Lin X, Xina H, Ma J (2013) Microstructure regulation of super activated carbon from biomass source corncob with enhanced hydrogen uptake. *Int J Hydrog Energy* 38(22):9243–9250
35. Figueroa-Torres MZ, Robau-Sánchez A, De la Torre-Sáenz L, Aguilar-Elguézabal A (2007) Hydrogen adsorption by nanostructured carbons synthesized by chemical activation. *Micro Meso Mater* 98(1–3):89–93
36. Tellez-Juárez MC, Fierro V, Zhao W, Fernández-Huerta N, Izquierdo MT, Reguera E, Celzard A (2014) Hydrogen storage in activated carbons produced from coals of different ranks: effect of oxygen content. *Int J Hydrog Energy* 39(10):4996–5002
37. Sevilla M, Mokaya R, Fuertes AB (2011) Ultrahigh surface area polypyrrole-based carbons with superior performance for hydrogen storage. *Energy Environ Sci* 4(8):2930–2936
38. Masikan E, Mokaya R (2013) Preparation of ultrahigh surface area porous carbons templated using zeolite 13X for enhanced hydrogen storage. *Prog Nat Sci Mater Int* 23(3):308–316
39. Yang Z, Xia Y, Mokaya R (2007) Enhanced hydrogen storage capacity of high surface area zeolite-like carbon materials. *J Am Chem Soc* 129(6):1673–1679
40. Zhao X, Xiao B, Fletcher AJ, Thomas KM (2005) Hydrogen adsorption on functionalized Nanoporous activated carbons. *J Phys Chem B* 109(18):8880–8888
41. Ströbel R, Jörissen L, Schliermann T, Trapp V, Schütz W, Bohmhammel K, Wolf G, Garcke J (1999) Hydrogen adsorption on carbon materials. *J Power Sources* 84(2):221–224
42. Hou P-X, Xu S-T, Ying Z, Yang Q-H, Liu C, Cheng H-M (2003) Hydrogen adsorption/desorption behavior of multi-walled carbon nanotubes with different diameters. *Carbon* 41(13):2471–2476
43. Kuchta B, Firllej L, Mohammadhosseini A, Boulet P, Beckner M, Romanos J, Pfeifer P (2012) Hypothetical high-surface-area carbons with exceptional hydrogen storage capacities: open carbon frameworks. *J Am Chem Soc* 134(36):15130–15137
44. Kuchta B, Firllej L, Mohammadhosseini A, Beckner M, Romanos J, Pfeifer P (2013) Open carbon frameworks – a search for optimal geometry for hydrogen storage. *J Mol Mod* 19(10):4079–4087
45. Firllej L, Pfeifer P, Kuchta B (2013) Understanding universal adsorption limits for hydrogen storage in Nano porous systems. *Adv Mater* 25(41):5971–5974
46. Pang JB, Hampsey JE, Wu ZW, Hu QY, Lu YF (2004) Hydrogen adsorption in mesoporous carbons. *Appl Phys Lett* 85(21):4887–4889
47. Gadiou R, Saadallah S-E, Piquero T, David P, Parmentier J, Vix-Guterl C (2005) The influence of textural properties on the adsorption of hydrogen on ordered nanostructured carbons. *Micro Meso Mater* 79(1–3):121–128
48. Ustinov EA, Gavrilov VY, Mel'gunov MS, Sokolov VV, Berveno VP, Berveno AV (2017) Characterization of activated carbons with low-temperature hydrogen adsorption. *Carbon* 121(1):563–573
49. Yushin G, Dash R, Jagiello J, Fischer JE, Gogotsi Y (2006) Carbide-derived carbons: effect of pore size on hydrogen uptake and heat of adsorption. *Adv Funct Mater* 16(17):2288–2293
50. Sethia G, Sayari A (2016) Activated carbon with optimum pore size distribution for hydrogen storage. *Carbon* 99:289–294
51. Gogotsi Y, Dash RK, Yushin G, Yildirim T, Laudisio G, Fischer JE (2005) Tailoring of nanoscale porosity in carbide-derived carbons for hydrogen storage. *J Am Chem Soc* 127(46):16006–16007
52. Sevilla M, Fuertes AB, Mokaya R (2011) Preparation and hydrogen storage capacity of highly porous activated carbon materials derived from polythiophene. *Int J Hydrog Energy* 36(24):15658–15663

53. Gogotsi Y, Portet C, Osswald S, Simmons JM, Yildirim T, Laudisio G, Fischer JE (2009) Importance of pore size in high-pressure hydrogen storage by porous carbons. *Int J Hydrog Energy* 34(15):6314–6319
54. Cabria I, Lopez MJ, Alonso JA (2007) The optimum average nanopore size for hydrogen storage in carbon nanoporous materials. *Carbon* 45:2649–2658
55. Garcia Blanco AA, de Oliveira JCA, Lopez R, Moreno-Pirajan JC, Giraldo L, Zgrablich G, Sapag K (2010) A study of the pore size distribution for activated carbon monoliths and their relationship with the storage of methane and hydrogen. *Colloids Surf A Physicochem Eng Asp* 357(1–3):74–83
56. Goler S, Coletti C, Tozzini V, Piazza V, Mashoff T, Beltram F, Pellegrini V, Heun S (2013) Influence of graphene curvature on hydrogen adsorption: toward hydrogen storage devices. *J Phys Chem C* 117(22):11506–11513
57. Murata K, Kaneko K, Kanoh H, Kasuya D, Takahashi K, Kokai F, Yudasaka M, Iijima S (2002) Adsorption mechanism of supercritical hydrogen in internal and interstitial nanospaces of single-wall carbon nanohorn assembly. *J Phys Chem B* 106(43):11132–11138
58. Ye Y, Ahn CC, Witham C, Fultz B, Liu J, Rinzler AG, Colbert D, Smith KA, Smalley RE (1999) Hydrogen adsorption and cohesive energy of single-walled carbon nanotubes. *Appl Phys Lett* 74(16):2307–2309
59. Yang FH, Lachawiec AJ, Yang RT (2006) Adsorption of spillover hydrogen atoms on Single-Wall carbon nanotubes. *Phys Chem B* 110(12):6236–6244
60. Ansón A, Jagiello J, Parra JB, Sanjuán ML, Benito AM, Maser WK, Martínez MT (2004) Porosity, surface area, surface energy, and hydrogen adsorption in nanostructured carbons. *J Phys Chem B* 108(40):15820–15826
61. Wang Q, Johnson JK (1999) Optimization of carbon nanotube arrays for hydrogen adsorption. *J Phys Chem B* 103(23):4809–4813
62. Wang Q, Johnson JK (1999b) Molecular simulation of hydrogen adsorption in single-walled carbon nanotubes and idealized carbon slit pores. *J Chem Phys* 110(1):577–586
63. Schimmel HG, Kearley GJ, Nijkamp MG, Visser CT, de Jong KP, Mulder FM (2003) Hydrogen adsorption in carbon nanostructures: comparison of nanotubes, fibers, and coals. *Chem Eur J* 9(19):4764–4770
64. Zhou L, Zhou Y, Sun Y (2004) A comparative study of hydrogen adsorption on superactivated carbon versus carbon nanotubes. *Int J Hydrog Energy* 29(5):475–479
65. Liu F, Zhang X, Cheng J, Tu J, Kong F, Huang W, Chen C (2003) Preparation of short carbon nanotubes by mechanical ball milling and their hydrogen adsorption behavior. *Carbon* 41(13):2527–2532
66. Darkrim Lamari F, Levesque D (2011) Hydrogen adsorption on functionalized graphene. *Carbon* 49(15):5196–5200
67. Firlej L, Roszak S, Kuchta B, Pfeifer P, Wexler C (2009) Enhanced hydrogen adsorption in boron substituted carbon nanospaces. *J Chem Phys* 131:164702
68. Roszak R, Firlej L, Roszak S, Pfeifer P, Kuchta B (2016) Hydrogen storage by adsorption in porous materials: is it possible? *Coll Surf A Physicochem Eng Asp* 496(10):69–76
69. Ariharan A, Viswanathan B, Nandhakumar V (2016) Hydrogen storage on boron substituted carbon materials. *Int J Hydrog Energy* 41(5):3527–3536
70. Kubas GJ, Ryan RR, Swanson BI, Vergamini PJ, Wasserman HJ (1984) Characterization of the first examples of isolable molecular hydrogen complexes,  $M(\text{CO})_3(\text{PR}_3)_2(\text{H}_2)$  ( $M = \text{molybdenum}$  or  $\text{tungsten}$ ;  $R = \text{cy}$  or  $\text{isopropyl}$ ). Evidence for a side-on bonded dihydrogen ligand. *J Am Chem Soc* 106(2):451–452
71. Giraudet S, Zhu Z (2011) Hydrogen adsorption in nitrogen enriched ordered mesoporous carbons doped with nickel nanoparticles. *Carbon* 49(2):398–405
72. Dillon AC, Jones KM, Bekkedahl TA, Kiang CH, Bethune DS, Heben MJ (1997) Storage of hydrogen in single-walled carbon nanotubes. *Nature* 386:377–379
73. Saha D, Deng S (2009) Hydrogen adsorption on ordered mesoporous carbons doped with Pd, Pt, Ni, and Ru. *Langmuir* 25(21):12550–12560

74. Nishihara H, Hou P-X, Li L-X, Ito M, Uchiyama M, Kaburagi T, Ikura A, Katamura J, Kawarada T, Mizuuchi K, Kyotani T (2009) High-pressure hydrogen storage in zeolite-templated carbon. *J Phys Chem C* 113(8):3189–3196
75. Contescu CI, Brown CM, Liu Y, Bhat VV, Gallego NC (2009) Detection of hydrogen spillover in palladium-modified activated carbon fibers during hydrogen adsorption. *J Phys Chem C* 113(14):5886–5890
76. Takagi H, Hatori H, Yamada Y, Matsuo S, Shiraishi M (2004) Hydrogen adsorption properties of activated carbons with modified surfaces. *J Alloys Compd* 385(1–2):257–263
77. Ahluwali RK, Peng JK (2009) Automotive hydrogen storage system using cryo-adsorption on activated carbon. *Int J Hydrog Energy* 34(13):5476–5487
78. Richard M-A, Cossemé D, Chandonia P-A, Chahine R, Mori D, Hirose K (2009) Preliminary evaluation of the performance of an adsorption-based hydrogen storage system. *AIChE J* 55(11):2985–2996
79. Kitagawa S, Kitaura R, Noro SI (2004) Functional Porous coordination polymers. *Angew Chem Int Ed* 43(18):2334–2375
80. Rowsell JLC, Yaghi OM (2004) Metal–organic frameworks: a new class of porous materials. *Micro Meso Mater* 73(1–2):3–14
81. Hoskins BF, Robson R (1989) Infinite polymeric frameworks consisting of three dimensionally linked rod-like segments. *J Am Chem Soc* 111(15):5962–5964
82. Phan A, Doonan CJ, Uribe-Romo FJ, Knobler CB, O’Keeffe M, Yaghi OM (2010) Synthesis, structure, and carbon dioxide capture properties of zeolitic imidazolate frameworks. *Acc Chem Res* 43(1):58–67
83. Ding S-Y, Wang W (2013) Covalent organic frameworks (COFs): from design to applications. *Chem Soc Rev* 42(2):548–568
84. Jiang J-X, Cooper AI (2010) Functional metal-organic frameworks: gas storage, separation and catalysis (M. Schröder Ed.). *Topics in Current Chemistry*, vol. 293, pp 1–33
85. Eddaoudi M, Kim J, Rosi N, Vodak D, Wachter J, O’Keeffe M, Yaghi OM (2002) Systematic design of pore size and functionality in isoreticular MOFs and their application in methane storage. *Science* 295(5554):469–472
86. Férey G (2008) Hybrid porous solids: past, present, future. *Chem Soc Rev* 37(1):191–214
87. Yaghi OM, O’Keeffe M, Ockwig NW, Chae HK, Eddaoudi M, Kim J (2003) Reticular synthesis and the design of new materials. *Nature* 423(6941):705–714
88. Yaghi OM, Li H (1995) Hydrothermal synthesis of a metal-organic framework containing large rectangular channels. *J Am Chem Soc* 117(41):10401–10402
89. Férey G (2001) Microporous solids: from organically templated inorganic skeletons to hybrid frameworks ... *Ecumenism in Chemistry*. *Chem Mater* 13(10):3084–3098
90. Kondo M, Yoshitomi T, Seki K, Matsuzaka H, Kitagawa S (1997) Three-dimensional framework with channeling cavities for small molecules:  $\{[M_2(4, 4'-bpy)_3(NO_3)_4] \cdot xH_2O\}_n$  (M = Co, Ni, Zn). *Angew Chem Int Ed* 36:1725–1727
91. Li J-R, Kuppler RJ, Zhou H-C (2009) Selective gas adsorption and separation in metal–organic frameworks. *Chem Soc Rev* 38(5):1477–1504
92. Murray LJ, Dinca M, Long JR (2009) Hydrogen storage in metal–organic frameworks. *Chem Soc Rev* 38(5):1294–1314
93. Rosi NL, Eckert J, Eddaoudi M, Vodak DT, Kim J, O’Keeffe M, Yaghi OM (2003) Hydrogen storage in microporous metal-organic frameworks. *Science* 300(5622):1127–1129
94. Han SS, Mendoza-Cortés JL, Goddard WA III (2009) Recent advances on simulation and theory of hydrogen storage in metal–organic frameworks and covalent organic frameworks. *Chem Soc Rev* 38(5):1460–1476
95. Kaye SS, Dailly A, Yaghi OM, Long JR (2007) Impact of preparation and handling on the hydrogen storage properties of  $Zn_4O(1,4\text{-benzenedicarboxylate})_3$  (MOF-5). *J Am Chem Soc* 129(46):14176–14177
96. Robson H, Lillerud KP (eds) (2001) *Verified syntheses of Zeolitic materials*. Elsevier, Amsterdam

97. Low JJ, Benin AI, Jakubczak P, Abrahamian JF, Faheem SA, Willis RR (2009) Virtual high throughput screening confirmed experimentally: porous coordination polymer hydration. *J Am Chem Soc* 131(43):15834–15842
98. Álvarez JR, Sánchez-González E, Pérez E, Schneider-Revueltas E, Martínez A, Tejada-Cruz A, Islas-Jácome A, González-Zamora E, Ibarra IA (2017) Structure stability of HKUST-1 towards water and ethanol and their effect on its CO<sub>2</sub> capture properties. *Dalton Trans* 46(28):9192–9200
99. Férey G, Mellot-Draznieks C, Serre C, Millange F, Dutour J, Surblé S, Margiolaki I (2005) A chromium terephthalate-based solid with unusually large pore volumes and surface area. *Science* 309(5743):2040–2042
100. Cavka JH, Jakobsen S, Olsbye U, Guillou N, Lamberti C, Bordiga S, Lillerud KP (2008) A new zirconium inorganic building brick forming metal organic frameworks with exceptional stability. *J Am Chem Soc* 130(42):13850–13851
101. Farha OK, Eryazici I, Jeong NC, Hauser BG, Wilmer CE, Sarjeant AA, Snurr RQ, Nguyen ST, Yazaydin AO, Hupp JT (2012) Metal–organic framework materials with ultrahigh surface areas: is the sky the limit? *J Am Chem Soc* 134(36):15016–15021
102. Panella B, Hirscher M, Pütter H, Müller U (2006) Hydrogen adsorption in metal–organic frameworks: Cu-MOFs and Zn-MOFs compared. *Adv Funct Mater* 16(4):520–524
103. Frost H, Düren T, Snurr RQ (2006) Effects of surface area, free volume, and heat of adsorption on hydrogen uptake in metal–organic frameworks. *J Phys Chem B* 110(19):9565–9570
104. Rowsell JLC, Eckert J, Yaghi OM (2005) Characterization of H<sub>2</sub> binding sites in prototypical metal–organic frameworks by inelastic neutron scattering. *J Am Chem Soc* 127(42):14904–14910
105. Yildirim T, Hartman MR (2005) Direct observation of hydrogen adsorption sites and Nanocage formation in metal-organic frameworks. *Phys Rev Lett* 95(21):215504
106. Yan Y, Lin X, Yang S, Blake AJ, Dailly A, Champness NR, Hubberstey P, Schröder M (2009) Exceptionally high H<sub>2</sub> storage by a metal–organic polyhedral framework. *Chem Commun* 9:1025–1027
107. Lin X, Telepeni I, Blake AJ, Dailly A, Brown CM, Simmons JM, Zoppi M, Walker GS, Thomas KM, Mays TJ, Hubberstey P, Champness NR, Schröder M (2009) High capacity hydrogen adsorption in Cu(II) Tetracarboxylate framework materials: the role of pore size, ligand functionalization, and exposed metal sites. *J Am Chem Soc* 131(6):2159–2171
108. Wong-Foy AG, Matzger AJ, Yaghi OM (2006) Exceptional H<sub>2</sub> saturation uptake in microporous metal–organic frameworks. *J Am Chem Soc* 128(11):3494–3495
109. Ahmed A, Liu YY, Purewal J, Tran LD, Wong-Foy AG, Veenstra M, Matzger AJ, Siegel DJ (2017) Balancing gravimetric and volumetric hydrogen density in MOFs. *Energy Environ Sci* 10(11):2459–2471
110. Chung YG, Camp J, Haranczyk M, Sikora BJ, Bury W, Krungleviciute V, Yildirim T, Farha OK, Sholl DS, Snurr RQ (2014) Computation-ready, experimental metal–organic frameworks: a tool to enable high-throughput screening of Nanoporous crystals. *Chem Mater* 26(21):6185–6192
111. Gómez-Gualdrón DA, Colón YJ, Zhang X, Wang TC, Chen Y-S, Hupp JT, Yildirim T, Farha OK, Zhang J, Snurr RQ (2016) Evaluating topologically diverse metal–organic frameworks for cryo-adsorbed hydrogen storage. *Energy Environ Sci* 9(10):3279–3289
112. Sillar K, Hofmann A, Sauer J (2009) Ab initio study of hydrogen adsorption in MOF-5. *J Am Chem Soc* 131(11):4143–4150
113. Bordiga S, Vitillo JG, Ricchiardi G, Regli L, Cocina D, Zecchina A, Arstad B, Bjrgen M, Hafizovic J, Lillerud KP (2005) Interaction of hydrogen with MOF-5. *J Phys Chem B* 109(39):18237–18242
114. Kubota Y, Takata M, Matsuda R, Kitaura R, Kitagawa S, Kato K, Sakata M, Kobayashi MC (2005) Direct observation of hydrogen molecules adsorbed onto a microporous coordination polymer. *Angew Chem Int Ed* 44(6):920–923
115. Chavan S, Vitillo JG, Gianolio D, Zavorotynska O, Civalleri B, Jakobsen S, Nilsen MH, Valenzano L, Lamberti C, Lillerud KP, Bordiga S (2012) H<sub>2</sub> storage in isostructural UiO-67 and UiO-66 MOFs. *Phys Chem Chem Phys* 14(5):1614–1626

116. Chun H, Dytbsev DN, Kim H, Kim K (2005) Synthesis, X-ray crystal structures, and gas sorption properties of Pillared Square grid nets based on paddle-wheel motifs: implications for hydrogen storage in porous materials. *Chem Eur J* 11(12):3521–3529
117. Dinca M, Long JR (2005) Strong H<sub>2</sub> binding and selective gas adsorption within the microporous coordination solid Mg<sub>3</sub>(O<sub>2</sub>C-C<sub>10</sub>H<sub>6</sub>-CO<sub>2</sub>)<sub>3</sub>. *J Am Chem Soc* 127(26):9376–9377
118. Han SS, Deng W-Q, Goddard WA III (2007) Improved designs of metal-organic frameworks for hydrogen storage. *Angew Chem Int Ed* 46(33):6289–6292
119. Dinca M, Long JR (2008) Hydrogen storage in microporous metal-organic frameworks with exposed metal sites. *Angew Chem Int Ed* 47(36):6766–6779
120. Getman RB, Bae Y-S, Wilmer CE, Snurr RQ (2012) Review and analysis of molecular simulations of methane, hydrogen, and acetylene storage in metal-organic frameworks. *Chem Rev* 112(2):703–723
121. Dinca M, Dailly A, Liu Y, Brown CM, Neumann DA, Long JR (2006) Hydrogen storage in a microporous metal-organic framework with exposed Mn<sub>2+</sub> coordination sites. *J Am Chem Soc* 128(51):16876–16883
122. Dinca M, Long JR (2007) High-enthalpy hydrogen adsorption in cation-exchanged variants of the microporous metal-organic framework Mn<sub>3</sub>[(Mn<sub>4</sub>Cl)<sub>3</sub>(BTT)<sub>8</sub>(CH<sub>3</sub>OH)<sub>10</sub>]<sub>2</sub>. *J Am Chem Soc* 129(36):11172–11176
123. Latroche M, Surlé S, Serre C, Mellot-Draznieks C, Llewellyn PL, Lee J-H, Chang J-S, Jung SH, Férey G (2006) Hydrogen storage in the giant-pore metal-organic frameworks MIL-100 and MIL-101. *Angew Chem Int Ed* 45(48):8227–8231
124. Dytbsev D, Serre C, Schmitz B, Panella B, Hirscher M, Latroche M, Llewellyn PL, Cordier S, Molard Y, Haouas M, Taulelle F, Férey G (2010) Influence of [Mo<sub>6</sub>Br<sub>8</sub>F<sub>6</sub>]<sup>2-</sup> cluster unit inclusion within the mesoporous solid MIL-101 on hydrogen storage performance. *Langmuir* 26(13):11283–11290
125. Prestipino C, Regli L, Vitillo JG, Bonino F, Damin A, Lamberti C, Zecchina A, Solari PL, Kongshaug KO, Bordiga S (2006) Local structure of framework Cu(II) in HKUST-1 Metallorganic framework: spectroscopic characterization upon activation and interaction with adsorbates. *Chem Mater* 18(5):1337–1346
126. Bordiga S, Regli L, Bonino F, Groppo E, Lamberti C, Xiao B, Wheatley PS, Morris RE, Zecchina A (2007) Adsorption properties of HKUST-1 toward hydrogen and other small molecules monitored by IR. *Phys Chem Chem Phys* 9(21):2676–2685
127. Yang QY, Zhong CL (2006) Understanding hydrogen adsorption in metal-organic frameworks with open metal sites: a computational study. *J Phys Chem B* 110(2):655–658
128. Dietzel PD, Morita Y, Blom R, Fjellvåg H (2005) An in situ high-temperature single-crystal investigation of a dehydrated metal-organic framework compound and field-induced magnetization of one-dimensional metal-oxygen chains. *Angew Chem Int Ed* 44(39):6354–6358
129. Dietzel PDC, Panella B, Hirscher M, Blom R, Fjellvåg H (2006) Hydrogen adsorption in a nickel based coordination polymer with open metal sites in the cylindrical cavities of the desolvated framework. *Chem Commun* 9:959–961
130. Rosi NL, Kim J, Eddaoudi M, Chen B, O’Keeffe M, Yaghi OM (2005) Rod packings and metal-organic frameworks constructed from rod-shaped secondary building units. *J Am Chem Soc* 127(5):1504–1518
131. Zhou W, Wu H, Yildirim T (2008) Enhanced H<sub>2</sub> adsorption in isostructural metal-organic frameworks with open metal sites: strong dependence of the binding strength on metal ions. *J Am Chem Soc* 130(46):15268–15269
132. Dietzel PDC, Georgiev PA, Eckert J, Blom R, Strässle T, Unruh T (2010) Interaction of hydrogen with accessible metal sites in the metal-organic frameworks M<sub>2</sub>(dhtp) (CPO-27-M; M = Ni, Co, Mg). *Chem Commun* 46(27):4962–4964
133. Vitillo JG, Regli L, Chavan S, Ricchiardi G, Spoto G, Dietzel PDC, Bordiga S, Zecchina A (2008) Role of exposed metal sites in hydrogen storage in MOFs. *J Am Chem Soc* 130(26):8386–8396

134. Liu Y, Kabbour H, Brown CM, Neumann DA, Ahn CC (2008) Increasing the density of adsorbed hydrogen with Coordinatively unsaturated metal centers in metal–organic frameworks. *Langmuir* 24(9):4772–4777
135. Meilikhov M, Yussenko K, Esken D, Turner S, Van Tendeloo G, Fischer RA (2010) Metals@MOFs – loading MOFs with metal nanoparticles for hybrid functions. *Eur J Inorg Chem* 24:3701–3714
136. Li Y, Yang RT (2006) Significantly enhanced hydrogen storage in metal–organic frameworks via spillover. *J Am Chem Soc* 128(3):726–727
137. Li Y, Yang RT (2008) Hydrogen storage in metal-organic and covalent-organic frameworks by spillover. *AICHE J* 54(1):269–279
138. Wang L, Yang RT (2008) New sorbents for hydrogen storage by hydrogen spillover – a review. *Energy Environ Sci* 1(2):268–279
139. Liu Y-Y, Zeng J-L, Zhang J, Xu F, Sun L-X (2007) Improved hydrogen storage in the modified metal-organic frameworks by hydrogen spillover effect. *Int J Hydrog Energy* 32(16):4005–4010
140. Proch S, Herrmannsdörfer J, Kempe R, Kern C, Jess A, Seyfarth L, Senker J (2008) Pt@MOF-177: synthesis, room-temperature hydrogen storage and oxidation catalysis. *Chem Eur J* 14(27):8204–8212
141. Zlotea C, Campesi R, Cuevas F, Leroy E, Dibandjo P, Volkringer C, Loiseau T, Férey G, Latroche M (2010) Pd nanoparticles embedded into a metal-organic framework: synthesis, structural characteristics, and hydrogen sorption properties. *J Am Chem Soc* 132(9):2991–2997
142. Blomqvist A, Moysés Araújo C, Srepusharawoot P, Ahuja R (2007) Li-decorated metal–organic framework 5: a route to achieving a suitable hydrogen storage medium. *PNAS* 104(51):20173–20176
143. Li A, Lu R-F, Wang Y, Wang X, Han K-L, Deng W-Q (2010) Lithium-doped conjugated microporous polymers for reversible hydrogen storage. *Angew Chem Int Ed* 49(19):3330–3333
144. Yang S, Lin X, Blake AJ, Thomas KM, Hubberstey P, Champness NR, Schröder M (2008) Enhancement of H<sub>2</sub> adsorption in Li<sup>+</sup>-exchanged co-ordination framework materials. *Chem Commun* 46:6108–6110
145. Rowsell JLC, Yaghi OM (2005) Strategies for hydrogen storage in metal–organic frameworks. *Angew Chem Int Ed Engl* 44(30):4670–4679
146. Ma S, Sun D, Ambrogio M, Fillinger JA, Parkin S, Zhou H-C (2007) Framework-catenation isomerism in metal–organic frameworks and its impact on hydrogen uptake. *J Am Chem Soc* 129(27):1858–1859
147. Zhao X, Xiao B, Fletcher AJ, Thomas KM, Bradshaw D, Rosseinsky MJ (2004) Hysteretic adsorption and desorption of hydrogen by nanoporous metal-organic frameworks. *Science* 306(5698):1012–1015
148. Zhao D, Yuan D, Zhou H-C (2008) The current status of hydrogen storage in metalorganic frameworks. *Energy Environ Sci* 1(2):222–235
149. Frost H, Snurr RQ (2007) Design requirements for metal-organic frameworks as hydrogen storage materials. *J Phys Chem C* 111(50):18794–18803
150. Thomas KM (2009) Adsorption and desorption of hydrogen on metal–organic framework materials for storage applications: comparison with other nanoporous materials. *Dalton Trans* 9:1487–1505
151. Ben T, Pei C, Zhang D, Xu J, Deng F, Jing X, Qiu S (2011) Gas storage in porous aromatic frameworks (PAFs). *Energy Environ Sci* 4(10):3991

# Chapter 11

## CO<sub>2</sub> Storage on Nanoporous Carbons



Marta Sevilla, Guillermo A. Ferrero, and Antonio B. Fuertes

### 11.1 Introduction

The control of anthropogenic CO<sub>2</sub> emissions is a matter of pressing importance in view of the significant role that this gas plays in global climate change. According to the 2016 report on “CO<sub>2</sub> emissions from fossil fuel combustion” by the International Energy Agency (IEA), in 2015 the average concentration of CO<sub>2</sub> (399 ppm) was about 40% higher than in the mid-1800s, and an average growth of 2 ppm/year has been recorded over the last 10 years [1]. Alarmingly, in April 2017, a new CO<sub>2</sub> level milestone was reached, i.e., 410 ppm, with a corresponding increase in global surface temperature of about 1 °C [2]. Of the many human activities that produce greenhouse gases, the use of energy represents by far the largest source of emissions. Despite the growth of non-fossil energy (such as nuclear, hydropower, and other renewable resources), considered as non-emitting, the share of fossil fuels within the world energy supply has remained relatively unchanged over the past four decades (>80% of the global total primary energy supply). Moreover, the IEA forecasts that the world’s energy consumption will increase by 48% between 2012 and 2040, with fossil fuels accounting for more than 75% of world energy use in 2040. Thereby, energy-related CO<sub>2</sub> emissions are predicted to increase 34% during this time span, with annual emissions rising from 32 billion metric tons in 2012 to 43 billion metric tons in 2040 [3]. There is therefore an urgent need for the development and deployment of efficient CO<sub>2</sub> capture and storage (CCS) technologies.

The most widely adopted approach for CO<sub>2</sub> capture is absorption using aqueous amine solutions. However, this technology suffers from several drawbacks (e.g., a high level of energy and solvent consumption, severe corrosion of the equipment,

---

M. Sevilla (✉) · G. A. Ferrero · A. B. Fuertes  
Instituto Nacional del Carbón (CSIC), Oviedo, Spain  
e-mail: [martasev@incar.csic.es](mailto:martasev@incar.csic.es)

toxicity, etc.) [4, 5], and, in consequence, there is great interest in developing other capture methods. Of the different alternatives, the use of porous materials to adsorb CO<sub>2</sub> by means of pressure (PSA), temperature (TSA), or vacuum swing adsorption (VSA) systems and their combinations is a promising alternative owing to its lower regeneration costs and energy consumption, long-term stability, non-corrosiveness, and non-toxicity. In relation with this alternative, a variety of porous materials have been investigated, including porous carbons, zeolites, metal-organic frameworks (MOFs), microporous polymers, and organic-inorganic hybrid sorbents [6–10]. Of these, porous carbons are the most advantageous in terms of cost, ready availability, large surface area, easy-to-design pore structure, hydrophobicity, and low energy requirements for regeneration. Consequently, intensive research efforts are being directed toward the development of high-performance adsorbents based on carbon materials.

There are two carbon capture technologies associated with different combustion processes for energy generation: (1) post-combustion, where CO<sub>2</sub> is removed from the flue gas after the combustion process, and (2) pre-combustion, where CO<sub>2</sub> is removed from the shifted-syngas after fuel gasification. A third possibility, known as oxy-fuel combustion, produces a stream almost entirely composed of CO<sub>2</sub>, so that no separation of CO<sub>2</sub> from a mixture is required. Post-combustion flue gas (1 bar, 30–80 °C) is typically composed of 12–15% CO<sub>2</sub>, 70–75% N<sub>2</sub>, 4–6% H<sub>2</sub>O, and 4% O<sub>2</sub> [10, 11]. On the other hand, shifted-syngas (~40 bar, <65 °C) is composed of >20% CO<sub>2</sub> and >50% H<sub>2</sub> [12, 13]. Therefore, post-combustion capture involves low pressures of CO<sub>2</sub>, whereas pre-combustion capture involves high CO<sub>2</sub> pressures, which demands, as will be explained in Section 11.2, a different tuning of the adsorbent's pore size distribution (PSD). Another difference worth noting is that a post-combustion adsorbent must show a high CO<sub>2</sub>/N<sub>2</sub> selectivity and a low water vapor adsorption, whereas a pre-combustion adsorbent must exhibit a high CO<sub>2</sub>/H<sub>2</sub> selectivity. Further requirements for a good CO<sub>2</sub> adsorbent are rapid adsorption-desorption kinetics (>1 mmol g<sup>-1</sup> min<sup>-1</sup>), stability against water vapor and acidic gases, stable adsorption over repeated cycles (>1000), and sufficient particle mechanical strength [10].

Given that natural gas consumption is rising as it is considered the cleanest of all the fossil fuels [3], another relevant carbon capture application which is attracting increasing attention is the process of natural gas purification. Natural gas wells typically contain considerable amounts of CO<sub>2</sub> (up to 50% depending on the origin) besides CH<sub>4</sub>, the removal of which is essential to prevent the corrosion of pipelines. As in the case of pre-combustion capture, natural gas upgrading takes place at high pressures, and so the adsorbent requirements are similar to those of pre-combustion carbon capture, except for the fact that in this case it is the selectivity of the adsorbent toward CO<sub>2</sub> vs. CH<sub>4</sub> that is important.

This chapter will cover the fundamentals of CO<sub>2</sub> adsorption by porous carbons and show the potential of these materials for carbon capture in different scenarios. The methodologies developed so far for the synthesis and control of the textural and chemical characteristics of porous carbons from a variety of precursors will be reviewed. Traditional activation approaches will be discussed, with reference to

recent advances (e.g., compactivation or melamine-mediated chemical activation) that have allowed a wider control over the textural properties of the materials produced, enabling them to be more easily adapted to the requirements of the targeted CO<sub>2</sub> application. More recent developments in carbon synthesis will also be discussed, such as nanocasting approaches, carbide-derived carbons, MOF-/COF-derived carbons, and novel polymerization approaches such as the use of deep eutectic solvents (DES). Finally, a comprehensive analysis of the performance of the materials produced in CO<sub>2</sub> capture will be presented.

## 11.2 Role of the Pore Structure of the Adsorbent on CO<sub>2</sub> Adsorption

The capture of CO<sub>2</sub> by porous carbons depends on two main factors: (a) the pore structure and (b) the surface chemical properties. The first factor determines the space available for accommodating the adsorbed gas, whereas the second influences the interaction forces between the CO<sub>2</sub> molecules and the carbon surface. The second factor will be analyzed in the next section. This section will provide a basis for understanding the relationship between the pore structure of the carbon and the amount of CO<sub>2</sub> it can adsorb. In this way, we expect to offer a useful guide for designing the porous structure of carbons intended for CO<sub>2</sub> adsorption.

In order to understand the adsorption of CO<sub>2</sub> on carbons, it is necessary to take into account the surface forces that determine the adsorptive properties. The extent of these forces depends greatly on the pore characteristics (i.e., their size and morphology), which determine the influence that the pore structure has on the adsorptive properties of porous carbons. These carbons are synthesized from non-graphitizable materials (i.e., biomass, polymers, saccharides, etc.), and, in consequence, they exhibit a disordered structure (turbostratic), which consists of carbon atoms arranged in a planar hexagonal network (graphene-like layers) lacking order in the third direction. However, these graphene-like layers still exhibit a more or less parallel stacking structure, as evidenced by the X-ray diffraction patterns, which show broad bands in the (002) and (100)/(101) regions (Fig. 11.1a). Inside this disordered structure, there are numerous interconnected nanovoids (pore network) that constitute the porosity of the carbon material (Fig. 11.1b) [14]. A reliable picture of the microstructure of porous carbons can be obtained from high-resolution transmission electron microscopy (HRTEM) micrographs, such as those displayed in Fig. 11.2 for a microporous carbon. These images show a highly disordered microstructure formed by graphene-like layers and numerous interlayer nanovoids that correspond to the micropores. These micropores are interconnected by narrow channels (constrictions) that control access to the microporous network. The constrictions are of great importance as they cause diffusional resistances during the adsorption process. For example, kinetic restrictions are evidenced when adsorption takes place at very low temperatures, as occurs when nitrogen is absorbed

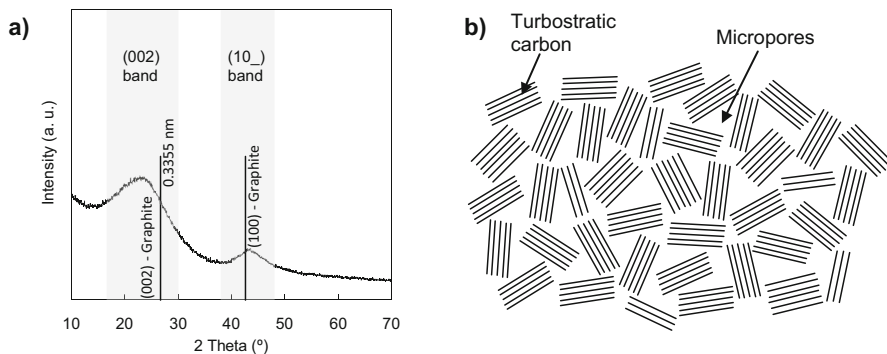


**Fig. 11.1** (a) XRD pattern and (b) model for a porous carbon

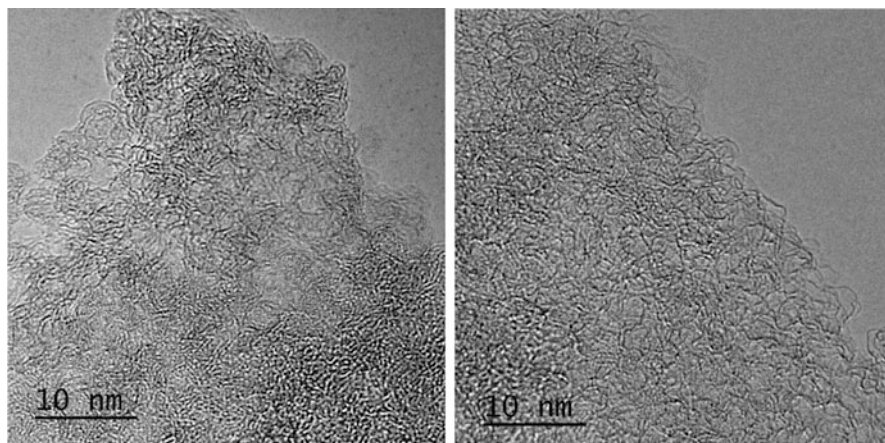


**Fig. 11.2** High-resolution transmission electron microscopy images obtained from a microporous carbon

in microporous carbon at  $-196\text{ }^{\circ}\text{C}$ . Another important structural feature is related to the morphology of the micropores. Micropores can be envisaged as nanospaces between quasi-planar graphene-like layers and so it is reasonable to assume that the shape of micropores is closer to a slit than a cylinder.

In general, the adsorptive capacity of porous carbons at low relative pressures mainly depends on the population of narrow micropores, whereas at high relative pressures, both micropores and mesopores determine the adsorption uptake. This assertion is key to understanding how  $\text{CO}_2$  is absorbed onto porous carbons. The process can be explained basically as follows. It is well-established that in the case of nonpolar adsorbate molecules and non-functionalized adsorbent surfaces, the adsorbate–adsorbent interaction energy is derived from short-range attractive and repulsive forces (non-specific interactions) [15]. The interaction energy is substantially enhanced when the adsorption takes place in very narrow pores

because of the overlapping of the potential fields from neighboring walls [16, 17]. Numerous simulation studies have been carried out to evaluate the relationship between the adsorption potential and the size of micropores [17–21]. An example is given in Fig. 11.3, which shows the modification of the CO<sub>2</sub> adsorption potential ( $\Phi/\Phi_0$ ) with the dimensionless distance from the pore center ( $z/\sigma$ ) ( $\sigma$  is the kinetic diameter of CO<sub>2</sub>  $\sim 0.33$  nm) for a graphite slit pore [22]. It can be seen that for  $w/\sigma \sim 3$  ( $w = L/2$ , where  $L$  is the pore width), the adsorption potential in the center of the pore starts to be negative due to the overlapping of the potential fields. As the pore width decreases, the potential minimum is greatly enhanced, and, for values  $w/\sigma < 1.2$  ( $L < 0.8$  nm), the double minimum is replaced by a single minimum. Finally, the adsorption potential attains the negative minimum for  $w/\sigma \sim 1$  ( $L \sim 0.66$  nm). This shows that, in the case of CO<sub>2</sub> molecules, the adsorption potential is greatly enhanced for micropores smaller than 0.8 nm. On the other hand, this enhancement in the adsorption potential is negligible for micropores  $> \sim 1$  nm. This enhanced adsorption potential can lead to the complete filling of the narrow micropores ( $< 0.8$  nm) at very low relative pressures ( $p/p_0 < \sim 0.01$ ). Under these circumstances, the adsorption mechanism consists of volume-filling rather than the surface coverage typical of meso-macroporous materials, and the adsorbate molecules occupying these narrow micropores are in a liquid-like state [23]. Clearly, this line of reasoning only holds true when the adsorption takes place at temperatures below the critical temperature of the adsorbate, which is 31 °C in

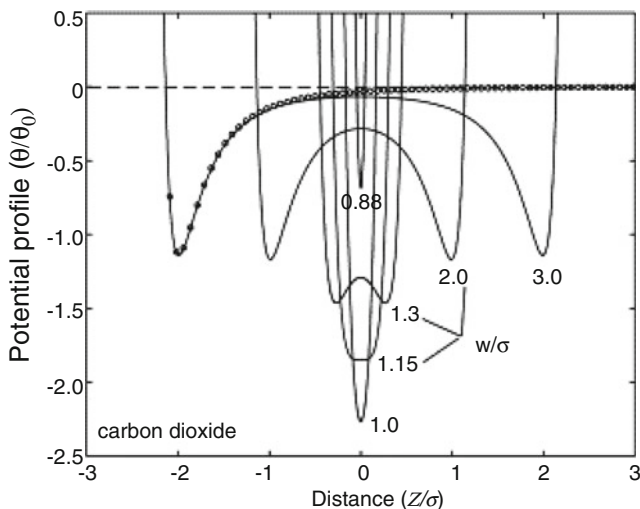


**Fig. 11.3** Adsorption energy in slit-shaped micropores. Normalized potential profile ( $\Phi/\Phi_0$ ) of CO<sub>2</sub> in a graphite slit-shape pore as a function of the pore half width ( $w$ ). The solid curves are the adsorbate–pore interaction potentials. The numbers on curves are ratios of the pore half width ( $w = L/2$ ) over the kinetic diameter ( $\sigma$ ) of CO<sub>2</sub>. The open circles are the interaction potential between a CO<sub>2</sub> molecule and a single pore wall or “free” surface. (Reproduced with permission from Ref. [22] © 2004, Elsevier)

the case of CO<sub>2</sub>. Given this situation, a description of the volume-filling mechanism has been provided by Dubinin, who deduced a relationship between the degree of micropore-filling and the partial pressure of the adsorbate (D–R equation) [24–28].

$$V = V_0 \exp \left[ -(A/\beta E_0)^2 \right] \quad (11.1)$$

where  $V$  is the volume filled at a temperature  $T$  and the relative pressure ( $p/p_0$ ),  $V_0$  is the micropore volume,  $A = RT \ln(p_0/p)$ , and  $E_0$  and  $\beta$  are the characteristic energy and the affinity coefficient ( $\beta = 0.35$  for CO<sub>2</sub>), respectively. The average width of the narrow micropores can be calculated by means of the empirical correlation proposed by Stoeckli et al. [29]:

$$L \text{ (nm)} = 10.8 / (E_0 - 11.4) \quad (11.2)$$

The above discussion constitutes a practical approach to understanding the role of the pore structure of carbons in relation to CO<sub>2</sub> capture under post-combustion conditions (i.e., temperatures in the 0–25 °C range and CO<sub>2</sub> pressures in the 0–1 bar range). Under these circumstances, the CO<sub>2</sub> relative pressure is very low (i.e., for a CO<sub>2</sub> partial pressure of 1 atm and an adsorption temperature of 25 °C ( $p_0 = 63.5$  atm),  $p/p_0 \sim 0.016$ ), and the adsorption of CO<sub>2</sub> will occur via a volume-filling mechanism. In consequence, at these low relative pressures, only those adsorbents with a large number of narrow micropores below  $\sim 0.8$  nm will be able to capture appreciable amounts of CO<sub>2</sub>. This suggests that the amount of CO<sub>2</sub> captured by non-functionalized porous carbons is mainly determined by the volume of micropores with a size below 0.8 nm. Conversely, other pores present in porous carbons, such as supermicropores (0.8–2 nm) or mesopores (>2 nm), are not relevant for CO<sub>2</sub> capture under post-combustion conditions (i.e.,  $T \sim 0$ –25 °C,  $p_{\text{CO}_2} \leq 1$  bar) because they are unable to adsorb significant amounts of CO<sub>2</sub> at the very low relative pressures that exist in such conditions. This is the reason for the lack of correlation between the CO<sub>2</sub> adsorption capacity of porous carbons at low pressure and their overall textural properties, such as total pore volume or BET surface area. Figure 11.4 presents a schematic illustration of the gas adsorption process in a porous carbon material with a pore network made up of ultramicropores (<0.7 nm), supermicropores (0.7 < pore width <2 nm), and mesopores (>2 nm).

The above conclusions deduced by applying the concepts provided by the adsorption theory have been fully confirmed by the experimental results obtained by different authors [30–34]. Thus, Wahby et al. synthesized a series of porous carbon molecular sieves both in the form of powders and monoliths, from petroleum pitch using KOH as the activating agent [35]. They observed it was the presence of narrow micropores and not the total available surface area that was the key factor defining the total adsorption capacity for CO<sub>2</sub>. Similarly, Martin et al. by analyzing the CO<sub>2</sub> adsorption on different polymeric porous carbons prepared by physical activation of a phenolic resin concluded that carbon dioxide capture under standard

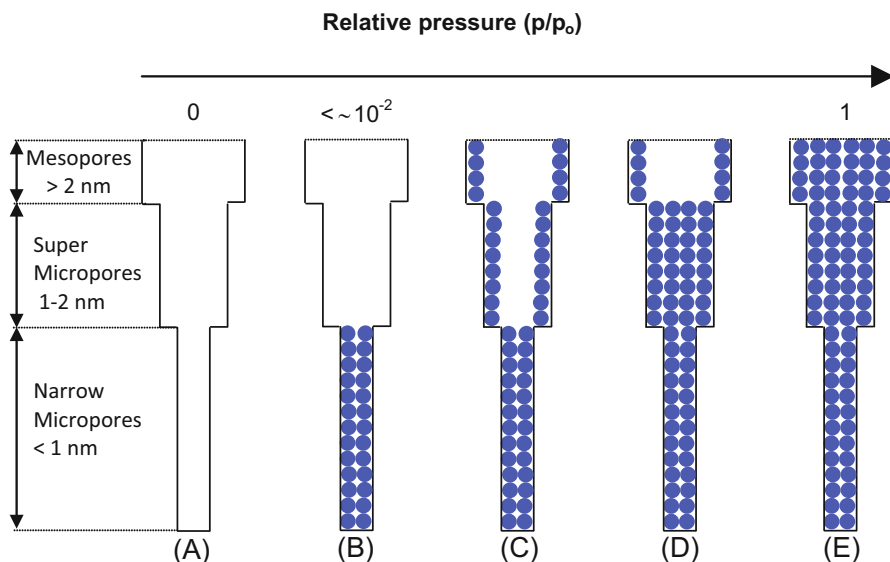


**Fig. 11.4** Schematic illustration of the gas adsorption process in a porous carbon material. In (a) the empty pore network, made up of narrow micropores, super-micropores, and mesopores, is represented. At very low relative pressures, only narrow micropores are filled according to the volume-filling mechanism, shown in (b). As the relative pressure rises, the surface of the supermicropores and mesopores is covered by adsorbed gas molecules (c). Finally, the pore volume is gradually filled (d) until it is completely full up at  $(p/p_0) = 1$ , as represented in (e). In the case of CO<sub>2</sub>, its adsorption at temperatures in the 0–25 °C range and at pressures of  $p_{\text{CO}_2} \leq 1$  atm is well-described by (b). As the CO<sub>2</sub> pressure increases, pores larger than 1 nm are gradually filled up until they are completely full up (maximum CO<sub>2</sub> uptake) at  $p/p_0 = 1$  [ $p_0$  (CO<sub>2</sub>)  $\sim$  34 atm at 0 °C and  $\sim$ 56 atm at 20 °C]

conditions (25 °C and 1 atm) involves exclusively the smaller micropores (<1 nm) [36]. Presser et al. used carbide-derived carbons (CDCs) to analyze the influence of micropore size on CO<sub>2</sub> adsorption at atmospheric and subatmospheric pressures [37]. These materials are particularly suitable for this purpose given that they have a quasi-unimodal micropore size distribution with a mean micropore size that can be controlled with precision. The pore structures of these CDCs have been correlated with the CO<sub>2</sub> sorption properties and are shown in Fig. 11.5. It can be seen that the correlation between the CO<sub>2</sub> uptake and the pore volume of pores smaller than 1.5 nm yields a coefficient of determination ( $R^2$ ) of 0.9699 at 1 bar (Fig. 11.5a) and 0.4813 at 0.1 bar (Fig. 11.5b). As the pore size limit decreases, the coefficients of determination increase to a maximum of 0.9958 for a limit of 0.8 nm at 1 bar (Fig. 11.5c) and 0.9468 for 0.5 nm at 0.1 bar (Fig. 11.5h). These results reveal that, at a pressure of 1 bar, CO<sub>2</sub> uptake mainly depends on pores smaller than 0.8 nm, whereas at a low partial pressure of 0.1 bar, the pores with a size below 0.5 nm are the most important contributors to CO<sub>2</sub> adsorption. Similarly, Wei et al. analyzed the CO<sub>2</sub> adsorption on bamboo-based KOH ACs and deduced that narrow micropores of size

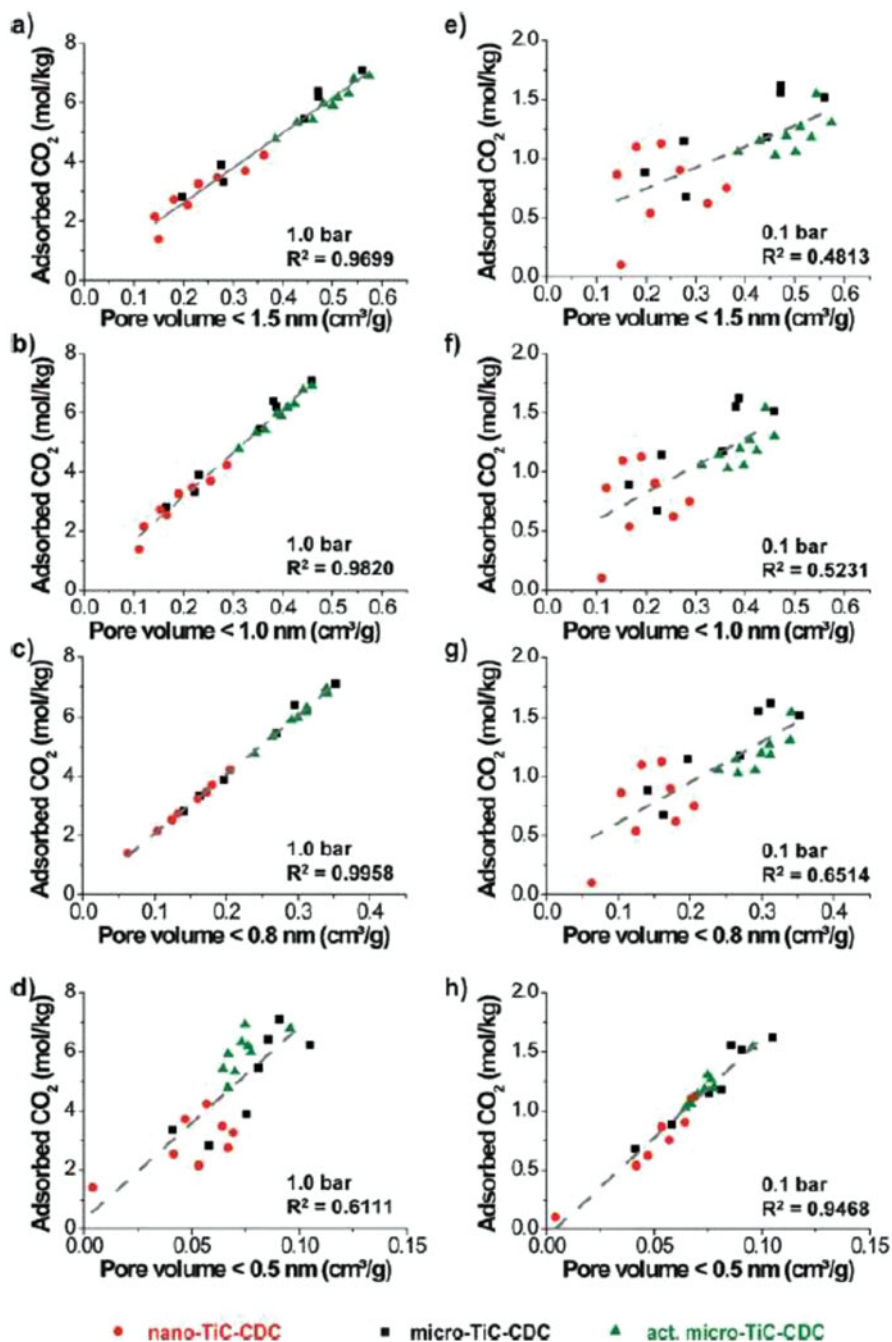


**Fig. 11.5** Correlation between the amount of CO<sub>2</sub> adsorbed at 1.0 bar (a–d) and 0.1 bar (e–h) for the volume of pores smaller 1.5 nm (a, e), 1.0 nm (b, f), 0.8 nm (c, g), and 0.5 nm (d, h). (Reproduced with permission from Ref. [37] © 2011, Royal Society of Chemistry)

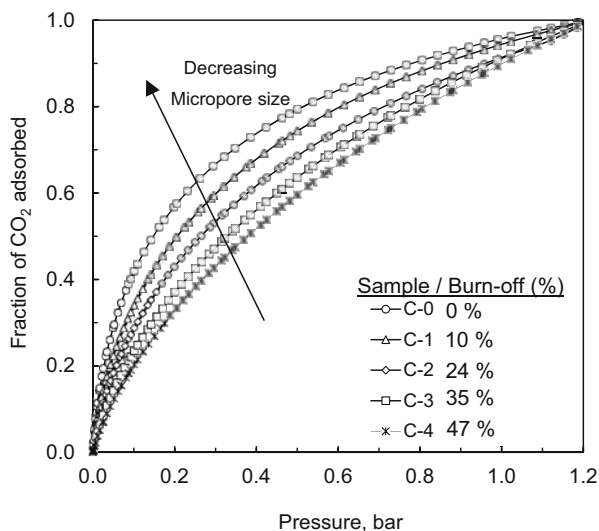


**Fig. 11.6** Comparison of the fraction of CO<sub>2</sub> adsorbed by porous carbons physically activated at different burn-offs. Adsorption temperature of 0 °C and  $p_{\text{CO}_2} = 1$  bar. (Reproduced with permission from Ref. [39] © 2013, American Chemical Society)

<0.82 nm are the main contributor at a pressure of 1 bar [38]. Sevilla et al. showed the importance of micropore size on CO<sub>2</sub> adsorption by comparing the shape of the CO<sub>2</sub> isotherms of non-activated materials and those of the corresponding activated carbons [39]. This is illustrated in Fig. 11.6, where the fraction of CO<sub>2</sub> adsorbed by porous carbons physically activated at different burn-offs is compared at an adsorption temperature of 0 °C. It can be seen that the fraction of CO<sub>2</sub> adsorbed at a given pressure decreases as the mean pore size increases with the degree of activation. This result clearly indicates that the adsorption potential is reduced with the enlargement of micropores as the activation progresses. Phenolic resin-based carbon microspheres activated with KOH were used by Wickramaratne and Jaroniec to evaluate the role of pore size on CO<sub>2</sub> adsorption [40]. They observed that these carbons exhibit a good CO<sub>2</sub> adsorption capacity which is attributed to the presence of small micropores (<0.8 nm).

When, however, the adsorption is performed at high pressures close to saturation (i.e., 34 or 64 bar at 0 or 25 °C, respectively), the adsorption of CO<sub>2</sub> occurs like that of N<sub>2</sub> (−196 °C) in comparable relative pressure ranges [41]. Under these circumstances, CO<sub>2</sub> uptake can be notably enhanced because both supermicropores and mesopores are now able to adsorb CO<sub>2</sub> via the coverage adsorption mechanism illustrated in Fig. 11.4. Because of this, the CO<sub>2</sub> uptake at high pressures shows a better correlation with the total pore volume or BET surface area, as reported by other authors [41–44]. Nevertheless, the best correlation achieved corresponds to the volume of pores of threshold pore size, like low pressure adsorption. This threshold pore size increases with the rise in pressure, since the adsorption potential within the

pores becomes large enough to favor capillary condensation [41, 45, 46]. It should be noted, however, that there is a certain discrepancy in the literature as to the value of the threshold pore size that determines the CO<sub>2</sub> adsorption capacity at a certain pressure depending on the kind of carbon material analyzed. For example, Casco et al. showed that for petroleum pitch-based KOH ACs, the CO<sub>2</sub> adsorption capacity at 45 bar/25 °C correlates well with the apparent surface area ( $R^2 = 0.9933$ ) and the volume of pores below 2 nm ( $R^2 = 0.9848$ ) and that the correlation worsens slightly for larger pores (<3.0 nm,  $R^2 = 0.9614$ ) [41]. On the other hand, Ashourirad et al. observed that both the surface excess and absolute CO<sub>2</sub> uptakes at 30 bar yield the best correlation with the volume of pores smaller than 2.2 nm ( $R^2 = 0.9968$  and 0.9949, respectively) in the case of benzimidazole-based KOH ACs [45]. He et al. studied polyaniline-based KOH-activated carbons and found a good correlation between the CO<sub>2</sub> adsorption capacity at 30 bar/25 °C and the cumulative pore volume of pores smaller than 3.95 nm ( $R^2 = 0.97$ ) [46]. In addition, these authors performed molecular simulations using grand canonical Monte Carlo (GCMC) and showed that, at pressures up to 50 bar, the difference in CO<sub>2</sub> density for small and large pores is not as significant as the difference at subatmospheric pressures, supporting the contribution of larger pores to the CO<sub>2</sub> adsorption capacity in high pressure applications. An intermediate situation between that of Ashourirad et al. and He et al. has been recently found by Sevilla et al. for glucose-based highly micro-mesoporous ACs prepared by means of melamine-mediated KOH chemical activation, where the CO<sub>2</sub> adsorption capacity at 30 bar/25 °C correlates well with the cumulative pore volume of pores smaller than 3 nm ( $R^2 = 0.99$ ) [47].

### 11.3 Chemical Doping and CO<sub>2</sub> Adsorption

As pointed out before, both the pore structure and the chemical characteristics are the main properties that determine the potential use of porous carbons. The usual way of modifying the chemical characteristics of carbon consists in incorporating into the graphene layer various types of foreign atoms (e.g., O, N, S, P, B, etc.) [48]. These heteroatoms have a different electronegativity to carbon atoms, causing a modification of the electron density map in the carbon framework. By means of DFT calculations, Zheng et al. analyzed the electronic densities of graphene layers doped with different heteroatoms [49]. The results, shown in Fig. 11.7, reveal that N and O heteroatoms are negatively charged and, in consequence, can act as electron donors (Lewis base). By contrast F, S, B, and P are positively charged and act as electron acceptors (Lewis acid). This alteration of the electronic density also affects the adjacent carbon atoms, thereby generating active sites that can act as catalytic centers. In this respect, numerous types of carbons doped with different heteroatoms have been successfully used as catalysts for a variety of reactions. In particular, carbons doped with nitrogen (an atom with a size similar to that of carbon) have been the most widely studied because they combine the abovementioned chemical properties with their easy incorporation into the carbon

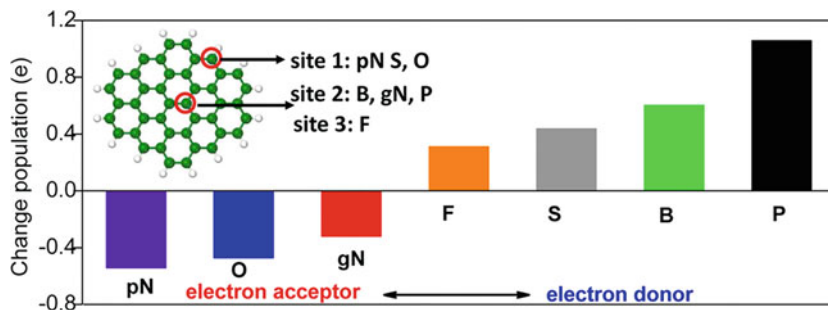


**Fig. 11.7** Electron population analysis of different heteroatoms in a graphene matrix. gN and pN represent the graphitic and pyridinic types of N. (Reproduced with permission from Ref. [49] © 2014, American Chemical Society)

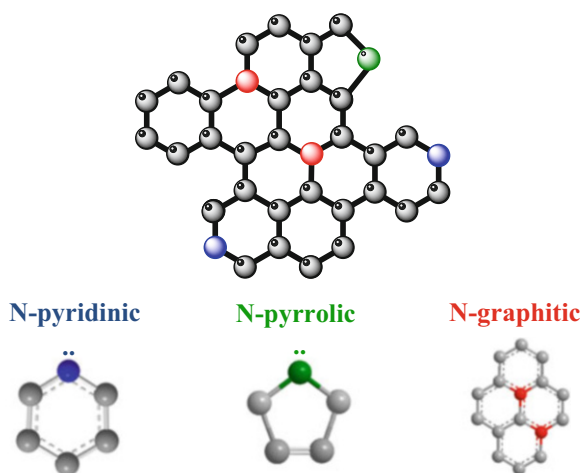


**Fig. 11.8** Schematic illustration of the main N-groups present in carbon

framework [50]. N-doped carbons have been extensively investigated as metal-free catalysts for water splitting [51, 52] and for the oxygen reduction reaction (ORR) [53, 54]. It has also been observed that the incorporation of nitrogen into porous carbons has a significant beneficial impact on their electrochemical properties. Consequently, N-doped porous carbons are used as electrodes in supercapacitors since they have a positive influence on electrochemical performance, including specific capacitance, rate capability, and cycle performance [55].

Carbon dioxide is a linear and nonpolar molecule with a slightly electropositive carbon atom and two slightly electronegative oxygen atoms. This configuration makes the carbon atom electron-deficient, and, in consequence, the CO<sub>2</sub> molecule can be considered as a weak Lewis acid. On the other hand, the N-groups present in N-doped carbons mainly appear in three different bonding configurations: (a) pyridinic-N, (b) pyrrolic-N, and (c) graphitic-N (Fig. 11.8). By means of DFT simu-

lations, it has been demonstrated that, independently of the type of N configuration, the nitrogen inserted into the graphene layers exhibits an electron donor behavior (Lewis base) [56]. In the case of pyridinic-N and pyrrolic-N, the enhanced basicity is associated with the lone pair of electrons, whereas for graphitic-N it is ascribed to delocalized  $\pi$ -orbitals. In view of this, the existence of specific interactions between the N atoms (Lewis base) present in a N-doped carbon and CO<sub>2</sub> molecules (Lewis acid) is a conceivable hypothesis. Thus, an enhancement of the CO<sub>2</sub> adsorption capacity of N-doped porous carbons can be expected unlike undoped materials. This hypothesis has generated an enormous number of works focused on the synthesis and characterization of N-doped porous carbons for CO<sub>2</sub> adsorption. Most of these studies simply assume that N-doping exerts a beneficial effect on CO<sub>2</sub> adsorption [57–77]. However, nowadays this assumption has not been fully demonstrated and it is still under discussion.

It has been established that N-doped porous carbons are very effective as electrocatalysts in a variety of reactions (i.e., ORR, HER, OER, etc.) and also as electrodes in supercapacitors. By contrast, in spite of the large number of works in this field, there is no conclusive evidence that proves unquestionably the beneficial effects of N-doping on CO<sub>2</sub> adsorption. This point has been critically analyzed by several authors, who have arrived at opposing conclusions. Thus, one group of authors believes that N-doped porous carbons exhibit higher CO<sub>2</sub> adsorption uptakes than undoped carbons. Among those who support this view are Hao et al. who compared the CO<sub>2</sub> adsorption capacity of a pristine N-doped porous carbon with the same sample treated with hydrochloric acid to neutralize the basic N-groups [70]. They claimed that, whereas the pore structure of the HCl-treated sample remained unchanged, the CO<sub>2</sub> uptake was 41% lower, which they ascribe to the deactivation of the N-groups. However, their measurements might have been affected by the presence of Cl<sup>-</sup> ions adsorbed on the carbon surface. Sanchez et al. analyzed the CO<sub>2</sub> adsorption of templated N-doped carbons and concluded that at 0 °C the CO<sub>2</sub> uptake mainly depends on the volume of narrow micropores and is unaffected by the presence of N-groups, whereas at higher temperatures (i.e., 20 °C or 50 °C), the N-groups exert a beneficial effect on CO<sub>2</sub> adsorption [78]. Babu et al. investigated the role of N-groups on CO<sub>2</sub> adsorption by using N-doped carbon nanotubes with a well-defined porosity containing only mesopores free of the interfering influence of micropores [79]. They concluded that N-groups have a beneficial effect on CO<sub>2</sub> adsorption at ambient conditions as well as at high pressures (~36 bar), as shown in Fig. 11.9. On the other hand, other authors consider that the N-groups present in porous carbons have only a marginal or no influence on CO<sub>2</sub> adsorption. Sevilla et al. investigated this matter by comparing the CO<sub>2</sub> performance of undoped and N-doped microporous carbon microspheres (~1  $\mu$ m) with similar textural properties (i.e., micropore size distribution, BET surface area, total pore volume, and micropore volume) [39]. It follows that, since undoped and N-doped samples only differ in their N content, a comparison of their CO<sub>2</sub> performances will provide information about the role that nitrogen functionalities in the porous carbons play in CO<sub>2</sub> adsorption. A comparison of the CO<sub>2</sub> uptakes measured at different temperatures in the -15 °C to +25 °C range ( $p_{\text{CO}_2} = 1$  bar) for undoped and N-doped carbons with analogous textural properties is provided

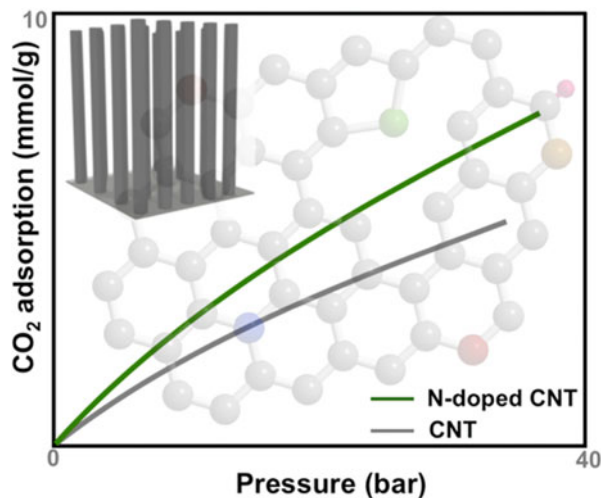


**Fig. 11.9** CO<sub>2</sub> adsorption isotherms up to 36 bar for pristine aligned carbon nanotubes (CNT) and N-doped CNT. (Reproduced with permission from Ref. [79] © 2017, American Chemical Society)

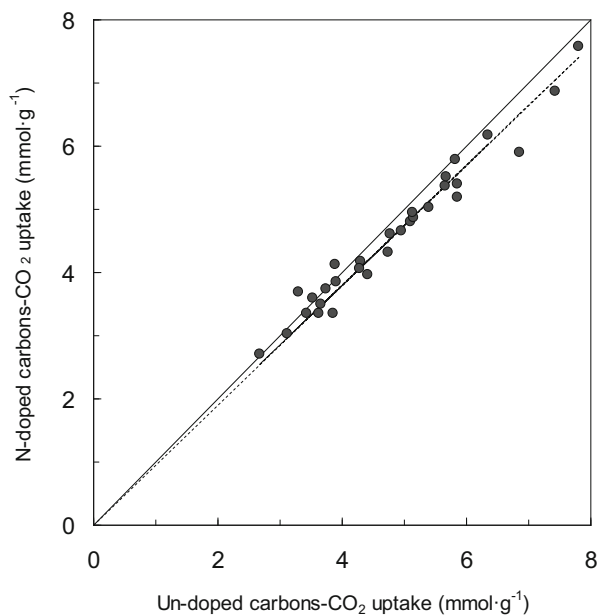


**Fig. 11.10** Comparison of the CO<sub>2</sub> uptake ( $p_{\text{CO}_2} = 1$  bar) of undoped (x-axis) and N-doped (y-axis) carbons. The dashed line shows the fitting of the experimental data ( $y = 0.95x$ ,  $R^2 = 0.9632$ ). (Reproduced with permission from Ref. [39] © 2013, American Chemical Society)

in Fig. 11.10. The graph shows that most of the represented points are near, or even below, the diagonal line, which suggests that the nitrogen moieties in the N-doped samples do not enhance CO<sub>2</sub> performance with respect to the undoped carbons. These results provide strong support for the view that the N heteroatoms present in the carbon framework of porous carbons do not significantly improve the uptake of CO<sub>2</sub>. This conclusion does not exclude certain marginal beneficial effects that might be expected from the weak acid/base Lewis interactions between the CO<sub>2</sub> molecules and the N-groups. Using a similar methodology, Adeniran and Mokaya compared a series of carbons with closely matched porosity, but differentiated by being either N-free or N-doped, and concluded that N-doping has no beneficial effect on CO<sub>2</sub> adsorption [34]. Similarly, Kumar et al., by means of a molecular simulation analysis, concluded that N-groups only marginally improve the adsorption of CO<sub>2</sub> [80].

A completely different scenario is offered by amine immobilization on porous carbons (often referred to as solid amine adsorbents). In this case, chemical adsorption is made possible by the amine groups grafted or loaded onto the porous carbon. Specifically, primary and secondary amines (and also sterically hindered amines) react directly with CO<sub>2</sub> and produce ammonium carbamate through the formation of zwitterions [81, 82]. The amine's lone electron pair first attacks the carbon atom in CO<sub>2</sub> (forming a zwitterion), then free base deprotonates the zwitterion to form the carbamate. Hence, the adsorption performance of carbons modified with primary or secondary amines depends on the amine's ability to split or bind to the proton [83]. Tertiary amines follow a different mechanism whereby CO<sub>2</sub> binds to the amine only in the presence of H<sub>2</sub>O. The mechanism involves the base-catalyzed hydration of CO<sub>2</sub> to form bicarbonate [82, 84]. Even though the selectivity of the porous carbon toward CO<sub>2</sub> is always improved by chemical adsorption, the degree of enhancement of the CO<sub>2</sub> uptake depends on the structure of the carbon support, the amount of loaded/grafted amine, and the type of amine. For example, pore blocking with the increase in the loading of amine may hinder the access of CO<sub>2</sub> to the active sites, thereby limiting the enhancement of CO<sub>2</sub> uptake [85]. In this regard, microporous adsorbents are more prone to pore blocking than mesoporous adsorbents [86]. On the other hand, the enhancement of CO<sub>2</sub> uptake usually occurs at temperatures higher than room temperature [85, 87, 88]. This is due to the fact that, at room temperature, the contribution of physisorption in amine-impregnated carbons is higher than chemisorption and physisorption is limited in the modified adsorbents due to micropore blocking by amines [87, 88]. For this reason, amine impregnation is not the best approach to increase the adsorption of CO<sub>2</sub> at room temperature. Other disadvantages of solid amine adsorbents are amine leaching/thermal instability, which reduces the cyclability of these materials compared to porous carbons [85, 89], and that regeneration cannot be accomplished merely by a change in pressure, but high temperature must also be applied [89, 90].

## 11.4 Preparation and Application of Porous Carbons for CO<sub>2</sub> Capture at Low Pressure

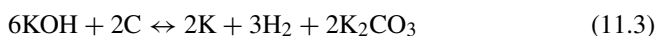
As mentioned in the Introduction, porous carbon materials have many interesting characteristics that make them suitable for use in gas adsorption and storage applications, including their large surface area and pore volume, high chemical and thermal stability, and tunable pore characteristics along with a low sensitivity to moisture [7, 91]. For these reasons, different carbon materials have been used as adsorbents for CO<sub>2</sub> capture. This section analyzes the use of a variety of porous carbon materials obtained from various types of precursors (i.e., biomass, polymers, zeolites, ionic liquids, MOFs, etc.) as CO<sub>2</sub> adsorbents at low pressure. To this end, special emphasis is placed on the description of the synthesis procedure, pore structure, and their performance as CO<sub>2</sub> adsorbents.

### 11.4.1 Carbon Materials Derived from Biomass

Although many types of carbon materials have been investigated and developed in recent years, carbon materials derived from biomass have proved to be one of the most attractive alternatives from the point of view of availability, cost, and sustainability. Thus, carbon materials can be fabricated from low-cost biomass wastes that have little or no economic value, such as coconut shells [75], bamboo [38], coffee grounds [92], sawdust [93], microalgae [94], rice husk [95], etc. The production of porous carbon materials from these renewable precursors is commonly accomplished by direct pyrolysis followed by an activation step [96, 97]. The activation step is usually required in order to develop the pore network [98], and it is usually performed by means of two different procedures: (1) chemical activation and (2) physical activation.

#### 11.4.1.1 Chemical Activation

Numerous chemical activation agents have been reported in the literature, such as NaOH, ZnCl<sub>2</sub>, H<sub>3</sub>PO<sub>4</sub>, KOH, K<sub>2</sub>CO<sub>3</sub>, etc. Of these, potassium hydroxide is the most widely used as it produces highly porous carbons (surface areas of above 2000 m<sup>2</sup> g<sup>-1</sup>) [99]. Even though it is well-known that KOH can efficiently generate micropores and small mesopores in the carbon framework, the exact mechanism of pore generation is still open to doubt because of the complexity involved. At temperatures as low as 400 °C, the redox reaction between KOH and C takes place, producing H<sub>2</sub>, K<sub>2</sub>CO<sub>3</sub>, and metallic K:



Lillo-Ródenas et al. proposed this reaction by combining thermodynamics studies with the experimental data obtained from temperature programmed desorption (TPD) experiments during the chemical activation of anthracite with KOH [100]. At temperatures higher than 600 °C, KOH would be completely consumed, and the resulting  $K_2CO_3$  would decompose into  $CO_2$  and  $K_2O$  at temperatures higher than 700 °C (reaction 11.4). At these high temperatures, the resulting  $CO_2$  and potassium compounds ( $K_2CO_3$  and  $K_2O$ ) can be reduced by carbon to produce CO (reaction 11.5) and metallic K (reactions 11.6 and 11.7), respectively.



Thus, the development of porosity and the increase in the specific surface area can be ascribed to the etching of carbon atoms by oxidation (reactions 11.3, 11.6, and 11.7) and the intercalation of in situ formed metallic potassium (reactions 11.3, 11.6, and 11.7) [100, 101]. In addition, the  $CO_2$  generated (reaction 11.4) contributes to the development of porosity via the carbon gasification process (reaction 11.5) [99]. It should also be noted that Otowa et al. proposed a different mechanism in which the main products are  $K_2O$ ,  $H_2O$ ,  $CO_2$ ,  $H_2$ , and  $K_2CO_3$  [102]. However, this study lacks experimental data to support the proposed activation mechanism.

As already mentioned, the use of KOH as activating agent leads to porous carbons with high BET surface areas ( $>3000 \text{ m}^2 \text{ g}^{-1}$ ) and large pore volumes ( $>2 \text{ cm}^3 \text{ g}^{-1}$ ) [42, 63, 103]. As an example, Wang et al. prepared an AC from celtuce leaves with a specific surface area as high as  $3400 \text{ m}^2 \text{ g}^{-1}$  and a pore volume of ca.  $1.9 \text{ cm}^3 \text{ g}^{-1}$  with a micro-mesoporous structure by using a KOH/precursor ratio equal to 4 and an activation temperature of 800 °C [104]. This porous carbon material shows a good  $CO_2$  adsorption capacity (25 °C) of  $1 \text{ mmol g}^{-1}$  at 0.15 bar and up to  $4.4 \text{ mmol g}^{-1}$  at 1 bar. On the other hand, Serafin et al. reported the synthesis of highly microporous carbons from different biomass precursors (pomegranate, kiwi, and carrot peels, tinder fungus, branches and mistletoe leaves, fern leaves, and sugar beet pulp) via a one-step KOH activation process under milder activation conditions (700 °C) [105]. The materials exhibit a Type I isotherm profile (see Fig. 11.11a), which is characteristic of microporous materials. These ACs possess moderate specific surface areas (in the  $585\text{--}1593 \text{ m}^2 \text{ g}^{-1}$  range) and a porosity made up mainly of narrow micropores so that they can adsorb up to  $1.25 \text{ mmol g}^{-1}$  and  $4.1 \text{ mmol g}^{-1}$  at 0.15 and 1 bar, respectively (at 25 °C) (Fig. 11.11b). In addition, they exhibit a  $CO_2/N_2$  adsorption ratio of 15.1 (evaluated using the ideal adsorption solution theory, IAST).

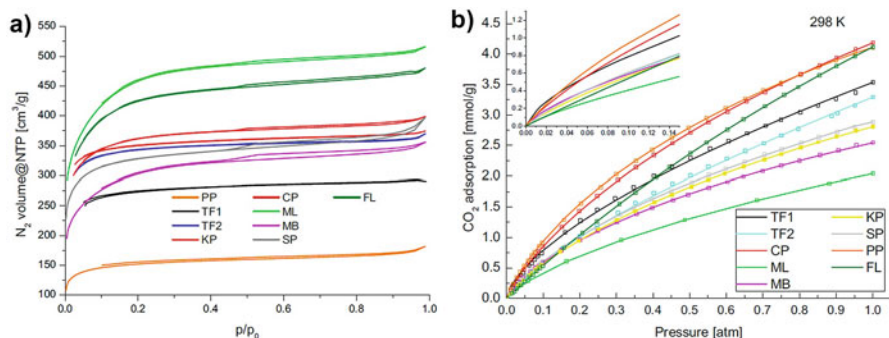


**Fig. 11.11** (a) Nitrogen sorption isotherms and (b) CO<sub>2</sub> adsorption isotherms at 25 °C of the activated carbons derived directly from biomass. (Reproduced with permission from Ref. [105] © 2017, American Chemical Society)

Selection of the starting biomass could be based on the presence of certain heteroatoms (e.g., nitrogen) that can be transferred to the carbon products so as to confer on them additional properties. In this regard, as mentioned in Sect. 11.3, there is a line of thought which claims that the incorporation of nitrogen into the carbon framework leads to an increase in CO<sub>2</sub> adsorption capacity and selectivity. This explains why numerous works have been published on the fabrication of N-doped porous carbons for CO<sub>2</sub> adsorption. For example, Chen et al. reported the synthesis of nitrogen-doped carbons by modification with urea and KOH activation of coconut shell [75]. Similarly, Yang et al. employed coconut shell as the carbon precursor to obtain N-doped porous carbon by combining ammoxidation with KOH activation [77]. These works emphasize the importance of microporosity and nitrogen content to obtain sorbents with high CO<sub>2</sub> adsorption capacities. A summary of the CO<sub>2</sub> uptakes (mmol g<sup>-1</sup>) at 0.15 and 1 bar and the selectivities at 25 °C of other N-doped as well as non-doped porous carbon materials obtained from different precursors and activating agents is given in Table 11.1.

Several authors have proposed the use of hydrochar, i.e., hydrothermally carbonized biomass, as carbon precursor instead of biomass because of its higher carbon yield and more homogeneous composition [97]. In this case, the synthesis procedure involves as first step the hydrothermal carbonization (HTC) of the biomass precursor, followed by chemical activation (usually KOH) [118]. This synthesis strategy was first reported in 2011 by Sevilla and Fuertes, who produced porous carbon materials by chemical activation of hydrothermally carbonized polysaccharides (starch and cellulose) and biomass (sawdust) [93]. They showed that the textural properties of these carbon materials can be designed by modifying the activation temperature and the amount of activating agent. The samples synthesized by using a KOH/hydrochar ratio of 2 and temperatures in the 600–700 °C range, exhibit moderate specific surface areas (e.g., 1390 m<sup>2</sup> g<sup>-1</sup> at 700 °C) and a porosity made up of narrow micropores with sizes of up to 1 nm, as illustrated in Fig. 11.12a, b. By contrast, the samples obtained at a ratio of KOH/hydrochar = 4 exhibit

**Table 11.1** A comparison of the low pressure CO<sub>2</sub> adsorption performances of porous carbon adsorbents derived from biomass

Carbon precursor	Sample	Activation method	CO <sub>2</sub> uptake at 25 °C (mmol g <sup>-1</sup> )		Selectivity (CO <sub>2</sub> /N <sub>2</sub> ) at 25 °C	References
			0.15 bar	1 bar		
Bamboo	Bamboo-3-873	Carbonization + KOH	1.5	4.5	8.6	[38]
Celtuce leaves	a-CL	Carbonization + KOH	1	4.4	–	[104]
Sawdust	SD2700D	Carbonization + KOH	1.3	4.6	–	[103]
Bean dreg	SK-0.5-700	Carbonization + KOH	–	4.2	–	[63]
Gelatin and starch	GSK1–700	Carbonization + KOH	1.2	3.8	51	[106]
Coconut shells	NC-650-1	Carbonization + KOH	1.3	4.3	29	[77]
Pine cone shell	PAC-650/2	Carbonization + KOH	1.2	4.7	17	[107]
Olive stones	AC_KOH	Carbonization + KOH	–	5.6 (at 0 °C)	–	[108]
Carrot peels	CP	KOH	1.15	4.2	8.1	[105]
Fern leaves	FL	KOH	0.71	4.1	5.6	[105]
Perennial cane ( <i>Arundo donax</i> )	KL B2	KOH	–	6.3 (at 0 °C)	–	[109]
Sawdust	AS-2-600	HTC+KOH	~1.3	4.8	5.4	[93]
Microalgae	AG-2-700	HTC+KOH	1	4.5	10	[94]
Sawdust	SD2700	HTC+KOH	1.3	4.6	21	[103]
Lignin waste	LAC2700	HTC+KOH	–	4.6	–	[110]
Empty fruit bunch	H250–800	HTC+KOH	1.2	3.7	11.2	[111]
Camellia japonica	ACCA.2700	HTC+KOH	1.5	5.0	–	[42]
Wood sawdust	SD2600P	HTC+KOH	2.0	5.8	–	[112]
Chitosan	AC-2-635	K <sub>2</sub> CO <sub>3</sub> (one-step activation process)	~0.8	3.9	21	[113]
Coconut shell	CACM32	H <sub>3</sub> PO <sub>4</sub>	–	3.7 (at 0 °C)	–	[114]
African palm stones	GACP48	H <sub>3</sub> PO <sub>4</sub>	–	4.2 (at 0 °C)	–	[115]
African palm stones	MZn40	ZnCl <sub>2</sub>	–	3.8 (at 0 °C)	–	[115]
African palm stones	MCa2	CaCl <sub>2</sub>	–	5.8 (at 0 °C)	–	[115]
Macadamia nut shell	700–900-60	CO <sub>2</sub>	1.057 (at 0.13 bar)	3.73	10.6	[116]
Olive stones	O-3-650-110	O <sub>2</sub>	1.36 (at 0 °C and 0.1 bar)	2.0	~30	[117]
Almond shells	A-3-650-83	O <sub>2</sub>	1.51 (at 0 °C and 0.1 bar)	2.1	~33	[117]

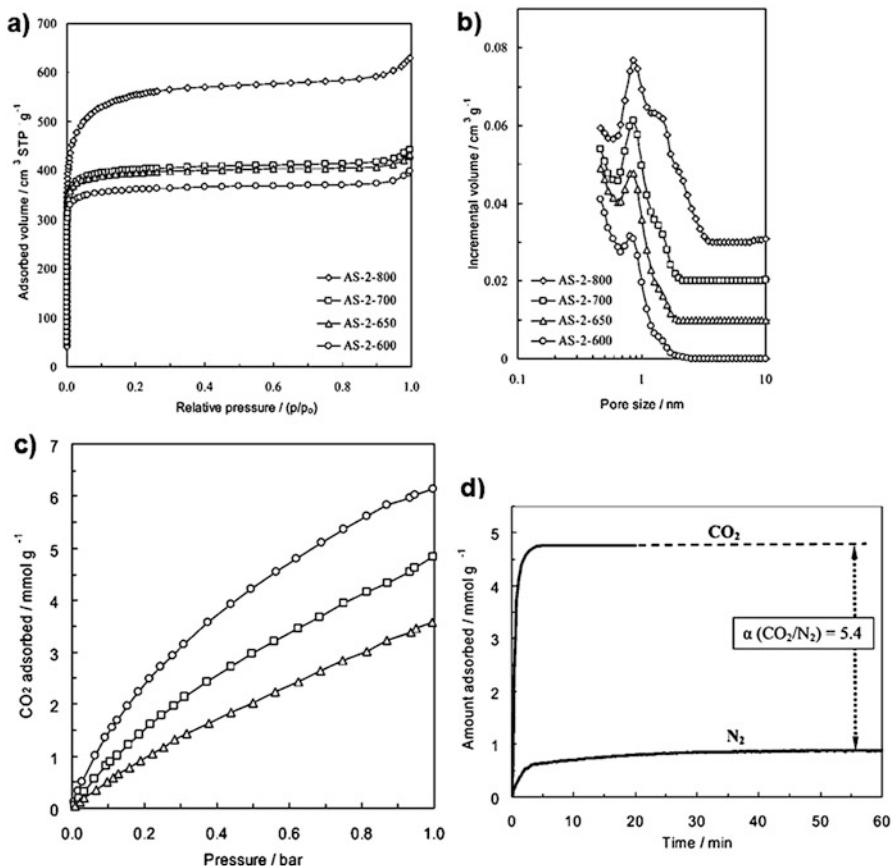


**Fig. 11.12** (a) N<sub>2</sub> sorption isotherms and (b) PSDs of activated carbons prepared from sawdust-derived hydrochar at different activation temperatures and with a (KOH/hydrochar) weight ratio of 2; (c) CO<sub>2</sub> adsorption isotherms at 0 °C (○), 25 °C (□), and 50 °C (△) for the porous carbon obtained when KOH/hydrochar = 2 and activation temperature = 600 °C; and (d) adsorption kinetics of CO<sub>2</sub> and N<sub>2</sub> at 25 °C for the AS-2-600 sample. (Reproduced with permission from Ref. [93] © 2011, Royal Society of Chemistry)

a higher pore development, with large specific surface areas (up to 2850 m<sup>2</sup> g<sup>-1</sup> at 800 °C) and pore volumes (up to 1.35 cm<sup>3</sup> g<sup>-1</sup> at 800 °C), and a lower proportion of narrow micropores. The ACs prepared under mild activation conditions display higher CO<sub>2</sub> uptakes than the ones obtained under more aggressive conditions (4.8 vs. 2.9 mmol g<sup>-1</sup>, respectively, at 1 atm/25 °C). This is due – as explained in Sect. 11.2 – to the abundance of narrow micropores (<0.8–1 nm) (Fig. 11.12c). The (CO<sub>2</sub>/N<sub>2</sub>) selectivity measured under equilibrium conditions is around 5.4 (as shown in Fig. 11.12d), and cycling stability was confirmed for 8 cycles of CO<sub>2</sub> adsorption-desorption. A significant advantage of this synthesis approach is that the product yield in the activating step is higher than when the biomass is directly

activated, which translates into a lower consumption of KOH for producing the same amount of AC [119]. This is important from a technological and environmental standpoint given the corrosive and toxic nature of KOH. Similarly, Coromina et al. prepared a series of KOH ACs from hydrochar derived from *Jujun grass* and *Camellia japonica* [42]. The activated carbons possess a narrow microporous structure and exhibit a remarkable CO<sub>2</sub> uptake of up to 5 mmol g<sup>-1</sup> at 1 bar/25 °C and 1.5 mmol g<sup>-1</sup> at 0.15 bar/25 °C. To date, a variety of biomass has been examined within this synthesis strategy, including seaweed [103], lignin waste [110], empty fruit bunches [111], or microalgae [94] (see Table 11.1).

Worth highlighting is the mechanochemical activation, or so-called compactivation methodology, developed by Mokaya's group, which allows the production of porous carbons with an unprecedented CO<sub>2</sub> storage capacity due to their higher pore development compared to that of analogous conventionally activated carbons but exhibiting a similar pore size [112]. Thus, the conundrum of how to increase the surface area and pore volume without generating larger pores would appear to have been solved. This process involves the compression (740 MPa) of mixtures of the activating agent (KOH) and biomass hydrochar into pellets or disks prior to thermal activation. In this way, a closer contact between the biomass carbon precursor and the activating agent (solid-solid interactions) during the early stages of the thermal treatment allows the activating agent to be used more efficiently, generating higher surface areas, but without any pore size expansion. Thus, while the shape of the isotherm remains unchanged for the compactivated and the activated samples, the specific surface area increases from 866 to 1066 m<sup>2</sup> g<sup>-1</sup>. In addition, the PSD shows little change in pore size with a slight contraction from 0.68 nm (activated) to 0.59 nm (compactivated). The compactivated sample exhibits a CO<sub>2</sub> uptake of 5.8 mmol g<sup>-1</sup> at 1 bar/25 °C (35% higher than the activated sample) and 2.0 mmol g<sup>-1</sup> at 0.15 bar/25 °C (54% higher than the activated sample). Moreover, the gravimetric and volumetric working capacities of the compactivated samples are greater than those of the activated ones, with values of 4.1 mmol g<sup>-1</sup>/171 g l<sup>-1</sup> (for PSA) and 2.9 mmol g<sup>-1</sup>/121 g l<sup>-1</sup> (for VSA) for flue gas CO<sub>2</sub> uptake.

Besides the widely used potassium hydroxide, other reagents have also been explored for chemical activation. For example, Fan et al. prepared nitrogen-doped microporous carbons (with a micropore fraction of over 90%) by using chitosan as the carbon precursor and K<sub>2</sub>CO<sub>3</sub> as the activating agent [113]. The textural properties of the obtained porous carbons were easily regulated by varying the ratio of K<sub>2</sub>CO<sub>3</sub>/chitosan and the activation temperature. The carbon material synthesized at 635 °C with a K<sub>2</sub>CO<sub>3</sub>/chitosan ratio of 2 exhibited a CO<sub>2</sub> uptake of 3.86 mmol g<sup>-1</sup> at 1 atm/25 °C and an extraordinary separation selectivity against N<sub>2</sub> of ~21. Likewise, Vargas et al. obtained a series of ACs by chemical activation of coconut shell and African palm stones with H<sub>3</sub>PO<sub>4</sub> [114]. The microporous carbon materials thus produced exhibited a CO<sub>2</sub> capture of ~ 3.7 mmol CO<sub>2</sub> g<sup>-1</sup>. Unlike KOH which acts as oxidant, H<sub>3</sub>PO<sub>4</sub> acts as dehydrating agent [120]. Another activating agent with a dehydration function is ZnCl<sub>2</sub>. As shown by Molina-Sabio and Rodriguez-Reinoso, both H<sub>3</sub>PO<sub>4</sub> and ZnCl<sub>2</sub>, besides having a dehydration function, act as templates for the development of microporosity, this microporosity

being smaller and more uniform in the case of ZnCl<sub>2</sub> owing to the smaller size of ZnCl<sub>2</sub> or its hydrates compared to the mixture of molecules of varying sizes present in the case of H<sub>3</sub>PO<sub>4</sub> (i.e., H<sub>3</sub>PO<sub>4</sub>, H<sub>4</sub>P<sub>2</sub>O<sub>5</sub>, H<sub>13</sub>P<sub>11</sub>O<sub>34</sub>) [121]. Later on, Vargas et al. used both activating agents to produce CO<sub>2</sub> adsorbents from African palm stones [115]. The materials thus obtained have a CO<sub>2</sub> adsorption capacity of between 3.8 mmol g<sup>-1</sup> (ZnCl<sub>2</sub>) and 4.2 mmol g<sup>-1</sup> (H<sub>3</sub>PO<sub>4</sub>) at atmospheric pressure and 0 °C. They also employed CaCl<sub>2</sub> as activating agent (in a CO<sub>2</sub> flow), which produces carbons with a narrow microporosity, the activation mechanism being similar to that of ZnCl<sub>2</sub>. In this case, the CO<sub>2</sub> uptake at 0 °C is analogous to that of ZnCl<sub>2</sub>-activated carbon (3.95 mmol g<sup>-1</sup>).

#### 11.4.1.2 Physical Activation

The production of porous carbons by physical activation entails the reaction at high temperature of the pyrolyzed carbon precursor with an oxidizing gas [98]. In this process, CO<sub>2</sub>, air (or O<sub>2</sub>), and steam are used as oxidizing gases. At high temperatures, these gases partially gasify the carbon framework to CO/CO<sub>2</sub>, and, as a consequence of this, a large number of pores are generated. Low-cost biomass wastes such as coconut shells [122], olive stones [62], almond shells [123], cotton stalks [124], or macadamia nut shells [116] have been used to produce CO<sub>2</sub> adsorbents by physical activation with CO<sub>2</sub>. For example, Plaza et al. synthesized activated carbons from macadamia nut shells by varying the activation time [116]. The carbon from macadamia can capture up to 1.2 mmol g<sup>-1</sup> at 0.15 bar/25 °C. As an alternative method, Plaza et al. explored the use of oxygen as activating agent to produce porous carbon from almond shells and olive stones [117]. It should be noted that the speed of the reaction of air or oxygen with carbon makes it difficult to control the process, resulting in excessive burn-off and the reduction of the activated carbon yield. However, they showed that the pore size distribution can be adequately tailored with an appropriate selection of the activation conditions. Thus, the carbon materials obtained under lower oxygen contents (3–5%) at mild temperatures (650 °C) display narrow micropores (0.5–0.5 nm), which are essential for the adsorption of CO<sub>2</sub> at low pressures. These adsorbents provide moderate CO<sub>2</sub> adsorption capacities (1.36 mmol g<sup>-1</sup> at 0.1 bar and 3.1 mmol g<sup>-1</sup> at 1 bar) and a high CO<sub>2</sub>/N<sub>2</sub> equilibrium selectivity (~33) for post-combustion capture.

### 11.4.2 Porous Carbons Derived from Polymers

Polymers are another kind of precursor typically used for the production of porous carbon materials due to their high carbon yield and absence of impurities, unlike biomass. N-containing polymers have been widely investigated in relation to CO<sub>2</sub> capture on the basis that the incorporation of nitrogen into the carbon framework enhances CO<sub>2</sub> adsorption (see discussion in Sect. 11.3). Thus, Sevilla et al. synthesized N-porous carbons from polypyrrole by KOH activation, achieving

a large specific surface area ( $\sim 3000 \text{ m}^2 \text{ g}^{-1}$ ), a high  $\text{CO}_2$  adsorption capacity ( $\sim 4 \text{ mmol g}^{-1}$  at 1 atm/25 °C), and a good cycling performance (6 cycles of adsorption-desorption) [125]. It should be noted that the materials with the highest  $\text{CO}_2$  adsorption capacity are those with the largest volume of narrow micropores and also the highest nitrogen content, and as a result the specific role of nitrogen cannot be ascertained. Szcześniak et al. also prepared a series of porous carbons from polypyrrole, although incorporating reduced graphene oxide into the one-step carbonization and KOH activation process [126]. They observed that the material with the highest volume of narrow micropores exhibits the best  $\text{CO}_2$  adsorption uptake ( $6.8 \text{ mmol g}^{-1}$  at 1 atm/0 °C), omitting the study of the influence of nitrogen. On the other hand, Men et al. using NaOH instead of KOH for the activation of polypyrrole managed to produce materials with surface areas of  $\sim 800 \text{ m}^2 \text{ g}^{-1}$  and micropore volumes of  $0.26 \text{ g cm}^{-3}$ , which resulted in  $\text{CO}_2$  uptakes of  $4 \text{ mmol g}^{-1}$  at 1 bar/25 °C [127]. Polyaniline is another commonly used polymer with a high nitrogen content. As an example, Silvestre-Albero et al. prepared a series of ACs by the carbonization of polyaniline followed by chemical activation with KOH or  $\text{K}_2\text{CO}_3$  [128]. They found that the best  $\text{CO}_2$  adsorption capacity corresponded to the material with the highest volume of narrow microporosity rather than the one with the largest BET surface area or nitrogen content. As can be seen from what has been said so far, the synthesis of porous materials from polypyrrole or polyaniline requires the use of an activation step (i.e., KOH) since the carbonization of these polymers leads to carbon materials with a poor pore development that limits their capacity to adsorb  $\text{CO}_2$ . This is a feature common to other N-rich polymers, such as imine-linked polymers or copolymers of resorcinol, formaldehyde, and lysine, which provided only limited  $\text{CO}_2$  uptakes when directly carbonized owing to their reduced specific surface area and micropore volume [70, 72]. As an alternative carbon source, polymers without nitrogen in their structure have also been used to produce highly microporous carbons with an excellent  $\text{CO}_2$  capture capacity ( $7\text{--}9 \text{ mmol g}^{-1}$  at 0 °C/1 bar and  $\sim 4.6 \text{ mmol g}^{-1}$  at 25 °C/1 bar) owing to their high volume of narrow micropores [40, 129, 130].

Del Monte's group demonstrated the use of different eutectic mixtures (the so-called deep eutectic solvents or DESs) as interesting alternatives for the synthesis of multifunctional hierarchical carbons [131, 132]. In this context, DESs act as all-in-one solvent-templating-reactant systems that offer an environmentally friendly and low-cost alternative to conventional syntheses in materials science. Specifically, resorcinol-based DESs can be used to prepare hierarchical porous carbon monoliths via formaldehyde polycondensation and subsequent carbonization. By applying this strategy, del Monte's group has synthesized different carbon materials for use as  $\text{CO}_2$  sorbents [64, 133, 134]. For example, they reported the synthesis of hierarchical nitrogen-doped carbon molecular sieves using deep eutectic solvents composed of resorcinol and 3-hydroxypyridine (as nitrogen source) and tetraethy-

ammonium bromide [133]. The carbons thus synthesized exhibited moderate CO<sub>2</sub> adsorption capacities of up to 2.7 mmol g<sup>-1</sup> (at 1 atm/25 °C) and outstanding CO<sub>2</sub>/N<sub>2</sub> selectivities of up to 14.4.

### 11.4.3 *Non-conventional Porous Carbon for CO<sub>2</sub> Adsorption*

The past few decades have witnessed a lot of progress in the synthesis of porous carbons by the use of non-conventional precursors or procedures that allow a tight control over the structural/textural/chemical properties of the materials produced. Thus, several authors have employed novel synthetic materials such as ionic liquids, metal-organic frameworks (MOFs), etc., as carbon precursors. In this regard, the attractive characteristics of ionic liquids-derived carbon materials, such as their high carbon yield, facile synthesis, large specific surface area, and the possibility of heteroatom-doping, make them alternative candidates for CO<sub>2</sub> capture [135–137]. For instance, Dai et al. reported the production of nitrogen-doped microporous carbons by means of the direct carbonization of an imidazolium-based ionic liquid [138]. The carbon materials thus produced were microporous, with a microporosity percentage of over 60% and a micropore volume of up to 0.31 cm<sup>3</sup> g<sup>-1</sup>. The optimized material exhibited a moderate CO<sub>2</sub> adsorption capacity of 4.4 mmol g<sup>-1</sup> (at 1 bar/0 °C). Although the authors attributed this value to the abundant nitrogen-modified basic sites, it is worth noting that this sample had the highest fraction of micropore volume.

Novel families of porous materials such as MOFs are also interesting precursors for the production of porous carbons. MOFs are highly crystalline inorganic-organic hybrids which are made by assembling organic linkers with metal ions or metal clusters through coordination bonds [139–141]. These materials have been used as CO<sub>2</sub> sorbents as it is possible to tune the pore size by controlling the length and functionality of the organic ligands and their high pore development [7, 142]. In addition, these compounds have proven to be effective templates for preparing microporous carbons, whereby the infiltration of other carbon sources can be avoided owing to their own high carbon content [143, 144]. In this way, these materials can act both as templates and carbon precursors for producing carbons with a uniform morphology and controllable porosity [145]. Srinivas et al. reported the creation of a new type of hierarchical porous carbon (HPC) by the direct carbonization of different MOF structures (MOF-5, MOF-74, MIL-53) and by applying an acid treatment to remove the residual metal [43]. The HPCs exhibited a large specific surface area (of up to ca. 2800 m<sup>2</sup> g<sup>-1</sup>), a high total pore volume (of up to 5.53 cm<sup>3</sup> g<sup>-1</sup>), and a micropore volume of 0.6 m<sup>3</sup> g<sup>-1</sup>, which led to a moderate CO<sub>2</sub> adsorption capacity of 3.0 mmol g<sup>-1</sup> at 1 bar/27 °C. This moderate value can be ascribed to the predominance of mesoporosity, which makes these materials the preferred choice for pre-combustion applications. Similarly, Zou et al. reported the synthesis of porous carbon materials by using zeolitic imidazolate frameworks (ZIFs), a subclass of MOFs [146]. The synthesis procedure

is based on the carbonization of different ZIFs (ZIF-8, ZIF-68, and ZIF-69) followed by a conventional chemical activation step using KOH (CZIF8a, CZIF68a, and CZIF69a). The materials exhibited large specific surface areas in the 1860–2430 m<sup>2</sup> g<sup>-1</sup> range, with pore sizes in the 0.8–1.5 nm range and standard CO<sub>2</sub> uptakes of 4.04–4.76 mmol g<sup>-1</sup> at 1 bar/0 °C.

The fabrication of porous carbon materials can also be achieved through the use of non-conventional procedures such as nanocasting. Within this context, the hard-templating route has been demonstrated to be a controllable method able to prepare carbons with a well-defined and precisely modulated size, shape, and pore network [147]. In the synthesis procedure, a carbon precursor is carbonized in the pore network of a porous inorganic solid which is used as a template. Afterward, the inorganic template is removed by acid or base leaching, and an inverse carbon replica is obtained. Usually, mesoporous silica materials have been used as templates, resulting in the production of mesoporous carbon materials [148], that require a subsequent chemical activation step to generate the micropores essential for CO<sub>2</sub> capture at low pressure. Sevilla and Fuertes have demonstrated the feasibility of fabricating highly porous carbons by means of the chemical activation of two kinds of mesoporous carbons obtained by using two different ordered mesostructured silicas as hard templates (SBA-15 and KIT-6) [149]. The activated carbon materials thus produced exhibited a large specific surface area and a porosity made up of mesopores inherited from the templated carbons and micropores derived from the chemical activation process, with a micropore fraction of over 70%. As a result, these materials were able to adsorb 3.3 mmol g<sup>-1</sup> (at 1 atm/25 °C), outperforming the commercial activated carbon M-30 (2.2 mmol g<sup>-1</sup> at 1 atm/25 °C). A similar procedure was employed by Han et al. to produce nitrogen-doped carbon materials by using tri-continuous mesoporous IBN-9 as template, p-diaminobenzene as the nitrogen-rich carbon precursor, and a KOH activation step to increase the micropore volume [58]. The material they developed exhibited a CO<sub>2</sub> uptake of up to 1.75 mmol g<sup>-1</sup> at 0.2 bar/25 °C and a remarkable CO<sub>2</sub>/N<sub>2</sub> selectivity of 25.

It is also worth noting that zeolites can be used as hard templates to directly synthesize highly microporous carbons with large specific surface areas without the need for an activation step. For example, microporous nitrogen-doped carbons that show moderate to high CO<sub>2</sub> adsorption capacities (2.4 and 4.4 mmol g<sup>-1</sup>, respectively, at 1 bar/25 °C) have been produced from the zeolites NaY [150] and EMC-2 [151]. Also worth mentioning is the use of compacted zeolite pellets, as in the compactation approach (see Sect. 11.4.1), by Mokaya's group [152]. The use of zeolites in pellet form yields a carbon material with a larger micropore surface area (25–40% higher), pore volume, and micropore volume compared to when they are used in powder form and, consequently, an enhanced CO<sub>2</sub> capture capacity (~50% higher). On the other hand, sulfur-doped microporous carbon materials have been prepared with zeolite EMC-2 as hard template and 2-thiophenemethanol as S-rich carbon precursor [153]. The sulfur-doped carbon exhibited a CO<sub>2</sub> uptake capacity 43% higher than its undoped counterpart under similar measurement conditions, although both samples had similar textural properties (i.e., micropore

surface area and total pore and micropore volumes). The authors attributed its performance to the micropore surface area and the presence of sulfur functional groups in the carbon framework, which increased its surface polarity and basicity and favored the adsorption of acidic CO<sub>2</sub> molecules. However, they did not undertake a detailed investigation to determine the influence of the pore size distribution. In fact, the authors omitted to compare the volume of narrow micropores which mainly determine the adsorptive capacity at low pressures.

Unlike the hard-templating method, the soft-templating approach produces ordered porous carbons by using block copolymer surfactants as organic templates (also called soft templates), thereby avoiding the need for a previous template synthesis step [148]. However, this approach is only valid for the synthesis of mesoporous carbons, which are not suitable for low pressure carbon capture. Nevertheless, some authors have employed this approach and have studied the low pressure CO<sub>2</sub> adsorption capacity of the materials produced. For example, Deng et al. synthesized ordered mesoporous carbons using a readily available triblock copolymer (Pluronic F127) as structure-directing agent and a mixture of phloroglucinol and formaldehyde as an inexpensive carbon precursor. The resulting materials had a moderate specific surface area ( $\sim 800 \text{ m}^2 \text{ g}^{-1}$ ) and a uniform mesopore size distribution, and so were able to adsorb only  $1.49 \text{ mmol CO}_2 \text{ g}^{-1}$  at 1 bar/25 °C [154]. Similarly, Yuan et al. synthesized ordered mesoporous carbons using Pluronic F127 as soft template and resorcinol and formaldehyde as carbon precursors [155]. In order to catalyze the reaction, they employed citric acid which also improved the microporosity of the carbon materials. As a result, the carbon materials with the largest narrow micropore volumes exhibited a CO<sub>2</sub> uptake of  $3.46 \text{ mmol g}^{-1}$  (1 bar/25 °C).

As discussed in Sect. 11.2, carbide-derived carbons (CDCs) are particularly suitable for carbon capture at low pressure taking into account their quasi-unimodal micropore size distribution with a mean micropore size that can be controlled with precision by modifying the synthesis conditions (chlorination temperature and metallic carbide precursor). The synthesis of CDCs is considered as a template approach in which the carbide precursor lattice acts as template, and the metal atoms are selectively etched layer by layer, most commonly by dry chlorine treatment [156, 157]. The first to report on the use of CDCs for carbon capture at low pressure were Presser et al. [37], who produced adsorbents with a remarkable CO<sub>2</sub> uptake at 0 °C of  $7.1 \text{ mmol g}^{-1}$  at 1 bar and  $1.51 \text{ mmol g}^{-1}$  at 0.1 bar by chlorination of TiC. They also studied the use of activation procedures (KOH and CO<sub>2</sub> activation) on CDCs to produce carbons with higher specific surface areas and pore volumes. However, they found that, under atmospheric conditions, the micropore volume dominated the amount of CO<sub>2</sub> adsorbed rather than the specific surface area and total pore volume, so that the pristine CDCs proved to be better CO<sub>2</sub> adsorbents for post-combustion conditions.

## 11.5 Porous Carbons for CO<sub>2</sub> Adsorption at High Pressures

As mentioned in the Introduction, two possible applications where CO<sub>2</sub> adsorption is performed at high pressure are pre-combustion CO<sub>2</sub> capture and natural gas purification. The study of these two applications is currently less widespread than post-combustion CO<sub>2</sub> capture owing to their less extended use. As a result, a small number of porous carbon adsorbents have been analyzed for these applications to date. The CO<sub>2</sub> uptakes at high pressure for porous carbon adsorbents reported so far in the literature are summarized in Table 11.2. As will be shown, the synthesis process adopted is virtually always based on an activation step, in most of the cases KOH chemical activation.

**Table 11.2** CO<sub>2</sub> uptake at high pressure for porous carbons reported in the literature

Material	CO <sub>2</sub> uptake at 20 bar, 25 °C <sup>a</sup> (mmol g <sup>-1</sup> )	Working capacity (PSA system) <sup>c</sup> (mmol g <sup>-1</sup> )	References
AMA-C-KOH (biomass-derived AC)	~13 (14) <sup>b</sup>	~ 10 (11)	[158]
ACCA4800 (hydrochar-derived AC)	21	18	[42]
AX-yM (hydrochar-derived AC)	20–21 (30–31)	18–19 (27.5–28.4)	[159]
G-3.6-2 (saccharide-derived AC)	24.1 (41.1)	22.6 (39.6)	[47]
KLB2 (biomass-derived AC)	ca. 13 (15.4) <sup>b,d</sup>	ca. 6.7 (9.1) <sup>d</sup>	[109]
NDAB3–500 (biomass-derived AC)	~11 (13.1) <sup>b</sup>	8.9 (11)	[160]
VR5–4:1 (mesophase pitch-derived AC)	22 (31.8)	19.4 (29.2)	[161]
A-rNPC (asphalt-derived AC)	21.1 (26) <sup>b</sup>	17.1 (22)	[162]
uGil-900 (asphalt-derived AC)	20.7 (26.6) <sup>b</sup>	18.1 (24)	[163]
PANI_30ZnNa550_800 (PANI-derived AC)	11.5 (14.6)	9.7 (12.8)	[164]
SU-AC-400 (PANI-derived AC)	22.5 (32.5)	18.2 (28.2)	[46]
CPC-700 (polymer-derived N-doped carbon)	21.4 (27.3) <sup>c</sup>	17.4 (23.3)	[165]
BIDC-3-700 (benzimidazole-derived AC)	21.7 (30.8) <sup>c</sup>	18.6 (27.7)	[45]
MPPY-4800 (polypyrrole-derived AC)	28.1 (45.6)	25.3 (42.8)	[166]
K-PAF-1-750 (PAF-derived AC)	~22.7 (30)	~18.2 (25.5)	[167]
HPC5b2–1100 (MOF-derived hierarchical porous carbons)	20.8 (27) <sup>b</sup>	17.1 (23.3)	[43]
CN2800 (activated CNT superstructures)	19.5	16.7	[168]
GODC-sol800 (activated GO)	16.4	~ 14.1	[44]
Maxsorb (commercial AC)	19 (25.5)	16.9 (23.4)	[169]

Values in parenthesis correspond to the difference in equilibrium adsorption capacity at 40 (or 30–35 bar) and 1 bar

<sup>a</sup>Values in parenthesis correspond to a pressure of 40 bar

<sup>b</sup>Uptake in parenthesis at 30 bar

<sup>c</sup>Uptake in parenthesis at 35 bar

<sup>d</sup>Values measured at 0 °C

<sup>e</sup>Defined as the difference in equilibrium adsorption capacity at 20 and 1 bar

Considering factors such as availability, environmental, and economic concerns, biomass-based carbons are also the most attractive materials for high pressure CO<sub>2</sub> adsorption. Ferrera-Lorenza et al. produced activated carbons for pre-combustion CO<sub>2</sub> capture and the separation/concentration of mixtures of CO<sub>2</sub>/CH<sub>4</sub> in natural gas feeds from an Agar-Agar industry, i.e., algae meal [158]. These authors prepared the adsorbents by means of chemical activation with KOH or K<sub>2</sub>CO<sub>3</sub>, using two approaches for the high temperature treatment, i.e., a conventional electrical furnace and a multimode microwave furnace. The material that showed the largest CO<sub>2</sub> adsorption capacity at 30 bar and 25 °C (ca. 14 mmol CO<sub>2</sub> g<sup>-1</sup>) was the material obtained by KOH activation in a conventional electrical furnace, which is the material with the highest pore development, i.e., a BET surface area of ca. 2000 m<sup>2</sup> g<sup>-1</sup> and pore volume of 0.91 cm<sup>3</sup> g<sup>-1</sup>. This material adsorbs 7.1 mmol CH<sub>4</sub> g<sup>-1</sup> and 0.85 mmol H<sub>2</sub> g<sup>-1</sup>, which translates into modest CO<sub>2</sub>/CH<sub>4</sub> and CO<sub>2</sub>/H<sub>2</sub> selectivities of ~2 and 16, respectively. The KOH-activated material, however, performs worse than one with an ultra-large textural development and a high proportion of mesoporosity such as Maxsorb (BET surface area = 3420 m<sup>2</sup> g<sup>-1</sup> and V<sub>p</sub> ~ 1.7 cm<sup>3</sup> g<sup>-1</sup>), whose CO<sub>2</sub> uptake is almost twice as high (25 mmol CO<sub>2</sub> g<sup>-1</sup>), although its CO<sub>2</sub>/CH<sub>4</sub> and CO<sub>2</sub>/H<sub>2</sub> selectivities are only slightly higher, i.e., 2.6 and 16.7, respectively.

More recently, Coromina et al. developed activated carbons with an enhanced CO<sub>2</sub> uptake for pre-combustion capture by the KOH chemical activation of hydrochar produced from Jujun grass and *Camellia japonica* [42]. Whereas mild activation conditions produced excellent adsorbents for low pressure applications (see Sect. 11.4.1.1), the use of harsh chemical activation conditions, i.e., a KOH/hydrochar weight ratio = 4 and activation temperatures between 700 and 800 °C, yielded adsorbents with good performances in high pressure applications. These porous carbons are characterized by high BET surface areas of 3000–3500 m<sup>2</sup> g<sup>-1</sup> and large pore volumes of ~1.6–1.9 cm<sup>3</sup> g<sup>-1</sup>. They are able to adsorb 19–21 mmol CO<sub>2</sub> g<sup>-1</sup> at 20 bar and 25 °C. Similarly, Sevilla et al. produced excellent adsorbents for high pressure CO<sub>2</sub> capture using a melamine-mediated KOH activation approach, with hydrochar produced from saccharides (starch and cellulose) and biomass (eucalyptus sawdust) as precursor (Fig. 11.13a) [159]. These porous carbons have ultra-large BET surface areas of up to 3500 m<sup>2</sup> g<sup>-1</sup> and pore volumes of up to ca. 2.4 cm<sup>3</sup> g<sup>-1</sup>. Importantly, they show a bimodal PSD in the micro-mesopore range with a well-balanced micro-mesoporosity (V<sub>micro</sub>/V<sub>meso</sub> ratio ~0.8–1.4), contrary to the materials produced by conventional KOH activation, which are predominantly microporous (>70% of their pore volume corresponds to micropore volume) (Fig. 11.13b). In this way, micro-mesoporous carbons are able to adsorb around 20–21 mmol CO<sub>2</sub> g<sup>-1</sup> at 20 bar and 25 °C vs. 19 mmol CO<sub>2</sub> g<sup>-1</sup> for the microporous carbons and notably 30–31 mmol CO<sub>2</sub> g<sup>-1</sup> at 40 bar vs. ~23 mmol CO<sub>2</sub> g<sup>-1</sup> in the case of the microporous carbons (Fig. 11.13c). Moreover, their abundant mesoporosity ensures the retention of low amounts of adsorbed gas at the regeneration pressures typically used in PSA systems (1–2 bar), which translates into enhanced working capacities (18–19 mmol CO<sub>2</sub> g<sup>-1</sup> between 20 and 1 bar and ~28 mmol CO<sub>2</sub> g<sup>-1</sup> between 40 and 1 bar) (Table 11.2).

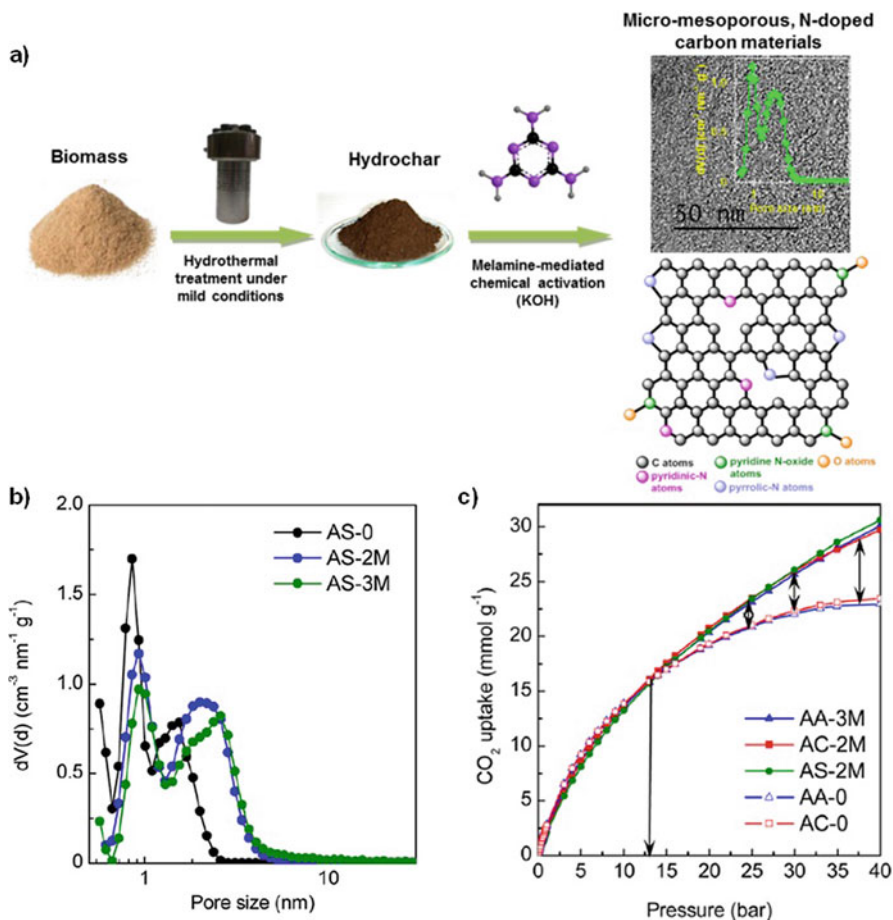


**Fig. 11.13** (a) Illustration of the synthesis methodology used for the production of highly porous micro-mesoporous, N-doped carbons from biomass-derived hydrochar, (b) PSDs of the porous carbons produced from starch-derived hydrochar in the absence (AA-0) and presence of melamine (AA-2 M and AA-3 M), and (c) high pressure  $\text{CO}_2$  isotherms of the microporous and micro-mesoporous carbons. (Reproduced with permission from Ref. [159] © 2016, American Chemical Society)

Using the same melamine-mediated activation approach, but with potassium oxalate instead of KOH as activating agent and saccharides as carbon precursor, Sevilla et al. very recently produced hierarchical micro-/mesoporous carbons with surface areas as high as  $3500 \text{ m}^2 \text{ g}^{-1}$ , pore volumes of up to  $2.7 \text{ cm}^3 \text{ g}^{-1}$ , and mesoporosity percentages of 50–60% [47]. As a result, these materials provided record-high room temperature  $\text{CO}_2$  uptakes of  $32\text{--}33 \text{ mmol g}^{-1}$  at 30 bar and  $44\text{--}49 \text{ mmol g}^{-1}$  at 50 bar. They also showed much higher PSA working capacities (see Table 11.2) than those of the best carbon adsorbents reported to date. Furthermore,

in view of the typical conditions of the pre-combustion gas (40% CO<sub>2</sub> and 55% H<sub>2</sub>, 40 bar), the best adsorbent provided a CO<sub>2</sub>/H<sub>2</sub> selectivity of 23 (calculated by using the IAST method), and in the case of the pure gases, an equilibrium CO<sub>2</sub>/H<sub>2</sub> selectivity of ca. 15 was achieved at 50 bar, rising to 16 at 40 bar. Overall, the optimized material combines an ultra-large CO<sub>2</sub> uptake, a high working capacity, and a good selectivity against H<sub>2</sub> under conditions relevant to pre-combustion capture, a combination of features that makes it a promising candidate for pre-combustion CO<sub>2</sub> capture. The work of Sevilla et al. demonstrates the importance of fine-tuning the porosity to suit a range of targeted pressures (i.e., depending on whether VSA or PSA systems are to be used) rather than just considering the final pressure.

Singh et al. have reported the production of pre-combustion adsorbents from the prolific waste biomass *Arundo donax* [109]. By direct activation with KOH and control of the ratio biomass/KOH ( $T = 600\text{ }^{\circ}\text{C}$ ), microporous carbons with BET surface areas of  $\sim 600\text{--}1100\text{ m}^2\text{ g}^{-1}$  and pore volumes of up to ca.  $0.6\text{ cm}^3\text{ g}^{-1}$  were produced. The CO<sub>2</sub> adsorption capacity of these materials was investigated at  $0\text{ }^{\circ}\text{C}$  up to 30 bar. Owing to the moderate pore development of these materials, especially in the mesopore region, the highest uptake recorded was  $15.4\text{ mmol CO}_2\text{ g}^{-1}$ . In addition, their enhanced narrow microporosity reduced their working capacity between 30 and 1 bar to only  $9.1\text{ mmol CO}_2\text{ g}^{-1}$ . Later on, the same authors prepared N-doped carbons from the same biomass, adding chitosan as N-dopant and using ZnCl<sub>2</sub> as activating agent [160]. In this way, porous carbons with a higher pore development were obtained. Thus, an optimized material, synthesized at  $500\text{ }^{\circ}\text{C}$  and with a ZnCl<sub>2</sub>/biomass ratio of 3, exhibited a BET surface area of ca.  $1900\text{ m}^2\text{ g}^{-1}$  and pore volume of  $1.0\text{ cm}^3\text{ g}^{-1}$ , besides a nitrogen content of 5.4 wt%. This material was able to adsorb  $13.1\text{ mmol CO}_2\text{ g}^{-1}$  at 30 bar/ $25\text{ }^{\circ}\text{C}$ , still well below the best values reported to date (see Table 11.2).

Porous carbons for high pressure CO<sub>2</sub> adsorption have also been produced from more traditional precursors such as coal or petroleum derivatives. For example, Casco et al. reported the production of a porous carbon with outstanding CO<sub>2</sub> uptakes of  $22\text{ mmol g}^{-1}$  at 20 bar and ca.  $32\text{ mmol g}^{-1}$  at 40 bar ( $25\text{ }^{\circ}\text{C}$ ) from petroleum pitch by chemical activation with KOH (VR5-4:1) [161]. An appropriate tuning of the pore structure consisting of a poorly developed narrow microporous structure and a highly developed wide microporous and small mesoporous network also led to outstanding working capacities of  $\sim 19\text{ mmol g}^{-1}$  between 20 and 1 bar and of  $\sim 29\text{ mmol g}^{-1}$  between 40 and 1 bar. Similarly, Jalilov et al. used asphalt for the synthesis of porous carbons with enhanced CO<sub>2</sub> uptakes for natural gas purification also by KOH chemical activation [162]. The highest CO<sub>2</sub> uptake at 30 bar and  $23\text{ }^{\circ}\text{C}$  (i.e.,  $26\text{ mmol g}^{-1}$ ) was recorded for the material post-treated with NH<sub>3</sub> at high temperature followed by H<sub>2</sub> treatment also at high temperature (see Fig. 11.14a). This material had a BET surface area of  $\sim 2600\text{ m}^2\text{ g}^{-1}$ , a pore volume of  $\sim 1.1\text{ cm}^3\text{ g}^{-1}$ , a micro-mesoporous pore network, and a surface N content of 4.5 wt%. The cycling stability of the material over 8 cycles of CO<sub>2</sub> adsorption-desorption was also confirmed. Furthermore, CO<sub>2</sub> adsorption was investigated at

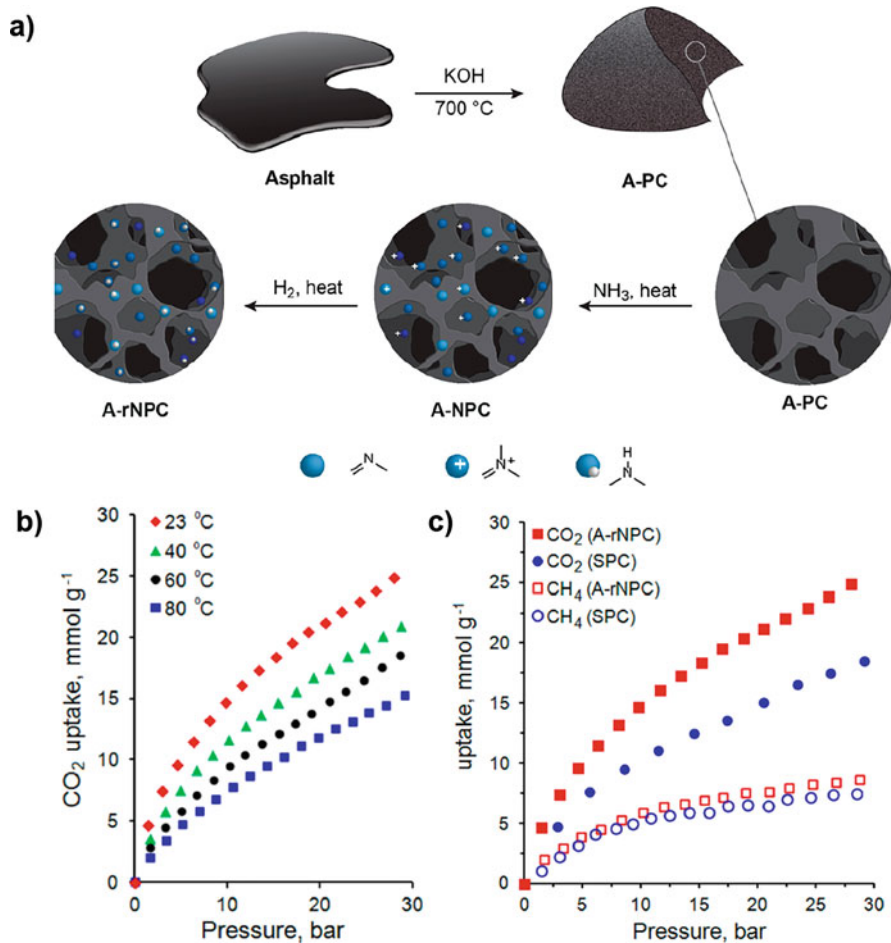


**Fig. 11.14** (a) Schematic illustration of the preparation of asphalt-derived porous carbons, (b) CO<sub>2</sub> uptake on A-rNPC as a function of temperature over the pressure range of 0–30 bar, and (c) CO<sub>2</sub> and CH<sub>4</sub> uptakes on A-rNPC at 23 °C over the pressure range of 0–30 bar. (Reproduced with permission from Ref. [162] © 2015, American Chemical Society)

different temperatures up to 80 °C, and the material was still able to adsorb 15 mmol CO<sub>2</sub> g<sup>-1</sup> at 80 °C (Fig. 11.14b). As the material was intended for use in natural gas purification, CH<sub>4</sub> adsorption was also analyzed (Fig. 11.14c). A CO<sub>2</sub>/CH<sub>4</sub> selectivity of 3 was recorded at 30 bar, the pressure chosen as the maximum pressure limit given that a 300 bar natural gas well-head pressure containing ~10% CO<sub>2</sub> has a 30 bar partial pressure of CO<sub>2</sub>. More recently, the same authors improved the previous synthesis methodology and as a result succeeded in producing ultra-high surface area porous carbons (4200 m<sup>2</sup> g<sup>-1</sup>) with a micro-mesoporous structure from asphalt [163]. The optimized material thus fabricated (uGil-900) showed very

good CO<sub>2</sub> uptakes of 26.6 and 35 mmol g<sup>-1</sup> (25 °C) at 30 and 54 bar, respectively, compared to CH<sub>4</sub> uptakes of 10.2 and 23.4 mmol g<sup>-1</sup> (25 °C) at 30 and >150 bar, respectively. This translates into a CO<sub>2</sub>/CH<sub>4</sub> selectivity of 1.1 for a 300 bar natural gas well-head pressure containing ~10% CO<sub>2</sub> and ~90% CH<sub>4</sub>. The cycling stability of the material was confirmed over 5 cycles of CO<sub>2</sub> or CH<sub>4</sub> adsorption-desorption. The study of this material for purposes of natural gas purification was complemented by performing CO<sub>2</sub> and CH<sub>4</sub> displacement measurements, which showed that the displacement of pre-adsorbed CH<sub>4</sub> by CO<sub>2</sub> was much faster than the other way around, the rate constant for displacement of pre-adsorbed CH<sub>4</sub> by CO<sub>2</sub> increasing with the rise in pressure, while the rate constant for the displacement of pre-adsorbed CO<sub>2</sub> by CH<sub>4</sub> remained constant. These results confirm the suitability of this material for natural gas upgrading.

Similar to low pressure CO<sub>2</sub> capture, N-rich polymers have also been widely employed to produce N-doped porous carbon materials for CO<sub>2</sub> capture at high pressure. Polyaniline (PANI) has been used by several authors to produce N-doped micro-mesoporous carbons by different methods. For example, Silvestre-Albero et al. followed a “salt templating” approach using a eutectic mixture of ZnCl<sub>2</sub> and NaCl [164]. The resulting porous carbons were characterized by BET surface areas of ~1400–1800 m<sup>2</sup> g<sup>-1</sup> and micropore and mesopore volumes of around 0.5–0.6 and 0.6–0.8 cm<sup>3</sup> g<sup>-1</sup>, respectively, besides a N content of 2–6 wt%. These materials were tested for CO<sub>2</sub> capture and storage at pressures of up to 40 bar and 25 °C. They exhibited moderate CO<sub>2</sub> uptakes in the ~10.5–14.6 mmol g<sup>-1</sup> range, and the surface nitrogen groups did not seem to influence the amount of CO<sub>2</sub> adsorbed. On the other hand, by the KOH activation of PANI hydrogel, He et al. produced N-doped porous carbon with ultra-large BET surface areas of up to 4200 m<sup>2</sup> g<sup>-1</sup> and abundant micro- and small mesopores (volume of pores <4 nm = 2.03 cm<sup>3</sup> g<sup>-1</sup>) [46]. The resulting carbon material (SU-AC-400) was thus able to provide a record-high CO<sub>2</sub> capture capacity at elevated pressures, i.e., 28.3 mmol g<sup>-1</sup> at 25 °C and 30 bar (and as much as 25.3 mmol g<sup>-1</sup> at 50 °C). In addition, the porous carbon showed a CO<sub>2</sub>/CH<sub>4</sub> selectivity of 11.2 (calculated using IAST, assuming an ideal mixture of 10% CO<sub>2</sub> and 90% CH<sub>4</sub> at a total pressure of 300 bar), and no reduction in CO<sub>2</sub> capture capacity was observed in the PSA system between 30 and 1 bar even after 10 cycles.

Ashourirad et al. also produced N-doped porous carbons by chemical activation of a benzimidazole-linked polymer with KOH. By employing a KOH/polymer ratio of 2 and controlling the temperature in the 550–800 °C range, porous carbons with BET surface areas in the range of ~1600–3200 m<sup>2</sup> g<sup>-1</sup>, micro- and mesopore volumes in the 0.6–0.8 and 0.1–0.8 cm<sup>3</sup> g<sup>-1</sup> range, and N contents in the 1–8 wt % ratio range were obtained [165]. The optimized material, i.e., the one activated at 700 °C (CPC-700), characterized by a surface area of 3242 m<sup>2</sup> g<sup>-1</sup> and a total pore volume of 1.51 cm<sup>3</sup> g<sup>-1</sup>, with 61% of the pore volume corresponding to micropores, provided an excellent CO<sub>2</sub> uptake of ca. 26 mmol g<sup>-1</sup> at 25 °C and 30 bar and a working capacity in the 30–1 bar range of 23 mmol g<sup>-1</sup>. The materials were also tested for CH<sub>4</sub> storage and showed CH<sub>4</sub> uptakes in the ~11–21 mmol g<sup>-1</sup> range at

25 °C and 65 bar. Thus, the equilibrium CO<sub>2</sub>/CH<sub>4</sub> adsorption ratio at 30 bar of the optimized material was 2.1. Later on, the same authors developed more economical N-doped porous carbons by using the monomer benzimidazole as precursor [45]. KOH activation was performed to generate porosity and to inhibit the sublimation of the precursor during the heat treatment through salt formation. Porous carbons with surface areas as high as 2500 m<sup>2</sup> g<sup>-1</sup> and pore volumes of up to 1.9 cm<sup>3</sup> g<sup>-1</sup> were synthesized in this way. N-doping in the 3–18 wt % range was also achieved. The material with the highest surface area, pore volume, and mesopore contribution (BIDC-3-700) showed the highest uptake, with a value of 28.1 mmol g<sup>-1</sup> at 25 °C and 30 bar, which almost matches that of the KOH-activated PANI hydrogel (see above). A good correlation ( $R^2 = 0.995$ ) was obtained between the excess and absolute uptakes at 30 bar and the volume of pores with a diameter smaller than 2.2 nm, confirming that micropores and small mesopores (2–4 nm) have a more pronounced effect at high pressures.

Very recently, Cox and Mokaya proved the colossal CO<sub>2</sub> capture capacity at high pressures of KOH-activated polypyrrole, another widely used N-rich polymer [170]. The material obtained under compactation, i.e., by compacting the mixture of polypyrrole and KOH at 740 MPa previous to the high temperature treatment (MPPY-4800), exhibited the highest CO<sub>2</sub> uptake reported to date for porous carbons, i.e., 37.2 mmol g<sup>-1</sup> at 25 °C/30 bar and 45.6 mmol g<sup>-1</sup> at 25 °C/40 bar, owing to the optimized combination of an ultra-high surface area (3934 m<sup>2</sup> g<sup>-1</sup>), pore volume (2.92 cm<sup>3</sup> g<sup>-1</sup>), and high mesoporosity (93%). KOH compactation seems therefore to be a powerful tool for boosting not only the CO<sub>2</sub> uptake of porous carbons at low pressure but also for high pressure applications. In order to prove the usefulness of the material for pre-combustion carbon capture, H<sub>2</sub> adsorption was also tested, and selectivity for CO<sub>2</sub>/H<sub>2</sub> mixtures with compositions similar to that of shifted-syngas was estimated using the IAST model. A CO<sub>2</sub>/H<sub>2</sub> selectivity  $\geq 18$  was estimated for a pressure of  $P \geq 40$  bar. This selectivity was higher than that of a microporous material used for comparison purposes ( $\sim 12$  for  $P \geq 20$  bar), which demonstrates the clear advantage of mesoporous carbons for removing CO<sub>2</sub> from syngas.

Also worthy of mention is the use of microporous polymers for the production of porous carbons with a good CO<sub>2</sub> adsorption capacity at high pressure. Li et al. synthesized a porous carbon (K-PAF-1-750) with a CO<sub>2</sub> uptake higher than 23 mmol g<sup>-1</sup> at  $P \geq 20$  bar and 25 °C by the KOH activation of a crystalline microporous polymer (PAF-1) [167]. The initial polymer also showed a high CO<sub>2</sub> uptake at high pressures (29.5 mmol g<sup>-1</sup> at 40 bar/25 °C). However, its structure was “soft,” which may be detrimental from the operation point of view. On the other hand, when the polymer was directly carbonized, the pores shrank and the surface area decreased to 1000 m<sup>2</sup> g<sup>-1</sup> [171]. These drawbacks however were circumvented by means of KOH activation. The activated material also exhibited a high CH<sub>4</sub> uptake of ca. 13 mmol g<sup>-1</sup> at 35 bar/25 °C, with the result that the equilibrium CO<sub>2</sub>/CH<sub>4</sub> adsorption ratio showed a value of 2.1 at this pressure, analogous to that of the KOH-activated benzimidazole-linked polymer (see above).

Another important characteristic of CO<sub>2</sub> sorbents affecting their practical application is its cost which has a direct bearing on the economic viability of CCS. Nevertheless, sophisticated carbon precursors such as MOFs have been explored for the purpose of producing CO<sub>2</sub> sorbents because of their advantageous characteristics. Thus, Srinivas et al. carbonized different MOFs at temperatures between 600 and 1100 °C, to produce hierarchical porous carbons (which combine micro-, meso-, and macropores) with surface areas of up to  $\sim 2700 \text{ m}^2 \text{ g}^{-1}$  and at the same time exceptionally high total pore volumes of up to  $5.5 \text{ cm}^3 \text{ g}^{-1}$  [43]. The best performing material, HPC5b2–1100, showed a CO<sub>2</sub> uptake of  $27.4 \text{ mmol g}^{-1}$  at 30 bar/27 °C (decreasing to around  $13 \text{ mmol g}^{-1}$  at 75 °C), without any sign of saturation owing to its ultra-large total pore volume (Fig. 11.15).

The works described so far clearly reveal the effectiveness of KOH in modulating and enhancing the gas storage properties of a variety of carbonaceous materials and polymers. As a consequence, it has also been studied as a tool to improve the gas storage properties of novel carbon structures such as carbon nanotubes (CNTs) or graphene/graphene oxide. CNTs are characterized by low surface areas and pore volumes ( $<500 \text{ m}^2 \text{ g}^{-1}$  and  $<0.4 \text{ cm}^3 \text{ g}^{-1}$ , respectively), which hampers their use in adsorption applications. However, Adeniran and Mokaya showed that KOH activation of low crystallinity CNTs yields highly porous CNT composites with surface areas of  $\sim 1500\text{--}3800 \text{ m}^2 \text{ g}^{-1}$  and pore volumes of  $0.83\text{--}2.98 \text{ cm}^3 \text{ g}^{-1}$  [168]. To be more specific, the materials synthesized under severer activation conditions, CN2800 and CN2900, with surface areas in the range of  $2600\text{--}2900 \text{ m}^2 \text{ g}^{-1}$  and pore volumes of  $\sim 1.6\text{--}1.9 \text{ cm}^3 \text{ g}^{-1}$ , 20–80% of which corresponds to mesopores, provided CO<sub>2</sub> uptakes of  $18\text{--}19.5 \text{ mmol g}^{-1}$  at 20 bar/25 °C. None of the CO<sub>2</sub>

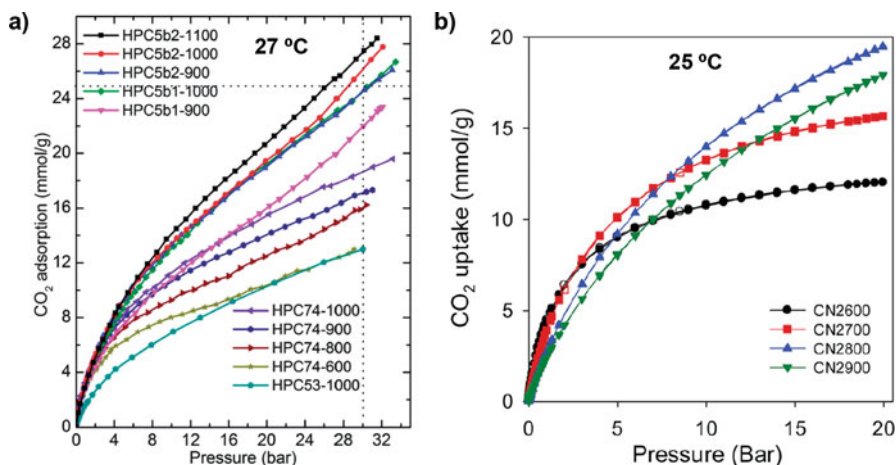


**Fig. 11.15** High pressure CO<sub>2</sub> adsorption isotherms of (a) hierarchical porous carbons fabricated by direct carbonization of different MOFs (Reproduced with permission from ref. [43] © 2014, Royal Society of Chemistry) and (b) CNT superstructures prepared by KOH activation (Reproduced with permission from Ref. [168] © 2015, Royal Society of Chemistry)

isotherms of these materials showed any sign of saturation at 20 bar, so that greater CO<sub>2</sub> uptakes could be achieved merely by increasing the pressure. It should be noted, however, that KOH activation was effective in this case because low crystallinity CNTs were used. When high crystallinity CNTs are used, only modest improvements in porosity are achieved [172]. Also, very severe activation conditions led to the loss of their tubular structure. Following a similar course of investigation, Srinivas et al. analyzed the production of high surface area carbons by the KOH chemical activation of a non-porous graphene oxide (GO) precursor [44]. They obtained porous carbons with surface areas in the 600–1900 m<sup>2</sup> g<sup>-1</sup> range and total pore volume of up to ca 1.7 cm<sup>3</sup> g<sup>-1</sup> and were able to tune the porosity parameters by regulating the activation temperature and the KOH/GO ratio. As usual, the more severe activation conditions yielded the materials with the highest surface areas values. These materials were also characterized by a hierarchical PSD in the micro-mesopore range. The best adsorbent provided a CO<sub>2</sub> uptake of 16.4 mmol CO<sub>2</sub> g<sup>-1</sup> at 20 bar/27 °C and a CH<sub>4</sub> uptake of ca. 11 at 35 bar/27 °C.

## 11.6 Conclusions and Perspectives

The aim of this chapter has been to show the potential of porous carbons for CO<sub>2</sub> adsorption at both low and high pressure, so that they can constitute an alternative to the current amine-based technology for carbon capture in a variety of applications (e.g., pre-combustion, post-combustion, natural gas upgrading). In addition, an effort has been made to provide a fundamental understanding of CO<sub>2</sub> adsorption on porous carbons and to show the important relationship between the pore structure of carbon and the amount of CO<sub>2</sub> that it can adsorb. In this way, useful guidelines have been provided for designing the porous structure of carbons with a view to specifically targeted CO<sub>2</sub> adsorption applications. However, in connection with the contribution of surface chemistry to CO<sub>2</sub> adsorption, there is still much controversy. The complexity arises from the need to synthesize materials with identical textural characteristics (PSD, surface area, and total pore volume) that differ only in their surface chemistry so that the precise contribution of surface chemistry can be ascertained. The issue is further clouded by the fact that carbon materials normally have a complex surface chemistry; they usually contain many kinds of oxygen groups, in addition to the specifically introduced nitrogen or sulfur groups.

It has been shown that porous carbons can be prepared from a variety of precursors, using a wide variety of synthesis methodologies. In spite of recent advances in porous carbon synthesis (nanocasting approaches, including hard- and soft-templating, CDCs, and MOFs), activation approaches continue to be the preferred choice for the production of porous carbons for reasons of scalability, simplicity, and cost. To date the most widely exploited approach for producing porous carbons with large CO<sub>2</sub> uptakes has been potassium hydroxide activation. On the other hand, biomass is regarded as the most suitable precursor from the point of view of sustainability, natural abundance, and cost. However, in order to

ensure the sustainability of the entire production process, greener and high-yield biomass transformation processes – alternatives to activation approaches – need to be developed. Such methodologies must aim at the precision-tailoring of the textural, structural, and chemical properties of the developed materials.

The evaluation of the CO<sub>2</sub> capture capacity of porous carbons (and other adsorbents) is normally carried out under equilibrium conditions and using pure gases. However, for the industrial deployment of this technology, simulated or real flue gas, shifted-syngas, and natural gas conditions should be studied in order to evaluate real CO<sub>2</sub> uptake under competitive conditions and its selectivity and stability in the presence of other components (e.g., water vapor or acidic gases). Furthermore, kinetics studies, although generally ignored, must be carried out since the process of carbon capture involves fast adsorption-desorption cycles.

**Acknowledgments** This work was financially supported by the FICYT Regional Project (GRUPIN14-102) and the Spanish MINECO-FEDER (CTQ2015-63552-R).

## References

1. Agency IE (2016) CO<sub>2</sub> emissions from fossil fuel combustion. OECD, Paris
2. Administration Noaa (2017) <https://www.esrl.noaa.gov/gmd/ccgg/trends/>
3. Agency IE (2016) World energy outlook. International Energy Agency, Paris
4. Rao AB, Rubin ES (2002) A technical, economic, and environmental assessment of amine-based CO<sub>2</sub> capture technology for power plant greenhouse gas control. *Environ Sci Technol* 36(20):4467–4475. <https://doi.org/10.1021/es0158861>
5. Aaron D, Tsouris C (2005) Separation of CO<sub>2</sub> from flue gas: a review. *Sep Sci Technol* 40(1–3):321–348. <https://doi.org/10.1081/SS-200042244>
6. Morris RE, Wheatley PS (2008) Gas storage in nanoporous materials. *Angew Chem Int Ed* 47(27):4966–4981. <https://doi.org/10.1002/anie.200703934>
7. Alonso A, Moral-Vico J, Abo Markeb A, Busquets-Fité M, Komilis D, Puentes V, Sánchez A, Font X (2017) Critical review of existing nanomaterial adsorbents to capture carbon dioxide and methane. *Sci Total Environ* 595(Suppl C):51–62. <https://doi.org/10.1016/j.scitotenv.2017.03.229>
8. Zhao Y, Liu X, Han Y (2015) Microporous carbonaceous adsorbents for CO<sub>2</sub> separation via selective adsorption. *RSC Adv* 5(38):30310–30330. <https://doi.org/10.1039/C5RA00569H>
9. X-q Z, Li W-c, Lu A-h (2015) Designed porous carbon materials for efficient CO<sub>2</sub> adsorption and separation. *New Carbon Mater* 30(6):481–501. [https://doi.org/10.1016/S1872-5805\(15\)60203-7](https://doi.org/10.1016/S1872-5805(15)60203-7)
10. Patel HA, Byun J, Yavuz CT (2016) Carbon dioxide capture adsorbents: chemistry and methods. *Chem Sus Chem*. <https://doi.org/10.1002/cssc.201601545>
11. Ling J, Ntiamoah A, Xiao P, Xu D, Webley P, Zhai Y (2014) Overview of CO<sub>2</sub> capture from flue gas streams by vacuum pressure swing adsorption technology. *Austin J Chem Eng* 1(2):1–7
12. Riboldi L, Bolland O (2016) Determining the potentials of PSA processes for CO<sub>2</sub> capture in Integrated Gasification Combined Cycle (IGCC). *Energy Procedia* 86:294–303. <https://doi.org/10.1016/j.egypro.2016.01.030>
13. Riboldi L, Bolland O (2015) Evaluating pressure swing adsorption as a CO<sub>2</sub> separation technique in coal-fired power plants. *Int J Greenhouse Gas Control* 39:1–16. <https://doi.org/10.1016/j.ijggc.2015.02.001>

14. Franklin RE (1951) Crystallite growth in graphitizing and non-graphitizing carbons. *Proc R Soc Lond A Math Phys Sci* 209(1097):196–218. <https://doi.org/10.1098/rspa.1951.0197>
15. Gregg SJ, Sing KSW (1991) Adsorption, surface area and porosity, vol Book, Whole. Academic Press, London [etc.]
16. Patrick JW (1995) Porosity in carbons: characterization and applications. Wiley, London
17. Everett DH, Powl JC (1976) Adsorption in slit-like and cylindrical micropores in the Henry's law region. A model for the microporosity of carbons. *J Chem Soc Faraday Trans 1* 72(0):619–636. <https://doi.org/10.1039/F19767200619>
18. Yin YF, McEnaney B, Mays TJ (1998) Dependence of GCEMC simulations of nitrogen adsorption on activated carbons on input parameters. *Carbon* 36(10):1425–1432. [https://doi.org/10.1016/S0008-6223\(98\)00134-1](https://doi.org/10.1016/S0008-6223(98)00134-1)
19. Cinke M, Li J, Bauschlicher CW, Ricca A, Meyyappan M (2003) CO<sub>2</sub> adsorption in single-walled carbon nanotubes. *Chem Phys Lett* 376(5):761–766
20. Montoya A, Mondragon F, Truong TN (2003) CO<sub>2</sub> adsorption on carbonaceous surfaces: a combined experimental and theoretical study. *Carbon* 41(1):29–39
21. Liu Y, Wilcox J (2012) Effects of surface heterogeneity on the adsorption of CO<sub>2</sub> in microporous carbons. *Environ Sci Technol* 46(3):1940–1947. <https://doi.org/10.1021/es204071g>
22. Cui X, Bustin RM, Dipple G (2004) Selective transport of CO<sub>2</sub>, CH<sub>4</sub>, and N<sub>2</sub> in coals: insights from modeling of experimental gas adsorption data. *Fuel* 83(3):293–303. <https://doi.org/10.1016/j.fuel.2003.09.001>
23. Rouquerol F, Rouquerol J, Sing K (1999) Adsorption by powders and porous solids: principles, methodology and applications. vol Book, Whole. Academic Press, San Diego
24. Dubinin M (1966) Chemistry and physics of carbon, vol 2. Marcel Dekker, New York, p 51
25. Dubinin M (1967) Adsorption in micropores. *J Colloid Interface Sci* 23(4):487–499
26. Dubinin M (1960) The potential theory of adsorption of gases and vapors for adsorbents with energetically nonuniform surfaces. *Chem Rev* 60(2):235–241
27. Bering B, Dubinin M, Serpinsky V (1966) Theory of volume filling for vapor adsorption. *J Colloid Interface Sci* 21(4):378–393
28. Dubinin MM, Plavnik G (1968) Microporous structures of carbonaceous adsorbents. *Carbon* 6(2):183–192
29. Stoeckli H, Rebstein P, Ballerini L (1990) On the assessment of microporosity in active carbons, a comparison of theoretical and experimental data. *Carbon* 28(6):907–909
30. Silvestre-Albero J, Wahby A, Sepulveda-Escribano A, Martínez-Escandell M, Kaneko K, Rodríguez-Reinoso F (2011) Ultrahigh CO<sub>2</sub> adsorption capacity on carbon molecular sieves at room temperature. *Chem Commun* 47(24):6840–6842. <https://doi.org/10.1039/C1CC11618E>
31. Zhang Z, Zhou J, Xing W, Xue Q, Yan Z, Zhuo S, Qiao SZ (2013) Critical role of small micropores in high CO<sub>2</sub> uptake. *Phys Chem Chem Phys* 15(7):2523–2529. <https://doi.org/10.1039/C2CP44436D>
32. Zhou J, Li Z, Xing W, Shen H, Bi X, Zhu T, Qiu Z, Zhuo S (2016) A new approach to tuning carbon ultramicropore size at Sub-Angstrom level for maximizing specific capacitance and CO<sub>2</sub> uptake. *Adv Funct Mater* 26(44):7955–7964. <https://doi.org/10.1002/adfm.201601904>
33. Lee JH, Kwac K, Lee HJ, Lim SY, Jung DS, Jung Y, Choi JW (2016) Optimal activation of porous carbon for high performance CO<sub>2</sub> capture. *Chem Nano Mat* 2(6):528–533. <https://doi.org/10.1002/cnma.201600082>
34. Adeniran B, Mokaya R (2016) Is N-doping in porous carbons beneficial for CO<sub>2</sub> storage? Experimental demonstration of the relative effects of pore size and N-doping. *Chem Mater* 28(3):994–1001. <https://doi.org/10.1021/acs.chemmater.5b05020>
35. Wahby A, Ramos-Fernández JM, Martínez-Escandell M, Sepúlveda-Escribano A, Silvestre-Albero J, Rodríguez-Reinoso F (2010) High-surface-area carbon molecular sieves for selective CO<sub>2</sub> adsorption. *Chem Sus Chem* 3(8):974–981. <https://doi.org/10.1002/cssc.201000083>
36. Martín CF, Plaza MG, Pis JJ, Rubiera F, Pevida C, Centeno TA (2010) On the limits of CO<sub>2</sub> capture capacity of carbons. *Sep Purif Technol* 74(2):225–229. <https://doi.org/10.1016/j.seppur.2010.06.009>

37. Presser V, McDonough J, Yeon SH, Gogotsi Y (2011) Effect of pore size on carbon dioxide sorption by carbide derived carbon. *Energy Environ Sci* 4(8):3059–3066
38. Wei H, Deng S, Hu B, Chen Z, Wang B, Huang J, Yu G (2012) Granular bamboo-derived activated carbon for high CO<sub>2</sub> adsorption: the dominant role of narrow micropores. *ChemSusChem* 5(12):2354–2360. <https://doi.org/10.1002/cssc.201200570>
39. Sevilla M, Parra JB, Fuertes AB (2013) Assessment of the role of micropore size and N-doping in CO<sub>2</sub> capture by porous carbons. *ACS Appl Mater Interfaces* 5(13):6360–6368. <https://doi.org/10.1021/am401423b>
40. Wickramaratne NP, Jaroniec M (2013) Importance of small micropores in CO<sub>2</sub> capture by phenolic resin-based activated carbon spheres. *J Mater Chem A* 1(1):112–116. <https://doi.org/10.1039/C2TA00388K>
41. Cazorla-Amorós D, Alcañiz-Monge J, Linares-Solano A (1996) Characterization of activated carbon fibers by CO<sub>2</sub> adsorption. *Langmuir* 12(11):2820–2824. <https://doi.org/10.1021/la960022s>
42. Coromina HM, Walsh DA, Mokaya R (2016) Biomass-derived activated carbon with simultaneously enhanced CO<sub>2</sub> uptake for both pre and post combustion capture applications. *J Mater Chem A* 4(1):280–289. <https://doi.org/10.1039/C5TA09202G>
43. Srinivas G, Krungleviciute V, Guo Z-X, Yildirim T (2014) Exceptional CO<sub>2</sub> capture in a hierarchically porous carbon with simultaneous high surface area and pore volume. *Energy Environ Sci* 7(1):335–342. <https://doi.org/10.1039/C3EE42918K>
44. Srinivas G, Burrell J, Yildirim T (2012) Graphene oxide derived carbons (GODCs): synthesis and gas adsorption properties. *Energy Environ Sci* 5(4):6453–6459. <https://doi.org/10.1039/C2EE21100A>
45. Ashourirad B, Arab P, Islamoglu T, Cychosz KA, Thommes M, El-Kaderi HM (2016) A cost-effective synthesis of heteroatom-doped porous carbons as efficient CO<sub>2</sub> sorbents. *J Mater Chem A* 4(38):14693–14702. <https://doi.org/10.1039/C6TA06251B>
46. He J, To JWF, Psarras PC, Yan H, Atkinson T, Holmes RT, Nordlund D, Bao Z, Wilcox J (2016) Tunable polyaniline-based porous carbon with ultrahigh surface area for CO<sub>2</sub> capture at elevated pressure. *Adv Energy Mater* 6(14):1502491-n/a. <https://doi.org/10.1002/aenm.201502491>
47. Sevilla M, Al-Jumaily ASM, Fuertes AB, Mokaya R (2018) Optimization of the pore structure of biomass-based carbons in relation to their use for CO<sub>2</sub> capture under low- and high-pressure regimes. *ACS Appl Mater Interfaces* 10(2):1623–1633. <https://doi.org/10.1021/acsami.7b10433>
48. Stein A, Wang Z, Fierke MA (2009) Functionalization of porous carbon materials with designed pore architecture. *Adv Mater* 21(3):265–293. <https://doi.org/10.1002/adma.200801492>
49. Zheng Y, Jiao Y, Li LH, Xing T, Chen Y, Jaroniec M, Qiao SZ (2014) Toward design of synergistically active carbon-based catalysts for electrocatalytic hydrogen evolution. *ACS Nano* 8(5):5290–5296. <https://doi.org/10.1021/nn501434a>
50. Shen W, Fan W (2013) Nitrogen-containing porous carbons: synthesis and application. *J Mater Chem A* 1(4):999–1013. <https://doi.org/10.1039/C2TA00028H>
51. Hu C, Dai L (2016) Carbon-based metal-free catalysts for electrocatalysis beyond the ORR. *Angew Chem Int Ed* 55(39):11736–11758. <https://doi.org/10.1002/anie.201509982>
52. Liu X, Dai L (2016) Carbon-based metal-free catalysts. *Nat Rev Mater* 1:16064. <https://doi.org/10.1038/natrevmats.2016.64>
53. Tang C, Zhang Q (2017) Nanocarbon for oxygen reduction electrocatalysis: dopants, edges, and defects. *Adv Mater* 29(13):1604103. <https://doi.org/10.1002/adma.201604103>
54. Shao M, Chang Q, Dodelet J-P, Chenitz R (2016) Recent advances in electrocatalysts for oxygen reduction reaction. *Chem Rev* 116(6):3594–3657. <https://doi.org/10.1021/acs.chemrev.5b00462>
55. Deng Y, Xie Y, Zou K, Ji X (2016) Review on recent advances in nitrogen-doped carbons: preparations and applications in supercapacitors. *J Mater Chem A* 4(4):1144–1173. <https://doi.org/10.1039/C5TA08620E>

56. Wu P, Du P, Zhang H, Cai C (2013) Microscopic effects of the bonding configuration of nitrogen-doped graphene on its reactivity toward hydrogen peroxide reduction reaction. *Phys Chem Chem Phys* 15(18):6920–6928. <https://doi.org/10.1039/C3CP50900A>
57. Wang L, Yang RT (2012) Significantly increased CO<sub>2</sub> adsorption performance of nanostructured templated carbon by tuning surface area and nitrogen doping. *J Phys Chem C* 116(1):1099–1106. <https://doi.org/10.1021/jp2100446>
58. Zhao Y, Zhao L, Yao KX, Yang Y, Zhang Q, Han Y (2012) Novel porous carbon materials with ultrahigh nitrogen contents for selective CO<sub>2</sub> capture. *J Mater Chem* 22(37):19726–19731. <https://doi.org/10.1039/C2JM33091A>
59. Liu L, Deng Q-F, Hou X-X, Yuan Z-Y (2012) User-friendly synthesis of nitrogen-containing polymer and microporous carbon spheres for efficient CO<sub>2</sub> capture. *J Mater Chem* 22(31):15540–15548. <https://doi.org/10.1039/c2jm31441j>
60. Wu Z, Webley PA, Zhao D (2012) Post-enrichment of nitrogen in soft-templated ordered mesoporous carbon materials for highly efficient phenol removal and CO<sub>2</sub> capture. *J Mater Chem* 22(22):11379–11389. <https://doi.org/10.1039/C2JM16183D>
61. Hao G-P, Li W-C, Qian D, Wang G-H, Zhang W-P, Zhang T, Wang A-Q, Schüth F, Bongard H-J, Lu A-H (2011) Structurally designed synthesis of mechanically stable poly(benzoxazine-co-resol)-based porous carbon monoliths and their application as high-performance CO<sub>2</sub> capture sorbents. *J Am Chem Soc* 133(29):11378–11388. <https://doi.org/10.1021/ja203857g>
62. Plaza MG, Pevida C, Arias B, Feroso J, Casal MD, Martín CF, Rubiera F, Pis JJ (2009) Development of low-cost biomass-based adsorbents for postcombustion CO<sub>2</sub> capture. *Fuel* 88(12):2442–2447. <https://doi.org/10.1016/j.fuel.2009.02.025>
63. Xing W, Liu C, Zhou Z, Zhang L, Zhou J, Zhuo S, Yan Z, Gao H, Wang G, Qiao SZ (2012) Superior CO<sub>2</sub> uptake of N-doped activated carbon through hydrogen-bonding interaction. *Energy Environ Sci* 5(6):7323–7327. <https://doi.org/10.1039/C2EE21653A>
64. Gutierrez MC, Carriazo D, Ania CO, Parra JB, Ferrer ML, del Monte F (2011) Deep eutectic solvents as both precursors and structure directing agents in the synthesis of nitrogen doped hierarchical carbons highly suitable for CO<sub>2</sub> capture. *Energy Environ Sci* 4(9):3535–3544. <https://doi.org/10.1039/C1EE01463C>
65. Zhao Y, Liu X, Yao KX, Zhao L, Han Y (2012) Superior capture of CO<sub>2</sub> achieved by introducing extra-framework cations into N-doped microporous carbon. *Chem Mater* 24(24):4725–4734. <https://doi.org/10.1021/cm303072n>
66. Zhong M, Natesakhawat S, Baltrus JP, Luebke D, Nulwala H, Matyjaszewski K, Kowalewski T (2012) Copolymer-templated nitrogen-enriched porous nanocarbons for CO<sub>2</sub> capture. *Chem Commun* 48(94):11516–11518. <https://doi.org/10.1039/C2CC36652E>
67. Nandi M, Okada K, Dutta A, Bhaumik A, Maruyama J, Derks D, Uyama H (2012) Unprecedented CO<sub>2</sub> uptake over highly porous N-doped activated carbon monoliths prepared by physical activation. *Chem Commun* 48(83):10283–10285. <https://doi.org/10.1039/C2CC35334B>
68. Thote JA, Iyer KS, Chatti R, Labhsetwar NK, Biniwale RB, Rayalu SS (2010) In situ nitrogen enriched carbon for carbon dioxide capture. *Carbon* 48(2):396–402. <https://doi.org/10.1016/j.carbon.2009.09.042>
69. Przepiórski J, Skrodziewicz M, Morawski AW (2004) High temperature ammonia treatment of activated carbon for enhancement of CO<sub>2</sub> adsorption. *Appl Surf Sci* 225(1):235–242. <https://doi.org/10.1016/j.apsusc.2003.10.006>
70. Hao G-P, Li W-C, Qian D, Lu A-H (2010) Rapid synthesis of nitrogen-doped porous carbon monolith for CO<sub>2</sub> capture. *Adv Mater* 22(7):853–857. <https://doi.org/10.1002/adma.200903765>
71. Wei J, Zhou D, Sun Z, Deng Y, Xia Y, Zhao D (2013) A controllable synthesis of rich nitrogen-doped ordered mesoporous carbon for CO<sub>2</sub> capture and supercapacitors. *Adv Funct Mater* 23(18):2322–2328. <https://doi.org/10.1002/adfm.201202764>
72. Wang J, Senkowska I, Oschatz M, Lohe MR, Borchardt L, Heerwig A, Liu Q, Kaskel S (2013) Imine-linked polymer-derived nitrogen-doped microporous carbons with excellent CO<sub>2</sub> capture properties. *ACS Appl Mater Interfaces* 5(8):3160–3167. <https://doi.org/10.1021/am400059t>

73. Sethia G, Sayari A (2015) Comprehensive study of ultra-microporous nitrogen-doped activated carbon for CO<sub>2</sub> capture. *Carbon* 93(Suppl C):68–80. <https://doi.org/10.1016/j.carbon.2015.05.017>
74. Gong J, Lin H, Antonietti M, Yuan J (2016) Nitrogen-doped porous carbon nanosheets derived from poly(ionic liquids): hierarchical pore structures for efficient CO<sub>2</sub> capture and dye removal. *J Mater Chem A* 4(19):7313–7321. <https://doi.org/10.1039/C6TA01945E>
75. Chen J, Yang J, Hu G, Hu X, Li Z, Shen S, Radosz M, Fan M (2016) Enhanced CO<sub>2</sub> capture capacity of nitrogen-doped biomass-derived porous carbons. *ACS Sustain Chem Eng* 4(3):1439–1445. <https://doi.org/10.1021/acssuschemeng.5b01425>
76. Wang Y, Zou H, Zeng S, Pan Y, Wang R, Wang X, Sun Q, Zhang Z, Qiu S (2015) A one-step carbonization route towards nitrogen-doped porous carbon hollow spheres with ultrahigh nitrogen content for CO<sub>2</sub> adsorption. *Chem Commun* 51(62):12423–12426. <https://doi.org/10.1039/C5CC03945B>
77. Yang M, Guo L, Hu G, Hu X, Xu L, Chen J, Dai W, Fan M (2015) Highly cost-effective nitrogen-doped porous coconut shell-based CO<sub>2</sub> sorbent synthesized by combining ammoxidation with KOH activation. *Environ Sci Technol* 49(11):7063–7070. <https://doi.org/10.1021/acs.est.5b01311>
78. Sánchez-Sánchez Á, Suárez-García F, Martínez-Alonso A, Tascón JMD (2014) Influence of porous texture and surface chemistry on the CO<sub>2</sub> adsorption capacity of porous carbons: acidic and basic site interactions. *ACS App Mater Interfaces* 6(23):21237–21247. <https://doi.org/10.1021/am506176e>
79. Babu DJ, Bruns M, Schneider R, Gerthsen D, Schneider JJ (2017) Understanding the influence of N-doping on the CO<sub>2</sub> adsorption characteristics in carbon nanomaterials. *J Phys Chem C* 121(1):616–626. <https://doi.org/10.1021/acs.jpcc.6b11686>
80. Kumar KV, Preuss K, Lu L, Guo ZX, Titirici MM (2015) Effect of nitrogen doping on the CO<sub>2</sub> adsorption behavior in nanoporous carbon structures: a molecular simulation study. *J Phys Chem C* 119(39):22310–22321. <https://doi.org/10.1021/acs.jpcc.5b06017>
81. D'Alessandro DM, Smit B, Long JR (2010) Carbon dioxide capture: prospects for new materials. *Angew Chem Int Ed* 49(35):6058–6082
82. Ko YG, Shin SS, Choi US (2011) Primary, secondary, and tertiary amines for CO<sub>2</sub> capture: designing for mesoporous CO<sub>2</sub> adsorbents. *J Colloid Interface Sci* 361(2):594–602. <https://doi.org/10.1016/j.jcis.2011.03.045>
83. Zelenak V, Halamova D, Gaberova L, Bloch E, Llewellyn P (2008) Amine-modified SBA-12 mesoporous silica for carbon dioxide capture: effect of amine basicity on sorption properties. *Microporous Mesoporous Mater* 116(1):358–364. <https://doi.org/10.1016/j.micromeso.2008.04.023>
84. Donaldson TL, Nguyen YN (1980) Carbon dioxide reaction kinetics and transport in aqueous amine membranes. *Ind Eng Chem Fundam* 19(3):260–266. <https://doi.org/10.1021/i160075a005>
85. Gholidoust A, Atkinson JD, Hashisho Z (2017) Enhancing CO<sub>2</sub> adsorption via amine-impregnated activated carbon from oil sands coke. *Energy Fuel* 31(2):1756–1763. <https://doi.org/10.1021/acs.energyfuels.6b02800>
86. Gibson JAA, Gromov AV, Brandani S, Campbell EEB (2015) The effect of pore structure on the CO<sub>2</sub> adsorption efficiency of polyamine impregnated porous carbons. *Microporous Mesoporous Mater* 208(Suppl C):129–139. <https://doi.org/10.1016/j.micromeso.2015.01.044>
87. Plaza MG, Pevida C, Arenillas A, Rubiera F, Pis JJ (2007) CO<sub>2</sub> capture by adsorption with nitrogen enriched carbons. *Fuel* 86(14):2204–2212. <https://doi.org/10.1016/j.fuel.2007.06.001>
88. Maroto-Valer MM, Tang Z, Zhang Y (2005) CO<sub>2</sub> capture by activated and impregnated anthracites. *Fuel Process Technol* 86(14):1487–1502. <https://doi.org/10.1016/j.fuproc.2005.01.003>
89. Keller L, Ohs B, Lenhart J, Abduly L, Blanke P, Wessling M (2018) High capacity polyethylenimine impregnated microtubes made of carbon nanotubes for CO<sub>2</sub> capture. *Carbon* 126(Suppl C):338–345. <https://doi.org/10.1016/j.carbon.2017.10.023>

90. Khalil SH, Aroua MK, Daud WMAW (2012) Study on the improvement of the capacity of amine-impregnated commercial activated carbon beds for CO<sub>2</sub> adsorbing. *Chem Eng J* 183(Suppl C):15–20. <https://doi.org/10.1016/j.cej.2011.12.011>
91. Lee S-Y, Park S-J (2015) A review on solid adsorbents for carbon dioxide capture. *J Ind Eng Chem* 23(Suppl C):1–11. <https://doi.org/10.1016/j.jiec.2014.09.001>
92. Travis W, Gadipelli S, Guo Z (2015) Superior CO<sub>2</sub> adsorption from waste coffee ground derived carbons. *RSC Adv* 5(37):29558–29562. <https://doi.org/10.1039/C4RA13026J>
93. Sevilla M, Fuertes AB (2011) Sustainable porous carbons with a superior performance for CO<sub>2</sub> capture. *Energy Environ Sci* 4(5):1765–1771
94. Sevilla M, Falco C, Titirici M-M, Fuertes AB (2012) High-performance CO<sub>2</sub> sorbents from algae. *RSC Adv* 2(33):12792–12797
95. Li D, Ma T, Zhang R, Tian Y, Qiao Y (2015) Preparation of porous carbons with high low-pressure CO<sub>2</sub> uptake by KOH activation of rice husk char. *Fuel* 139(Suppl C):68–70. <https://doi.org/10.1016/j.fuel.2014.08.027>
96. Lu A-H, Hao G-P, Zhang X-Q (2014) Porous carbons for carbon dioxide capture. In: *Porous materials for carbon dioxide capture*. Springer, Berlin, pp 15–77
97. Titirici M-M, White RJ, Falco C, Sevilla M (2012) Black perspectives for a green future: hydrothermal carbons for environment protection and energy storage. *Energy Environ Sci* 5(5):6796–6822. <https://doi.org/10.1039/c2ee21166a>
98. Sevilla M, Mokaya R (2014) Energy storage applications of activated carbons: supercapacitors and hydrogen storage. *Energy Environ Sci* 7(4):1250–1280. <https://doi.org/10.1039/C3EE43525C>
99. Wang J, Kaskel S (2012) KOH activation of carbon-based materials for energy storage. *J Mater Chem* 22(45):23710–23725. <https://doi.org/10.1039/c2jm34066f>
100. Lillo-Ródenas MA, Cazorla-Amorós D, Linares-Solano A (2003) Understanding chemical reactions between carbons and NaOH and KOH: an insight into the chemical activation mechanism. *Carbon* 41(2):267–275. [https://doi.org/10.1016/S0008-6223\(02\)00279-8](https://doi.org/10.1016/S0008-6223(02)00279-8)
101. Lozano-Castelló D, Calo JM, Cazorla-Amorós D, Linares-Solano A (2007) Carbon activation with KOH as explored by temperature programmed techniques, and the effects of hydrogen. *Carbon* 45(13):2529–2536. <https://doi.org/10.1016/j.carbon.2007.08.021>
102. Otowa T, Tanibata R, Itoh M (1993) Production and adsorption characteristics of MAXSORB: high-surface-area active carbon. *Gas Sep Purif* 7(4):241–245. [https://doi.org/10.1016/0950-4214\(93\)80024-Q](https://doi.org/10.1016/0950-4214(93)80024-Q)
103. Balahmar N, Al-Jumaily AS, Mokaya R (2017) Biomass to porous carbon in one step: directly activated biomass for high performance CO<sub>2</sub> storage. *J Mater Chem A* 5(24):12330–12339. <https://doi.org/10.1039/C7TA01722G>
104. Wang R, Wang P, Yan X, Lang J, Peng C, Xue Q (2012) Promising porous carbon derived from celctue leaves with outstanding supercapacitance and CO<sub>2</sub> capture performance. *ACS Appl Mater Interfaces* 4(11):5800–5806. <https://doi.org/10.1021/am302077c>
105. Serafin J, Narkiewicz U, Morawski AW, Wróbel RJ, Michalkiewicz B (2017) Highly microporous activated carbons from biomass for CO<sub>2</sub> capture and effective micropores at different conditions. *J CO<sub>2</sub> Util* 18(Suppl C):73–79. <https://doi.org/10.1016/j.jcou.2017.01.006>
106. Alabadi A, Razzaque S, Yang Y, Chen S, Tan B (2015) Highly porous activated carbon materials from carbonized biomass with high CO<sub>2</sub> capturing capacity. *Chem Eng J* 281(Suppl C):606–612. <https://doi.org/10.1016/j.cej.2015.06.032>
107. Li K, Tian S, Jiang J, Wang J, Chen X, Yan F (2016) Pine cone shell-based activated carbon used for CO<sub>2</sub> adsorption. *J Mater Chem A* 4(14):5223–5234. <https://doi.org/10.1039/C5TA09908K>
108. Moussa M, Bader N, Querejeta N, Durán I, Pevida C, Ouederni A (2017) Toward sustainable hydrogen storage and carbon dioxide capture in post-combustion conditions. *J Environ Chem Eng* 5(2):1628–1637. <https://doi.org/10.1016/j.jece.2017.03.003>
109. Singh G, Kim IY, Lakhi KS, Srivastava P, Naidu R, Vinu A (2017) Single step synthesis of activated bio-carbons with a high surface area and their excellent CO<sub>2</sub> adsorption capacity. *Carbon* 116(Suppl C):448–455. <https://doi.org/10.1016/j.carbon.2017.02.015>

110. Sangchoom W, Mokaya R (2015) Valorization of lignin waste: carbons from hydrothermal carbonization of renewable lignin as superior sorbents for CO<sub>2</sub> and hydrogen storage. *ACS Sustain Chem Eng* 3(7):1658–1667. <https://doi.org/10.1021/acssuschemeng.5b00351>
111. Parshetti GK, Chowdhury S, Balasubramanian R (2015) Biomass derived low-cost microporous adsorbents for efficient CO<sub>2</sub> capture. *Fuel* 148(Suppl C):246–254. <https://doi.org/10.1016/j.fuel.2015.01.032>
112. Balahmar N, Mitchell AC, Mokaya R (2015) Generalized mechanochemical synthesis of biomass-derived sustainable carbons for high performance CO<sub>2</sub> storage. *Adv Energy Mater* 5(22):1500867. <https://doi.org/10.1002/aenm.201500867>
113. Fan X, Zhang L, Zhang G, Shu Z, Shi J (2013) Chitosan derived nitrogen-doped microporous carbons for high performance CO<sub>2</sub> capture. *Carbon* 61(Suppl C):423–430. <https://doi.org/10.1016/j.carbon.2013.05.026>
114. Vargas DP, Giraldo L, Silvestre-Albero J, Moreno-Piraján JC (2011) CO<sub>2</sub> adsorption on binderless activated carbon monoliths. *Adsorption* 17(3):497–504. <https://doi.org/10.1007/s10450-010-9309-z>
115. Vargas DP, Giraldo L, Moreno-Piraján J (2012) CO<sub>2</sub> adsorption on granular and monolith carbonaceous materials. *J Anal Appl Pyrolysis* 96:146–152
116. Bae J-S, Su S (2013) Macadamia nut shell-derived carbon composites for post combustion CO<sub>2</sub> capture. *Int J Greenhouse Gas Control* 19(Suppl C):174–182. <https://doi.org/10.1016/j.ijggc.2013.08.013>
117. Plaza MG, González AS, Pis JJ, Rubiera F, Pevida C (2014) Production of microporous biochars by single-step oxidation: effect of activation conditions on CO<sub>2</sub> capture. *Appl Energy* 114(Suppl C):551–562. <https://doi.org/10.1016/j.apenergy.2013.09.058>
118. Sevilla M, Fuertes AB, Mokaya R (2011) High density hydrogen storage in superactivated carbons from hydrothermally carbonized renewable organic materials. *Energy Environ Sci* 4(4):1400–1410. <https://doi.org/10.1039/C0EE00347F>
119. Sevilla M, Yu L, Ania CO, Titirici M-M (2014) Supercapacitive behavior of two glucose-derived microporous carbons: direct pyrolysis versus hydrothermal carbonization. *Chem Electro Chem* 1(12):2138–2145. <https://doi.org/10.1002/celec.201402233>
120. Jagtoyen M, Derbyshire F (1998) Activated carbons from yellow poplar and white oak by H<sub>3</sub>PO<sub>4</sub> activation. *Carbon* 36(7):1085–1097. [https://doi.org/10.1016/S0008-6223\(98\)00082-7](https://doi.org/10.1016/S0008-6223(98)00082-7)
121. Molina-Sabio M, Rodríguez-Reinoso F (2004) Role of chemical activation in the development of carbon porosity. *Colloids Surf A Physicochem Eng Asp* 241(1–3):15–25. <https://doi.org/10.1016/j.colsurfa.2004.04.007>
122. Ello AS, de Souza LKC, Trokourey A, Jaroniec M (2013) Coconut shell-based microporous carbons for CO<sub>2</sub> capture. *Microporous Mesoporous Mater* 180(Suppl C):280–283. <https://doi.org/10.1016/j.micromeso.2013.07.008>
123. Plaza MG, Pevida C, Martín CF, Feroso J, Pis JJ, Rubiera F (2010) Developing almond shell-derived activated carbons as CO<sub>2</sub> adsorbents. *Sep Purif Technol* 71(1):102–106. <https://doi.org/10.1016/j.seppur.2009.11.008>
124. Xiong Z, Shihong Z, Haiping Y, Tao S, Yingquan C, Hanping C (2013) Influence of NH<sub>3</sub>/CO<sub>2</sub> modification on the characteristic of biochar and the CO<sub>2</sub> capture. *Bioenergy Res* 6(4):1147–1153
125. Sevilla M, Valle-Vigón P, Fuertes AB (2011) N-doped polypyrrole-based porous carbons for CO<sub>2</sub> capture. *Adv Funct Mater* 21(14):2781–2787. <https://doi.org/10.1002/adfm.201100291>
126. Szcześniak B, Osuchowski Ł, Choma J, Jaroniec M (2017) Highly porous carbons obtained by activation of polypyrrole/reduced graphene oxide as effective adsorbents for CO<sub>2</sub>, H<sub>2</sub> and C<sub>6</sub>H<sub>6</sub>. *J Porous Mater* 25:1–7
127. Meng L-Y, Park S-J (2014) One-pot synthetic method to prepare highly N-doped nanoporous carbons for CO<sub>2</sub> adsorption. *Mater Chem Phys* 143(3):1158–1163. <https://doi.org/10.1016/j.matchemphys.2013.11.016>
128. Silvestre-Albero A, Silvestre-Albero J, Martínez-Escandell M, Rodríguez-Reinoso F (2014) Micro/mesoporous activated carbons derived from polyaniline: promising candidates for CO<sub>2</sub> adsorption. *Ind Eng Chem Res* 53(40):15398–15405. <https://doi.org/10.1021/ie5013129>

129. Wickramaratne NP, Jaroniec M (2013) Activated carbon spheres for CO<sub>2</sub> adsorption. *ACS Appl Mater Interfaces* 5(5):1849–1855. <https://doi.org/10.1021/am400112m>
130. Grundy M, Ye Z (2014) Cross-linked polymers of diethynylbenzene and phenylacetylene as new polymer precursors for high-yield synthesis of high-performance nanoporous activated carbons for supercapacitors, hydrogen storage, and CO<sub>2</sub> capture. *J Mater Chem A* 2(47):20316–20330. <https://doi.org/10.1039/C4TA04038D>
131. Carriazo D, Serrano MC, Gutierrez MC, Ferrer ML, del Monte F (2012) Deep-eutectic solvents playing multiple roles in the synthesis of polymers and related materials. *Chem Soc Rev* 41(14):4996–5014. <https://doi.org/10.1039/C2CS15353J>
132. del Monte F, Carriazo D, Serrano MC, Gutiérrez MC, Ferrer ML (2014) Deep eutectic solvents in polymerizations: a greener alternative to conventional syntheses. *ChemSusChem* 7(4):999–1009. <https://doi.org/10.1002/cssc.201300864>
133. Patino J, Gutierrez MC, Carriazo D, Ania CO, Fierro JLG, Ferrer ML, del Monte F (2014) DES assisted synthesis of hierarchical nitrogen-doped carbon molecular sieves for selective CO<sub>2</sub> versus N<sub>2</sub> adsorption. *J Mater Chem A* 2(23):8719–8729. <https://doi.org/10.1039/C4TA00562G>
134. Patino J, Gutierrez MC, Carriazo D, Ania CO, Parra JB, Ferrer ML, Fd M (2012) Deep eutectic assisted synthesis of carbon adsorbents highly suitable for low-pressure separation of CO<sub>2</sub>-CH<sub>4</sub> gas mixtures. *Energy Environ Sci* 5(9):8699–8707. <https://doi.org/10.1039/C2EE22029F>
135. Zhang S, Miran MS, Ikoma A, Dokko K, Watanabe M (2014) Protic ionic liquids and salts as versatile carbon precursors. *J Am Chem Soc* 136(5):1690–1693. <https://doi.org/10.1021/ja411981c>
136. Zhang S, Dokko K, Watanabe M (2014) Direct synthesis of nitrogen-doped carbon materials from protic ionic liquids and protic salts: structural and physicochemical correlations between precursor and carbon. *Chem Mater* 26(9):2915–2926. <https://doi.org/10.1021/cm5006168>
137. Fechler N, Fellinger T-P, Antonietti M (2013) “Salt templating”: a simple and sustainable pathway toward highly porous functional carbons from ionic liquids. *Adv Mater* 25(1):75–79. <https://doi.org/10.1002/adma.201203422>
138. Zhu X, Hillesheim PC, Mahurin SM, Wang C, Tian C, Brown S, Luo H, Veith GM, Han KS, Hagaman EW, Liu H, Dai S (2012) Efficient CO<sub>2</sub> capture by porous, nitrogen-doped carbonaceous adsorbents derived from task-specific ionic liquids. *Chem Sus Chem* 5(10):1912–1917. <https://doi.org/10.1002/cssc.201200355>
139. Ma S, Zhou H-C (2010) Gas storage in porous metal-organic frameworks for clean energy applications. *Chem Commun* 46(1):44–53. <https://doi.org/10.1039/B916295J>
140. Chen B, Xiang S, Qian G (2010) Metal–organic frameworks with functional pores for recognition of small molecules. *Acc Chem Res* 43(8):1115–1124. <https://doi.org/10.1021/ar100023y>
141. Makal TA, Yakovenko AA, Zhou H-C (2011) Isomerism in metal–organic frameworks: “framework isomers”. *J Phys Chem Lett* 2(14):1682–1689. <https://doi.org/10.1021/jz200424h>
142. Liu J, Thallapally PK, McGrail BP, Brown DR, Liu J (2012) Progress in adsorption-based CO<sub>2</sub> capture by metal-organic frameworks. *Chem Soc Rev* 41(6):2308–2322. <https://doi.org/10.1039/C1CS15221A>
143. Radhakrishnan L, Reboul J, Furukawa S, Srinivasu P, Kitagawa S, Yamauchi Y (2011) Preparation of microporous carbon fibers through carbonization of Al-based porous coordination polymer (Al-PCP) with furfuryl alcohol. *Chem Mater* 23(5):1225–1231. <https://doi.org/10.1021/cm102921y>
144. Liu B, Shioyama H, Akita T, Xu Q (2008) Metal-organic framework as a template for porous carbon synthesis. *J Am Chem Soc* 130(16):5390–5391. <https://doi.org/10.1021/ja7106146>
145. Hu M, Reboul J, Furukawa S, Torad NL, Ji Q, Srinivasu P, Ariga K, Kitagawa S, Yamauchi Y (2012) Direct carbonization of Al-based porous coordination polymer for synthesis of nanoporous carbon. *J Am Chem Soc* 134(6):2864–2867. <https://doi.org/10.1021/ja208940u>

146. Wang Q, Xia W, Guo W, An L, Xia D, Zou R (2013) Functional zeolitic-imidazolate-framework-templated porous carbon materials for CO<sub>2</sub> capture and enhanced capacitors. *Chem Asian J* 8(8):1879–1885. <https://doi.org/10.1002/asia.201300147>
147. Liu Y, Goebel J, Yin Y (2013) Templated synthesis of nanostructured materials. *Chem Soc Rev* 42(7):2610–2653. <https://doi.org/10.1039/C2CS35369E>
148. Inagaki M, Toyoda M, Soneda Y, Tsujimura S, Morishita T (2016) Templated mesoporous carbons: synthesis and applications. *Carbon* 107(Suppl C):448–473. <https://doi.org/10.1016/j.carbon.2016.06.003>
149. Sevilla M, Fuertes AB (2012) CO<sub>2</sub> adsorption by activated templated carbons. *J Colloid Interface Sci* 366(1):147–154. <https://doi.org/10.1016/j.jcis.2011.09.038>
150. Zhou J, Li W, Zhang Z, Xing W, Zhuo S (2012) Carbon dioxide adsorption performance of N-doped zeolite Y templated carbons. *RSC Adv* 2(1):161–167. <https://doi.org/10.1039/C1RA00247C>
151. Xia Y, Mokaya R, Walker GS, Zhu Y (2011) Superior CO<sub>2</sub> adsorption capacity on N-doped, high-surface-area, microporous carbons templated from zeolite. *Adv Energy Mater* 1(4):678–683. <https://doi.org/10.1002/aenm.201100061>
152. Balahmar N, Lowbridge AM, Mokaya R (2016) Templating of carbon in zeolites under pressure: synthesis of pelletized zeolite templated carbons with improved porosity and packing density for superior gas (CO<sub>2</sub> and H<sub>2</sub>) uptake properties. *J Mater Chem A* 4(37):14254–14266. <https://doi.org/10.1039/C6TA06176A>
153. Xia Y, Zhu Y, Tang Y (2012) Preparation of sulfur-doped microporous carbons for the storage of hydrogen and carbon dioxide. *Carbon* 50(15):5543–5553. <https://doi.org/10.1016/j.carbon.2012.07.044>
154. Saha D, Deng S (2010) Adsorption equilibrium and kinetics of CO<sub>2</sub>, CH<sub>4</sub>, N<sub>2</sub>O, and NH<sub>3</sub> on ordered mesoporous carbon. *J Colloid Interface Sci* 345(2):402–409. <https://doi.org/10.1016/j.jcis.2010.01.076>
155. Liu L, Deng Q-F, Ma T-Y, Lin X-Z, Hou X-X, Liu Y-P, Yuan Z-Y (2011) Ordered mesoporous carbons: citric acid-catalyzed synthesis, nitrogen doping and CO<sub>2</sub> capture. *J Mater Chem* 21(40):16001–16009. <https://doi.org/10.1039/C1JM12887F>
156. Presser V, Heon M, Gogotsi Y (2011) Carbide-derived carbons – from porous networks to nanotubes and graphene. *Adv Funct Mater* 21(5):810–833. <https://doi.org/10.1002/adfm.201002094>
157. Cambaz ZG, Yushin GN, Gogotsi Y, Vyshnyakova KL, Pereselenyeva LN (2006) Formation of carbide-derived carbon on β-silicon carbide whiskers. *J Am Ceram Soc* 89(2):509–514. <https://doi.org/10.1111/j.1551-2916.2005.00780.x>
158. Ferrera-Lorenzo N, Fuente E, Suárez-Ruiz I, Ruiz B (2014) Sustainable activated carbons of macroalgae waste from the Agar–Agar industry. Prospects as adsorbent for gas storage at high pressures. *Chem Eng J* 250(Suppl C):128–136. <https://doi.org/10.1016/j.cej.2014.03.119>
159. Sevilla M, Sangchoom W, Balahmar N, Fuertes AB, Mokaya R (2016) Highly porous renewable carbons for enhanced storage of energy-related gases (H<sub>2</sub> and CO<sub>2</sub>) at high pressures. *ACS Sustain Chem Eng* 4(9):4710–4716. <https://doi.org/10.1021/acssuschemeng.6b00809>
160. Singh G, Kim IY, Lakhi KS, Joseph S, Srivastava P, Naidu R, Vinu A (2017) Heteroatom functionalized activated porous biocarbons and their excellent performance for CO<sub>2</sub> capture at high pressure. *J Mater Chem A* 5(40):21196–21204. <https://doi.org/10.1039/C7TA07186H>
161. Casco ME, Martínez-Escandell M, Silvestre-Albero J, Rodríguez-Reinoso F (2014) Effect of the porous structure in carbon materials for CO<sub>2</sub> capture at atmospheric and high-pressure. *Carbon* 67:230–235. <https://doi.org/10.1016/j.carbon.2013.09.086>
162. Jalilov AS, Ruan G, Hwang C-C, Schipper DE, Tour JJ, Li Y, Fei H, Samuel ELG, Tour JM (2015) Asphalt-derived high surface area activated porous carbons for carbon dioxide capture. *ACS Appl Mater Interfaces* 7(2):1376–1382. <https://doi.org/10.1021/am508858x>
163. Jalilov AS, Li Y, Tian J, Tour JM (2017) Ultra-high surface area activated porous asphalt for CO<sub>2</sub> capture through competitive adsorption at high pressures. *Adv Energy Mater* 7(1):1600693. <https://doi.org/10.1002/aenm.201600693>

164. Silvestre-Albero A, Silvestre-Albero J, Martinez-Escandell M, Molina-Sabio M, Kovacs A, Rodriguez-Reinoso F (2015) Novel synthesis of a micro-mesoporous nitrogen-doped nanostructured carbon from polyaniline. *Microporous Mesoporous Mater* 218(Suppl C):199–205. <https://doi.org/10.1016/j.micromeso.2015.07.023>
165. Ashourirad B, Sekizkardes AK, Altarawneh S, El-Kaderi HM (2015) Exceptional gas adsorption properties by nitrogen-doped porous carbons derived from benzimidazole-linked polymers. *Chem Mater* 27(4):1349–1358. <https://doi.org/10.1021/cm504435m>
166. Cox M, Mokaya R (2017) Ultra-high surface area mesoporous carbons for colossal pre combustion CO<sub>2</sub> capture and storage as materials for hydrogen purification. *Sust Energy Fuels* 1(6):1414–1424. <https://doi.org/10.1039/C7SE00300E>
167. Li Y, Ben T, Zhang B, Fu Y, Qiu S (2013) Ultrahigh gas storage both at low and high pressures in KOH-activated carbonized porous aromatic frameworks. *Sci Rep* 3:2420. <https://doi.org/10.1038/srep02420http://www.nature.com/articles/srep02420#supplementary-information>
168. Adeniran B, Mokaya R (2015) Low temperature synthesized carbon nanotube superstructures with superior CO<sub>2</sub> and hydrogen storage capacity. *J Mater Chem A* 3(9):5148–5161. <https://doi.org/10.1039/c4ta06539e>
169. Himeno S, Komatsu T, Fujita S (2005) High-pressure adsorption equilibria of methane and carbon dioxide on several activated carbons. *J Chem Eng Data* 50(2):369–376. <https://doi.org/10.1021/je049786x>
170. Cox M, Mokaya R (2017) Ultra-high surface area mesoporous carbons for colossal pre combustion CO<sub>2</sub> capture and storage as materials for hydrogen purification. *Sustain Energy Fuels* 1(6):1414–1424. <https://doi.org/10.1039/C7SE00300E>
171. Ben T, Li Y, Zhu L, Zhang D, Cao D, Xiang Z, Yao X, Qiu S (2012) Selective adsorption of carbon dioxide by carbonized porous aromatic framework (PAF). *Energy Environ Sci* 5(8):8370–8376. <https://doi.org/10.1039/C2EE21935B>
172. Raymundo-Piñero E, Azañs P, Cacciaguerra T, Cazorla-Amorós D, Linares-Solano A, Béguin F (2005) KOH and NaOH activation mechanisms of multiwalled carbon nanotubes with different structural organisation. *Carbon* 43(4):786–795. <https://doi.org/10.1016/j.carbon.2004.11.005>

# Chapter 12

## CO<sub>2</sub> Storage on Metal-Organic Frameworks



Yunsheng Ma, Hideki Tanaka, and Ryotaro Matsuda

### 12.1 Introduction

The increasing concentration of carbon dioxide (CO<sub>2</sub>) in the atmosphere is thought to be one of the main contributors to rising global temperatures and climate change. Therefore, considerable research effort is dedicated to minimizing atmospheric CO<sub>2</sub> levels. A promising method for CO<sub>2</sub> amelioration is its adsorption onto suitable solids. Activated carbon and zeolite are the most commonly used and researched adsorbents for CO<sub>2</sub> separation and storage. Since the first observations of gas adsorption by porous coordination polymers (PCPs) and the metal-organic frameworks (MOFs) MOF-5 [1] and copper benzene-1,3,5-tricarboxylate (CuBTC) [2], these kinds of porous materials have been considered highly promising as gas separation and storage media [3]. The most attractive features of MOFs are their extremely high surface areas (up to 10,000 m<sup>2</sup> g<sup>-1</sup>), high porosities (up to 90%), and tunable pore sizes [4]. With the rapidly growing number of research articles on this topic, many new MOFs that display excellent CO<sub>2</sub> capture ability have been identified. Accordingly, in this chapter, we present a brief review of the theory and development of CO<sub>2</sub> separation and storage using MOFs.

---

Y. Ma · R. Matsuda (✉)

Department of Chemistry and Biotechnology, School of Engineering, Nagoya University,  
Nagoya, Japan

e-mail: [ryotaro.matsuda@chembio.nagoya-u.ac.jp](mailto:ryotaro.matsuda@chembio.nagoya-u.ac.jp)

H. Tanaka

Research Initiative for Supra-Materials, Interdisciplinary Cluster for Cutting Edge Research,  
Shinshu University, Wakasato 4-17-1, Nagano, Japan

e-mail: [htanaka@shinshu-u.ac.jp](mailto:htanaka@shinshu-u.ac.jp)

© Springer Nature Singapore Pte Ltd. 2019

K. Kaneko, F. Rodríguez-Reinoso (eds.), *Nanoporous Materials for Gas Storage*,  
Green Energy and Technology, [https://doi.org/10.1007/978-981-13-3504-4\\_12](https://doi.org/10.1007/978-981-13-3504-4_12)

331

## 12.2 Strategies of CO<sub>2</sub> Adsorption

MOFs with high adsorption capacities are required for their application to CO<sub>2</sub> capture. For this reason, extensive research has been dedicated to enhancing the CO<sub>2</sub> adsorption abilities of MOFs by modifying the chemical environments of the metal sites and organic ligands therein [5]. These excellent works on CO<sub>2</sub> adsorption can be classified depending on the strategy employed. Here, we begin our discussion with MOFs that have interaction sites, which can be further classified into metal and ligand sites. Subsequently, CO<sub>2</sub> adsorption under high pressure is discussed. Finally, we highlight some recent progress in the study of the crystal structures of MOFs containing CO<sub>2</sub> molecules.

### 12.2.1 MOFs Having Interaction Sites

#### 12.2.1.1 Open Metal Sites

In some MOFs, the metal ions are partially coordinated with solvent molecules, such as H<sub>2</sub>O and dimethylformamide (DMF), which can be removed by the application of heat and/or low pressure. This allows unsaturated metal centers (UMCs), also called open metal sites (OMSs), to be generated on the pore surfaces [6, 7]. These OMSs exhibit strong binding affinity to CO<sub>2</sub> molecules at low pressure. M-MOF-74 (M = Mg, Co, Fe, Zn, Ni) and CPO-27, which are synthesized by the reaction of 2,5-dihydroxyterephthalic acid (DOBDC) and metal ions, represent a family of MOFs with very high densities of OMSs. The use of different metal ions results in materials with different CO<sub>2</sub> adsorption capacities. For example, Mg-MOF-74 presents the highest CO<sub>2</sub> uptake up to 180 ml/g (26 wt %) at 1 bar and 296 K (Mg/DOBDC in Fig. 12.1) [8]. In comparison, the corresponding isostructural analogues of M-MOF-74, i.e., those prepared with M = Co, Ni, or Zn, exhibit much lower CO<sub>2</sub> adsorption capacities. The ionic character of the Mg-O bond in Mg-MOF-74 and the large surface area and pore volume of its framework are largely responsible for its superior CO<sub>2</sub> adsorption capacity [8].

M<sub>3</sub>(BTC)<sub>2</sub> (M = Cu, Cr, Ni, Zn, Mo, Ru) is another representative class of MOFs that exhibit high densities of OMSs. They comprise M paddle wheels and benzene-1,3,5-tricarboxylic acid (BTC) ligands (Fig. 12.2) [9]. Ru<sub>3</sub>(BTC)<sub>2</sub> exhibits the highest heat of adsorption, indicating high CO<sub>2</sub> uptake by the material. This demonstrates that the choice of metal has a significant impact on the interactions between the adsorbate gas and the framework. The strong affinity toward CO<sub>2</sub> and high heat of adsorption of Ru<sub>3</sub>(BTC)<sub>2</sub> may be due to the high positive charge of Ru(5+).

The effect of OMSs in the MIL-100 (Cr, V, Sc) series has also been studied [10]. It was reported that the enthalpy of adsorption followed the trend Cr > V > Sc, indicating differences in the binding strength of the cationic metal sites with CO<sub>2</sub> molecules. This can be explained by the differences in the density of the positive charge, which depend on the identity of the metal.

**Fig. 12.1** CO<sub>2</sub> sorption isotherms (296 K, 0–1 atm) of the M/DOBDC series. The inset shows the low-pressure region (0–0.1 atm). Reprinted with the permission from ref. [8]. Copyright (2008) American Chemical Society

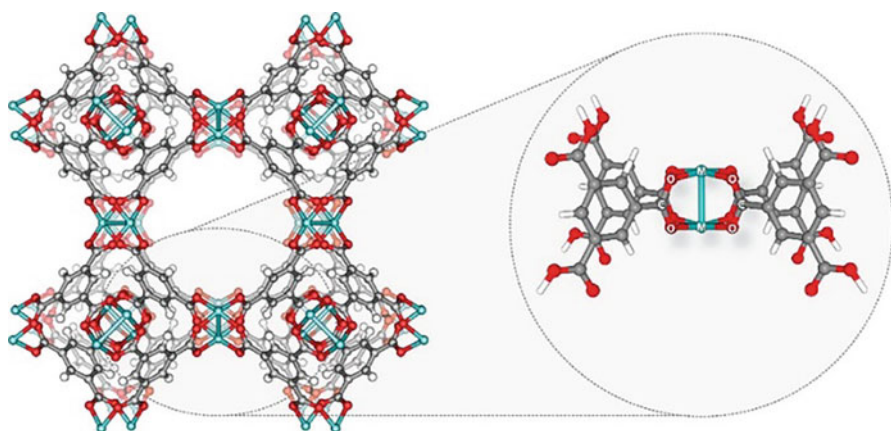
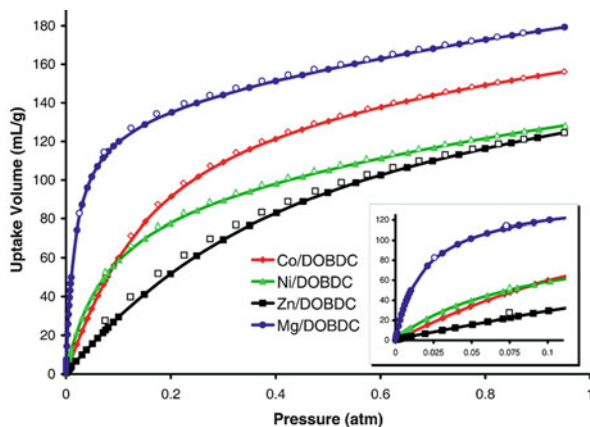


**Fig. 12.2** Portion of the crystal structure of M<sub>3</sub>(BTC)<sub>2</sub>. Reprinted with the permission from ref. [9b]. Copyright (2017) American Chemical Society

Clearly, the presence of OMSs can dramatically enhance the affinity of a material with CO<sub>2</sub>. However, the pore size and surface area of the framework play very important roles in its adsorption capacity. The CO<sub>2</sub> adsorption capacities and surface areas for several isostructural MOFs are listed in Table 12.1.

### 12.2.1.2 Doping with Metals Ions

It is widely recognized that the presence of strong nanospace-scale electrostatic fields can endow a material with high CO<sub>2</sub> sorption. The doping of pore spaces with metal ions is a particularly effective method for generating such strong electrostatic fields, which can improve the interactions between CO<sub>2</sub> molecules and frameworks.

Mu et al. performed a computational study to investigate the effects of doping metals (Li, Na, K, Rb, Cs, Mg, Ca, Al, and Ga) on each side of the aromatic rings in MOF-5 on its selective CO<sub>2</sub> adsorption [11]. The simulation indicated that

**Table 12.1** CO<sub>2</sub> adsorption capacity and surface area for the isostructural MOFs

MOF	S <sub>BET</sub> m <sup>2</sup> /g	Condition	CO <sub>2</sub> adsorption capacity wt % <sup>a</sup>	Q <sub>st</sub> kJ/mol	Ref.
Mg-MOF74	1495	1 bar, 296 K	26	47	[8]
Co-MOF74	1080	1 bar, 296 K	24	37	[8]
Zn-MOF74	816	1 bar, 296 K	18		[8]
Ni-MOF74	1070	1 bar, 296 K	20	41	[8]
Cu <sub>3</sub> (BTC) <sub>2</sub>	1734	1 bar, 315 K	11	29.8	[9a]
Cr <sub>3</sub> (BTC) <sub>2</sub>	2031	1 bar, 314 K	11	26.7	[9a]
Ni <sub>3</sub> (BTC) <sub>2</sub> (Me <sub>2</sub> NH) <sub>2</sub> (H <sub>2</sub> O)	1047	1 bar, 313 K	9.0	36.8	[9a]
Mo <sub>3</sub> (BTC) <sub>2</sub> (DMF) <sub>0.5</sub>	1689	1 bar, 314 K	7.2	25.6	[9a]
Ru <sub>3</sub> (BTC) <sub>2</sub> (BTC) <sub>0.5</sub>	1180	1 bar, 313 K	11	32.6	[9a]
MIL-100(Sc)				48	[10]
MIL-100(V)				54	[10]
MIL-100(Cr)				63	[10]

<sup>a</sup>The data were calculated as  $100 \times \text{weight of CO}_2 / (\text{weight of CO}_2 + \text{weight of adsorbent})$  [wt %]

the presence of alkali metal atoms strongly enhances the adsorption ability and selectivity for CO<sub>2</sub> in a CO<sub>2</sub>/CH<sub>4</sub> mixture. Furthermore, Lau et al. reported that the CO<sub>2</sub> adsorption capacity of UiO-66 is enhanced by up to 81% upon partially exchanging the Ti with Zr. It was found that the Ti-exchanged UiO-66 has a smaller pore size than that of UiO-66, resulting in a larger isosteric heat of adsorption and thereby superior CO<sub>2</sub> adsorption [12]. M-SNU-100 (M = Li<sup>+</sup>, Mg<sup>2+</sup>, Ca<sup>2+</sup>, Co<sup>2+</sup>, Ni<sup>2+</sup>) samples exhibit higher isosteric heat values than pristine SNU-100 (34.5–37.4 kJ mol<sup>-1</sup> vs. 29.3 kJ mol<sup>-1</sup>), which can be ascribed to the electrostatic interactions between CO<sub>2</sub> molecules and metal ions in the anionic SNU-100 pores [13].

### 12.2.1.3 N-Rich MOFs

Uncoordinated N atoms in the pores of MOFs can enhance CO<sub>2</sub> adsorption affinity owing to the base-acid and electrostatic interactions between basic N sites and polarizable CO<sub>2</sub> molecules [14]. For example, IFMC-1 is constructed from N-rich 4,5-di(1H-tetrazol-5-yl)-2H-1,2,3-triazole ligands and Zn<sup>2+</sup> and presents a large number of uncoordinated N atoms in its pores. Accordingly, IFMC-1 exhibits a high CO<sub>2</sub> adsorption capacity and CO<sub>2</sub>/N<sub>2</sub> selectivity [15].

Using bis-triazolate ligands and tetrahedral Zn<sup>2+</sup> ions, Zhang et al. synthesized the flexible MOF [Zn<sub>2</sub>(btm)<sub>2</sub>]<sub>2</sub>·4H<sub>2</sub>O (MAF-23·4H<sub>2</sub>O), which is functionalized with pairs of uncoordinated triazolate N-donors that act as guest chelating sites, providing a very high CO<sub>2</sub> adsorption enthalpy. Its dynamic CO<sub>2</sub> sorption behavior was studied using single-crystal X-ray diffraction [16]. A very small amount of CO<sub>2</sub> gas was loaded into the crystal to investigate the host-guest interactions at near-zero coverage. The electron density difference map revealed just one linear

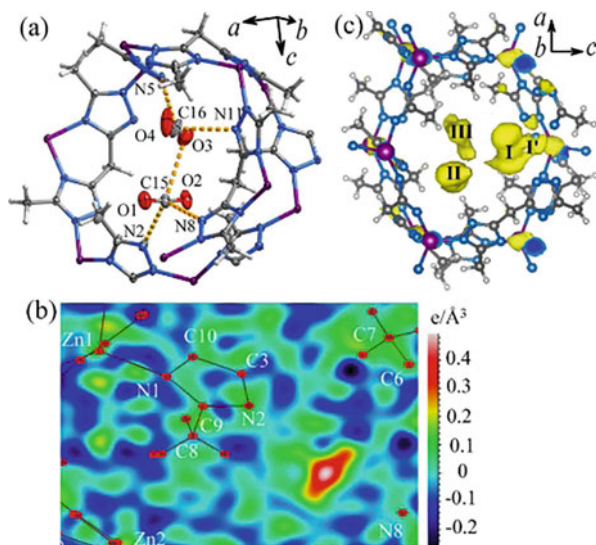
three-electron peak at site I, demonstrating that site I is the strongest CO<sub>2</sub> binding site. The structures obtained for crystals loaded with different amounts of CO<sub>2</sub> further illustrated the dynamic adsorption behavior of the compound (Fig. 12.3).

### 12.2.1.4 Amine Functionalization

Hydrogen-bond interactions between CO<sub>2</sub> molecules and a framework can enhance its CO<sub>2</sub> adsorption. Amine-functionalized MOFs are the most investigated for this purpose because their basic amine groups display strong affinity to acidic CO<sub>2</sub> molecules [17]. Three routes have been employed to prepare amine-functionalized MOFs: (i) in situ synthesis, (ii) post-modification with amines, and (iii) physical mixing of unfunctionalized MOFs and polyamines.

The in situ method is by far the most used. 2-Amino-1,4-benzenedicarboxylate (NH<sub>2</sub>BDC) has been used to construct several amine-functionalized MOFs, such as IRMOF-3 [18], NH<sub>2</sub>-UiO-66 [19], NH<sub>2</sub>-MIL-101(Cr) [20], and NH<sub>2</sub>-MIL-53(Fe) [21]. The incorporation of alkylamines into MOFs endows more active Lewis basic sites for CO<sub>2</sub> capture and thereby significantly enhances the CO<sub>2</sub> adsorption uptake at low pressures. Férey et al. reported the first alkylamine-modified MOF, i.e., ethylenediamine-modified MIL-101(Cr), through post-synthetic functionalization of the open Cr<sup>3+</sup> sites [22]. Furthermore, Long et al. synthesized ethylenediamine-modified CuBTTri (en-CuBTTri, where BTri = 1,3,5-tri(1H-1,2,3-triazol-4-yl)benzene) through post-synthetic functionalization of the open Cu sites and investigated its performance for CO<sub>2</sub> adsorption (Fig. 12.4) [23]. The resulting en-CuBTTri exhibits an extremely high isosteric heat of CO<sub>2</sub> adsorption at zero coverage (up to 90 kJ mol<sup>-1</sup>) but unfortunately only a slight enhancement of

**Fig. 12.3** (a) ORTEP plot of the single-crystal X-ray structure of MAF-23·1.5CO<sub>2</sub> (probability ellipsoids drawn at 30%). (b) 2D electron density difference map ( $F_o - F_c$ ) for MAF-23·0.07CO<sub>2</sub> showing the presence of CO<sub>2</sub> at site I. (c) 3D electron density map ( $F_o - F_c$ ) of MAF-23·2.8CO<sub>2</sub> (isosurfaces drawn at 0.60). Reprinted with the permission from ref. [16]. Copyright (2012) American Chemical Society



CO<sub>2</sub> uptake, which is most likely due to difficulty in loading ethylenediamine into the internal pores of CuBTri.

Diamine-modified mmen-Mg<sub>2</sub>(dobpdc) (Fig. 12.5) [24], en-Mg<sub>2</sub>(dobpdc) [25], and dmen-Mg<sub>2</sub>(dobpdc) [26] (dmen = N,N-dimethylethylenediamine) have been synthesized and show excellent CO<sub>2</sub> capture abilities, even at ultra-dilute levels. In this series, the OMSs of MOFs play an important role, anchoring one end of the diamine and leaving the other end available to capture CO<sub>2</sub>.

MIL-101(Cr) is an ideal platform for physical impregnation with polyalkylamines because it has a large surface area as well as thermal and chemical stability. In addition, MIL-101 possesses OMSs and Cr-OH groups that serve as Lewis acid sites to anchor polyethyleneimine (PEI) (Fig. 12.6). The amine/MIL-101 composite exhibits dramatically enhanced CO<sub>2</sub> adsorption capacity at low pressure [27].

**Fig. 12.4** A portion of the structure of the sodalite-type framework of CuBTri showing surface functionalization of a coordinatively unsaturated Cu<sup>2+</sup> site with ethylenediamine, followed by attack by an amino group on CO<sub>2</sub>. Reprinted with the permission from ref. [23]. Copyright (2009) American Chemical Society

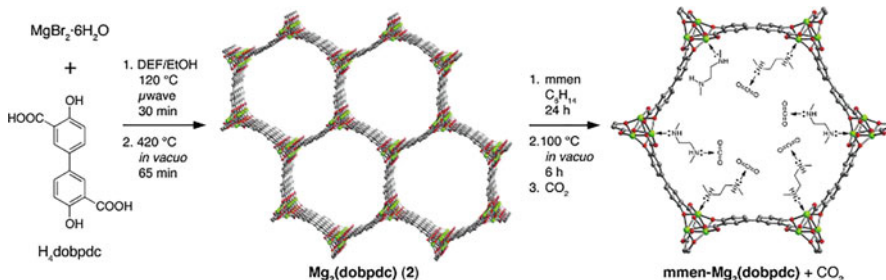
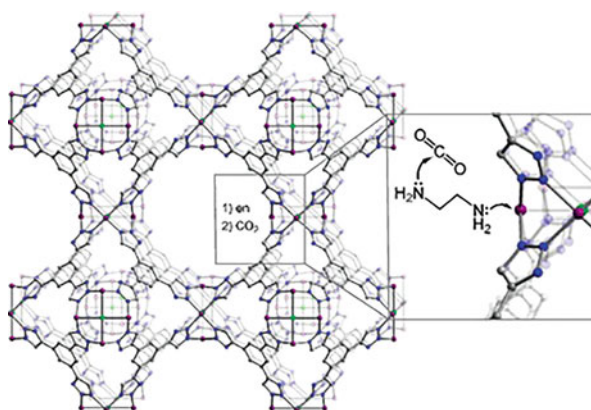


**Fig. 12.5** Synthetic route for mmen-Mg<sub>2</sub>(dobpdc). Reprinted with the permission from ref. [24]. Copyright (2012) American Chemical Society

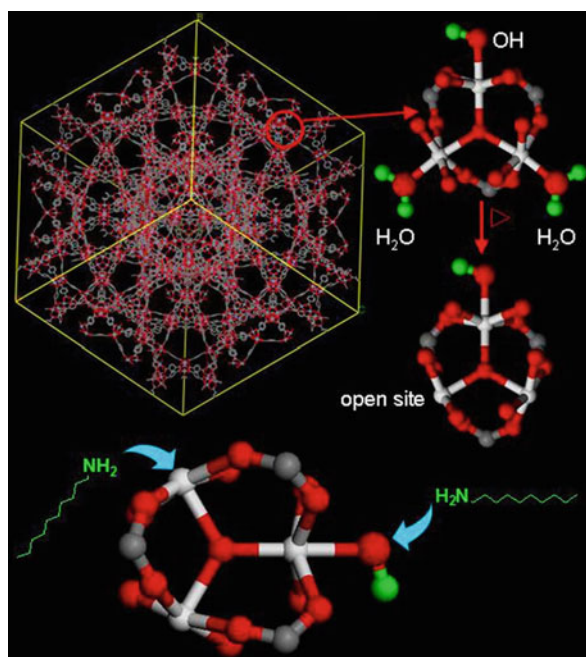
### 12.2.1.5 Pore-Size Control

The pore size of a framework is critical to its adsorption capacity for CO<sub>2</sub>. The kinetic diameter of a CO<sub>2</sub> molecule is 0.33 nm. Thus, materials with MOF pore sizes in the range 0.3–0.4 nm are ideal candidates for CO<sub>2</sub> capture. It has been observed that, at low pressure, CO<sub>2</sub> uptake in a MOF correlates with the heat of adsorption, which is an index of adsorption affinity that depends on pore size.

A representative example is the ultra-microporous SIFSIX-3-M (M = Zn, Cu, Ni) series, which is constructed with pyrazine linking ligands that adopt a pillared formation. This series of MOFs shows excellent CO<sub>2</sub> uptake at low pressures, which can be explained by the fact that these MOFs have micropores with sizes in the range 0.35–0.4 nm and moderate surface areas (Fig. 12.7). It is worthy of mention that SIFSIX-3-Cu shows a remarkable CO<sub>2</sub> adsorption capacity of 1.24 mmol g<sup>-1</sup> (5.2 wt %) at 400 ppm and 298 K, which is by far the highest recorded under atmospheric conditions [28].

Modifying ligands with appropriate substituents is an efficient method for decreasing the pore size of MOFs. For example, UiO-66-(CH<sub>3</sub>)<sub>2</sub> has two methyl groups on the linkers and therefore exhibits smaller pore sizes compared with those of UiO-66 and UiO-66-NH<sub>2</sub>. Adsorption experiments have revealed that it exhibits enhanced CO<sub>2</sub> uptake, which is due to the stronger interactions between CO<sub>2</sub> molecules and the framework [29].

**Fig. 12.6** Illustration of the interactions between PEI and MIL-101 [27]. Copyright (2013) Springer Nature



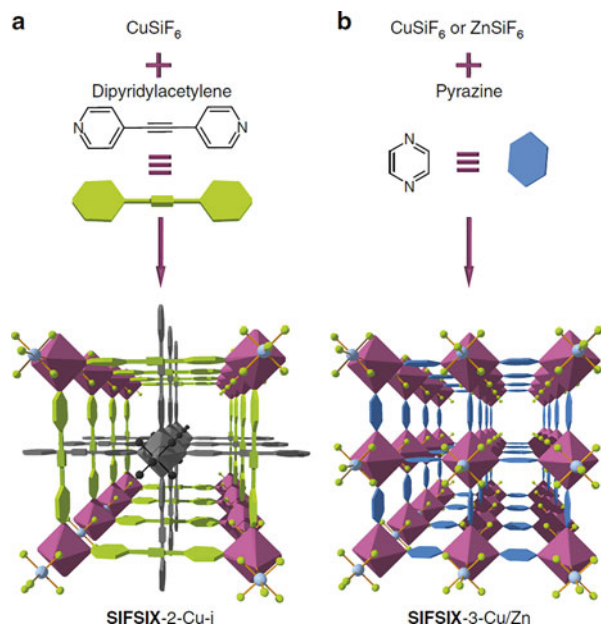


**Fig. 12.7** Pore-size tuning in SIFSIX-3 [28]. Copyright (2014) Springer Nature

Feng et al. reported a pore-space-partition strategy to adjust channel size by inserting symmetry-matching regulated ligands. As shown in Fig. 12.8, MIL-88-type structures were selected as a prototype framework because these highly flexible frameworks allow a ligand with C3 symmetry to fit into the channel. By introducing tripyridyl-type ligands into the MIL-88-type structures, a family of Ni-trimer-based MOFs (CPM-33a, CPM-33b, CPM-34, CPM-35, and CPM-37) were synthesized [30]. The channel segments are 4.5 Å in length and exhibit superior  $\text{CO}_2$  uptake capacity.

Interpenetration or catenation is also a proven strategy for reducing the pore dimensions in order to enhance the interactions between  $\text{CO}_2$  and a framework. For example, catenated isorecticular MOFs (IRMOFs) such as IRMOF-9, IRMOF-11, and IRMOF-13 have better  $\text{CO}_2$  over  $\text{CH}_4$  selectivity compared with those of their non-interpenetrated counterparts (Fig. 12.9) [31]. Recently, Kim et al. reported that catenation in CuTATB-60 leads to both higher surface area and enhanced network stability compared to the non-catenated counterpart, CuTATB-30. Moreover, CuTATB-60 shows higher  $\text{CO}_2$  adsorption capacity ( $189 \text{ mg g}^{-1}$ ) than CuTATB-30 [32].

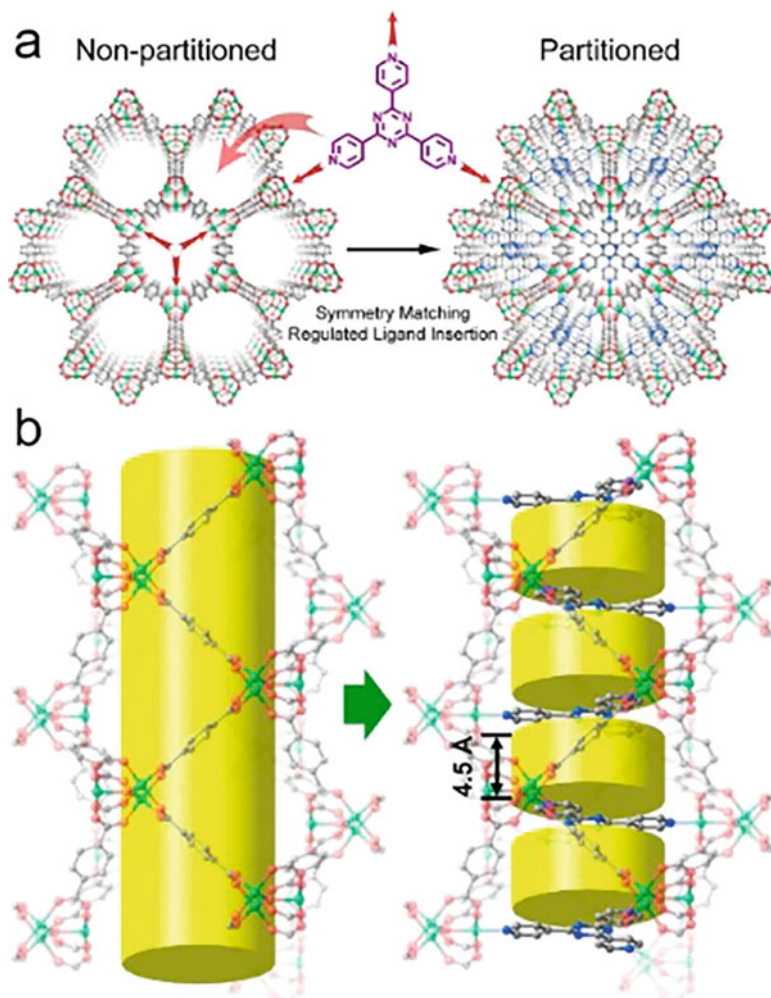


**Fig. 12.8** Illustration of pore space partition through regulated symmetry-matching ligand insertion. (a) Viewed along *c* axis and (b) side view of the channels before and after partition. Reprinted with the permission from ref. [30]. Copyright (2015) American Chemical Society

### 12.2.2 Flexible MOFs for CO<sub>2</sub> Adsorption

Flexible MOFs show S-shaped or multistep adsorption isotherms, leading to hysteresis in their charge and discharge pressures. Flexibility is expected to be a useful property for practical gas storage materials. The MIL (Materials of the Institut Lavoisier) series of hybrid porous materials synthesized by Férey and co-workers are promising candidates for flexible adsorption materials. MIL-53(Al) and MIL-

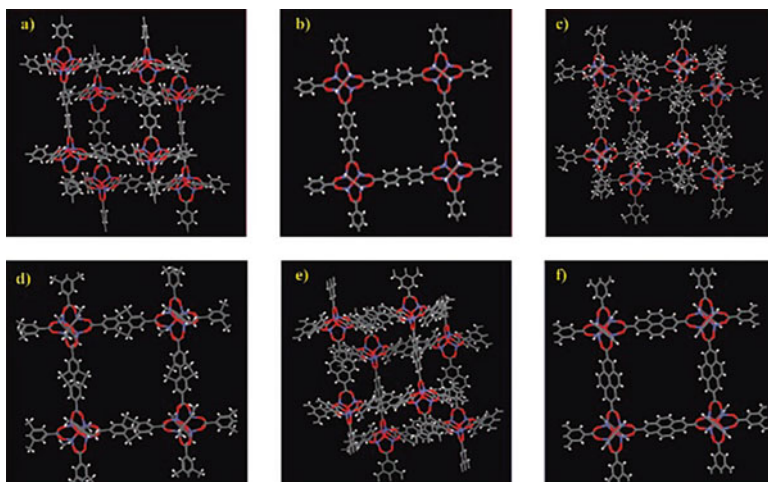


**Fig. 12.9** Crystal structures of the IRMOFs used for the simulation in ref. 31: (a) IRMOF-9, (b) IRMOF-10, (c) IRMOF-11, (d) IRMOF-12, (e) IRMOF-13, and (f) IRMOF-14. Reprinted with the permission from ref. [31]. Copyright (2008) American Chemical Society

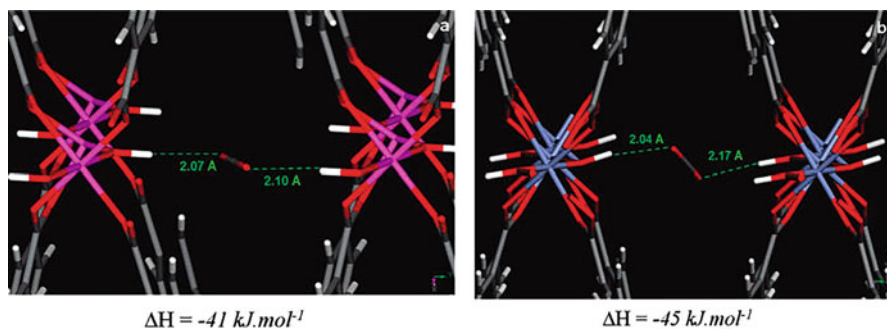


**Fig. 12.10** Interaction of one CO<sub>2</sub> molecule with two μ<sub>2</sub>-OH groups on opposing sides of a pore wall in MIL-53 narrow-pore structures containing Al (a) and Cr (b) [33]. Copyright (2007) Springer Nature

53(Cr) exhibit significant breathing effects upon CO<sub>2</sub> adsorption (Fig. 12.10) [33]. Detailed structural studies have shown that the μ<sub>2</sub>-OH group in M(OH)(O<sub>2</sub>C-C<sub>6</sub>H<sub>4</sub>-CO<sub>2</sub>) exhibits hydrogen-bond interactions with CO<sub>2</sub> molecules. The formation of electron donor-acceptor complexes between CO<sub>2</sub> molecules and hydroxyl groups was observed by Vimont et al. through IR spectroscopy measurements. This result demonstrates that CO<sub>2</sub> molecules act as electron acceptors in adsorption processes [34].

Matsuda et al. reported the flexible 3D MOF {[Cd<sub>2</sub>(pzdc)<sub>2</sub>L(H<sub>2</sub>O)<sub>2</sub>]}<sub>n</sub>·5H<sub>2</sub>O·(EtOH)<sub>n</sub>, which contains a rotatable pillar [35]. The framework shows reversible single-crystal-to-single-crystal transformations in response to the removal and rebinding

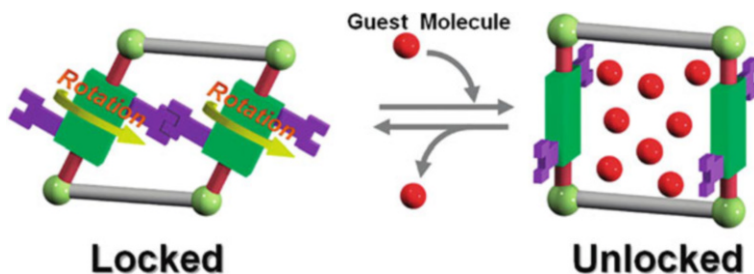


**Fig. 12.11** A rotational module as a molecular gate with locking/unlocking interactions triggered by guest inclusion. Reprinted with the permission from ref. [35]. Copyright (2009) American Chemical Society

of guest molecules. Its CO<sub>2</sub> adsorption isotherm shows a gate-opening profile, which is derived from the locking/unlocking behavior of the rotational module (Fig. 12.11).

Adsorption behavior of gas mixture on the flexible MOFs accompanied by their structural transitions cannot be predicted by the ideal adsorption solution theory (IAST) method, which is the conventional method to estimate an adsorption isotherm of gas mixture with the use of experimental single component adsorption isotherms on a rigid porous solid. Therefore, in research and development of the flexible MOFs for CO<sub>2</sub> capture and storage, a new strategy for evaluating their adsorption characteristics of CO<sub>2</sub> gas mixture needs to be developed. Recently, Coudert et al. proposed the osmotic framework adsorption solution theory (OFAST) [36, 37], which is the method combining the IAST method and a thermodynamic model for estimating the change in Helmholtz free energy of flexible MOF,  $\Delta F$ , during its structural transition (“breathing” or “gating”) induced by gas adsorption. The thermodynamic model was also developed by Coudert et al. [38] and was successfully applied to demonstrate the adsorption of pure CO<sub>2</sub> on MIL-53(Al) at 304 K, which shows sharp two steps in the adsorption isotherm coming from the structural transitions between so-called narrow-pore (**np**) and large-pore (**lp**) structures (Fig. 12.12a). The Helmholtz free energy change of MIL-53(Al),  $\Delta F_{lp \rightarrow np}$ , was determined by fitting two Langmuir-type adsorption isotherms to each region of the experimental adsorption isotherm of MIL-53(Al) having **np** and **lp** structures and then setting the osmotic free energy profiles obtained by integrating the obtained Langmuir-type adsorption isotherms with respect to CO<sub>2</sub> gas pressure so that they intersect at the experimental breathing pressure corresponding to the **np**  $\rightarrow$  **lp** transition (Fig. 12.12b). This strategy successfully described the experimental CO<sub>2</sub> adsorption isotherm on MIL-53(Al) showing both the **lp**  $\rightarrow$  **np** and **np**  $\rightarrow$  **lp** transitions and provided  $\Delta F_{lp \rightarrow np} \approx 2.5$  kJ/mol per unit cell of MIL-53(Al). Coudert et al. then used the OFAST method to predict a diagram of stability of the **np** and **lp** phases of MIL-53(Al) upon adsorption of CO<sub>2</sub>/CH<sub>4</sub> mixtures at 304 K as a function of total gas pressure and mixture composition (Fig. 12.13) by assuming  $\Delta F_{lp \rightarrow np} = 2.5$  kJ/mol per unit cell [36]. The two total adsorption isotherms of

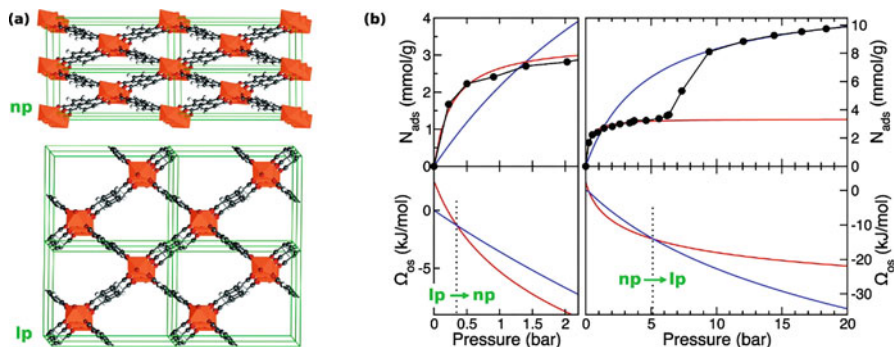


**Fig. 12.12** (a) Narrow-pore (**np**) and large-pore (**lp**) structures of MIL-53(Al). (b) (upper) Experimental adsorption isotherm of CO<sub>2</sub> on MIL-53(Al) at 304 K and Langmuir-type adsorption isotherms fit over the range of 0–5 bar and 9–30 bar (in red and blue, respectively). (lower) Osmotic free energy profiles as a function of CO<sub>2</sub> pressure for the **lp** (in blue) and **np** (in red) structures of MIL-53(Al). Reprinted with the permission from ref. [38]. Copyright (2008) American Chemical Society

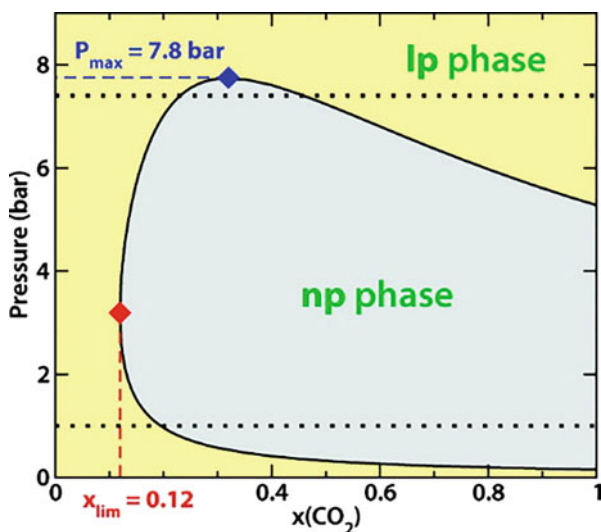
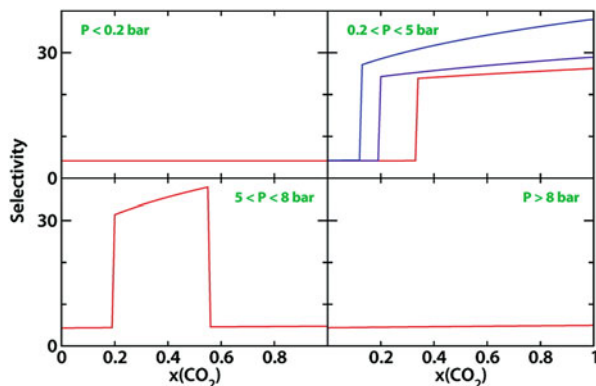


**Fig. 12.13** Predicted diagram of stability of the **np** and **lp** phases of MIL-53(Al) upon adsorption of a CO<sub>2</sub>/CH<sub>4</sub> mixture at 304 K, as a function of total pressure and mixture composition. Reprinted with the permission from ref. [36]. Copyright (2009) American Chemical Society

CO<sub>2</sub>/CH<sub>4</sub> mixture on the **np** and **lp** structures, which are required to obtain the phase diagram using the OFAST method, were evaluated by the IAST method using the Langmuir-type adsorption isotherms fitted to the corresponding parts of experimental adsorption isotherms for pure CO<sub>2</sub> and CH<sub>4</sub>. Note that they assumed the adsorption isotherm of pure CH<sub>4</sub> on the **lp** structure of MIL-53(Al) reduced by about 74% as the one on the **np** structure because the **lp** → **np** transition by CH<sub>4</sub>

**Fig. 12.14** Curves of CO<sub>2</sub> selectivity as a function of CO<sub>2</sub> composition in CO<sub>2</sub>/CH<sub>4</sub> gas mixture for MIL-53(Al) at different total pressures (0.1, 0.5, 1, 4, 7, and 10 bar) and 304 K. Reprinted with the permission from ref. [36]. Copyright (2009) American Chemical Society



adsorption cannot be experimentally observed. They showed that the **np** structure of MIL-53(Al) can have larger CO<sub>2</sub> selectivity (20–40) than the **lp** structure and interestingly predicted that the **np** structure can be only observed when the mole fraction of CO<sub>2</sub> in the CO<sub>2</sub>/CH<sub>4</sub> mixture gas of 7 bar is in the range of 0.2–0.56 (Fig. 12.14). A few years after the non-monotonic phase behavior of MIL-53(Al) was predicted, Coudert and his co-workers performed a combined experimental and theoretical study for CO<sub>2</sub>/CH<sub>4</sub> mixture adsorption on MIL-53(Al) as a function of temperature, pressure, and mixture composition and succeeded in validating the OFAST model [37].

As mentioned above, the flexible MOFs can provide relatively large CO<sub>2</sub> selectivity because their framework can deform to fit adsorbed CO<sub>2</sub> molecules and to enhance intermolecular interactions. And, the steep rise in the CO<sub>2</sub> adsorption amount caused by the breathing or gating can realize large CO<sub>2</sub> working capacity with small pressure swing. Another significant issue to utilize the flexible MOFs for CO<sub>2</sub> capture and storage is adsorption kinetics for CO<sub>2</sub> gas mixture. A very limited number of breakthrough experiments for CO<sub>2</sub> gas mixture using the flexible MOFs have been reported in the literature: MIL-53(Al) [39], MIL-53(Cr) [40], [Zn(5NO<sub>2</sub>-ip)(bpy)]<sub>n</sub> (CID-5, 5NO<sub>2</sub>-ip = 5-nitroisophthalate, bpy = 4,4'-bipyridyl) [41], [Zn(5MeO-ip)(bpy)]<sub>n</sub> (CID-6, 5MeO-ip = 5-methoxyisophthalate) [41], and [Cu(BF<sub>4</sub>)<sub>2</sub>(bpy)<sub>2</sub>]<sub>n</sub> (ELM-11) [42]. Finsy et al. [39] pioneered the breakthrough measurements for the flexible MOFs and reported the breakthrough curves of CO<sub>2</sub>/CH<sub>4</sub> mixtures for a fixed bed of MIL-53(Al) pellets. Hamon et al. also performed breakthrough curves measurements for MIL-53(Cr) using CO<sub>2</sub>/CH<sub>4</sub> mixtures at 303 K (Fig. 12.15) [40]. CH<sub>4</sub> first breaks because the **np** structure of MIL-53(Cr) strongly interacts with the CO<sub>2</sub> molecules similarly to the **np** structure of MIL-53(Al); however, the breakthrough curves for two mixtures (CO<sub>2</sub>:CH<sub>4</sub> = 50:50 at 0.1 MPa and CO<sub>2</sub>:CH<sub>4</sub> = 75:25 at 1.0 MPa) show different profiles. For the mixture of CO<sub>2</sub>:CH<sub>4</sub> = 50:50, the breakthrough curves of CO<sub>2</sub> and CH<sub>4</sub> were changed gradually, which is due to a partial transformation of MIL-53(Cr) from **lp** to **np** structure. On the other hand, for the mixture of CO<sub>2</sub>:CH<sub>4</sub> = 75:25, the CH<sub>4</sub> breakthrough curve exhibits unusual two peaks, and they coincide with the

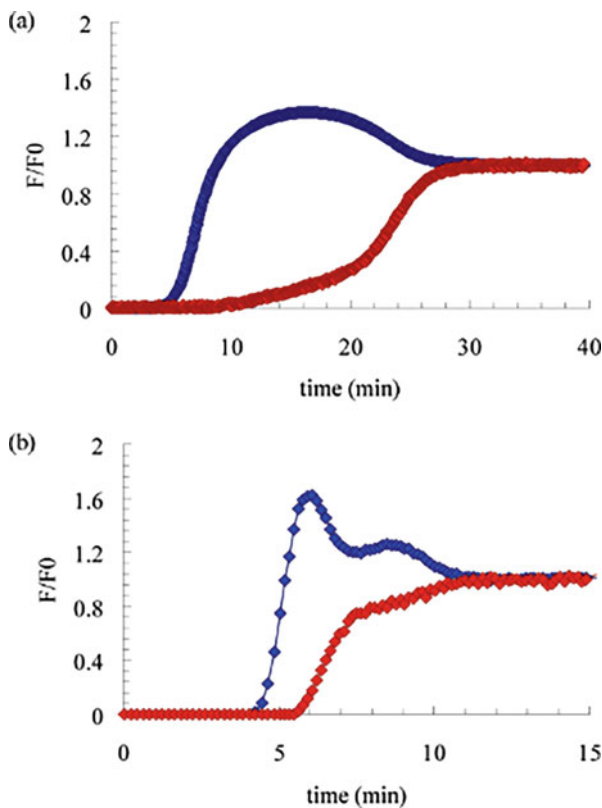


**Fig. 12.15** Breakthrough curves for CO<sub>2</sub>/CH<sub>4</sub> gas mixtures on MIL-53(Cr) at 303 K: CO<sub>2</sub> in red and CH<sub>4</sub> in blue: (a) CO<sub>2</sub>:CH<sub>4</sub> = 50:50 at 0.1 MPa and (b) CO<sub>2</sub>:CH<sub>4</sub> = 75:25 at 1.0 MPa. Reprinted with the permission from ref. [40]. Copyright (2009) American Chemical Society

change in slope of the CO<sub>2</sub> breakthrough curve. The authors attribute the first peak of CH<sub>4</sub> breakthrough curve to the adsorption of CO<sub>2</sub> accompanied by the **lp** → **np** transition and the second one to the exclusion of adsorbed CH<sub>4</sub> due to the widening of pores of MIL-53(Cr) by the **np** → **lp** transition. Another important finding is that the partial pressures of CO<sub>2</sub> at the maximum of CH<sub>4</sub> breakthrough curves for the two mixtures are both close to the **lp** → **np** transition pressure for pure CO<sub>2</sub> adsorption. This indicates that the driving force for the breathing transformation is the partial pressure of CO<sub>2</sub>, and the same behavior was also reported for the gate opening of CID-5 induced by adsorption of CO<sub>2</sub>/CH<sub>4</sub> mixture at 0.8 MPa and 273 K [41]. These facts suggest that the flexible MOFs can no longer adsorb the CO<sub>2</sub> molecules when the partial pressure of CO<sub>2</sub> in a gas mixture decreases below their specific breathing or gating pressure and thus a pure effluent gas cannot be obtained, which is one of the problems to be solved to effectively utilize the flexible MOFs for CO<sub>2</sub> capture and storage.

Thermal management of adsorption column is also an important issue on CO<sub>2</sub> capture and storage. When a CO<sub>2</sub> gas mixture is rapidly and adiabatically introduced into the adsorption column, the temperature rise due to exothermic heat released by adsorption suppresses the adsorption amount of CO<sub>2</sub>, and on the other hand, the impact of cooling due to the abrupt desorption leads to a decrease in the CO<sub>2</sub> working capacity. Recently, Mason et al. [43] reported that the flexible MOFs have suitable characteristics for CH<sub>4</sub> storage: the endothermic expansion of the framework due to the gate opening effectively offsets the exothermic heat of CH<sub>4</sub> adsorption, and the gate closing acts in an opposite way. They focused on [Co(bdp)]<sub>n</sub> (bdp = 1,4-benzenedipyrazolate) and [Fe(bdp)]<sub>n</sub>, which exhibit a typical gate adsorption of CH<sub>4</sub>, and showed that the heat released by CH<sub>4</sub> adsorption due to the gate opening of [Co(bdp)]<sub>n</sub> is reduced by 28%. Moreover, very recently, Hiraide et al. [44] reported that the thermal management capabilities of ELM-11 showing the two-step gating for CO<sub>2</sub> at lower and higher pressures (Fig. 12.16) are nearly identical and the efficiencies reach 41% and 44% at 298 K, respectively. These facts indicate that the flexible MOFs have indeed intrinsic thermal management capability and it must be useful for CO<sub>2</sub> capture and storage.

### 12.2.3 CO<sub>2</sub> Capture Under Humid Conditions

Although MOF materials have shown high CO<sub>2</sub> capture capabilities, their main drawback is their high sensitivity toward H<sub>2</sub>O. For example, the coordination bonds between organic ligands (e.g., carboxylate) and metal ions can be broken by H<sub>2</sub>O

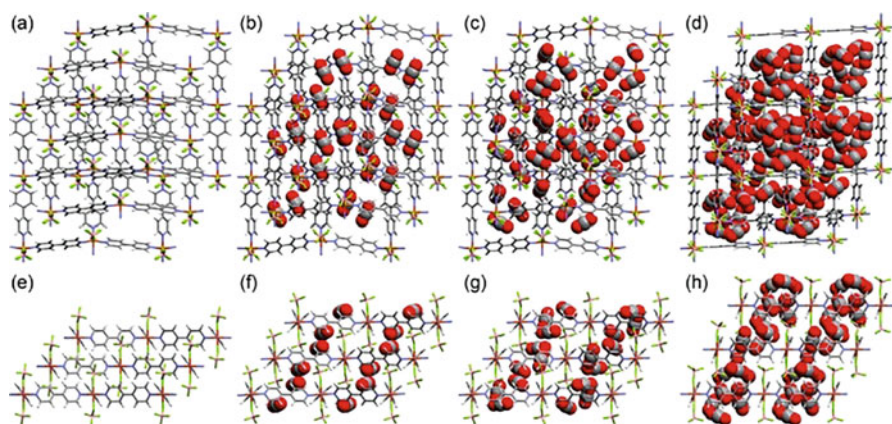


**Fig. 12.16** Crystal structures of ELM-11 with different CO<sub>2</sub> loadings at 195 K: top views of (a) ELM-11, (b) ELM-11 encapsulating 2CO<sub>2</sub> per monomer unit of Cu(BF<sub>4</sub>)<sub>2</sub>(bpy)<sub>2</sub> after gating at lower pressure, (c) ELM-11 encapsulating 3CO<sub>2</sub>, and (d) ELM-11 encapsulating 6CO<sub>2</sub> after gating at higher pressure; and (e), (f), (g), and (h) are side views of (a), (b), (c), and (d), respectively. Reprinted with the permission from ref. [44]. Copyright (2017) American Chemical Society

molecules. In addition, water molecules can compete with  $\text{CO}_2$  molecules for occupancy of the active sites in MOF materials, resulting in drastically decreased overall  $\text{CO}_2$  capture capacity [45]. Thus, MOFs must exhibit water stability for real-world application to  $\text{CO}_2$  capture. Three strategies have been applied to achieve water-stable MOFs: (i) high-valence metal ions ( $\text{Zr}^{4+}$ ,  $\text{Al}^{3+}$ ) coordinated to carboxylates (e.g., UiO-66, MIL-101), (ii) the construction of metal azolate frameworks (e.g., ZIF-8, MAF-23), and (iii) the functionalization of MOFs with hydrophobic functional groups [46].

MIL-53(Cr) has a 3D structure comprising  $\text{CrO}_4(\text{OH})_2$  octahedra and 1,4-benzenedicarboxylate (BDC) linkers and is water stable. Llewellyn et al. found that its diamond-shaped channels exhibit a breathing effect when it is under ambient conditions (hydrated) and activated (dehydrated) [47]. The observation of  $\text{CO}_2$  uptake by hydrated MIL-53(Cr) at 20 bar presents the possibility of using preabsorbed water in MOFs for the capture of  $\text{CO}_2$ .

MIL-100(Fe) presented very interesting and promising results (Fig. 12.17). At 3% relative humidity (RH), its  $\text{CO}_2$  uptake reaches  $26 \text{ mg g}^{-1}$  with an adsorption enthalpy of  $-43 \text{ kJ mol}^{-1}$ , which are similar results to those for anhydrous

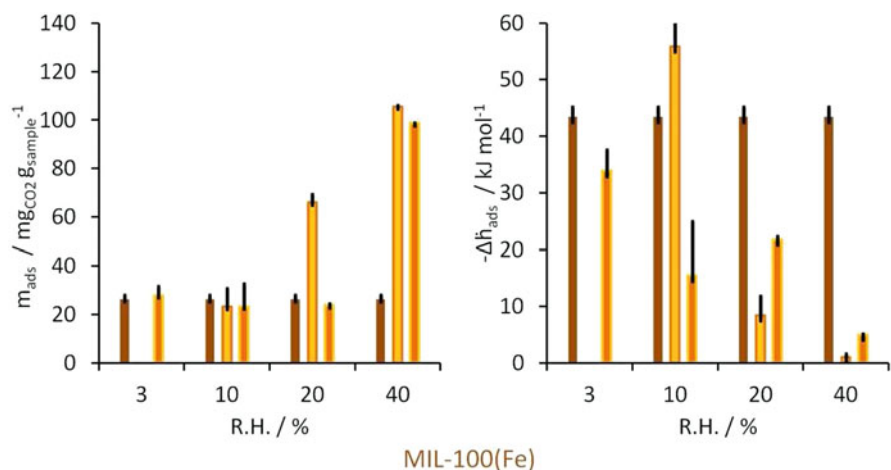


**Fig. 12.17** Dynamic  $\text{CO}_2$  adsorption for MIL-100 (Fe). Reprinted with the permission from ref. [48]. Copyright (2012) American Chemical Society

CO<sub>2</sub>. However, at 20% RH, the overall CO<sub>2</sub> uptake is significantly augmented to 66 mg g<sup>-1</sup>. Remarkably, a total CO<sub>2</sub> capture of 105 mg g<sup>-1</sup> is observed at 40% RH, which is five times higher than that under anhydrous conditions [48].

Water-accelerated CO<sub>2</sub> adsorption by MOFs can also be observed in InOF-1 [49], NOTT-400, and NOTT-401 [50]. It is hypothesized that an initial adsorption domain is created when these MOF materials adsorb a small quantity of water. Once these water molecules are “pinned” to the μ<sub>2</sub>-OH groups, a reduction in the size of the micropores takes place, providing better packing of CO<sub>2</sub> molecules and thus having a positive impact on the overall CO<sub>2</sub> capture.

The incorporation of different solvents, such as EtOH, within the pores of the MOFs was also investigated. When a small amount of EtOH (2.63 wt%) is pre-adsorbed on InOF-1, the CO<sub>2</sub> capture is enhanced 2.7-fold in comparison to that of the fully activated material. This study showed that EtOH molecules would be involved in hydrogen bonds with the μ<sub>2</sub>-OH groups. Thus, a bottleneck is formed owing to the hydrogen bonding of the EtOH molecule. The formation of O=C=O(δ<sup>-</sup>)...H(δ<sup>+</sup>) hydrogen bonds in the bottleneck facilitates the adsorption of CO<sub>2</sub> molecules [51].

It is expected that more exciting results regarding the confinement of different solvents within the pores of MOF materials will be reported in due course, presenting a new and vast research field.

## 12.3 High-Pressure CO<sub>2</sub> Adsorption

MOFs with very large pore sizes are thought to be useful for the adsorption of large amounts of CO<sub>2</sub>. In principle, the construction of stable MOFs bearing large pores is possible by choosing suitable ligands (Fig. 12.18) and metal ions. To date, several MOFs with large pores, such as MOF-210 [4], PCN-68 [52], NU-100 [53], and Al-soc-MOF [54], have been constructed and studied for CO<sub>2</sub> adsorption, providing interesting results.

Both gravimetric and volumetric capacities are used to evaluate the adsorption capacity of an MOF for CO<sub>2</sub> capture. The gravimetric capacity (wt%), i.e., the quantity of CO<sub>2</sub> adsorbed within a unit mass of material, dictates the mass of the MOF required to form an adsorbent bed. The volumetric capacity (cm<sup>3</sup> cm<sup>-3</sup>) is how densely the CO<sub>2</sub> can be stored within a material and has a significant influence on the volume of the adsorbent bed. The high internal surface areas of MOFs present the possibility to achieve large CO<sub>2</sub> adsorption capacities, especially under high pressure. Under high pressure, CO<sub>2</sub> molecules can be more efficiently packed onto pore surfaces. Thus, materials with large surface areas normally exhibit larger capacities at high pressure. For example, at 50 bar, the gravimetric CO<sub>2</sub> adsorption capacity of MOF-210 reaches 74.2 wt%, which is approximately 2.4 g g<sup>-1</sup>. The high-pressure adsorption capacities for selected MOFs are listed in Table 12.2 [55]. It can be seen that several materials with modest surface areas with OMSs also show high CO<sub>2</sub> adsorption.

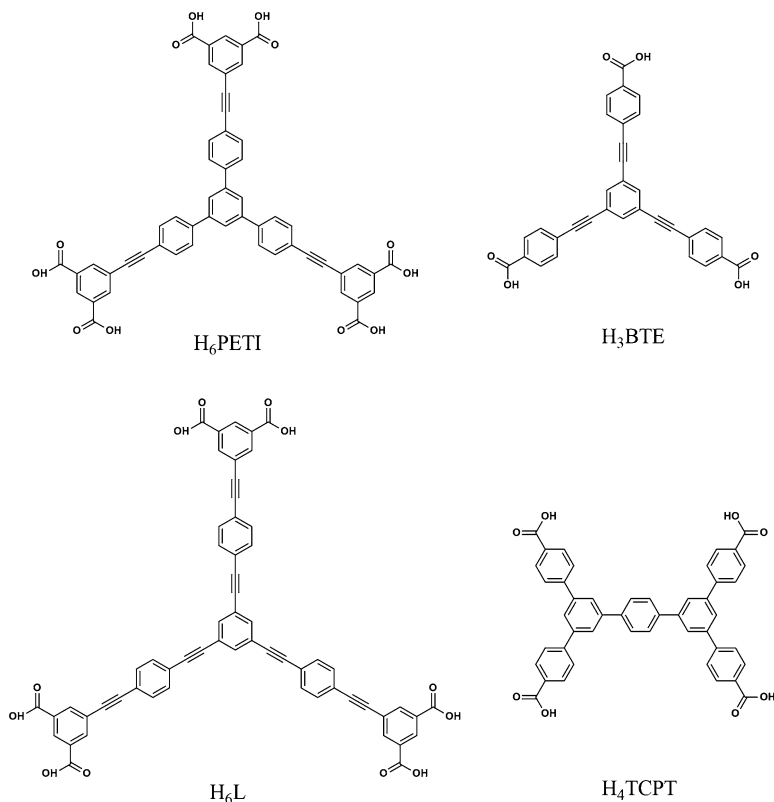


**Fig. 12.18** Selected ligands used for building MOFs with large pore

## 12.4 CO<sub>2</sub> State in MOFs

A knowledge of the states of gases in MOF nanopores permits a deeper understanding of the interactions at play during adsorption and ultimately provides guidance for designing improved MOFs for gas adsorption. Accordingly, in 2005, Matsuda et al. used synchrotron X-ray powder diffraction to examine C<sub>2</sub>H<sub>2</sub> states in the channels of CPL-1 ([Cu(pzdc)(pyz)], where pzdc = 2,3-pyrazinedicarboxylate and pyz = pyrazine) (Fig. 12.19) [66]. The material adopts different structures corresponding to an intermediate and a saturated phase with different C<sub>2</sub>H<sub>2</sub> loadings. These phases exhibit different framework-C<sub>2</sub>H<sub>2</sub> interactions. At lower loadings, a metastable phase is formed featuring an interaction between two metal-coordinated carboxylate O atoms and C<sub>2</sub>H<sub>2</sub>. However, under saturated conditions, a slight rotation of the C<sub>2</sub>H<sub>2</sub> molecules occurs, allowing the formation of stronger C-H...O hydrogen bonds with two uncoordinated O atoms of the carboxylates. Subsequently, rotation of the pyrazine rings of the framework is observed. These specific host-guest interactions provide a clear rationale for the enhanced adsorption of C<sub>2</sub>H<sub>2</sub> over CO<sub>2</sub>, especially at low pressures.

**Table 12.2** High-pressure CO<sub>2</sub> adsorption capacities in selected MOFs

MOF	Formula	Surface area (m <sup>2</sup> /g)		CO <sub>2</sub> adsorption capacity			Ref.
		S <sub>BET</sub>	S <sub>Langmuir</sub>	wt %	P (bar)	T (K)	
MOF-210	[Zn <sub>4</sub> O(BTE) <sub>4</sub> ] <sub>3</sub> (BPDC)]	6240	10,400	74.2	50	298	[4]
MOF-200	[Zn <sub>4</sub> O(BBC) <sub>2</sub> (H <sub>2</sub> O) <sub>3</sub> ]	4530	10,400	73.9	50	298	[4]
MOF-205	[Zn <sub>4</sub> O(BTB) <sub>4</sub> ] <sub>3</sub> (NDC)]	4460	6170	62.6	50	298	[4]
MOF-177	[Zn <sub>4</sub> O(BTB) <sub>2</sub> ]	4500	5340	60.8	50	298	[4]
PCN-68	[Cu <sub>3</sub> (H <sub>2</sub> O) <sub>3</sub> (ptei)]	5109	6033	57.2	35	298	[52]
NU-100	[Cu <sub>3</sub> (TCEPEB)]	6143		69.8	40	298	[53]
Al-soc-MOF-1	[Al <sub>3</sub> O(TCPT) <sub>1.5</sub> (H <sub>2</sub> O) <sub>3</sub> ] <sub>3</sub> [Cl <sup>-</sup> ]	5585	6530	66.7	40	298	[54]
MOF-74	[Zn <sub>4</sub> O(FMA) <sub>3</sub> ]	1120	1618	69.0	28	300	[56]
	[Mg <sub>2</sub> (dobdc)]	1542		68.9	36	278	[57]
Co21-MOF-5	[Zn <sub>3.16</sub> Co <sub>0.84</sub> (BDC) <sub>3</sub> ]		2900	65.0	10	273	[58]
MOF-5	[Zn <sub>4</sub> O(BDC) <sub>3</sub> ]		2900	58.0	10	273	[58]
Be-BTB	[Be <sub>12</sub> (OH) <sub>12</sub> (BTB) <sub>4</sub> ]	4030	4400	58.5	40	313	[59]
DUT-9	[Ni <sub>5</sub> O <sub>2</sub> (BTB) <sub>2</sub> ]			62.1	47	298	[60]
MIL-101(Cr)	[Cr <sub>3</sub> O(H <sub>2</sub> O) <sub>2</sub> F(BDC) <sub>3</sub> ]	4230		56.9	50	304	[61]
MIL-100	[Cr <sub>3</sub> O(H <sub>2</sub> O) <sub>3</sub> F(BTC) <sub>2</sub> ]	1900		44.2	50	304	[61]
HKUST-1	[Cu <sub>3</sub> (BTC) <sub>2</sub> ]	1270		42.8	300	313	[62]
ZIF-8	[Zn(MeIm) <sub>2</sub> ]	1264		35.0	30	298	[63]
MIL-53	[Al(OH)(BDC)]			30.6	25	304	[64]
UIO-66	[Zr <sub>6</sub> O <sub>4</sub> (OH) <sub>4</sub> (BDC) <sub>6</sub> ]			24.3	18	303	[65]

Adapted with permission from ref. 55. Copyright (2012) American Chemical Society

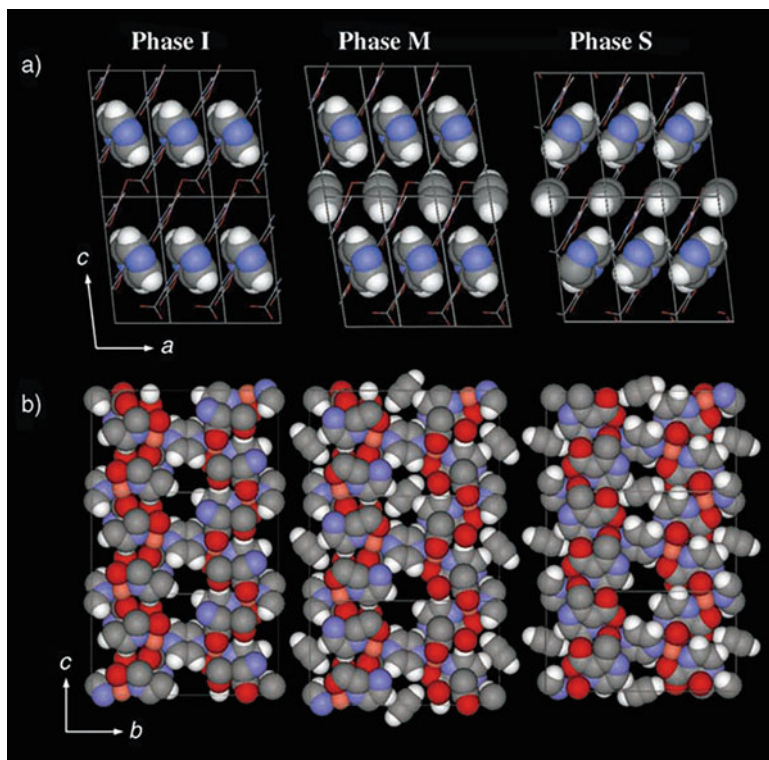


**Fig. 12.19** Crystal structures of CPL-1 in its evacuated form and with channels partially filled (intermediate phase) and filled (fully adsorbed phase) viewed along the *a*-axis showing changes in acetylene-to-framework C-H...O hydrogen bonding upon increasing gas loading. Adapted with permission from ref. [66b]. Copyright (2006) John Wiley and Sons

Over the last decade, crystallographic characterization of CO<sub>2</sub>-loaded MOFs by single-crystal or powder diffraction using either X-rays or neutrons (Table 12.3) has progressed dramatically. Here, two examples are given to demonstrate the different states possible for CO<sub>2</sub> in specific nanopores as revealed using single-crystal X-ray diffraction. In 2010, Shimizu et al. studied the states of CO<sub>2</sub> inside [Zn<sub>2</sub>(Atz)<sub>2</sub>(ox)], a Zn-based MOF comprising amino-functionalized 1,2,4-triazole (Atz) and oxalate (ox) ligands [67]. There are two independent CO<sub>2</sub> binding sites: one near the free amino groups, denoted as CO<sub>2</sub>-I, and another close to the oxalates, denoted as CO<sub>2</sub>-II. Occupancies of 0.8 and 0.5 for CO<sub>2</sub>-I and CO<sub>2</sub>-II were consistent with gravimetric adsorption measurements. The CO<sub>2</sub>-I forms an N<sup>δ-</sup>...C<sup>δ+</sup> interaction between the N atom of the amino group and the C atom of a CO<sub>2</sub> molecule at a distance of 3.151(8) Å ( $\Sigma_{vdW} = 3.25$  Å). Weak hydrogen bonds were observed between the amino groups and the CO<sub>2</sub> O atoms. Furthermore, a characteristic cooperative T-shaped O<sup>δ-</sup>...C<sup>δ+</sup> interaction between the two independent CO<sub>2</sub> molecules was identified.

**Table 12.3** Crystallographic studies of MOFs containing adsorbed CO<sub>2</sub> molecules

MOF	Formula	Analytic method	Temperature (K)	Gas loading	Ref.
MAF-23	[Zn <sub>2</sub> (BTM) <sub>2</sub> ]	SCXRD	195	0–1.5 CO <sub>2</sub> /Cu	[16]
PCP-N	[Zn <sub>2</sub> (Atz) <sub>2</sub> (ox)]	SCXRD	123–293	0.65 CO <sub>2</sub> /Zn	[67]
	[Fe(ppt) <sub>2</sub> ]	SCXRD	173	0.95 bar	[68]
MAF-2	[Cu(pyrdc)(bpp)]	SCXRD	195		[69]
	[Cu(etz)]	SCXRD	123	0.8 bar	[70]
MCF-27	[Sc <sub>2</sub> (BDC) <sub>3</sub> ]	SCXRD	235	1 bar	[71]
	[LiZn(BTC)]	SCXRD	195		[72]
MAF-X7	(Me <sub>2</sub> NH)(Hdmf)[Co <sub>2</sub> Cl <sub>4</sub> (ppt) <sub>2</sub> ]	SCXRD	120	1 bar	[73]
MIL-53 (Cr)	[Cr(OH)(BDC)] hydrated and dehydrated	PXRD		1–15 bar	[47]
MIL-53 (Cr)	[Cr(OH)(BDC)]	PXRD	293	0–10 bar	[74]
CPO-27-Ni	[Ni <sub>2</sub> (dhtp)(H <sub>2</sub> O) <sub>2</sub> ]	PXRD	100	0.2–0.5 bar	[75]
YO-MOF	[Zn <sub>2</sub> (L <sub>1</sub> )(L <sub>2</sub> )]	PXRD-PDF analysis	260-RT	1 bar	[76]
MIL-47(V)	[V(O)(BDC)]	PXRD	303	0–30.9 bar	[77]
DMOF-(BME) <sub>2</sub>	[Zn <sub>2</sub> (BME-BDC) <sub>2</sub> (DABCO)]	PXRD	195	0–1 bar	[78]
MIL-53(Fe)	[Fe(OH)(BDC)]	PXRD	230	0–8.8 bar	[79]
MIL-53(Sc)	[Sc(OH)(BDC)]	PXRD	196	0–0.9 bar	[80]
ELM-11	[Cu(BF <sub>4</sub> ) <sub>2</sub> (bpy) <sub>2</sub> ]	PXRD	195–298	2, 3, 6 CO <sub>2</sub> /Cu	[81]
HKUST-1	[Cu <sub>3</sub> (BTC) <sub>2</sub> ]	NPD	20	1.07–1.47 CO <sub>2</sub> /Cu	[82]
CPO-27-Mg	[Mg <sub>2</sub> (dhtp)(H <sub>2</sub> O) <sub>2</sub> ]	NPD	20	0.64 CO <sub>2</sub> /Mg	[82]
CPO-27-Mg	[Mg <sub>2</sub> (dhtp)(H <sub>2</sub> O) <sub>2</sub> ]	NPD	20	0.5 and 1.75 CO <sub>2</sub> /Mg	[83]

Abbreviations: *NPD* neutron powder diffraction, *PXRD* powder X-ray diffraction, *SCXRD* single-crystal X-ray diffraction, *PDF* pair distribution function

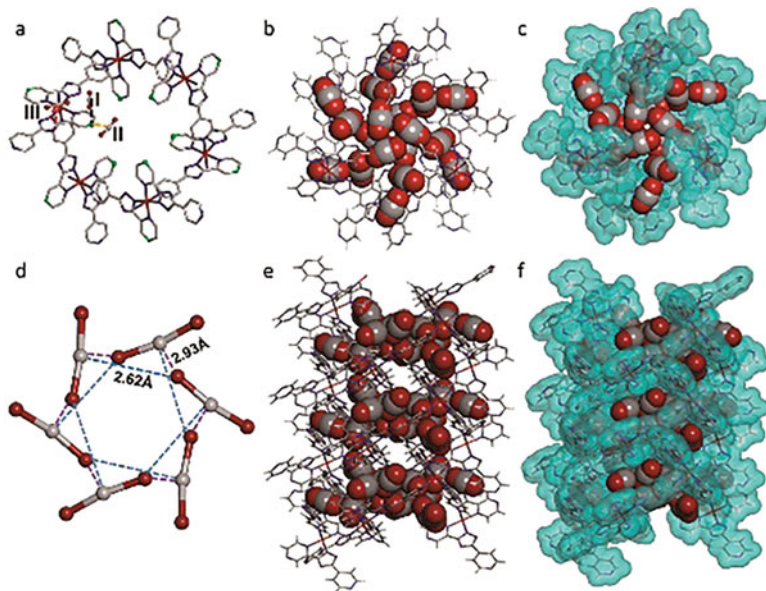


**Fig. 12.20** Representation of the different binding modes for CO<sub>2</sub> molecules in [Fe(ppt)<sub>2</sub>] $\cdot$ 5CO<sub>2</sub> at 173 K. Reprinted with the permission from ref. [68]. Copyright (2015) American Chemical Society

In 2015, Matsuda et al. investigated the general state of CO<sub>2</sub> in flexible [Fe(ppt)<sub>2</sub>] $\cdot$ 5CO<sub>2</sub> (Hppt = 3-(2-pyrazinyl)-5-(4-pyridyl)-1,2,4-triazole) [68]. There are 2.5 CO<sub>2</sub> molecules in the asymmetric unit, supporting the adsorption data. The adsorption sites of three types of independent CO<sub>2</sub> are shown as CO<sub>2</sub>–I, CO<sub>2</sub>–II, and CO<sub>2</sub>–III (Fig. 12.20). It was observed that CO<sub>2</sub>–I and CO<sub>2</sub>–II closely interact with the N atom of pyrazine. The distances between the carbon atom of CO<sub>2</sub> and the N atom are very close to the sum of the van der Waals radii of carbon (1.70 Å) and nitrogen (1.55 Å) (i.e., C12 $\cdots$ N2 = 3.23 Å and C13 $\cdots$ N2 = 3.38 Å). Strong guest-guest interactions among CO<sub>2</sub>–II molecules with slipped-parallel and T-shaped geometries (O $\cdots$ C = 2.62 and 2.93 Å) promote the formation of an unprecedented six-membered cluster. Furthermore, CO<sub>2</sub>–I interacts with CO<sub>2</sub>–III forming a T-shaped dimer (C $\cdots$ O = 2.47 Å), indicative of the formation of a more stable dimer.

Most of the MOFs will lose their crystallinity upon activation; thus the powder diffraction analysis is one powerful tool to study the gas information in the pores. Theory calculation and experimental data are always being analyzed together to give the correct information. In 2013, Düren et al. studied the breathing behavior of flexible MIL-53(Sc) with ab initio molecular dynamic simulations and in situ X-ray powder diffraction experiments (Fig. 12.21) [80]. The temperature-dependent structural changes and the structural response to variable sorbate uptake have been successfully predicted. The intermediate and large-pore phases were determined with increasing CO<sub>2</sub> pressure. The molecular-level interactions revealed the origin

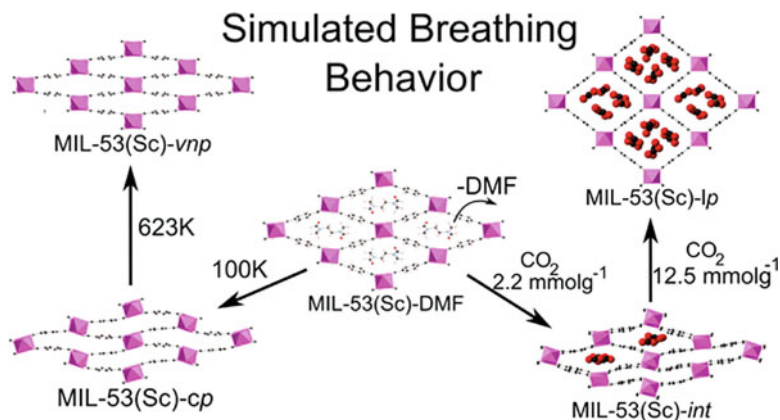


**Fig. 12.21** Simulated breathing behavior of MIL-53(Sc). Reprinted with the permission from ref. [80]. Copyright (2013) American Chemical Society

of the breathing behavior of MIL-53(Sc), which demonstrate the power of the theory calculation and X-ray diffraction studies.

It would be necessary to enhance the sorption capacity to use MOFs as real-world CO<sub>2</sub> storage materials. The key to improving capacity is to enhance the interactions between the CO<sub>2</sub> and the framework. The combination of multiple strategies, such as creating OMSSs, amine functionalization, and pore-size control, should be tailored to achieve ideal MOFs with high CO<sub>2</sub> capture abilities. In addition, suitable pore volumes and very high surface areas should also be applied by the correct design of organic ligands.

## References

1. Li H, Eddaoudi M, O’Keeffe M, Yaghi OM (1999) Design and synthesis of an exceptionally stable and highly porous metal-organic framework. *Nature* 402(6759):276–279. <https://doi.org/10.1038/46248>
2. Chui SSY, Lo SMF, Charmant JPH, Orpen AG, Williams ID (1999) A chemically functionalizable nanoporous material [Cu<sub>3</sub>(TMA)<sub>2</sub>(H<sub>2</sub>O)<sub>3</sub>]<sub>n</sub>. *Science* 283(5405):1148–1150. <https://doi.org/10.1126/science.283.5405.1148>
3. Kitagawa S, Kitaura R, Noro S (2004) Functional porous coordination polymers. *Angew Chem Int Ed* 43(18):2334–2375. <https://doi.org/10.1002/anie.200300610>
4. Furukawa H, Ko N, Go YB, Aratani N, Choi SB, Choi E, Yazaydin AO, Snurr RQ, O’Keeffe M, Yaghi OM (2010) Ultrahigh porosity in metal-organic frameworks. *Science* 329(5990):424–428. <https://doi.org/10.1126/science.1192160>
5. Li JR, Sculley J, Zhou HC (2012) Metal-organic frameworks for separations. *Chem Rev* 112(2):869–932. <https://doi.org/10.1021/cr200190s>
6. Chen B, Eddaoudi M, Reineke TM, O’Keeffe M, Yaghi OM (2000) Cu<sub>2</sub>(ATC)·6H<sub>2</sub>O: design of open metal sites in porous metal-organic crystals (ATC: 1,3,5,7-adamantane tetracarboxylate). *J Am Chem Soc* 122(46):11559–11560. <https://doi.org/10.1021/ja003159k>

7. Park J, Kim H, Han SS, Jung Y (2012) Tuning metal–organic frameworks with open-metal sites and its origin for enhancing CO<sub>2</sub> affinity by metal substitution. *J Phys Chem Lett* 3(7):826–829. <https://doi.org/10.1021/jz300047n>
8. Caskey SR, Wong-Foy AG, Matzger AJ (2008) Dramatic tuning of carbon dioxide uptake via metal substitution in a coordination polymer with cylindrical pores. *J Am Chem Soc* 130(33):10870–10871. <https://doi.org/10.1021/ja8036096>
9. (a) Wade CR, Dincă M (2012) Investigation of the synthesis, activation, and isosteric heats of CO<sub>2</sub> adsorption of the isostructural series of metal–organic frameworks M<sub>3</sub>(BTC)<sub>2</sub> (M = Cr, Fe, Ni, Cu, Mo, Ru). *Dalton Trans* 41(26):7931–7938. <https://doi.org/10.1039/c2dt30372h>; (b) Ketrat S, Maihom T, Wannakao S, Probst M, Nokbin S, Limtrakul J (2017) Coordinatively unsaturated metal–organic frameworks M<sub>3</sub>(btc)<sub>2</sub> (M = Cr, Fe, Co, Ni, Cu, and Zn) catalyzing the oxidation of CO by N<sub>2</sub>O: insight from DFT calculations. *Inorg Chem* 56(22):14005–14012. <https://doi.org/10.1021/acs.inorgchem.7b02143>
10. Cabello CP, Rumori P, Palomino GT (2014) Carbon dioxide adsorption on MIL-100(M) (M = Cr, V, Sc) metal–organic frameworks: IR spectroscopic and thermodynamic studies. *Microporous Mesoporous Mater* 190:234–239. <https://doi.org/10.1016/j.micromeso.2014.02.015>
11. Mu W, Liu D, Zhong C (2011) A computational study of the effect of doping metals on CO<sub>2</sub>/CH<sub>4</sub> separation in metal–organic frameworks. *Microporous Mesoporous Mater* 143(1):66–72. <https://doi.org/10.1016/j.micromeso.2011.02.009>
12. Lau CH, Babarao R, Hill MR (2013) A route to drastic increase of CO<sub>2</sub> uptake in Zr metal organic framework UiO-66. *Chem Commun* 49:3634–3636. <https://doi.org/10.1039/C3CC40470Fz>
13. Park HJ, Suh MP (2013) Enhanced isosteric heat, selectivity, and uptake capacity of CO<sub>2</sub> adsorption in a metal–organic framework by impregnated metal ions. *Chem Sci* 4:685–690. <https://doi.org/10.1039/C2SC21253F>
14. Zhang JP, Zhang YB, Lin JB, Chen XM (2012) Metal azolate frameworks: from crystal engineering to functional materials. *Chem Rev* 112(2):1001–1033. <https://doi.org/10.1021/cr200139g>
15. Qin JS, Du DY, Li WL, Zhang JP, Li SL, Su ZM, Wang XL, Xu Q, Shao KZ, Lan YQ (2012) N-rich zeolite-like metal–organic framework with sodalite topology: high CO<sub>2</sub> uptake, selective gas adsorption and efficient drug delivery. *Chem Sci* 3:2114–2118. <https://doi.org/10.1039/C2SC00017B>
16. Liao PQ, Zhou DD, Zhu AX, Jiang L, Lin RB, Zhang JP, Chen XM (2012) Strong and dynamic CO<sub>2</sub> sorption in a flexible porous framework possessing guest chelating claws. *J Am Chem Soc* 134(42):17380–17383. <https://doi.org/10.1021/ja3073512>
17. Lin Y, Kong C, Chen L (2016) Amine-functionalized metal–organic frameworks: structure, synthesis and applications. *RSC Adv* 6:32598–32614. <https://doi.org/10.1039/C6RA01536K>
18. Eddaoudi M, Kim J, Rosi N, Vodak D, Wachter J, O’Keeffe M, Yaghi OM (2002) Systematic design of pore size and functionality in isoreticular MOFs and their application in methane storage. *Science* 295(5554):469–472. <https://doi.org/10.1126/science.1067208>
19. Vermoortele F, Ameloot R, Vimont A, Serre C, Vos DD (2011) An amino-modified Zr-terephthalate metal–organic framework as an acid–base catalyst for cross-aldol condensation. *Chem Commun* 47:1521–1523. <https://doi.org/10.1039/C0CC03038D>
20. Lin Y, Kong C, Chen L (2012) Direct synthesis of amine-functionalized MIL-101(Cr) nanoparticles and application for CO<sub>2</sub> capture. *RSC Adv* 2:6417–6419. <https://doi.org/10.1039/C2RA20641B>
21. Chen XY, Vinh-Thang H, Rodrigue D, Kaliaguine S (2012) Amine-functionalized MIL-53 metal–organic framework in polyimide mixed matrix membranes for CO<sub>2</sub>/CH<sub>4</sub> separation. *Ind Eng Chem Res* 51(19):6895–6906. <https://doi.org/10.1021/ie3004336>
22. Hwang YK, Hong DY, Chang JS, Jung SH, Seo YK, Kim J, Vimont A, Daturi M, Serre C, Férey G (2008) Amine grafting on coordinatively unsaturated metal centers of MOFs: consequences for catalysis and metal encapsulation. *Angew Chem Int Ed* 47(22):4144–4148. <https://doi.org/10.1002/anie.200705998>

23. Demessence A, D'Alessandro DM, Foo ML, Long JR (2009) Strong CO<sub>2</sub> binding in a water-stable, triazolate-bridged metal–organic framework functionalized with ethylenediamine. *J Am Chem Soc* 131(25):8784–8786. <https://doi.org/10.1021/ja903411w>
24. McDonald TM, Lee WR, Mason JA, Wiers BM, Hong CS, Long JR (2012) Capture of carbon dioxide from air and flue gas in the alkylamine-appended metal–organic framework mmen-Mg<sub>2</sub>(dobpdc). *J Am Chem Soc* 134(16):7056–7065. <https://doi.org/10.1021/ja300034j>
25. Lee WR, Hwang SY, Ryu DW, Lim KS, Han SS, Moon D, Choi J, Hong CS (2014) Diamine-functionalized metal–organic framework: exceptionally high CO<sub>2</sub> capacities from ambient air and flue gas, ultrafast CO<sub>2</sub> uptake rate, and adsorption mechanism. *Energy Environ Sci* 7:744–751. <https://doi.org/10.1039/C3EE42328J>
26. Lee WR, Jo H, Yang LM, Lee H, Ryu DW, Lim KS, Song JH, Min DY, Han SS, Seo JG, Park YK, Moon D, Hong CS (2015) Exceptional CO<sub>2</sub> working capacity in a heterodiamine-grafted metal–organic framework. *Chem Sci* 6:3697–3705. <https://doi.org/10.1039/C5SC01191D>
27. Lin Y, Yan Q, Kong C, Chen L (2013) Polyethyleneimine incorporated metal-organic frameworks adsorbent for highly selective CO<sub>2</sub> capture. *Sci Rep* 3:1859. <https://doi.org/10.1038/srep01859>
28. Shekhah O, Belmabkhout Y, Chen Z, Guillerm V, Cairns A, Adil K, Eddaoudi M (2014) Made-to-order metal-organic frameworks for trace carbon dioxide removal and air capture. *Nat Commun* 5:4228. <https://doi.org/10.1038/ncomms5228>
29. Huang Y, Qin W, Li Z, Li Y (2012) Enhanced stability and CO<sub>2</sub> affinity of a UiO-66 type metal–organic framework decorated with dimethyl groups. *Dalton Trans* 41:9283–9285. <https://doi.org/10.1039/C2DT30950E>
30. Zhao X, Bu XH, Zhai G, Tran H, Feng PY (2015) Pore space partition by symmetry-matching regulated ligand insertion and dramatic tuning on carbon dioxide uptake. *J Am Chem Soc* 137(4):1396–1399. <https://doi.org/10.1021/ja512137t>
31. Liu B, Yang Q, Xue C, Zhong C, Chen B, Smit B (2008) Enhanced adsorption selectivity of hydrogen/methane mixtures in metal–organic frameworks with interpenetration: a molecular simulation study. *J Phys Chem C* 112(26):9854–9860. <https://doi.org/10.1021/jp802343n>
32. Kim J, Yang ST, Choi SB, Sim J, Kim J, Ahn WS (2011) Control of catenation in CuTATB-n metal–organic frameworks by sonochemical synthesis and its effect on CO<sub>2</sub> adsorption. *J Mater Chem* 21:3070–3076. <https://doi.org/10.1039/C0JM03318A>
33. Ramsahye NA, Maurin G, Bourrelly S, Llewellyn PL, Devic T, Serre C, Loiseau T, Férey G (2007) Adsorption of CO<sub>2</sub> in metal organic frameworks of different metal centres: Grand Canonical Monte Carlo simulations compared to experiments. *Adsorption* 13(5–6):461–467. <https://doi.org/10.1007/s10450-007-9025-5>
34. Vimont A, Travert A, Bazin P, Lavalley JC, Daturi M, Serre C, Férey G, Bourrelly S, Llewellyn PL (2007) Evidence of CO<sub>2</sub> molecule acting as an electron acceptor on a nanoporous metal–organic-framework MIL-53 or Cr<sup>3+</sup>(OH)(O<sub>2</sub>C–C<sub>6</sub>H<sub>4</sub>–CO<sub>2</sub>). *Chem Commun*:3291–3293. <https://doi.org/10.1039/B703468G>
35. Seo J, Matsuda R, Sakamoto H, Bonneau C, Kitagawa S (2009) A pillared-layer coordination polymer with a rotatable pillar acting as a molecular gate for guest molecules. *J Am Chem Soc* 131(35):12792–12800. <https://doi.org/10.1021/ja904363b>
36. Coudert F, Mellot-Draznieks C, Fuchs AH, Boutin A (2009) Prediction of breathing and gate-opening transitions upon binary mixture adsorption in metal–organic frameworks. *J Am Chem Soc* 131(32):11329–11331. <https://doi.org/10.1021/ja904123f>
37. Ortiz AU, Springuel-Huet MA, Coudert F, Fuchs AH, Boutin A (2012) Predicting mixture coadsorption in soft porous crystals: experimental and theoretical study of CO<sub>2</sub>/CH<sub>4</sub> in MIL-53(Al). *Langmuir* 28(1):494–498. <https://doi.org/10.1021/la203925y>
38. Coudert F, Jeffroy M, Fuchs AH, Boutin A, Mellot-Draznieks C (2008) Thermodynamics of guest-induced structural transitions in hybrid organic–inorganic frameworks. *J Am Chem Soc* 130(43):14294–14302. <https://doi.org/10.1021/ja805129c>
39. Finsy V, Ma L, Alaerts L, De Vos DE, Baron GV, Denayer JFM (2009) Separation of CO<sub>2</sub>/CH<sub>4</sub> mixtures with the MIL-53(Al) metal–organic framework. *Microporous Mesoporous Mater* 120(3):221–227. <https://doi.org/10.1016/j.micromeso.2008.11.007>

40. Hamon L, Llewellyn PL, Devic T, Ghoufi A, Clet G, Guillerm V, Pirngruber GD, Maurin G, Serre C, Driver G, Beek W, Jolimaître E, Vimont A, Daturi M, Férey G (2009) Co-adsorption and separation of CO<sub>2</sub>–CH<sub>4</sub> mixtures in the highly flexible MIL-53(Cr) MOF. *J Am Chem Soc* 131(47):17490–17499. <https://doi.org/10.1021/ja907556q>
41. Horike S, Inubushi Y, Hori T, Fukushima T, Kitagawa S (2012) A solid solution approach to 2D coordination polymers for CH<sub>4</sub>/CO<sub>2</sub> and CH<sub>4</sub>/C<sub>2</sub>H<sub>6</sub> gas separation: equilibrium and kinetic studies. *Chem Sci* 3:116–120. <https://doi.org/10.1039/C1SC00591J>
42. Sotomayor FJ, Lastoskie CM (2017) Predicting the breakthrough performance of “gating” adsorbents using osmotic framework-adsorbed solution theory. *Langmuir* 33(42):11670–11678. <https://doi.org/10.1021/acs.langmuir.7b02036>
43. Mason JA, Oktawiec J, Taylor MK, Hudson MR, Rodriguez J, Bachman JE, Gonzalez MI, Cervellino A, Guagliardi A, Brown CM, Llewellyn PL, Masciocchi N, Long JR (2015) Methane storage in flexible metal–organic frameworks with intrinsic thermal management. *Nature* 527(7578):357–361. <https://doi.org/10.1038/nature15732>
44. Hiraide S, Tanaka H, Ishikawa N, Miyahara MT (2017) Intrinsic thermal management capabilities of flexible metal–organic frameworks for carbon dioxide separation and capture. *ACS Appl Mater Interfaces* 9(46):41066–41077. <https://doi.org/10.1021/acsami.7b13771>
45. Low JJ, Benin AI, Jakubczak P, Abrahamian JF, Faheem SA, Willis RR Virtual high throughput screening confirmed experimentally: porous coordination polymer hydration. *J Am Chem Soc* 131(43):15834–15842. <https://doi.org/10.1021/ja9061344>
46. Bosch M, Zhang M, Zhou HC (2014) Increasing the stability of metal-organic frameworks. *Adv Chem*:182327. <https://doi.org/10.1155/2014/182327>
47. Llewellyn PL, Bourrelly S, Serre C, Filinchuk Y, Férey G (2006) How hydration drastically improves adsorption selectivity for CO<sub>2</sub> over CH<sub>4</sub> in the flexible chromium terephthalate MIL-53. *Angew Chem Int Ed* 45(46):7751–7754. <https://doi.org/10.1002/anie.200602278>
48. Soubeyrand-Lenoir E, Vagner C, Yoon JW, Bazin P, Ragon F, Hwang YK, Serre C, Chang JS, Llewellyn PL (2012) How water fosters a remarkable 5-fold increase in low-pressure CO<sub>2</sub> uptake within mesoporous MIL-100(Fe). *J Am Chem Soc* 134(24):10174–10181. <https://doi.org/10.1021/ja302787x>
49. Qian J, Jiang F, Yuan D, Wu M, Zhang S, Zhang L, Hong M (2012) Highly selective carbon dioxide adsorption in a water-stable indium–organic framework material. *Chem Commun* 48:9696–9698. <https://doi.org/10.1039/C2CC35068H>
50. Álvarez JR, Peralta RA, Balmaseda J, González-Zamora E, Ibarra IA (2015) Water adsorption properties of a Sc(III) porous coordination polymer for CO<sub>2</sub> capture applications. *Inorg Chem Front* 2:1080–1084. <https://doi.org/10.1039/C5QI00176E>
51. Gonzalez-Zamora E, Ibarra IA (2017) CO<sub>2</sub> capture under humid conditions in metal–organic frameworks. *Mater Chem Front* 1:1471–1484. <https://doi.org/10.1039/C6QM00301J>
52. Yuan D, Zhao D, Sun D, Zhou HC (2010) An isorecticular series of metal–organic frameworks with dendritic hexacarboxylate ligands and exceptionally high gas-uptake capacity. *Angew Chem Int Ed* 49(31):5357–5361. <https://doi.org/10.1002/anie.201001009>
53. Farha OK, Yazaydin AO, Eryazici I, Malliakas CD, Hauser BG, Kanatzidis MG, Nguyen ST, Snurr RQ, Hupp JT (2010) De novo synthesis of a metal–organic framework material featuring ultrahigh surface area and gas storage capacities. *Nat Chem* 2:944–948. <https://doi.org/10.1038/NCHEM.834>
54. Alezi D, Belmabkhout Y, Suyetin M, Bhatt PM, Weselinski LJ, Solovyeva V, Adil K, Spanopoulos I, Trikalitis PN, Emwas AH, Eddaoudi M (2015) MOF crystal chemistry paving the way to gas storage needs: aluminum-based soc-MOF for CH<sub>4</sub>, O<sub>2</sub>, and CO<sub>2</sub> storage. *J Am Chem Soc* 137(41):13308–13318. <https://doi.org/10.1021/jacs.5b07053>
55. Sumida K, Rogow DL, Mason JA, McDonald TM, Bloch ED, Herm ZR, Bae TH, Long JR Carbon dioxide capture in metal–organic frameworks. *Chem Rev* 112(2):724–781. <https://doi.org/10.1021/cr2003272>
56. Xue M, Liu Y, Schaffino RM, Xiang S, Zhao X, Zhu GS, Qiu SL, Chen B New prototype isorecticular metal–organic framework Zn<sub>4</sub>O(FMA)<sub>3</sub> for Gas Storage. *Inorg Chem* 48(11):4649–4651. <https://doi.org/10.1021/ic900486r>

57. Dietzel PDC, Besikiotis V, Blom R (2009) Application of metal-organic frameworks with coordinatively unsaturated metal sites in storage and separation of methane and carbon dioxide. *J Mater Chem* 19:7362–7370. <https://doi.org/10.1039/B911242A>
58. Botas JA, Calleja G, Sanchez-Sanchez M, Orcajo MG Cobalt doping of the MOF-5 framework and its effect on gas-adsorption properties. *Langmuir* 26(8):5300–5303. <https://doi.org/10.1021/la100423a>
59. Herm ZR, Swisher JA, Smit B, Krishna R, Long JR (2011) Metal-organic frameworks as adsorbents for hydrogen purification and precombustion carbon dioxide capture. *J Am Chem Soc* 133(15):5664–5667. <https://doi.org/10.1021/ja111411q>
60. Gedrich K, Senkowska I, Klein N, Stoeck U, Henschel A, Lohe MR, Baburin IA, Mueller U, Kaskel S (2010) A highly porous metal-organic framework with open nickel sites. *Angew Chem Int Ed* 49(45):8489–8492. <https://doi.org/10.1002/anie.201001735>
61. Llewellyn PL, Bourrelly S, Serre C, Vimont A, Daturi M, Hamon L, Weireld GD, Chang JS, Hong DY, Hwang YK, Jung SH, Férey G (2008) High uptakes of CO<sub>2</sub> and CH<sub>4</sub> in mesoporous metal-organic frameworks MIL-100 and MIL-101. *Langmuir* 24(14):7245–7250. <https://doi.org/10.1021/la800227x>
62. Moellmer J, Moeller A, Dreisbach F, Glaeser R, Staudt R (2011) High pressure adsorption of hydrogen, nitrogen, carbon dioxide and methane on the metal-organic framework HKUST-1. *Microporous Mesoporous Mater* 138(1–3):140–148. <https://doi.org/10.1016/j.micromeso.2010.09.013>
63. Nune SK, Thallapally PK, Dohnalkova A, Wang C, Liu J, Exarhos GJ (2010) Synthesis and properties of nano zeolitic imidazolate frameworks. *Chem Commun* 46:4878–4880. <https://doi.org/10.1039/C002088E>
64. Bourrelly S, Llewellyn PL, Serre C, Millange F, Loiseau T, Férey G (2005) Different adsorption behaviors of methane and carbon dioxide in the isotypic nanoporous metal terephthalates MIL-53 and MIL-47. *J Am Chem Soc* 127(39):13519–13521. <https://doi.org/10.1021/ja054668v>
65. Wiersum AD, Soubeyrand-Lenoir E, Yang QY, Moulin B, Guillerme V, Yahia MB, Bourrelly S, Vimont A, Miller S, Vagner C, Daturi M, Clet G, Serre C, Maurin G, Llewellyn PL (2011) An evaluation of UiO-66 for gas-based applications. *Chem Asian J* 6(12):3270–3280. <https://doi.org/10.1002/asia.201100201>
66. (a) Matsuda R, Kitaura R, Kitagawa S, Kubota Y, Belosludov RV, Kobayashi TC, Sakamoto H, Chiba T, Takata M, Kawazoe Y, Mita Y (2005) Highly controlled acetylene accommodation in a metal-organic microporous material. *Nature* 436(7048):238–241. <https://doi.org/10.1038/nature03852>; (b) Kubota Y, Takata M, Matsuda R, Kitaura R, Kitagawa S, Kobayashi TC (2006) Metastable sorption state of a metal-organic porous material determined by in situ synchrotron powder diffraction. *Angew Chem Int Ed* 45(30):4932–4936. <https://doi.org/10.1002/anie.200600976>
67. Vaidhyanathan R, Iremonger SS, Shimizu GK, Boyd PG, Alavi S, Woo TK (2010) Direct observation and quantification of CO<sub>2</sub> binding within an amine-functionalized nanoporous solid. *Science* 330(6004):650–653. <https://doi.org/10.1126/science.1194237>
68. Ma Y, Matsuda R, Sato H, Hijikata Y, Li L, Kusaka S, Foo M, Xue F, Akiyama G, Yuan R, Kitagawa S (2005) A convenient strategy for designing a soft nanospace: an atomic exchange in a ligand with isostructural frameworks. *J Am Chem Soc* 137(50):15825–15832. <https://doi.org/10.1021/jacs.5b09666>
69. Maji TK, Mostafa G, Matsuda R, Kitagawa S (2005) Guest-induced asymmetry in a metal-organic porous solid with reversible single-crystal-to-single-crystal structural transformation. *J Am Chem Soc* 127(49):17152–17153. <https://doi.org/10.1021/ja0561439>
70. Zhang JP, Chen XM (2009) Optimized acetylene/carbon dioxide sorption in a dynamic porous crystal. *J Am Chem Soc* 131(15):5516–5521. <https://doi.org/10.1021/ja8089872>
71. Miller SR, Wright PA, Devic T, Serre C, Férey G, Llewellyn PL, Denoyel R, Gaberova L, Filinchuk Y (2009) Single crystal X-ray diffraction studies of carbon dioxide and fuel-related gases adsorbed on the small pore scandium terephthalate metal organic framework, Sc<sub>2</sub>(O<sub>2</sub>CC<sub>6</sub>H<sub>4</sub>CO<sub>2</sub>)<sub>3</sub>. *Langmuir* 25(6):3618–3626. <https://doi.org/10.1021/la803788u>

72. Xie LH, Lin JB, Liu XM, Wang Y, Zhang WX, Zhang JP, Chen XM (2010) Porous coordination polymer with flexibility imparted by coordinatively changeable lithium ions on the pore surface. *Inorg Chem* 49(3):1158–1165. <https://doi.org/10.1021/ic902077j>
73. Lin J, Xue W, Zhang J, Chen X (2011) An ionic porous coordination framework exhibiting high CO<sub>2</sub> affinity and CO<sub>2</sub>/CH<sub>4</sub> selectivity. *Chem Commun* 47:926–928. <https://doi.org/10.1039/C0CC04089D>
74. Serre C, Bourrelly S, Vimont A, Ramsahye NA, Maurin G, Llewellyn PL, Daturi M, Filinchuk Y, Leynaud O, Barnes P, Férey G (2007) An explanation for the very large breathing effect of a metal–organic framework during CO<sub>2</sub> adsorption. *Adv Mater* 19(17):2246–2251. <https://doi.org/10.1002/adma.200602645>
75. Dietzel PDC, Johnsen RE, Fjellvåg H, Bordiga S, Groppo E, Chavan S, Blom R Adsorption properties and structure of CO<sub>2</sub> adsorbed on open coordination sites of metal–organic framework Ni<sub>2</sub>(dhtp) from gas adsorption, IR spectroscopy and X-ray diffraction. *Chem Commun*:5125–5127. <https://doi.org/10.1039/B810574J>
76. Mulfort KL, Farha OK, Malliakas CD, Kanatzidis MG, Hupp JT (2010) An interpenetrated framework material with hysteretic CO<sub>2</sub> uptake. *Chem Eur J* 16(1):276–281. <https://doi.org/10.1002/chem.200902104>
77. Leclerc H, Devic T, Devautour-Vinot S, Bazin P, Audebrand N, Férey G, Daturi M, Vimont A, Clet G (2011) Influence of the oxidation state of the metal center on the flexibility and adsorption properties of a porous metal organic framework: MIL-47(V). *J Phys Chem C* 115(40):19828–19840. <https://doi.org/10.1021/jp206655y>
78. Henke S, Wieland DCF, Meilikhov M, Paulus M, Sternemann C, Yussenko K, Fischer RA (2011) Multiple phase-transitions upon selective CO<sub>2</sub> adsorption in an alkyl ether functionalized metal–organic framework—an in situ X-ray diffraction study. *CrystEngComm* 13:6399–6404. <https://doi.org/10.1039/C1CE05446E>
79. Devic T, Salles F, Bourrelly S, Moulin B, Maurin G, Horcajada P, Serre C, Vimont A, Lavalley JC, Leclerc H, Clet G, Daturi M, Llewellyn PL, Filinchuk Y, Férey G (2012) Effect of the organic functionalization of flexible MOFs on the adsorption of CO<sub>2</sub>. *J Mater Chem* 22:10266–10273. <https://doi.org/10.1039/C2JM15887F>
80. Chen L, Mowat JP, Fairen-Jimenez D, Morrison CA, Thompson SP, Wright PA, Duren T (2013) Elucidating the breathing of the metal–organic framework MIL-53(Sc) with ab initio molecular dynamics simulations and in situ X-ray powder diffraction experiments. *J Am Chem Soc* 135(42):15763–15773. <https://doi.org/10.1021/ja403453g>
81. (a) Tanaka H, Hiraide S, Kondo A, Miyahara MT (2015) Modeling and visualization of CO<sub>2</sub> adsorption on elastic layer-structured metal–organic framework-11: toward a better understanding of gate adsorption behavior. *J Phys Chem C* 119(21):11533–11543. <https://doi.org/10.1021/jp512870p>; (b) Hiraide S, Tanaka H, Miyahara MT (2016) Understanding gate adsorption behaviour of CO<sub>2</sub> on elastic layer-structured metal–organic framework-11. *Dalton Trans* 45:4193–4202. <https://doi.org/10.1039/C5DT03476K>
82. Wu H, Simmons JM, Srinivas G, Zhou W, Yildirim T (2010) Adsorption sites and binding nature of CO<sub>2</sub> in prototypical metal–organic frameworks: a combined neutron diffraction and first-principles study. *J Phys Chem Lett* 1(13):1946–1951. <https://doi.org/10.1021/jz100558r>
83. Queen WL, Brown CM, Britt DK, Zajdel P, Hudson MR, Yaghi OM (2011) Site-specific CO<sub>2</sub> adsorption and zero thermal expansion in an anisotropic pore network. *J Phys Chem C* 115(50):24915–24919. <https://doi.org/10.1021/jp208529p>

# Chapter 13

## CO<sub>2</sub> Storage on Zeolites and Other Adsorbents



Maria João Regufe, Ana Mafalda Ribeiro, Alexandre F. P. Ferreira, and Alírio Rodrigues

### 13.1 Adsorption at Ambient Pressure

Over the last years, CO<sub>2</sub> adsorption on zeolites and other type of materials, such as hydrotalcites and metal oxides, has been studied for application in adsorption processes to fight the global warming and to reduce the anthropogenic greenhouse gas emissions, especially CO<sub>2</sub>, the most important of these gases. The required adsorbent and process design depend on the conditions of the stream to be treated.

There are three main techniques to capture and storage CO<sub>2</sub>: the post-combustion process, pre-combustion process and oxy-fuel process. Characterized by CO<sub>2</sub> separation from flue gases resulting from a combustion process, post-combustion capture normally targets streams with 8–15% of CO<sub>2</sub> diluted in inert gases such as nitrogen, argon and small amounts of H<sub>2</sub>O and O<sub>2</sub> [1]. This type of capture can be applied to conventional coal- or gas-fired power plants [2]. The conditions of flue gases are usually ambient pressure and moderate/high temperatures, between 320 and 400 K [2]. One of the main advantages of the post-combustion capture is the flexibility, and changes to the combustion cycle are not needed. However, the resulting low CO<sub>2</sub> concentration in flue gases is not the most favourable scenario for adsorption processes.

In the oxy-fuel process, coal, oil or natural gas is burned using pure oxygen instead of air, and depending on the conditions, the produced exhaust stream has approximately 3–15% of CO<sub>2</sub>.

---

M. J. Regufe (✉) · A. M. Ribeiro · A. F. P. Ferreira · A. Rodrigues  
LSRE-Laboratory of Separation and Reaction Engineering, Associate Laboratory LSRE/LCM,  
Faculdade de Engenharia, Universidade do Porto, Porto, Portugal  
e-mail: [mjregufe@fe.up.pt](mailto:mjregufe@fe.up.pt)

It is in these two contexts, post-combustion and oxy-fuel processes, due to the low-pressure streams with low CO<sub>2</sub> molar fractions that research has focused on the development of adsorbents with high adsorption capacity. Numerous studies have demonstrated that there are several zeolites topologies and structures able to fulfil this condition [3, 4]. The success of CO<sub>2</sub> capture/storage depends on the development of new materials with some important properties.

### 13.1.1 Zeolites

Zeolites are a type of material that may occur naturally or can be synthesized. The networks of interconnecting channels/cages contained in the zeolites structures are formed by uniform pores with molecular sizes between 0.5 and 1.2 nm [5]. Their properties as molecular sieving and strong electrostatic interactions with the adsorbate, specially, CO<sub>2</sub>, make these materials promising adsorbents for CO<sub>2</sub> storage [6]. High adsorption capacity at low partial pressures of CO<sub>2</sub> and low capacities of N<sub>2</sub> lead to a high CO<sub>2</sub>/N<sub>2</sub> selectivity, being this property one of the most aimed by the researchers. Other important characteristics as stability and fast kinetics of adsorption/desorption are important for process development and are affected by several properties such as shape of materials, pore diameters, charge densities, alkali-metal cations and others, as will be explored in the next subchapters.

CO<sub>2</sub> storage on zeolites at low pressures has been explored by many groups in several experimental and computational screening/performance studies [3, 7–9].

The zeolite 13X is one of the most applied zeolites for CO<sub>2</sub> capture due to its high adsorption capacity. Depending on the shaping procedure, there are several reported values in the literature. Choudhary et al. [10] investigated the adsorption on 13X pellets (0.2–0.3 mm) using a gravimetric method, obtaining a value of 2.47 mol/kg at 0.1 bar and 305 K. In another work, Siriwardane et al. [7] studied the potential use of pressure swing adsorption (PSA) and temperature swing adsorption (TSA) processes for CO<sub>2</sub> capture, and the adsorption properties of 13X were studied with a volumetric set-up. At 0.1 bar and 304 K, an adsorbed amount of 3.65 mol/kg was assessed. Adsorption equilibrium isotherms of CO<sub>2</sub> on 13X were also determined by Cavenati et al. [11] and Siriwardane et al. [3], in 8 × 12 mesh particles and extrudates (1.6 mm) at 0.1 bar and 298 K, and values of 2.05 and 2.49 mol/kg were obtained, respectively. To improve the capacity, some modifications on shaping procedure were investigated, as example, the reduction of the binder content or even its total removal or transformation, producing binderless particles. Lee et al. [12] and Choudhary et al. [10] studied different samples of zeolite 13X, pellets (0.2–0.3 mm) and extrudates, produced without binder (binder-free), and an improved capacity was verified. CO<sub>2</sub> adsorbed amounts of 5.63 and 6.27 mol/kg at 1 bar and 305 K/298 K were obtained, respectively. In accordance with this increase of capacity is the reported value by Moreira et al. [13] (4.97 mol/kg at 1 bar and 323 K), in this study zeolite 13X binderless spheres were used. Another type of modification reported in several studies is the ion exchange with different cations in

the structure to increase the strength of interactions between the adsorbent and the molecules of the adsorbate. Moura et al. [14] presented a work of cation-exchanged 13X binderless beads with Li<sup>+</sup>, NH<sub>4</sub><sup>+</sup>, Ba<sup>2+</sup> and Fe<sup>3+</sup>. The reported values of CO<sub>2</sub> adsorption capacity at 1 bar and 298 K were 6.98, 5.31, 4.86 and 3.36 mol/kg for the following materials, from larger to smaller, FeX > BaX > NH<sub>4</sub>X > LiX.

Synthetic faujasite zeolites (FAU-type structure) can be divided as zeolite type X and zeolite type Y, depending on the silica (SiO<sub>2</sub>)-to-alumina (Al<sub>2</sub>O<sub>3</sub>) ratio (Si/Al ratio) of their framework. The first one has values of Si/Al ratio between 2 and 3, while in the second one, this ratio is 3 or higher. This property influences the CO<sub>2</sub> adsorption capacity. Choudhary et al. [10] and Liu et al. [15] reported values of CO<sub>2</sub> adsorption capacity on NaY samples of 1.23 and 1.77 mol/kg at 0.1 bar, which corresponds to 10% of CO<sub>2</sub> in a stream at 1 bar, and 305/303 K, respectively. Once again, a binder-free sample presented a higher CO<sub>2</sub> capacity of 5.38 (1 bar and 305 K) as reported by Choudhary et al. [10].

Zeolites type A, as 4A and 5A, are also evaluated regarding their performance for CO<sub>2</sub> adsorption, due to some advantages presented, such as the relatively simple structure, the stability to dehydration and the capacity to adsorb small molecules. The partial calcium exchange of the zeolite 4A results in the zeolite 5A, containing then fewer cations than 4A, and consequently has a greater adsorption capacity [16]. This property can be verified comparing the works of Saha et al. [17] and Siriwardane et al. [3], that showed values of CO<sub>2</sub> adsorption capacity of 3.24 and 1.25 mol/kg (0.1 bar and 298 K), for 5A and 4A, respectively. Mendes et al. [18] reported adsorption equilibrium isotherms on binderless beads. A high value of capacity was achieved, 3.38 mol/kg at 0.1 bar and 305 K.

ZSM-5 is a zeolite, which becomes acid with the presence of H<sup>+</sup> cation in its structure, to compensate the excess of positive charges due to high Si/Al ratio. When compared with the materials analysed before, the values reported for CO<sub>2</sub> capacity in ZSM-5 are lower than the ones for 13X, 5A and 4A, at the same conditions. An example is the work developed by Dunne et al. [19], reporting values of 0.92 and 0.57 mol/kg at 0.1 bar and 297 K for Na-ZSM-5 and H-ZSM-5, respectively.

Ion-exchange studies in the synthetic eight-membered-ring zeolite ZK-5 is reported by Liu et al. [15] as a novel CO<sub>2</sub> adsorbent. Adsorption equilibrium isotherms at 0.1 bar and 303 K showed that Li-ZK-5 presented the highest CO<sub>2</sub> adsorption capacity (3.38 mol/kg) and the samples Ca-ZK-5 and Mg-ZK-5 were the worse ion-exchange option in terms of capacity (1.46 mol/kg).

In addition to the synthetic zeolites, natural zeolites have been also investigated. A gravimetric method was used to obtain the CO<sub>2</sub> adsorption equilibrium on Na-mordenite by Choudhary et al. [10]. CO<sub>2</sub> adsorption capacity reported is 0.82 mol/kg at 0.1 bar and 298 K, which is a low value when compared with a binder-free sample, which presents an adsorption capacity value of 2.94 mol/kg at 1 bar and 298 K, as reported by the same authors.

Three natural zeolites, erionite (ZAPS), mordenite (ZNT) and clinoptilolite (ZN-19) were reported by Hernández-Huesca et al. [20] for the adsorption of CO<sub>2</sub>, and the adsorption capacities obtained were 2.66, 1.66 and 1.62 mol/kg at 0.1 and 290 K,

respectively. The authors verified that the adsorption of CO<sub>2</sub> was not affected by mass transfer problems.

Also Siriwardane et al. [7], considering the cost of the adsorbent as a major factor that needs to be considered for the process to be economical, reported a work on three natural zeolites, with low cost and easily obtained. In this research, natural herschelite-sodium chabazite (sodium aluminosilicate), clinoptilolite (sodium aluminosilicate) and another form of clinoptilolite (potassium calcium aluminosilicate) were evaluated for CO<sub>2</sub> capture, and values of 0.82, 0.40 and 0.08 mol/kg were obtained at 1 bar and 298 K, respectively, for three referred materials.

Table 13.1 shows different values of pure CO<sub>2</sub> adsorption capacity for several natural and synthetic zeolites.

Pressure swing adsorption (PSA) and temperature swing adsorption (TSA) are the two major processes targeted in the available literature using zeolites for CO<sub>2</sub> capture. Considering the composition of the gas streams to treat, as conclusion and based on literature, the best separation of CO<sub>2</sub> from N<sub>2</sub> can be achieved using zeolite 13X, as synthetic material, or chabazite as natural one [2].

### **13.1.2 Silicoaluminophosphates (SAPOs) and Aluminophosphates (AIPOs)**

Silicoaluminophosphates (SAPOs) and aluminophosphates (AIPOs) are crystalline and porous phosphates that have been studied for CO<sub>2</sub> adsorption. This type of materials can have narrow pore openings with eight-ring windows in the structure.

The structure of SAPOs possesses negatively charged frameworks like zeolites, composed of oxides of Al, Si and P. AIPOs structure is an intermediate framework, in which atoms of Si(IV) are replaced by P(V). Then, AIPOs are constituted by Al and P covalent oxides connected together, with phosphorus in an oxidation state of (V), resulting in a neutral framework with no charge balancing cations resembling to microporous silicas [21].

In SAPOs, the neutral framework is obtained due to the compensation of the negative charges by exchangeable cations [21], as happens in zeolites. Consequently, the overall electrical field gradient on SAPOs is higher than on AIPOs structure, however still lower than on low-silica zeolites.

With these properties, AIPOs present some hydrophobic characteristics, whereas SAPOs have hydrophilic properties, but still lower than zeolites. The hydrophilicity is an important property of the materials due to the presence of water vapour in the gas streams [22].

Some of SAPOs and AIPOs materials have structures very similar to zeolites, while others have unique structures. From this type of materials, SAPO-34 is the most studied one for CO<sub>2</sub> adsorption. Three-dimensional cages, small pore diameter (<0.38 nm) and moderate acidic surface properties have been attracting the attention to this material, which has the same global structure of natural zeolite chabazite

**Table 13.1** Adsorption capacity of CO<sub>2</sub> for some zeolites

Material	Property/size	<i>T</i> (K)	<i>P</i> (bar)	<i>q</i> (mol/kg)	References
13X	8 × 12 mesh	298	0.1	2.05	[3]
	Pellets 0.2–0.3 mm	305	0.1	2.47	[10]
	Unknown	304	0.1	3.65	[7]
	Extrudates 1.6 mm	298	0.1	2.49	[11]
	Binder-free pellets 0.2–0.3 mm	305	1.0	5.63	[12]
	Binder-free spheres	298	1.0	6.27	[10]
	Binder-less beads 1.2–2 mm	323	1.0	4.97	[13]
LiX	Binder-free spheres 2 mm	298	1.0	6.98	[14]
NH <sub>4</sub> X				5.31	
BaX				4.86	
FeX				3.36	
NaY	Pellets 0.2–0.3 mm	305	0.1	1.23	[10]
	Unknown	303	0.1	1.77	[15]
	Binder-free	305	1.0	5.38	[10]
4A	Unknown	298	0.1	1.25	[3]
5A	Binder-free beads 1.2–2 mm	305	0.1	3.38	[18]
	Unknown	298	0.1	3.24	[17]
Na ZSM-5	Unknown	297	0.1	0.92	[19]
H ZSM-5				0.57	
Ca-ZK-5	Unknown	303	0.1	1.46	[15]
Mg-ZK-5				1.46	
K-ZK-5				2.63	
Na-ZK-5				3.10	
Li-ZK-5				3.38	
H-ZK-5				0.86	
Na-Mordenite				Pellets 0.2–0.3 mm binder free	
	1.0	2.94			
Erionite (ZAPS)	Unknown	290	0.1	2.66	[20]
Mordenite (ZNT)				1.66	
Clinoptilolite (ZN-19)				1.62	
Chabazite	Unknown	298	1.0	0.82	[7]
Clinoptilolite (Na)				0.40	
Clinoptilolite (K)				0.08	

(CHA). In terms of CO<sub>2</sub> adsorption capacity, value of 1.98 mol/kg at 1 bar and 297 K was reported by Li et al. [23]. Other SAPOs materials have also been studied, as the case of SAPO-42 and SAPO-56. Hernández-Maldonado et al. [24] reported a value of 1.06 mol/kg at 1 bar and 298 K for SAPO-42, while SAPO-56 showed a CO<sub>2</sub> uptake of 3.65 mol/kg at 1 bar and 293 K, as reported by Bacsik et al. [25]. The kinetic diameter of CO<sub>2</sub> and N<sub>2</sub> are 0.33 and 0.37 nm, respectively [24]. Therefore,

SAPO-34 can be selected as the appropriate molecular sieve for CO<sub>2</sub>/N<sub>2</sub> separation, because its pore size (<0.38 nm) is approximately equal to nitrogen and higher than CO<sub>2</sub>. Other types of SAPOs, such as SAPO-5, SAPO-41 and SAPO-11 which have pore sizes larger than 0.38 nm, are not selective for this separation [26, 27].

As in zeolites, ion-exchanged SAPOs have been explored, in order to improve the adsorption capacity. The substitution must be made with care because SAPOs tend to lose the crystallinity due to the high concentration of H<sup>+</sup> ions released in the exchange process, destroying the framework [21]. Then, some investigations tested the enhancement of performance with cations such as Sr<sup>2+</sup>, Ce<sup>3+</sup>, Ti<sup>3+</sup>, Mg<sup>2+</sup>, Ca<sup>2+</sup>, Ag<sup>+</sup> or Na<sup>+</sup> [28–30]. The referred works demonstrated that adsorption capacity of CO<sub>2</sub> at low partial pressures of this gas is enhanced by the Sr<sup>2+</sup> cation. Rivera-Ramos et al. [28] demonstrated that Sr-SAPO-34 has a good performance for CO<sub>2</sub> adsorption in low-pressure region (2.93 mol/kg at 1 bar and 298 K for Sr-SAPO-34) and that the cation exchanged did not have significant impact in mass transfer resistance nor caused pore blocking. In terms of overall adsorption performance, the exchanged materials exhibited the following trend: Ce<sup>3+</sup> < Ti<sup>3+</sup> < Mg<sup>2+</sup> < Ca<sup>2+</sup> < Ag<sup>+</sup> < Na<sup>+</sup> < Sr<sup>2+</sup>.

AlPOs are not so well studied like SAPOs and zeolites for CO<sub>2</sub> capture, because in general, these materials have values of CO<sub>2</sub> uptake lower than the other two ones. The hydrophobic properties of AlPOs reduce the strength of interactions between CO<sub>2</sub> molecules and adsorbent. AlPOs have low capacities, such as in case of AlPO-53, AlPO-17, AlPO-18, AlPO-21, AlPO-25 and AlPO-53 [21]. These were registered in CO<sub>2</sub> adsorption capacity, as in AlPO-17, which has a lower CO<sub>2</sub> uptake than SAPO-17, although both have the same basic structure (2.30 mol/kg and 3.30 mol/kg, respectively, at 1 bar and 273 K) [31, 32]. The reduction can be justified by the absence of cation sites in AlPOs, which implies a lack of chemisorbed CO<sub>2</sub> [21].

### 13.1.3 Porous Silicates, Metal Salts and Metal Oxides

Other types of materials used to remove CO<sub>2</sub> from post-combustion processes are chemisorbents. A wide range of materials acts by chemisorption definition, i.e. in the exposed surface of material occurs a chemical reaction and molecules are adsorbed (explored in Sect. 13.3).

The use of amines onto various supports as porous mesoporous silicas, including SBA-15, SBA-12, MCM-41 and MCM-48, and silica microspheres have been studied to improve the CO<sub>2</sub> capacity [1]. MCM-41 is a silicious material that was studied by Serna-Guerrero et al. [33] for CO<sub>2</sub> capture at ambient pressure and temperature conditions, obtaining a value of 0.62 mol/kg for the adsorption capacity at 1 bar and 298 K for the adsorbent without amines treatment. In order to improve the adsorption capacity, different studies assessed different options of treatment [34–36], including grafting with polyethyleneimine, leading to an increase for 2.52 mol/kg (1 bar and 353 K), as demonstrated by Son et al. [37] (see Fig. 13.1).

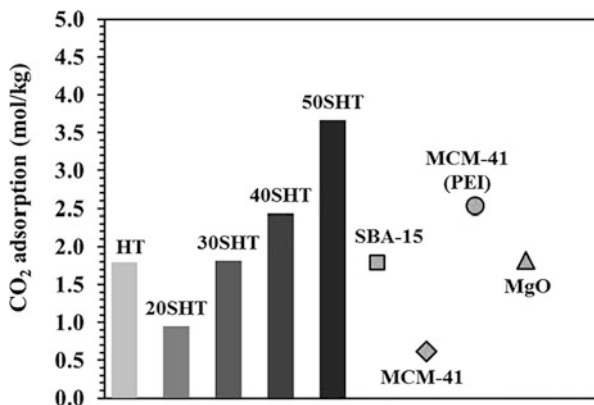


**Fig. 13.1** Comparison between CO<sub>2</sub> adsorption capacities for several materials: hydrotalcite (HT, 1 bar, 343 K) [51], 20% of hydrotalcite on SBA-15 supported (20SHT, 1 bar, 343 K) [51], 30% of hydrotalcite on SBA-15 supported (30SHT, 1 bar, 343 K) [51], 40% of hydrotalcite on SBA-15 supported (40SHT, 1 bar, 343 K) [51], 50% of hydrotalcite on SBA-15 supported (50SHT, 1 bar, 343 K) [51], SBA-15 (1 bar, 343 K) [51], MCM-41 (1 bar, 298 K) [33], MCM-41 with polyethyleneimine (MCM-41 PEI, 1 bar, 353 K) [37] and MgO (1 bar, 373 K) [39]

In addition, metal oxides such as calcium oxide (CaO), magnesium oxide (MgO) and lithium metal oxides (Li<sub>2</sub>ZrO<sub>3</sub> and Li<sub>4</sub>SiO<sub>4</sub>); metal salts from alkali metals, as lithium silicates and lithium zirconates; hydrotalcites; and double salts are also included in nanoporous materials and have been receiving considerable attention for their possible application at high temperatures. CaO oxide has been studied because it is a raw material available in high quantity and low cost, presenting a high CO<sub>2</sub> adsorption capacity [38]. CaO and MgO present good perspectives for CO<sub>2</sub> capture due to their accessibility and favourable thermodynamics [39]. Gunathilake et al. [40] reported a value of 3.85 mol/kg of CO<sub>2</sub> adsorbed at 1 bar and 393 K for a sample of CaO-SiO<sub>2</sub>. MgO sample was studied by Liu et al. [41] and a value of 1.82 mol/kg at 1 bar and 298 K was obtained. On the other hand, oxides as Li<sub>2</sub>ZrO<sub>3</sub> and Li<sub>4</sub>SiO<sub>4</sub> having lithium in their structure are more expensive. Ochoa-Fernández et al. [42] studied the CO<sub>2</sub> adsorption properties using a tapered element oscillating microbalance (TEOM) on a lithium zirconate sample, and 5.0 mol/kg of CO<sub>2</sub> was obtained at 1 bar and 673 K.

Hydrotalcites (HTs) are materials with a structure represented by  $\left[ \left( M_{1-x}^{2+} M_x^{3+} (\text{OH})_2 \right)^{x+} \cdot \left( A_{x/n}^{n-} \cdot m\text{H}_2\text{O} \right)^{x-} \right]$ , where M<sup>2+</sup> can be Mg<sup>2+</sup>, Ni<sup>2+</sup>, Zn<sup>2+</sup>, Cu<sup>2+</sup> or Mn<sup>2+</sup>, M<sup>3+</sup> can be Al<sup>3+</sup>, Fe<sup>3+</sup> or Cr<sup>3+</sup> and A<sup>n-</sup> can be CO<sub>3</sub><sup>2-</sup>, SO<sub>4</sub><sup>2-</sup>, NO<sub>3</sub><sup>-</sup>, OH<sup>-</sup>. These anionic clays are composed of layers of positively charged metallic oxide, like Mg(OH)<sub>2</sub> layers, with trivalent cations substituting the divalent cations at the centre of octahedral sites of the hydroxide sheet whose vertex contains hydroxide ions. Each -OH is shared by three octahedral cations and points to the interlayer regions [43, 44]. They can be used at high

temperatures, up to 573 K. However, the regeneration step can be more difficult and high temperature may be required [45]. Diverse works have studied CO<sub>2</sub> adsorption on hydrotalcites. The works of Yong et al. [46], Yong et al. [47] and Ram Reddy et al. [48] reported adsorption capacities of 0.52, 0.50 and 0.25 mol/kg, respectively, for CO<sub>2</sub> on different hydrotalcite samples at 1 bar and 573 K. Yong et al. [44] investigated the adsorption capacity of carbon dioxide on several samples of hydrotalcite-like materials and the effects of some modifications, such as exchange cations, temperature, chemical modification and others. An order for adsorption capacity was being established as Ni-Al (0.35 mol/kg) > Mg-Al (0.22 mol/kg) > Zn-Al (0.14 mol/kg) > Co-Al (0.11 mol/kg) > Cu-Al (0.07 mol/kg) at 0.1 bar and 298 K. Wu et al. [49] studied a potassium-promoted hydrotalcite-like material prepared with potassium nitrate as the K precursor (Mg30-K), obtaining 0.54 mol/kg of capacity at 0.1 bar (and 0.05 of partial pressure of CO<sub>2</sub>) and 711 K. Miguel et al. [50] prepared a series of HTs and gallium-substituted HTs (HTs-10Ga) by co-precipitation and later modified by impregnation with alkali (K and Cs) and alkaline-earth (Sr) metals. The obtained materials were tested and screened for CO<sub>2</sub> sorption at 573 K, up to a maximum pressure of about 1 bar. The adsorption order, in a volume base, at 1 bar was HT-10Ga-20 K (2.01 mmol/cm<sup>3</sup>) > HT-20 K (1.80 mmol/cm<sup>3</sup>) > HT-10Ga-20Cs (1.45 mmol/cm<sup>3</sup>) > HT-10Ga (0.49 mmol/cm<sup>3</sup>) > HT-10Ga-20Sr (0.37 mmol/cm<sup>3</sup>). However, this order suffers a significant change when the materials are compared in a mass base, HT-20 K (2.14 mol/kg) > HT-10Ga-20 K (1.82 mol/kg) > HT-10Ga-20Cs (1.22 mol/kg) > HT-10Ga (0.57 mol/kg) > HT-10Ga-20Sr (0.48 mol/kg) [50] (Table 13.2).

**Table 13.2** Adsorption capacity of CO<sub>2</sub> for some hydrotalcite samples and for one lithium zirconate adsorbent

Material	Partial pressure of CO <sub>2</sub>	<i>T</i> (K)	<i>P</i> (bar)	<i>q</i> (mol/kg)	References
Hydroalците	1	573	1.0	0.52	[46]
			1.0	0.50	[47]
			1.1	0.25	[48]
Ni-Al	1	298	0.1	0.35	[44]
Mg-Al				0.22	
Co-Al				0.11	
Cu-Al				0.07	
Zn-Al				0.14	
Lithium zirconate	1	673	1.0	5.00	[42]
Mg30-K	0.05	711	0.1	0.54	[49]
HT-10Ga-20K	1	573	1.0	2.14	[50]
HT-20 K				1.82	
HT-10Ga-20Cs				1.22	
HT-10Ga				0.57	
HT-10Ga-20Sr				0.48	

Pramod et al. [51] presented some results of Mg–Al hydrotalcite (Mg/Al = 2) supported on SBA-15; the composite materials present different loadings of hydrotalcite (HT) and were prepared by precipitation-deposition method. The increase of HT percentage in the composites was proved to be a good option to increase the adsorption capacity of CO<sub>2</sub> up to a maximum of 3.67 mol/kg (50% of HT loading in the composite of SBA-15) at 343 K and 1 bar, when compared with a value of 1.80 mol/kg and 1.79 mol/kg for SBA-15 and HT, respectively [28]. The values of these adsorption capacities are compared in Fig. 13.1.

## 13.2 Adsorption at High Pressure

Another type of process considered is the pre-combustion CO<sub>2</sub> capture, applicable, for example, to two types of plants: integrated gasification combined cycle (IGCC) and natural gas combined cycle (NGCC). The synthesis gas (syngas) produced in gasification process is a mixture of hydrogen, carbon monoxide, carbon dioxide and small amount of other compounds, such as methane and water, at elevated pressures (>10 bar) conditions. The water gas shift reaction produces hydrogen and carbon dioxide at high pressure and slightly elevated temperature, i.e. 5–40 bar and 313 K. Generally, in these applications, the partial pressure of CO<sub>2</sub> is up to 40% mol of CO<sub>2</sub>, implying that the adsorbents with high saturation capacity at high CO<sub>2</sub> partial pressures should be chosen [52]. Contrary to the results presented in Sect. 13.1 Adsorption at Room Pressure, here high operating pressures will be given attention; therefore high selectivity and high capacity, both evaluated at low pressures, are not important [53]. Ideal adsorbents have good working capacity between high and moderate pressures (1 bar).

Porous solid adsorbents and liquid solvents are materials currently under consideration as potential candidates for the pre-combustion CO<sub>2</sub> capture. Studies of adsorbents with sufficient CO<sub>2</sub> capacity at high pressure are scarcer than studies of adsorption at room pressure.

### 13.2.1 Zeolites

Many works are based on improving the adsorptive properties of zeolites, to be competitive with liquid solvents for processes at high pressures. These solid adsorbents must be less sensitive to steam and must also offer substantially greater capacity and selectivity for CO<sub>2</sub> than currently available physical adsorbents [54]. However, as temperature increases, zeolites have significantly lower capacity [55, 56].

As for applications at room pressures, zeolite 13X remains among the most studied adsorbent at high pressures conditions. From granulates (mesh 8 × 12), spheres (2 mm) to extrudates (1.6 mm), 13X had been studied in various forms,

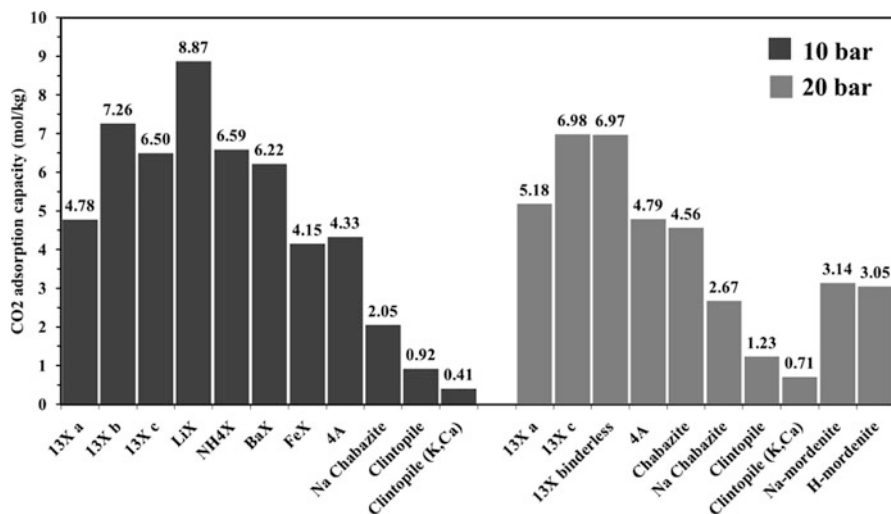


**Fig. 13.2** Adsorption capacity of CO<sub>2</sub> for some adsorbent materials at 298 K: 13X in 8 × 12 mesh form (13X a, [3]); 13X binder-free spheres (13X b, [14]); 13X extrudates by CECA (13X c, [11]); LiX, NH<sub>4</sub>X, BaX and FeX in binder-free spheres ([14]); 4A in 4 × 8 mesh form ([3]); sodium chabazite, sodium aluminosilicate (Na-chabazite, clintopile and clintopile KCa, respectively [7]); sodium mordenite and hydrogen mordenite (Na-mordenite and H-mordenite, [58])

such as in the works of Siriwardane et al. [3], Moura et al. [14] and Cavenati et al. [11], respectively, with adsorption equilibrium capacities at 10 bar and 298 K of 4.78, 7.26 and 6.50 mol/kg (named by 13X a, 13X b and 13X c in Fig. 13.2). The first and third mentioned works have also measurements at 20 bar and 298 K, and values of 5.18 and 6.98 mol/kg of CO<sub>2</sub> were obtained. In addition, Moreira et al. [13] studied a binderless 13X, and in this study, an adsorption capacity of 6.97 mol/kg at 20 bar and 298 K was obtained.

Ion exchange with different cations was reported by Moura et al. [14] in binderless beads. In contrast with the results reported at room pressure, in this case, at 10 bar and 298 K, zeolite with Li<sup>+</sup> was the best material in terms of CO<sub>2</sub> capacity (8.87 mol/kg), followed by NH<sub>4</sub><sup>+</sup> (6.59 mol/kg), Ba<sup>2+</sup> (6.22 mol/kg) and finally Fe<sup>3+</sup> (4.15 mol/kg).

In zeolite 4A, the adsorption capacity of CO<sub>2</sub> at 10 and 20 bar is very similar, which indicates that this material is already saturated at these pressures. This comparison can be made with values reported by Siriwardane et al. [3] (4.33 mol/kg at 10 bar and 4.79 mol/kg at 20 bar, both at 298 K).

Natural zeolites were also investigated at high pressures for CO<sub>2</sub> capture. Siriwardane et al. [7] reported a study on three natural materials, sodium chabazite, sodium clintopile and potassium calcium clintopile. The results obtained experimentally were 2.05 and 2.67 mol/kg for the chabazite, 0.92 and 1.23 mol/kg for the sodium clintopile and 0.41 and 0.71 mol/kg for the potassium calcium clintopile, at 10 and 20 bar, respectively. Watson et al. [57] presented a much higher value of

4.56 mol/kg for CO<sub>2</sub> adsorption at 20 bar and 298 K on another natural chabazite. Delgado et al. [58] studied the effect of the Na<sup>+</sup> and H<sup>+</sup> substitution on natural mordenite on the adsorption capacity of carbon dioxide. Na-mordenite showed a value of 3.14 mol/kg and H-mordenite of 3.05 mol/kg at 20 bar and 298 K.

Figure 13.2 presents a comparison between the discussed adsorption capacities on the different materials.

### 13.2.2 Other Materials

Mesoporous silica adsorbents and hydrotalcites have been extensively studied at relevant temperatures (between 473 and 773 K) but predominantly at low pressures (up to 1 bar) [59]. The performance of these classes of materials was evaluated in few works at high pressures. MCM-41 silica samples were prepared at different temperatures in the presence of cetyltrimethylammonium bromide by Belmabkhout et al. [60]. Adsorption equilibrium isotherms were reported for the different prepared materials, and the highest capacity was obtained for the material prepared at 373 K. The CO<sub>2</sub> adsorption capacity obtained was 4.77 mol/kg at 10 bar and 298 K (Table 13.3). The capacity increases up to 14.6 mol/kg at 40 bar and 298 K.

In the case of hydrotalcites, lower CO<sub>2</sub> adsorption capacities are reported. Hanif et al. [61] reported the synthesis of Mg-Al hydrotalcites by three procedures, and a comparison between CO<sub>2</sub> adsorption capacities at different temperatures was done. Sample named HTA-CP is composed of magnesium nitrate hexahydrate and aluminium nitrate nonahydrate and was produced by conventional co-precipitation method. Hydrotalcite produced by an ultrasound assisted co-precipitation technique was labelled as HTA-US. Finally, HTA-MW corresponds to a sample developed by a microwave-assisted reaction method. CO<sub>2</sub> adsorption capacities at 10 bar and 573 K were reported, and values of 1.59, 1.36 and 1.49 mol/kg, respectively, were obtained (Table 13.3). In addition to these three samples, other three were prepared by 20 wt% impregnation with K<sub>2</sub>CO<sub>3</sub> on the previously synthesized hydrotalcites by wet impregnation method. These were defined as HTA-CP-20 K, HTA-US-20 K and HTA-MW-20 K, names related with the original samples. Respectively, 1.83, 1.76 and 2.37 mol/kg of CO<sub>2</sub> adsorption capacity were reported (Table 13.3). In

**Table 13.3** Adsorption capacity of CO<sub>2</sub> for one mesoporous silica sample and for some hydrotalcite samples

Material	<i>T</i> (K)	<i>P</i> (bar)	<i>q</i> (mol/kg)	References
MCM-41100 T	298	10	4.77	[60]
HTA-CP	573	10	1.36	[61]
HTA-MW			1.49	
HTA-US			1.59	
HTA-CP-20 K	573	10	1.83	[61]
HTA-US-20 K		9.1	1.76	
HTA-MW-20 K		10	2.37	

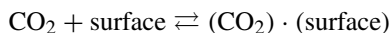
all cases, an increase of capacity was observed relatively to the nonimpregnated samples. The reported values were measured at 10 bar (except HTA-MW-20 that was at 9.1 bar) and 573 K.

### 13.3 Porosity and Mechanism of Adsorption

The mechanism of adsorption in a material depends on some parameters, such as thermodynamic conditions, surface structures and interactions between the adsorbed particles (adsorbate-adsorbate) and between the surface and the particles (adsorbate-adsorbent). For this, the structure of the pore walls is strongly responsible for the mechanism of adsorption in the material. In the case of zeolites, complex systems of pores with channels and cages form a 3D ordered porous system/crystalline wall structure, and the mechanism is mostly determined by the characteristic sites of adsorption [62]. Indeed, the well-defined micropores structure may present high selectivity between different molecules. The selectivity, responsible for the adsorptive gas separation, can be achieved by the following mechanisms: equilibrium, steric, kinetic and quantum sieving effect.

The thermodynamic equilibrium is one of the important properties of any adsorbent, and it is usually characterized by the adsorption equilibrium isotherms. Two methods are most commonly used for adsorption equilibrium isotherms determination, gravimetric and volumetric [63]. The preferential adsorption of some components over others in the interactions between adsorbate and the surface of solid packing material (adsorbent) is key in equilibrium-based separation ability. Diverse properties as polarizability, magnetic susceptibility, permanent dipole moment and quadrupole moment are indicative of the strength of interaction [64]. For example, for CO<sub>2</sub>, the relevant molecular properties is the kinetic diameter, 3.30 Å, the polarizability of  $29.1 \times 10^{-25} \text{ cm}^3$  and quadrupole moment of  $4.30 \times 10^{-26} \text{ esu}\cdot\text{cm}^2$ . The gases that have high dipole or quadrupole moment, as CO<sub>2</sub>, interact strongly with the electric field created by structural cations that promote the adsorption. Indeed, the strong affinity and the environmental friendly character are two of the most important properties of zeolites, giving to these nanoporous materials a great potential for adsorption and consequently for CO<sub>2</sub> storage.

The interaction between CO<sub>2</sub> molecule and adsorbent surface, pole-ion and pole-pole attractions between the quadrupole of CO<sub>2</sub> and the ionic and polar sites of the surface can be explained by van der Waals interactions [2], as following represented:



Generally, microporous materials, as zeolites, present an isotherm of type I, which has a monotonic curve and approaches a saturation limit at high partial pressures [63]. There are some models to represent this behaviour, being the

Langmuir model the simplest one. Langmuir theory is one of the first theories of adsorption, and together with the BET model are the most frequently used models in the experimental adsorption data analysis to explain the interactions in the materials. In these models, the adsorption is explained only taking into account the vertical components interactions, assuming that the lateral interactions between particles of adsorbate have no influence [62]. In order to account for lateral interaction as well as adsorbate molecules mobility, other models were developed such as Freundlich, Langmuir-Freundlich, Toth and Nitta [65].

However, in addition to this equilibrium selectivity, steric effects may also be present in these types of materials, because of size and/or shape exclusion, and it is a very important phenomenon to consider to explain the involved mechanisms. The ion-exchange character of zeolites can be used to tune their pore size. Then, depending on the cations present in the structure, different pore sizes can be obtained which makes these materials ideal molecular sieves [66]. For example, large molecules are sieved in pores with smaller sizes, such as in the case of zeolite 3A, which can be easily obtained from 4A by exchanging the sodium ions by potassium ions. As example the zeolite 3A can be used in dehydration of gases or alcohols where all hydrocarbons are excluded by size [67].

Kinetic selectivity arises from the difference between the diffusion rates of molecules. The suitability of adsorbents for industrial application should be assessed because if a material has high capacity but slow kinetics, it might not be ideal. However, the slow kinetics of one component relative to another can be exploited. Therefore, kinetic selectivity can be an option when equilibrium selectivity is not present or as complement to the equilibrium separation [67]. To describe the behaviour of adsorption in a material, it is important to define a diffusion model. In many studies, conditions that ensure that the system may be considered isothermal are employed. For example, Hernández-Huesca et al. [20] presented the CO<sub>2</sub> uptake curves on an erionite (ERI), natural zeolite at 293 K, and the results demonstrated that 70% of the total capacity of material is obtained after 20 s [20]. However, when this is not the case, the uptake curve results must be represented by non-isothermal models, and the heat effects during adsorption should be considered [68].

Adsorbent materials are composed of crystals of active phase shaped into extrudates or pellets with or without binder. Microporosity is present in the crystal domain, while macro- and mesoporosity appear due to the shaping process, particle domain. Micropore diffusion within the crystals is sometimes responsible for the overall of mass transfer resistance, while there are other cases where the macro-/mesopore diffusion is the controlling mechanism. It is also possible that diffusion in both types of pores contribute equally [69]. Therefore, bidisperse pore diffusion models must be considered.

To conclude, the selection of material for a process depends on the operation conditions and the composition of the stream to treat. In order to know the feasibility of separation, since different separation/adsorption mechanism can be exploited.

### 13.4 Selective Adsorption and Capacity

Adsorption selectivity is determined based on the adsorption capacity of the adsorbent for each component of the gas stream. Accordingly the selection of the separation process to be used and the performance that can be obtained is directly determined by the characteristics of the adsorbent [65]. There are some intrinsic properties of each zeolite material and of each adsorbate, which contribute to different values of selectivity and capacity of adsorption [70]. The main properties that could influence the zeolites performance in CO<sub>2</sub> adsorption capacity are:

- Basicity
- Polarizing power, distribution, size, charge and number of exchangeable cations
- Size and shape of the pores
- Silica/alumina ratio
- Dimension of adsorbates molecules
- Carbonates species formation
- Presence of water
- Pressure and temperature

The structure of zeolites consists on different SiO<sub>4</sub> and AlO<sub>4</sub> tetrahedral arrangements, in which each atom of oxygen is shared between two tetrahedrals of the structure. When compared with silicon (Si<sup>4+</sup>), aluminium (Al<sup>3+</sup>) has one more negative charge, leading to a framework with one negative charge for each aluminium atom that must be balanced by the exchangeable cation. In other words, for each Si<sup>4+</sup> ion replaced by an Al<sup>3+</sup>, the charge must be balanced by having other positive ions, such as Li<sup>+</sup>, Na<sup>+</sup>, K<sup>+</sup>, 1/2Ba<sup>2+</sup>, 1/2Ca<sup>2+</sup>, 1/2Zn<sup>2+</sup>, 1/2Mg<sup>2+</sup> and others. Cations are the most electropositive atoms in the zeolite, and typically, they are not located in the framework rings in a perfectly symmetrical fashion. The approximation of these cations to the zeolite framework induces a high electric field gradient within the cavities, and this forms a structure with basic or acid properties. In the main zeolite adsorbents, the basicity degree is higher than the acidity, and herewith the strength of electric field induced by the presence of exchange cations. Therefore, the adsorption capacity is higher for molecules with acid properties and greater permanent quadrupole moment, such as CO<sub>2</sub>. Then the basicity of zeolites is an important property [71]. Some authors indicate that the basic strength of cationic zeolites containing cations of group I-A increases by following order: Li<sup>+</sup> < Na<sup>+</sup> < K<sup>+</sup> < Rb<sup>+</sup> < Cs<sup>+</sup> [71].

The polarizing power of the exchangeable cations and their distribution, size and number also influences the local electric field and the polarization of adsorbed molecules on the structures. Polarization power can be defined as the ability of a cation to distort an anion. The tendency of the anion to become polarized by the cation is known as its polarizability. These two definitions are related with the formation of covalent/ionic bonds. Small cations, large anions and larges charges benefit the polarizing power and polarizability. In this way, polarizing power of the cations increases as the ionic radius decreases. Then, using the same cations referred

**Table 13.4** Relation between Si/Al ratios and CO<sub>2</sub> adsorption capacities

Si/Al ratio	<i>T</i> (K)	<i>P</i> (bar)	CO <sub>2</sub> adsorption capacity (mol/kg)
15	309	0.8	1.87
30	309	0.9	1.60
60	309	0.8	1.28
280	313	1.0	1.24

Ref. [76]

in basicity effect, the diameters of cations are Li<sup>+</sup> (1.4 Å) < Na<sup>+</sup> (1.9 Å) < K<sup>+</sup> (2.7 Å) < Rb<sup>+</sup> (2.9 Å) < Cs<sup>+</sup> (3.3 Å). The polarity of cations assume exactly the inverse order [72]. Katoh et al. [73] presented a work of adsorption characteristics of alkali metal ion-exchanged ZSM-5 zeolites. An increase of adsorption capacity according with the increase of cations diameter was verified (except with the Cs<sup>+</sup> cation substitution).

Another factor that influences the capacity and rate of adsorption is the pore size. When molecules penetrate in the pores at low loadings (lower pressure), first, these molecules occupy the most energetically favourable positions, that is, positions where adsorbate-pore interactions are higher than adsorbate-adsorbate interactions. At lower pressure, the density of the adsorbed molecules is highest in smaller pores due to the overlap of attractive potentials of each wall. As the pressure increases, the molecules occupy the central region of the pores, resulting in an increase of packing density. This effect is more important in zeolites with larger pores. This combined effect results in zeolites with smaller pores having higher capacity at lower partial pressures (NaA > NaX > NaY) and zeolites with larger pores having higher saturation capacity [74].

In addition to the pressure, effects of temperature, quadrupoles interactions and molecules elongation influence the density of the adsorbate within the pore.

Si/Al ration is another important factor that influences the CO<sub>2</sub> adsorption capacity. Zeolites can be classified based on the Si/Al ratio. Low-silica zeolites (Si/Al between 1 and 1.5) are represented by A and X zeolites. Natural zeolites such as erionite, chabazite, clinoptilolite, mordenite and synthetic zeolites, as L, Y, omega and large-pore mordenite, can be classified as intermediate silica zeolites with Si/Al ratios between 2 and 5. Values between 10 and 4000 are high-silica zeolites, and examples from this group are ZSM-5, ZSM-11, EU-1, EU-2 and beta, developed by direct synthesis, and mordenite, erionite and highly silicious variant of Y without any chemical framework modification [75]. In the case of CO<sub>2</sub> adsorption, Si/Al factor is very important due to the high quadrupole moment of CO<sub>2</sub>. Selectivity and adsorption capacity for CO<sub>2</sub> is favoured on zeolites with small Si/Al ratio, as described by Calleja et al. [76], which verified a decrease of capacity with the increase of Si/Al ratio in H-ZSM-5 zeolite (see Table 13.4).

Depending on the feed composition to treat, the adsorbent should be selected in order to increase the CO<sub>2</sub> capacity when compared with capacity for the other molecules, such as N<sub>2</sub> in post-combustion CO<sub>2</sub> capture and CH<sub>4</sub> in natural gas upgrade.

The dimension of the adsorbate molecules is another critical factor for adsorption process. CO<sub>2</sub> has a diameter of 3.3 Å. Depending on the zeolite, cavities with different sizes and shapes will be formed, and this is a decisive factor to determine which molecules can be or not be adsorbed in the material. Several zeolites present pore sizes much higher than the CO<sub>2</sub> molecule. For example, Na-A, Na-X, Na-Y and Ca-X have different pore sizes of 4.2, 7.4, 7.9 and 7.6 Å, respectively. Therefore, the materials do not presented any restrictions in relation to the kinetic diameter of adsorbed molecule. Then, in these cases, the porosity of zeolite cavities is a selective factor for the adsorption process [47].

Parallel to the chemisorption process, formation of carbonated species can occur with the interaction between CO<sub>2</sub> and oxygen bridging aluminium and silicon atoms [77]. These species formed at the surface of zeolites can be a significantly limiting factor for CO<sub>2</sub> adsorption due to the blocking of the cations present in the surface of the structure. Related with this factor is the presence of water. The presence of water can decrease the CO<sub>2</sub> adsorption capacity because of two main factors. H<sub>2</sub>O vapour may facilitate the formation of hydroxyl groups at the surface and, consequently, the formation of bicarbonates [10]. Then, the accessibility of CO<sub>2</sub> to the zeolite surface is reduced by the presence of these carbonates, limiting the adsorption of the molecules. Secondly, the polar water molecules adsorb strongly on the exchangeable cations, leading to a reduction of the strength and heterogeneity of the zeolites electric field [47].

For other adsorbents, such as hydrotalcites, the adsorption capacity of CO<sub>2</sub> is also influenced by diverse factors, such as type of cations and anions contained in the structure, water content, temperature conditions and chemical modifications [44, 78]. Yong et al. [44] published a review on CO<sub>2</sub> adsorption on hydrotalcites, and diverse factors were analysed. The main conclusions of this work were that in order to improve the CO<sub>2</sub> capacity:

- An optimum aluminium content on the hydrotalcite structure should be found.
- Larger or higher charge of anions leads to a high CO<sub>2</sub> adsorption capacity.
- Small amount of water is benefit for CO<sub>2</sub> adsorption.
- An optimal chemical modification, in terms of compound and quantity, improves the CO<sub>2</sub> capacity.

## 13.5 Cyclability

The successfully implementation of an adsorbent in an industrial process depends greatly on the ability to regenerate it, that is, on the cyclic working capacity.

As referred, zeolites are adsorbent materials with high selectivity, especially for molecules with electric n-poles, such as carbon dioxide, due to the presence of aluminium and extra-framework cations in their structure. However, in the desorption step, the removal of the adsorbed molecules is very difficult due to the strong interactions, leading to expensive, long and complex regeneration steps,

that may, consequently, reduce the performance of the process. In order to achieve acceptable cyclic working capacity either high vacuum or high temperature may be required.

Tagliabue et al. [79] presented a study on the performance of sodium-exchanged FAU zeolites through pure adsorption equilibrium isotherms and cycles of adsorption and desorption. The working capacity was evaluated through the desorbed amount of CO<sub>2</sub> between 5 bar and 0.5 bar. Three binder-free samples were tested, zeolite X, zeolite Y and dealuminated zeolite Y (DAY), with different Si/Al ratios of 2.5, 5.6 and 13.6, respectively. In terms of working capacity, the results obtained were inversely proportional to the zeolite aluminium content, i.e. DAY > Y > X. The stronger adsorption sites in zeolite X structure hinders the CO<sub>2</sub> desorption [56].

The adsorption of CO<sub>2</sub>/N<sub>2</sub> mixtures on ion-exchanged ZSM-5 zeolites was assessed by Katoh et al. [73]. The authors performed fixed-bed adsorption studies of CO<sub>2</sub>/N<sub>2</sub> (20.1/79.9) mixtures at different temperatures and pressures with regeneration in two steps, initially just by changing the feed stream to helium and later by increasing the temperature. The amount desorbed in each regeneration step was, respectively, denominated of weakly adsorbed and strongly adsorbed. Table 13.5 presents the determined percentage of strongly CO<sub>2</sub> adsorbed amount for the different ion-exchanged ZSM-5 zeolites for different temperatures. It can be seen that these values are higher for lower temperatures and strongly depend on the cation present on the framework.

Sanz-Pérez et al. [80] and Mittal et al. [81] studied the reuse and recycling of amine-functionalized silica materials.

In the first study, SBA-15-based adsorbents were prepared by grafting with diethylenetriamine (DT) or by polyethyleneimine (PEI) impregnation. The lifespan of adsorbent materials was evaluated through several adsorption-desorption cycles experiments performed at 383 K during 60 and 75 min for SBA-DT and SBA-PEI, respectively. In the case of SBA-DT, 96% of initial CO<sub>2</sub> uptake was maintained even after 15 cycles, and for SBA-PEI 88% of the initial capacity was kept, demonstrating that both samples exhibited a good cyclic behaviour. As can be seen in Fig. 13.3, during the successive cycles, the adsorption capacity was maintained practically constant, although a small reduction was attained in the first cycles. To ensure that these conditions of pressure and temperature were enough for a complete desorption, five additional cycles were carried out at 383 K during 120 min, and the results obtained were analogues to the previous ones. Also, Mittal et al. [81]

**Table 13.5** Percentage of strongly CO<sub>2</sub> adsorbed amount for the different ion-exchanged ZSM-5 zeolites for different temperatures

Material	% of strongly CO <sub>2</sub> adsorbed			
	303 K	333 K	373 K	423 K
Li-ZSM-5	20.5	16.5	0	0
Na-ZSM-5	44.0	26.7	0	0
K-ZSM-5	33.3	14.8	0	0
Rb-ZSM-5	25.0	3.1	0	0
Cs-ZSM-5	5.6	0	0	0

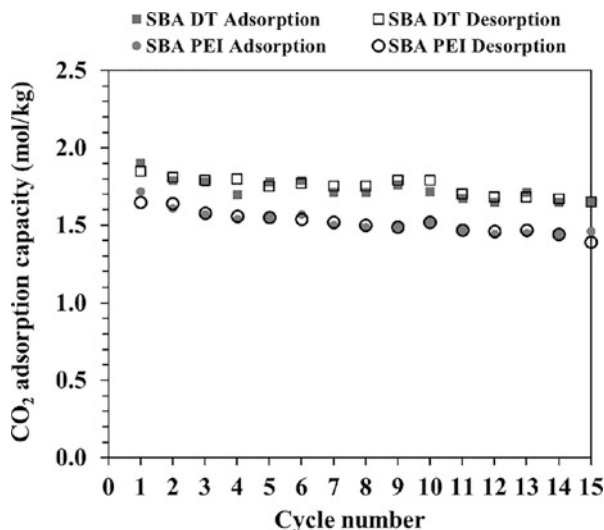


**Fig. 13.3** Amount of CO<sub>2</sub> adsorbed (full symbols) and desorbed (empty symbols) on SBA-ST (squares) and SBA-PEI (circles) for 15 cycles. (Reprinted from ref. [82], Copyright 2017, with permission from Elsevier)

published results on a N-(3-trimethoxysilylpropyl) diethylenetriamine grafted SBA-15 material in which a loss of only 7% of the initial CO<sub>2</sub> adsorption capacity was obtained even after 100 cycles.

A mesoporous MgO sample prepared by Bhagiyalakshmi et al. [83] was also evaluated by sorption/desorption cycles of carbon dioxide at 298 K (Fig. 13.4). The results obtained showed the absence of any significant change in carbon dioxide adsorption capacity over three cycles.

Oliveira et al. [83] evaluated the regenerability of a commercial hydrotalcite in extrudate form (MG30) impregnated with K<sub>2</sub>CO<sub>3</sub>. Adsorption/desorption cycles were performed at 676 K and 2 bar total pressure by feeding, in the adsorption step 20% of CO<sub>2</sub> and 26.5% of water vapour in helium and in the desorption step 26.5% of water vapour in helium. The calculated adsorption capacity in the first cycle was 0.84 mol/kg, and, after 75 cycles, a decrease of only 8% was obtained (0.77 mol/kg).

Wu et al. [49] performed a similar study on a hydrotalcite sample impregnated with potassium nitrate MG30-K<sup>N</sup>. The stability of the material was assessed by submitting it to cyclic adsorption and regeneration operation at 1 bar. The adsorption was carried out with a 0.5/0.5 mixture of CO<sub>2</sub> and water vapour at 656 K, while for the desorption a stream with helium and water vapour (0.5/0.5) was employed. After 10 cycles a decrease of 7% (from 1.13 mol/kg to 1.05 mol/kg) was observed for isothermal regeneration (Fig. 13.5). If thermal swing regeneration is employed, that is, increase the temperature to 708 K, a similar decrease in capacity is observed after 10 cycles (Fig. 13.5), but the time required for regeneration is reduced in half.

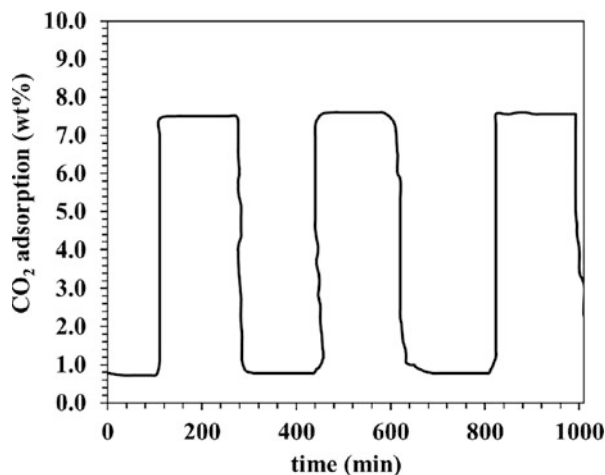


**Fig. 13.4** Cycles of CO<sub>2</sub> adsorption/desorption with N<sub>2</sub> at 298 K on mesoporous MgO. (Reprinted from ref. [82], Copyright 2010, with permission from Elsevier)

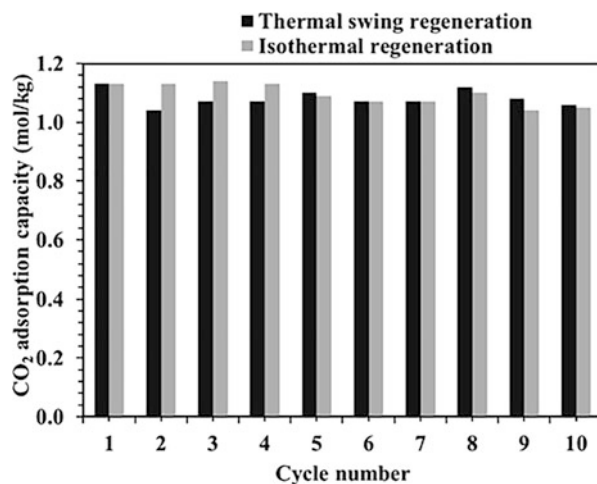


**Fig. 13.5** Adsorption capacities of CO<sub>2</sub> on Mg30-K<sup>N</sup> at 656 K for ten adsorption/desorption cycles with temperature swing regeneration and isothermal regeneration. (Adapted from Wu et al. [49])

## References

1. Songolzadeh M, Soleimani M, Takht Ravanchi M, Songolzadeh R (2014) Carbon dioxide separation from flue gases: a technological review emphasizing reduction in greenhouse gas emissions. *Sci World J* 2014:1–34
2. Samanta A, Zhao A, Shimizu GKH, Sarkar P, Gupta R (2012) Post-combustion CO<sub>2</sub> capture using solid sorbents: a review. *Ind Eng Chem Res* 51(4):1438–1463

3. Siriwardane RV, Shen M-S, Fisher EP, Poston JA (2001) Adsorption of CO<sub>2</sub> on molecular sieves and activated carbon. *Energy Fuel* 15(2):279–284
4. Chue KT, Kim JN, Yoo YJ, Cho SH, Yang RT (1995) Comparison of activated carbon and zeolite 13X for CO<sub>2</sub> recovery from flue gas by pressure swing adsorption. *Ind Eng Chem Res* 34(2):591–598
5. Chester AW, Derouane EG (2009) *Zeolite characterization and catalysis*. Springer
6. Zhang J, Singh R, Webley PA (2008) Alkali and alkaline-earth cation exchanged chabazite zeolites for adsorption based CO<sub>2</sub> capture. *Microporous Mesoporous Mater* 111(1):478–487
7. Siriwardane RV, Shen M-S, Fisher EP (2003) Adsorption of CO<sub>2</sub>, N<sub>2</sub>, and O<sub>2</sub> on natural zeolites. *Energy Fuel* 17(3):571–576
8. Xu X, Zhao X, Sun L, Liu X (2009) Adsorption separation of carbon dioxide, methane and nitrogen on monoethanol amine modified  $\beta$ -zeolite. *J Nat Gas Chem* 18(2):167–172
9. Liu B, Smit B (2009) Comparative molecular simulation study of CO<sub>2</sub>/N<sub>2</sub> and CH<sub>4</sub>/N<sub>2</sub> separation in zeolites and metal–organic frameworks. *Langmuir* 25(10):5918–5926
10. Choudhary VR, Mayadevi S, Singh AP (1995) Sorption isotherms of methane, ethane, ethene and carbon dioxide on NaX, NaY and Na-mordenite zeolites. *J Chem Soc Faraday Trans* 91(17):2935–2944
11. Cavenati S, Grande CA, Rodrigues AE (2004) Adsorption equilibrium of methane, carbon dioxide, and nitrogen on zeolite 13X at high pressures. *J Chem Eng Data* 49(4):1095–1101
12. Lee J-S, Kim J-H, Kim J-T, Suh J-K, Lee J-M, Lee C-H (2002) Adsorption equilibria of CO<sub>2</sub> on zeolite 13X and zeolite X/activated carbon composite. *J Chem Eng Data* 47(5):1237–1242
13. Moreira MA, Ribeiro AM, Ferreira AFP, Rodrigues AE (2017) Cryogenic pressure temperature swing adsorption process for natural gas upgrade. *Sep Purif Technol* 173:339–356
14. Moura PAS, Bezerra DP, Villarrasa-Garcia E, Bastos-Neto M, Azevedo DCS (2016) Adsorption equilibria of CO<sub>2</sub> and CH<sub>4</sub> in cation-exchanged zeolites 13X. *Adsorption* 22(1):71–80
15. Liu Q, Pham T, Porosoff MD, Lobo RF (2012) ZK-5: a CO<sub>2</sub>-selective zeolite with high working capacity at ambient temperature and pressure. *ChemSusChem* 5(11):2237–2242
16. Seff K, Shoemaker DP (1967) The structures of zeolite sorption complexes. I. The structures of dehydrated zeolite 5A and its iodine sorption complex. *Acta Crystallogr* 22(2):162–170
17. Saha D, Bao Z, Jia F, Deng S (2010) Adsorption of CO<sub>2</sub>, CH<sub>4</sub>, N<sub>2</sub>O, and N<sub>2</sub> on MOF-5, MOF-177, and zeolite 5A. *Environ Sci Technol* 44(5):1820–1826
18. Mendes PAP, Ribeiro AM, Gleichmann K, Ferreira AFP, Rodrigues AE (2017) Separation of CO<sub>2</sub>/N<sub>2</sub> on binderless 5A zeolite. *J CO<sub>2</sub> Util* 20:224–233
19. Dunne JA, Mariwala R, Rao M, Sircar S, Gorte RJ, Myers AL (1996) Calorimetric heats of adsorption and adsorption isotherms. I. O<sub>2</sub>, N<sub>2</sub>, Ar, CO<sub>2</sub>, CH<sub>4</sub>, C<sub>2</sub>H<sub>6</sub>, and SF<sub>6</sub> on silicalite. *Langmuir* 12(24):5888–5895
20. Hernández-Huesca R, Díaz L, Aguilar-Armenta G (1999) Adsorption equilibria and kinetics of CO<sub>2</sub>, CH<sub>4</sub> and N<sub>2</sub> in natural zeolites. *Sep Purif Technol* 15(2):163–173
21. Cheung O, Hedin N (2014) Zeolites and related sorbents with narrow pores for CO<sub>2</sub> separation from flue gas. *RSC Adv* 4(28):14480–14494
22. Jänchen J, Stach H (2012) Adsorption properties of porous materials for solar thermal energy storage and heat pump applications. *Energy Procedia* 30:289–293
23. Li S, Falconer JL, Noble RD (2004) SAPO-34 membranes for CO<sub>2</sub>/CH<sub>4</sub> separation. *J Membr Sci* 241(1):121–135
24. Hernández-Maldonado AJ, Yang RT, Chinn D, Munson CL (2003) Partially calcined gismondine type silicoaluminophosphate SAPO-43: isopropylamine elimination and separation of carbon dioxide, hydrogen sulfide, and water. *Langmuir* 19(6):2193–2200
25. Bacsik Z, Cheung O, Vasiliev P, Hedin N (2016) Selective separation of CO<sub>2</sub> and CH<sub>4</sub> for biogas upgrading on zeolite NaKA and SAPO-56. *Appl Energy* 162:613–621
26. Ashraf Talesh S, Fatemi S, Hashemi SJ, Emrani P (2008) Synthesis the fine particles of SAPO molecular sieve for effective separation of carbon dioxide from methane
27. Wendelbo R, Akporiaye D, Andersen A, Dahl IM, Mostad HB (1996) Synthesis, characterization and catalytic testing of SAPO-18, MgAPO-18, and ZnAPO-18 in the MTO reaction. *Appl Catal A Gen* 142(2):L197–L207

28. Rivera-Ramos ME, Ruiz-Mercado GJ, Hernández-Maldonado AJ (2008) Separation of CO<sub>2</sub> from light gas mixtures using ion-exchanged silicoaluminophosphate nanoporous sorbents. *Ind Eng Chem Res* 47(15):5602–5610
29. Arévalo-Hidalgo AG, Santana JA, Fu R, Ishikawa Y, Hernández-Maldonado AJ (2010) Separation of CO<sub>2</sub> from light gas mixtures using nanoporous silicoaluminophosphate sorbents: effect of multiple-step ion exchange and adsorption mechanism via computational studies. *Microporous Mesoporous Mater* 130(1):142–153
30. Hong M, Li S, Funke HF, Falconer JL, Noble RD (2007) Ion-exchanged SAPO-34 membranes for light gas separations. *Microporous Mesoporous Mater* 106(1):140–146
31. Cheung O, Liu Q, Bacsik Z, Hedin N (2012) Silicoaluminophosphates as CO<sub>2</sub> sorbents. *Microporous Mesoporous Mater* 156:90–96
32. Liu Q, Cheung NCO, Garcia-Bennett AE, Hedin N (2011) Aluminophosphates for CO<sub>2</sub> separation. *ChemSusChem* 4(1):91–97
33. Serna-Guerrero R, Belmabkhout Y, Sayari A (2010) Further investigations of CO<sub>2</sub> capture using triamine-grafted pore-expanded mesoporous silica. *Chem Eng J* 158(3):513–519
34. Ebrahimi-Gatkash M, Younesi H, Shahbazi A, Heidari A (2017) Amino-functionalized mesoporous MCM-41 silica as an efficient adsorbent for water treatment: batch and fixed-bed column adsorption of the nitrate anion. *Appl Water Sci* 7(4):1887–1901
35. Ghorbani M, Mostafa Nowee S, Ramezani N, Raji F (2016) A new nanostructured material amino functionalized mesoporous silica synthesized via co-condensation method for Pb(II) and Ni(II) ion sorption from aqueous solution. *Hydrometallurgy* 161:117–126
36. Klinthong W, Chao K-J, Tan C-S (2013) CO<sub>2</sub> capture by As-synthesized amine-functionalized MCM-41 prepared through direct synthesis under basic condition. *Ind Eng Chem Res* 52(29):9834–9842
37. Son W-J, Choi J-S, Ahn W-S (2008) Adsorptive removal of carbon dioxide using polyethyleneimine-loaded mesoporous silica materials. *Microporous Mesoporous Mater* 113(1):31–40
38. Lee ZH, Lee KT, Bhatia S, Mohamed AR (2012) Post-combustion carbon dioxide capture: evolution towards utilization of nanomaterials. *Renew Sust Energy Rev* 16(5):2599–2609
39. Kumar S, Saxena SK (2014) A comparative study of CO<sub>2</sub> sorption properties for different oxides. *Mat Renew Sustain Energy* 3(3):30
40. Gunathilake C, Jaroniec M (2016) Mesoporous calcium oxide-silica and magnesium oxide-silica composites for CO<sub>2</sub> capture at ambient and elevated temperatures. *J Mater Chem A* 4(28):10914–10924
41. Liu S, Zhang X, Li J, Zhao N, Wei W, Sun Y (2008) Preparation and application of stabilized mesoporous MgO–ZrO<sub>2</sub> solid base. *Catal Commun* 9(7):1527–1532
42. Ochoa-Fernández E, Rusten HK, Jakobsen HA, Rønning M, Holmen A, Chen D (2005) Sorption enhanced hydrogen production by steam methane reforming using Li<sub>2</sub>ZrO<sub>3</sub> as sorbent: sorption kinetics and reactor simulation. *Catal Today* 106(1):41–46
43. Soares J, Casarin GL, José HJ, Moreira RFP, Rodrigues AE (2005) Experimental and theoretical analysis for the CO<sub>2</sub> adsorption on hydrotalcite. *Adsorption* 11(1):237–241
44. Yong Z, Rodrigues AE (2002) Hydrotalcite-like compounds as adsorbents for carbon dioxide. *Energy Convers Manag* 43(14):1865–1876
45. Aschenbrenner O, McGuire P, Alsamaq S, Wang J, Supasitmongkol S, Al-Duri B, Styring P, Wood J (2011) Adsorption of carbon dioxide on hydrotalcite-like compounds of different compositions. *Chem Eng Res Des* 89(9):1711–1721
46. Yong Z, Mata V, Rodrigues AE (2002) Adsorption of carbon dioxide at high temperature – a review. *Sep Purif Technol* 26(2):195–205
47. Yong Z, Rodrigues AE (2001) Adsorption of carbon dioxide onto Hydrotalcite-like compounds (HTLcs) at high temperatures. *Ind Eng Chem Res* 40(1):204–209
48. Ram Reddy MK, Xu ZP, Lu GQ, Diniz da Costa JC (2006) Layered double hydroxides for CO<sub>2</sub> capture: structure evolution and regeneration. *Ind Eng Chem Res* 45(22):7504–7509
49. Wu YJ, Li P, Yu JG, Cunha AF, Rodrigues AE (2013) K-promoted hydrotalcites for CO<sub>2</sub> capture in sorption enhanced reactions. *Chem Eng Technol* 36(4):567–574

50. Miguel CV, Trujillano R, Rives V, Vicente MA, Ferreira AFP, Rodrigues AE, Mendes A, Madeira LM (2014) High temperature CO<sub>2</sub> sorption with gallium-substituted and promoted hydrotalcites. *Sep Purif Technol* 127:202–211
51. Pramod CV, Uppendur K, Mohan V, Sarma DS, Dhar GM, Prasad PSS, Raju BD, Rao KSR (2015) Hydrotalcite-SBA-15 composite material for efficient carbondioxide capture. *J CO<sub>2</sub> Utilization* 12:109–115
52. Hinkov I, Lamari F, Langlois P, Dicko M, Chilev C, Pentchev I (2016) Carbon dioxide capture by adsorption (review). *J Chem Technol Metal* 51:609–626
53. Riboldi L, Bolland O (2017) Overview on pressure swing adsorption (PSA) as CO<sub>2</sub> capture technology: state-of-the-art, limits and potentials. *Energy Procedia* 114:2390–2400
54. Hinkov I, Lamari FD, Langlois P, Dicko M, Chilev C, Pentchev I (2016) Carbon dioxide capture by adsorption (review). *J Chem Technol Metal* 51(6):609–626
55. Siriwardane RV, Shen M-S, Fisher EP, Losch J (2005) Adsorption of CO<sub>2</sub> on zeolites at moderate temperatures. *Energy Fuel* 19(3):1153–1159
56. Stevens RW, Siriwardane RV, Logan J (2008) In situ fourier transform infrared (FTIR) investigation of CO<sub>2</sub> adsorption onto zeolite materials. *Energy Fuel* 22(5):3070–3079
57. Watson GC, Jensen NK, Rufford TE, Chan KI, May EF (2012) Volumetric adsorption measurements of N<sub>2</sub>, CO<sub>2</sub>, CH<sub>4</sub>, and a CO<sub>2</sub> + CH<sub>4</sub> mixture on a natural chabazite from (5 to 3000) kPa. *J Chem Eng Data* 57(1):93–101
58. Delgado JA, Uguina MA, Gómez JM, Ortega L (2006) Adsorption equilibrium of carbon dioxide, methane and nitrogen onto Na- and H-mordenite at high pressures. *Sep Purif Technol* 48(3):223–228
59. Bhatta LKG, Subramanyam S, Chengala MD, Olivera S, Venkatesh K (2015) Progress in hydrotalcite like compounds and metal-based oxides for CO<sub>2</sub> capture: a review. *J Clean Prod* 103:171–196
60. Belmabkhout Y, Serna-Guerrero R, Sayari A (2009) Adsorption of CO<sub>2</sub> from dry gases on MCM-41 silica at ambient temperature and high pressure. 1: pure CO<sub>2</sub> adsorption. *Chem Eng Sci* 64(17):3721–3728
61. Hanif A, Dasgupta S, Divekar S, Arya A, Garg MO, Nanoti A (2014) A study on high temperature CO<sub>2</sub> capture by improved hydrotalcite sorbents. *Chem Eng J* 236:91–99
62. Kuchta B, Firllej L, Maurin G (2005) Modeling of adsorption in nanopores. *J Mol Model* 11(4):293–300
63. Thommes M, Kaneko K, Neimark Alexander V, Olivier James P, Rodriguez-Reinoso F, Rouquerol J, Sing Kenneth SW (2015) Physisorption of gases, with special reference to the evaluation of surface area and pore size distribution (IUPAC technical report). *Pure Appl Chem* 87(9–10):1051–1069
64. Zhou K, Chaemchuen S, Verpoort F (2017) Alternative materials in technologies for biogas upgrading via CO<sub>2</sub> capture. *Renew Sust Energ Rev* 79:1414–1441
65. Do DD (1998) Adsorption analysis: equilibria and kinetics, Chemical engineer series, vol 2. Imperial College Press, London
66. Barany S (2004) Role of interfaces in environmental protection. Springer, Dordrecht
67. Yang RT (2003) Adsorbents: fundamentals and applications. Wiley, Hoboken
68. Ruthven DM, Lee L-K, Yucel H (1980) Kinetics of non-isothermal sorption in molecular sieve crystals. *AICHE J* 26(1):16–23
69. Zhao Z, Cui X, Ma J, Li R (2007) Adsorption of carbon dioxide on alkali-modified zeolite 13X adsorbents. *Int J Greenhouse Gas Cont* 1(3):355–359
70. Yang RT (2003) Adsorbents: fundamentals and applications. John Wiley & Sons, Inc, Hoboken, pp 1–410
71. Huang M, Kaliaguine S (1992) Zeolite basicity characterized by pyrrole chemisorption: an infrared study. *J Chem Soc Faraday Trans* 88(5):751–758
72. Xu B, Kevan L (1992) Formation of alkali metal particles in alkali metal cation exchanged X zeolite exposed to alkali metal vapor: control of metal particle identity. *J Phys Chem* 96(6):2642–2645

73. Katoh M, Yoshikawa T, Tomonari T, Katayama K, Tomida T (2000) Adsorption characteristics of ion-exchanged ZSM-5 zeolites for CO<sub>2</sub>/N<sub>2</sub> mixtures. *J Colloid Interface Sci* 226(1):145–150
74. Quirke N (2005) Adsorption and transport at the nanoscale. CRC Press/Taylor and Francis Group, London
75. Visakh PM, Morlanes MJM (2016) Nanomaterials and nanocomposites: zero- to three-dimensional materials and their composites. Wiley-VCH Verlag GmbH & Co. KGaA, Weinheim
76. Calleja G, Pau J, Calles JA (1998) Pure and multicomponent adsorption equilibrium of carbon dioxide, ethylene, and propane on ZSM-5 zeolites with different Si/Al ratios. *J Chem Eng Data* 43(6):994–1003
77. Angell CL, Howell MV (1969) Infrared spectroscopic investigations of zeolites and adsorbed molecules. Part V. carbon dioxide. *Can J Chem* 47(20):3831–3836
78. Bhatta KGL, Seetharamu S, Madhusoodana C, Olivera S, Venkatesh K (2015) Progress in hydrotalcite like compounds and metal-based oxides for CO<sub>2</sub> capture: a review. *J Clean Prod* 103:171
79. Tagliabue M, Rizzo C, Onorati NB, Gambarotta EF, Carati A, Bazzano F (2012) Regenerability of zeolites as adsorbents for natural gas sweetening: a case-study. *Fuel* 93:238–244
80. Sanz-Pérez ES, Dantas TCM, Arencibia A, Calleja G, Guedes APMA, Araujo AS, Sanz R (2017) Reuse and recycling of amine-functionalized silica materials for CO<sub>2</sub> adsorption. *Chem Eng J* 308:1021–1033
81. Mittal N, Samanta A, Sarkar P, Gupta R (2015) Postcombustion CO<sub>2</sub> capture using N-(3-trimethoxysilylpropyl)diethylenetriamine-grafted solid adsorbent. *Energy Sci Eng* 3(3):207–220
82. Bhagiyalakshmi M, Lee JY, Jang HT (2010) Synthesis of mesoporous magnesium oxide: its application to CO<sub>2</sub> chemisorption. *Int J Greenhouse Gas Cont* 4(1):51–56
83. Oliveira ELG, Grande CA, Rodrigues AE (2008) CO<sub>2</sub> sorption on hydrotalcite and alkali-modified (K and Cs) hydrotalcites at high temperatures. *Sep Purif Technol* 62(1):137–147

# Chapter 14

## Clathrate-Mediated Gas Storage in Nanoporous Materials



J. Silvestre-Albero

### 14.1 Introduction

The adsorption and storage of light gas molecules (for instance, CH<sub>4</sub> and H<sub>2</sub>) in a minimum space volume is one of the most important challenges nowadays in materials science for a wide range of applications. For instance, as described in previous chapters, the development of a storage technology able to achieve a high volumetric capacity (v/v) for methane is mandatory to widen the applicability of methane as a fuel for onboard automotive applications or for long-distance transportation. Something similar accounts for hydrogen when dealing with devices running with fuel-cell technology. The low volumetric capacity of hydrogen at standard pressure and temperature conditions (STP) constitutes a handicap in applications such as stationary power, portable power, and transportation. One of the main characteristics of these gas molecules is the absence of attractive intermolecular interactions (strong repulsive interactions are found in the case of H<sub>2</sub>) with the corresponding difficulty to achieve a high packing density and the corresponding low energy density per unit volume. Among the different possibilities to increase the storage density, the most relevant approaches nowadays are either compression at high pressures (for instance, 25 MPa for CH<sub>4</sub> or 70 MPa for H<sub>2</sub>), with the associated safety, economical, and technological limitations, or liquefaction at cryogenic temperatures (112 K for methane or below 20 K for hydrogen), with the associated economical and technological concerns.

---

J. Silvestre-Albero (✉)

Laboratorio de Materiales Avanzados, Departamento de Química Inorgánica-Instituto Universitario de Materiales, Universidad de Alicante, Alicante, Spain  
e-mail: [joaquin.silvestre@ua.es](mailto:joaquin.silvestre@ua.es)

Physisorption of gases in nanoporous materials constitutes a promising alternative to densify these molecules. As described in previous chapters, high-surface area materials such as zeolites, activated carbons, and metal-organic frameworks are among the most promising candidates. However, actual storage values are still limited, preferentially at moderate pressures, and new approaches must be designed and developed to reach the actual DOE targets, for instance, 263 v/v or 0.5 g/g, for methane, and 4.5 wt.% or 0.030 kg/L, for hydrogen (target for 2020) [1, 2]. A potential alternative to increase the storage capacity for these supercritical gases at moderate temperature and pressure conditions is based on a natural process, i.e., the formation of gas clathrates deep under the sea in sediments or in the permafrost.

Gas hydrates are solid crystalline structures constituted by water molecules arranged in a 3D network through hydrogen bonding and small gas molecules trapped in the inner cavities. These are nonstoichiometric compounds that form when water and the gas molecules are in contact at low temperature and high pressure. Taking into account that the average cavity radius ranges from 3.91 nm to 5.71 nm, depending on the type of cavity and the hydrate structure formed, these water networks can accommodate different molecules such as light hydrocarbons, hydrogen, carbon dioxide, and so on [3]. Figure 14.1 and Table 14.1 describe the common hydrate unit crystal structures, their structural parameters, and the potential guest molecules trapped.

Gas hydrates have been widely evaluated in the last 30–40 years due to their abundance in nature, preferentially deep under the sea and in the permafrost. These natural hydrates contain preferentially methane in a cubic I structure, so that one volume of hydrate contains 180 volumes (STP) of gas (considering that all cavities

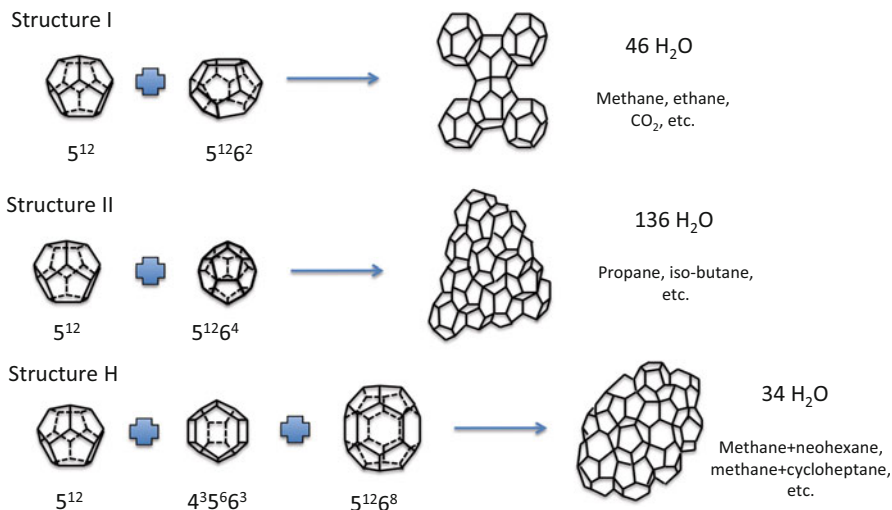


**Fig. 14.1** Three common hydrate crystal structures and their corresponding building units. (Reprinted by permission from Springer Nature, Ref. [3], copyright 2003)

**Table 14.1** Description of the unit cell parameters for the different hydrate crystal structures

Hydrate crystal structure	I		II		H		
	Small	Large	Small	Large	Small	Medium	Large
Description	$5^{12}$	$5^{12}6^2$	$5^{12}$	$5^{12}6^4$	$5^{12}$	$4^35^66^3$	$5^{12}6^8$
Number of cavities per unit cell	2	6	16	8	3	2	1
Average cavity radius (Å)	3.95	4.33	3.91	4.73	$3.91^a$	$4.06^a$	$5.71^a$

Reprinted by permission from Springer Nature, Ref. [3], copyright 2003

<sup>a</sup>Estimated from geometric models

are filled with methane). Taking into account that this amount corresponds to a gas concentration similar to the one achieved in compressed natural gas (for instance, methane gas at 273 K and 18 MPa), the possibility to store methane as a crystalline solid has become an attractive alternative to improve the storage capacity at moderate pressure and temperature conditions. Compared to liquefied or compressed alternatives, gas hydrates are stable even at temperatures above the freezing point of water and at moderate pressures (below 10 MPa in the specific case of methane hydrate), thus reducing significantly the transportation requirements. Despite the benefits of gas hydrates to store large quantities of gas, there are several drawbacks that limit the application of this technology in the transportation sector. Gas hydrates require a large amount of water compared to gas (see, for instance, the composition in Fig. 14.1 for the different crystal structures), the transportation of this additional weight attributed to water being a limitation for the efficiency of the process. Another limitation concerns the slow nucleation and growth kinetics under bulk conditions (when using pure water). The solid hydrate film formed in the initial steps at the gas-liquid interface acts as a barrier so that additional gas molecules cannot reach the growing interface, thus limiting any further growth. Last but not least, another drawback of bulk hydrates concerns the limited dissociation and methane recovery under practical conditions. For instance, Stern et al. reported only 7% hydrate dissociation after 24 h at 268.15 K and atmospheric pressure [4]. Although the first limitation cannot be solved due to the necessity of water in the formulation, there are a large number of publications in the literature dealing with the enhancement of the hydrate formation/dissociation kinetics. Among them, the most widely evaluated are magnetic stirring, to renovate the gas-liquid interface [5]; incorporation of additives (for instance, sodium dodecyl sulfate – SDS) [6, 7]; and nucleation in the presence of an inorganic material (for instance, oxides, clays, carbon materials) [8]. Among these possibilities, the nucleation and growth of gas hydrates in the presence of an inorganic material, preferentially a nanoporous system, constitutes a promising alternative due to the large versatility in the design of the structural network in terms of surface chemistry (presence of surface functionalities) and porosity (pore size and shape), with the possibility to tailor the gas-framework interactions and indirectly the hydrate formation process. Furthermore, the presence of nanoconfinement effects in the inner cavities can be used to promote the hydrate crystal growth and dissociation.

Last but not least, it is important to highlight that although natural hydrates contain preferentially methane, the cage size allows the incorporation of other guest molecules, as described in Fig. 14.1. Even multiple occupancies have been described in the literature for small gas molecules (for instance, hydrogen) [9–13]. Mao et al. described the artificial synthesis of hydrogen hydrates at extremely high pressures (above 180–220 MPa) and 300 K [9]. The presence of a H<sub>2</sub>/H<sub>2</sub>O molar ratio of 1:2 in the sII structure was associated with multiple occupancy with clusters of two H<sub>2</sub> molecules in the small cages and up to four H<sub>2</sub> molecules in the larger ones. Multiple occupation allows an increased storage of hydrogen in bulk hydrates with values around 5.3 wt.% hydrogen stored at 200–300 MPa and 240 K–249 K [13]. Although these values are very promising taking into account the DOE targets, the extreme conditions for hydrogen hydrate formation exclude at the moment any implementation on a commercial scale. However, the large versatility of gas hydrates to accommodate different guest molecules opens the gate toward another application that will also be briefly described in this chapter, i.e., the possibility to perform in situ molecular replacement (for instance, CH<sub>4</sub> replacement by CO<sub>2</sub>) under confined conditions.

## 14.2 Crystal Growth in Confined Nanospace

As described in previous chapters, nanoporous materials are constituted by a network of cavities in the nanometer scale able to accommodate molecules under a different environment compared to the bulk phase. Taking into account that a solid surface exerts electrostatic interactions (attractive and repulsive van der Waals interactions) on a given molecule nearby, the presence of two walls facing each other in a porous system gives rise to an enhancement in the adsorption potential, thus providing to the adsorbed molecule or atom unique properties. In a recent paper, Fujimori et al. demonstrated that nanoconfinement effects in carbon nanotubes could promote the formation of monoatomic sulfur chains with exceptional conductive properties [14]. While bulk sulfur requires ultrahigh pressures (above 90 GPa) to become metallic, one-dimensional confined sulfur chains become conductive at ambient pressures. Urita et al. described an outstanding compression factor in the confined nanospace of single-walled carbon nanohorns [15]. Under ambient pressure conditions, the authors successfully achieved the phase transition from B1 to B2 in KI crystals, a conversion process that usually requires pressures above 1.9 GPa under bulk conditions. The presence of supercompression functions in the confined space of nanotubular materials anticipated the potential of these nanoporous systems to promote the growth of other kinds of confined crystals, for instance, gas hydrates, under milder pressure and temperature conditions compared to the bulk system.

One of the pioneering studies about the gas hydrate formation process in confined nanospace dates back to 1992 [16]. Handa et al. extended the concept of water activity from van der Waals and coworkers [17] to describe the stability of gas

hydrates in the restricted space of mesoporous silica. According to this model, water activity decreases in confined space, and, when the water activity decreases, the hydrate formation process must take place at a higher pressure at a given temperature or at a lower temperature at a given pressure. It is well known that the freezing point of pure water is also shifted to lower temperatures when confined in the restricted space of nanoporous materials, the decrease in the melting temperature being larger for narrower pores [18]. Consequently, these premises clearly anticipate that the activity of water will be different under geometrical constraints, and consequently, phase equilibria and thermodynamic properties of confined hydrates will differ considerably from the bulk system. Thermodynamics of gas hydrates in confined nanospace are well defined by the Gibbs-Thomson equation.

$$\Delta P = \frac{4 \sigma_{lh} \cos \theta}{w} \quad (14.1)$$

where  $\sigma_{lh}$  is the surface tension between liquid water and the hydrate phases onto which water spreads with a contact angle  $\theta$  that is assumed to be zero. According to Eq. 14.1, the formation pressure in confined nanospace is

$$P_f = P_{ff} + \Delta P \quad (14.2)$$

where  $P_{ff}$  is the pressure of hydrate formation in free water, i.e.,  $P_{ff} = 3.18$  MPa.

According to Eqs. 14.1 and 14.2, the formation pressure for gas hydrates in confined nanospace increases with the decrease in the pore dimensions ( $w$ ) due to capillary effects, in such a way that hydrates must appear first in macropores ( $w > 50$  nm), followed by mesopores and finally micropores. Perrin et al. estimated the formation pressure for hydrates in mesopores at around 5.3 MPa, assuming that water is still liquid in such pores [19]. Concerning the role of the microporosity in the hydrate formation process, the situation is less clear due to the absence of characterization techniques able to evaluate the reaction processes taken place in these narrow constrictions. Taking into account that the unit cell for methane hydrate in sI structure has a lattice constant of 1.2 nm, pores below this value would be a priori useless to trap gas in the form of hydrate. However, the presence of gas adsorption processes at high pressures, above 5–8 MPa, in wet samples does not allow to ascertain a clear image about the processes taken place in these cavities, i.e., either methane compression in the unfilled pores or the formation of a defective nanohydrate [19, 20]. Miyawaki et al. proposed the formation of nano-ordered hydrates of methane in carbon cavities around 1.1 nm, these defective hydrates having a composition of methane-to-water of 1:2 [20]. The model proposed for these nanohydrates based on GCMC simulations involves a first layer of methane molecules adsorbed on the pore wall and the water molecules repelled from the graphitic pores associated with each other in the central space of the micropore forming a zigzag chain through hydrogen bonding. Unfortunately, these structures growing in micropores have never been identified due to their restricted size, and, consequently, care must be taken when trying to anticipate the role

of micropores in the methane hydrate formation process. In any case, assuming a perfect stoichiometry for hydrates growing in purely microporous materials or materials with a certain amount of small mesopores, the methane storage density within the hydrate will never exceed 180 v/v or 0.128 g/cm<sup>3</sup>, a storage density that is slightly lower than that reported for microporous materials under dry conditions (e.g., activated carbons or metal-organic frameworks may reach the range of 0.20–0.25 g/cm<sup>3</sup> assuming a purely physisorption phenomena) [21–23]. Consequently, the concept of gas storage through gas hydrate would be more meaningful for nanoporous materials with a wide pore size distribution (PSD), so that narrow pores can contribute with conventional physisorption processes, while larger pores, traditionally not participating in the dry adsorption process at high pressure (pores above 5 nm) [24], could be useful promoting the nucleation and growth of gas hydrate nanocrystals. The optimization of the adsorption process (physisorption + hydrate formation) is even more important considering the additional weight of the storage system after incorporation of water, i.e., methane transportation via confined gas hydrates will be more attractive volumetrically, more methane adsorbed in the volume of the host nanoporous system, rather than gravimetrically. In any case, Eqs. 14.1 and 14.2 clearly anticipate that gas hydrate growth in confined nanospace is thermodynamically inhibited due to the reduced pore water activity although, as will be described later, the presence of a nanoporous system exhibits an important promoting effect in the formation kinetics and extent of hydrate formation (yield) [25].

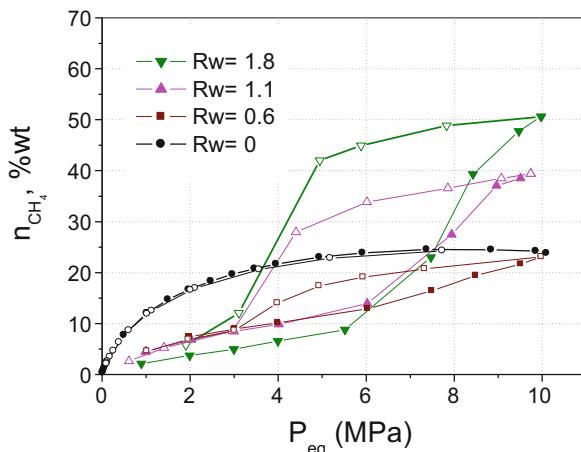
Another important parameter in confined hydrates concerns the amount of bound and freezing water [18]. The proportion of these two kinds of water molecules highly depends on the pore size and the nature of the pore walls, i.e., the presence of specific water-framework interactions. For instance, Smirnov et al. suggested these two kinds of water molecules to explain the absence of methane hydrate formation below a given water content (1.2 wt.%) in bituminous coal, i.e., weakly bound water to coal can form hydrate, while strongly interacting water does not [26]. The knowledge of amount of water molecules prone to form hydrates is highly important since it will define the water-to-hydrate ratio and, indirectly, the hydrate yield. As it will be discussed in the subsequent sections, the water-to-hydrate yield highly depends on the amount of water incorporated and the nature of the nanoporous solid evaluated. In this chapter we will focus in carbon materials, metal-organic frameworks, zeolites, clays, and silicas as host structures to promote the nucleation and growth of gas hydrates and methane as preferential guest molecule.

### 14.3 Gas Hydrates in Carbon Materials

Carbon materials are among the most widely investigated nanoporous structures to host gas hydrates. Carbon materials have been traditionally identified as hydrophobic system, so that the adsorption mechanism of water on such surfaces is markedly different from other molecules (e.g., hydrocarbons or nitrogen). Grand canonical

Monte Carlo simulations in large micropores/small mesopores have predicted that water adsorption takes place via the formation of peculiar three-dimensional clusters and networks in specific active sites (surface defects or functionalities), due to the presence of larger fluid-fluid interaction compared to fluid-solid ones [27]. The presence of low interactions with the carbon surface will be of paramount importance to promote the water-to-hydrate yield compared to other, more hydrophilic, nanoporous solids. One of the pioneering studies about methane hydrate formation in carbon materials dates back to 1992 [20]. Miyawaki et al. evaluated the adsorption of methane at subatmospheric pressure (up to 0.03 MPa) in wet carbon materials (activated carbon fibers and activated pitch-based carbons) at 303 K [20]. Despite the small pore size in these carbon materials (below 1.1 nm) and the low pressure applied, these authors proposed the formation of methane nanohydrates with a methane-to-water stoichiometry of 1:2, these structures being formed only in pores above 1.05 nm. These studies also anticipate the dependence of the hydrate formation process in the fractional filling ( $\phi_w$ ) of micropores by pre-adsorbed water. A promoting effect of the fractional filling in the amount of methane stored in wet carbon materials was also described by Celzard et al. and Casco et al. but under more realistic pressure and temperature conditions, i.e., 275 K and up to 8–10 MPa [28, 29]. High-pressure methane isotherms in these activated carbon materials are characterized by (1) an initial region at low pressures (below 4–5 MPa) with a lower adsorption capacity compared to the dry carbon and associated with the blocking of the porosity by pre-adsorbed water, (2) a subsequent jump in the amount adsorbed at 5–8 MPa attributed to the methane hydrate formation in wide pores (a pressure slightly larger than that found in bulk water at the same temperature,  $P_{ff} = 3.18$  MPa [30]), and (3) a final region above 8 MPa attributed to the methane hydrate formation in smaller pores (mesopores or even micropores), although the compression of physisorbed methane in narrow micropores cannot be ruled out. The different steps in the high-pressure methane adsorption isotherm in wet carbons can be clearly appreciated in Fig. 14.2. As it can be observed, samples with a low water content are dominated preferentially by a blocking effect, and larger water contents are required to overpass the adsorption capacity of the dry material. In the specific case of these carbon materials produced from petroleum pitch, the maximum amount adsorbed at 10 MPa was as high as 50 wt.% for the saturated sample  $R_w = 1.8$ , high above the dry carbon (24 wt.%) [29]. Interestingly, the incorporation of additional water above saturation ( $R_w = 4.1$ ) could improve the storage capacity up to 63 wt.%, with the additional appearance of a step in the adsorption isotherm at low pressures ( $P_f = 3.5$  MPa) attributed to methane hydrate formation in macropores or in the external surface. In any case, compared to the dry carbon, gas hydrate formation in nanoporous carbons is associated with a large hysteresis loop due to the metastability of the formation process. At this point it is important to highlight that these hydrate crystals in confined nanospace were synthesized within minutes (around 60 min), i.e., the presence of the activated carbon promotes the hydrate nucleation and growth kinetics compared to the bulk system due to the improved gas-liquid interphase. Yang et al. suggested an increase in the methane hydrate formation kinetics upon a decrease in the formation

**Fig. 14.2** High-pressure methane adsorption/desorption isotherms on petroleum-pitch-derived activated carbons at 275 K and under different water saturation ratios ( $R_w$  = weight water/weight carbon). The isotherm for the dry sample is included for the sake of comparison [29]



temperature or an increase in the methane pressure in the presence of carbon [30]. Furthermore, these studies suggested an optimum in the water-to-carbon mass ratio, the amount of methane stored decreasing drastically afterward due to the appearance of bulk water emerging above the wet carbon bed.

Another important parameter defining the methane hydrate formation in confined nanospace concerns the pore size of the carbon material. Recent studies from Borchardt et al. using a variety of model carbon materials (micro-, meso-, and macroporous) have anticipated that the pore size has a dominant role not only in the total methane adsorption capacity under wet conditions but also in the water-to-hydrate yield [31]. An important point to highlight is the performance of the bulk water, i.e., in the absence of the carbon host structure. As it can be appreciated in Fig. 14.3, pure water does not adsorb methane over the whole pressure range evaluated and under the equilibrium conditions usually used for these kinds of isotherms (after a few days under pressure). Incorporation of carbon has a promoting effect in the methane hydrate formation, the final amount adsorbed highly depending on the pore size. A closer look to the isotherms clearly shows that all samples exhibit important blocking effects exerted by water below 2 MPa. However, the amount of methane adsorbed drastically increases in the 2–4 MPa range, independently of the pore size. This performance unambiguously corresponds to methane hydrate formation. Methane adsorption capacity in the microporous carbon material ( $C_{micro}$ , pore size 0.8 nm) is limited to 180 mg/g under wet conditions, most probably due to steric limitations in small cavities (“hydrate stoichiometry 1  $CH_4$ ·2.5  $H_2O$ ”). A similar poor performance is observed for a macroporous carbon material ( $C_{macro}$ ) obtained from pinewood. However, the scenario changes completely for model mesoporous carbons. These carbons exhibit an improvement in the methane adsorption capacity compared to the dry samples of 120 and 173% for the 10 and 25 nm samples, respectively. Furthermore, the stoichiometry of the methane hydrate formed in the mesoporous cavities is 1  $CH_4$ ·6.3  $H_2O$ , very close to the stoichiometry of the natural

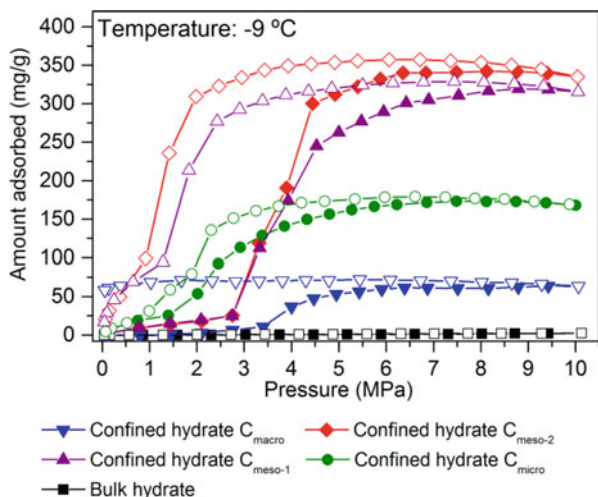


**Fig. 14.3** High-pressure methane adsorption/desorption isotherms at 264 K in a variety of model carbon materials:  $C_{\text{micro}}$  (0.8 nm),  $C_{\text{meso1}}$  (10 nm),  $C_{\text{meso2}}$  (25 nm), and  $C_{\text{macro}}$  (10,000 nm). Bulk water is included for the sake of comparison. (Reproduced from Ref. [31] with permission from the PCCP Owner Societies)

hydrates. In summary, these results clearly show that compared to the bulk system where mass transfer limits the hydrate formation process, carbon materials promote the diffusion rate between gas and water, thus promoting the hydrate formation rate.

Siangsai et al. studied the effect of the activated carbon particle size in the methane hydrate formation process [32]. High-pressure gas adsorption experiments (8 MPa and 276 K) show that the water-to-hydrate ratio is larger in activated carbons with a large particle size (up 96.5%), due to the larger interstitial pore space between the activated carbon particles. However, the methane recovery after desorption was larger for the smaller particles. Smaller particles also show improved formation kinetics due to the larger contact area between methane and water. In situ thermal evaluations anticipate two distinct growth steps, the first one probably due to the formation of a first hydrate film in the interstitial space at the gas-liquid interphase and the second one attributed to hydrate formation in the core of the interparticle space through cracks formed in the external hydrate film. A similar two-step growth process has been described in the literature for other nanoporous materials [33]. Particle size, pore space, and interconnectivity were also postulated as critical parameters playing an important role in the methane hydrate formation in porous media [34]. Direct observation of the hydrate growth in silica sand and activated carbon using a conventional microscope allowed Babu et al. to propose that in the presence of activated carbon beds, hydrate nucleation starts on the surface of the carbon grains, while in the specific case of silica, the hydrate crystals grow in the interstitial pore space. Furthermore, for larger activated carbon particles, these authors observed the presence of transient hydrate crystal formation/dissociation

within the hydrate stability region. Similar observations were reported by Jung et al. for methane hydrates formed in capillary pores, thus anticipating the complexity of the nucleation and growth process [35].

One of the open questions in the nucleation and growth of methane hydrates in the presence of carbon materials concerns the formation mechanism. It is widely accepted in the literature that the carbon surface acts as the nucleation site promoting the formation of the first nuclei, the presence of an improved water-gas interphase being responsible for the improved kinetics compared to the bulk phase. Based on the kinetic model of Skovborg et al. [36] that assumes the transfer of gas from the bulk gas phase to the bulk water as the rate-determining step, Yan et al. suggested that the surface of carbon acts as nucleation center for the methane hydrate formation rather than the water/gas interface, as it is the case for bulk hydrates [25, 30]. As it can be observed in Fig. 14.4, water is adsorbed on the carbon surface wetting the large cavities (mesopores and macropores) as a film, thus providing an efficient contact area between methane and water able to promote the methane hydrate formation process. As described above, the situation in micropores is still an open question due to the limited space for hydrate growth (the thermodynamically critical size of a stable hydrate nucleus is estimated to be 8–11 nm [5]) and the different water adsorption mechanisms compared to larger pores.

According to the proposed mechanism, liquid water films form on the surface of the carbon cavities, the formation of hydrate being initiated at the water/carbon interface. The preferential growth on the carbon surface avoids the drawbacks associated with the bulk systems, i.e., the formation of a hydrate film limiting

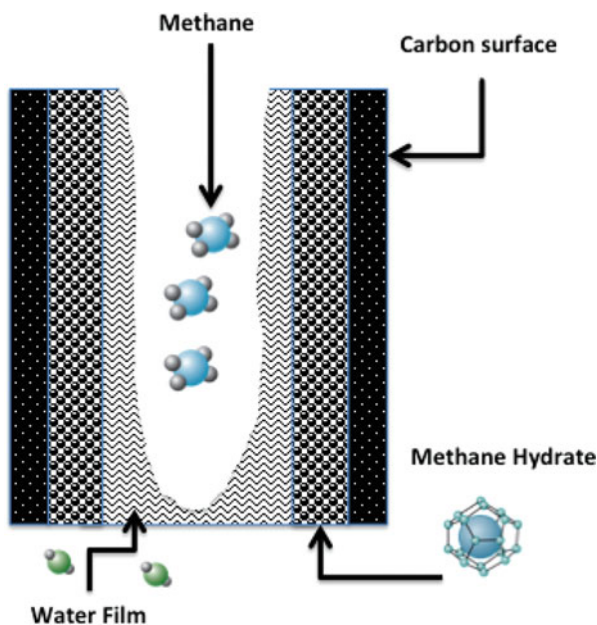


**Fig. 14.4** Physical model for methane hydrate formation in porous activated carbon. (Reprinted with the permission from Ref. [30]. Copyright 2005 American Chemical Society)

subsequent growth. Under these conditions, the formation of additional hydrate crystals is controlled by the transfer rate of gas through the water film rather than through the hydrate film. Based on this assumption, Skovborg et al. proposed the following equation to describe the hydrate formation rate in wet carbon materials [36]:

$$\frac{-d_n}{d_t} = K_L A_L (x_i - x_e) \quad (14.3)$$

where  $K_L$  and  $A_L$  are the coefficient of mass transfer of gas through liquid film and the total area of mass transfer between gas and water and  $(x_i - x_e)$  is the methane concentration difference between the water/gas interface and the water/hydrate interface. This model clearly explains the promoting effect of carbon in the gas hydrate formation process in terms of nucleation and growth kinetics and water-to-hydrate yield, due to the presence of an optimized water/gas interface. Furthermore, carbon as a host structure also promotes the gas hydrate dissociation compared to the bulk phase (self-preservation effects are not observed in confined hydrates) [37]. The rapid dissociation of the confined hydrates is crucial for a technological application of these hydrates, since it defines extent and kinetics of methane recovery. An additional thermodynamic promotion of the carbon surface due to the ordered adsorption of water clusters prone to form hydrates cannot be ruled out [25].

As described above, the promoting effect of confined water in the gas hydrate formation process is rarely reflected in the total methane adsorption capacity per gram of sample (unless the mass of dry carbon is considered in the calculations) but rather in the volumetric adsorption capacity. While the presence of water increases the weight of the adsorbent (water + carbon), the final volume is rather similar before and after water pre-impregnation. Yan et al. reported storage values around 140 v/v at 280 K and 8.76 MPa for carbon materials [30]. Larger values were reported for mesoporous activated carbons (up to 248 v/v) at 275 K and 8 MPa [38]. Celzard et al. reported a similar improvement in the methane storage capacity, in volumetric basis, for coconut shell-derived microporous activated carbons [28]. The incorporation of water improved the storage capacity at 8 MPa and 275 K from 160 v/v in the dry carbon up to 230 v/v. These results clearly anticipate the potential of natural gas hydrates (NHG) confined in carbon materials as a future alternative for high-pressure methane storage.

One of the open questions in this specific topic concerns the crystal structure of the confined hydrates. As described above, the nucleation and growth process in micropores is still a matter of debate since there are no experimental evidences about the nature of the potential hydrate grown under these steric constrictions (crystal size in micropores would be too small to be evaluated with conventional techniques). However, the crystal structure of the methane hydrates confined in larger cavities has been evaluated using synchrotron X-ray diffraction measurements [29, 31]. These studies have shown that hydrate crystals in carbon materials with a wide pore size distribution exhibit a sI crystal structure with an average crystal size around 10–50 nm, thus corresponding to hydrate grown in mesocavities. The

presence of the sI structure has been confirmed using inelastic neutron scattering experiments [29]. These experiments show the rotation of the trapped methane molecules as a free rotor at low energy transfer,  $E = \pm 0.99$  meV ( $7.98$  cm<sup>-1</sup>),  $E_1 = 2.3$  meV ( $18.54$  cm<sup>-1</sup>), and  $E_2 = 3.3$  meV ( $26.61$  cm<sup>-1</sup>). Interestingly, these inelastic rotational lines perfectly fit with those found in natural methane hydrates from the Pacific seafloor [39].

Although the main interest in gas storage through hydrate formation involves methane, there are few studies in the literature dealing with gas hydrates confined in carbon materials containing other molecules, for instance, CO<sub>2</sub> or H<sub>2</sub> [40–42]. Compared to methane, CO<sub>2</sub> hydrate formation takes place at a lower threshold pressure (ca. 1.5 MPa) due to the higher thermodynamic stability, activated carbon promoting the water-to-hydrate yield, and the formation kinetics in a similar manner to experiments performed with methane. Sun et al. reported a lower H<sub>2</sub>O/CO<sub>2</sub> molar ratio than theoretical due to the high solubility of CO<sub>2</sub> in water, in addition to the CO<sub>2</sub> trapped in the form of hydrate [41]. At this point it is important to highlight that the possibility to choose the guest molecule within the hydrate structure opens the gate toward the in situ replacement of CH<sub>4</sub> by CO<sub>2</sub>. This technology has been successfully applied for bulk systems and deep-sea water sediments so that CO<sub>2</sub> can be stabilized in natural hydrates for long-term storage while recovering the methane as a fuel [43, 44]. Although the replacement of CH<sub>4</sub> by CO<sub>2</sub> is thermodynamically favorable, the extent of the reaction (extremely slow kinetics have been reported so far for bulk systems) and its efficiency in real systems are not easy due to multiple factors and coexisting processes (e.g., pressure- and temperature-dependent solubility, interfacial properties, etc.) [43]. Recent studies from Casco et al. have shown that the in situ replacement of CH<sub>4</sub> by CO<sub>2</sub> can be done relatively fast (within minutes) in gas hydrates confined in activated carbons [40]. As it can be observed in Fig. 14.5, methane hydrates confined in high-surface area carbon materials are stable up to 263 K under a CO<sub>2</sub> pressure of 1 MPa. Despite the presence of a given CO<sub>2</sub> pressure, CO<sub>2</sub> molecules are not able to replace methane under these conditions. Confined hydrates lose the trapped methane at 267 K changing immediately to a hexagonal ice structure. However, a subsequent increase in the CO<sub>2</sub> pressure up to 1.5 MPa (lower panel) promotes the incorporation of CO<sub>2</sub> in the ice network, CO<sub>2</sub> hydrate being formed within minutes. It is important to highlight that these hydrates are fully reversible, i.e., methane and CO<sub>2</sub> can be replaced upon request and during several cycles with complete reversibility. These results open the gate toward the application of confined gas hydrates in transportation units where methane can be delivered as a fuel, the CO<sub>2</sub> produced during its combustion being trapped in the same crystals.

Concerning hydrogen confined hydrates, the number of studies described in the literature is rather limited [42]. Saha et al. reported an enhanced hydrogen storage capacity in ordered mesoporous carbon materials through clathrate formation in the presence of H<sub>2</sub>O/THF mixtures. At 270 K and 16.3 MPa, the total amount of hydrogen adsorbed was enhanced from 0.58 wt.% in the dry carbon up to 0.78 wt.% in wet conditions [42]. However, these pressures are still too large for a potential application of hydrogen storage through hydrates.

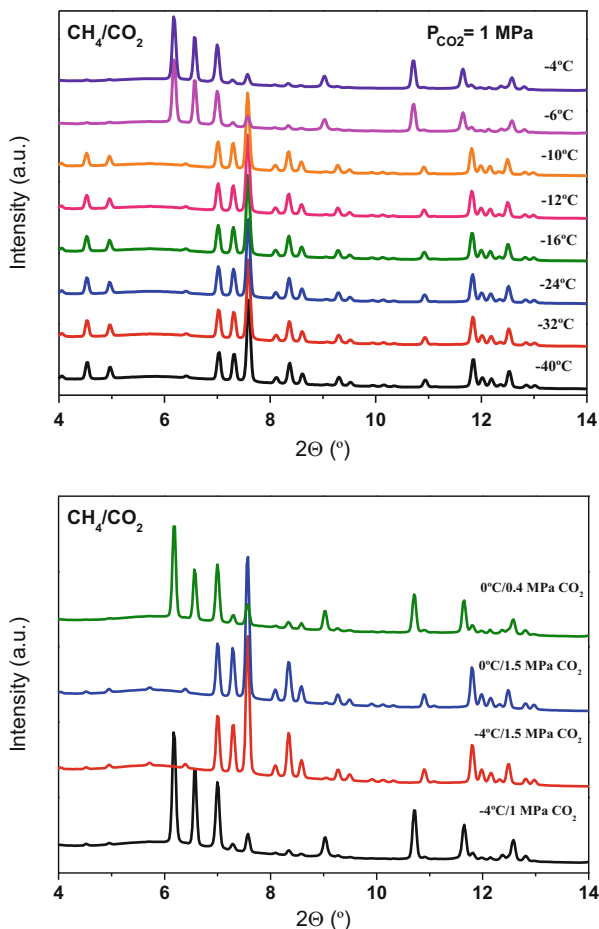


**Fig. 14.5** (Upper panel) Synchrotron X-ray diffraction pattern of the methane hydrate at temperatures from 233 K up to 269 K under a CO<sub>2</sub> pressure of 1 MPa; (lower panel) synchrotron X-ray diffraction pattern of the last sample in upper figure (sample at 269 K and 1 MPa) after an initial pressurization with CO<sub>2</sub> up to 1.5 MPa followed by a decrease in temperature to 273 K and a further decrease in pressure to 0.4 MPa (Reproduced from Ref. [40] by permission of John Wiley & Sons Ltd)

## 14.4 Gas Hydrates in Metal-Organic Frameworks (MOFs)

Although metal-organic framework materials have been widely applied in gas adsorption and storage processes with excellent results, as described in previous chapters, their application as a host structure to promote nucleation and growth of gas hydrates is rather scarce. The low number of studies dealing with the application of MOFs for gas hydrate must be attributed to (1) the poor structural stability of a number of MOFs in the presence of humidity; (2) the hydrophilic nature of a

number of MOFs, thus limiting the amount of water prone to form hydrate; and (3) the presence of preferentially microporous and/or small mesoporous cavities in the majority of conventional MOFs, thus limiting the growth of large hydrate crystals. Taking into account that the methane hydrate unit cell is 1.2 nm, a great number of MOFs will not allow more than 1–2 confined unit cells with the limited storage capacity. Compared to actual values of high-pressure methane storage capacity in dry conditions (e.g., MOF-905 reaches 240 v/v at 8 MPa [45], HKUST-1 in monolithic form reaches 263 v/v at 6.5 MPa [46] or 270 v/v in powder form [47], among others), it is quite easy to believe that actual MOFs will not be able to overpass these excellent values through the hydrate formation route. Despite these drawbacks, there have been some attempts in the literature trying to use MOFs as a host structure for methane hydrates. For instance, Kim et al. evaluated the methane hydrate formation in MIL-53 saturated with water [48]. Using high-resolution powder diffraction, the authors identified the formation of methane hydrate with a *sI* structure. However, these hydrate crystals were grown preferentially in meso/macropores in the interparticle space rather than in the inner micropores of the MOF due to their small size (MIL-53 has pores around 0.6 nm in size). The phase equilibrium in MIL-53 confined hydrates ( $\text{CH}_4$  and  $\text{CO}_2$ ) exhibits an important thermodynamic inhibition compared to the bulk hydrates due to the lower activity of water in smaller interparticle cavities. Mu et al. performed similar high-pressure methane adsorption experiments in hydrophobic ZIF-8 using different water contents [49]. Under wet conditions ZIF-8 was able to improve the methane adsorption capacity from 5.9 mmol/g up to 9.3 mmol/g at 276.85 K and 2.85 MPa. Unfortunately, the methane hydrates grown in the presence of ZIF-8 were not confined within the microporous network but rather in the interparticle space [50]. Casco et al. compared the ability of a hydrophilic (MIL-100) and a hydrophobic (ZIF-8) MOFs toward the methane hydrate formation in wet conditions at 275 K and up to 10 MPa [50]. As it can be observed in Fig. 14.6, in a hydrophilic environment such as MIL-100 (Fe), the presence of preferential water-framework interactions inhibits the hydrate formation process in the intrinsic porosity of the metal-organic framework. The high-pressure adsorption capacity of the wet sample is quite poor compared to the dry sample due to the preferential blocking of the porosity by water. Interestingly, the scenario changes completely for a hydrophobic network such as ZIF-8. As it can be appreciated in Fig. 14.6, the wet samples exhibit a similar adsorption profile to the dry MOF up to 3–4 MPa, the adsorption performance changing drastically afterward. Above this threshold pressure, there is a sudden jump in the adsorption capacity that correlates with the amount of water incorporated. These results confirm the preferential hydrate formation in the interparticle space, while the intrinsic microporosity (non-wettable) only participates in the adsorption process through pure physisorption (physisorption taking place below 3 MPa).

In summary, gas hydrate studies using metal-organic frameworks as a host structure clearly anticipate the complexity of the gas hydrate nucleation and growth process in these materials. Actual data clearly show that hydrophobic surfaces are prone to promote the formation process with a high yield although it is necessary to develop MOFs able to accommodate water inside their intrinsic cavities despite

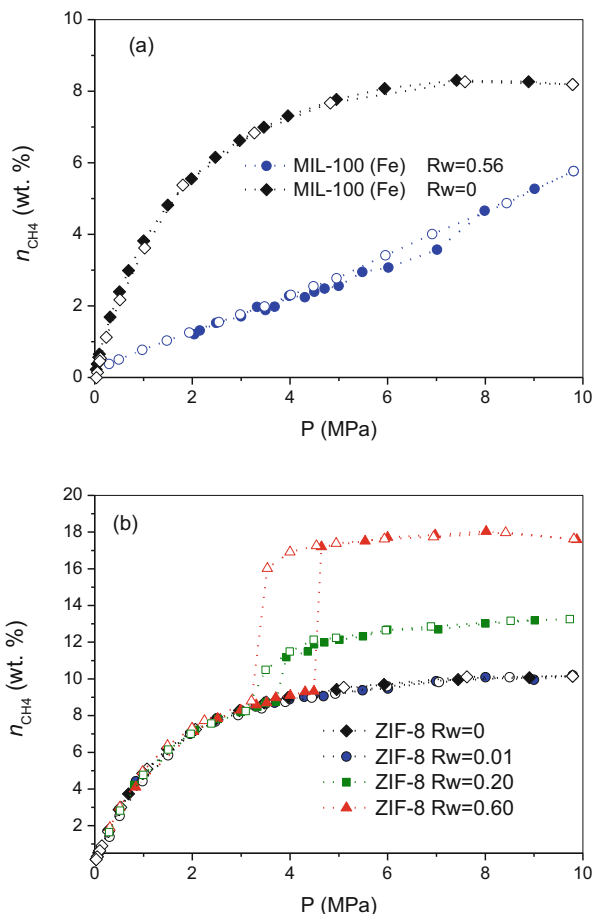


**Fig. 14.6** High-pressure methane adsorption/desorption isotherms at 275 K and up to 10 MPa for (a) MIL-100 (Fe) and (b) ZIF-8 before and after pre-humidification with different water contents ( $R_w$  is amount of water g/g) (Reprinted with permission from [50])

their hydrophobic nature. Last but not least, it is important to highlight that even under these conditions, it is not easy to anticipate a priori if these MOF-confined hydrates will be able to overpass the excellent performance of the dry materials.

## 14.5 Gas Hydrates in Zeolites and Other Adsorbents

In a similar manner to MOFs, the number of studies in the literature dealing with gas hydrate formation in zeolites is very limited. To our knowledge there is only one study from Kim et al. about the role of synthetic and natural zeolites (5A and 13X) in the methane hydrate formation process [51]. In the presence of a

zeolite suspension lower than 0.01 wt.%, zeolite 13X gives rise to a 5.1 times increase in the methane consumption compared to distilled water. Higher zeolite concentrations became detrimental due to the rapid formation of methane hydrate at the interfacial area between methane gas and distilled water. Unfortunately, there are no experimental evidences about the location of these hydrate crystals, but, based on the purely microporous network of these zeolites (pore cavity in zeolite 13X is around 0.73 nm), it is easy to anticipate that hydrate formation would take place in the interparticle space rather than in the inner porous structure. Surprisingly, phase equilibrium data show a thermodynamic promotion of the methane hydrate formation in the presence of the zeolites, a behavior that is completely opposed to the observations with carbon materials.

Contrary to zeolites, the number of studies dealing with gas hydrate formation in clays is large, most probably associated with the necessity to understand methane hydrates grown in natural sediments. Swelling clays such as montmorillonite have been described in the literature as a host structure to promote methane hydrate formation in the interlamellar space. Guggenheim et al. observed an increased  $d$  value (interlayer space) of pre-humidified montmorillonite from  $\cong 0.98$  nm (for a 2:1 silicate layer) to 2.2 nm upon pressurization at 4.1 MPa [52]. This result was attributed to the formation of methane hydrate crystals intercalated between 2:1 layers. These observations were supported by molecular dynamic (MD) simulations [53]. MD simulations predict a certain disordering in the hydrate clusters intercalated in the montmorillonite with three different configurations for methane: (1) coordinated by water within a quasi-stable methane hydrate cluster, (2) coordinated to the siloxane surface of the clay and the water associated with the methane hydrate cluster, and (3) coordinated by water after diffusing from the methane hydrate cluster. An expansion of the basal spacing from 1.538 nm up to 1.606 nm was also reported for smectite clays upon pressurization with methane [54]. Molecular dynamic simulations suggested that methane molecules in the hydrate-like structure are solvated by nearly 12–13 water molecules and coordinated with 5–6 tetrahedral oxygen atoms from the clay surface in the interlayer of the simulated smectites [55]. Phase equilibrium showed a slight promotion of the clay in the methane hydrate formation, in close agreement with previous data in zeolites. At this point it is important to highlight that these observations in hydrophilic materials are completely opposed to the inhibition observed for hydrophobic carbons, i.e., water activity depends on the nature of the nanoporous material, in close agreement with Eq. 14.1 [17]. Further studies in swelled clays reported that phase equilibria of gas hydrates in clay sediments are largely dependent on the morphological characteristics of the clay, such as pore size and water content [56].

The most widely evaluated oxide for confined methane hydrates is without doubts silica and silica-based materials. The large interest for silica is due to the necessity to understand the mechanism of gas hydrate formation and dissociation in the Earth's porous media and the subsequent recovery of methane. There are a number of studies in the literature dealing with porous silica and silica sand that report a large water-to-hydrate conversion in the presence of the inorganic media. For instance, Linga et al. reported water-to-hydrate values above 70% (even up to

94.7%) at 8.0 MPa and temperatures around 274–277 K for water-saturated silica sands [57, 58]. The water-to-hydrate yield achieved in the presence of the silica sand was larger than the one achieved under conventional stirring conditions, thus confirming the promoting effect of the silica surface [58]. The enhanced hydrate formation in the presence of the silica sand has been attributed to the presence of multiple nucleation events, as suggested by temperature profiles, thus avoiding costly mechanical agitation [58–60].

The role of silica in the methane hydrate formation process highly depends on the size of the intrinsic cavities and, indirectly, on the decreased capillary-pressure-induced water activity (an excellent description of the thermodynamics in confined nanospace can be found elsewhere [61]). Uchida et al. evaluated different porous glasses with pores between 10 and 50 nm and observed that the temperature shift for methane hydrate dissociation was proportional to the decrease in the pore diameter [62]. This result was consistent with the depressed melting point of ice when confined in small pores [18]. The calculated density for the hydrate formed in the porosity of porous glasses was  $914 \text{ Kg/m}^3$ , and the latent heat of dissociation for confined hydrates was reported as  $45.92 \text{ kJ/mol}$  (slightly smaller than bulk hydrates) [62]. A widening of the pore size range evaluated for porous glasses from 4 nm up to 10 nm confirm the instability of methane hydrates confined in cavities [63]. At a fixed temperature, the dissociation pressure is higher for smaller pore sizes, whereas, at a fixed pressure, the dissociation temperature is lower for smaller pore sizes. These changes in confined environments are in close agreement with the Gibbs-Thomson equation with the interfacial tensions as the fitting parameter. Similar studies using silica gels with pore radii of 7.5, 5.0 and 3.0 nm confirmed the increased dissociation pressure in pores [64]. Smith et al. suggested that for pores with radii below 4.3 nm and at 263 K, there is a sudden shift in the equilibrium pressure for methane hydrate formation mainly due to the presence of liquid water, while for larger pores the equilibrium pressure resembles that of bulk due to the presence of ice, i.e., zero surface tension between hydrate and water ice [64]. Handa et al. evaluated the methane hydrate formation in porous silica gels of 0.7 nm [16]. Experimental results show that the methane hydrate dissociation pressure is higher by 20–100% compared to bulk hydrates (the reduction in the thermodynamic stability compared to the bulk hydrate can be seen in Fig. 14.7). Calorimetric measurements of the dissociation process suggest that after the initial dissociation into ice and gas, the hydrate becomes totally encapsulated between the pore walls and the ice caps formed at the pore opening, so that the trapped hydrate remains stable up to the melting point of the pore ice (about 70% of the pore hydrate remains intact). These observations are similar to those observed for bulk hydrates where self-stabilization was reported after the formation of a shielding layer of ice [65]. The composition of these confined hydrates in silica gel was  $1 \text{ CH}_4 \cdot 5.94 \text{ H}_2\text{O}$ , in close agreement with the sI structure.

One of the open questions when dealing with nanoporous silica as a host structure is the reaction mechanism taking place during the methane hydrate nucleation process. Molecular dynamics (MD) simulations predict that the crystal growth of methane hydrate tends to be away from the hydroxylated silica surface, while

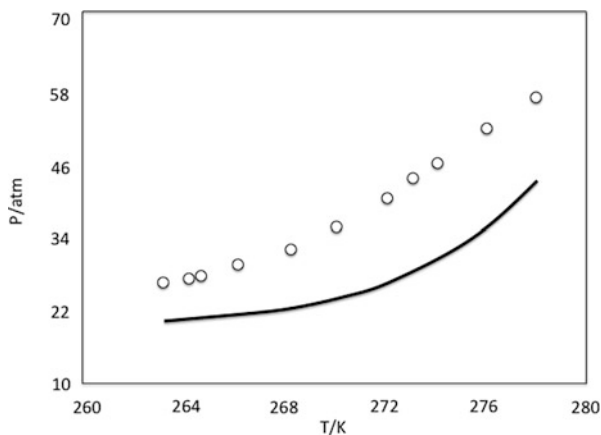


**Fig. 14.7** Equilibrium pressure of methane hydrate in a silica gel with a pore size of 0.7 nm as a function of temperature. Solid line corresponds to the methane hydrate in bulk phase. (Reprinted with permission from [16])

disordered water arrangements are formed in the vicinity of the silica surface with a thickness of about 0.5 nm [66]. This behavior is completely opposed to the mechanism suggested for carbon materials where surface sites act as nucleation centers. However, under appropriate conditions the hydroxylated silica surface can accumulate methane bubbles and serve as a kind of “source” for methane molecules, facilitating crystal growth in the middle of the cavities. The ratio for methane molecules trapped in small and large hydrate cages predicted by MD is close to the ideal value in the sI structure.

In summary, theoretical predictions and experimental evidences clearly show that silica-based materials are excellent host structures to promote the methane hydrate formation and dissociation. Although these two processes are thermodynamically inhibited under confined conditions due to the capillary-induced lower water activity, the incorporation of the nanoporous solid gives rise to increased kinetics and an enhancement of the water-to-hydrate yield. Under these conditions, the high-pressure methane adsorption capacity can reach values as high as 175 v/v at 273.2 K and 8.6 MPa when using dry water [67] and 206 v/v for silica powder at 8.8 MPa and 288 K [68] (in these specific cases, MHs are non-confined since silicas are nonporous).

## References

1. See the DOE MOVE program at <http://arpa-e.energy.gov/?q=arpa-e-programs/move>. Accessed Jan
2. See the DOE program at <https://energy.gov/eere/fuelcells/hydrogen-storage>. Accessed Jan 2018

3. Sloan ED Jr (2003) Fundamental principles and applications of natural gas hydrates. *Nature* 426:353–359
4. Stern LA, Kirby SH, Durham WB (1996) Peculiarities of methane clathrate hydrate formation and solid-state deformation, including possible superheating of water ice. *Science* 273:1843–1848
5. Englezos P, Kalogerakis N, Dholabhai PD, Bishnoi PR (1987) Kinetics of formation of methane and ethane gas hydrates. *Chem Eng Sci* 42:2647–2658
6. Zhong Y, Rogers RE (2000) Surfactant effects on gas hydrate formation. *Chem Eng Sci* 55:4175–4187
7. Zhang JS, Lee S, Lee JW (2007) Kinetics of methane hydrate formation from SDS solution. *Ind Eng Chem* 46:6353–6359
8. Borchardt L, Casco ME, Silvestre-Albero J (2018) Methane hydrate in confined spaces—an alternative energy storage system. *PhysChemPhys* 19(11):1298–1314
9. Mao WL, Mao H-K, Goncharov AF, Struzhkin VV, Guo Q, Hu J, Shu J, Hemley RJ, Somayazulu M, Zhao Y (2002) Hydrogen cluster in clathrate hydrate. *Science* 297:2247–2249 +10
10. Strobel TA, Koh CA, Sloan ED (2007) Hydrogen storage properties of clathrate hydrate materials. *Fluid Phase Equilib* 261:382–389
11. Struzhkin VV, Militzer B, Mao WL, Mao HK, Hemley RJ (2007) Hydrogen storage in molecular clathrates. *Chem Rev* 107:4133–4151
12. Veluswamy HP, Kumar R, Linga P (2014) Hydrogen storage in clathrate hydrates: current state of the art and future directions. *Appl Energy* 122:112–132
13. Mao WL, Mao HK (2004) Hydrogen storage in molecular compounds. *PNAS* 101:708–710
14. Fujimori T, Morelos-Gómez A, Zhu Z, Muramatsu H, Futamura R, Urita K, Terrones M, Hayashi T, Endo M, Hong SY, Choi YC, Tománek D, Kaneko K (2013) Conducting linear chains of Sulphur inside carbon nanotubes. *Nat Commun* 4:2162
15. Urita K, Shiga Y, Fujimori T, Iiyama T, Hattori Y, Kanoh H, Ohba T, Tanaka H, Yudasaka M, Iijima S, Moriguchi I, Okino F, Endo M, Kaneko K (2011) Confinement in carbon nanospace-induced production of KI nanocrystals of high-pressure phase. *J Am Chem Soc* 133:10344–10347
16. Handa YP, Stupin D (1992) Thermodynamic properties and dissociation characteristics of methane and propane hydrates in 70- Å-radius silica gel pores. *J Phys Chem* 96:8599–8603
17. Van der Waals JH, Platteeuw JC (1959) Clathrate solutions. *Adv Chem Phys* (Prigogine Ed) Interscience Publisher Inc 2:1–57
18. Handa YP, Zakrzewski M, Fairbridge C (1992) Effect of restricted geometries on the structure and thermodynamic properties of ice. *J Phys Chem* 96:8594–8599
19. Perrin A, Celzard A, Mareché JF, Furdin G (2003) Methane storage within dry and wet active carbons: a comparative study. *Energy Fuel* 17:1283–1291
20. Miyawaki J, Kanda T, Suzuki T, Okui T, Maeda Y, Kaneko K (1998) Macroscopic evidence of enhanced formation of methane nanohydrates in hydrophobic nanospaces. *J Phys Chem B* 102:2187–2192
21. Rodríguez-Reinoso F, Almansa C, Molina-Sabio M (2005) Contribution to the evaluation of the density of methane adsorbed on activated carbon. *J Phys Chem B* 109:20227–20231
22. Chen XS, McEnaney B, Mays TJ, Alcañiz-Monge J, Cazorla-Amoros D, Linares-Solano A (1997) Theoretical and experimental studies of methane adsorption on microporous carbons. *Carbon* 35:1251–1258
23. García-Blanco AA, Vallone AF, Korili SA, Gil A, Sapag K (2016) A comparative study of several microporous materials to store methane by adsorption. *Microp Mesop Mater* 224:323–331
24. Casco ME, Martínez-Escandell M, Gadea-Ramos E, Kaneko K, Silvestre-Albero J, Rodríguez-Reinoso F (2015) High-pressure methane storage in porous materials: are carbon materials in the pole position? *Chem Mater* 27:959–964
25. Cha SB, Ouar H, Wildeman TR, Sloan ED (1988) A third-surface effect on hydrate formation. *J Phys Chem* 92:6492–6494

26. Smirnov VG, Manakov AY, Ukraintseva EA, Villevald GV, Karpova TD, Dyrdin VV, Lyrshchikov SY, Ismagilov ZR, Terekhova IS, Ogienko AG (2016) Formation and decomposition of methane hydrate in coal. *Fuel* 166:188–195
27. Müller EA, Rull LF, Vega LF, Gubbins KE (1996) Adsorption of water on activated carbons: a molecular simulation study. *J Phys Chem* 100:1189–1196
28. Celzard A, Marêché JF (2006) Optimal wetting of active carbons for methane hydrate formation. *Fuel* 85:957–966
29. Casco ME, Silvestre-Albero J, Ramírez-Cuesta AJ, Rey F, Jordá JL, Bansode A, Urakawa A, Peral I, Martínez-Escandell M, Kaneko K, Rodríguez-Reinoso F (2015) Methane hydrate formation in confined nanospace can surpass nature. *Nat Commun* 6:6432
30. Yan L, Chen G, Pang W, Liu J (2005) Experimental and modeling study on hydrate formation in wet activated carbon. *J Phys Chem B* 109:6025–6030
31. Borchardt L, Nickel W, Casco M, Senkovska I, Bon V, Wallacher D, Grimm N, Krause S, Silvestre-Albero J (2016) Illuminating solid gas storage in confined spaces—methane hydrate formation in porous model carbons. *Phys Chem Chem Phys* 18:20607–20614
32. Siangsai A, Rangsunvigit P, Kitiyanan B, Kulprathipanja S, Linga P (2015) Investigation on the roles of activated carbon particle sizes on methane hydrate formation and dissociation. *Chem Eng Sci* 126:383–389
33. Jin Y, Konno Y, Nagao J (2012) Growth of methane clathrate hydrates in porous media. *Energy Fuels* 26:2242–2247
34. Babu P, Yee D, Linga P, Palmer A, Khoo BC, Tan TS, Rangsunvigit P (2013) Morphology of methane hydrate formation in porous media. *Energy Fuel* 27:3364–3372
35. Jung J-W, Santamaria JC (2012) Hydrate formation and growth in pores. *J Cryst Growth* 345:61–68
36. Skovborg P, Rasmussen P (1994) A mass transport limited model for the growth of methane and ethane gas hydrates. *ChemEngSci* 49:1131–1143
37. Liang M, Chen G, Sun C, Yan L, Liu J, Ma Q (2005) Experimental and modeling study on decomposition kinetics of methane hydrates in different media. *J Phys Chem B* 109:19034–19041
38. Mahboub MJ, Ahmadvpour A, Rashidi H (2012) Improving methane storage on wet activated carbons at various amounts of water. *J Fuel Chem Technol* 40:385–389
39. Gutt C, Asmussen B, Press W, Merkl C, Casalta H, Greinert J, Bohrmann G, Tse JS, Hüller A (1999) Quantum rotations in natural methane-clathrates from the Pacific Sea-floor. *Europhys Lett* 48:269–275
40. Casco ME, Jordá JL, Rey F, Fauth F, Martínez-Escandell M, Rodríguez-Reinoso F, Ramos-Fernández EV, Silvestre-Albero J (2016) High-performance of gas hydrates in confined nanospace for reversible CH<sub>4</sub>/CO<sub>2</sub> storage. *Chem Eur J* 22:10028–10035
41. Sun Y, Wang Y, Zhang Y, Zhou Y, Zhou L (2007) CO<sub>2</sub> sorption in activated carbon in the presence of water. *Chem Phys Lett* 437:14–16
42. Saha D, Deng S (2009) Enhanced hydrogen adsorption in ordered mesoporous carbon through clathrates formation. *Int J Hydr Energy* 34:8583–8588
43. Cha M, Shin K, Lee H, Moudrakovski IL, Ripmeester JA, Seo Y (2015) Kinetics of methane hydrate replacement with carbon dioxide and nitrogen gas mixture using in situ NMR spectroscopy. *Environ Sci Technol* 49:1964–1971
44. Babu P, Yang SHB, Dasgupta S, Linga P (2014) Methane production from natural gas hydrates via carbon dioxide fixation. *Energy Proc* 61:1776–1779
45. Jiang J, Furukawa H, Zhang Y-B, Yaghi OM (2016) High methane storage working capacity in metal-organic frameworks with acrylate links. *J Am Chem Soc* 138:10244–10251
46. Tian T, Zeng Z, Vulpe D, Casco ME, Divitini G, Midgley PA, Silvestre-Albero J, Tan J-C, Moghadam PZ, Fairen-Jimenez D (2018) A sol-gel monolithic metal-organic framework with enhanced methane uptake. *Nat Mater* 17:174–179
47. Peng Y, Krungleviciute V, Eryazici I, Hupp JT, Farha OK, Yildirim T (2013) Methane storage in metal-organic frameworks: current records, surprise findings, and challenges. *J Am Chem Soc* 135:11887–11894

48. Kim D, Ahn Y-H, Lee H (2015) Phase equilibria of CO<sub>2</sub> and CH<sub>4</sub> hydrates in intergranular meso/macro pores of MIL-53 metal organic framework. *J Chem Eng Data* 60:2178–2185
49. Mu L, Liu B, Liu H, Yang Y, Sun C, Chen G (2012) A novel method to improve the gas storage capacity in ZIF-8. *J Mater Chem* 22:12246–12252
50. Casco ME, Rey F, Jordá JL, Rudic S, Fauth F, Martínez-Escandell M, Rodríguez-Reinoso F, Ramos-Fernández EV, Silvestre-Albero J (2016) Paving the way for methane hydrate formation on metal-organic frameworks (MOFs). *Chem Sci* 7:3658–3666
51. Kim N-J, Park S-S, Shin S-W, Hyun J-H, Chun W (2015) An experimental investigation into the effects of zeolites on the formation of methane hydrates. *Int J Energy Res* 39:26–32
52. Guggenheim S, Koster von Groos AF (2003) New gas-hydrate phase: synthesis and stability of clay-methane hydrate intercalate. *Geology* 31:653–656
53. Cygan RT, Guggenheim S, Koster van Groos AF (2004) Molecular models for the intercalation of methane hydrate complexes in montmorillonite clay. *J Phys Chem B* 108:15141–15149
54. Seo Y-J, Seol J, Yeon S-H, Koh D-Y, Cha M, Kang S-P, Seo Y-T, Bahk J-J, Lee J, Lee H (2009) Structural, mineralogical, and rheological properties of methane hydrates in smectite clays. *J Chem Eng Data* 54:1284–1291
55. Zhou Q, Lu X, Liu X, Zhang L, He H, Zhu J, Yuan P (2011) Hydration of methane intercalated in Na-smectites with distinct layer charge: insights from molecular simulations. *J Colloid Interf Sci* 355:237–242
56. Kim D, Ahn Y-H, Kim S-J, Lee JY, Lee J, Seo Y-J, Lee H (2015) Gas hydrate in crystalline-swelled clay: the effect of pore dimension on hydrate formation and phase equilibria. *J Phys Chem C* 119:22148–22153
57. Linga P, Haligva C, Nam SC, Ripmeester JA, Englezos P (2009) Gas hydrate formation in a variable volume bed of silica sand particles. *Energy Fuel* 23:5496–5507
58. Linga P, Daraboina N, Ripmeester JA, Englezos P (2012) Enhanced rate of gas hydrate formation in a fixed bed column filled with sand compared to a stirred vessel. *Chem Eng Sci* 68:617–623
59. Bagherzadeh SA, Moudrakovski IL, Ripmeester JA, Englezos P (2011) Magnetic resonance imaging of gas hydrate formation in a bed of silica sand particles. *Energy Fuel* 25:3083–3092
60. Prasad PSR (2015) Methane hydrate formation and dissociation in the presence of hollow silica. *J Chem Eng Data* 60:304–310
61. Anderson R, Llamedo M, Tohidi B, Burgass RW (2003) Characteristics of clathrate hydrate equilibria in mesopores and interpretation of experimental data. *J Phys Chem B* 107:3500–3506
62. Uchida T, Ebinuma T, Ishizaki T (1999) Dissociation condition measurements of methane hydrate in confined small pores of porous glass. *J Phys Chem B* 103:3659–3662
63. Uchida T, Ebinuma T, Takeya S, Nagao J, Narita H (2002) Effects of pore sizes on dissociation temperatures and pressures of methane, carbon dioxide, and propane hydrates in porous media. *J Phys Chem B* 106:820–826
64. Smith DH, Wilder JW, Seshadri K (2002) Methane hydrate equilibria in silica gels with broad pore-size distributions. *AIChE J* 48:393–400
65. Handa YP (1986) Calorimetric determination of the compositions, enthalpies of dissociation, and heat capacities in the range 85 to 270 K for clathrate hydrates of xenon and krypton. *J Chem Thermod* 18:891–902
66. Liang S, Rozmanov D, Kusalik PG (2011) Crystal growth simulations of methane hydrates in the presence of silica surfaces. *Phys Chem Chem Phys* 13:19856–19864
67. Wang W, Bray CL, Adams DJ, Cooper AI (2008) Methane storage in dry water gas hydrates. *J Am Chem Soc* 130:11608–11609
68. Prasad PSR, Sowjanya Y, Chari VD (2014) Enhancement in methane storage capacity in gas hydrates formed in hollow silica. *J Phys Chem C* 118:7759–7764